Thèse n° 10 249

# III-V Nitride Semiconductors Deposited At Low Temperature For Photovoltaic Applications

Présentée le 16 juin 2023

Faculté des sciences et techniques de l'ingénieur
Laboratoire de photovoltaïque et couches minces électroniques
Programme doctoral en physique

pour l'obtention du grade de Docteur ès Sciences

par

**Jonathan Emanuel THOMET**

Acceptée sur proposition du jury

Prof. R. Houdré, président du jury
Dr A. Hessler-Wyser, Dr N. Würsch, directeurs de thèse
Prof. T. Nelis, rapporteur
Dr G. Christmann, rapporteur
Prof. A. Fontcuberta i Morral, rapporteuse

École polytechnique fédérale de Lausanne

2023

Si tu peux voir détruit l'ouvrage de ta vie Et sans dire un seul mot te mettre à rebâtir,
Ou perdre en un seul coup le gain de cent parties Sans un geste et sans un soupir;

Si tu peux être amant sans être fou d'amour, Si tu peux être fort sans cesser d'être tendre,
Et, te sentant haï, sans haïr à ton tour, Pourtant lutter et te défendre;

Si tu peux supporter d'entendre tes paroles Travesties par des gueux pour exciter des sots,
Et d'entendre mentir sur toi leurs bouches folles Sans mentir toi-même d'un mot;

Si tu peux rester digne en étant populaire, Si tu peux rester peuple en conseillant les rois,
Et si tu peux aimer tous tes amis en frères, Sans qu'aucun d'eux soit tout pour toi;

Si tu sais méditer, observer et connaître, Sans jamais devenir sceptique ou destructeur;
Rêver, mais sans laisser ton rêve être ton maître, Penser sans n'être que penseur;

Si tu sais être dur, sans jamais être en rage, Si tu sais être brave et jamais imprudent,
Si tu sais être bon, si tu sais être sage, Sans être moral et pédant;

Si tu peux rencontrer Triomphe après Défaite Et recevoir ces deux menteurs d'un même front,
Si tu peux conserver ton courage et ta tête Quand tous les autres les perdront,

Alors les Rois les Dieux la Chance et la Victoire
Seront à tout jamais tes esclaves soumis,
Et, ce qui vaut bien mieux que les Rois et la Gloire,

Tu seras un homme mon fils!

— *Rudyard Kipling (1910), traduit par André Maurois (1918)*

À mon Père éternel,
À son Fils victorieux,
À son Esprit vivifiant.

# Acknowledgements

Ce manuscrit est le fruit de quatre années de travaux réalisés au laboratoire de photovoltaïque et couches minces électroniques (PV-lab) de Microcity à Neuchâtel, une antenne de l'École Polytechnique Fédérale de Lausanne. Elles ont été partiellement financées par la bourse n° 200021_182171 "SALTO" du Fond National Suisse, et partiellement par le fond iPrecise de l'OFEN.

Je suis dans la reconnaissance pour ces quatre années de ma vie passées à PV-lab. Quelle chouette aventure!

Je souhaite tout d'abord remercier Christophe Ballif, professeur à l'EPFL et directeur du PV-lab, pour la possibilité qu'il m'a donnée de travailler dans son laboratoire. Je remercie également grandement Aïcha Hessler-Wyser et Nicolas Wyrsch, ma directrice et mon co-directeur de thèse, pour le soin qu'ils ont pris à me guider au cours de ces quatre années. Merci également à Mathieu Boccard et à Franz-Josef Haug pour les conseils et discussions hebdomadaires qui m'ont permis de faire des pas de géants. Merci aussi à Anna Fontcuberta i Morral, à Gabriel Christmann et à Thomas Nelis d'avoir accepté d'être expert-rapporteurs de cette thèse.

Merci à tous les acteurs externes de qui j'ai pu profiter pour approfondir ma connaissance et mon experience: Abdelhak Bensaoula et son équipe de TofWerk pour l'étude TOFMS, Olha Sereda et son équipe au CSEM pour les mesures XRD, Marco Cantoni et son équipe pour leur mise à disposition de différents microscopes électroniques à l'EPFL, Michel Stchakovsky et son équipe pour leur approfondissement de l'ellipsométrie à Horibas Paris, et finalement à l'équipe de crystallographie d'EMPA Dübendorf pour leur excellent cours sur la XRD.

Un grand merci à toutes les personnes que j'ai rencontrées dans mon errance scientifique, et qui m'ont aidé à faire un pas de plus. En tout premier l'équipe technique sans laquelle PV-lab ne serait pas ce qu'il est aujourd'hui et sans laquelle cette thèse perdrait bien des plumes: Cédric Bucher, Aymeric Schafflützel, Nicolas Fürst, Sylvain Dunand et les deux Joël (Spitznagel et Currit). Merci à Karine Frossard pour les soins qu'elle a pour ce laboratoire et l'énorme boulot administratif qu'elle abat. Merci à feu l'équipe hétéro-jonctions pour leur accueil et leur patience avec le petit débutant que j'étais: Luca Antognini, Jean Cattin, Angela Fioretti, Vincent Paratte, Jan Haschke. Merci à l'actuelle équipe haute température de m'avoir si bien intégré malgré l'écart qui nous séparait: Ezgi Genç et Audrey Morisset. Merci également à Caroline Hain à la BFH de Bienne pour ses excellentes discussions et sa rigueur scientifique.

Merci encore à toutes celles et ceux qui ont versé une partie de leur sueur, de leur sang et de leur temps dans cette thèse: Julie Dréon, Julien Hurni, Aman Singh, Sofia Libraro, Nils Toggwyler, Mélanie Rouèche et Antoine Devincenti. Sans vous également, ce document aurait bien moins de pages.

Merci encore à mon fidèle collègue de bureau, Daniel Jacobs, pour sa patience malgré mes écouteurs toujours réglés au max. Merci également à Noémie Jeannin pour les moments jeux vidéos, et à Janina Löffler pour l'introduction au yoga qui ne m'a jamais vraiment plu en fait! Merci à mes parents pour leur soutien inconditionnel malgré leurs quelques lacunes dans le domaine photovoltaïque, et merci surtout à ma femme, Yasmine, qui a su rester forte et porter notre petite tribu alors que j'étais bien trop occupé à rédiger.

Et un merci tout particulier à Samira Frey d'avoir été mon amie durant ces quatre années (et pour la suite de nos vies j'espère!). Pour les cheveux tirés sur les AMCPs, pour les cafés en guise de petits-déjeuners, pour les jeux vidéos, pour les memes et les soirées un peu trop arrosées, pour les cours de français et d'allemand, et pour les discussions profondes. Le temps aurait vraiment été long sans toi, je te souhaite bonne chance pour la suite.

*Neuchâtel, 26 janvier 2022* Jonathan Emanuel Thomet

# Abstract

This thesis reports on the study of low temperature and low-cost approaches for depositing indium gallium nitride (InGaN) thin films for photovoltaic (PV) applications. A particular focus is put on plasma-enhanced vapour deposition and co-sputtering as two potentially viable options to alleviate the drawbacks of conventional methods for InGaN deposition, primarily related to silicon wafer degradation at elevated temperatures, high fabrication costs, and phase separation. Our ultimate aim was to assess the suitability of layers prepared using simplified methods for integration as either the absorber or as contacts of a Si-solar cell.

Concerning plasma-enhanced chemical vapor deposition (PECVD), a detailed study of the effect of growth parameters on layer quality and optoelectronic properties is presented. In particular, lowering the growth rate generally improves the main quality metrics of Urbach energy $E_U$, crystallite size, and resistivity. It is also demonstrated that the InGaN bandgap (BG) follows the quadratic Vegard's law with respect to indium content $X_{\mathrm{In}}$, but that the bowing of said law is influenced by the growth rate as well. Using a time-of-flight mass spectrometer (TOF-MS) allowed for a deeper analysis of plasma dynamics, revealing the critical importance of different factors leading to deposition of higher quality. In particular, higher-quality layers are achieved by promoting a stronger dissociation, by a more efficient evacuation of the plasma by-products and by starting the plasma before injecting the precursors containing carbon. Combining data from more than 250 depositions, a model of the main quality metrics as a function of all but one deposition parameter (the radio frequency) is presented, allowing identification of the optimal processing conditions. Based on this study, the optimised InGaN PECVD layer does not perform well enough to act as the absorber layer of a PV device. The main shortcomings at this stage are related to poor performance in doping density, optical properties (particularly the Urbach energy) and crystallinity. However, the quality metrics of these layers were good enough to enable possible applications as selective-contact layers for c-Si cells. These possibilities were investigated by fabricating c-Si cells with the PECVD InGaN layers playing different roles (passivating, n-selective or even just as a transition to the metal contact) using flat wafers and different indium contents without doping. A champion cell efficiency of 13 % was achieved using the highest indium content in the InGaN-metal contact configuration. For other structures, it was found that the InGaN layers have low conductivity and poor selectivity, limiting their ability to function as passivating contacts.

The second studied process for low-cost, low-temperature InGaN deposition was physical vapor deposition (PVD) (co-)sputtering. Here an analysis of the deposition parameters revealed a vital role of the pressure on essential layer characteristics. An acceptable electrical

performance with germanium doping is demonstrated, albeit with weak dopant activation and somewhat stronger resistivity with silicon doping but at a lower doping density. Epitaxy of undoped gallium nitride (GaN) on sapphire is demonstrated, but this process is unstable with respect to increasing the silicon doping level. Similarly to PECVD, increasing the indium content of the layer helps to decrease the resistivity, but still to values at least two orders of magnitude greater than the standard (n)a-Si:H layer usually used for contacting absorbers in heterojunction c-Si cells. For reasons similar to those affecting our PECVD films, but in particular, due to a lack of p-doping, it is concluded that the optimised InGaN layer does not perform well enough to act as an absorber but has acceptable characteristics for a contact application. It is also observed that the "barely sufficient" layer properties (be it optical, electrical or structural) do not improve the cell performances compared to state-of-the-art literature values. However, electrical power is also produced by the solar cell under standard test conditions. Again, the main two issues with these contacts are their too-high resistivity (decreasing the open-circuit voltage and worsening the fill factor) and their poor selectivity (decreasing the short-circuit current density, worsening the fill factor and inducing S-shaping of the J-V curve).
Even though the absorber path had to be discarded, **optimisation at all the levels of the InGaN layer (but especially the crystallinity) seems possible. It should lead to better cell performances if more time and research are dedicated to InGaN materials for photovoltaic applications**.

Keywords: InN, GaN, InGaN, indium, gallium, nitride, PECVD, PVD, sputtering, co-sputtering, deposition, photovoltaics, silicon, solar cell, thin films, contact, tandem, absorber, design of experiment, germanium doping, silicon doping, characterisation, electron microscopy, J-V curve, TOFMS, TMG, TMI, ammonia, epitaxy.

# Résumé

Cette thèse porte sur l'étude et l'utilisation de procédés à basse température pour le dépôt de couches minces de composés de nitrure de gallium et d'indium afin de pallier certains des inconvénients actuels de son dépôt sur silicium pour des applications photovoltaïques (principalement la dégradation des substrats de silicium, les coûts de fabrication élevés et la séparation de phase). Le but est d'évaluer s'il est possible de les intégrer soit comme absorbeur soit comme contact d'une cellule solaire.

Le premier des procédés testés est le dépôt chimique en phase vapeur amélioré par plasma (PECVD), avec lequel il est mis en évidence que la diminution du taux de croissance améliore généralement les métriques de qualité des caractéristiques de la couche (énergie d'Urbach $E_U$, taille des cristallites, résistivité). Il est également démontré que la bande interdite de l'InGaN suit la loi quadratique de Vegard par rapport à la teneur en indium $X_{\mathrm{In}}$, mais que l'inflexion de cette loi est également influencée par le taux de croissance. L'utilisation d'un spectromètre de masse à temps de vol a permis une analyse plus approfondie de la dynamique du plasma, et l'importance clé de différents facteurs conduisant à un dépôt de couche de plus haute qualité est présentée. En particulier, une meilleure qualité de couche est obtenue principalement en favorisant une dissociation plus forte, par une évacuation plus efficace des sous-produits du plasma et en démarrant le plasma avant d'injecter les précurseurs contenant du carbone. Finalement, la plupart des différentes caractéristiques et mesures de qualité de la couche sont modélisées en fonction de tous les paramètres de dépôt sauf un (la radiofréquence), ce qui donne des indications sur les conditions de dépôt qui devraient conduire à une couche optimisée. Il est conclu que le dépôt optimisé de couche InGaN par PECVD n'est pas assez performant pour servir d'absorbeur à un dispositif photovoltaïque à ce stade de la recherche. Ceci est dû au dopage p qui n'a pas pu être atteint, et aux propriétés optiques, électriques et de crystallinité qui n'étaient pas assez satisfaisantes. Cependant, les performances étaient suffisamment bonnes pour conserver un certain potentiel pour une application de contact sur des cellules solaires à base de silicium crystallin. Cette voie a donc été suivie et différents types de contacts (passivant, sélectif à électrons ou même simplement comme transition vers le contact métallique) ont été testés avec trois architectures de cellules solaires utilisant des substrats plats et différentes teneurs en indium, sans dopage. Une puissance électrique est extraite et le meilleur rendement de la meilleure cellule atteint à peine 13 %. Ce résultat a été obtenu à la teneur en indium la plus élevée, dans la configuration de contact InGaN-métal. En comparaison, les autres architectures ont prouvé que les couches InGaN ont une résistivité

trop élevée et de mauvaises caractéristiques de sélectivité, ce qui impacte son pouvoir de passivation.
Le second procédé étudié est le dépôt physique en phase vapeur (PVD) par (co-)pulvérisation cathodique, qui met en évidence le fort rôle de la pression sur les caractéristiques de base de la couche. Celle-ci atteint des performances électriques acceptables avec un dopage au germanium mais démontre une faible activation des dopants. Avec un dopage au silicium, les performances électriques sont moindres, mais la teneur en silicium est inférieure à celle du germanium, démontrant une meilleure activation des dopants. L'épitaxie du nitrure de gallium non dopé sur saphir est démontrée mais reste instable avec un niveau de dopage croissant en silicium. De même que pour le PECVD, l'augmentation de la teneur en indium de la couche permet de diminuer la résistivité, mais toujours à des valeurs d'au moins deux ordres de grandeur supérieurs à la couche standard (n)a-Si:H habituellement utilisée pour contacter l'absorbeur. Pour les mêmes raisons que pour le PECVD, mais surtout parce que le dopage p n'a pas pu être réalisé aussi bien, il est conclu que la couche optimisée de InGaN n'est pas assez performante pour servir d'absorbeur, mais présente des caractéristiques acceptables pour une application de contact. Il est également observé qu'en effet, les propriétés de la couche "à peine suffisantes" (qu'elles soient optiques, électriques ou structurelles) n'améliorent pas les performances de la cellule par rapport aux valeurs de l'état de l'art de la littérature. Cependant, une puissance électrique est également produite par la cellule solaire sous des conditions de test standard. Là encore, les deux principaux problèmes liés à ces contacts sont leur résistivité trop élevée (qui diminue le tension de courant ouvert et aggrave le facteur de remplissage) et leur mauvaise sélectivité (qui diminue la densité de courant de court-circuit, aggrave le facteur de remplissage et induit une forme en S de la courbe J-V).
Même si la recherche sur l'absorbeur a dû être écartée, une optimisation à tous les niveaux (mais surtout la cristallinité) de la couche d'InGaN semble possible et devrait conduire à de meilleures performances de la cellule, si plus de temps et de recherche sont consacrés aux matériaux InGaN pour les applications PV.

Mots clés : InN, GaN, InGaN, indium, gallium, nitrure, PECVD, PVD, pulvérisation, co-pulvérisation, dépôt, photovoltaïque, silicium, cellule solaire, films minces, contact, tandem, absorbeur, design d'expérience, dopage au germanium, dopage au silicium, caractérisation, microscopie électronique, courbe J-V, TOFMS, TMG, TMI, ammoniac, épitaxie.

# Contents

**Acknowledgements** **i**

**Abstract** **iii**

**Résumé** **v**

**Contents** **vii**

**List of figures** **xi**

**List of tables** **xv**

**List of acronyms** **xvii**

**1 Introduction** **1**

**2 Solar cell state of the art** **5**
2.1 Solar cell operation . . . . . 5
2.1.1 The p-n junction . . . . . 5
2.1.2 The solar cell . . . . . 8
2.1.3 The losses . . . . . 9
2.2 Physical properties of InN, GaN and InGaN . . . . . 12
2.3 Solar cell integration . . . . . 17
2.3.1 Is In/GaN a good candidate for solar cell integration? . . . . . 17
2.3.2 Reaching a competitive solar cell price . . . . . 18
2.3.3 In/GaN challenges . . . . . 18
2.4 Research questions . . . . . 19

**3 Experimental methods** **23**
3.1 Film fabrication . . . . . 23
3.1.1 PECVD processes . . . . . 23
3.1.2 PVD processes . . . . . 26
3.2 Means of characterization . . . . . 28
3.2.1 Plasma diagnostics: time-of-flight mass spectrometry . . . . . 28
3.2.2 Photon-matter interactions . . . . . 30
3.2.3 Electron microscopy and related tools of characterizations . . . . . 45

3.2.4 Electrical characterizations . . . . . 50
3.2.5 Other means of characterization: profilometry . . . . . 55
3.3 Design of Experiment . . . . . 55
3.3.1 Operation . . . . . 55
3.3.2 Result quality analysis . . . . . 59

**4 InGaN by PECVD 67**
4.1 GaN & InN: influence of the deposition parameters . . . . . 67
4.2 InGaN: influence of the deposition parameters . . . . . 70
4.2.1 Nitrogen source: $N_2$ . . . . . 71
4.2.2 Nitrogen source: $NH_3$ . . . . . 76
4.2.3 InGaN PECVD: key take aways & next steps . . . . . 79
4.3 Time-of-flight mass spectrometer . . . . . 80
4.3.1 Motivation & procedure . . . . . 80
4.3.2 Ammonia synthesis and dissociation . . . . . 80
4.3.3 DOE: frequency, power, pressure . . . . . 83
4.3.4 TOF-MS and layer characteristics . . . . . 85
4.3.5 InGaN PECVD, TOFMS: key takeaways & next steps . . . . . 102
4.4 Design of experiment with all the PECVD layers . . . . . 104
4.4.1 Motivation . . . . . 104
4.4.2 Procedure . . . . . 104
4.4.3 Thickness . . . . . 106
4.4.4 Optical bandgap . . . . . 116
4.4.5 Unstrained XRD crystallite size . . . . . 125
4.4.6 InGaN Urbach energy . . . . . 129
4.4.7 Indium content . . . . . 131
4.4.8 InGaN PECVD DOE: key takeaways & next steps . . . . . 134
4.5 PECVD results: wrap-up & conclusions . . . . . 138

**5 InGaN by PVD 141**
5.1 Sputtered GaN layer characteristics . . . . . 141
5.1.1 Optical properties . . . . . 142
5.1.2 Growth rate . . . . . 142
5.1.3 Structural properties – XRD . . . . . 144
5.1.4 Structural properties – SEM & TEM . . . . . 146
5.1.5 Link with Thornton Diagram . . . . . 151
5.1.6 Sputtered GaN: key takeaways & next steps . . . . . 153
5.2 Effect of the germanium doping on the GaN layer characteristics . . . . . 153
5.2.1 Growth rate and thickness . . . . . 154
5.2.2 Optical properties . . . . . 155
5.2.3 Structural properties . . . . . 156
5.2.4 Electrical properties . . . . . 156
5.2.5 Germanium doping: key takeaways & next steps . . . . . 158

5.3 Effect of the silicon doping on the GaN layer characteristics . . . . . 160
5.3.1 Silicon content influence . . . . . 160
5.3.2 Substrate temperature influence . . . . . 164
5.3.3 Annealing temperature influence . . . . . 166
5.3.4 Silicon doping: key takeaways & next steps . . . . . 169
5.4 Effect of the silicon doping on the GaN epitaxy on sapphire . . . . . 169
5.4.1 Motivation . . . . . 169
5.4.2 Basic characteristics . . . . . 170
5.4.3 TEM study . . . . . 173
5.4.4 TKD study . . . . . 176
5.4.5 GaN epitaxy on sapphire: key takeaways . . . . . 179
5.5 Effects of the indium content on the layer characteristics . . . . . 179
5.5.1 Motivation . . . . . 179
5.5.2 Single InGaN target . . . . . 180
5.5.3 Co-sputtering . . . . . 181
5.5.4 PVD InGaN: key takeaways & next steps . . . . . 184
5.6 PVD results: Wrap-up and conclusions . . . . . 185

**6 InGaN contacts 187**
6.1 In/GaN contacts by PECVD . . . . . 188
6.1.1 Setup of the experiment . . . . . 188
6.1.2 Results . . . . . 191
6.1.3 In/GaN PECVD contact: key takeaways & next steps . . . . . 194
6.2 Doped GaN contacts by PVD . . . . . 194
6.2.1 Doped with germanium . . . . . 195
6.2.2 Doped with silicon . . . . . 199
6.3 InGaN contacts by PVD . . . . . 210
6.3.1 Introduction . . . . . 210
6.3.2 Architectures . . . . . 210
6.3.3 Results . . . . . 212
6.3.4 InGaN PVD contact: key takeaways & next steps . . . . . 214
6.4 Contacts: wrap-up and conclusions . . . . . 215

**7 Conclusion 217**

**A Further theoretical development 221**
A.1 Raman: other parasitic vibrational modes . . . . . 221
A.2 Ellipsometry: from Fresnel coefficients to the complex index of refraction . . . 221
A.3 XRD: other powerful tools . . . . . 225
A.3.1 The Williamson-Hall plot . . . . . 225
A.3.2 The Young's modulus . . . . . 226
A.3.3 The rocking curve . . . . . 228
A.4 Design of experiment deepening . . . . . 228

A.4.1 Designs . . . . . 228
A.4.2 Cook's distance . . . . . 234

**B Deeper analysis of some results 235**
B.1 More details on the influence of deposition parameters on the InGaN layers deposited by PECVD . . . . . 235
B.1.1 Plasma dynamics . . . . . 235
B.1.2 Substrates and data extraction . . . . . 236
B.1.3 ANOVA tables of the different InN DOEs . . . . . 237
B.1.4 3D view of the fit . . . . . 238
B.2 Details of the InGaN PECVD DOEs . . . . . 238
B.2.1 Thickness . . . . . 239
B.2.2 Optical bandgap . . . . . 245
B.2.3 Unstrained XRD grain size . . . . . 250
B.2.4 InGaN Urbach energy . . . . . 253
B.2.5 Indium content . . . . . 255
B.3 GaN by PVD: lost figures . . . . . 256
B.3.1 Effects of deposition parameters – Pressure on structural properties . . . 256
B.3.2 Effect of germanium doping – optical properties . . . . . 256
B.3.3 Effect of germanium doping – electrical properties . . . . . 257
B.3.4 Dark fields of a GaN/Sa PVD epitaxial layer . . . . . 257
B.4 InGaN contacts by PVD, J-V curves . . . . . 259

**C Other noteworthy results 269**
C.1 A-Si:H contacts . . . . . 269
C.1.1 A-Si:H at 400 °: optimization . . . . . 269
C.1.2 Passivation & lifetime . . . . . 272
C.1.3 A-Si:H contacts: key takeaways & next steps . . . . . 274

**Bibliography 275**

**Curriculum Vitae 293**

# List of Figures


1.1 Introduction: PV module cost evolution . . . . . 2
1.2 Introduction: solar cell evolution, from PERC to tandem . . . . . 3

2.1 Solar cell state of the art, operation . . . . . 6
2.2 Solar cell state of the art, operation: visualisation of some loss types . . . . . 13
2.3 Solar cell state of the art, InN and GaN physical properties: crystal . . . . . 15
2.4 Solar cell state of the art, InN and GaN physical properties: bandgap . . . . . 16

3.1 Experimental methods, film fabrication: schematic of the System B . . . . . 26
3.2 Experimental methods, film fabrication: schematic of the Univex . . . . . 29
3.3 Experimental methods, plasma diagnostics: peak integration . . . . . 31
3.4 Experimental methods, Raman: vibrational modes of wurtzite In/GaN bulk. . . 34
3.5 Experimental methods, ellipsometry: a modelled stack of layers . . . . . 37
3.6 Experimental methods, spectroscopy: tool and measurement method. . . . . 39
3.7 Experimental methods, XRD: Bragg's law for X-ray diffraction use . . . . . 43
3.8 Experimental methods, electron microscopy: interactions . . . . . 45
3.9 Experimental methods, electron microscopy: configurations . . . . . 47
3.10 Experimental methods, Hall: measurement setup . . . . . 52
3.11 Experimental methods, DOE: useful analysis tools . . . . . 61
3.12 Experimental methods, DOE: two ANOVA elements . . . . . 64
3.13 Experimental methods, DOE: degrees of freedom distribution . . . . . 66

4.1 GaN PECVD, deposition parameters: temperature, TMG, $N_2$ and $H_2$ . . . . . 68
4.2 In/GaN PECVD, deposition parameters: InN XRD . . . . . 70
4.3 In/GaN PECVD, deposition parameters: XRD & spectro vs $X_{\mathrm{In}}$ . . . . . 72
4.4 In/GaN PECVD, deposition parameters: indium content determination . . . . . 73
4.5 In/GaN PECVD, deposition parameters: $E_{04}^{\mathrm{InGaN}}$ vs $X_{\mathrm{In}}$ . . . . . 74
4.6 In/GaN PECVD, deposition parameters: Urbach energy and parameter space . 76
4.7 In/GaN PECVD, deposition parameters: TEM InN and GaN . . . . . 78
4.8 In/GaN PECVD, deposition parameters: XRD & spectro, $N_2$ vs $NH_3$ . . . . . 78
4.9 In/GaN PECVD, TOFMS: $NH_3$ synthesis . . . . . 81
4.10 In/GaN PECVD, TOFMS: $N_2$ synthesis . . . . . 82
4.11 In/GaN PECVD, TOFMS: plasma flicker . . . . . 87
4.12 In/GaN PECVD, TOFMS: InGaN and GaN absorption coefficient . . . . . 88

4.13 In/GaN PECVD, TOFMS: GaN layer SEM & TEM . . . . . 89
4.14 In/GaN PECVD, TOFMS: InN layers, basic characteristics . . . . . 90
4.15 In/GaN PECVD, TOFMS: InN layer, SEM & TEM . . . . . 92
4.16 In/GaN PECVD, TOFMS: peak evolution over time, InN . . . . . 93
4.17 In/GaN PECVD, TOFMS: InN SEM topview . . . . . 95
4.18 In/GaN PECVD, TOFMS: InGaN layers by XRD . . . . . 96
4.19 In/GaN PECVD, TOFMS: InGaN SEM & TEM . . . . . 97
4.20 In/GaN PECVD, TOFMS: crystallite size distribution . . . . . 98
4.21 In/GaN PECVD, TOFMS: TMB dissociation . . . . . 99
4.22 In/GaN PECVD, TOFMS: B-doped GaN $P_{41}$ . . . . . 100
4.23 In/GaN PECVD, TOFMS: $SiH_4$ dissociation . . . . . 101
4.24 In/GaN PECVD, DOE: GaN thickness model, quality analysis . . . . . 109
4.25 In/GaN PECVD, DOE: InN thickness model, quality analysis . . . . . 112
4.26 In/GaN PECVD, DOE: InGaN thickness models, quality analysis . . . . . 115
4.27 In/GaN PECVD, DOE: GaN optical bandgap model, quality analysis . . . . . 118
4.28 In/GaN PECVD, DOE: InN optical bandgap models, quality analysis . . . . . 121
4.29 In/GaN PECVD, DOE: InGaN optical bandgap models, quality analysis . . . . . 124
4.30 In/GaN PECVD, DOE: InN crystallite size model, quality analysis . . . . . 127
4.31 In/GaN PECVD, DOE: InGaN crystallite size model, quality analysis . . . . . 129
4.32 In/GaN PECVD, DOE: InGaN Urbach energy model, quality analysis . . . . . 131
4.33 In/GaN PECVD, DOE: indium content model, quality analysis . . . . . 134

5.1 PVD GaN, characteristics: optical properties vs temperature & thickness . . . . 143
5.2 PVD GaN, characteristics: optical characteristics vs pressure . . . . . 143
5.3 PVD GaN, characteristics: growth rate vs pressure & temperature . . . . . 144
5.4 PVD GaN, characteristics: XRD vs temperature, thickness and substrate . . . . . 145
5.5 PVD GaN, characteristics: XRD results of previous figure summarised . . . . . 147
5.6 PVD GaN, characteristics: strain vs pressure . . . . . 148
5.7 PVD GaN, characteristics: SEM cross-section at different pressures . . . . . 148
5.8 PVD GaN, characteristics: SEM top view at different pressures & temperatures . 149
5.9 PVD GaN, characteristics: depolarisation of a TEM diffraction profile . . . . . 149
5.10 PVD GaN, characteristics: FT on an HRTEM micrograph . . . . . 150
5.11 PVD GaN, characteristics: effect of the substrate on the structure . . . . . 151
5.12 PVD GaN, characteristics: link with the Thornton Diagram . . . . . 152
5.13 Ge-doped PVD GaN: growth rate & thickness vs pressure, doping & annealing . 155
5.14 Ge-doped PVD GaN: optical properties vs pressure, doping & annealing . . . . 156
5.15 Ge-doped PVD GaN: XRD vs doping & annealing . . . . . 157
5.16 Ge-doped PVD GaN: Arrhenius plots vs annealing . . . . . 158
5.17 Ge-doped PVD GaN: $\rho$ & $E_A$ vs pressure, doping & annealing . . . . . 159
5.18 Si-doped PVD GaN: optical & electrical properties vs doping . . . . . 161
5.19 Si-doped PVD GaN: Raman crystallinity vs doping . . . . . 162
5.20 Si-doped PVD GaN: XRD crystallinity vs doping . . . . . 163

5.21 Si-doped PVD GaN: optical and electrical properties vs temperature . . . . . 165
5.22 Si-doped PVD GaN: Raman crystallinity vs temperature . . . . . 166
5.23 Si-doped PVD GaN: XRD crystallinity vs temperature . . . . . 167
5.24 Si-doped PVD GaN: optical & electrical properties vs annealing temperature . . 168
5.25 PVD GaN(Si) on Sa, epitaxy: unit cells merging . . . . . 170
5.26 PVD GaN(Si) on Sa, epitaxy: structural, electrical & optical layer properties . . . 172
5.27 PVD GaN(Si) on Sa, epitaxy: HRTEM and diffraction figure of two interfaces . . 174
5.28 PVD GaN(Si) on Sa, epitaxy: TEM analysis of the doped GaN layer . . . . . 175
5.29 PVD GaN(Si) on Sa, epitaxy: TKD study of the undoped GaN layer . . . . . 177
5.30 PVD GaN(Si) on Sa, epitaxy: TKD study of the doped GaN layer . . . . . 178
5.31 PVD InGaN: optical and structural layer properties . . . . . 181
5.32 PVD InGaN, co-sputtering: indium content gradient . . . . . 182
5.33 PVD InGaN, co-sputtering: problems with textured solar cells . . . . . 182
5.34 PVD InGaN, co-sputtering: layer properties . . . . . 183

6.1 In/GaN PECVD contact: Absorption coefficient and optical bandgap . . . . . 189
6.2 In/GaN PECVD contact: three tested architectures . . . . . 190
6.3 In/GaN PECVD contact: J-V characteristics . . . . . 192
6.4 In/GaN PECVD contact: effect of temperature and annealing . . . . . 194
6.5 Ge-doped GaN PVD contact: architectures . . . . . 195
6.6 Ge-doped GaN PVD contact: J-V curves . . . . . 197
6.7 Si-doped GaN PVD contact: architectures . . . . . 200
6.8 Si-doped GaN PVD contact: lifetime vs architecture . . . . . 201
6.9 Si-doped GaN PVD contact: J-V curves & performances . . . . . 202
6.10 Si-doped GaN PVD contact: DITO i-n band diagram . . . . . 204
6.11 Si-doped GaN PVD contact: temperature & irradiation influence . . . . . 206
6.12 Si-doped GaN PVD contact: lifetime vs doping & thickness . . . . . 207
6.13 Si-doped GaN PVD contact: J-V vs doping & thickness . . . . . 208
6.14 InGaN PVD contact: architectures & band diagram . . . . . 211
6.15 InGaN PVD contact: cell performances . . . . . 213

A.1 Experimental methods, ellipsometry: ∥- and ⊥-polarised light . . . . . 223
A.2 Experimental methods, XRD: Elaborates of stress . . . . . 227
A.3 Experimental methods, DOE: four 3D designs of experiments . . . . . 230

B.1 In/GaN PECVD, deposition parameters: 3D view of the fitted model . . . . . 239
B.2 In/GaN PECVD, DOE: GaN thickness model, added model plot . . . . . 240
B.3 In/GaN PECVD, DOE: GaN thickness model, Cook distance . . . . . 241
B.4 In/GaN PECVD, DOE: InN thickness model, added model plot . . . . . 241
B.5 In/GaN PECVD, DOE: InN thickness model, Cook distance . . . . . 242
B.6 In/GaN PECVD, DOE: InN thickness model, two particular effects . . . . . 242
B.7 In/GaN PECVD, DOE: InGaN thickness models, model plot & Cook . . . . . 243
B.8 In/GaN PECVD, DOE: InGaN thickness models, two particular effects . . . . . 244

B.9 In/GaN PECVD, DOE: GaN optical bandgap model, model plot and $a_{Ar}$ . . . . . 246
B.10 In/GaN PECVD, DOE: GaN optical bandgap model, Cook distance . . . . . 246
B.11 In/GaN PECVD, DOE: InN optical bandgap models, model plots & Cook . . . . 247
B.12 In/GaN PECVD, DOE: InN optical bandgap model, two particular effects . . . . 248
B.13 In/GaN PECVD, DOE: InGaN optical bandgap model, model plots & Cook . . . 249
B.14 In/GaN PECVD, DOE: InGaN optical bandgap model, one particular effect . . . 250
B.15 In/GaN PECVD, DOE: InN crystallite size model, added model plot . . . . . 251
B.16 In/GaN PECVD, DOE: InN crystallite size model, Cook distance . . . . . 252
B.17 In/GaN PECVD, DOE: InGaN crystallite size model, added model plot . . . . . 252
B.18 In/GaN PECVD, DOE: InGaN crystallite size model, Cook distance . . . . . 253
B.19 In/GaN PECVD, DOE: InGaN Urbach energy model, added model plot . . . . . 254
B.20 In/GaN PECVD, DOE: InGaN Urbach energy model, Cook distance . . . . . 254
B.21 In/GaN PECVD, DOE: indium content model, added model plot . . . . . 255
B.22 In/GaN PECVD, DOE: indium content model, Cook distance . . . . . 256
B.23 PVD GaN, characteristics: XRD vs temperature & pressure at 100 nm on Si . . . 257
B.24 PVD GaN, characteristics: XRD vs temperature & pressure at 100 nm on Sa . . . 258
B.25 PVD GaN, characteristics: XRD vs thickness & pressure at 400 °C on Si . . . . . 259
B.26 PVD GaN, characteristics: XRD vs thickness & pressure at 400 °C on Sa . . . . . 260
B.27 Ge-doped PVD GaN: absorption coefficients . . . . . 263
B.28 Ge-doped PVD GaN: Arrhenius plots . . . . . 264
B.29 PVD GaN(Si) on Sa, epitaxy: TEM analysis of the undoped GaN layer . . . . . 265
B.30 InGaN PVD contact: J-V curves, hole architecture . . . . . 266
B.31 InGaN PVD contact: J-V curves, electron architecture . . . . . 267

C.1 a-Si:H PECVD contact: Fabrication process . . . . . 269
C.2 a-Si:H PECVD contact: hydrogen content and temperature . . . . . 271
C.3 a-Si:H PECVD contact: effect of the doping . . . . . 272
C.4 A-Si:H PECVD contact: architecture used to test the passivation . . . . . 273

# List of Tables


1.1 Introduction: global shares of primary energy consumption by source in 2021 . 1

2.1 Solar cell state of the art, InN and GaN physical properties . . . . . 14

3.1 Experimental methods, photon-matter interactions: energy ranges . . . . . 32
3.2 Experimental methods, Raman: vibrational modes of wurtzite In/GaN bulk . . 33
3.3 Experimental methods, DOE: ANOVA table . . . . . 66

4.1 InN PECVD, deposition parameters: six InN layers . . . . . 69
4.2 In/GaN PECVD, deposition parameters: InN and GaN optimisation . . . . . 71
4.3 In/GaN PECVD, deposition parameters: $E_{04}$ vs $g$, best fit . . . . . 75
4.4 In/GaN PECVD, deposition parameters: parameter space with $NH_3$ . . . . . 77
4.5 In/GaN PECVD, TOFMS: frequency, power and pressure DOEs . . . . . 84
4.6 In/GaN PECVD, TOFMS: deposition parameters and layer characteristics . . . . 86
4.7 In/GaN PECVD, TOFMS: InGaN XRD results . . . . . 98
4.8 In/GaN PECVD, DOE: GaN thickness model, input and quality metrics . . . . . 108
4.9 In/GaN PECVD, DOE: InN thickness model input and quality metrics . . . . . 111
4.10 In/GaN PECVD, DOE: InGaN thickness models, input and quality metrics . . . 114
4.11 In/GaN PECVD, DOE: InGaN thickness models, problematic extrema . . . . . 115
4.12 In/GaN PECVD, DOE: GaN optical bandgap model, input and quality metrics . 117
4.13 In/GaN PECVD, DOE: InN optical bandgap models, input and quality metrics . 120
4.14 In/GaN PECVD, DOE: InGaN optical bandgap models, input and quality metrics 122
4.15 In/GaN PECVD, DOE: InN crystallite size model, input and quality metrics . . . 126
4.16 In/GaN PECVD, DOE: InGaN crystallite size model, input and quality metrics . 128
4.17 In/GaN PECVD, DOE: InGaN Urbach energy model, input and quality metrics . 130
4.18 In/GaN PECVD, DOE: indium content model, input and quality metrics . . . . 133
4.19 In/GaN PECVD, DOE: synthesis of all the DOE models . . . . . 135
4.20 In/GaN PECVD, DOE: best-predicted layers . . . . . 138

5.1 PVD GaN, characteristics: optical and structural properties dependence on temperature, pressure and thickness . . . . . 144
5.2 Ge-doped PVD GaN: comparison with literature . . . . . 159
5.3 PVD GaN(Si) on Sa, epitaxy: basic layer characteristics . . . . . 171
5.4 PVD GaN(Si) on Sa, epitaxy: EDS of two layers . . . . . 173

5.5 PVD InGaN: optical & electrical layer properties . . . . . 180

6.1 Contacts: band alignment physical quantities . . . . . 188
6.2 In/GaN PECVD contact: In/GaN layer characteristics . . . . . 189
6.3 InGaN PVD contact: best result & literature . . . . . 214

A.1 Experimental methods, Raman: other parasitic vibrational modes . . . . . 222
A.2 Experimental methods, XRD: InN and GaN elastic stiffness constants . . . . . 227
A.3 Experimental methods, DOE: the table of the $2^{n-g}$ plan . . . . . 232

B.1 In/GaN PECVD, deposition parameters: $g^{\mathrm{InN}}$ Anova table . . . . . 237
B.2 In/GaN PECVD, deposition parameters: $E_{04}^{\mathrm{InN}}$ Anova table . . . . . 237
B.3 In/GaN PECVD, deposition parameters: $CrSz^{\mathrm{InN}}$ Anova table . . . . . 238
B.4 In/GaN PECVD, deposition parameters: models' evaluation . . . . . 238
B.5 In/GaN PECVD, DOE: GaN thickness model, coefficient details . . . . . 241
B.6 In/GaN PECVD, DOE: InN thickness model, coefficient details . . . . . 242
B.7 In/GaN PECVD, DOE: InGaN thickness models, coefficient details . . . . . 245
B.8 In/GaN PECVD, DOE: GaN optical bandgap model, coefficient details . . . . . 246
B.9 In/GaN PECVD, DOE: InN optical bandgap models, coefficient details . . . . . 248
B.10 In/GaN PECVD, DOE: InGaN optical bandgap models, coefficient details . . . . 250
B.11 In/GaN PECVD, DOE: InN crystallite size model, coefficient details . . . . . 252
B.12 In/GaN PECVD, DOE: InGaN crystallite size model, coefficient details . . . . . 253
B.13 In/GaN PECVD, DOE: InGaN Urbach energy model, coefficient details . . . . . 254
B.14 In/GaN PECVD, DOE: indium content model, coefficient details . . . . . 256
B.15 Ge-doped PVD GaN: optical and electrical properties vs Ge power . . . . . 261
B.16 Ge-doped PVD GaN: optical and electrical properties vs pressure & annealing . 262

C.1 A-Si:H PECVD contact: passivation results. . . . . 273

# List of acronyms

| | |
|---|---|
| **3kD** | $3^k$ design |
| **4-PP** | four point probe |
| *FF* | fill factor |
| *TA* | total absorptance |
| *TR* | total reflectance |
| *TT* | total transmittance |
| $I_{SC}$ | short-circuit current |
| $J_{MPP}$ | current density at the maximum power point |
| $J_{SC}$ | short-circuit current density |
| $V_{MPP}$ | voltage at the maximum power point |
| $V_{OC}$ | open-circuit voltage |
| **a-Si** | amorphous silicon |
| **AM** | air mass coefficient |
| **AM1.5G** | mid-latitudes global air mass coefficient |
| **ANOVA** | analysis of variance |
| **B-M** | Burstein-Moss |
| **BF** | bright field image |
| **BG** | bandgap |
| **BSE** | backscattered electron |
| **c-Si** | crystalline silicon |
| **CB** | conduction band |
| **CCD** | central composite design |
| **CdTe** | cadmium telluride |
| **CI** | confidence interval |
| **CIGS** | copper indium gallium selenide |
| **CVD** | chemical vapor deposition |
| **DF** | dark field image |
| **DLC** | dark lateral conductivity |
| **DOE** | design of experiment |
| **DSSC** | dye-synthesized solar cell |
| **e-h pair** | electron-hole pair |

| | |
|---|---|
| **EBSD** | electron backscattered diffraction |
| **EDS/EDX** | energy-dispersive X-ray spectroscopy |
| **ERD** | elastic recoil detection |
| **FCA** | free carrier absorption |
| **FFD** | full factorial design |
| **FIB** | focused ion beam |
| **FrFD** | fractional factorial design |
| **FTIR** | Fourrier-transform infrared spectroscopy |
| **FWHM** | full width at half maximum |
| **GaN** | gallium nitride |
| **GIXRD** | grazing incidence X-ray diffraction |
| **high-*T*** | high temperature |
| **IBC** | interdigitated back contact |
| **InGaN** | indium gallium nitride |
| **InN** | indium nitride |
| **IR** | infrared |
| **ITO** | indium tin oxyde |
| **LL** | load lock |
| **low-*T*** | low temperature |
| **LOWESS** | locally weighted scatterplot smoothing |
| **MBE** | molecular beam epitaxy |
| **MFC** | mass-flow control |
| **MOCVD** | metal-organic chemical vapor deposition |
| **MPP** | maximum power point |
| **NIST** | national institute of standards and technology |
| **NUDM** | non-uniform deformation model |
| **OPV** | organic photovoltaic cell |
| **PAALD** | plasma-assisted atomic layer deposition |
| **PAMBE** | plasma-assisted molecular beam epitaxy |
| **PECVD** | plasma-enhanced chemical vapor deposition |
| **PERC** | passivated emitter rear contact |
| **PL** | photoluminescence |
| **PSC** | perovskite solar cell |
| **PV** | photovoltaic |
| **PVD** | physical vapor deposition |
| **RBS** | Rutherford backscattering |
| **RF** | radiofrequency |
| **RLC** | resistor-inductor-capacitor circuit |
| **RT** | room temperature |
| **SAED** | selected area electron diffraction |

| | |
|---|---|
| **SC** | semiconductor |
| **SE** | secondary electron |
| **SEM** | scanning electron microscope |
| **SHJ** | silicon heterojunction |
| **SSC** | silicon solar cell |
| **STC** | standard test conditions |
| **STEM** | scanning transmission electron microscope |
| **T-L** | Tauc-Lorentz |
| **TCO** | transparent conductive oxyde |
| **TEG** | triethylgallium |
| **TEI** | triethylindium |
| **TEM** | transmission electron microscope |
| **TKD** | transmission Kikuchi diffraction |
| **TLM** | transfer length measurement |
| **TMG** | trimethylgallium |
| **TMI** | trimethylindium |
| **TOF-MS** | time-of-flight mass spectrometer |
| **TOPCON** | tunnel oxide passivated contact |
| **UDEDM** | uniform deformation energy density model |
| **UDM** | uniform deformation model |
| **UV** | ultraviolet |
| **VB** | valence band |
| **VIF** | variance inflation factor |
| **VIS** | visible |
| **XRD** | X-ray diffraction |

# 1 Introduction

Given the present climate crisis, renewable energies are increasingly promoted and used by both the public and governments. But change remains slow; in 2021, just after the Covid crisis, the global share of fossil fuels is still more than 80% (see table 1.1), despite continuously rung alarms from scientists since 1912 [180].

Table 1.1: Introduction: global shares of primary energy consumption by source in 2021, calculated according to the substitution method [157] with a conversion factor of 40.6%, using here only the BP Statistical Review of World Energy 2021 [25]. See also the International Energy Agency (IEA) report [83] or Our World in Data [73].

| Primary energy source | Global consumption [EJ] | Global share [%] |
|---:|:---:|:---:|
| Natural Oil | 184.21 | 31.0 |
| Natural Coal | 160.10 | 26.9 |
| Natural Gas | 145.35 | 24.4 |
| Hydraulic energy | 40.26 | 6.8 |
| Nuclear energy | 25.31 | 4.3 |
| Wind energy | 20.32 | 3.4 |
| Solar energy | 11.27 | 1.9 |
| Other renewable energies | 8.32 | 1.4 |
| **Total 2021** | **595.15** | 100 |

Solar energy is the best candidate for a quick and stable energy transition. Indeed, the solar module's versatility allows it to be installed virtually anywhere the sun shines: next to highways or train tracks, on most roofs, or even as the cover of a wall, quickly producing power. As a new technology compared to fossil fuels, its learning rate shows a sharper decrease in price per unit of power (today at around 3 cts/W, see figure 1.1). This price drop is so pronounced that installing new PV power plants rather than building fossil-fuel-based ones is now more economical. This considerable price evolution is mainly driven by the increase in the PV technology efficiency and the production up-scaling. These two dimensions are critical in making solar cells cheaper and more competitive and must be improved constantly.

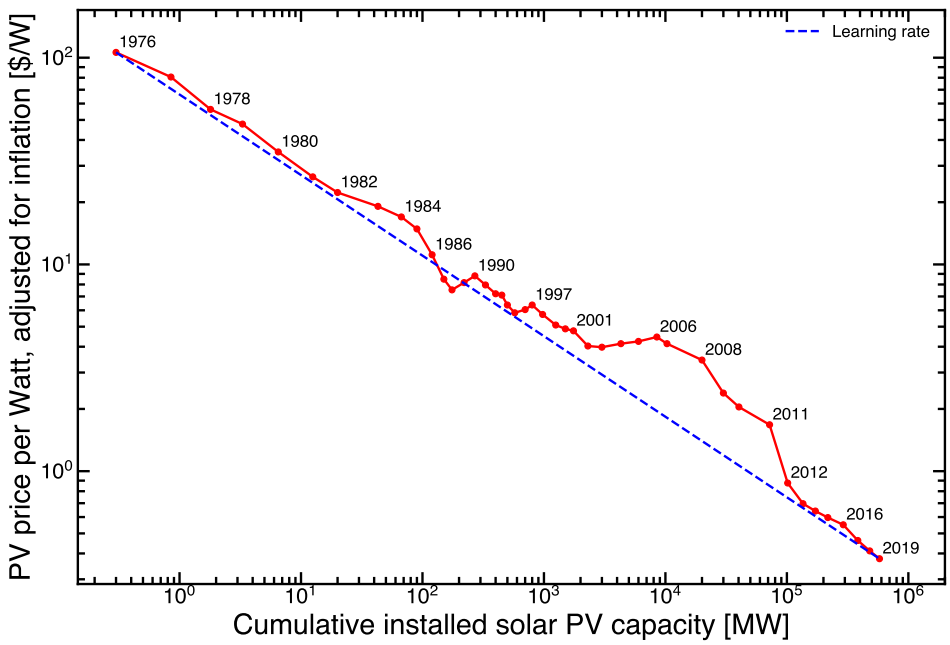


Figure 1.1: PV module cost evolution, with its learning rate, from 1976 to 2019 [94].

The first generation of solar cells was based on crystalline silicon (c-Si), a mature technology mass-produced in the seventies. We call those cells "crystalline silicon cells". The second generation sees its thickness reduced and is mainly made up of amorphous silicon (a-Si), copper indium gallium selenide (CIGS) and cadmium telluride (CdTe). It was mass-produced in the early eighties and is referred to as "thin film technologies". The third generation consists of organic photovoltaic cell (OPV), perovskite solar cell (PSC), and dye-synthesized solar cell (DSSC). The first cells ever produced by this generation date back to the early nineties. Its main new feature is its flexibility, and this generation is called "emerging PV". Sadly, it has not penetrated the market yet [144]. InGaN is a material that belongs to the second generation of solar cells.

While it is critical to boost the efficiency of solar cells, single junction solar cells are limited in their conversion power by nature. If we were to consider a perfect solar cell at a temperature of 25 °C, illuminated by the mid-latitudes global air mass coefficient (AM1.5G) spectrum [12], and assuming radiative emission from the front and rear side of the solar cell, its maximal possible efficiency would be $\eta = 33\,\%$, with a bandgap of 1.4 eV [117, 152, 27]. This is mainly due to the radiative losses of the electrons excited by photons having an energy higher than the bandgap. Only two leading solutions have been found to overcome this theoretical limit: increase the solar power concentration by using a lens before the solar cell, or use more than one junction in a single solar cell. The highest efficiency solar cell ever produced is a six-junction concentrated PV solar cell with an efficiency of 47.1 % [66], which is obviously not marketable for terrestrial applications.

If we stick to c-Si only, we can afford a more detailed history of the technology and of the architecture evolution (figure 1.2). After the first primary structure was developed to capture photons with silicon, passivated emitter rear contact (PERC) solar cells were introduced in 1989 [22]. Their back was coated with a reflective layer, forcing light to go through the whole cell again for more absorption, preventing losses at the back in the process, for demonstrated efficiencies of up to 23 % (theoretical maximum efficiency: 24.5 %). After that came the tunnel oxide passivated contact (TOPCON), introduced in 2013 [58]. As an upgrade from the PERC technology, a tunnel oxide layer and a polysilicon layer are added to the rear side (respectively, steps 2 and 3 of figure 1.2). The thin tunnel oxide layer passivates the interface between the absorber and the contact [37], facilitated by the highly doped polysilicon layer [154], for demonstrated efficiencies of up to 26 % (theoretical maximum efficiency: 28.5 %). The next step would be to move the front contacts at the back to remove the front bus bars shading completely; this is called the interdigitated back contact (IBC) solar cell technology [99]. Without shading and with ideal conditions, this technology allows for the highest theoretical efficiency for c-Si-based solar cells (29.4 %), with the downside of a more expensive and complex manufacturing process [199]. And eventually, the last way to increase the efficiency even further would be to use another higher energy absorber at the front, like perovskite or InGaN. These kinds of technologies, under ideal conditions, have a theoretically achievable efficiency of 43 % [191] and recently overcame the highly symbolic 30 % efficiency threshold [192].

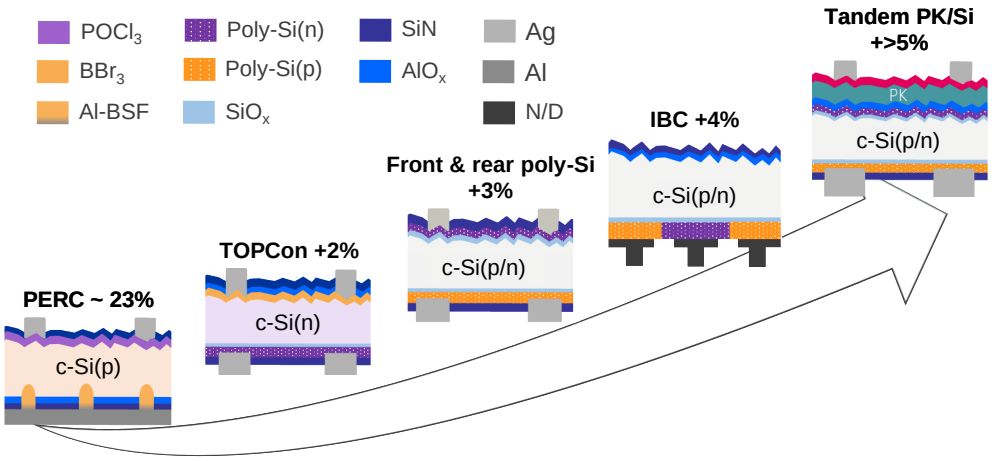


Figure 1.2: Solar cell evolution, from PERC to tandem [22, 58, 99, 191]. Values in red are already obtained.

In the currently industrialised c-Si solar cell architectures, the primary source of current losses stems from recombination at the metal contacts. Thus, developing novel contact structures to reduce recombination at the metal/c-Si interface is an essential research topic among the c-Si PV community. These novel contact structures are referred to as "passivating contacts" as their main feature is to "passivate" electrically active defects at the metal/c-Si interface (*e.g.* by saturating them with hydrogen). One of the candidates for this kind of feature is also the versatile III-N technology, where its tunable BG and structural properties align pretty

conveniently with the present silicon technology (see section 2.3 for more details). Using InGaN as contact has already been explored, but it was produced with high-temperature deposition processes.

**The goal of this thesis is to explore the feasibility of integrating InGaN materials into the PV technology, but at lower temperature deposition processes**, such as PECVD or sputtering. This research is undertaken to mitigate the high cost, the disadvantages and the defects linked to the standard high temperature (high-$T$) deposition process such as metal-organic chemical vapor deposition (MOCVD). Being able to produce InGaN layers with similar properties bat at a lower deposition temperature is a roadmap for further developments in multiple fields: InGaN absorber, passivating or selecting contacts and low-$T$ InGaN applications. Most of my work focussed on PECVD III-N material development. Still, I initiated and supervised several student projects (e.g. semester, master or internship projects), also included in this thesis to present a complete study. Here is what the reader will find in the current view:

**Chapter 2** details the current state-of-the-art of InGaN technology for PV applications, including the following research questions (presented in more detail in section 2.4):

1. Is it possible to produce InGaN materials at low temperatures?
2. If yes, how compatible are the layer characteristics for PV application?
3. If they are compatible enough, how stable do they remain when p- or n-doping is added?
4. If it is stable enough, once integrated, how well does it compare with standard c-Si solar cell technology?

**Chapter 3** presents the experimental methods based on the present work. The rest of the thesis will address the research questions.

**Chapters 4 & 5** addresses the first three research questions, where InGaN layers deposited by PECVD and PVD are fully analysed and presented.

**Chapter 6** will address the fourth and last research question. The integration quality of In/GaN layers in a solar cell as contacts using both a PECVD and a sputtering process are presented here. This chapter also includes a small study on taking advantage of the possibility of high-$T$ processes in System B to presumably quicken the production process of standard silicon solar cells, potentially making it cheaper.

**The rest** of the thesis includes a conclusion, annexes, an extensive bibliography and other extras.

Enjoy!

# 2 Solar cell state of the art

## 2.1 Solar cell operation

This section is a reminder of how solar cells work. It will focus on the essentials, assuming the reader is already familiar with most of the PV field. A more thorough study can be found in the literature [129, 116].

In short, the following events will lead to the production of electricity from a solar cell (also refer to figure 2.1 for a visual representation):

1. Photons in sunlight hit the solar panel and are absorbed by semiconducting materials.
2. Electrons (negatively charged) are knocked loose from filled states in the valence band (VB) into empty states in the conduction band (CB), leaving holes behind.
3. Due to the electronic p-n junction configuration and its metallic contacts, electrons and holes are separated and collected selectively at the two metallic contacts.
4. When reaching the metallic contact, direct current (DC) electricity is produced.

### 2.1.1 The p-n junction

In intrinsic semiconductors (SCs), the CB and VB are close enough so that with a little bit of energy, electrons can cross the BG. According to fundamental solid state physics [158, 14], for a three-dimensional material, the free electrons concentration $n$ in the CB is the integral of the product of the Fermi-Dirac distribution function $F(E, E_F)$ centred on the Fermi level $E_F$ and the density of states $N(E)$.

$$F(E, E_F) = \left(1 + \exp\left(\frac{E - E_F}{k_B T}\right)\right)^{-1} \tag{2.1}$$

$$N(E) = \frac{\sqrt{128}\pi \left(m_e^*\right)^{3/2}}{h^3} (E - E_C)^{1/2}$$

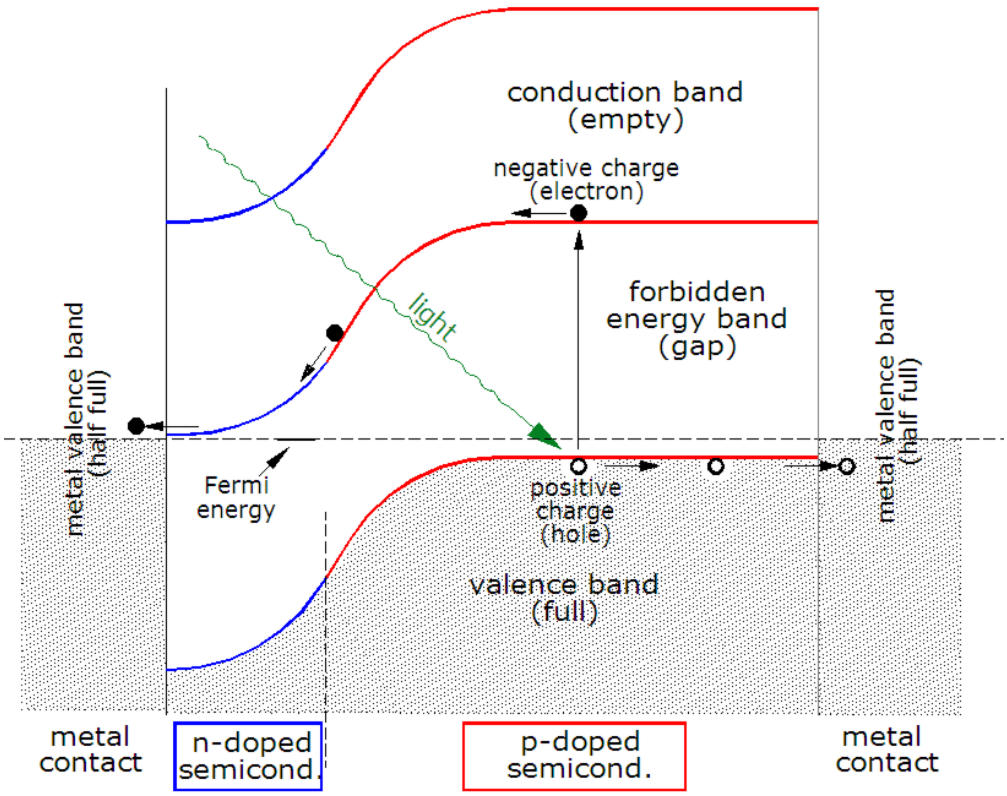


Figure 2.1: Solar cell state of the art, operation. This figure was created and generously shared by GianniG46 on Wikipedia [172].

$$
\begin{aligned}
n &= \int_{E_C}^{\infty} F(E\,E_F) \cdot N(E)\,\mathrm{d}E \\
n &= N_C \exp\left(\frac{E_F - E_C}{k_B T}\right) \qquad (2.2) \\
N_C &= \left(\frac{32\pi m_e^* k_B T}{h^2}\right)^{3/2}
\end{aligned}
$$

where similar development is used for the holes in the VB (with $p$ and $N_A$). It follows that:

$$
E_F = \frac{E_C + E_V}{2} + \frac{3k_B T}{4} \ln\left(\frac{m_h^*}{m_e^*}\right) \qquad (2.3)
$$

$$
\begin{aligned}
np &= N_V N_C \exp\left(\frac{-E_g}{k_B T}\right) \\
&\equiv n_i^2 \qquad (2.4)
\end{aligned}
$$

where $n_i$ is defined as the "intrinsic carrier density" that only changes with respect to temperature and BG. We see that for intrinsic SCs, the Fermi level tends to increase slightly with temperature. The Fermi level significantly changes with doping, where for an n-type material with fully ionised impurities in concentration $N_D$ or for a p-type material with fully ionised impurities in concentration $N_A$, we have

$$E_F - E_C = k_B T \ln\left(\frac{N_D}{N_C}\right) \tag{2.5a}$$

$$E_V - E_F = k_B T \ln\left(\frac{N_A}{N_V}\right) \tag{2.5b}$$

As an example, for intrinsic c-Si at 300 K in the dark, the bandgap $E_g = E_C - E_F = 1.12\,\text{eV}$, $N_C = 2.86 \cdot 10^{19}\,\text{cm}^{-3}$ with $m_e^* = 1.09 m_e$, and $n_i^2 = 9.33 \cdot 10^{19}\,\text{cm}^{-6}$. Adding a Boron concentration of $N_A = 10^{17}\,\text{cm}^{-3}$ to intrinsic c-Si will shift $E_F$ down, just 149 meV above the VB (assuming that all the impurities are fully ionised). Nevertheless, the product of equation 2.4 remains valid even for doped SCs. This means that doping a SC to a certain level will create a so-called "majority carrier" and its counterpart "minority carrier", where their concentration can be approximated as follows (here for an n-doping example, similarly applicable to p-doping):

$$n_0 \approx N_D^+ \approx N_D$$

$$p_0 = \frac{n_i^2}{N_D} \ll n_0$$

A solar cell is a p-n junction in which electron-hole pair (e-h pair) are created by illumination. The most straightforward p-n junction is created by merging two SC pieces, where one is p-doped (red side of figure 2.1), and the other is n-doped (blue side of the exact figure). At the interface, the electrons of the n-doped side will move across thanks to thermal diffusion and recombine with the holes of the other side, both leaving behind their ionised dopants. This will create a "space charge region" (SCR), eventually leading to the appearance of an electric potential. This electric potential will create a so-called "drift current" in the opposite direction until equilibrium is reached and the two currents cancel one another. The SCR is described by multiple properties (size, band-bending, current density, etc.); here are some equations describing the different current densities $\vec{J}$ passing through it (in this case, the $n$ subscript refers to electrons, but it is also applicable to holes).

$$\vec{J}_n^{diffusion} = eD_n \vec{\nabla} n$$

$$D_n = \frac{k_B T}{e} \mu_n$$

$$\vec{J}_n^{drift} = en\mu_n\vec{E}$$
$$\vec{J}_{tot} = \vec{J}_p + \vec{J}_n = e\left(D_n\vec{\nabla}n - D_p\vec{\nabla}p\right) + e\left(n\mu_n + p\mu_p\right) \tag{2.6}$$

where $D_n$ is defined as the "diffusion constant", $\vec{\nabla}n$ refers to a gradient in the charge carrier level across the SC (perpendicularly to the interface), $\mu_n$ is the electron mobility (usually in $\frac{\text{cm}^2}{\text{Vs}}$) and $\vec{E}$ is the electric field within the SCR. This is still all in the dark, and without going into further detail but assuming that the p-n junction is infinitely thick, we can define the so-called "dark J-V curve", which describes the current density as a function of an externally applied voltage:

$$J(V) = J_0 \cdot \exp\left(\frac{eV}{k_B T}\right) \tag{2.7}$$
$$J_0 = J_{0n} + J_{0p}$$
$$J_{0n} = \frac{eD_p p_{n0}}{L_p} = \frac{eD_p n_i^2}{N_D L_p}$$
$$J_{0n} = \frac{eD_n n_{p0}}{L_n} = \frac{eD_n n_i^2}{N_A L_n}$$

where $J_0$ is called the "diode saturation current density". Taking over the terminology from transistor technology, $J_{0n}$ is often called the "emitter saturation current density" and $J_{0p}$ is often called the "base saturation current density". $L_p$ refers to the diffusion length for holes in the n-doped part of the junction, the distance an electron usually travels before recombining. The same applies to $L_n$ and electrons in the p-doped region. Note that given the different diffusion coefficients of electrons and holes, these two lengths are different (usually smaller for the holes).

### 2.1.2 The solar cell

If light is shone on such a device, it will generate e-h pairs that will diffuse towards the contacts more or less quickly. To model that, an e-h pair generation factor $G(x)$ is introduced everywhere in the device, where excess minority carriers create a current flowing backwards to the junction overall. If they cross the SCR, they become majority carriers on the other side. Assuming a constant generation factor $G$ across the whole thickness, a simple term is added to equation 2.7:

$$J(V) = J_0\left[\exp\left(\frac{eV}{k_B T}\right)\right] - J_L \tag{2.8}$$
$$J_L = eG\left(L_n + L_p + W\right) \tag{2.9}$$

where $W$ is the SCR width. From there, all the cell characteristics can be described:

**Short-circuit current density ($J_{SC}$):** is the maximum possible current density that a solar cell can deliver, and that happens when the voltage is zero (hence the "short circuit" term). This characteristic depends on the illuminated area, the number of photons reaching the solar cell, the incident light spectrum (which is here standardised), the solar cell's optical properties (and especially the optical losses due to reflection, shadowing, or parasitic absorption), and the minority-carrier collection probability; all of which can be optimised. In the ideal case, $J_{SC} = J_L$.

**Open-circuit voltage ($V_{OC}$):** is the maximum possible voltage that a solar cell can deliver, and that happens when the current is zero (hence the "open circuit" term). Solving equation 2.8 for $V$ with $J = 0$ yields

$$V_{OC} = \frac{k_B T}{q} \ln\left(\frac{J_L}{J_0} + 1\right) \tag{2.10}$$

where $J_0$ contributes an additional dependence on $T$.

**Maximum power density ($P_{max}$):** is the maximum power density that a cell can deliver, following $P = VJ$. On the J-V curve, between the zero power points at $J_{SC}$ and $V_{OC}$, there exists a maximum power point (MPP), associated with a current density at the maximum power point ($J_{MPP}$) and a voltage at the maximum power point ($V_{MPP}$). This optimal point can be obtained when the derivative of the power density is zero, hence:

$$\begin{aligned} \frac{\mathrm{d}P}{\mathrm{d}V} &= 0 \\ V_{MPP} &= V_{OC} - \frac{k_B T}{q} \ln\left(\frac{q V_{MPP}}{k_B T} + 1\right) \end{aligned} \tag{2.11}$$

**Fill factor ($FF$):** is the ratio between the $P_{max}$ and the product of $J_{SC}$ and $V_{OC}$. It measures the J-V curve "squareness". A low $FF$ signifies high-rate recombination mechanisms or parasitic resistive losses.

$$FF = \frac{V_{MPP} \cdot J_{MPP}}{V_{OC} \cdot J_{SC}} \tag{2.12}$$

**Energy conversion efficiency ($\eta$):** compares the electrical power produced by the solar cell with the illumination power reaching it, 1000 W under STC.

$$\eta = \frac{P_{max}}{P_{in}} \tag{2.13}$$

### 2.1.3 The losses

The model presented in the last section is simple but sufficient to grasp the fundamental dynamics of a solar cell. A more complicated one could consider the solar cell's finite size, an exponential decrease of the photo-generated current with respect to the depth, and, more

importantly, losses. This section focuses on the different ways that a solar cell may be deficient, how it reflects on the J-V curve, and what are the standard solutions (or rather trade-offs) set in place to overcome them. This non-exhaustive list only aims to present the leading causes of losses; their amplitudes mainly depend on solar cell technology. Part of this list is also visually schematised in figure 2.2 at the end of this section.

**Optical losses** are related to lost photons before they can produce an e-h pair inside the solar cell. These will mainly decrease the generation of e-h pairs, decreasing the produced current, mainly impacting the $J_{SC}$.

**Reflection:** when reaching the surface of a solar cell, light can be reflected (see equations A.7a, A.7b or 3.16a for a detailed description), which will decrease the number of photons entering the cell. This problem is usually reduced in two ways: by texturing the front surface (if the photon is reflected at a certain angle, it may have one more chance to enter the solar cell before being lost) and by adding an anti-reflective coating on the front side of the solar cell (normally adapted to a certain wavelength and angle only).

**Passing through:** photons may cross the solar cell without being absorbed and exit at the rear. This problem is usually reduced in three ways: by texturing both the front and the back side (this time for better optical confinement within the solar cell), by adding a reflective coating on the back side of the cell so that light has to cross it a second time, or by making the absorber thicker.

**Spectral losses, low energy:** if the photon does not have enough energy to produce an e-h pair, it will simply not interact with the solar cell and will count toward a decrease in efficiency. To capture low-energy photons, the bandgap of the absorber must be reduced, increasing its photocurrent but decreasing its voltage; a trade-off has to be found here, or one can resort to multiple-junction solar cells.

**Thermalisation:** if a photon has higher energy than the BG, it will promote an electron from the VB to a level higher than the bottom of the CB. “Thermalisation” is the process of this electron descending back to the lowest available energy state at the bottom of the CB, losing heat or emitting phonons. Thermalisation can also affect holes, where an electron deep in the VB is promoted low in the CB, leaving a hole behind that will thermalise until it reaches the top of the VB. These losses can be addressed by either increasing the bandgap of the junction (but that will decrease the $J_{SC}$ because fewer photons are absorbed) or by using multiple absorbers.

**Shading:** occurs when something prevents the photons from penetrating the solar cell. Specifically, shading usually refers to the conducting wire network (traditionally made of silver) printed at the front to collect the charges. Reducing shading by reducing the thickness of these wires may increase the resistance of said wires, impacting the *FF*. Another solution is to switch to IBC technology, which complicates the production process and results in more expensive solar cells.

**Parasitic absorption:** refers to light that is absorbed without the generation of e-h pair. This could be absorption in the front transparent conductive oxyde (TCO), the $SiN_x$ anti-reflective coating, the highly doped layers, or the rear reflector.

**Recombination losses:** are losses related to electrons recombining with holes before reaching the metallic contacts. These may affect the produced current and voltage, mainly the $V_{OC}$. In a general case, if the e-h pair creation occurs further from the junction than a diffusion length, it will likely recombine. This can be solved by having a thinner absorber.

**Radiative recombination:** is simply a direct band-to-band recombination of an electron with a hole, emitting a photon carrying the energy of the BG, possibly assisted with a phonon in the case of an indirect BG. This recombination rate will depend on the concentration of the different charge carriers implied in the different parts of the solar cell, hence on the doping level and the generation rate (or injection regime). These physical limits cannot be overcome but moderated by playing with the desired charge carrier concentration. Typically, high concentrations of charge carriers in a direct BG SC will produce a high radiative recombination rate.

**Auger recombination:** is a recombination process where energy is transferred to another charge carrier, either an electron excited very high into the CB or a hole excited very low in the VB, which then relaxes back by a thermalisation process.

**Shockley-Read-Hall (SRH) recombination:** refers to recombination via a deep energy level that is more than about 100 meV away from the band edges, within the BG. These deep energy levels (sometimes called traps or recombination centres) can be generated by dangling bonds, undesired contaminants, etc. Dangling bonds can be found within the crystal matrix (structural defect, threading dislocation, lattice mismatch, etc.), at the grain boundary for multicrystalline devices, at the interface between the different layers of the solar cell, or more commonly, at the perimeter of the solar cell where the crystal ends (see next point). In III-V SCs, the recombination due to lattice misfit dislocations is more identified to surface recombination (see next point) rather than SRH recombination. Undesired contaminants are not acting like a dopant but rather as an attractor for both holes and electrons, easing their recombination. To solve this issue, one has to work with single-crystal materials: fewer texturisation, larger crystals, fewer contaminants with cleaner processes, better passivation, etc.

**Surface recombination:** comprises recombinations that occur at the edge of the solar cell, or more importantly, at each interface between two layers, because the crystal ends or changes there, causing intermediate energy states to appear in the middle of the BG. They can be addressed by passivating the recombination centres, usually with hydrogen, or using a field effect generated by band-bending near the interface.

**Traps:** are also states in the BG, but they are located closer to the band edges in terms of energy. Thus, a trapped charge can be released by thermal excitation before recombination.

**Electrical losses** are usually associated with resistive losses in the external metallisation or local defects that short-circuit the junction. They will mainly impact the *FF*.

**Series resistance:** is the combined intrinsic resistance of all the elements of the solar cell stacked together. There is always some series resistance in a solar cell. Still, if one of its components is not well-designed (a too-thick tunnel junction, for example), the series resistance may increase, leading to sagging of the current-controlled portion of the J-V curve towards the origin. If it becomes high enough to dominate, the $J_{SC}$ decreases, and the solar cell's behaviour can become comparable to a simple resistor. *N.B.*: the series resistance includes the contact resistance at the interface between the solar cell and the metallic contact collecting the charges.

**Shunt resistance:** is mainly used when describing the solar cell with an equivalent circuit and represents a low-resistance path allowing electric currents to avoid the intended path. Shunts are so deadly for electronics that they must be avoided at all costs, and the shunt resistance should be as high as possible using the equivalent circuit. A shunt in the solar cell usually originates from a large recombination centre, for example, a dust particle integrated into the layer stack or perimeter losses at the edges of wafer-based cells. A low series resistance due to a shunt will impact the *FF* by reducing the $V_{OC}$.

**Thermal losses:** refer to the heating of the solar cell. This heating will, by definition, broaden the Fermi-Dirac distribution (equation 2.1). Referring to equation 2.10 and assuming that the $J_0$ of the cell is dominated by the $J_0$ of the bulk, solving equation 2.4 leads to a linear relationship of the $V_{OC}$ with temperature. In other words, if all the assumptions mentioned here are met, the $V_{OC}$ decreases linearly with temperature. This is why it is advantageous to use solar cells in a cooled environment or with SCs that are less sensitive to temperature changes, if possible. The heating can come from an external source, from the sun illumination, or the operating cell itself: the small resistances in the path of the charge carriers will emit heat that will further reduce the $V_{OC}$. But if other dynamics start to dominate the solar cell, the effect of temperature may not be that straightforward.

## 2.2 Physical properties of InN, GaN and InGaN

The physical properties of indium nitride (InN) and GaN are presented in table 2.1. Let "In/GaN" be defined as the generic term describing both InN, GaN and InGaN. In/GaN is naturally arranged in a hexagonal Wurtzite crystal structure (exact space group: $P6_3$, see figure 2.3a), but can be forced in a cubic zincblende crystal structure (exact space group: $F\bar{4}3m$) when the substrate under it is well chosen [2]. The "ideal" structure, where the nearest-neighbour environment of each atom is the same as in zincblende, is achieved when $c/a = \sqrt{8/3} \approx 1.6330$ and $u = 3/8 = 0.375$ (space group $P6_3mc$) where the $u$ parameter is the ratio between $c$ and the height of the first plateau of atoms that are different than the ones in the basal plane unit cell. In the extreme case where $u = 1/2$, the crystal integrates the specific $P6_3/mmc$ space

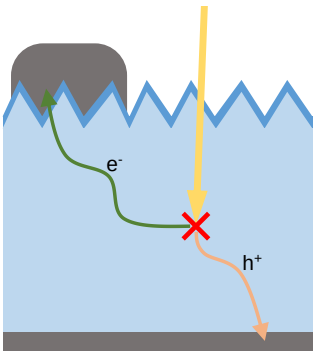


(a) Normal cell operation: the light (yellow arrow) is absorbed, creates an e-h pair that is extracted by the contacts.

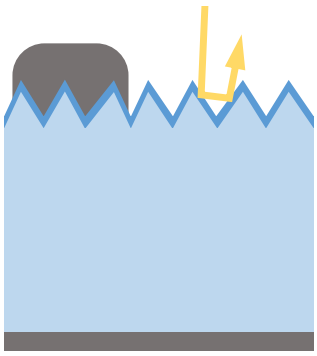

(b) Reflection: the light is reflected before entering the solar cell.

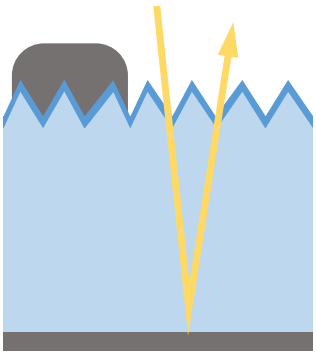

(c) Passing through (and here reflected at the back), due to either no absorption or too low photon energy.

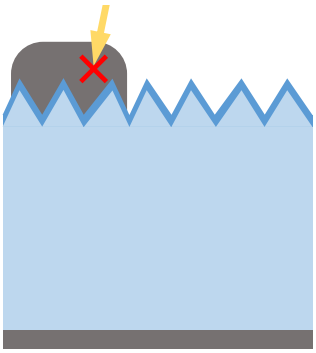

(d) Shading by the metallic contact.

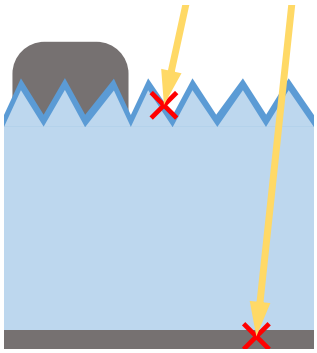

(e) Parasitic absorption: the photon is absorbed in the solar but does not produce an e-h pair.

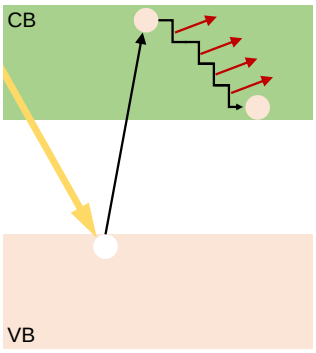


(f) Thermalization, where some energy is lost by the electron falling here to the bottom of the CB. Also applicable with a hole.

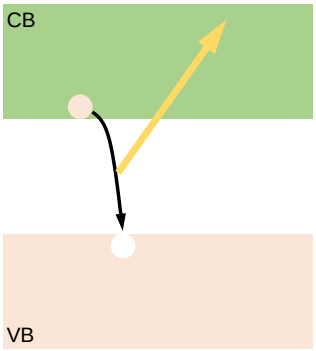


(g) Radiative recombination.

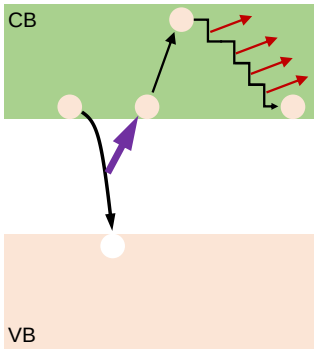


(h) Auger recombination followed by thermalisation of the excited charge carrier. Also applicable to holes.

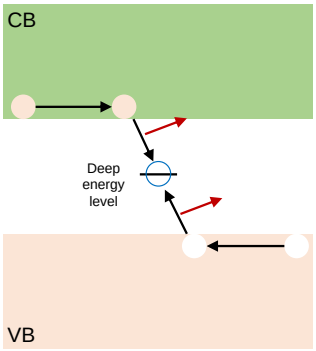


(i) SRH recombination via a deep energy level.

Figure 2.2: Solar cell state of the art, operation: visualisation of some loss types amongst the one presented here. The yellow arrow represents a photon; the red arrow represents an energy loss; the black arrow represents a change of energy state for the charge carrier.

Table 2.1: Solar cell state of the art, InN and GaN physical properties, arranged in a Wurtzite configuration, and with a direct bandgap. The values are valid at 300 °K, and often vary with temperature. $In_xGa_{1-x}N$ values vary linearly with the indium content $X_{In} = \frac{In}{In+Ga}$ (In & Ga in at. %, $X_{In}$ in %). The BG is the only physical quantity that varies in a quadratic way with $X_{In}$, named Vegard's law (see equation 2.14 and figure 2.4).

| Physical property name | Symbol | Unit | InN | GaN | InN sources | GaN sources |
|---|---|---|---|---|---|---|
| Lattice parameter | $a$ | Å | 3.5377 | 3.1881 | [136, 137] | [103, 102] |
| Lattice parameter | $c$ | Å | 5.7037 | 5.1856 | [136, 137] | [103, 102] |
| Lattice parameter | $c/a$ | - | 1.6123 | 1.6265 | [136, 137] | [103, 102] |
| u-parameter | $u$ | Å | 0.379 | 0.377 | [136, 137] | [103, 102] |
| Spontaneous polarization | $P_{SP}$ | $C/m^2$ | -0.032 | -0.029 | [18] | [18] |
| Resistivity | $\rho$ | $\Omega$ cm | 0.46 | $10^5$ | [132] | [124] |
| Electron mobility | $\mu$ | $cm^2/V{\cdot}s$ | 3200 | 1500 | [80] | [107] |
| Electron effective mass | $m_e^*$ | $m_e$ | 0.055 | 0.20 | [118] | [168] |
| Hole effective mass | $m_h^*$ | $m_e$ | 2.80 | 0.9 | [118] | [168] |
| Refractive index, $\lambda = 633$ nm | $n_{633}$ | - | 2.95 | 2.50 | [7] | [7] |
| Dielectric constant | $\varepsilon_\Gamma$ | - | 15.3 | 8.9 | [45] | [45] |
| Bandgap | $E_g$, BG | eV | 0.65 | 3.42 | [91, 188, 193] | [91, 193] |
| Electron affinity | $EA$ | eV | 5.80 | 4.00 | [176] | [176] |
| Abs. coeff. at BG + 0.2 eV | $\alpha_{E_g}$ | $cm^{-1}$ | $3 \cdot 10^{-4}$ | $10^5$ | [126] | [127] |
| Molar mass | $M$ | g/mol | 128.83 | 83.730 | [184] | [184] |
| Density | $\rho$ | $g/cm^3$ | 6.81 | 6.10 | [184] | [184] |
| Thermal expansion | $\alpha_a$ | $\mu K^{-1}$ | 3.09 | 5.59 | [137] | [103] |
| Thermal expansion | $\alpha_c$ | $\mu K^{-1}$ | 2.79 | 7.75 | [137] | [103] |

group [41]. These particular cases are not often found in In/GaN crystals, and their natural lack of symmetry along the c-axis will induce a spontaneous polarisation $P_{SP}$. This spontaneous polarisation will be added to the piezoelectric polarisation $P_{PZ}$ induced by mechanical stress, usually due to a lattice mismatch with the used substrate. The total polarization $P$ is simply their sum $P = P_{SP} + P_{PZ}$.

See figure 2.3c and related figure 2.3b for a more detailed description of the In/GaN BG. Physical properties of InGaN all vary linearly with the indium content $X_{In} = \frac{In}{In+Ga}$ (In & Ga in at. %, $X_{In}$ in %), except for the direct InGaN BG $E_g^{InGaN}$. The latter varies in a quadratic fashion with $X_{In}$ instead, or is said to follow Vegard's law, as shown in figure 2.4, and as described in equation 2.14. Vegard's law depends on a bowing parameter $b$, usually ranging from 1.32 eV to 2.87 eV, for strained and relaxed layers respectively [133].

$$E_g^{InGaN}(X_{In}) = X_{In}E_g^{InN} + (1 - X_{In})E_g^{GaN} - bX_{In}(1 - X_{In}) \tag{2.14}$$

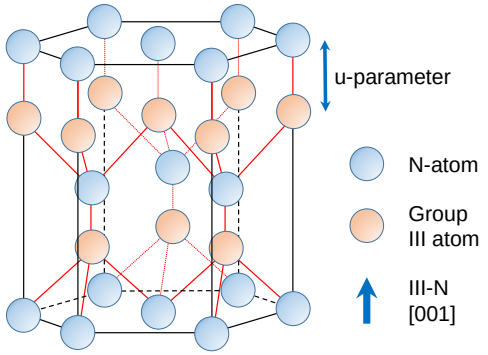


(a) Wurtzite structure of In/GaN, where three unit cells are merged. The specific space group is $P6_3mc$.

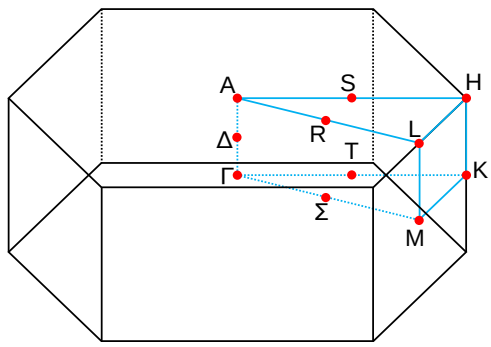


(b) Schematic (not to scale) Brillouin zone of a hexagonal Wurtzite crystal structure.

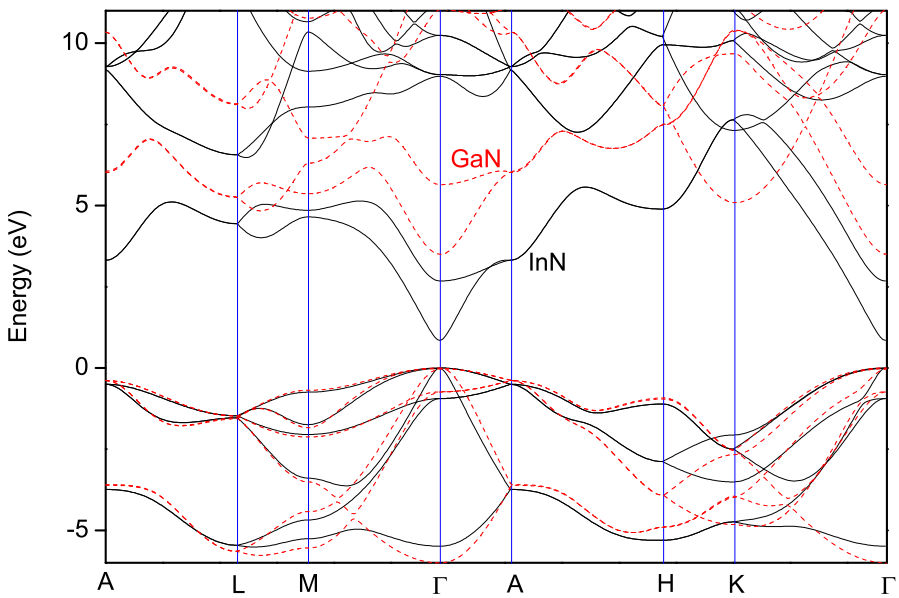


(c) Pseudopotential band structure for InN (plain black) and GaN (dashed red). The figure is generously shared by Bulutay *et al.* [29, 40].

Figure 2.3: Solar cell state of the art, InN and GaN physical properties: structural arrangement.

Comparing In/GaN's bandgap with the one of c-Si with respect to the vacuum level (see figure 2.4b), InGaN films with < 45 % In/(In+Ga) have a CB that is higher than c-Si's VB, which should theoretically result in an Ohmic junction between the two materials [3]. An InGaN/Si tandem solar cell configuration would guarantee a low resistance contact between the two sub-cells [55].

The "Fermi level energy" $E_F$ of a solid-state body refers to the energy level in the band structure that has a 50 % chance of being electronically occupied at any given time, by definition of

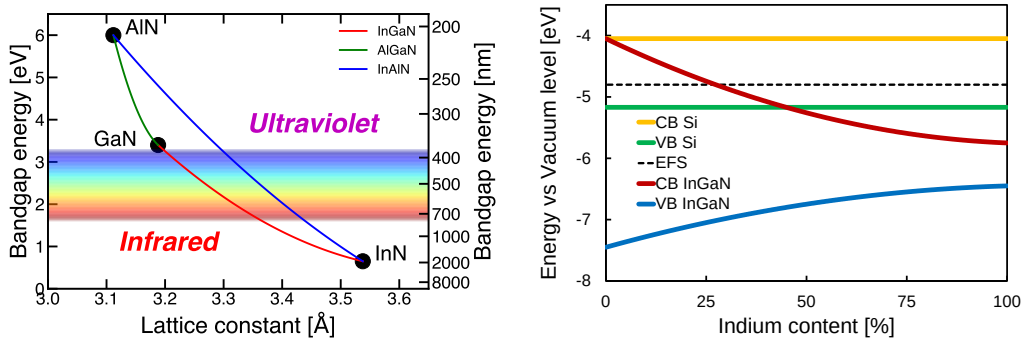


(a) Vegard's law (quadratic relationship between the bandgap and the indium content $X_{\text{In}} = \frac{\text{In}}{\text{In+Ga}}$, In & Ga in at. %, $X_{\text{In}}$ in %) for the In-Ga-Al – nitride group. The Si atoms in the (111) plane have a comparable inter-atomic distance (3.8500 Å) with the In/GaN atoms in the (001) plane.

(b) Band energy position with respect to the vacuum level for intrinsic silicon and intrinsic InGaN. The dashed black line is the Fermi level stabilisation energy $E_{FS}$, which penetrates the InGaN conduction band for the content of In/(In+Ga) higher than 30 % [188].

Figure 2.4: Solar cell state of the art, InN and GaN physical properties: bandgap.

the Fermi-Dirac distribution (see equation 2.1). The "Fermi level stabilisation energy" $E_{FS}$ is defined by Walukiewicz *et al.* as "a reference level for the electronic part of defect annihilation energies". It is shown that the position of the stabilisation energy with respect to the band edges determines the maximum free carrier concentration, which can be obtained through doping" [186]. In other words, in a III-N SC, the position of $E_{FS}$ with respect to the band edges determines the doping density observed in highly defective films. Again according to Walukiewicz, the stabilisation of $E_F$ at $E_{FS}$ "corresponds to a minimum free energy of the defect system in quasi-equilibrium with the free carrier gas" [186]. $E_{FS}$ is located 4.9 eV under the vacuum level [105]. For GaN layers, that energy value falls in the middle of the bandgap, slightly closer to the CB than the VB, thus defects are expected to be created in the mid-gap region, countering the effect of extrinsic doping. On the contrary, $E_{FS}$ penetrates the CB of InGaN compounds for In/(In+Ga) ratios of about 30 % or more (see figure 2.4b) [188]. This induces defects inside the conduction band and naturally leads to an n-type behaviour in defective layers, often degeneratively.

If $E_F$ is intrinsically lower than $E_{FS}$, donor-like defects will form preferentially during growth until $E_F$ approaches $E_{FS}$. Similarly, if $E_F$ is higher than $E_{FS}$, acceptor-like states will grow preferentially. Generally for InGaN, but particularly for InN, a high density of donor-type defects yields a strong free carrier absorption (FCA) in the infrared (IR) and a high optical BG due to the Burstein-Moss (B-M) effect. This led to erroneous reports of 1.7 eV for the BG of InN [4], whereas it stands at 0.7 eV [188].

## 2.3 Solar cell integration

### 2.3.1 Is In/GaN a good candidate for solar cell integration?

Single junction silicon solar cells are slowly but steadily approaching their maximum theoretical efficiency of $\eta_{max}^{c-Si} = 29.4\,\%$ [9]. Alternative materials or structures must be investigated to overcome this theoretical limit. The first efficiency improvement that can be taken is to change the BG of the absorber for a more optimised one with respect to the solar spectrum; the theoretical efficiency limit can be pushed to $\eta = 33\,\%$, with a bandgap of 1.4 eV absorber[117, 152, 27]. Other improvement paths would be to implement the already existing concentrated solar cell technology or to increase the number of absorbers by stacking them on top of one another, where the most simple structure would imply a silicon bottom absorber and a higher energy top absorber. This configuration is a particular case of a tandem solar cell that contains two absorbers: the one with the largest BG placed at the front. All of this can be combined, and today the highest efficiency solar cell ever produced is a six-junction concentrated PV solar cell with an efficiency of 47.1 % [66]. Considering all that, the InGaN alloy is a potentially promising candidate for the following reasons (refer to table 2.1 for more details):

- Tunable BG from the IR to the ultraviolet (UV), spanning across almost the entire solar spectrum (see figure 2.4a).
- Because of this tunable BG, high-efficiency multi-junctions solar cells could be produced (theoretical efficiency of $\eta_{\max^5} = 67\%$ for a five junctions solar cell [97]).
- An InGaN/Si tandem configuration would benefit from the low-cost Si bottom absorber. The optimal indium content of the InGaN top absorber for the maximum possible efficiency ($\eta_{\max^2} = 43\%$, [191]) would be $X_{\mathrm{In}} = \frac{\mathrm{In}}{\mathrm{In+Ga}} = 45$ (In & Ga in at. %, $X_{\mathrm{In}}$ in %, giving a BG value of 1.8 eV). Coincidentally, the same composition enables a perfect alignment between c-Si's VB and InGaN's CB, forming a low resistance contact for the series connection of the two sub-cells (see figure 2.4b) [3, 188, 79].
- Because of its high absorption coefficient, only a few hundreds of nanometers of InGaN on top of a silicon wafer are necessary to absorb most of the higher energy solar light, making the rare earth element indium more cost-effective. In contrast, the optimal thickness of silicon alone is 80 $\mu$m [9], more than a hundred times more.
- This material has other advantages such as: direct BG, high electron mobility and superior radiation resistance [194].
- Alternatively, using InGaN alloys as carrier-selective contacts (CSC) in combination with a silicon PV absorber is another application with high potential interest. In that case, low In-content InGaN alloy (or even GaN) can be used, provided it can be highly n-doped.

For these reasons, there are two leading roles for which InGaN has some potential in a solar cell: as an absorber or as an n-contact. Thus, low-$T$ InGaN layers for PV applications have development potential, but some challenges must be addressed.

### 2.3.2 Reaching a competitive solar cell price

Is developing In/GaN layers for PV use worth the money? If used as a contact or in a tandem configuration, what would it take to make this type of cell as competitive as the current commercial ones? How could an InGaN/Si tandem solar cell be sold for three cts/W, the actual price of a TOPCON solar cell? The short answer is that it seems possible, but the cost inputs and the process steps constantly evolve. In 2018, III-V solar modules often exceeded 150 $/W, 400 times the cost of mainstream silicon-based solar cells at the time (30 cts/W) [78]. But by considering upscaling the production volume and improving the fabrication process, a long-term scenario predicts a III-V/Si tandem solar cell with a net efficiency of 35 % at the cost of 66 cts/W [54]. The higher-than-30 % efficiency achieved here would allow for a 9 cts/W of savings compared to today's prices for silicon solar cell (SSC). That alone justifies the research in III-V materials as potential top-cell in a tandem configuration, even though silicon-based solar cell prices will also evolve in the same way as the long-term InGaN scenario. And if these costs cannot be brought to these levels, cheaper alternative top-cell materials will be required to continue to push the efficiency limit. Typically, a joint research team from EPFL and CSEM achieved a record-breaking efficiency of 31.25 % for a PK/Si tandem solar cell recently [192]. Another model predicts that silicon-based tandem PV modules will become increasingly attractive because of the disparity in the silicon module and area-related balance-of-system learning rates [200]. As mentioned in this study, "The critical challenge to realising this future is the demonstration of a wide-bandgap PV technology with efficiency above approximately 20 %, an areal cost below 100 $/m$^2$, the ability to be integrated with silicon PV cells with little coupling loss (in at least a four-terminal configuration), and sufficient durability to justify 25-year warranties".

### 2.3.3 In/GaN challenges

#### 2.3.3.1 In/GaN p-doping

As stated in section 2.2, really little indium content and slight instability during growth is needed to pin $E_F$ on $E_{FS}$ inside the conduction band, according to the amphoteric defect model [187, 194, 185]. This will naturally or intrinsically n-dope InN and In-rich InGaN materials so that p-dopants' effectiveness inside them is highly reduced, or their concentration must be exaggerated. The causes for the pinning of $E_F$ on $E_{FS}$ leading to degeneracy and the B-M shift of the BG are diverse, according to literature. H, O and N vacancies are shallow donors, while In vacancies act as acceptors in the InN crystal. Here, H vacancies leading to dangling bonds seem to be the main cause for undesired natural n-type doping of InN. The vacancy (or intrinsic defect) concentration can range up to $10^{20} - 10^{21}$ cm$^{-3}$ in thin films, but can be reduced down to $10^{18}$ cm$^{-3}$ by just increasing the film thickness, because the surface effects mentioned in the next paragraph [123, 188]. Oxygen contamination and positively charged nitrogen vacancies along dislocations may be another cause for this behaviour [143].

The particularity of the pinning of $E_F$ inside the CB due to dangling bonds implies some interesting surface effects. Indeed, close to the surface (no more than 5 nm deep), the concentration of intrinsic donors dramatically increases, effectively creating a subsurface depletion region. This can hinder some optical and electrical characterisations, such as spectroscopy and Hall effect measurements, and must be considered when performing them. Not all measurements are affected: photoluminescence (PL) for example, probes 100 nm under the surface, and a relatively good signal can be extracted [123, 188]. But more importantly, it will hinder the InN layer performances when integrated into a device without considering its passivation carefully.

Another reason for the difficulty of growing p-type InGaN layers resides in the limited solubility and the large thermal activation energy of its acceptors (usually Mg). Indeed, larger activation energy lowers dopants' ionisation efficiency, lowering free carrier concentration. This effect is even more pronounced with increasing indium content. This low solubility is mainly due to the formation of $Mg_2N_3$ precipitates during growth [55]. But by controlling the kinetics of Mg incorporation using a low substrate temperature and a specific growth procedure, highly p-type III-nitride films with hole concentrations exceeding $7 \cdot 10^{19}\,\mathrm{cm}^{-3}$ can be produced [71].

#### 2.3.3.2 Growth temperature

Thin films of In/GaN are usually deposited by MOCVD, or by molecular beam epitaxy (MBE), with the occasional assistance of a remote plasma to produce nitrogen radicals, and is then called plasma-assisted molecular beam epitaxy (PAMBE). These are high-$T$ deposition methods [20], 600 °C and higher, which imply three significant drawbacks: (1) favoured InN and GaN phase segregation [140], (2) high manufacturing costs [54], and (3) inability to use glass or other temperature-sensitive substrates [20]. Moreover, in the case of monolithically MOCVD-grown InGaN/Si tandem solar cells, electronically active defects in the bulk of the c-Si wafer can be created by such high temperatures if no specific precautions are taken, which decreases the device efficiency [50, 202]. Growing In/GaN films at lower temperatures would alleviate all these issues, provided sufficient layer quality can be achieved. Plasma-based methods, such as plasma-assisted atomic layer deposition (PAALD) or PECVD, are often used to grow electronic-quality materials at low-$T$ [15, 150, 101, 153], and are therefore also attractive for InGaN compounds.

## 2.4 Research questions

The introduction presented some facts about the current climatic crisis and why the PV technology can be considered the dominating solution to remedy it. Solar cell technologies underwent different (r)evolutions, and many manners to capture solar energy are now available.

The heterojunction solar cell's essence is to reduce surface recombination losses by using a wide BG material to contact the material. Amorphous silicon is the primary candidate for silicon-based cells because this material has a higher BG than silicon, can be n- or p-doped and allows the passivation of silicon by hydrogenation [1]. Different materials to replace a-Si layers are investigated because it has been shown that low transparency and low thermal stability limit the efficiency of the SHJ. Low transparency determines the extracted current density due to the parasitic absorption of light in the amorphous layers. Electron-hole pairs generated in the top layers recombine due to surface recombination and do not contribute to the cell's output current [48]. Transition metal oxides (TMOs) such as $MoO_x$ or $TiO_x$ have been used with promising results, but the poor stability of these materials during solar cell fabrication has been a limiting factor. III-V nitrides are wide BG materials with excellent thermal and chemical stability, and they offer a good alternative to TMO materials. Furthermore, they have been studied for other optoelectronic applications, such as UV lasers and LEDs. indium gallium nitride (InGaN) is an excellent candidate due to its high transparency at low indium content (GaN BG of 3.4 eV) and good band alignment with crystalline silicon (see figure 2.4b). Since the conduction bands of InGaN and Si are well aligned, and the optical BG of InGaN is much higher than Si, InGaN is well suited for electron selective contacts [3]. Furthermore, numerous different deposition techniques exist for InGaN, and n-type doping has been well studied. The downside is that it is usually deposited at high temperatures, with expensive processes that may damage the rest of the solar cell; the goal would be to maintain the quality metrics while lowering the temperature.

This work contributes to the field of absorbing layers for tandem solar cells and carrier-selective layers for silicon heterojunction solar cells. Low-temperature growth (< 400 °C) of InGaN by PECVD or by radiofrequency co-sputtering using a solid GaN target and a solid InGaN target is investigated on glass, silicon and sapphire substrates. Different deposition conditions and film thicknesses are explored as their effect on crystallinity and refractive index, optical BG and Urbach energy, etc. Since the final application of these InGaN layers is to be used as an absorber or as electron-selective contact, these films must have the following properties, which will therefore be the numerical objectives of the experimental results:

- Because doping of a material is much more efficient in the presence of a crystalline material [149], a high crystallinity is sought. But since it is difficult to quantify and compare the degree of crystallinity, this objective is not quantified. However, the degree of crystallinity obtained here is not performant enough to achieve satisfactory electrical results without doping.
- Low electrical resistivity, ideally as low as that of a (n) a-Si layer as used in solar cells (<0.1 Ω cm) [204]
- High transparency of the layers, and thus to obtain an optical BG much higher than amorphous silicon ($E_{04} > 1.8$ eV) [48]
- To obtain better solar cells than the normal SHJ cells, an efficiency higher than 25 %, with a fill factor, short circuit current and open circuit voltage in the order of 80 %, 40 (textured) or 30 (flat) mA/cm$^2$ and 730 mV [115].

Even though depositing InGaN at low-$T$ and using InGaN in solar cells has already been done before, depositing InGaN at low-$T$ for an application in solar cells is innovative. Thus, the present work aims to answer the following four research questions:

1. Is it possible to produce InGaN materials at low-$T$?
2. If yes, how compatible are the characteristics of these layers for PV application?
3. If they are compatible enough, how stable do they remain when p- or n-doping is added?
4. If it is stable enough, once integrated, how well does it compare with standard c-Si solar cells?

In case of success, a new pathway for cheap tandem solar cells can potentially be open, thanks to the low-$T$ deposition processes compared to the expensive and energy-intensive high-$T$ fabrication processes of state-of-the-art III-V materials. Alternatively, it could open the pathway for a more efficient electron contact.

***Nota Bene:*** the "indium content" $X_{\mathrm{In}}$ wording will often be used in this thesis. It does not refer to the atomic or weighted portion of the material that is indium, but rather to the indium to III-material ratio, mathematically expressed as $\frac{\mathrm{In}}{\mathrm{In+Ga}}$, where In & Ga are reported in atomic per cent, and $X_{\mathrm{In}}$ in per cent. Unless specifically stated otherwise, the nitrogen part is assumed to constitute 50 at. % of the layers in every case. This means that "an indium content of 100 %" corresponds in fact to an InN (or $In_{0.5}N_{0.5}$) layer, "an indium content of 0 %" corresponds to a GaN (or $Ga_{0.5}N_{0.5}$) layer, and "an indium content of 30 %" (for example) corresponds to a stoichiometry that could be written in multiple ways: $In_{30}Ga_{70}N$, $In_{0.3}Ga_{0.7}N$, or even $In_{15}Ga_{35}N_{50}$.

# 3 Experimental methods

In the previous chapter, InGaN materials were presented as a good candidate for PV applications, with their related physical quantities reported from the literature. This chapter presents the experimental methods that will enable the measurement of said physical quantities to probe the quality of the material produced. The first part refers to the deposition techniques used to produce InGaN films, the middle part refers to characterisation techniques, and the last part presents a mathematical tool used at different research steps: the design of experiment (DOE).

## 3.1 Film fabrication

High-quality films can be deposited through a physical or a chemical process in a large panel of creative ways. For example, one can use a pure source such as a target, precursors arranged in complex molecules, a dyeing process, etc. In the framework of this research, only PECVD and PVD sputtering were used and are presented here.

### 3.1.1 PECVD processes

Chemical vapor deposition (CVD) is a vacuum deposition method that uses volatile precursors that react and decompose on the flat substrate surface to produce a layer. A pumping system removes volatile by-products of the chemical reaction and the gas flow through the chamber. This chemical reaction can be enhanced by using cold plasma, inside which the precursors react and decompose and drift towards the flat substrate instead of directly reacting at its surface. With plasma, this process is called PECVD (for plasma-enhanced CVD).

#### 3.1.1.1 What is a plasma?

After solid, liquid and gaseous, plasma is considered the $4^{th}$ fundamental state of matter. Although the world population is unfamiliar with this fundamental state of matter, it makes

up most of our universe (excluding dark matter and dark energy). Various types of plasma exist, but the most common one consists of a specific density of electrons, ions, and possibly some neutral particles. "Hot plasmas" are characterised by a similar temperature for the electrons and the ions. In contrast, electrons have a much higher temperature than the ions in "cold plasma". This is possible because of the small mass and cross-section of the electrons compared to all the other constituents of the plasma. Cold plasmas are advantageous for chemical use because the high-$T$ electrons enable interesting high-$T$ chemistry while the low-$T$ ions allow for simple reactor designs. However, whatever the plasma type, it needs to be powered, usually by applying an electric field to accelerate the charged particles [166].

#### 3.1.1.2 Parallel plate reactor deposition process

In a parallel plate reactor, PECVD processes follow quite a simple procedure involving complex physics. Usually, a flat substrate is hung from above the plasma, inside the chamber, to a grounded and heated sample holder. After vacuuming the chamber to rid it of any undesired impurities that may be incorporated in the layer, "precursors" are introduced in the chamber with a flow controlled by a "mass-flow control" (MFC), through a "showerhead" just below the substrate, that is also heated to a controlled temperature. The showerhead is not grounded but electrically insulated from the rest of the chamber, and a voltage is applied to it to feed and power the plasma. In the case of a radiofrequency (RF) source, a matching box is used alongside the RF generator to minimise the reflected power by matching the impedance between the transmitter and receiver (in this case, the plasma) by tuning a series and a parallel adjustable capacitor. Indeed, the power generator, the matching box and the plasma act like a resistor-inductor-capacitor circuit (RLC) in series, where the minimised reflected power is reached when the matchings are tuned to the resonance frequency of the equivalent RLC circuit. The plasma is lit up either spontaneously or with a spark igniter. A turbo and a primary pump usually pump the chamber, and a butterfly valve controls the pressure inside the chamber.

For the In/GaN PECVD depositions presented in this thesis, the precursors are the following: $N_2$-bubbled trimethylindium (TMI) for the indium source, trimethylgallium (TMG) for the gallium source, pure nitrogen $N_2$ or ammonia $NH_3$ for the nitrogen source, and other gases that may influence the deposition or the layer characteristics, such as argon Ar and hydrogen $H_2$. Dopants could be carbon or silicon from methane $CH_4$ of silane $SiH_4$ for either kind of doping or carbon dioxide $CO_2$ for n-doping. Most of these precursors will break down into radicals or possibly into atoms, which will recombine into different species and will eventually drift towards the flat substrate to be deposited. This whole process was studied in the framework of this thesis, and its detailed unfolding is presented in the result section 4.3, page 80.

In a cold plasma, electrons have a temperature (or kinetic energy) far more significant than one of the ions. This implies that at the edge of a cold plasma (called the "plasma sheath"), electrons will fly off more efficiently and negatively charge the surface that the plasma is in

contact with. This will slowly create a countering electric field (called the "Debey shielding"). At some point, an equilibrium is reached where plasma electrons no longer cross the plasma sheath. The transition region has a thickness of one Debey length $\lambda_D$ (see equation 3.1, about 0.1 mm in laboratory plasmas). However, this electric potential will attract the ions from inside the positive plasma, which will drive them towards the substrate, and be deposited with a kinetic energy corresponding to the electric field created by the electrons [82].

$$\lambda_D = \sqrt{\frac{\varepsilon_0 k_B T_e}{n_e q^2}} \tag{3.1}$$

where $\varepsilon_0$ is the vacuum permittivity, $T_e$ is the electron temperature, $n_e$ is their density, and $q$ is the fundamental charge. This equation is only valid when the background medium can be treated as a vacuum ($\varepsilon_r = 1$) and when the mobility of ions is negligible compared to the process's timescale.

#### 3.1.1.3 PECVD using System B

System B is not sold by a supplier "as is", but is more of an accretion of different parts. It consists of one load lock (LL) and two chambers that are primarily pumped by a Leybold Trivac D4B with a 1-ph 220 V 50 Hz motor (chamber 1), an Alcatel 2005SD Pascal dual stage rotary vane vacuum pump (chamber 2), and a Leybold Trivac Hanning Elektro-Werke E8CD4B1-162 (LL). Both chambers are connected to a Pfeiffer TMH-261 Turbo Pump (a switch allows the choice between the two chambers). The RF power is generated by a Leader LG-3211 signal generator and amplified by an Amplifier Research 50A220. The gas flows are controlled by different Brooks GF080CXXC Series metal-sealed thermal mass flow controllers & meters. The pressure is probed by an Inficon Capacitance Diaphragm Gauge CDG025D P/N 378-001 for processing pressures (between 0.1 and 1 mbar) in chamber 1, by a MKS Baratron 622C unheated absolute capacitance manometer for processing pressures in chamber 2, and by two PFEIFFER PKR 251 full range vacuum gauge P/N PT R26 000 for high vacuum pressures, one for each chamber. An adaptive pressure controller PM-3 for VAT series 64 control valves controls the butterfly valve, connected to a VAT F61 butterfly control vacuum valve.

In/GaN films were deposited by PECVD in a parallel plate reactor at various RF powers and frequencies, at pressures ranging between 400 – 800 $\mu$bar and over a temperature range of 150 – 400 °C. Unless stated otherwise, In/GaN layers were co-deposited on glass, polished (001) silicon wafers, and a TEM grid, without pre- or post-treatment. Because of its lower volatility, TMI was bubbled with nitrogen, as shown in figure 3.1. The lowest reachable TMG and $N_2$-bubbled TMI flow rates were 0.05 and 0.3 sccm, respectively.

In terms of errors linked to the operation of System B, the MFCs may have fluctuations of ±0.2 % during the deposition, more significant than the precision of said MFC of ±0.05 %. So

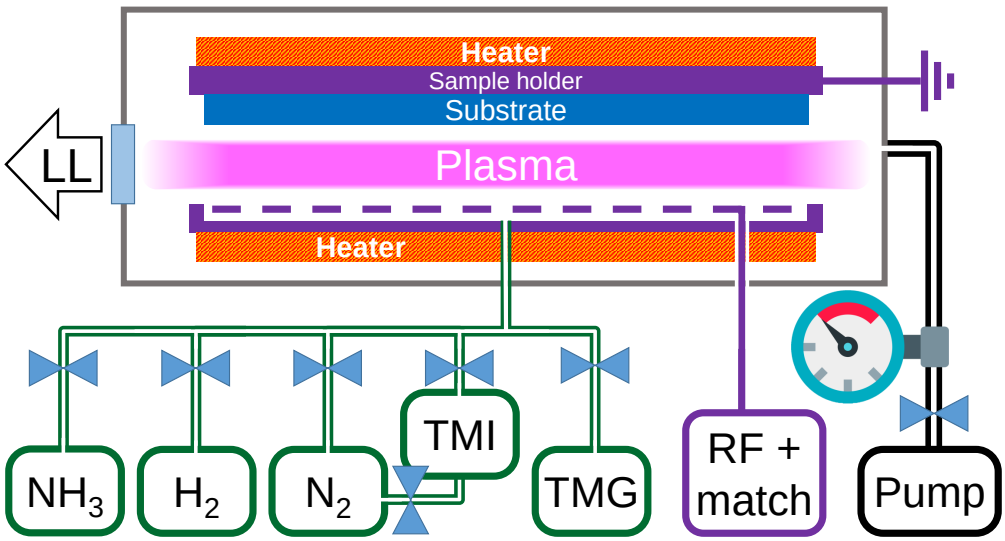


Figure 3.1: Experimental methods, film fabrication: schematic of the RF-PECVD setup used in this thesis. The TMI bottle is bubbled with a small flow of $N_2$, and the wafer hangs "face down" above the plasma. "LL" stands for "Load Lock".

this fixed value will be considered instead and will give rise to errors like the ones presented in table 4.6a, for example. Other deposition parameters can be tuned for a PECVD deposition, where the set pressure also fluctuates wider ($\pm 2\,\mu$bar) than the probe's precision. The RF is usually set to 110 MHz with an accuracy of $\pm 10^{-4}$ and is abbreviated to $\pm 0$. Still, the power is analogue and tuned with the help of a needle, hence its considerable uncertainty of $\pm 4$ W. The temperature is precisely set, but the probe is placed further from the deposition surface, hence its uncertainty of $\pm 2\,°$C. Finally, the time is taken with a precise stopwatch and starts and stops instantaneously, allowing a small error on that measurement of 1 s.

### 3.1.2 PVD processes

Another way to grow high-quality layers is through PVD processes. These processes are characteristics of a source (solid or liquid) vaporised, transported, and deposited in a solid phase, usually under a vacuum. Among other ways to produce such deposition would be by vaporising a source by heating it in a vacuum (sublimation) or by bombarding a solid source in a vacuum with heavy atoms to tear out and expel the source atoms towards the substrate. The second procedure is the primary deposition method used in this thesis for InGaN and is called "sputtering". The first method will be referred to as the "Joule effect" and is usually used to deposit metallic contacts.

#### 3.1.2.1 Dynamics of a sputtering process

Sputtering gas (nitrogen in our case) is introduced inside the chamber at a given pressure. A local high-energy plasma is started right next to the negatively biased target, thanks to which the positive ions of the plasma hit the target at speed proportional to the bias, enough to sputter some target's atoms, with kinetic energy up to tens of eV. Usually, the plasma is an RF alternating one to avoid charging the target, particularly when the latter is insulating. In our case, since the sputtering gas is nitrogen and the target is either InGaN or GaN, "reactive sputtering" can occur, where the sputtered gallium atoms can also react with the radical nitrogen atoms of the plasma before reaching the substrate. The nitrogen from the target also feeds the local plasma. Then, depending on the chamber pressure, the sputtered particles fly either in a straight line and remain un-thermalised (low pressure, $< 10^{-9}$ bar) or follow a random walk while getting thermalised (high pressure, $> 10^{-5}$ mbar) onto the substrate [110]. Suppose the plasma power is high enough and the chamber pressure is low enough. In that case, the sputtered atoms may have enough energy to "re-sputter" the deposited layer off the substrate or even etch it. For compound targets such as the ones used in this thesis, the compound can be formed on the target surface, in-flight or substrate, depending on the process parameters. Depending on the deposition conditions and the substrate temperature, the sputtered particles may still have enough energy to behave like adatoms and re-arrange when reaching the substrate.

The bias difference applied to the target affects almost linearly the film's growth rate, but only if the incident ions have more kinetic energy than the target material's binding energy. The ionisation degree of the plasma is also strongly linked to the potential difference. Too high voltage induces damage in the target and the films due to the target's high bombardment energy, which causes high-energy particles. Moreover, since each surface is negatively charged in a plasma (including the sample if not electrically grounded), the positively charged particles hit the substrate with high energy and damage the films. The main issue of reactive sputtering processes comes from forming an insulating layer on the target (if the target is metallic) or if that insulating layer is naturally present (which is the case of a solid gallium nitride target). This causes positive charging of the target, which leads to electric arcs and stops the deposition process. The applied voltage is either pulsed (pulsed DC sputtering and HiPIMS) or modulated in the radio wave range (RF sputtering) to counter this phenomenon. This work will focus on RF sputtering because it is the sputtering type used to deposit the In/GaN thin films.

The chamber's working pressure is a crucial parameter linked to the mean free path that changes the growth rate and the bombardment energy. These two parameters influence the films' optical, electrical, and structural properties. The pressure must be such that the product between distance and pressure satisfies Paschen's law to initiate a plasma. This limits the pressure range of the process to $10^{-3} - 10^{-2}$ mbar and depends on the electrode material and the gas used. Low pressure induces a large mean free path and reduces the probability of a particle having a collision before hitting either the target or the substrate. Thus, particles have more energy, resulting in a higher growth rate and film density. By reducing the pressure, the

deposition process is limited by the number of particles in the plasma and reduces the growth rate at shallow pressure. A higher deposition pressure reduces particle energy due to a higher collision probability. This reduces the growth rate but generally results in fewer layer defects and a more homogeneous thickness deposition.

The temperature of the substrate has a substantial influence on the film properties. Higher temperature leads to faster adatom mobility and better film crystallinity. At higher temperatures, desorption of adatoms at the sample's surface induces a decrease in growth rate [95]. The effect of the temperature over the material crystallinity and the optical properties has been studied by Jeffries *et al.* [87]. They reported better transparency but a loss of crystallinity at low temperatures (< 400 °C).

#### 3.1.2.2 Sputtering using the Univex

The sputtering depositions were performed in a Lexbold Univex 450 B standard Experimental Vacuum Coating System, P/N 502932V901, with a chamber diameter of 490 mm, equipped with electron-beam evaporators with heatable and coolable chamber walls and with a COOLVAC 3010 cryopump. The pressure was swept between 0.85 and 12 $\mu$bar, the temperature between 200 and 400 °C, and the power stayed constant at 150 W against the InGaN or GaN target. When co-sputtered with a dopant (germanium or silicon), the tested power on the doping target was set between 0 and 100 W.

Fewer deposition parameters can be tuned for the sputtering process and are associated with errors. Most of the setup is digital here, meaning that the errors on the values are pretty minor compared to System B. For the target power, an error of 0.1 W was chosen. The time error, however, is set to ±5 s because of the latency period necessary to open the shutters in front of the targets to start the deposition. The rest is the same as System B: ±2 °C for the temperature, and ±2 % relative error regarding the pressure.

## 3.2 Means of characterization

### 3.2.1 Plasma diagnostics: time-of-flight mass spectrometry

As seen in section 3.1.1.2, PECVD processes are subject to multiple input parameters, making the plasma dynamics pretty complex, and errors are easily induced. But there are ways to gain insight into the plasma processes thanks to a time-of-flight mass spectrometer (TOF-MS).

Time-of-flight mass spectrometry measurements were performed using a TOFWERK process gas analysis time-of-flight mass spectrometer (TOF-MS), "pgaTOF". The working principle relies on kinematics, where a molecule is ionised and accelerated through an electric potential $U$, called an "extractor". The acceleration depends on the charge $q$ and the mass $m$, where a lighter or a more charged molecule will display a faster exit speed $V$. After some "time of flight"

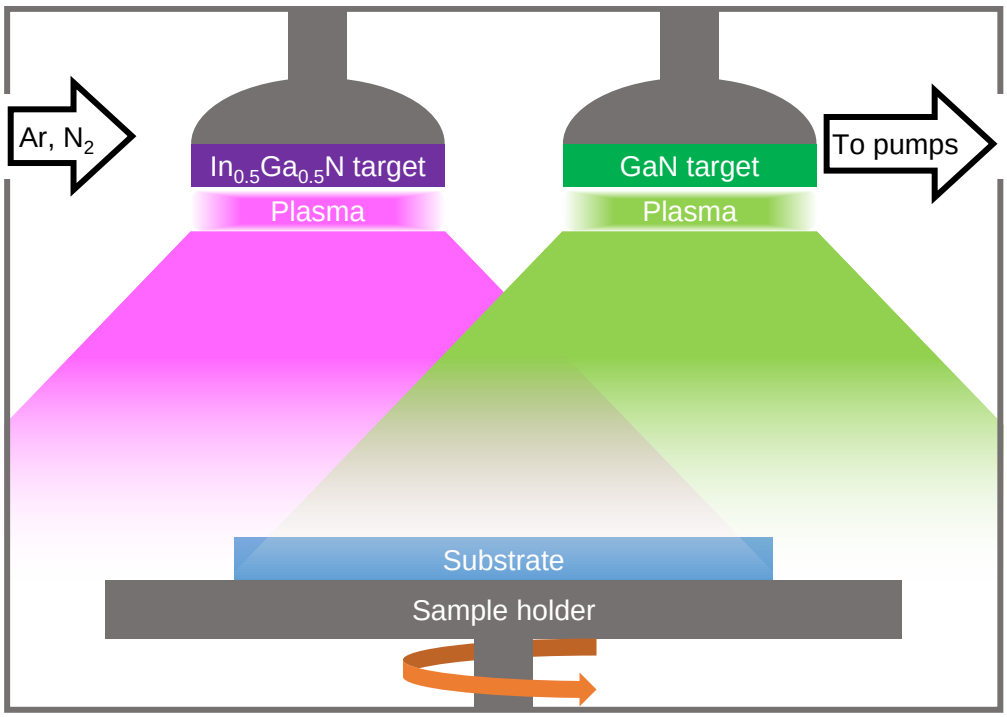


Figure 3.2: Experimental methods, film fabrication: schematic of a co-sputtering process, using two targets. The etching gases are introduced and activated in a plasma close to the target for efficient etching.

$t_{\mathrm{TOF}}$ across a "flight tube" of length $d$, all the charged molecules hit a detector, the heaviest last. Depending on the arrival time, a $m/q$ value can be extracted, and a molecule can be identified.

$$
\begin{aligned}
E_{\mathrm{kin}} &= \frac{1}{2} m V^2 \\
E_{\mathrm{pot}} &= qU \\
t_{\mathrm{TOF}} &= \frac{d}{\sqrt{2U}} \sqrt{\frac{m}{q}} = k \sqrt{\frac{m}{q}}
\end{aligned}
\tag{3.2}
$$

where $k$ is a constant that depends on the TOF-MS working parameters $d$ and $U$. Given the nature of the process, the extracted signal must be pulsed to give enough time for the heavier species to reach the detector before the lighter ones from the next pulse arrive. Of course, the period of the pulse can be tuned to detect heavier molecules, or lighter ones, down to the single hydrogen atom. Knowing all these aforementioned tunings, it is possible from the intensity of an identified peak to extract the exact number of its molecules per pulse and thus its real concentration in the flow passing through the extractor, which should reflect its concentration at the probed location. Therefore this tool was attached to the exhaust tube of System B and allowed the analysis of non-charged plasma by-products. For a plasma

by-product to be detected, it has to go through two pin-holes protecting the necessary high vacuum of the TOF-MS (less than 1 nbar) from the relatively high pressure of the deposition process (around 0.5 mbar). This is why charged molecules ejected from the plasma can not be detected in this configuration; they quickly encounter a wall on which to stick. Analysing the plasma by-products with a TOF-MS can lead to a back-analysis of the plasma dynamics that took place during a deposition process and how a given parameter change can, for example, reduce carbon assimilation in the layer.

Depending on the molecule, some share almost the same mass-to-charge ratio, such as, for example, $C_2HO^+$ (41.002 u/C), $C_2H_3N^+$ (41.026 u/C), $C_3H_5{}^+$ (41.039 u/C), and $BMe_2{}^+$ (41.056 u/C) (see more details about the detection of these exact species in section 4.3.4.4, page 98). Given the time resolution of the detector, the TOF-MS that was used for this thesis is precise enough to differentiate between these species all at once. That would not have been anywhere possible with a "standard" quadrupole mass spectrometer, which lacks that precision. Another perk of the TOF-MS is that a wide range of mass-to-charge ratios can be probed simultaneously, while the standard MS can only probe one ratio at a time. This feature allowed the quick observation of unexpected species in the exhaust pipe.

The different $m/q$ values are usually recorded as a function of time. This means that the TOF-MS eventually outputs two signals that can be analysed: the spectrum of all $m/q$ values at a precise time (or averaged over a certain period), and the evolution over time of certain $m/q$ values, where a change in these critical values are usually linked to changes made during the deposition process. See figure 4.23 page 101, displaying both types of signals. The latter kind of information is, in fact, the integral of the signal (the surface of the peak) around the observed peak of interest, $\pm 0.5$ u/C (see figure 3.3 for a visual understanding). In other words, analysing the evolution of, for example, the peak n° 30 in figure 4.23 (referred to as "$P_{30}$") amounts to observe the added contributions of all the present species that have a $m/q = 30$ u/C ratio over time: $SiH_2{}^+$ and $CH_4N^+$ in this example. To differentiate the respective contribution of each species showing a similar $m/q$ value, the peak of interest must be deconvoluted at every timestamp, and their integral must be displayed again as a function of time. Here, the tool has more of a role of identification; no error is considered.

### 3.2.2 Photon-matter interactions

When light encounters tangible elements, it becomes altered following quantum mechanics (or Maxwell's equations for lower energies), where the nature of the interaction mainly depends on the energy of the electromagnetic wave (see table 3.1). This section explores how one can probe a material's characteristics using electromagnetic waves, most of which are used in this thesis.

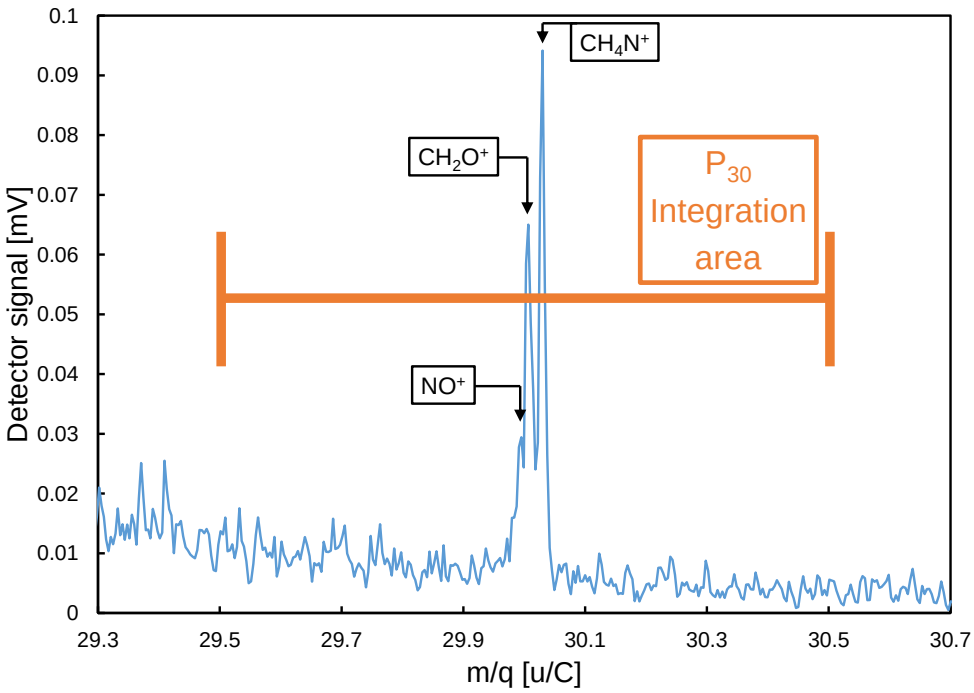


Figure 3.3: Experimental methods, plasma diagnostics: peak integration of $P_{30}$ is done between 29.5 and 30.5 u/c. Over time, different species contribute to the evolution of $P_{30}$, and a deconvolution may be necessary.

#### 3.2.2.1 Raman spectroscopy

Raman measurements were performed using a MonoVista Confocal Raman System (MonoVista CRS+) setup from Spectroscopy & Imaging GmbH, with a UV laser wavelength of 325 nm. Unless stated otherwise, Raman spectroscopy was always performed on layers deposited on silicon wafers. It identifies the vibrational modes of the crystal and relates them to crystallinity and stress measurements of the probed layer. Raman spectroscopy relies on the inelastic scattering of photons, known as Raman scattering, where the scattered beam's energy loss (or gain) relates to vibrational signatures, such as phonon energy from the system or molecular vibrations. The challenge in this kind of measurement is to filter out the coherent elastic reflected light to observe only the inelastic one. Raman shifts are typically reported in wavenumbers $[\mathrm{cm}^{-1}]$. The typical In/GaN observed modes are displayed in table 3.2 and correspond to a lattice vibration displayed in figure 3.4. Assuming that the $A_1$(LO) peak is a sum of Gaussian or Lorentzian functions, it can be deconvoluted into different chemical bonding signatures, also displayed in the middle part of the same table. Apart from that, other artefacts or parasitic signatures can appear in this range of energy. These may be attributed to the silicon substrate, water vapour, or other contaminant. The main contributions are displayed in table A.1, in appendix A.1.

Table 3.1: Experimental methods, photon-matter interactions: energy ranges. The energy range is generously rounded.

| Energy range | Interaction description |
|---|---|
| $10\,\text{cm} < \lambda$<br>$10\,\mu\text{eV} > E$ | **Radiowaves** have just enough energy to cause polar molecules to vibrate back and forth, slightly increasing the temperature of the medium. They can also push electrons of metal, creating small oscillating currents that can be detected as signals (hence their name: "radiowaves"). Similarly, this is equivalent to a SC's FCA's energy range. |
| $1\,\text{mm} < \lambda < 10\,\text{cm}$<br>$1\,\text{meV} > E > 10\,\mu\text{eV}$ | **Microwaves** can rotate and wring molecules, and produce heat as a result of that molecular motion, only for non-metals. For metals, the effect is the same as radiowaves: microwave will create internal electrical currents, generating heat. |
| $750\,\text{nm} < \lambda < 1\,\text{mm}$<br>$1.6\,\text{eV} > E > 1\,\text{meV}$ | **Infrared** will produce molecular vibrations that will quickly heat non-metallic materials. For metals, an even stronger internal current is generated. |
| $380\,\text{nm} < \lambda < 750\,\text{nm}$<br>$3.2\,\text{eV} > E > 1.6\,\text{eV}$ | Only **visible light** will trigger a photosensitive response in the human retina. This range of electromagnetic energy can promote electrons to higher energy levels. |
| $10\,\text{nm} < \lambda < 380\,\text{nm}$<br>$100\,\text{eV} > E > 3.2\,\text{eV}$ | **Ultraviolet** light triggers the photoelectric effect, or photoionisation, whose discovery granted Einstein its Nobel prize. |
| $10\,\text{pm} < \lambda < 10\,\text{nm}$<br>$100\,\text{keV} > E > 100\,\text{eV}$ | **X-ray** energies are far above the ionisation energies of atoms. They cannot be absorbed in electron transitions between states for most atoms. Because of that, X-ray photons can only interact with one electron by knocking it out of an atom. |
| $\lambda < 10\,\text{pm}$<br>$E > 100\,\text{keV}$ | **Gamma rays** are even more powerful ionizing radiations. The minuscule wavelength allows it to pass between the atoms and penetrate deep into matter and organic tissues. These electromagnetic waves are also capable of spontaneously creating an electron-positron pair. |

Among the six main vibrational modes mentioned in table 3.2 and displayed in figure 3.4, $A_1$(LO) and $E_1$(LO) are the ones that relate to the layer crystallinity: the sharper they are, the more crystalline the layer. And similarly, as with X-ray diffraction (XRD) (see section 3.2.2.5), an x-shift of the peak position relates to stress in the layer.

Since the intensity of the peak depends on the measurement conditions, its arbitrary units usually do not correlate to physical quantities. However, it is possible to compare the area of the peaks with each other. This technique is frequently used to determine the Raman

Table 3.2: Experimental methods, Raman: vibrational modes of wurtzite In/GaN bulk in $cm^{-1}$ [169, 59, 174, 167, 96, 175, 146, 74, 13] (part 1/3). The $A_1$(LO) peak can be deconvoluted to extract different stretching vibration signatures [122, 67] (part 2/3). Other In- or Ga-related vibration modes are displayed in the third part of the table with their sources. The abbreviations TA, LA, TO and LO stand for "Transverse Acoustic", "Longitudinal Acoustic", "Transverse Optical" and "Longitudinal Optical", respectively.

| Signature mode | GaN [$cm^{-1}$] | InN [$cm^{-1}$] |
|---|---|---|
| $E_2^L$ | 144 | 87 |
| $A_1$(TO) | 532 | 447 |
| $E_1$(TO) | 559 | 476 |
| $E_2^H$ | 568 | 488 |
| $A_1$(LO) | 734 | 586 |
| $E_1$(LO) | 741 | 593 |
| N – Ga – H | 720.28 | |
| Ga – N | 736 | |
| H – Ga – Ga | 755.46 | |
| Ga – N – H | 775.06 | |
| GaN – C [108] | 610 | |
| CB electron plasmon [19] | | ~ 2000 |
| In – H stretching [19] | | 1650 – 1700 |

crystallinity $\chi_C$ of silicon layers [100, 177], defining the portion of the layer that is crystalline, expressed as such:

$$\chi_C = \frac{I_c}{I_c + yI_a} \qquad y = \frac{I_c \alpha_c}{I_a \alpha_a} \tag{3.3}$$

where $I_c$ is the area of the integrated c-Si peak at 520 $cm^{-1}$, $I_a$ is the cumulated area of the two integrated a-Si and $\mu$c-Si peaks at 480 and 510 $cm^{-1}$ respectively, $y$ is a cross-section ratio, where $\alpha_c$ and $\alpha_a$ are the absorption coefficients of the fully crystalline and fully amorphous layer, respectively, at the same laser wavelength. In the literature, this value varies between 0.8 and 1.7 for a 514.5 nm laser [100]. In this work, it will be determined using ellipsometry and spectroscopy.

The information extracted from the Raman measurement originates from a Gaussian fitting of the peaks of interest. The error on the amplitude $A$, peak position $\mu$ and width $\sigma$ will depend on the peak itself and the quality of the signal but should not be larger than 1 % relative, 0.2 $cm^{-1}$ and 0.2 $cm^{-1}$ respectively.

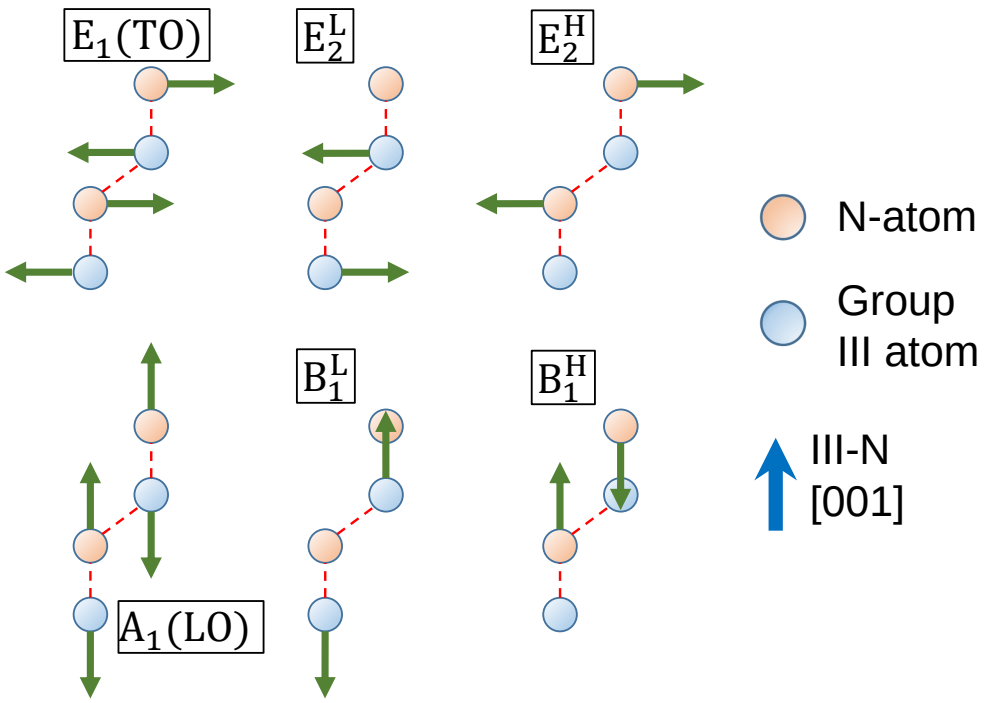


Figure 3.4: Experimental methods, Raman: vibrational modes of wurtzite In/GaN bulk. Compare with figure 2.3a.

#### 3.2.2.2 Fourier-transform infrared spectroscopy

Fourrier-transform infrared spectroscopy (FTIR) measurements were performed by means of a VERTEX 80 FTIR spectrometer from Bruker. Unless stated otherwise, FTIR was always performed on layers deposited on silicon wafers. The same information as with the Raman can be probed here (crystallinity and vibrational modes), but in an absorption mode (not in an emission mode, like for the Raman) and at higher energies. By integrating certain peaks of the exported spectrum and comparing them, it is also possible to determine the concentration of certain species or a type of bond within the layer.

Typical measurements were averaged on 64 scans. FTIR uses the IR spectrum (precisely between 0.05 and 0.75 eV for this thesis) to probe different absorption modes in the deposited layer. Contrary to Raman spectroscopy which excites vibrational states to extract emission peaks by inelastic excitation, FTIR shines IR light through a sample and then collects it in our case. In this way, the observed energies are absorbed by the layer's vibrational states and then subtracted from the transmitted spectrum, at identifiable energies. The setup is purged with $N_2$ to reduce artefacts from $H_2O$ and $CO_2$ absorption otherwise present throughout the whole beam path. Like with Raman spectroscopy, the spectrum is usually expressed in $cm^{-1}$.

At this energy level, the substrate (usually a c-Si wafer) also alters the signal and must be considered. Given the thinness of the layer $d_L$ and of the wafer $d_{Si}$ compared to the IR

wavelength, interferences can be neglected, and only the exponential decay law is applied across the whole layer stack.

$$I_L = I_0 \cdot \exp(-\alpha_S d_S) \cdot \exp(-\alpha_L d_L) \tag{3.4a}$$

$$I_S = I_0 \cdot \exp(-\alpha_S d_S) \tag{3.4b}$$

where $I_0$ is the intensity of the incident beam, $I_L$ is the intensity of the transmitted beam through the layer and the substrate, while $I_S$ is the one through the substrate alone, and $\alpha$ is the absorption coefficient (of the layer or the substrate). By measuring the bare substrate and the layer on top of the substrate, it is possible to extract the absorption coefficient of the layer [90, 88]:

$$\alpha_L = \frac{\ln\left(\frac{I_L}{I_S}\right)}{-d_L} \tag{3.5}$$

The same method used for Raman spectroscopy can then be used here for FTIR, where the area of peak signatures can be compared among the samples, for example, to determine the qualitative carbon concentration of the layer of In/GaN [84].

It is also possible to use FTIR measurements to quantify the real concentration of a signature peak. For the sake of example, let us consider the three Si – H peaks centred around 2060 $\mathrm{cm}^{-1}$ (see table A.1 in appendix A.1). Indeed, the absorption coefficient extracted in equation 3.5 is expressed in $\mathrm{cm}^{-1}$, so the area under the peak $A_{2060}$ should correspond to a surface density of the Si – H bond, by a factor $A^s_{\mathrm{Si-H}}$. Dividing it by the thickness will result in a bulk concentration in $\mathrm{cm}^{-3}$. According to the literature [49, 160, 161, 28], the surface concentration [Si – H] and the bulk concentration $C_{\mathrm{Si-H}}$ will be determined by the following equations:

$$\begin{aligned}[\mathrm{Si-H}] &= \frac{cn\omega_t\mu}{2\pi^2 e_s^{*2}} \int \frac{\alpha(\omega)}{\omega} \mathrm{d}\omega \\ &= nA^s_{\mathrm{Si-H}} \cdot A_{2060}\end{aligned} \tag{3.6}$$

$$C_{\mathrm{Si-H}} = \frac{nA^s_{\mathrm{Si-H}}}{d} \cdot A_{2060} \tag{3.7}$$

where $c$ is the speed of light, $n$ is the refractive index, $\omega_t$ is the peak position, $\mu$ is the Si – H reduced mass, and $e_s^*$ is the Si – H bond effective charge. Different values exist for the factor $A^s_X$, whereas the following will be chosen [76, 183]: $A^s_{\mathrm{Si-H}} = 2.58 \cdot 10^{19}$. The last step would be to determine the hydrogen concentration of the layer $C_{\mathrm{H}}$, instead of the Si – H bond

concentration $C_{\text{Si-H}}$. For an a-Si:H layer containing a little bit of carbon for stability, this concentration is obtained as follows [183]:

$$C_{\text{H}} = \frac{C_{\text{Si-H}} + C_{\text{C-H}}}{C_{\text{Si}} + C_{\text{C}} + C_{\text{Si-H}} + C_{\text{C-H}}} \tag{3.8}$$

where $C_{\text{C-H}}$ can also be determined by an FTIR measurement using the triple-combined peak around 2960 $\text{cm}^{-1}$, with $A^{s}_{\text{C-H}} = 1.35 \cdot 10^{21}\,\text{cm}^{-2}$ (also in table A.1) [90]. However, $C_{\text{Si}}$ and $C_{\text{C}}$ have to be determined with another method, such as elastic recoil detection (ERD) or Rutherford backscattering (RBS). These methods can also help to calibrate the FTIR and precisely determine the components of the constants implied in the different concentration determinations.

Similarly to the Raman, the information extracted from the FTIR tool depends on the fitting quality, and the errors considered for the raw measurement are the same. They are then propagated to the values of interest with the uncertainty propagation method, generalised in the following equation (consider applying this to equation 3.7 for example, where $C_{\text{Si-H}}$ depends on three measurements with each its error: $n$, $A^{s}_{\text{Si-H}}$ and $d$):

$$\Delta f(x,y,z) = \sqrt{\left(\frac{\partial f}{\partial x}\right)^2 \cdot \Delta x^2 + \left(\frac{\partial f}{\partial y}\right)^2 \cdot \Delta y^2 + \left(\frac{\partial f}{\partial z}\right)^2 \cdot \Delta z^2} \tag{3.9}$$

where $\Delta f$ is the propagated uncertainty calculated from the measurement errors $\Delta x$, $\Delta y$ and $\Delta z$.

#### 3.2.2.3 Ellipsometry

Ellipsometry measurements were performed using a Horiba UVISEL ellipsometer. Unless stated otherwise, ellipsometry was always completed on layers deposited on glass wafers. It allows the measurement of the layer's optical properties, its thickness and even some electrical properties can be deduced in some cases. Ellipsometry takes advantage of polarised light, where the interaction with matter will induce a phase shift in the reflected photon's polarisation, depending on the nature and thickness of each probed layer, the photon energy and the incident angle.[I] More details about the ellipsometry measurement and functioning are in appendix A.2

The complex dielectric permittivity (described in equation A.6 in appendix A.2) that was extracted from the ellipsometry measurement does not correspond to the physical quantities

[I] Ellipsometry measurements can also be performed in transmission mode.

of natural material, but rather to the stack of layers probed as a whole. Therefore it is often called pseudo dielectric function, whereas the properties of the individual layers can only be extracted by modelling. Hence, the modelling of the stack of layers becomes relevant here.

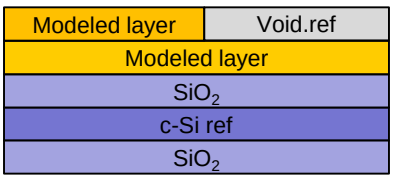


Figure 3.5: Experimental methods, ellipsometry: a modelled stack of layers for the ellipsometry measurement, with a silicon wafer here.

In the present thesis, the chosen model will primarily constitute the analysed layer on top of the substrate. The layer consists of the bulk and a roughness layer (a mix of 50% of the bulk layer and 50% of vacuum) on top. Reference data will model the substrate and will not take part in the fitting of the model. The only fitted parameters are the thicknesses of the film and the roughness layer and the modelled properties of the layer. See figure 3.5 for a better understanding.

The real and imaginary parts of the optical properties of solids are energy-dependent. This dependency can be described by so-called "dispersion formulae", classified into the following groups: empirical formulae, classical oscillator models, amorphous and multiple oscillator models, and transition-based models. Each has its strength and weaknesses; the goal is to describe best the three kinds of absorptions in the material: interband absorption, intraband absorption, and FCA. The choice was set on a combination of a Tauc-Lorentz (T-L) oscillator for the main absorption above the BG and a Drude oscillator for the FCA. The T-L oscillator uses five parameters ($\varepsilon_0$, $E_g$, $A$, $E$ and $C$) and models the dielectric constant in the following way [170]:

$$\varepsilon_r(E) = \varepsilon^{\infty} + \frac{2P}{\pi}\int_{E_g}^{\infty} \frac{\xi\varepsilon_i(\xi)}{\xi^2 - E^2}\mathrm{d}\xi \tag{3.10a}$$

$$\varepsilon_i(E) = \begin{cases} \frac{1}{E}\cdot\frac{AE_0C(E-E_g)^2}{(E^2-E_0^2)^2+C^2E^2} & , E > E_g \\ 0 & , E < E_g \end{cases} \tag{3.10b}$$

where $P$ is the Cauchy principal value containing the residues of the integral at poles located in the lower half of the complex plane and along the real axis. The Drude model uses two parameters ($\omega_p$ and $\Gamma_d$) and models the dielectric constant in the following way:

$$\varepsilon_r(\omega) = 1 - \frac{\omega_p^2}{\omega^2 + \Gamma_d^2} \tag{3.11a}$$

$$\varepsilon_i(\omega) = \frac{\omega_p^2 \cdot \Gamma_d}{\omega\left(\omega^2 + \Gamma_d^2\right)} \tag{3.11b}$$

$$\omega_p = \sqrt{\frac{Ne^2}{m\varepsilon_0}} \tag{3.11c}$$

In particular, the Drude part of this composed dispersion describes the FCA, which can be linked to the electrical properties of the layers. Indeed, based on the work of Fujiwara [64] and Humlicek *et al.* [81], the carrier concentration $n$, the resistivity $\rho$ and the mobility $\mu$ of the characterised layer can be extracted in the following way:

$$n = \frac{m^* \varepsilon_0 \varepsilon^\infty \omega_p^2}{(e\hbar)^2} \tag{3.12}$$

$$\rho = 7435 \frac{\Gamma_d}{\omega_p^2} \tag{3.13}$$

$$\mu = \frac{e\hbar}{m^* \Gamma_d} \tag{3.14}$$

These parameters depend on the effective electron mass $m^*$, displayed in table 2.1. However, these values also depend on the defect concentration and will be corrected accordingly (see figure 13 of Walukiewicz *et al.*'s work [188]), usually to a value of $m^* = 0.25 m_e$.

Instead of using $R^2_{adj}$ like for the design of experiment method (see equation 3.48, page 60), here the goodness of fit will be tested by the chi-square test [165], defined as:

$$\chi^2 = \sum_i \frac{(O_i - E_i)^2}{E_i} \tag{3.15}$$

where $i$ refers to one of the experimental points, $O$ refers to the observed value, while $E$ is the expected one, be it $\Delta$ or $\Psi$. The downside of this test is that a high number of points are necessary to be significant. But its advantage lies in its versatility: any observation linked to the optically probed layer can be included in the fitting process. In that sense, experimental ellipsometry measurements can be coupled with FTIR and spectroscopic experimental measurements, referred to as "multi-modelling".

However, for multi-modelling to make sense, one must verify that the layer stays the same throughout all measurements methods: be it the thicknesses of the bulk and roughness layers, as well as the optical properties modelled by the T-L and Drude dispersions. And indeed, depending on the substrate, some changes may appear, where an amorphous substrate such as glass will generally induce less crystallinity, less conductivity, and a less dense layer (resulting

in a higher thickness) compared to a silicon wafer. The layer must also remain homogeneous on the substrate surface, where the probed volume may differ and be slightly mislocated between the other methods. If all the assumptions linked to physical properties conservation between the different characterisations are verified, then multi-modelling makes sense.

In terms of error, they are usually given by the fit process performed by the Horiba software used with the Horiba UVISEL ellipsometer and are generally insignificant. However, since some of these values are often compared with other tool results (thickness with the profilometer, optical characteristics with the spectrometer), and since the probed area might slightly change between measurements, a more significant constant error is considered to englobe all those differences. Mainly, the error on the thickness is chosen as ±10 nm and the error on the bandgaps is determined as ±0.03 eV.

#### 3.2.2.4 Spectroscopy

UV-VIS-IR spectroscopy measurements were performed using a Perkin Elmer – Lambda 950 spectrometer for optical transmission and absorption using an integrating sphere. Unless stated otherwise, UV-VIS-IR spectroscopy was always completed on layers deposited on glass wafers. Spectroscopy results are similar to ellipsometry results, but the light here is not polarised, and the extracted values are not modelled. It allows the extraction of the absorption coefficient, from which three values can be exported: the optical BG $E_{04}$, the Tauc-BG $E_T$ and the Urbach energy $E_U$.

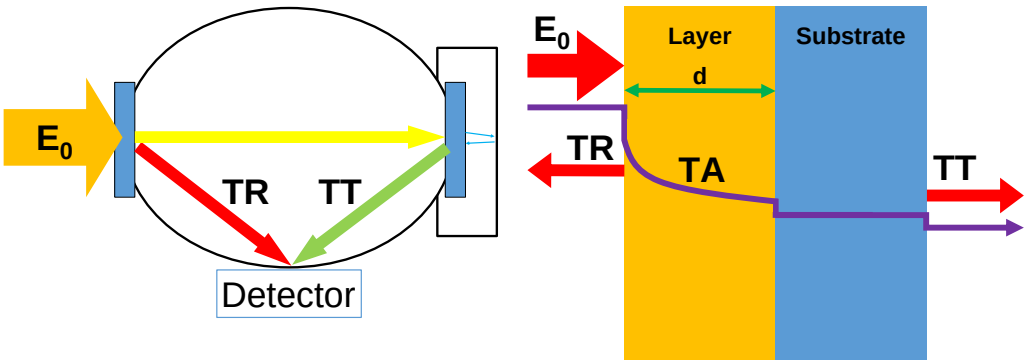


(a) UV-VIS-IR spectroscometer using an integrating sphere. The total transmission *TT* and total reflectance *TR* configurations place the layer (the blue rectangle) before and after the integrating sphere, respectively. The *TR* measurements do not take the reflection against the black absorbing cover (blue arrows) into account.

(b) Zoom in on the layer and its substrate: total transmittance *TT*, total reflectance *TR* and total absorbtance *TA* of a layer of thickness $d$. Interface interferences and internal reflections are not taken into account. The purple arrow denotes the light intensity decrease along the path.

Figure 3.6: Experimental methods, UV-VIS-IR spectroscopy: tool and measurement method for total transmission *TT*, total reflectance *TR*, and the deduced total absorptance *TA*.

The incident light is normal to the surface, a particular case of the set of equations A.4. Indeed, when $\theta_i = \theta_t = 0$, then at any interface, we have

$$R_{\parallel} = R_{\perp} \equiv R = \left| \frac{n_i - n_t}{n_i + n_t} \right| \tag{3.16a}$$

$$T = 1 - R \tag{3.16b}$$

However, the contribution to the signal from the layer alone cannot be extracted because of the unknown interaction between the layer and the substrate. In other words, there is no way to separate the contribution of the substrate from one of the layers, mainly because of all the internal reflections due to the comparable wavelength of the probing light. This was indeed not a problem with the FTIR (see equation 3.5), but applying here the same method is not possible since internal interferences have to be taken into account. So instead of considering each contribution, one solution is to measure the total transmittance ($TT$) and total reflectance ($TR$) of the whole stack (layer and substrate), which are, by definition, the fraction of the incident light that was transmitted and reflected respectively. These two fractions do not comprise the whole light intensity; a fraction of the incident light was absorbed, referred to as the total absorptance ($TA$).

$$1 = TT + TR + TA \tag{3.17}$$

By assuming that only the layer absorbs part of the incident light when the bandgap of the substrate is large enough and by assuming that the absorption follows an exponential decay law with respect to the crossed thickness (as schematised by the purple line in the "layer" region of figure 3.6b), then an approximation for the absorption coefficient $\alpha$ can be extracted.

$$I(x) = I_0 e^{-\alpha x}$$

where $I_0$ is the light penetrating the layer $I_0 = TA + TT = 1 - TR$, and $I(x = d)$ is the light transmitted through the layer $TT$. It follows that

$$\alpha = \frac{\ln\left(\frac{TT}{1-TR}\right)}{-d} \tag{3.18}$$

From the absorption coefficient $\alpha$, a few methods exist to determine the BG of the probed layer [201], each with their advantages and inconveniences, but only three of them will be

presented here. There is more than one way to assess the BG because in disordered SC, tail states in the CB and VB start to appear, and the definition of "BG" becomes blurry.

The first one has already been presented in the ellipsometry section, where the T-L BG $E_{TL}$ is extracted from a fitting procedure and corresponds to the beginning of the absorption inside the material. However, because of the presence of these tail states, the value of the T-L BG may be slightly underestimated. Indeed, the fitting procedure may be slightly off compared to the other two because of the imperfections inducing a high defect concentration in the materials characterised here.

The second method is the Tauc-BG $E_T$. As in the crystalline case, it assumes that the density of electron states close to the VB and CB extrema is proportional to the square root of the photon energy. By fitting this kind of relationship on the absorption coefficient spectra, or by fitting a line on the "$(\alpha/E)^{1/r}$ versus $E$" plot, the bandgap is determined at a zero absorption, where the exponent here depends on the type of transition (allowed or not, direct or indirect). This type of BG considers tail states and is particularly suited for non-crystalline materials but has the disadvantage of a fitting procedure. In particular, crystalline In/GaN has a direct BG (see figure 2.3c, supposedly $r = 1/2$). Still, the results are off by about 1 eV compared to the indirect allowed transition value for the exponent $r = 2$. On top of that, an important quantity of defects in the BG will contribute to energy transitions similar to the ones of a perfect material; they will deform the absorption curve precisely where the fit is performed. Because of all these reasons, the third method is preferred.

The third BG determination method is straightforward and derives from spectroscopy: the so-called "optical bandgap" $E_{04}$ is the energy value at which $\alpha = 10'000\,\mathrm{cm}^{-1}$. This definition is mainly used when the tail states extend so much that there is a continuous non-zero state density between the intrinsic CB and VB edges. At that point, the energy levels inside the bandgap are not forbidden anymore, although absorbing less than $10'000\,\mathrm{cm}^{-1}$, hence the blurry definition of "bandgap" in that case. This third method is chosen because the "non-zero state density between the CB and the VB" is observed in most of the layers. In particular, the first method perfectly works for sharp band edges, and the second method can tolerate an exponentially decreasing state density which will be perfectly fitted. The high defect density mentioned in the previous paragraph will, in fact, not impact the absorption rate at high values such as $10'000\,\mathrm{cm}^{-3}$, which allows for a way more consistent approach. Its downside is that this optical BG is overestimated compared to the other methods.

Among all the results that UV-visible (VIS)-IR spectroscopy has to offer, this last one serves as a quality metric: the measurement of the Urbach energy $E_U$. $E_U$ is evaluated by fitting the tail region of the absorption coefficient below the bandgap to the exponential given by equation 3.19 [181], where $\alpha_0$ and $E_1$ are the two empirical fitting parameters. A lousy quality SC will have an Urbach energy above 0.1 eV, while a relatively good SC will manage to reach values below 50 meV.

$$\alpha(E) = \alpha_0 \cdot \exp\left(\frac{E - E_1}{E_U}\right) \tag{3.19}$$

Regarding uncertainty, the measurement of $TT$ and $TR$ is precise with a ±1 % absolute error. When propagated to physical quantities such as $E_{04}$ (see equation 3.9). Considering the error discussion at the end of the previous section, a larger error is considered for the extracted values $E_{04}$, $E_T$ and $E_U$, respectively of ±0.03 eV, ±0.03 eV and 4 meV.

#### 3.2.2.5 X-ray diffraction

X-ray diffraction (XRD) measurements were performed using a Multi-Purpose Diffractometer (MPD) PANalytical Xpert Multipurpose X-ray Diffraction (XRD) System. Unless stated otherwise, XRD was always performed on layers deposited on silicon wafers. It allows the detection of interplanar distances in a crystal, and the result post-processing allows the measurement of the crystallinity and the strain inside a layer and the deduction of the indium content $X_{\mathrm{In}}$. This section is fully based on Mote *et al.*'s article [125].

XRD is a versatile non-destructive method that probes structural properties like phase composition, structure and texture. The measurement is performed by shining a sample with X-ray photons and collecting them after the interaction. Usually, electrons strike a copper source, and the photons produced are filtered and directed so that only the K-$\alpha$ transition is shone out of the source in a parallel fashion. The Cu K-$\alpha$ transition emits photons at 8.04 keV, corresponding to a wavelength of 1.54059 Å. Given their energy range, the X-ray photons will mainly interact with matter by photoelectric absorption, Compton scattering (inelastic) and Raylight scattering (elastic). Here, we are interested in the elastic interaction, so the detector is equipped with the same filter as the source. For the present thesis, only the reflected interaction is considered, but it is also possible to perform XRD in transmission mode.

The basic principle of XRD uses constructive and destructive wavelength recombination. Indeed, given the comparable length between the Cu K-$\alpha$ photon wavelength and the interplanar distance of the probed sample, there are specific angles at which the reflected photons all maintain the same phase, producing constructive interference. This will induce a signal peak whose associated angle $\theta$ is linked to a certain interplanar distance. This constructive interference is only met when Bragg's law is fulfilled:

$$n\lambda = 2d\sin(\theta) \tag{3.20}$$

where $\lambda$ is the photon wavelength, $n$ must be an integer to have constructive recombination (usually 1, sometimes 2), $d$ is the interplanar distance, and $\theta$ is the incident Bragg angle. See

figure 3.7 for a better visual understanding. Varying incident and reflected x-ray beams in a symmetric way is referred to as the "Bragg-Brentano geometry". In this particular geometry, the diffracted angle is always twice the incident angle.

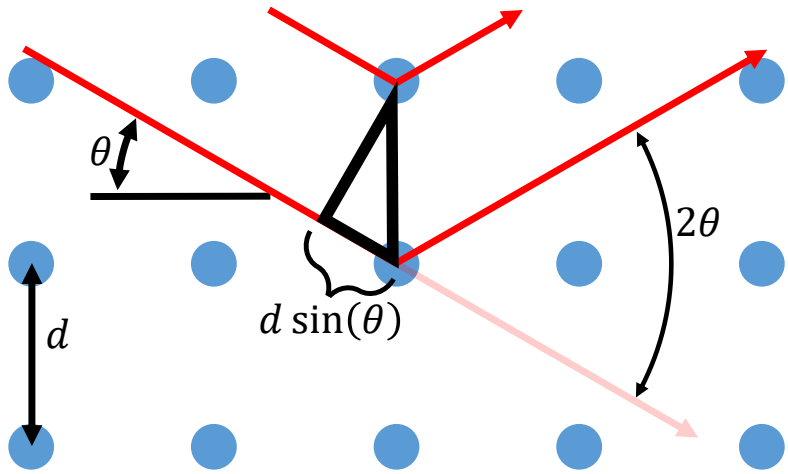


Figure 3.7: Experimental methods, XRD: Bragg's law visualisation in a Bragg-Brentano geometry, where $\lambda$ is the photon wavelength, $n$ is an integer, $d$ is the interplanar distance, and $\theta$ is the incident angle. See also equation 3.20.

It is possible to determine the indium content $X_{\text{In}} = \frac{\text{In}}{\text{In+Ga}}$ (In & Ga in at. %, $X_{\text{In}}$ in %) of an InGaN layer using XRD. Indeed, the interplanar distance varies linearly with $X_{\text{In}}$, depending on lattice parameters taking values between the ones presented in table 2.1. This means the peaks will follow a $\sim \sin^{-1}$ shift that can be back-calculated to amount to the indium content. This is usually done with the (002) peak if it is not merged with the forbidden (004) peak of the silicon wafer; in that case, the (110) peak is usually used instead. Compared to EDS, the extracted $X_{\text{In}}$ value is usually reliable since the peak position is exact.

The set of peaks acquired by varying the angle will then act as a fingerprint for phase identification, where a specific set of interplanar distances are expected to be observed. Indeed, each peak can be identified to a particular plane family $(hkl)$ (with Miller indices), wherein in a hexagonal configuration such as the In/GaN one, the interplanar distance $d$ is expressed as:

$$\frac{1}{d} = \frac{4}{3}\left(\frac{h^2 + hk + k^2}{a^2}\right) + \frac{l^2}{c^2} \tag{3.21}$$

where $a$ and $c$ are the lattice constants. If the phase is identified and at least two non-colinear peak positions are accurately measured, then $a$ and $c$ can be deduced. For a peak to be classified as a reflection, its intensity $N_{\text{Peak}}$ must be significantly higher than the background intensity $N_{\text{Background}}$:

$$N_{\text{Peak}} > N_{\text{Background}} + 3 \cdot \sqrt{N_{\text{Background}}} \tag{3.22}$$

The percentage of crystallinity $\%C$ is defined as

$$\chi_C = \frac{\Sigma_i \text{Area of peak } i}{\text{Total area}} \tag{3.23}$$

Other than the peak position and the peak area, the measured peak width $(\beta_{hkl})_{\text{measured}}$ is a quadratic composition of the actual peak width due to the probed layer $\beta_{hkl}$, and the additional width due to the instrument $(\beta_{hkl})_{\text{instrument}}$ (all in radians). The actual peak width can be broadened either because of strain $\varepsilon$ in the layer (uniform or non-uniform, see equations A.16 in appendix A.3), or slimmed because of a larger crystallite size $D$. When the layer is not under stress, the Scherrer equation [139, 119] gives a quick way to determine the crystallite size:

$$\beta_{hkl} = \sqrt{(\beta_{hkl})^2_{\text{measured}} - (\beta_{hkl})^2_{\text{instrumental}}} \tag{3.24}$$

$$D = \frac{K\lambda}{\beta_{hkl}\cos(\theta)} \tag{3.25}$$

where $(\beta_{hkl})_{\text{instrumental}}$ is extracted by experimentally measuring the width of a perfect powder of reference, and $K$ is a dimensionless shape factor that takes a value of 0.9. A deeper strain analysis linked to the peak width can be found in appendix A.3. Finally, two last tools: the preferential orientation is computed by comparing the normalised strength of the different diffracted peaks with each other, and the degree of crystallinity is calculated by integrating the total diffraction signal (without substrate peaks) and dividing the integral by the signal's total sum.

The error on all these values is extracted from the fit procedure (the error of one of the fit parameters is equal to the square root of its corresponding diagonal element in the dispersion matrix, see equation 3.52 and following paragraph for its explanation), and are propagated to other physical quantities through the uncertainty propagation method (see equation 3.9). However, these errors alone do not consider the tool's calibration error, and a more significant error is deemed to include the latter. In particular, the indium content determined by XRD is estimated with an error of ±0.5 % absolute, the crystallite size with ±0.01 nm and the lattice parameters with ±0.002 nm.

This thesis mentions two other possible configurations: grazing incidence X-ray diffraction (GIXRD), where the incident x-rays have a fixed low angle of incidence (usually $\omega = 4°$), and rotating the sample to improve particle statistics.

### 3.2.3 Electron microscopy and related tools of characterizations

#### 3.2.3.1 Working principle

Electrons can interact with matter in many more diverse ways than light can, depending on their incident energy. This section explores the many ways one can probe a material's characteristics using energetic electrons, based on four lectures given at the EPFL [32, 33, 98, 31] and their related sources. Nowadays, electron microscopes can emit electrons at a few hundred electronvolts only. At these energies or higher, if an electron encounters an atom, it will interact with its nucleus and the electron cloud differently, as described in figure 3.8.

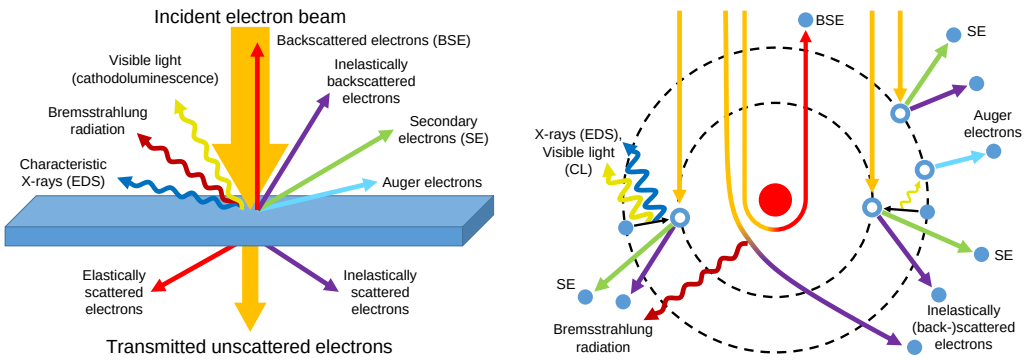


(a) All the signal types can be collected in an electron microscope, where the blue sheet represents the probed sample. Each type of signal requires a different type of detector, and some of the signals can be collected differently.

(b) Origin of all the signal types of figure 3.8a: interaction between the incident electrons (orange arrows) and the atom of the probed material. The electrons are the filled blue dots, whereas the hollow ones represent an ejected electron. The Bohr model is used here only to visualise the energies in play better.

Figure 3.8: Experimental methods, electronic microscopy: interactions. The flat lines represent electrons, while the wavy ones represent photons. The colour code is the same between the two figures: **incident electron**, **elastically scattered electron**, **inelastically scattered electron**, **secondary electron**, **Auger electron**, **visible light**, **Bremmstrahlung radiation**, **characteristic X-rays**. Most electron charges are absorbed in the sample and evacuated away from the impact area if the sample is conductive enough (which is also a measurable signal) or may induce parasitic charging effects if the sample is resistive.

Why are high-energy electrons used instead of the traditional light microscope? This is due to the wave-particle duality in quantum mechanics, stating that all massive particles exhibit wave-light behaviour depending on their momentum. French scientist De Broglie developed this theory in his thesis in 1924 [47, 46], based on the Planck-Einstein relationship shown in equation 3.26 [52]:

$$E = h\nu = \frac{ch}{\lambda} \tag{3.26}$$

$$\lambda_B = \frac{h}{p} = \frac{h}{\gamma m_0 v} \tag{3.27}$$

where $\gamma$ is the Lorentz factor for relativistic particles. The De Broglie wavelength $\lambda_B$ of a particle diminishes with increasing mass or speed, with, for example, $\lambda_B = 0.01221$ nm for an electron accelerated by a 10 kV electric potential. Such wavelength ranges will interact with the material's crystalline structure in the same way as X-rays (see section 3.2.2.5). For a coherent electron flux, the fulfilled Bragg condition will induce diffraction by the crystal, providing information on the crystal structure. The advantages of electrons are that they are lighter and smaller than other common particles (such as protons or neutrons), which will induce a higher interaction volume (which may be undesirable, depending on the measurement) while causing minimal damage. They are also highly quickly produced and controlled, and given their De Broglie wavelength (which is smaller than light's), they allow for higher resolution than traditional light microscopes.

Different types of electron microscopes with varying modes of operation and other kinds of information can be collected.

#### 3.2.3.2 Types of electron microscopes

Whatever the type of electron microscope, the electrons are generated by an electron gun and accelerated by a high voltage. They pass through magnetic lenses, apertures and deflectors until they reach the sample. If the signal is collected after passing through the sample (*e.g.* for (S)TEM), another set of magnetic lenses may guide the electrons towards the appropriate detector to form an image. Unless stated otherwise, electron microscopy is always performed on layers deposited on silicon wafers or on transmission electron microscope (TEM) grids to prevent charging effects.

**Scanning electron microscope (SEM):** The electron beam is focused on the sample and scans its surface thanks to scanning coils. The signal (SE and BSE) is collected on the same side as the incident beam, and an image is reconstructed point per point. The microscope used during this thesis was a ZEISS GeminiSEM 450 microscope with electron energy ranges between 1 – 20 keV. See figure 3.9a.

**Transmission electron microscope (TEM):** a parallel beam of electrons is shone on the sample, and the reconstructed image is collected after crossing the probed sample, similar to a traditional light microscope. But the particularity of having a parallel beam of electrons makes it possible also to collect a diffraction pattern when the image is extracted out of the focal plane rather than on the image plane. The more coherent the beam, the better the contrast in the diffraction pattern. The TEM that was used during this thesis

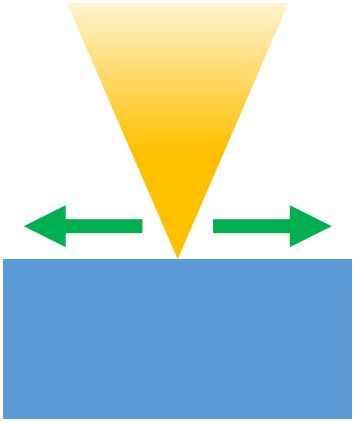

(a) SEM configuration. The focused beam scans the thick sample's surface.

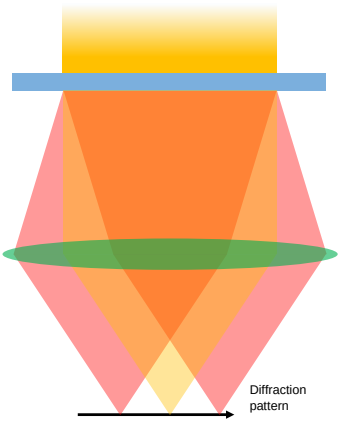


(b) TEM configuration, diffraction mode. The lens system after the thin sample (schematised in green) forms the diffraction pattern on the screen.

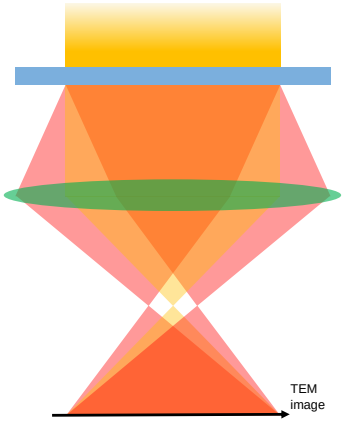


(c) TEM configuration, image mode. The lens system after the thin sample (schematised in green) forms the TEM image on the screen.

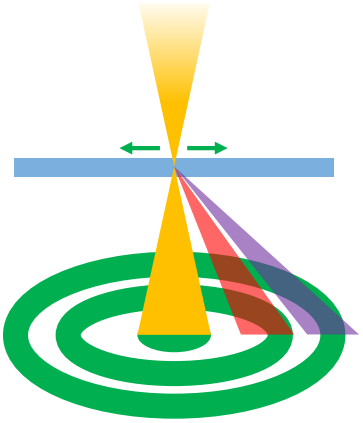

(d) STEM configuration. The focused beam scans the thin sample, and different ring detectors (green rings) are used for scattered electrons.

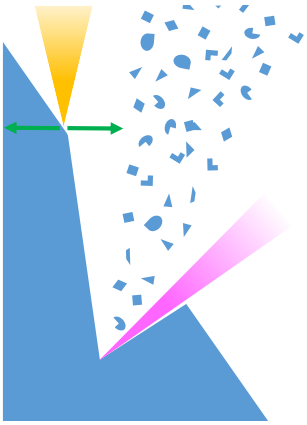

(e) FIB configuration. The gallium beam (in pink) erodes the surface, while an SEM scans the surface to visualise the work in progress.

Figure 3.9: Experimental methods, electronic microscopy: ***Highly simplified*** schematics of different microscope configurations: SEM, TEM, STEM, FIB. The blue surface is the probed sample, the green element denotes what can be tuned, the orange surfaces represent the incident and unscattered electrons, the red ones represent the elastically scattered electrons, and the purple ones are the inelastically scattered electrons.

was an FEI Co. Talos F200X 200 keV field emission (scanning) transmission electron microscope (STEM/TEM). The electron energy was set to 200 keV. See figures 3.9b and 3.9c.

**Scanning transmission electron microscope (STEM):** the electron beam is focused on a thin sample and scans it; the transmitted signal is collected after the probed sample. Different ring detectors are used to collect the transmitted electrons (bright field image BF, centre), the elastically scattered electrons (dark field image DF, first ring detector) and the inelastically scattered electrons (high-angle annular dark field HAADF, outermost detector ring). The ZEISS GeminiSEM 450 microscope can also perform such measurements, where only the sample holder is changed, and ring detectors are inserted. The electron energy was set to 20 keV for such experiments. See figure 3.9d.

**Focused ion beam (FIB):** heavy atoms (usually galium) are focused on a sample. Even though secondary electrons (SEs) for imaging by scanning are also produced when the ion beam interacts with the sample, the former is used for milling, precise machining (sputtering), chemically assisted deposition or etching. This is why an FIB is often accompanied by a SEM column to monitor the operation of the ions. This thesis used this tool to produce cross-section lamellae of a layer for TEM analysis. The used FIB was a Zeiss NVision 40 CrossBeam with focused ion beam (FIB) and high-resolution field emission SEM. See figure 3.9e.

#### 3.2.3.3 Types of electron microscope signals and operation modes

Here are only listed the signals used in this thesis and the different operation modes.

**Secondary electrons (SEs)** have low kinetic energy ($< 20$ eV), which means that only the ones produced at the surface can escape the sample and be collected. They are collected by a standard Everhart-Thornley SE detector or by an in-lens SE detector (topography contrast in both cases). These contrasts can be obtained in an SEM only.

**Backscattered electrons (BSEs)** have the same kinetic energy as the incident beam. They are incident electrons that diffuse randomly in all directions within the sample but are preferentially reflected in the same direction as the incident angle by turning around a nucleus (see figure 3.8b). Those are the electrons that are collected to form a signal. This back-scattering depends on the mass of the impacted atom, and hence they give Z-contrast information. They are only collected in a SEM.

**TEM images** are identical to images extracted from a traditional light microscope, where the sample illuminated by a parallel beam has its image reconstructed on the detector, here a phosphorous screen or a charge-coupled device CCD camera. However, given the De Broglie wavelength of the electrons at 200 keV in a TEM, this can even allow for contrasts showing columns of atoms that can later be post-processed by an image-processing tool to extract crystallite orientation, for example (HRTEM).

**Bright field images (BFs)** are images composed of all transmitted electrons that were not diffracted. This kind of contrast can be obtained in a TEM (200 keV) or a STEM ($20-200$ keV). The detector is either a phosphorous screen or a charge-coupled device CCD camera (TEM case) or a semiconductor detector (STEM case).

**Dark field images (DFs)** is an image only composed of transmitted elastically diffracted electrons. The bright areas in these images denote highly crystalline regions and can help identify or measure crystallite size and orientation. This kind of contrast can be obtained in a TEM or a STEM with ways to enhance the image further in both cases. In a STEM, the ring detector is usually broken down into four quarters, where the signal of each one can be added or subtracted from the others, or even not taken into account, for better contrast. In a TEM, an objective aperture can be inserted in the back focal plane to let pass through the electrons of only one diffraction spot. In this way, the TEM image will only display the crystallites responsible for that specific diffraction spot in white. The tools used to collect this data are the same as for the bright field, with identical energies.

**Diffraction patterns** are formed on the focal plane of a TEM (200 keV), with ellastically scattered electrons. Depending on the probed area and material, the diffraction pattern can look like an arranged array, a superposition of multiple arranged arrays or even circular patterns. These correspond to a single high-quality crystal in the illuminated area, multiple high-quality crystals, or nanocrystals. More complex cases may even arise. In the first two cases, the crystal orientations can be identified by comparing the observed diffraction patterns with simulated ones, and the third case (circular patterns) can be de-polarized. It should give similar results as XRD (see section 3.2.2.5). Whatever the diffraction figure, information can be extracted using simulating software such as JEMS. The depth of diffraction figure analysis is pretty vast, where stacking faults, strains, or richer information can be extracted; for this, we refer the reader to the literature. In a TEM, a selected area aperture can be used in the image plane to reduce parasitic contrasts in the diffraction figure for better identification. The detector is either a phosphorous screen or a charge-coupled device CCD camera.

**Transmission Kikuchi diffraction (TKD)** collects ellastically scattered electrons on an electron backscattered diffraction (EBSD) detector directly after transmission through a thin sample. This signal should not be confused with backscattered Kikuchi diffraction (BKD) or electron backscattered diffraction (EBSD). The electrons that exit the sample coherently interact with the crystal close to the surface; it behaves like a street light entering a dark room through blinds, and Kikuchi lines are formed on the screen. These can precisely identify the crystal structure, stress and orientation. In this case, the electron beam needs to be focused (which also enables mapping), and this kind of data is usually collected in a SEM (20 keV) with a special kind of sample holder.

**Characteristics X-rays** X-Max 50 mm$^2$ EDS detector (Oxford Instruments) was used for EDS measurements, where specific energies are identifiers of an element inside the layer. For gallium, indium and nitride, the interesting energy transition produces a 1.098 keV $L_\alpha$, a 3.286 keV $L_\alpha$ and a 0.392 keV $K_\alpha$ X-ray, respectively. To ensure the ionisation of these species, at least twice the highest interesting energy is needed for the electrons; thus, a 7 keV electron beam was used for this kind of measurement in a SEM (which enables mapping). This measurement type can also be performed in a STEM or a TEM. The indium content can be extracted from this measurement, whereas $X_{\mathrm{In}} = \frac{\mathrm{In}}{\mathrm{In+Ga}}$ (In & Ga in at. %, $X_{\mathrm{In}}$ in %). Since such values depend on the peak intensity amidst a

usually noisy signal, the error chosen for such value is ±1 % absolute instead of the 0.5 % traditionally taken. This choice is made because light elements such as nitrogen are in high quantities in the deposited layers.

### 3.2.4 Electrical characterizations

Due to the precision of the instruments used for electrical characterisations (usually less than 0.2 % relative), the error bars would usually be thinner than a single point, so they are removed in all related figures. However, if a physical quantity is extracted from them, uncertainty propagation is still applied (see equation 3.9). For example, the resistivity measured from the four-terminal sensing depends on the layer thickness, which has a significant uncertainty that will impact the resistivity uncertainty.

#### 3.2.4.1 Four-terminal sensing

Four-terminal sensing measurements were performed using a Lucas Labs resistivity test stand S-302-6. Unless stated otherwise, four-terminal sensing was always completed on layers deposited on glass wafers. It allows the measurement of the resistivity of a layer, provided its thickness is known. Four-terminal sensing or four point probe (4-PP) measurements is one of the quickest measurements possible. Four aligned contacts are pressed against the sample, with a current imposed on the two external contacts. This set current generates a voltage drop across the measured line according to Ohm's law $U = RI$, and a voltage can be measured between the two internal contacts. By doing so, the contact resistance for the measured voltage is negligible because the sensor uses only a tiny portion of the current to measure the resistance between the two internal contacts. Given the geometry of the contacts or the distance between them, a factor could be applied. It is also possible to do this measurement in a squared configuration by correcting it with another factor (see next section on the Hall effect).

Since the distance between the two internal pins is known, the extracted value is the sheet resistance $R_{\square}$, measured in $\Omega\square$. The fundamental unit of sheet resistance is, in fact, $\Omega$. Still, the idea behind this name is to imagine a square of any dimension (aspect ratio of 1) and constant thickness, where two opposite sides are connected. The measured resistance between the two sides of the square corresponds to the sheet resistance. If the surface has an aspect ratio of 3 and the contacts run along the shorter sides, the measured resistance would be three times its sheet resistance. Finally, multiplying the sheet resistance with the film thickness d will give the bulk resistivity (usually presented in [$\Omega$ cm]) [36].

$$\rho = R_{\square} \cdot d \tag{3.28}$$

#### 3.2.4.2 Transfer length measurement

Transfer length measurements (TLMs) were performed by means of a Signatone H100 Probe Station System, added with multiple Signatone S-725-PRM X-Y-Z economic micropositioners, P/N 08113045. It allows the measurement of the resistivity of a layer and the contact resistance, provided the layer thickness, and the contact dimensions are known. Unless stated otherwise, TLM was always performed on layers deposited on glass wafers. This technique involves depositing multiple aligned metallic contacts on the probed layer, differently spaced out. The resistance between two contacts is measured by applying a voltage and measuring a current. The current flows from the first probe to the metallic contact, then through the metal-SC junction, into the probed layer, through the SC-metal junction again, in the second metallic contact, and eventually out of the second probe. The measured resistance is then the sum of the resistance of the layer and the two metal-junction resistance. When the distance is varied on multiple measurements, a plot of the resistance versus the inter-contact distance can be drawn; the slope of the line is the sheet resistance, and the intercept with the y-axis is two times the contact resistances [155].

#### 3.2.4.3 Hall effect

Hall effect measurements were performed using an Ecopia Hall effect measurement system (HMS) 5000. Unless stated otherwise, Hall effect measurements were always performed on layers deposited on glass wafers. The working principle relies on the Lorentz force, undergone by charged particles moving across a magnetic field. In our case, four contacts are placed in a squared fashion, and a current is applied between two opposing contacts. The magnetic field is directed perpendicular to the surface and will deflect the charge carriers, inducing a voltage perpendicular to the two contacts. Charges will accumulate until an equilibrium is reached between the Lorentz force and the induced electric field; when that happens, the so-called "Hall voltage" $U_H$ is measured between the other pair of contacts (see figure 3.10 for a visual representation). The Hall voltage depends on the Lorentz force, which depends on the speed of the charged particles (or drift velocities), which in turn depends on the physical properties of the layer (such as charge carrier mobility or concentration) [111, 72].

$$\mathbf{F} = q\,(\mathbf{E} + \mathbf{V} \times \mathbf{B}) \tag{3.29}$$

where at equilibrium, **F=0**. Taking the charge and vector direction into account, it follows that:

$$VB = E$$
$$U_H = VBw$$

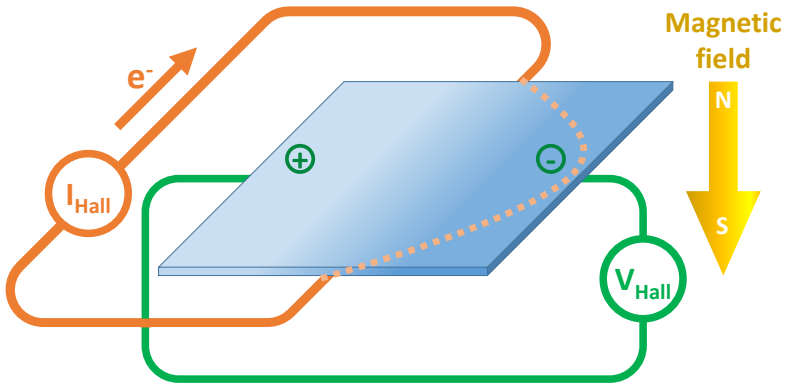


Figure 3.10: Experimental methods, Hall: voltage measurement setup of a layer with a thickness $d$ and length $w$ between the two green contacts.

where $w$ is the distance between the two contacts measuring $U_H$. From the Drude theory for free electrons in metals [156], using $d$ as the layer thickness and $n$ as the free electron density, we can define the current $I$ passing through the layer and substitute into the previous equation.

$$I = ndwqV$$
$$U_H = \frac{IB}{ndq}$$

Using the mobility dependent resistivity $\rho = 1/\mu qn$, we obtain two useful expressions for the Hall mobility $\mu_H$ and the free carrier concentration $n$:

$$\mu = \frac{1}{\rho nq} \tag{3.30}$$
$$n = \frac{IB}{dqU_H} \tag{3.31}$$

And to measure $\rho$, the Van der Pauw equation (here below) is solved for the four contacts in a square configuration, where a current $I_{kl}$ is imposed between two contacts, and a voltage $U_{ij}$ is measured between the two others:

$$1 = \exp\left(\frac{-\pi R_1}{R_\square}\right) + \exp\left(\frac{-\pi R_2}{R_\square}\right) \tag{3.32}$$
$$R_1 = \frac{U_{ij}}{I_{kl}}, \qquad R_2 = \frac{U_{ik}}{I_{jl}}$$

where $R_\square$ is the sheet resistance, for which the equation has to be solved, the bulk resistivity is extracted according to equation 3.28.

#### 3.2.4.4 Dark lateral conductivity

The goal of this tool is to use the dependence of the resistivity on the temperature to deduce the activation energy of the probed material. The activation energy measures the energy between the Fermi level and the closest energy band of a solid.

Similarly to system B, dark lateral conductivity (DLC) measurements were performed using a patchwork of different tools. The chamber was vacuumed by an Alcatel 2005SD Pascal dual-stage rotary vane vacuum pump, and a Leybold Thermovac TM220 S2 gauged the pressure. A TECON 501 Programmable Controller monitored the temperature of the heating body, and the different electrical sources and monitoring devices were two Keithley 617 programmable electrometers and a Keithley 705 System Scanning Thermometer. A metallic contact was deposited on the layers of known dimensions and separation distance, and the experiment took place under $N_2$ atmosphere at a bit less than 1 bar. The $N_2$ atmosphere is necessary because at higher temperatures, if it were done in the atmosphere, there would be an increased risk of oxidation of the layer. Unless stated otherwise, DLC was always performed on layers deposited on silicon wafers because of the too-hot temperature for glass.

The doping level of a SC will change the fermi level energy. Whatever the material, this change in the Fermi level energy or the electron concentration due to doping or temperature will be reflected in the conductivity $\sigma$ of the layer because the conductivity is proportional to the product of mobility and carrier concentration (see equation 3.33). That is where DLC measurements come into play.

Because the layers could already be photoactive, the whole experiment is performed in the dark. And because the heating could promote the oxidation of the layer (similarly to annealing, for example), the entire measurement is performed under a nitrogen atmosphere. After being contacted, the sample is first heated, and its conductivity $\sigma(T)$ is measured during its cooling down, during which the conductivity is expected to follow the Arrhenius equation (displayed in equation 3.34). The measure is not done during the heating up of the material because a hysteresis effect is observed, and the cooling down gives more linear results.

$$\sigma = q\left(n\mu_e + p\mu_h\right) \tag{3.33}$$

$$\sigma(T) = \sigma_0 \exp\left(\frac{-E_A}{k_B T}\right) \tag{3.34}$$

$$\ln(\sigma) = \frac{-E_A}{k_B}\frac{1}{T} + \ln(\sigma_0) \tag{3.35}$$

where $E_A$ is the Arrhenius activation energy. Comparing equations 2.2, 3.33 and 3.34, this activation energy corresponds to the difference between the Fermi level energy $E_F$ and the closest band, be it valence or conduction. And here, one can fit equation 3.34 onto the $\sigma$ versus $T$ data points or fit a straight line across the points displayed in the $\ln(\sigma)$ versus $1/T$

plot (equation 3.35), where the activation energy will then be extracted from the slope, and the extrapolated conductivity at infinite temperature $\sigma_0$ is the ordinate at the origin. This measurement will serve as a metric of the active layer doping, where a more doped layer will display a lower activation energy.

#### 3.2.4.5 Quasi-steady-state photoconductance

Quasi-steady state photoconductance measurements were performed using a Sinton instruments WCT-120TS – Temperature dependent lifetime measurement. Unless stated otherwise, quasi-steady state photoconductance measurements were always performed on layers deposited on silicon wafers. By placing a photo-active sample on a coil and under a flash, excess charge carriers density $\Delta n$ is generated at a rate $G$, increasing the conductance for a moment before recombining. This perturbation can then be measured inductively by a coil and compared to a reference sample. The lifetime can be extracted using the formula presented by Nagel *et al.* [128, 163].

$$\tau_{eff} = \frac{\Delta n}{G - \frac{\partial \Delta n}{\partial t}} \tag{3.36}$$

where $G$ is the photogeneration rate determined thanks to the flash intensity, $\Delta n$ is measured inductively by the coil, and the subscript "*eff*" refers to the lifetime at a fixed $\Delta n$ value. The lifetime measurement provides a metric for the surface passivation quality of a wafer.

#### 3.2.4.6 Current-voltage cell characterization

Current-voltage cell characterisation was performed using a WXS-90S-L2, AM1.5G class AAA solar simulator from Wacom Electric Co., Ltd. (Japan). A Keithley-2601A source meter was used to sweep the voltage and simultaneously record the generated electrical current. A chuck contacts the rear side of the solar cell, while 4-point probes get the fingers at the front. A $2 \times 2\,\mathrm{cm}^2$ shadow mask was used to restrict the illuminated region, avoiding carrier generation outside the active cell area. The measurements were performed under standard test conditions, *i. e.* at a $25\,°C$ temperature maintained by Peltier elements cooled by a water chiller, at a one sun illumination ($1000\,W/\mathrm{m}^2$), and using the AM1.5G spectrum.

This measurement determines all the performances of a solar cell as described at the end of section 2.1.2: the $V_{\mathrm{OC}}$, the $J_{\mathrm{SC}}$, the $FF$ and the efficiency $\eta$.

### 3.2.5 Other means of characterization: profilometry

The physical thickness was assessed with an Ambios Technology XP-2 profilometer, with a Tensor instruments Alpha Step 500 Profilometer, and confirmed with the ellipsometry multi-modelling (see section 3.2.2.3). Unless stated otherwise, profilometry was always performed on layers deposited on silicon wafers. In these contact profilometers, a diamond tip is slid on the surface along a line (1D scan), and the height variation generates an analogue signal, converted into a digital one, as a function of the position. The parameters that will influence the precision of the measurement are the tip diameter and the contact force, as well as the plasticity of the layer. With the mentioned tools, the accuracy can reach under 10 nm, and as already discussed previously (see the end of section 3.2.2.3), this will be considered as the error on the thickness measurement (±10 nm). The scanned step can be created by a lift-off procedure using tape or ink traces that can be removed after the deposition.

## 3.3 Design of Experiment

This whole section is based on the work of Hinkelmann and his peers, published in their book [77]. Please refer to it for more details on the design of experiment (DOE) techniques presented here.

### 3.3.1 Operation

> No matter how complex the process is, the data quality is the essence of the process. An efficient design of the experiment is essential for improving the data quality.
>
> (Subir Ghosh in [77], p. 284)

#### 3.3.1.1 Motivation & Definitions

Usually, a single finding depends on combining a few conclusions obtained through multiple experiments based on many runs, which all depend on input variables. Often, one experiment consists in finding an optimal outcome value for one given input variable while keeping the others constant. The usual way to proceed would be to vary that parameter on an interesting range through many trials and then select the parameter value giving the outcome closest to the desired or optimal result. This empirical approach allows the extraction of trends and helps to perfect the research object without relying on comparison with heavy multiple existing phenomenon formulations. For example, it may be difficult to precisely formulate the influence of the plasma frequency used for the deposition of an InGaN layer on the $V_{OC}$ of an InGaN/Si tandem solar cell.

To define things, the term "Design of Experiment" (DOE) refers to a method that allows for an efficient quantitative prediction of one experimental "outcome" $y$ (or "dependent variable") that varies as a function of $k$ "input parameters" $x_i$ (or "independent variables"). Qualitative input parameters or outcomes can also be considered, but only the quantitative case will be discussed here. This quantitative prediction is based on a "model" that is fitted on a set of $n$ outcomes measured after $n$ "runs" are performed, whose collections of input parameters were precisely designed so that said prediction is the most reliable with the lowest cost possible. This procedure provides more efficient ways to develop an entire process rather than optimising one factor at a time (OFAT), as described at the end of the previous paragraph. Furthermore, it allows highlighting the combined influence of parameters, which is not visible with the OFAT approach.

Of course, this method has its limits. The actual state of nature will pass through the model's lens, with some noise and (hopefully not) unconsidered influence. Indeed, multiple factors can affect the results without the experimenter having any control over them. However, "Correlation does not imply causation"; hence designed experiments are preferred to observational studies. The DOE then ensures that the tests result in clear conclusions, in a simplified and efficient way, without reducing data quality.

#### 3.3.1.2 Models

> Remember that all models are wrong; the practical question is how wrong they have to be not to be useful.
>
> (Box and Draper in [23], p. 74)

For example, let us consider an outcome $y$ that depends on $k = 3$ input parameters $x_1$, $x_2$ and $x_3$. Since the relationship between these input parameters and the outcome has yet to be discovered, one of the best approaches is linearising the unknown relationship using Taylor's power series. For the sake of simplicity, we will develop it to the second level.

$$y(x_1, x_2, x_3) = a_0 + a_1 x_1 + a_2 x_2 + a_3 x_3 \tag{3.37a}$$

$$+ a_{12} x_1 x_2 + a_{13} x_1 x_3 + a_{23} x_2 x_3 \tag{3.37b}$$

$$+ a_{11} x_1^2 + a_{22} x_2^2 + a_{33} x_3^2 + R_3 \tag{3.37c}$$

where equation 3.37 is the full quadratic model, with the right-hand-side of part 3.37a describes the "main effects" (and a "constant" effect $a_0$), part 3.37b contains the "interaction effects", and part 3.37c defines the "quadratic effects" (with the error $R_3$). Any simple or complicated $a_i x_i$ combination is called an "effect". The $a_i$ terms are called the "coefficients",

and the goal of the DOE method is precisely to calculate their value to have a complete model fully predicting the outcome $y$. The $a_0$ term represents the effect of the constant. The number of effects (or coefficients) is defined as $p$ (for the model described in equation 3.37, $p = 10$). The range on which all the input parameters fluctuate defines the "experimental design space" of dimension $k$, within which the quantitative prediction remains valid. With multiple experiments, the model can be translated into a matrix form:

$$
\begin{aligned}
y_1 &= a_0 + a_1 x_{1_1} + a_2 x_{2_1} + \cdots + a_{22} x_{2_1}^2 + a_{33} x_{3_1}^2 + R_{3_1} \\
\vdots \quad & \quad \vdots \qquad\qquad\qquad\qquad \vdots \\
y_n &= a_0 + a_1 x_{1_n} + a_2 x_{2_n} + \cdots + a_{22} x_{2_n}^2 + a_{33} x_{3_n}^2 + R_{3_n} \\
&\downarrow \\
\begin{pmatrix} y_1 \\ \vdots \\ y_n \end{pmatrix} &= \begin{pmatrix} 1 & x_{1_1} & \cdots & x_{3_1}^2 \\ \vdots & \vdots & \ddots & \vdots \\ 1 & x_{1_n} & \cdots & x_{3_n}^2 \end{pmatrix} \begin{pmatrix} a_0 \\ \vdots \\ a_{33} \end{pmatrix} + \begin{pmatrix} R_{3_1} \\ \vdots \\ R_{3_n} \end{pmatrix} \\
&\downarrow \\
\vec{Y} &= X\vec{\alpha} + \vec{\varepsilon} \qquad (3.38) \\
\hat{y}(x_1, x_2, x_3) &= \vec{f}(x_1, x_2, x_3) \bullet \vec{\alpha} \qquad (3.39)
\end{aligned}
$$

where $\vec{Y}$ is the "vector of experimental outcomes", $X$ is the "matrix of experiment" (or "model matrix"), $\vec{\alpha}$ is the "vector of coefficients", and $\vec{\varepsilon}$ is the "vector of residuals" (or "vector of experimental errors"). Constructing the "essay matrix" $E$ by only keeping the columns of $X$ corresponding to linear terms is possible. Finally, $\hat{y}$ is the vector of expected outcomes (read next paragraph), and $\vec{f}$ is called the "model coordinates" and is a vertical vector composed of all the effects, the constant included. From there on, the goal is to manipulate equation 3.38 to deduce the vector of coefficients $\vec{\alpha}$. Note that a few calculation steps are not displayed in the subsequent development.

$$
\begin{aligned}
\vec{Y} &= X\vec{\alpha} + \vec{\varepsilon} \\
\vec{\alpha} &= \left(X^T X\right)^{-1} X^T \vec{Y} - \left(X^T X\right)^{-1} X^T \vec{\varepsilon} \\
\mathbb{E}(\vec{\alpha}) &= \left(X^T X\right)^{-1} X^T \mathbb{E}\left(\vec{Y}\right) \\
\hat{\vec{\alpha}} &= D X^T \hat{\vec{Y}} \qquad (3.40) \\
D &= \left(X^T X\right)^{-1} \qquad (3.41)
\end{aligned}
$$

where $\mathbb{E}$ is the "expectation operator" (and we expect the vector of residuals to be zero), $\hat{\vec{\alpha}}$ is the "estimated vector of coefficients", and $D$ is the "dispersion matrix". Equation 3.40 is often called the "least square fit of the estimates". **Deducing $\vec{\alpha}$ is the objective, $\vec{Y}$ is measured, and $X$ (hence $D$) can be designed**. We see the importance of the dispersion matrix (of dimensions $p \times p$) because it represents the transfer of variance between the factors and the input parameters.

For the sake of simplicity, it is possible to standardise the input variables. This means the unit is dropped when a range of values is probed for a variable; the lowest value is set to -1 and the highest to +1. The values in between are linearly corrected between -1 and +1, and the matrix of experiments $X$ is only filled with values between -1 and +1. This allows for a fair comparison between the variables and allows the deduction of the most significant effects on the outcome, and designs are overall more symmetrical. But more importantly, if the input variables are standardised, the orthogonality of the dispersion matrix becomes relevant to the DOE process because it reflects the orthogonality of the model. This is the first aspect of performing experimental runs where the question of the design matters.

The correlation matrix $C$ is a central tool in DOE. It is a $p \times p$ matrix which, with standardised input variables, can be deduced from the dispersion matrix:

$$C_{ij} = \frac{D_{ij}}{\sqrt{D_{ii} D_{jj}}} \tag{3.42}$$

A correlation defines the strength of the linear relationship between two effects. This means that a correlation value of +1 indicates a perfect positive linear correlation between two effects, and that has to be avoided because it would mean that after an experiment, the influence of the two effects cannot be distinguished. On the contrary, if a correlation matrix element is zero, the influences of two effects are entirely distinguishable. It is said that the two effects are "orthogonal" to one another. This is where the design becomes essential: the effects' correlation can be optimised to 0 if the experiment is well-designed. On the contrary, with an ill-designed experiment, it is sometimes difficult to distinguish which correlated effects significantly impact the outcome $y$. The diagonal of the correlation matrix comprises ones where each effect is entirely positively correlated to itself.

When the number of effects is too large for a comprehensive reading of the correlation matrix, it is sometimes faster to calculate the "variance inflation factors" (VIFs), which convey the increase of the variance of an estimated effect due to collinearity. Its square root reflects how much larger the standard error is, compared with what it would be if that variable were uncorrelated with the other predictor variables in the model. It is thus desirable to lower the VIFs as close to one as possible. Again, this can be achieved with a well-designed experiment.

$$VIF(\hat{a}_i) = \text{diag}_i\left(C^{-1}\right) \tag{3.43}$$

Finally, one last key element that can be established is the "Standardized Response Variance". It is a function that is defined on the "experimental space" of $p$ dimensions (not to be confused with the experimental design space of $k$ dimensions). The value this function takes defines the fraction of the "experimental error" $s^2$ (or "mean squared error", a constant that can be determined after performing all the runs, defined in equation 3.50, page 61) that will be transferred to the effect of a given model, at a particular value of the input parameters, using the model coordinate $\vec{f}$ established in equation 3.39.

$$\frac{\text{var}_Y(x_i)}{s^2} = \vec{f}^T(x_i)\, D\vec{f}(x_i) \tag{3.44}$$

Given the chosen design, some effect values will be accompanied by more variation in the model, while other parts of the experimental space will show slight variance. This may be useful when a particular volume of the experimental space needs to be modelled more precisely. Choosing a design that will induce symmetries in this function will also prove helpful, as discussed in appendix A.4, page 228.

### 3.3.2 Result quality analysis

#### 3.3.2.1 Basic outcomes

Until now, no run has been performed, and no outcome has been collected. The design and the model have to be chosen depending on the actual knowledge of the existing system and on what is interesting to observe to extract desired values. Once the runs are performed, the designed model can be fitted on the set of $n$ experimental outcomes, and conclusions can be drawn. A few key tools can be defined for a thorough insight into the modelling process. Again, let $n$ be the number of runs of an experiment with $y_1, \cdots, y_n$ outcomes, then $f_1, \cdots, f_n$ are the outcomes predicted by the model $f(x_1, \cdots, x_k)$ where $k$ is the number of input variables and $p$ is the number of effects or the number of coefficients $a_i$ in the model (constant included). Using the average of all the outcomes $\bar{y}$ (or "grand mean"), the following tools can be defined:

$$\begin{aligned} \bar{y} &= \frac{y_1 + \cdots + y_n}{n} \\ SS_{tot} &= \sum_{i=1}^{n} \left(y_i - \bar{y}\right)^2 \end{aligned} \tag{3.45}$$

$$SS_{res} = \sum_{i=1}^{n} \left(y_i - f_i\right)^2 \tag{3.46}$$

$$R^2 = 1 - \frac{SS_{res}}{SS_{tot}} \tag{3.47}$$

$$R^2_{adj} = 1 - \frac{SS_{res}}{SS_{tot}} \cdot \frac{n-1}{n-p} \tag{3.48}$$

$$RMSE = \sqrt{\frac{SS_{res}}{n}} \tag{3.49}$$

**The "sum of squares"** $SS_{tot}$ (see equation 3.45, figure 3.11a). It allows for an evaluation of the overall variance of a dataset from its mean. When fitting the dataset with a function or a model, the fitting process aims to minimise this value. Unit in $[y^2]$.

**The "residual sum of squares"** $SS_{res}$ (see equation 3.46, figure 3.11b). When $SS_{tot}$ (see above) has been minimised, there is still some error between the dataset and the model. $SS_{res}$ measures the variation of errors in a regression model or how badly the model explains the data. Unit in $[y^2]$

**The "coefficient of determination"** $R^2$ (see equation 3.47). By definition of the two above, $R^2$ is the proportion of variation in the data the model predicts. Unit in [%], where a value closer to 1 is desired.

**The "adjusted coefficient of determination"** $R^2_{adj}$ (see equation 3.48). Increasing $R^2$ is easily achieved by increasing the number of effect terms $p$. To have a fair evaluation of the quality of the model and to prevent overfitting, the adjusted coefficient of determination $R^2_{adj}$ penalises the addition of new effect terms to the model. The penalty is objectively chosen, but the standard in statistics nowadays is developed by Mordecai Ezekiel [198]. Unit in [%].

**The "root mean square error" RMSE** (or "root mean square deviation", see equation 3.49). It estimates the average difference between the dataset values and the model's predictions. Unit in $[y]$, which is the reason why it makes this tool useful.

If the model does explain the dataset well, then the residuals should behave like noise, *i.e.*, following a normal distribution. A plot of the residuals with respect to a normal distribution is called a "normal probability plot of residuals", or just "normal plot". There are two ways to perform a normal plot: one can either use the cumulative distribution function (called a "normal P-P plot", where "P" stands for "Probability"), or one can directly use the gaussian curve instead (like in figure 3.11c, called a "normal Q-Q plot", where "Q" stands for "Quantile"). Since the residuals behave like noise, the points in such a plot are expected to be scattered evenly around the central diagonal line, representing the normal distribution fitted to the residuals. Suppose the scattering is uneven or follows a recognisable pattern. In that case, the noise still depends on an unaccounted effect, and a more complex model may be elaborated.

Considering the optimised coefficients $a_i$, their variance can be calculated at this point. The "variance of the coefficients" $\widehat{\text{var}}\left(\hat{\hat{\alpha}}\right)$ is calculated using the "mean square error" $s^2$, where

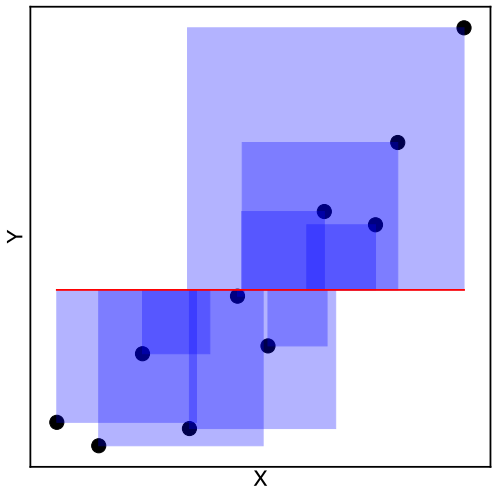


(a) Sum of squares $SS_{tot}$, where the red line is placed at the overall mean value $\bar{y} = \frac{y_1+\cdots+y_n}{n}$. The blue squares represent the square of the difference between $\bar{y}$ and the experimental $y$-value.

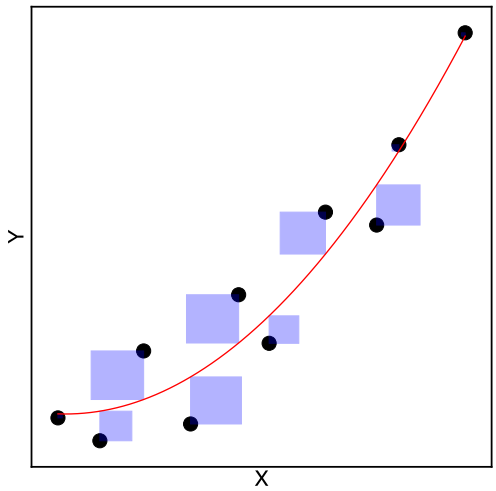


(b) Sum of squares of residuals $SS_{res}$, where the red line shows the $y = a_0 + a_{11}x_1^2$ model used, for $a_i$ coefficients that minimize $SS_{tot}$. The blue squares represent the squares of the residuals for each point.

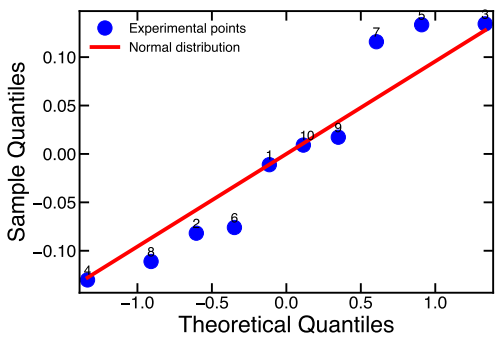


(c) Q-Q normal probability plot of residuals, or normal plot. For a good model, residuals are expected to be scattered evenly around the central diagonal line, representing the normal distribution.

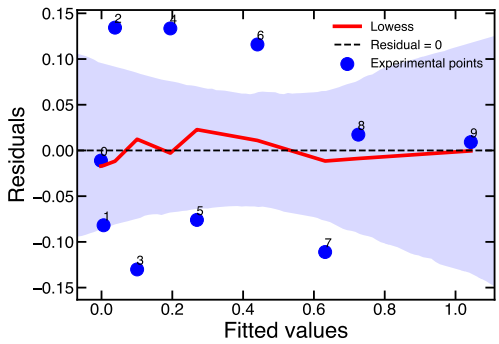


(d) Residuals versus fitted values. Helps identify which experimental point has the most influence on the whole model (or on one isolated effect in the case of an added variable plot).

Figure 3.11: Experimental methods, DOE: four of the most used tools for DOE result analysis that can be visualised through a plot. The same set of points is used in these four examples, where the points follow a pure quadratic behaviour with some implemented noise; hence the chosen model is $y = a_0 + a_{11}x_1^2$.

$\nu = n - p$ is the degree of freedom of the model. The following mathematical development is the continuation of equation 3.40 page 57, the least square fit of the estimates.

$$s^2 = \frac{\|\vec{\varepsilon}\|^2}{\nu} \tag{3.50}$$

$$\begin{aligned}\widehat{\mathrm{var}}\left(\hat{\vec{\alpha}}\right) &= \widehat{\mathrm{var}}\left(DX^T\vec{Y}\right)\\ &= \widehat{\mathrm{var}}\left(DX^T\right)\widehat{\mathrm{var}}\left(\vec{Y}\right)\\ &= D\cdot\widehat{\mathrm{var}}\left(\vec{Y}\right)\\ \widehat{\mathrm{var}}\left(\hat{\vec{\alpha}}\right) &= D\begin{pmatrix}1\\ \vdots\\ 1\end{pmatrix}s^2 \qquad (3.51)\\ CI_\beta(a_i) &= t_{\alpha/2,\nu}\sqrt{D_{ii}s^2} \qquad (3.52)\end{aligned}$$

where $CI_\beta$ is the $\beta$ "confidence interval of half effects" (also simply called "error of half effects", but only when using $\beta = 95\%$ for a 95 % confidence interval), where $\alpha = 1-\beta$. $t_{\alpha/2,\nu}$ is the quantile of the student distribution for the probability $\alpha/2$ and degree of freedom $\nu$ ($t_{0.025,\nu}$ for a 95 % confidence interval). In other words, this last equation expresses the error on each fitted parameter, which depends on the dispersion matrix $D$ and on the error of each measurement (expressed here in the $s$ term, see equation 3.50).

When performing a linear regression with a single effect, a scatter plot of the output against its related effects provides a good indication of the nature of the relationship (like in figure 3.11b, where the only other effect is the constant with $a_0 \approx 0$). If there is more than one non-constant effect, things become visually more complicated. Although it can still be helpful to generate scatter plots of the output against each independent effect while keeping the others constant at an arbitrary value, this will not reflect the influence of the other independent effects in the model with respect to the observed independent effect. We want to look at the relationship between the dependent variable (the output) and one effect, but conditional to all the others. In other words, we want to illustrate the incremental influence on the output of a specified effect of the model caused by removing the influence of all other effects. The "added variable plot", also called "partial regression (leverage) plot", does precisely that.

To discern the relationship between the output and the $i^{\text{th}}$ effect $a_i x_i$, the so-called "partial residuals" are computed by regressing the output versus all the effects, except the $i^{\text{th}}$ one. These partial residuals constitute the $y$-axis of the added variable plot. The $i^{\text{th}}$ effect is then regressed on these partial residuals, and the "final residuals" of this operation constitutes the $x$-axis of the added variable plot. The final residuals are exactly the residuals of the whole model. In other words, the y-axis represents the part of the response values unexplained by the "uninteresting" effects (except the interesting $i^{\text{th}}$ one), and the x-axis represents the part of the $a_i x_i$ values unexplained by the other effects. Therefore, the fitted straight line represents how the new information introduced by adding $a_i x_i$ to the model can explain the unexplained part of the response values. If the slope of the fitted line is close to zero and the confidence bounds can include a horizontal line, then the plot indicates that the new information from $a_i x_i$ does not explain the unexplained part of the response values well. That is, $a_i x_i$ is not significant in the model fit.

The notable strengths of this plot are that (1) the fitted line has a slope equal to the coefficient $a_i$ of the probed $i^{\text{th}}$ effect and a zero intercept. (2) The residuals in the $x$-axis of this plot are the

same as those of the least squares fit of the original full model unless they are adjusted. (3) The influence of the individual outcome values can be pinpointed on the coefficient estimation easily: the absence of a highly influential point would drastically change the slope $a_i$ of the fitted line. (4) Finally, the homoscedasticity and linearity brought by said effect can be visually assessed.

Ideally, the added variable plot should be performed for every effect, but it may be too dense when the model has many of them. It is, however, possible to treat the whole model as one effect and plot an "added model plot". Here, outliers are experimental output points that have the most influence on the model. In this case, the $y$-axis represents the residuals of the experimental values regressed by a constant. Be it an added model plot or an added variable plot, a 95% interval can then be added to the fitted line. See figure 3.11d for an example.

#### 3.3.2.2 ANOVA table

Analysis of variance (ANOVA) is a procedure for assigning sample variance to different sources and deciding whether these variations are significant for the model. The total variance $SS_{tot}$ is already defined in equation 3.45. Geometrically speaking, $SS_{tot}$ can also be seen as the squared length of the $\vec{Y}$ vector (see equation 3.38 and the black arrow in figure 3.12a) in a space of $n$ dimensions, that is not necessarily orthogonal. This variance $SS_{tot}$ is the sum of two variances: the "variance of the regression" $SS_R$ (sometimes referred to as the "variance of the model", it corresponds to the red arrow in figure 3.11a), with $p$ degrees of freedom (or p dimensions in the n-dimensional space presented in figure 3.12a), and the "variance of the error" $SS_E$ (sometimes referred to as the "variance of the residuals", or "residual sum of squares"). See also equation 3.46, $SS_E \equiv SS_{res}$ corresponds to the pink arrow in figure 3.11a), with $n - p = \nu$ degrees of freedom, where $p$ is the number of effects in the model.

$$SS_{tot} = SS_R + SS_E \tag{3.53}$$

$$\sum_{i=1}^{n} \left(y_i - \bar{y}\right)^2 = \sum_{i=1}^{n} \left(f_i - \bar{y}\right)^2 + \sum_{i=1}^{n} \left(y_i - f_i\right)^2 \tag{3.54}$$

where $f_i$ is the $i^{\text{th}}$ model predicted value, $y_i$ it the $i^{\text{th}}$ experimental output, and $\bar{y}$ is the grand mean. It is, of course, possible to extract the individual contribution to the variance of each effect $a_i x_i$, where each coefficient sum of square $SS_{x_i}$ is usually calculated sequentially. This means that the first coefficient linked to the first effect is chosen to minimise the first intermediate residual sum of squares out of the total sum of squares. The second coefficient is then chosen to minimise the second intermediate residual sum of squares out of the first intermediate residual sum of squares. And so on, until all coefficients have been processed. Taking figure 3.12a again, this corresponds to the breaking down the red arrow in as many arrows as there are effects, where the blue arrow, the constant, is usually the first of them.

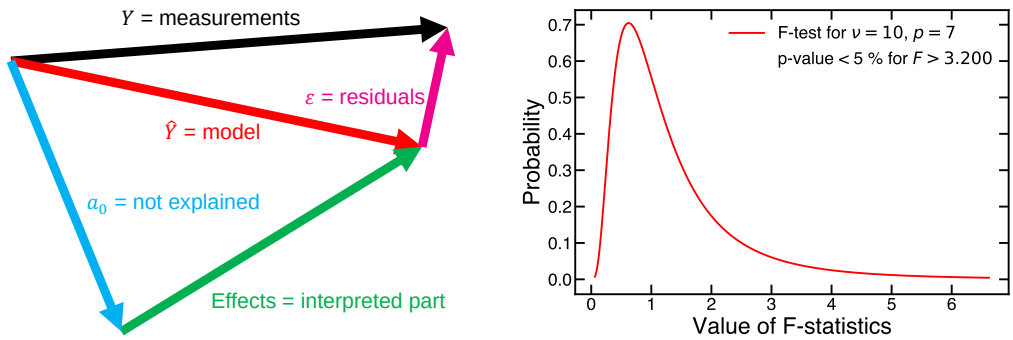


(a) Geometrical representation of a model approaching experimental values. The arrows evolve in this $n$ dimensional space, which is not necessarily orthogonal. The square of the length of each vector represents a variance discussed in this section.

(b) F-distribution and p-value. In this example, a model with $p = 7$ effects was fitted on $n = 17$ outcomes. The model tested is significant if $F > 3.2$ (p-value < 5 %).

Figure 3.12: Experimental methods, DOE: a visual representation of two ANOVA elements.

The next element appearing in an ANOVA table is the "mean squares" $MS$ of each source of variance. It is established by dividing the sum of squares by its associated degrees of freedom. This value will be the basis for an F-statistic test, or simply "F-test" $F$. An F-test is a catch-all term but is generally used to refer to the comparison of two variances using a Fisher–Snedecor distribution $f$ (see equation 3.55 and figure 3.12b). Here, the goal is to compare the variance explained by the model (or by each of its $p$ elements individually) with the unexplained variance, *i.e.*, the error variance. Hence, $F = {}^{MS_R}/_{MS_E}$.

This F-value displayed in the ANOVA table will then be used to extract a p-value, the probability of obtaining test results at least as extreme as a result observed, under the assumption that the null hypothesis "the two variances are identical" is correct. The null hypothesis can be rejected if the p-value is low enough (the standard threshold is 5%). The contribution of an individual effect is significant for the model. Suppose the p-value is greater than the established threshold. In that case, the null hypothesis cannot be rejected, and the effect's contribution is not significant for predicting an outcome.

$$f\left(F, \nu, p\right) = \frac{\sqrt{\frac{(\nu F)^{\nu} p^{p}}{(\nu F + p)^{n}}}}{F B\left(\frac{\nu}{2}, \frac{p}{2}\right)} \tag{3.55}$$

$$B\left(x, y\right) = \int_0^1 t^{x-1} (1-t)^{y-1} \, dt \tag{3.56}$$

where $B\left(x, y\right)$ is called the "beta function".

Finally, some models can be insufficiently complete. For example, trying to fit a linear model through a set of points arranged in a quadratic fashion is not optimal. In such cases, one says that the model is underfitting the data, and depending on the dataset, there is a quantitative way to decide when too much of the error in the prediction is due to "lack of (model) fit". However, this can only be observed when the two following conditions are met:

1. There is at least one replicated point in the design. Among the four designs presented in the section A.4, this condition is only met for the CCD, where the central point is run multiple times. In such cases, it is possible to calculate a "pure error sum of squares" $SS_{PE}$.
2. The model is not saturated, meaning there are fewer parameters as there are observations ($p < n$). If $p = n$, then the model fits the experimental outputs perfectly, so it is impossible to assess the "lack of fit sum of squares" $SS_{LF}$.

If these two conditions are met, the variance on the error $SS_E$ can be decomposed in a sum of two variances: the pure error sum of squares $SS_{PE}$, and the lack of fit sum of squares $SS_{LF}$. Let $c$ be the number of distinct points in the design where $n_j$ is the number of repeated runs of the $j^{\text{th}}$ distinct design point. The variance due to pure error compares each observed outcome $y_i$ with the experimental local average $\bar{y}_j$ of the $j^{\text{th}}$ design point. On the other hand, the lack of fit compares each fitted outcome $f_i$ with the experimental local average $\bar{y}_j$, weighted by the number of repetitions $n_j$. Then:

$$SS_E = SS_{PE} + SS_{LF}$$

$$\bar{y}_j = \frac{1}{n_j} \sum_{k=1}^{n_j} y_{jk} \tag{3.57}$$

$$SS_{PE} = \sum_{j=1}^{c} \sum_{k=1}^{n_j} \left(y_{jk} - \bar{y}_j\right)^2 \tag{3.58}$$

$$SS_{LF} = \sum_{j=1}^{c} n_j \left(f_j - \bar{y}_j\right)^2 \tag{3.59}$$

Once these two sum of squares are determined, the same procedure can be followed, where the $MS$ is evaluated by dividing each $SS$ term by its corresponding degree of freedom. The degree of freedom due to pure error corresponds to the number of repeated design points: $DF_{PE} = n - c$. It follows that $DF_{LF} = DF_E - DF_{PE} = c - p$, and we indeed realise the reason for the two mentioned conditions for the possible calculation of a lack of fit: if there is no replicated point in a design, then $c = n$ and $DF_{PE} = 0$. Suppose the model is saturated, $p = n$ and $DF_{LF} = 0$. See figure 3.13 for a summary of the degrees of freedom distribution.

Then, the lack of fit statistical test assesses if $MS_{LF}$ is significantly different than $MS_{PE}$. Their ratio is computed in the Fisher–Snedecor distribution, and a p-value is extracted. Given the

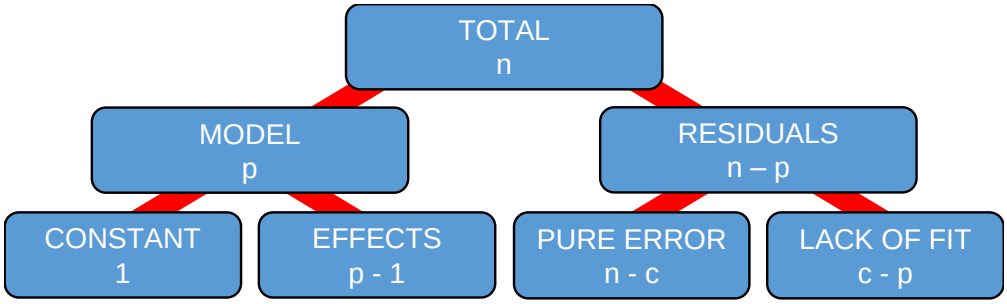


Figure 3.13: Experimental methods, DOE: degrees of freedom distribution.

nature of the statistical test, the null hypothesis can be defined as "The relationship assumed in the model is reasonable, *i.e.*, there is no lack of fit in this model". Here, it is desirable not to be able to reject the null hypothesis, where a p-value more significant than 5% is targeted.

And with this, the analysis of variance is complete, where table 3.3 summarises all the terms evaluated in this section.

Table 3.3: Experimental methods, DOE: ANOVA table. This table shows how every term is evaluated based on the equations presented in this section. In the chosen design and model, there are $n$ outcomes, $p$ effects, and $c$ distinct points. It is also interesting to evaluate the significance of the variation of each effect of the model, given by each term of $SS_R$, with respect to $SS_E$.

| Source of variance | Sum of Squares | Degrees of Freedom | Mean Squares | F-statistic | p-value |
|---|---|---|---|---|---|
| Label | $SS$ | $DF$ | $MS$ | $F$ | $p$ |
| Model | $\sum_{i=1}^{n}\left(f_i-\bar{y}\right)^2$ | $p$ | $\frac{SS_R}{p}$ | $\frac{MS_R}{MS_E}$ | $f\left(F_R, p, n-p\right)$ |
| Errors | $\sum_{i=1}^{n}\left(y_i-f_i\right)^2$ | $n-p$ | $\frac{SS_E}{n-p}$ | | |
| Lack of fit | $\sum_{j=1}^{c} n_j\left(f_j-\bar{y}_j\right)^2$ | $c-p$ | $\frac{SS_{LF}}{c-p}$ | $\frac{MS_{LF}}{MS_{PE}}$ | $f\left(F_{LF}, c-p, n-c\right)$ |
| Pure error | $\sum_{j=1}^{c}\sum_{k=1}^{n_j}\left(y_{jk}-\bar{y}_j\right)^2$ | $n-c$ | $\frac{SS_{PE}}{n-c}$ | | |
| Total | $\sum_{i=1}^{n}\left(y_i-\bar{y}\right)^2$ | $n$ | | | |

# 4 InGaN by PECVD

This chapter presents studies related to InGaN layers deposited by PECVD. The first section explores the effect of simple deposition parameters, such as the temperature or the flow of one precursor, on essential layer characteristics, such as the bandgap, the growth rate, or the crystallinity. After this is discussed, a small study on the effect of the growth rate on the bowing parameter of InGaN's Vegard's law is presented. Then, a more in-depth analysis of the plasma dynamics follows, thanks to the TOF-MS. Finally, the DOE method is applied to all the deposited layers to confirm all observed in the first sections of the present chapter.

The overall goal of this chapter is to explore the three first research questions, which are the following:

1. Is it possible to produce InGaN materials at low temperatures?
2. If yes, how compatible are the characteristics of these layers for PV application?
3. If they are compatible enough, how stable do they remain when p- or n-doping is added?

The layer characteristics that are aimed at are the ones presented in table 2.1. However, the following quality metrics will be used here: the Urbach energy $E_U$ that should be inferior to at least 100 meV, and the crystallite size *CrSz* that should be in the same range as the thickness of the layer considered. In detail for GaN, the aims are the following: a BG of 3.4 eV, a refractive index of 2.50 (a sign of a dense layer), and a measurable resistivity of $10^5\,\Omega$ cm (also achievable thanks to doping). In detail, for the InN, the aims are the following: a BG of 0.7 eV, a refractive index of 2.95 (a sign of a dense layer), and a resistivity of $0.45\,\Omega$ cm (also possible thanks to doping). Depending on the best performances achieved in this chapter, these key values will also help determine if the PECVD III-N layers can be used as an absorber or as a contact.

## 4.1 GaN & InN: influence of the deposition parameters

In this section, Aman Singh deposited and characterised the layers for his semester project in PV-lab under my and Mathieu Boccard's supervision and leadership. I then analysed and eventually integrated these results in writing a paper on the InGaN BG dependence on the

growth rate, mainly presented in the next section. This first section aims to (re-)acquire basic knowledge on how specific deposition parameters influence essential layer characteristics. For that purpose, GaN layers were deposited under different conditions, and the main results are presented in figure 4.1.

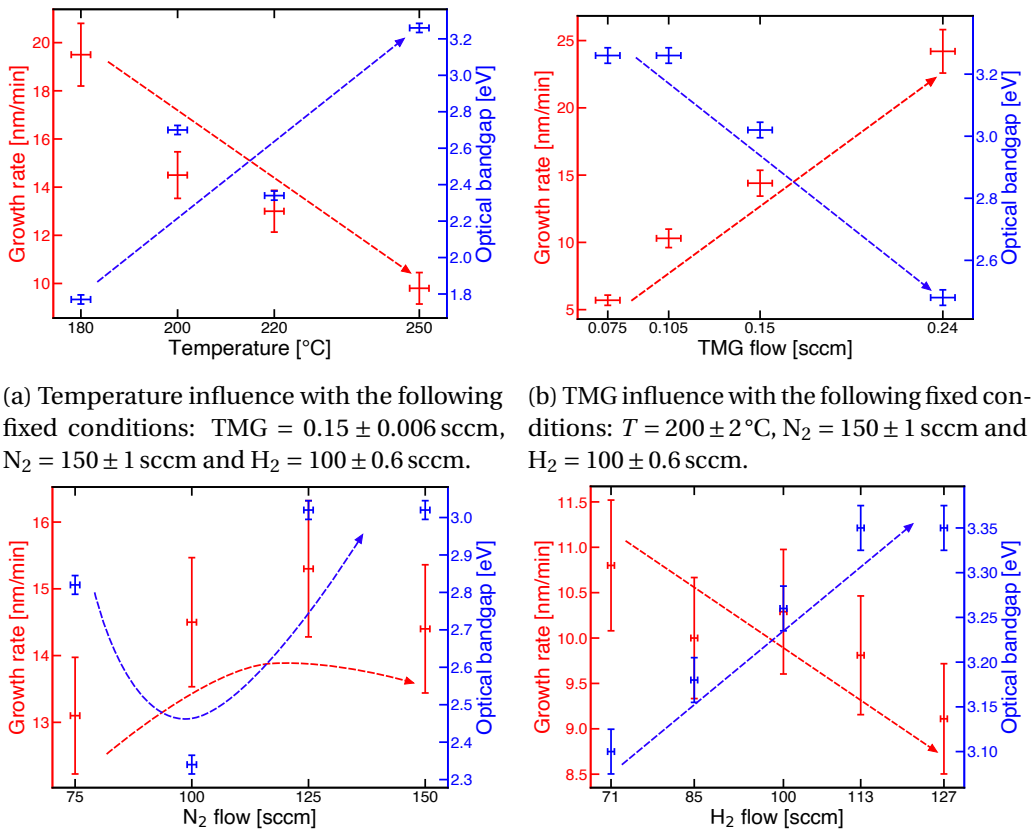


(a) Temperature influence with the following fixed conditions: TMG = $0.15 \pm 0.006$ sccm, $N_2 = 150 \pm 1$ sccm and $H_2 = 100 \pm 0.6$ sccm.

(b) TMG influence with the following fixed conditions: $T = 200 \pm 2\,°C$, $N_2 = 150 \pm 1$ sccm and $H_2 = 100 \pm 0.6$ sccm.

(c) $N_2$ influence with the following fixed conditions: TMG = $0.15 \pm 0.006$ sccm, $T = 200 \pm 2\,°C$ and $H_2 = 100 \pm 0.6$ sccm.

(d) $H_2$ influence with the following fixed conditions: TMG = $0.15 \pm 0.006$ sccm, $N_2 = 150 \pm 1$ sccm and $T = 200 \pm 2\,°C$.

Figure 4.1: GaN PECVD, deposition parameters: temperature, TMG, $N_2$ and $H_2$ effect on the growth rate and the optical BG on a glass substrates. Dashed trendlines are added to help the reader's eye.

If we first analyse the effect of these four deposition parameters on the optical BG, with an ideal value of 3.40 eV in mind, we see that it is better approached at high temperature, at low TMG and high $N_2$ and $H_2$ flows. These observed trends will also lower the growth rate, except for the nitrogen flow. A BG value closer to literature ones means that the optical quality metrics hold better features. In other words, the optical characteristics of the layers are of higher quality when the deposition parameters are tuned in the way described here or, more generally, when the growth rate is reduced. Decreasing the growth rate is here a key element of the deposition of In/GaN by PECVD, since it gives more time for the adatoms to arrange themselves, decreasing the grain boundary density and improving the crystallinity of the deposited layer, which will also have a positive impact on the optical and electrical properties.

Decreasing the growth rate can be achieved by reducing the TMG flow: fewer metallic atoms are present in the plasma and deposited on the layer. Increasing the temperature will give more energy to the surface adatoms to reach a lower energy state when binding with the layer; this will decrease the growth rate and densify the layer. Hydrogen, on its part, will promote the dissociation of the TMG molecule, making more radicals available for the growth of the material. However, it will also have a diluting power of the other precursors and an etching effect on the already deposited layer, with an overall net decrease in the growth rate when its flow increases. Nitrogen also has two counter-balancing effects when increased: more dilution but more nitrogen radicals to react with the metallic atoms. However, since nitrogen is not the limiting factor in growth rate, the diluting effect counter-balances the deposition effect by far, and the dilution is expected to increase. However, this is not what was observed in figure 4.1c, which is difficult to explain. Fioretti *et al.* [60] also observed an increase of the Raman crystallinity when decreasing the growth rate at a fixed $N_2$:TMG ratio, but also an increase of the crystallinity when increasing the $N_2$:TMG ratio at a fixed growth rate. On the nitrogen effect, we will conclude that it is better to increase the dilution, as expected.

Table 4.1: In/GaN PECVD, deposition parameters: six InN layers on a glass substrate. The nitrogen flow was fixed at $150 \pm 1$ sccm, and the temperature at $250 \pm 2$ °C.

| N° | $N_2^{TMI}$ $\pm 0.04$ [sccm] | $H_2$ $\pm 0.6$ [sccm] | Time $\pm 1/60$ [min] | $g$ [nm/min] | $E_{04}$ [eV] |
|---|---|---|---|---|---|
| 1 | 2.4 | 50 | 16 | $10.0 \pm 0.7$ | - |
| 2 | 2.0 | 70 | 20 | $7.30 \pm 0.49$ | - |
| 3 | 1.7 | 71 | 23 | $6.96 \pm 0.46$ | - |
| 4 | 1.5 | 60 | 23 | $5.52 \pm 0.37$ | - |
| 5 | 1.2 | 51 | 30 | $4.47 \pm 0.30$ | $1.70 \pm 0.03$ |
| 6 | 1.2 | 85 | 30 | $4.10 \pm 0.27$ | $1.70 \pm 0.03$ |

For the InN, among the deposited layers, only six are presented here, in table 4.1; they are enough to represent most of the trends found in the InN deposition by the System B. Similar to what was observed for GaN, the growth rate of InN depends significantly on the TMI flow rate. At a growth rate of around 5.5 nm/min and above, the InN films display a metallic behaviour, showing no optical bandgap. It is also observed that lowering the growth rate causes the absorption values to go down in the range of $1-2$ eV. At a growth rate of around 4.5 nm/min, an optical BG of $1.70 \pm 0.03$ eV is measured, corresponding to what is found in the literature for $E_{04}$. Below this growth rate, the optical bandgap remains the same. However, the Urbach energy (tail) is reduced with a lowering growth rate (not shown here).

A highly defective film growth mechanism could explain this behaviour. Continuous defect states across the BG lead to significant optical absorption at high growth rates below the BG energy. As the growth rate is lowered, these defects become less pronounced, especially in the midgap region, which brings the optical absorption down in this range. The band edges, however, are dominated by defect states arising from dangling bonds on the surface, which are less affected by the growth rate. Due to these dangling bonds, the optical absorption at

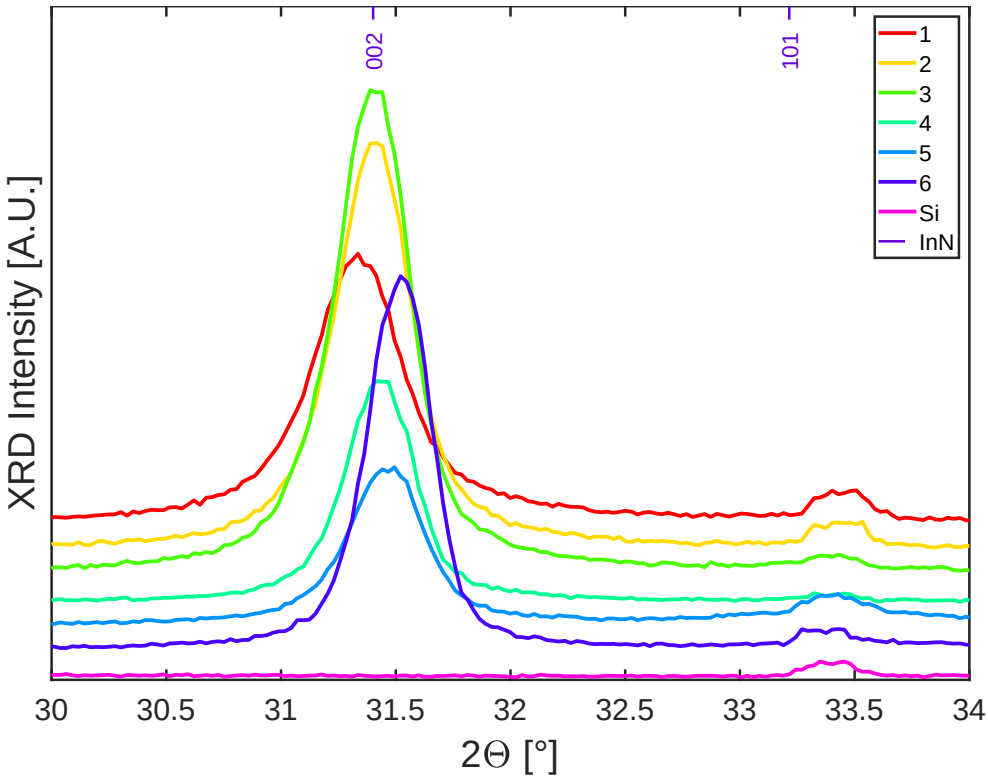


Figure 4.2: In/GaN PECVD, deposition parameters: InN XRD (002) peak on a silicon substrate (pink line). See table 4.1 for more details on the deposition conditions that produced these layers.

low energies is significant even at the lowest growth rates. The fact that lower growth rates show smaller Urbach energies, leading to a sharper drop close to the band edges, also bolsters this hypothesis. This hypothesis can be further tested and validated by adding a surface passivation layer and studying its effect on the optical absorption curve.

Figure 4.2 shows the XRD pattern of the InN films. All films show a very intense InN (002) peak, indicating preferential orientation along the plane. However, weak peaks corresponding to InN planes of (103), (112) and (004) were also detected (not shown here). The InN (002) peak for all samples was shifted to lower angles compared to the bulk value of 31.40°, indicating the presence of residual tensile stress in the films along the hexagonal c-axis. With an increase in growth rates, the amount of peak shift increases, implying an increase in residual stress. The peak is centred at $31.16 \pm 0.01°$ for the lowest growth rate of $4.10 \pm 0.27$ nm/min, while the centre is at $30.90 \pm 0.01°$ for the highest growth rate of $10 \pm 0.7$ nm/min.

## 4.2 InGaN: influence of the deposition parameters

Some of the layers presented in this section were deposited and characterised by four master students that were realising their semester project on InGaN PECVD development under

my and Mathieu Boccard's supervision: Nils Toggwyler, Aman Singh, Mélanie Rouèche and Antoine Devincenti. This section inspired most of what is published in the Journal of Vacuum Science and Technology A (JVST-A) [53].

An InN or GaN layer with low defect concentration should have an optical BG $E_{04}$ close to its electronic BG value (0.7 eV or 3.4 eV, respectively), large crystallite size, and a low Urbach energy (preferentially below 0.05 eV). In this section, InGaN layers were first deposited using $N_2$ as the nitrogen source, the results of which are presented in section 4.2.1. It is shown how the defect concentration changes depending on the growth rate. Table 4.2 shows the details of the deposition parameters used with $N_2$. To further reduce the growth rate, InN and GaN layers were then grown using ammonia as the nitrogen source, and the results are presented in section 4.2.2.

Table 4.2: In/GaN PECVD, deposition parameters: the partially explored parameter space for InN and GaN baseline optimisation. The arrows on the right-hand side show the qualitative effects of a parameter increase on three film characteristics: the growth rate $g$ on glass, the optical BG $E_{04}$ of InN or GaN layers on glass, and the crystallite size on silicon. For example, increasing the temperature will decrease the growth rate, bringing InN layer's optical BG closer to 0.7 eV or GaN layer's optical BG closer to 3.4 eV, and increase the grain size. The pressure and power were kept constant, at $500 \pm 2\,\mu$bar and $30 \pm 3$ W respectively.

| Dep. Param. | Min. | Max. | Error | Unit | g | $E_{04}$ InN | $E_{04}$ GaN | Cr. Sz. |
|---|---|---|---|---|---|---|---|---|
| TMI | 0.3 | 2.0 | 0.04 | sccm | ↑ | = | | = |
| TMG | 0.05 | 0.09 | 0.006 | sccm | ↑ | | = | = |
| $N_2$ | 75 | 150 | 1 | sccm | ↓ | = | = | = |
| $H_2$ | 50 | 100 | 0.6 | sccm | = | ↓ | ↑ | ↑ |
| Temperature $T$ | 180 | 250 | 2 | °C | ↓ | ↓ | ↑ | ↑ |
| Time $t$ | 10 | 30 | 1/60 | min | = | = | = | = |

### 4.2.1 Nitrogen source: $N_2$

InGaN layers were deposited by PECVD, and different indium contents ($19\,\% \leq X_{\mathrm{In}} \leq 72\,\%$) and growth rates ($4.1 \leq g \leq 8.4$ nm/min) were investigated. Optimised InN and GaN experimental layer characteristics define the extremes of this variation.

XRD measurements of In/GaN layers deposited on untreated (001) c-Si wafers show a (002) preferential growth, whereas the $In_{0.3}Ga_{0.7}N$ layer also shows a (100) peak (see figure 4.3a). Based on similar works on the growth of ZnO [56, 130], it is proposed that this behaviour is due to the initial layer being aligned along the c-axis, which is consistent with the lowest surface free energy of the (002) plane in wurtzite InGaN or ZnO. This also implies that our growth conditions are not in thermodynamic equilibrium, which leads to the apparition of non-minimum surface free energy (NMSE) grain in the initial layer, whose preferential orientation will grow faster perpendicularly to the substrate. Different deposition conditions

could alter the overall preferential orientation, where the main adjusting factors would be temperature and layer thickness.

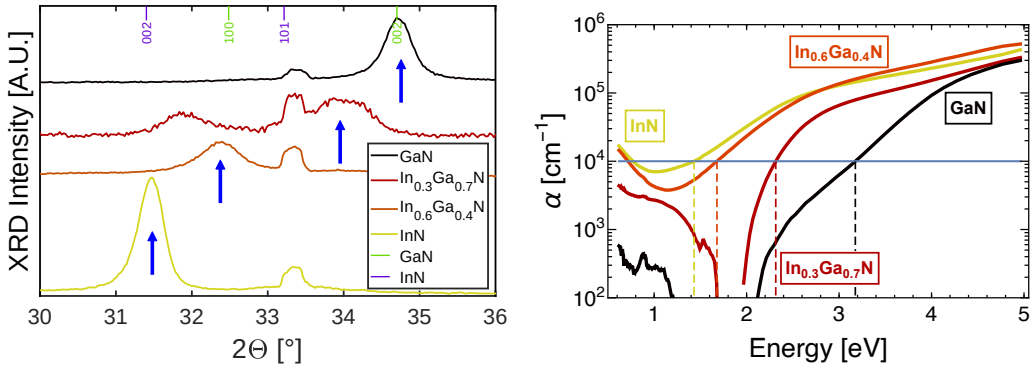


(a) InGaN XRD patterns on a silicon substrate. The blue arrows follow the (002) peak. The small peak at 33.2 ° is identified as the 200 forbidden reflection of the c-Si wafer. No phase segregation is observed. $In_{0.3}Ga_{0.7}N$ signal is multiplied by 5.

(b) InGaN Absorption coefficient spectra on a glass substrate. The optical BG $E_{04}$ is indicated by the vertical dashed line of the corresponding colour.

Figure 4.3: In/GaN PECVD, deposition parameters: XRD patterns and absorption coefficient for the InN, $In_{0.6}Ga_{0.4}N$, $In_{0.3}Ga_{0.7}N$ and GaN layers. InGaN BG and lattice parameter shift with indium concentration.

InN layers display sharper peaks than GaN, which in turn are sharper than InGaN ones. This implies that InN layers contain the largest crystals (~ 30 nm) of the three species (not shown in a figure). No InN or GaN phase segregation is observed in any InGaN layer probed by XRD. Phase separation relies on multiple factors. In any alloy, it requires long-range diffusion; thus, a correlation between phase separation and growth rate is expected. The different interatomic distance between GaN and InN can also give rise to a phase miscibility gap that increases with indium content [162]. At high temperatures, this phenomenon is also exacerbated by the high vapour pressure of InN with respect to that of GaN, leading to low indium incorporation in the InGaN layer. It is assumed that the reason for an absence of phase separation in the layers presented here is their thinness (less than 150 nm) and the choice of the deposition parameters used for growing the films: the use of relatively low growth temperatures, low growth rate, low growth pressure and high V/III flow ratio [20].

Compared to InN and GaN XRD reference peaks, InGaN XRD 110 peaks are then used to assess the indium content $X_{In} = \frac{In}{In+Ga}$ (In & Ga in at. %, $X_{In}$ in %) of the layers that were crystalline enough, which are compared to the values extracted from EDS measurements (see figure 4.4b). Both methods confirm one another within a ±3% error margin and are thus deemed reliable. For the modelling of the optical BG as a function of $X_{In}$, the XRD result is chosen for its higher reliability and simplicity compared to EDS. Indeed, when using EDS, ZAF corrections are applied to convert apparent concentrations (raw peak intensity) into (semi-quantitative) concentrations corrected for inter-element matrix effects. Very simplistically, Z is the atomic

number correction related to the stopping power of the element; A is the absorption correction - less energetic X-rays from lighter elements are absorbed upon leaving the sample by heavier elements; F is the fluorescence correction - A more energetic X-ray leaving the sample can fluoresce a lower energy X-ray from a lighter element. The ZAF routine is iterative; it needs information on concentrations to proceed, but these are absent at the start. So the results from the first iteration are fed back to the second, and so on, until a limit is reached that is statistically satisfactory. On the other hand, the XRD peaks position varies with the inverse of the sinus of the interplanar distance (see figure 4.4a and refer to Bragg's law in equation 3.20), which in turn depends linearly on the indium content $X_{\mathrm{In}}$.

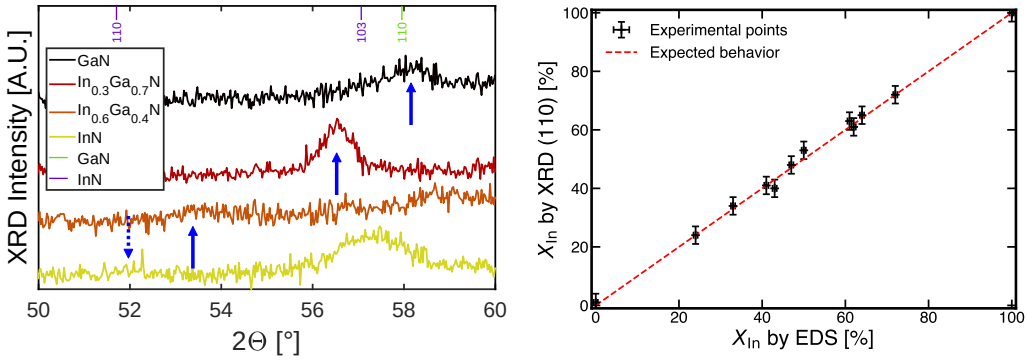


(a) For the same layers as the ones presented in figure 4.3, XRD 110 peak (followed by the blue arrow, not visible for the InN layer), that was used to determine the indium content $X_{\mathrm{In}}$.

(b) Comparison between the indium content determined by XRD (using the 110 peak) and EDS. The difference between the two measurements is less than 3 % in absolute value.

Figure 4.4: In/GaN PECVD, deposition parameters: determination of the indium content of InGaN layers by XRD & EDS on a silicon substrate.

Figure 4.3b shows that the optical BGs $E_{04}$ are determined from the intersection with the horizontal blue line, as stated in the experimental method (page 41, section 3.2.2.4). Due to their ternary nature, InGaN layers are expected to obey Vegard's law, with a bowing parameter $b$ (see equation 4.1a) [133]. Figure 4.5 shows the optical BG $E_{04}$ as a function of the indium content $X_{\mathrm{In}}$ for different growth rates. The points are widely spread out, and a single bowing parameter cannot be extracted. However, if we consider the variation of $E_{04}$ for a fixed growth rate, Vegard's law is respected for each growth rate, and it is observed that a higher growth rate yields a higher $b$ parameter than for lower growth rates. Thus, the bowing parameter of Vegard's law seems to depend on the growth rate $g$.

$$E_g^{\mathrm{InGaN}}(X_{\mathrm{In}}) = X_{\mathrm{In}} E_g^{\mathrm{InN}} + (1 - X_{\mathrm{In}}) E_g^{\mathrm{GaN}} - b X_{\mathrm{In}}(1 - X_{\mathrm{In}}) \tag{4.1a}$$

$$E_g^{\mathrm{InN}} = a_1^{\mathrm{InN}} g + a_2^{\mathrm{InN}} \tag{4.1b}$$

$$E_g^{\mathrm{GaN}} = a_1^{\mathrm{GaN}} g + a_2^{\mathrm{GaN}} \tag{4.1c}$$

$$b = a_1^b g + a_2^b \tag{4.1d}$$

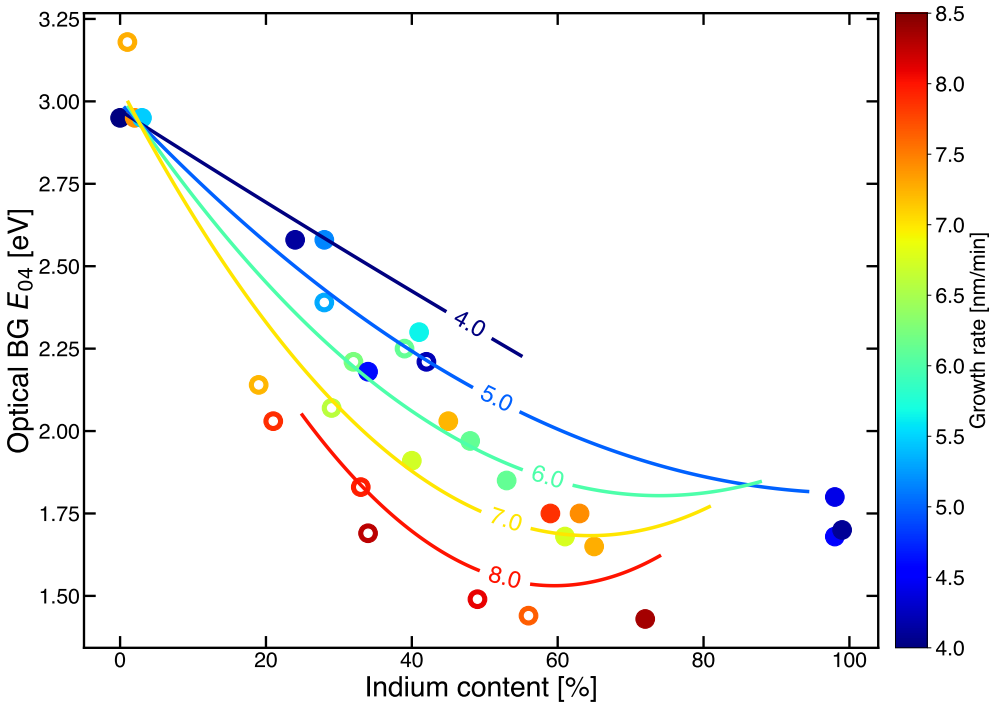


Figure 4.5: In/GaN PECVD, deposition parameters: growth rate fitted isocurves on the optical BG as a function of the indium content $X_{\mathrm{In}} = \frac{\mathrm{In}}{\mathrm{In+Ga}}$ (In & Ga in at. %, $X_{\mathrm{In}}$ in %). The bowing parameter visibly increases with increasing growth rates. The open symbols correspond to layers whose crystallinity was not good enough for the indium content to be determined by XRD. The EDS value was taken instead for those layers. The error on the indium content is ±3 %, the error on $E_{04}$ is ±0.03 eV.

To test this observation, a model based on Vegard's law is developed by letting Vegard's three parameters (the GaN BG $E_g^{\mathrm{GaN}}$, the InN BG $E_g^{\mathrm{In}}$, and the bowing parameter $b$) depend on the growth rate $g$. The dependency is chosen to be linear for each of the three parameters as a first approximation, as detailed in the set of equations 4.1. Six empirical fit parameters are then chosen for the lowest sum of squares of residuals of the model over the experimental points: $a_1^{\mathrm{InN}}$, $a_2^{\mathrm{InN}}$, $a_1^{\mathrm{GaN}}$, $a_2^{\mathrm{GaN}}$, $a_1^b$ and $a_2^b$. Given Vegard's law's configuration, this means that on top of having a quadratic dependency on the indium content $X_{\mathrm{In}}$, the BG of InGaN layers also has a linear dependency on the growth rate $g$.

This model is fitted to the experimental points without constraints, where each point represents an InGaN layer with measured growth rate $g$, indium content $X_{\mathrm{In}}$, and optical BG $E_{04}$. The resulting fit parameters and statistics are presented in table 4.3. The model is in excellent agreement with experiments, with a fit residual under 10 %. According to this model, Vegard's bowing parameter $b$ increases with increasing growth rate, reaching 4.33 eV at a growth rate of 8 nm/min. The low values reach 0.10 eV (almost no bowing) for the lowest growth rate of 4 nm/min. Orsal and co-authors have shown that the bowing parameter usually takes values between 1 eV and 3 eV for InGaN compounds [133].

Table 4.3: In/GaN PECVD, deposition parameters: coefficients of best fit for the modified Vegard's model. This includes different goodness of fit evaluations: residual sum of square $SS_{res}$, coefficient of determination $R^2$ and Mordecai Ezekiel's adjusted coefficient of determination $R^2_{adj}$ [198].

| Coefficient | Value | Std. dev. |
|---|---|---|
| $a_1^{\mathrm{InN}}$ | 0.143 | 0.088 |
| $a_2^{\mathrm{InN}}$ | 1.097 | 0.411 |
| $a_1^{\mathrm{GaN}}$ | 0.0240 | 0.0466 |
| $a_2^{\mathrm{GaN}}$ | 2.876 | 0.286 |
| $a_1^{b}$ | 1.056 | 0.280 |
| $a_2^{b}$ | -4.116 | 1.514 |
| $SS_{res}$ | 0.472 | |
| $R^2$ | 92.9 % | |
| $R^2_{Adj}$ | 91.1 % | |

According to Walukiewicz *et al.* [188], InN layers with an optical BG above 1 eV indicate a high electron concentration. Hall effect measurements on an InN layer ($E_{04} = 1.70 \pm 0.03$ eV) confirmed an electron concentration of $n = 1.90 \pm 0.05 \cdot 10^{21}\,\mathrm{cm}^{-3}$ and a mobility of $\mu = 33.4 \pm 0.8\,\mathrm{cm}^2/\mathrm{Vs}$. This is coherent with the ellipsometry measurement (assuming an effective mass of $0.25 m_e$ in the Drude model [64]) and indeed confirms the link between the BG and the electron concentration proposed by Walukiewicz *et al.*, based on the Burstein-Moss effect. Such high electron concentrations imply that these layers can be considered unsuitable for PV absorbers as the high carrier concentration would likely entail a short lifetime due to Auger recombination. InGaN layers with lower indium content are also suspected to be degenerately doped.

Given the behaviour of the bowing parameter in the model, we infer that for degenerately doped layers, a relatively better crystallinity and, in turn, a lower sub-band absorption is reached at a lower growth rate. This claim is supported by a general decrease in the Urbach energy of all the layers with decreasing growth rate for any $X_{\mathrm{In}}$, as shown in figure 4.6a. The lower growth rate gives enough time to the adsorbates to arrange themselves with fewer native defects or carbon impurities [92], leading to a lower Burstein-Moss shift and a lower Urbach energy, along with better crystallinity. A reduction in the defect concentration decreases the sub-BG absorption and results in a sharper band edge and a higher optical BG for GaN, or a lower optical BG for InN. This also explains the smaller bowing parameter for lower growth rates. Moreover, since the Fermi level stabilisation energy $E_{FS}$ lies within the conduction band (respectively BG) for InN (respectively GaN), InN layers are more easily degenerately doped. Thus, it is also observed that the growth rate has a more substantial influence on the InN BG than on the GaN bandgap, which is manifested in the $a_1^{\mathrm{GaN}}$ factor being smaller than the $a_1^{\mathrm{InN}}$ one [182]. In terms of XRD measurements, the lowest growth rates yield a higher XRD intensity (see filled symbols in figures 4.5 and 4.6b). Peaks almost systematically appear for a growth rate below 6 nm/min.

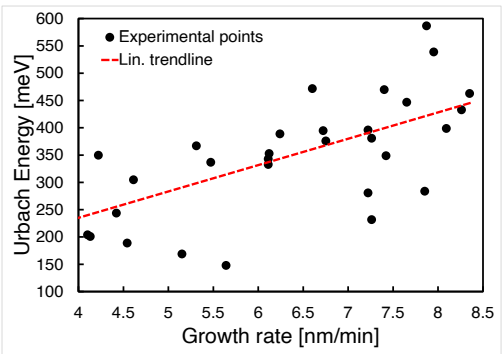


(a) Urbach energy of all the InGaN layers on a glass substrate, without taking the indium content into account (which in turn induces more spreading of the points). The linear trendline over all the points (only painted here to guide the eye) shows a sharper band edge absorption for lower growth rates. The error bars are removed for clarity; ±10 % relative to the growth rate, and ±4 meV for the Urbach energy.

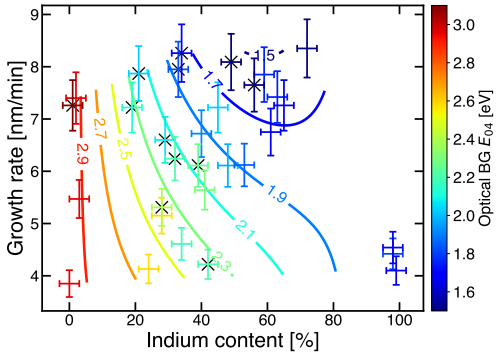


(b) Optical BG fitted isocurves on the growth rate as a function of the indium content $X_{\mathrm{In}}$. The points with an additional "X" symbol correspond to layers whose crystallinity was not good enough for $X_{\mathrm{In}}$ to be determined by XRD. For those layers, the EDS value was taken instead.

Figure 4.6: In/GaN PECVD, deposition parameters: Urbach energy and parameter space.

Unfortunately, growth rates lower than 4 nm/min, which should further improve the crystallinity, could not be reached due to the instrumental limits of our system. This limit is also visible in figure 4.6b, where indium contents $X_{\mathrm{In}}$ between 5-20 % and 60-95 % (at low growth rate) are not achieved due to low TMI or TMG flow rates, and this parameter space could not be explored. One solution would be to increase the density of atomic nitrogen or hydrogen to reach a different metallic composition in the plasma. However, a change in the precursors was preferred and used: $NH_3$ instead of $N_2$, as $NH_3$ yields more free nitrogen radicals than $N_2$ in similar plasma conditions. This allows a higher dilution and hence a lower growth rate, enabling a broader parameter space exploration. Only InN and GaN layers were deposited with ammonia; the results are presented in the following subsection.

### 4.2.2 Nitrogen source: $NH_3$

Ammonia was used as a nitrogen source to achieve lower growth rates for InN and GaN layers. Due to its lower bonding energy than dinitrogen, ammonia has a higher dissociation rate, leading to higher atomic nitrogen density in the plasma.

Given the similar parameter space explored with ammonia for InN and GaN layers, the deposition parameters have the same expected influence as with $N_2$. Hydrogen and plasma power are expected to increase the growth rate due to an increased dissociation of TMG (or TMI) molecules. However, this is not observed because, within the explored parameter space, the TMG (or TMI) is already fully dissociated, leading to the growth being limited by metallic precursor flow rates [60]. For more details, see table 4.4, which is extracted from a DOE on InN

layers whose details are presented in appendix B.1.3. Using $NH_3$, InN and GaN layers could be deposited with growth rates down to 1.5 nm/min.

Table 4.4: In/GaN PECVD, deposition parameters: partially explored parameter space for InN and GaN baseline optimisation with ammonia. The arrows on the right-hand side show the qualitative effects of a parameter increase on three film characteristics: the growth rate $g$ on glass, the optical BG $E_{04}$ on glass, and the crystallite size on silicon; like in table 4.2. These results were extracted using a DOE on InN layers, whose ANOVA tables B.1, B.2 and B.3 are available in appendix B.1.3.

| Dep. Param. | Min. | Max. | Error | Unit | $g$ | $E_{04}$ InN | $E_{04}$ GaN | Cr. Sz. |
|---|---|---|---|---|---|---|---|---|
| TMI | 1 | 2 | 0.04 | sccm | ↑ | = | | = |
| TMG | 0.4 | 2 | 0.006 | sccm | ↑ | | = | = |
| $NH_3$ | 15 | 25 | 0.08 | sccm | ↓ | = | = | = |
| $H_2$ | 0 | 150 | 0.6 | sccm | = | ↓ | ↑ | ↑ |
| Pressure ($Pr$) | 480 | 520 | 2 | $\mu$bar | = | = | = | = |
| Power ($Po$) | 20 | 30 | 3 | W | = | ↓ | ↑ | = |
| Temperature ($T$) | 180 | 250 | 2 | °C | ↓ | ↓ | ↑ | ↑ |
| Time ($t$) | 16 | 120 | 1/60 | min | = | = | = | = |

Regarding their crystallinity features, figure 4.7 shows clear nanocrystals of up to 30 nm, observed with a TEM. Note that no preferential orientation is visible on the diffraction pattern, which is expected as the layers are deposited on amorphous carbon films. XRD measurements reveal higher peak intensities for both InN and GaN layers than with the $N_2$ source, but with a similar crystallite size (see the similar full width at half maximum (FWHM) of the peaks in figure 4.8a). For a more precise estimation of the crystallite size using XRD, see equation B.1c, along with corresponding table B.3 in section B.1.3. This implies that the crystallites do not span the entire thickness of the layer.

In terms of optical properties, the GaN layer displays the same features as with di-nitrogen, as shown in figure 4.8b, with an Urbach energy around $290 \pm 1$ meV. On the contrary, the InN layer deposited with ammonia exhibits an Urbach energy of $187 \pm 2$ meV, while the one deposited using di-nitrogen has an Urbach energy of $463 \pm 3$ meV. Assuming that the electron concentration remains in the same order of magnitude, the Burstein-Moss effect will lead to the same shift. However, since there are fewer sub-BG defects when growing the layer with ammonia, the band tail is reduced, and the optical BG is pushed to higher values. Thus, despite the persistent Burstein-Moss effect, deposition with ammonia improves the layer quality noticeably for InN more than for GaN. The FCA feature nevertheless remains present for all the layers, implying an out-of-equilibrium deposition and that they still cannot be used effectively as absorbers for PV applications.

In conclusion, using ammonia to reduce the growth rate effectively improves crystallinity and reduces sub-BG absorption. However, the defect concentration responsible for the FCA and the Burstein-Moss effect is still persistent and too high for possible PV integration as an absorber. Indeed, fewer defects are necessary for possible extrinsic doping of the layer, with a

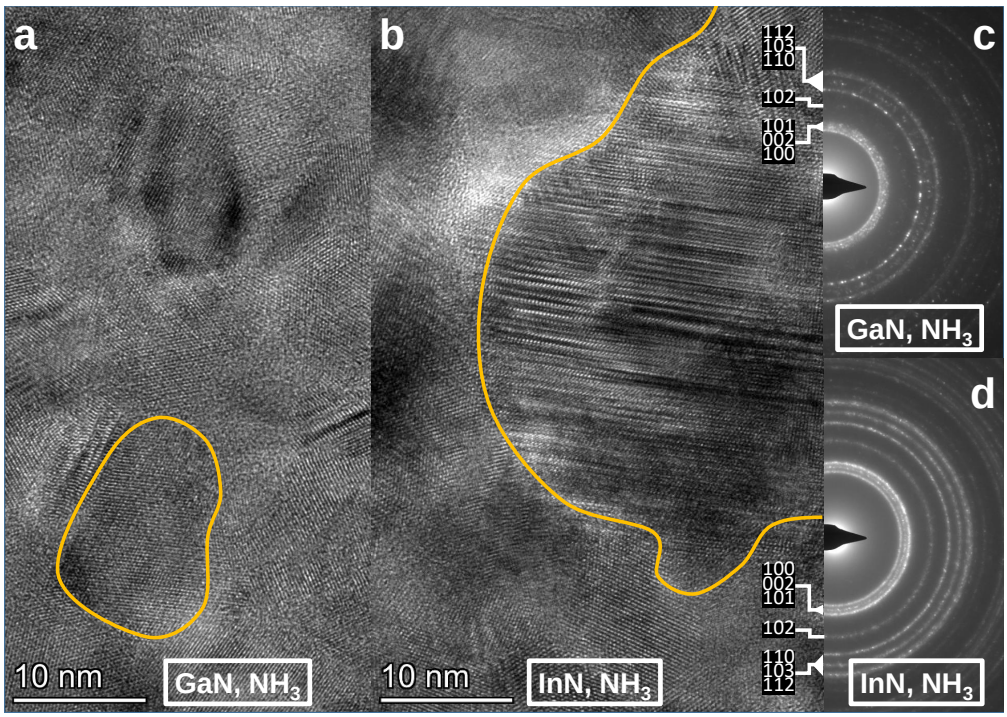


Figure 4.7: In/GaN PECVD, deposition parameters: HRTEM micrographs of a GaN layer (a) and an InN layer (b) grown by PECVD on an amorphous carbon TEM grid film with $NH_3$ at low growth rates (less than 2 nm/min). Their respectively associated diffraction patterns are shown in figures (c) and (d). High-quality crystals of sizes ranging from 10 – 30 nm can be observed.

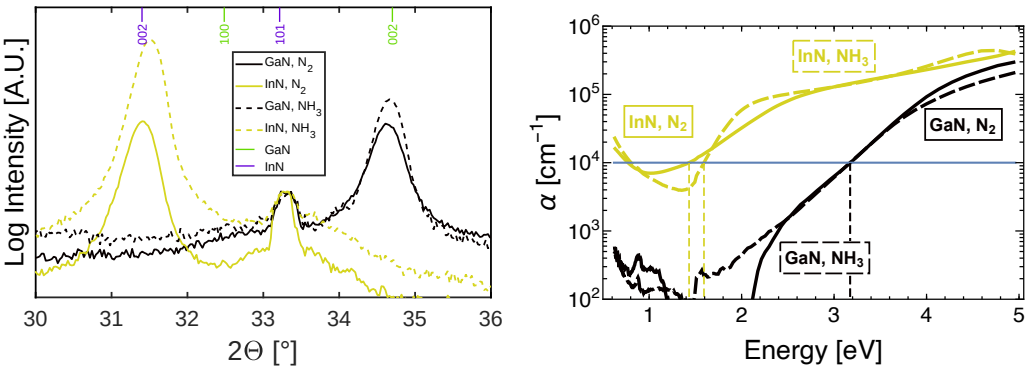


(a) XRD patterns of InN (yellow) and GaN (black) layers deposited on a silicon substrate using $N_2$ (solid) and $NH_3$ (dashed). The thickness is similar, and the signal is normalised on the silicon peak at 33.3°. The peak intensity is higher for layers with a lower growth rate, achieved using ammonia.

(b) Comparison between InN and GaN layers grown on a glass substrate using either $NH_3$ or $N_2$ as the nitrogen source. For the layers grown with ammonia, a growth rate below 2 nm/min could be reached.

Figure 4.8: In/GaN PECVD, deposition parameters: Urbach energy and parameter space.

much cleaner band edge. Regarding electron transport, since the layer is a conglomerate of crystallites, charge carriers have a high probability of recombining at the grain boundaries. However, by reducing the growth rate with ammonia, we can prove that the crystallite size increases, the Urbach energy is reduced, and the crystallinity is improved, which are steps in the right direction.

### 4.2.3 InGaN PECVD: key take aways & next steps

InGaN layers with varying chemical compositions were deposited using PECVD and $N_2$. A 3D fit was performed (model in equation 4.1 and results in table 4.3) describing the variation of their optical BG with the growth rate and the indium content $X_{\mathrm{In}} = \frac{\mathrm{In}}{\mathrm{In+Ga}}$ (In & Ga in at. %, $X_{\mathrm{In}}$ in %). An excellent fit with experimental values is observed within the parameter space explored here (19 at. % $\leq X_{\mathrm{In}} \leq$ 72 at. %, and $4.1 \leq g \leq 8.4$ nm/min). XRD peaks in InGaN layers shift according to their indium content, and no phase segregation was observed in any layer.

Optical measurements show that most layers are electronically degenerate and, thus, unsuitable for PV applications. This behaviour is explained using the position of the Fermi level stabilisation energy and the concentration of intrinsic defects created during deposition. To avoid this degeneration, the defect concentration needs to be reduced.

Even though they are degenerate, no clear relation could be established between the electron concentration and the growth rate since the layers were too resistive for reliable Hall effect measurements. Thus, it would be interesting to vary the growth rate at a constant In/(In+Ga) ratio to observe the dependence of the electron concentration on the growth rate with less resistive samples. That would allow for a comparison between our results and those of Walukiewicz *et al.* (see figure 14 of their paper [188]).

Ammonia is helpful since it gives rise to a higher density of nitrogen radicals in the plasma. This allows for higher metallic precursor flows without the detrimental growth of metal-rich films. Larger crystallites and lower Urbach energy were achieved, but the InN or GaN layers developed with ammonia still show high extents of degeneracy, manifested by a persistent FCA and Burstein-Moss shift. By improving these characteristics, maybe with the help of annealing or higher deposition temperatures, extrinsic doping and integration as a carrier contact in a silicon heterojunction configuration can be achieved.

As an outlook, the unexplored parameter space mentioned in section 4.2.1 can also be probed thanks to ammonia. InN and GaN layers can still be improved with growth rates lower than 1 nm/min, to reach an Urbach energy below 0.1 eV. Post-deposition annealing or higher deposition temperatures can also help extend the crystallite size even further [38]. Other calculation details are presented in Appendix B.1, such as the 3D fit of the model and the ANOVA tables of the different DOEs performed here.

## 4.3 Time-of-flight mass spectrometer

### 4.3.1 Motivation & procedure

PECVD depositions are pretty complex; many knobs can be turned, and many parameters can be tuned. The plasma dynamics linked to these parameters can be complex, even more so when mixed.

This section aims to better understand the plasma dynamics during the deposition and link some observations to deposition events and layer characteristics. This will lead to better control and forecast of the layer characteristics or may prove helpful to optimise the deposition process faster. Different findings are presented in this section: the importance of a low base pressure, how ammonia is synthesised and dissociated, the links between specific deposition parameters and certain layer characteristics, and a small analysis of plasma by-products.

The tool used for that is a TOF-MS. For more details about its functioning and connection to System B, please consult section 3.2.1. Please also note that when the evolution of a peak of interest is presented (such as in figure 4.9b), it will always follow this pattern unless stated otherwise:

1. The plasma is turned off, but the precursor gases flow through the chamber at a stable rate, hence the non-zero signal.
2. The plasma is turned on, resulting in either a sharp increase or decrease
3. The event of interest for which the figure is used happens during the plasma deposition.
4. The plasma is turned off, resolving the system to the initial state.

As stated in section 3.2.1, the first observed result given by a TOF-MS is a spectrum of all the $m/q$ intensities, usually from 2 to 300 u/C. This spectrum is extracted for every pulsed bundle of molecules. Hence it follows a certain evolution over time. Some strategic $m/q$ values are linked to certain species, like for example $NH_3{}^+$ that peaks at the 17.026 u/C position. "Following peak Id. $P_{17}$" then means following the evolution over time of the area under the peak with $m/q = 17$ u/C. For this example, the considered area is integrated from the spectrum between 16.5 and 17.5 u/C (see figure 3.3). However, multiple species may contribute to the peak's surface, and its evolution over time must be considered with care since the most contributing species to the peak area may also change over time. But the main point to consider is the following: each peak is linked to one or multiple species, and its evolution reflects the evolution of the concentration of these species in the measured gas.

### 4.3.2 Ammonia synthesis and dissociation

Only simple gases were introduced in the chamber for the first few tests with the TOF-MS, and the plasma was lit up. During one of those, hydrogen ($100 \pm 0.6$ sccm) and nitrogen ($20 \pm 1$ sccm) was introduced to see if ammonia was produced, and $NH_3$ was indeed synthesised. At $500 \pm 2\,\mu$bar, $250 \pm 2$ °C and $110 \pm 0$ MHz, the plasma power was then varied, and it was

observed that the synthesised ammonia was proportional to the applied power. This is all described in figure 4.9. This process also indicates a good dissociation of the two injected precursors, even at low power.

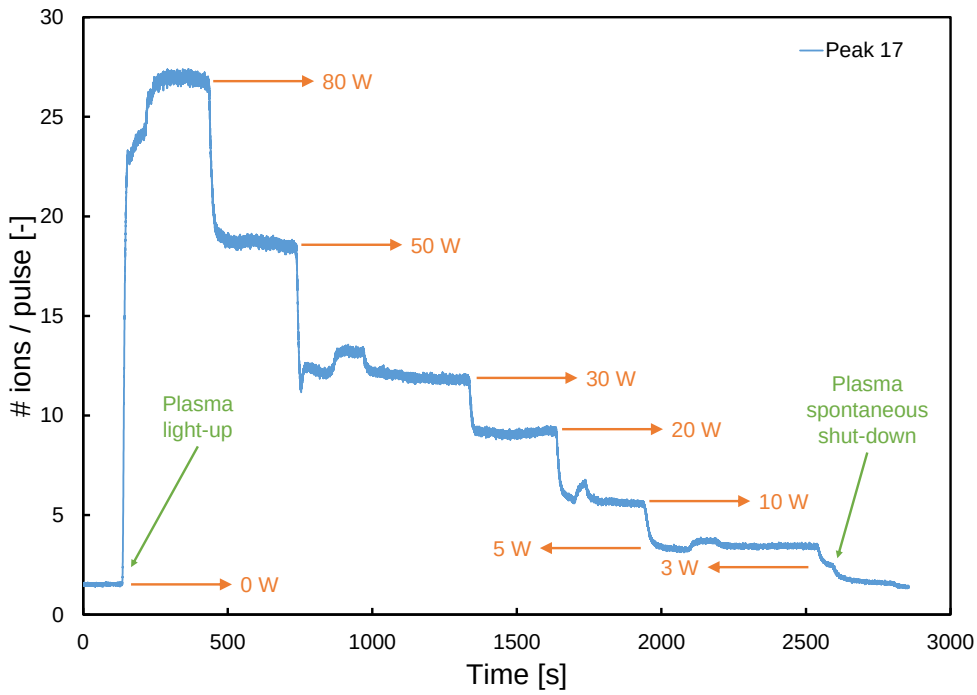


(a) Evolution of the $NH_3$ peak (n° 17) over time, with different applied powers. The plasma is turned on, and the peak rises rapidly: ammonia is synthesised. The small bumps are due to slight pressure and power corrections.

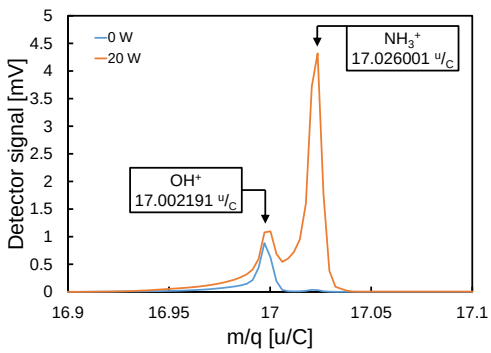


(b) Peak n° 17 ($OH^+$ and $NH_3{}^+$): difference between no plasma "0 W" and an applied power of 20 W.

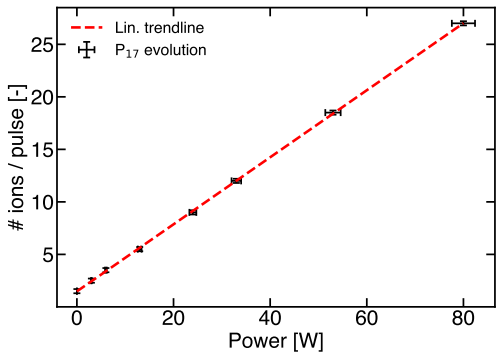


(c) Ammonia synthesis as a function of the applied power, linear relationship.

Figure 4.9: In/GaN PECVD, TOFMS: $NH_3$ synthesis as a function of the applied plasma power, from $N_2$ ($20 \pm 1$ sccm) and $H_2$ ($100 \pm 0.6$ sccm). This was performed at $250 \pm 2$ °C, $500 \pm 2\,\mu$bar and $110 \pm 0$ MHz.

Before the plasma is turned on, the TOF-MS already detects the $OH^+$ species, which comes from residual air or a leak that may still be present within the system somewhere. This is

visible with the non-zero value of the curve before the plasma light-up in figure 4.9a, which is the integration of the area under the blue curve of figure 4.9b. This contribution is also represented in the y-intercept of figure 4.9c. More interesting is the rate at which ammonia is produced, where a linear relationship with power is observed. According to Shah *et al.* [159], since the relationship between the plasma power and the ammonia yield is still linear, our case represents the linear regime, and the ammonia yield should be around 3 % at 80 W. See Figure 9 of Shah *et al.*'s paper for more detailed and complex dynamics between the two precursors, their dissociated species and the plasma electrons.

The same phenomenon happens in reverse: the dissociation rate of ammonia is also proportional to the plasma power density. This is shown in figure 4.10, where this time, the nitrogen peak is followed over time ($P_{28} - N_2{}^+$) while the power was changed. The same conclusions as for the synthesis of ammonia can be drawn: the relationship here seems to be still linear, although a quadratic relationship may be starting here, and not all the ammonia is wholly dissociated, but only a fraction of it, some of which also recombines into ammonia.

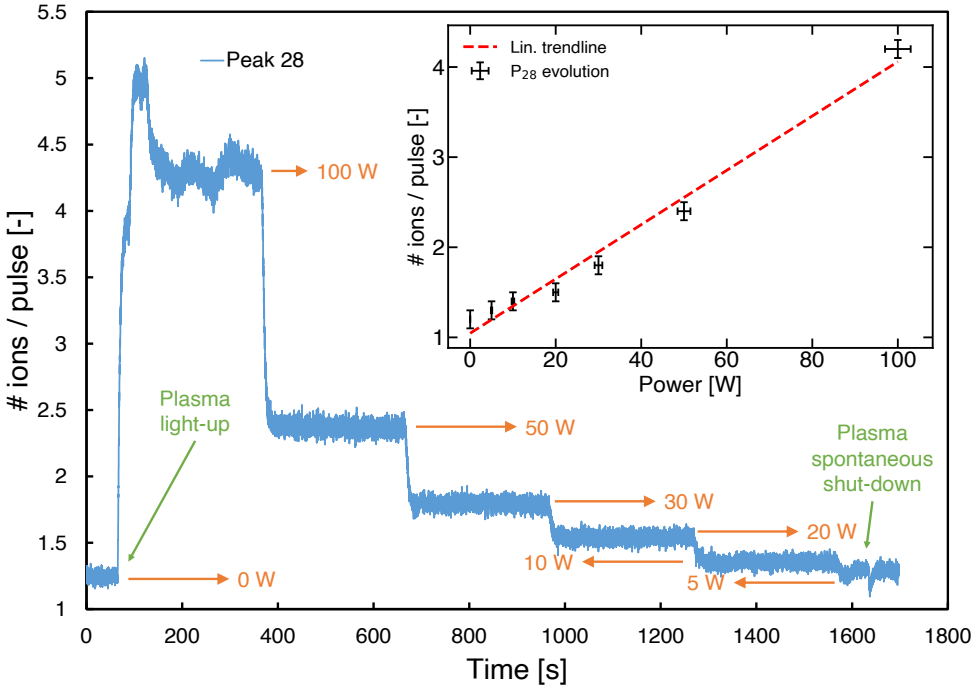


Figure 4.10: In/GaN PECVD, TOFMS: $N_2$ synthesis as a function of the applied plasma power, from $NH_3$ ($30 \pm 0.08$ sccm) and $H_2$ ($50 \pm 0.6$ sccm) by following the evolution of the $N_2$ peak (n° 28) over time, with different applied powers. This was performed at $250 \pm 2$ °C, $500 \pm 2\,\mu$bar and $110 \pm 0$ MHz. The plasma is turned on initially, and the peak rises rapidly: nitrogen is synthesised. The small bumps are due to slight pressure and power corrections. Inset: $N_2$ synthesis as a function of the applied power & linear trendline (dashed red).

### 4.3.3 DOE: frequency, power, pressure

A small DOE could be performed. In contrast, TOFWERK's TOF-MS was still connected to System B. Since the effect of the different precursors on the layer characteristics are already well-known, this short study focused on the RF, power and pressure of the plasma. The frequency was probed over three values (105, 110 and $115 \pm 0$ MHz), the power over two values ($30 \pm 2$ and $100 \pm 4$ W), and the pressure over three values (450, 500 and $550 \pm 2\,\mu$bar). For readability, these three input parameters are all standardised (see the standardisation process described on page 58). All the other deposition parameters were kept constant at the values given in the following table, and the TOF-MS configuration remained untouched during the whole process:

| TMG [sccm] | $N_2^{TMI}$ [sccm] | $N_2$ [sccm] | $H_2$ [sccm] | $NH_3$ [sccm] | Temperature [°C] |
|---|---|---|---|---|---|
| $0.5 \pm 0.006$ | $2.0 \pm 0.04$ | $20 \pm 1$ | $100 \pm 0.6$ | $30 \pm 0.08$ | $250 \pm 2$ |

By design, the input parameters are all orthogonal to one another; there is no correlation factor between any of them in any of the models presented here. By design as well, 18 measurements points are recorded, corresponding to 18 graphs such as the one in figure 4.11 (where the m/q value spans the whole range from 1 to 300 u/c) from which several peaks can be analysed; these are the output parameters. In other words, the numerical value that, for example, $P_{28}$ can take corresponds to the value given on the y-axis of a graph similar to figure 4.9a or 4.16 while the plasma is lit up. This value is modelled as a function of the pressure, frequency and power. With model quality metrics, the chosen peaks and the species that they refer to are displayed in table 4.5, and the models with standardised input values are presented in equations 4.2. The analysed peaks are not deconvoluted, so that they will be the added contribution of all the indistinguishable species.

$$P_{17} = 172.10 + 23.48Pr \tag{4.2a}$$

$$P_{28} = 203.94 - 3.14F + 27.76Pr + 2.63Po - 4.87F \cdot Pr - 4.52F \cdot Po + 8.05F^2 \tag{4.2b}$$

$$1000P_{69} = 25.47 + 7.16F \cdot Po + 3.69F^2 \tag{4.2c}$$

$$10'000P_{99} = 71.92 + 92.46F \cdot Po + 110.45F^2 \tag{4.2d}$$

$$1000P_{115} = 32.67 + 3.32F - 2.30Po + 3.99F \cdot Po - 8.22F^2 \tag{4.2e}$$

$$10'000P_{145} = 30.41 + 2.25Pr + 1.78Po - 1.93F + 2.47F \cdot Po + 6.85F^2 \tag{4.2f}$$

$$10P_{30} = 19.45 - 2.59F + 3.52Pr - 3.87Po + 2.32F \cdot Po + 4F^2 \tag{4.2g}$$

$$100P_{41} = 40.76 - 3.65F + 5.40Pr - 2.43Po - 2.39F \cdot Pr + 2F \cdot Po + 4.79F^2 \tag{4.2h}$$

$$100P_{44} = 13.82 + 0.49F + 2.10Pr - 0.34Po + 3.2F^2 \tag{4.2i}$$

$$1000P_{54} = 27.92 - 1.75F + 4.04Pr - 1.77Po + 1.51F \cdot Po + 3.49F^2 \tag{4.2j}$$

Table 4.5: In/GaN PECVD, TOFMS: DOE results on the frequency, the power and the pressure. The peak identifier ("peak Id.", first column) refers to the $^{m}/_{q}$ value observed, which corresponds to one or multiple distinct species (second column). At the bottom of the table are peaks related only to plasma by-products.

| Peak Id. | Species | $R^2_{\text{adj}}$ [%] | $p_M$ [%] | Highest p-value |
|---|---|---|---|---|
| $P_{17}$ | $NH_3^+$ | 88.7 | $3.34 \cdot 10^{-7}$ | All < 5 % |
| $P_{28}$ | $N_2^+$ | 93.8 | $4.76 \cdot 10^{-7}$ | $F = 10.8\,\%$ |
| $P_{69}$ | $Ga^+$ | 81.5 | $1.25 \cdot 10^{-4}$ | All < 5 % |
| $P_{99}$ | $Ga\,(CH_3)_2^+$ | 74.8 | $1.28 \cdot 10^{-3}$ | All < 5 % |
| $P_{115}$ | $In^+$ | 92.7 | $5.08 \cdot 10^{-7}$ | All < 5 % |
| $P_{145}$ | $In\,(CH_3)_2^+$ | 52.8 | 1.22 | All > 5 % |
| $P_{30}$ | $C_2H_6^+$, $CH_4N^+$, $CH_2O^+$ | 91.9 | $4.82 \cdot 10^{-5}$ | All < 5 % |
| $P_{41}$ | $C_3H_5^+$ | 83.2 | $1.01 \cdot 10^{-2}$ | All < 5 % |
| $P_{44}$ | $CO_2^+$, $CH_4N_2^+$ | 96.3 | $5.99 \cdot 10^{-8}$ | All < 5 % |
| $P_{54}$ | $C_3H_5N^+$, $C_4H_6^+$ | 91.8 | $5.23 \cdot 10^{-5}$ | All < 5 % |

As a reminder, those species reach the TOF-MS after going through the plasma. The simplest model would be the first one, described in equation 4.2a, and can be interpreted as such: "the quantity of ammonia that reaches the TOF-MS slightly increases when the plasma pressure is increased". This is almost the same for nitrogen ($P_{28}$, equation 4.2b), where the dominant term is the pressure as well. This is expected since these two precursors (with hydrogen, which was not modelled here) are main diluting precursors that are never entirely dissociated within the plasma; changing the pressure of the plasma is effectively changing their partial pressure, influencing the number of their species that will reach the TOF-MS. The plasma power influences the ammonia synthesis, and it is surprising to see it missing in the $P_{17}$ equation, even though ammonia, hydrogen and nitrogen are all injected here. For the layer, this means that increasing the pressure will increase; in fact, the dilution power of these species and the growth rate should be slowed down, with all the benefits that this brings: higher crystallinity, better optical properties, etc. These two models (and their interpretation) are reliable at about 90 %, with excellent $p_M$ value.

For the TMG and TMI, the atomic signal ($P_{69}$ & $P_{115}$) is more reliable than the two-methyl molecule one ($P_{99}$ & $P_{145}$). This is also reflected in the extremely low peak signal intensity with the high number in front of related equations (equations 4.2c to 4.2f), but the model remains pretty noisy (reflected in the lower $R^2_{\text{adj}}$ value). This is explained because the plasma easily breaks the TMG/me, and no such molecule reaches the TOF-MS, while some Ga or In atoms can leave the plasma and drift until the TOF-MS is reached. Considering the two complex ones unreliable because of their low $R^2_{\text{adj}}$ and high $p_M$ values (equations 4.2d and 4.2f) and only focusing on the two atomic ones (equations 4.2c and 4.2f), we see that the two dominant effects are $a_{F \cdot Po}$ and $a_{F^2}$. Since the combined effect of power and frequencies generally helps break down the precursor molecules, it makes sense to see an interacting term appear here; more of these atomic species are produced when this interaction effect is increased. For the

$a_{F^2}$ effect, it seems that it has a different effect depending on the considered molecule, where more atomic gallium can escape the plasma and reach the TOF-MS than atomic indium when the frequency is pushed to one of the two extreme values of the considered parameter range. As a consequence of the layer, it is concluded that a better molecule dissociation is obtained when increasing the frequency and the power, where the effect will be stronger for indium (because less of it escapes the plasma compared to gallium).

As far as by-products are concerned, please be aware that there is no oxygen in the precursors: it probably comes from a leak in the TOF-MS as already discussed in the previous section. The signal given by the molecules containing oxygen should then remain constant. We notice that the structure of the fitted models is pretty similar: they all have the three linear terms and the $a_{F^2}$ effect, and three of the four have the $a_{F \cdot Po}$ effect, but with different signs in front of them. They are all four reliable ($R^2_{\text{adj}} > 90\,\%$ except for $P_{41}$) with a good $p_M$ value (except for $P_{41}$ again). Here, the role of hydrogen is important since it passivates the plasma by-products, such as the methyl groups of the decomposed complex TMG and TMI molecules. A rule of thumb is that the longer the methyl chain (or, the more complex the by-product) reaches the TOF-MS, the less effective the hydrogen passivation of these waste products at the plasma sheath, giving them more possibilities to recombine among themselves. So it is better to search to favour $P_{30}$ while simultaneously preventing $P_{54}$ from rising. This is difficultly done since most of the effects have the same polarity. But since the input parameters have been standardised, we can play with the strength of each of them on the effects. Increasing the frequency will create more $P_{30}$ by-products than $P_{54}$ ones, and the same goes with the power. However, increased pressure will favour more the $P_{54}$ by-products than the $P_{30}$ ones, so the pressure should be decreased.

In summary, for the layer, a lower pressure, higher power and higher frequency will mean less carbon-rich or carbon chains plasma by-products that are more easily evacuated and less integrated into the layer, producing a layer with fewer impurities and less carbon in general.

### 4.3.4 TOF-MS and layer characteristics

Thirteen layers were deposited and characterised; the TOF-MS results were then linked to some layer characteristics, which allows to understand better the importance of specific deposition parameters and their overall influence on layer deposition. The deposition parameters are presented in table 4.6a, and each layer type is developed in the following sections. Since this section would be difficult to read if the evolution of the peak was to be presented for every layer, only one is shown in figure 4.16; everything went as expected for this layer. Other unique or problematic layers are presented in more detail. Finally, each layer's characteristics are presented in table 4.6b, where only layers n° 1 and 8 were discarded since their depositions were problematic.

Table 4.6: In/GaN PECVD, TOFMS: deposition parameters and layer characteristics.

(a) Layer characterization with the TOFMS: deposition parameters. Note that (not indicated in the table) layers 11, 12 and 13 were fabricated with an additional element: phosphorous (expected to produce GaNP), boron (expected to produce BGaN) and traces of silicon (expected to produce GaN(Si)) respectively. These layers were deposited at $500 \pm 2\,\mu$bar, $110 \pm 0$ MHz, $250 \pm 2$ °C and $100 \pm 4$ W, except for layers n° 1 and 2 deposited at $30 \pm 2$ W.

| Layer n° | TMG ±0.006 [sccm] | $N_2^{TMI}$ ±0.04 [sccm] | $N_2$ ±1 [sccm] | $H_2$ ±0.6 [sccm] | $NH_3$ ±0.08 [sccm] | Ar ±0.25 [sccm] | Time ±1 s [min] | Thickness ±10 [nm] |
|---|---|---|---|---|---|---|---|---|
| 1 | 0.45 | | | | 10 | 5 | 14.3 | - |
| 2 | | 2.0 | 60 | 75 | | | 20 | 129.3 |
| 3 | | 2.0 | 60 | 75 | | 5 | 20 | 66.9 |
| 4 | | 1.0 | 60 | 75 | | 5 | 20 | 25.9 |
| 5 | | 3.0 | 10 | 100 | 30 | | 20 | 67.3 |
| 6 | | 1.4 | 10 | 100 | 30 | | 20 | 43.2 |
| 7 | 0.45 | | 20 | 100 | 30 | | 20 | 13.3 |
| 8 | 0.70 | | 20 | 100 | 30 | | 20 | - |
| 9 | 0.15 | 1.4 | 20 | 100 | 30 | | 30 | 68.6 |
| 10 | 0.07 | 3.0 | 20 | 100 | 30 | | 30 | 94.7 |
| 11 | 0.50 | | 20 | 100 | 30 | | 30 | 805.4 |
| 12 | 0.50 | | 20 | 100 | 30 | | 30 | 41.3 |
| 13 | 0.50 | | 20 | 100 | 30 | | 30 | 89.4 |

(b) Layer characterization with the TOFMS: layer characteristics. Layers n° 1 and 8 were not characterised because of plasma flickers during the deposition that rendered them unusable. EDS was not performed for the InN layers.

| Layer n° | $E_{04}$ ±0.03 [eV] | $E_T$ [eV] | $E_U$ [meV] | $n_{633}$ ±0.02 [−] | $X_{In}$ ±3 [%] | $CrSz$ ±0.01 [nm] |
|---|---|---|---|---|---|---|
| 2 | 1.71 | $1.60 \pm 0.01$ | $252 \pm 1$ | 2.47 | | 32.93 |
| 3 | 1.45 | $1.17 \pm 0.01$ | $247 \pm 1$ | 1.38 | | 25.88 |
| 4 | 1.24 | $1.07 \pm 0.01$ | $240 \pm 1$ | 2.86 | | 15.44 |
| 5 | - | $0.14 \pm 0.01$ | $504 \pm 1$ | 2.00 | | 13.19 |
| 6 | 0.76 | $0.54 \pm 0.01$ | $447 \pm 1$ | 1.90 | | 27.77 |
| 7 | 2.67 | $3.25 \pm 0.04$ | $305 \pm 9$ | 2.25 | 20 | 19.16 |
| 9 | 3.14 | $2.99 \pm 0.10$ | $176 \pm 2$ | 2.32 | 4 | 31.88 |
| 10 | 2.36 | $2.15 \pm 0.03$ | $173 \pm 2$ | 2.38 | 37 | 16.45 |
| 11 | 4.46 | $3.51 \pm 0.07$ | $417 \pm 12$ | 1.90 | 0 | - |
| 12 | 3.24 | $3.10 \pm 0.05$ | $172 \pm 2$ | 2.25 | 0 | 24.93 |
| 13 | 1.94 | $2.75 \pm 0.02$ | $486 \pm 2$ | 2.33 | 0 | - |

#### 4.3.4.1 GaN layers

Referring to table 4.6, three intrinsic GaN layers were deposited, and three other GaN layers with a dopant. This section analyses the intrinsic ones, layers n° 1, 7 and 8. However, only

layer n° 7 did not have deposition problems; layer n° 1 was deposited just after a cleaning of the system, which sullied it, and the plasma flickered during the deposition of layer n° 8 for an unknown reason. It is, however, interesting to probe a bit more into what happened during a plasma flicker of layer n° 8, even though the origin of the perturbation could not be identified. This is shown in figure 4.11. Highly complex molecules could be identified during this perturbation, confirmed by their isotopic peaks, such as $P_{229}$ – TMG – H – TMG. But in general, many methyl groups assemble to form long C-chains. This means that when the plasma flickers, a lot of recombination occurs that would otherwise not happen, leading to contamination and degradation of the layer.

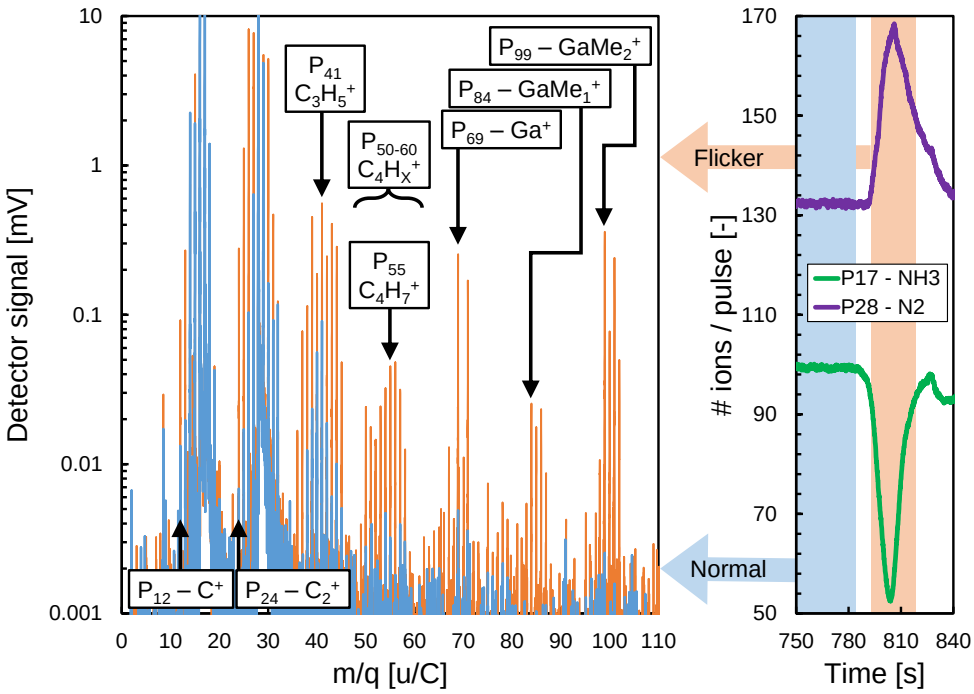


Figure 4.11: In/GaN PECVD, TOFMS: Plasma flicker. The right plot shows the evolution over time of the $P_{28}$ – $N_2$ and $P_{17}$ – $NH_3$ peaks in purple and green respectively. The small bump occurs during a plasma flicker, for which the orange spectra TOFMS $m/Q$ vs intensity graph is also displayed here. The blue spectra show the "normal" $m/Q$ vs intensity graph outside a plasma flickering.

Highly complex carbon chains were not observed for the one well-deposited GaN layer ($P_{78}$ – $C_6H_6{}^+$ or $P_{91}$ – $C_7H_7{}^+$ for example). The longest observed carbon chain was $P_{41}$ – $C_3H_5{}^+$, sign of a clean deposition. There should not be any indium in this layer, but some still showed up, indicating contamination from the previous InN depositions. Indeed, $P_{115}$ – $In^+$ did not move when the pressure was changed, when the precursors were injected or when the plasma was lit up; sadly, the TOF-MS itself may be contaminated. However, the signal from the small $P_{145}$ – $InMe_2{}^+$ did vary with plasma light-up, a sign that TMI was still present inside the chamber before the deposition started and was dissociated during the deposition. This is verified by

EDS, where a Ga:In ratio of 4 is noted (see table 4.6b). Nothing is unusual: the TMG is fully dissociated, but Ga is not fully / efficiently used.

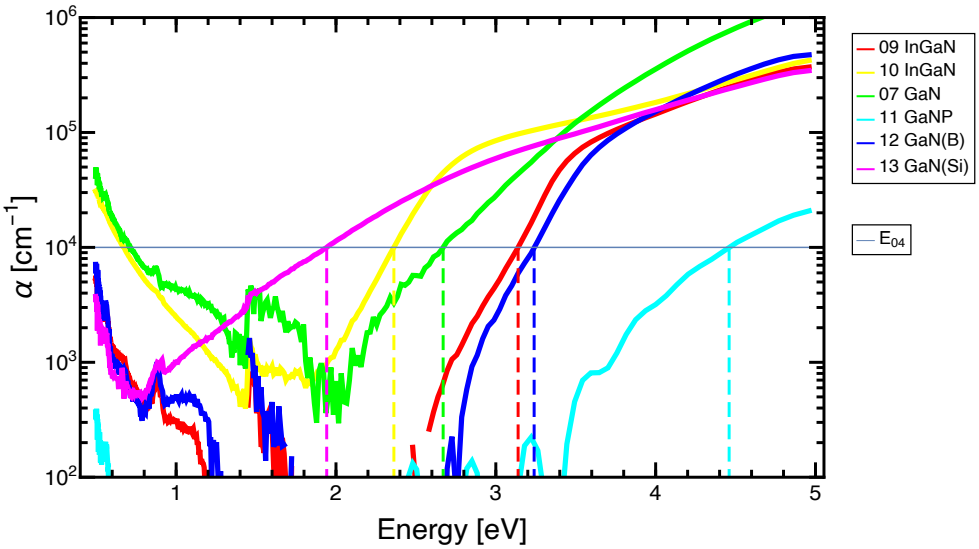


Figure 4.12: In/GaN PECVD, TOFMS: absorption coefficient of InGaN, GaN and doped GaN layers deposited on glass substrates.

In terms of layer characteristics, the good GaN layer only shows a slight XRD crystallinity (small (002) peak from which a crystallite size of 19 nm can be deduced, not presented here), coherent with the TEM results. Indeed, crystallite sizes of up to 15 nm were observed by TEM, without any preferential orientation (certainly because of the amorphous carbon film, compare figures 4.13a & 4.13c). The presence of indium in the GaN layer is also confirmed by deconvoluting the diffraction figure, where the peaks' shift to lower angles is a sign of a more considerable interplanar distance, coherent with the larger indium atom (see figure 4.13b). The EDS also confirmed a low level of carbon and oxygen within the layer, coherent with the TOF-MS observation. Finally, when considering the absorption coefficient (see figure 4.12), the lowered optical BG also hints towards indium contamination. The Urbach energy is not that good, and there is FCA; indeed, a few signs of indium contamination again, but also a symptom of a too-thin layer, more difficult to characterise precisely.

To solve the problems caused by indium contamination, a lower base pressure must be reached before the deposition. Given the slow growth rate, a longer deposition time would produce a thicker, more stable layer with a higher crystallinity and better-defined band edge. Apart from that, the deposition was well done, and only a tiny carbon contamination was guessed based on the short carbo-hydrate chains observed with the TOF-MS.

#### 4.3.4.2 InN layers

This section probes all the InN layers that were deposited and analysed with the TOF-MS. Their deposition parameters are presented in table 4.6a, their absorption coefficient and

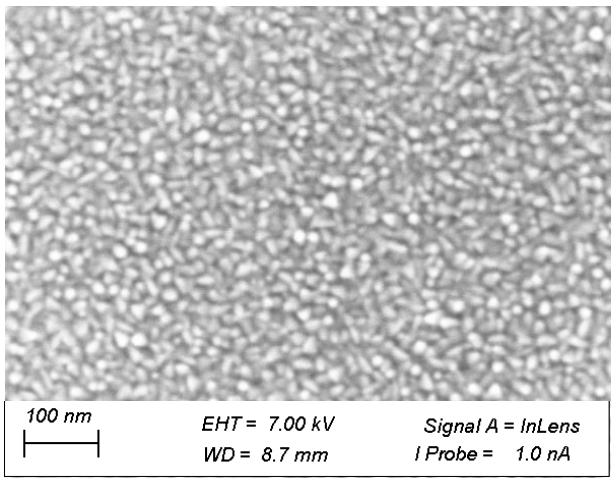


(a) Top surface on a (100) silicon wafer, SEM.

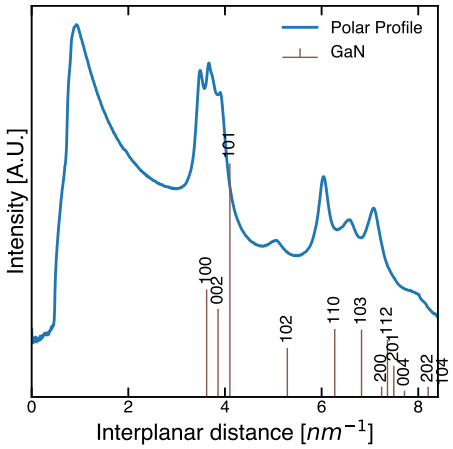


(b) Depolarization of the diffraction figure presented in figure 4.13c.

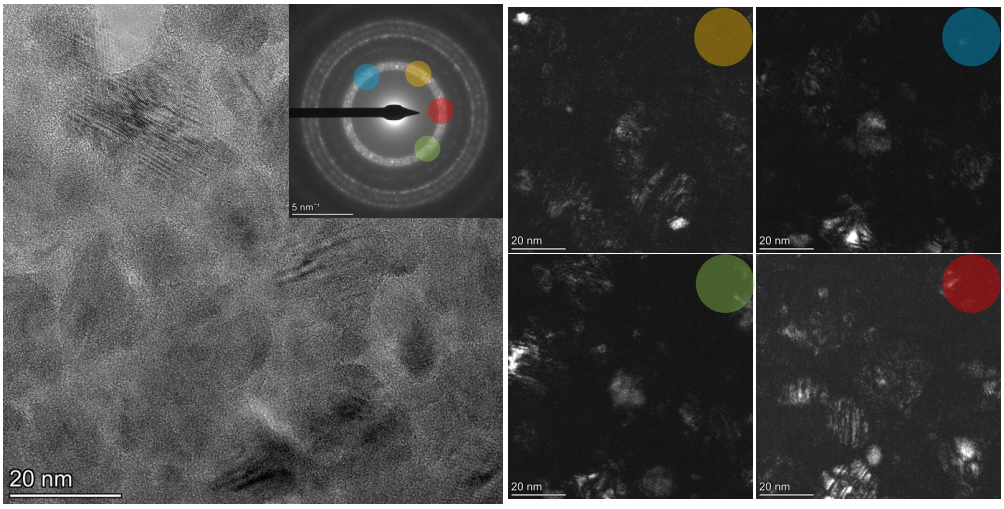


(c) TEM diffraction figure and associated DFs, layer deposited on a TEM grid.

Figure 4.13: In/GaN PECVD, TOFMS: GaN layer, small electron microscopy study.

XRD features are shown in figure 4.14, from which essential characteristics are extracted and presented in table 4.6b.

The TOF-MS shows that the TMI is completely dissociated because the $InMe_2{}^+$ signal completely disappears from the spectrum (noise levels). Carbo-hydrates of up to $C_3H_X$ atoms appear as a sign of a good evacuation of the methyl group, mainly thanks to hydrogen. When neither ammonia nor argon is used (layer 2 of table 4.6), ammonia is still observed as a plasma by-product. This implies that nitrogen and hydrogen are well-dissociated and available to react with the indium atoms inside the plasma. Such layers are expected to contain low contamination levels or defects; a sharp band edge should reflect that. Indeed, the Urbach energy is pretty standard when there is neither ammonia nor argon, with good crystallinity. The first InN layer has some gallium traces because the base pressure was not low enough.

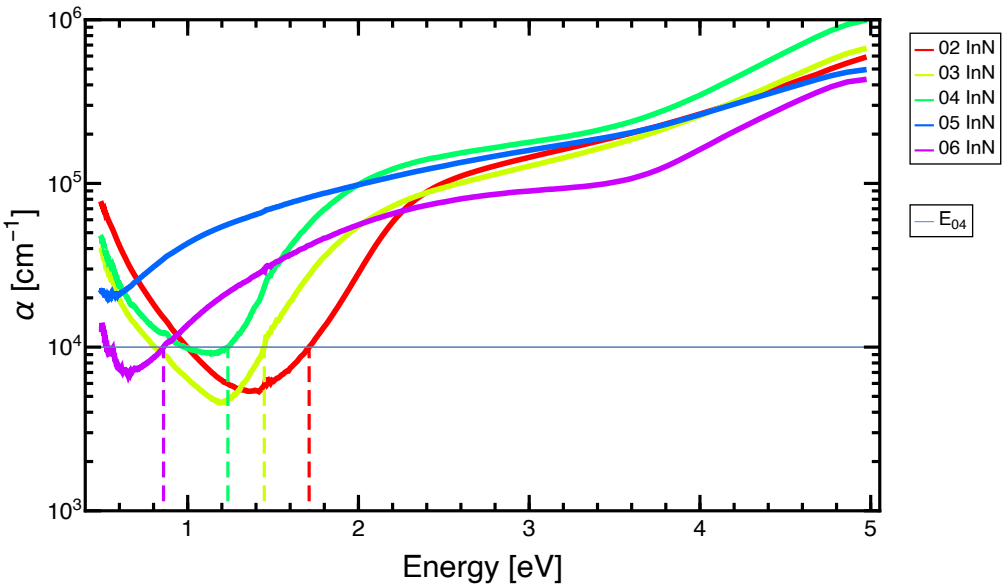


(a) Absorption coefficient on a glass substrate.

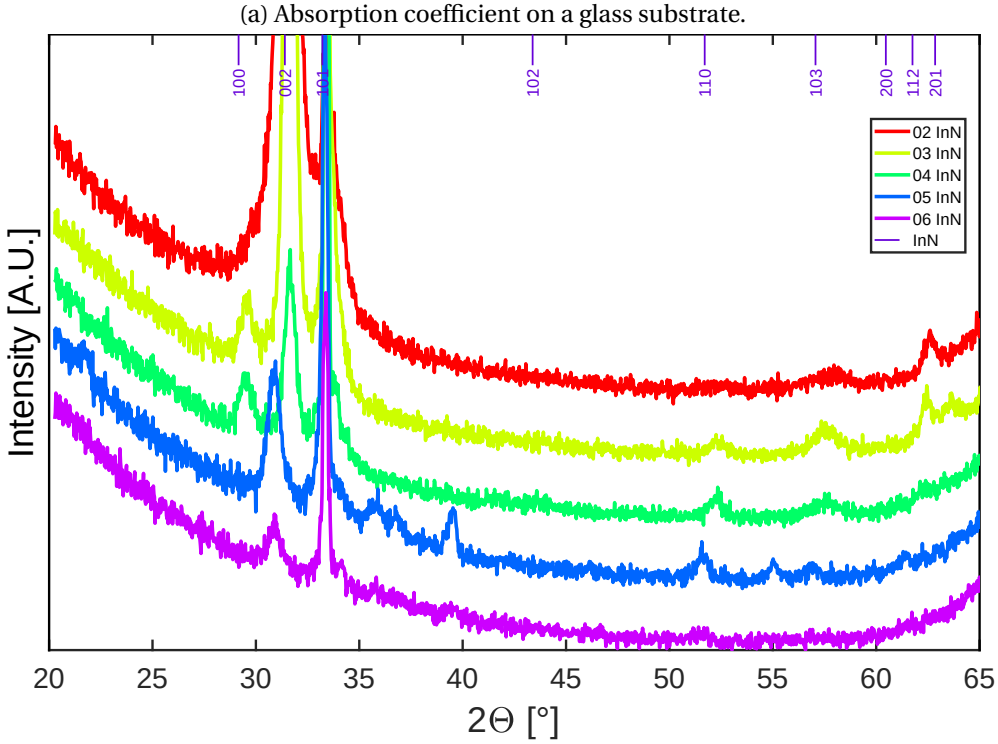


(b) XRD pattern on a silicon substrate. The sharp peak at 33.3° is attributed to the silicon wafer.

Figure 4.14: In/GaN PECVD, TOFMS: InN layers, absorption coefficient and XRD pattern.

The base pressure level is essential because it gives more time for the contaminants inside the chamber to be evacuated and drastically decreases their unwanted presence inside the layer. The contamination of the first InN layers was made evident here thanks to the TOF-MS.

Indeed, there still were some traces of complex hydrocarbons ($P_{78}$ — $C_6H_6{}^+$?) that are stable through the whole process and whose peak intensity does not change when lighting up the plasma. That means it is either a contamination of the tool or a non-reactive species. In either case, it can be due to the high base pressure reached before this deposition ($1.40 \cdot 10^{-5}$ mbar), and it is a warning to wait further for the system to be under high vacuum.

This can be compared with a deposition with argon added to the previous mix, with the power increased to 100 W and with a lower base pressure (layers 3 and 4 of table 4.6). Compared to the first InN layer, in figure 4.14a, the edge is sharper, the optical BG is at lower energy, and the FCA is reduced. This is due to the addition of argon, increased power, or decreased deposition rate. Link with TOF-MS results: the layers deposited in these conditions (higher power, with argon and at a lower growth rate) are the ones that have the least sub-bandgap absorption states. This means fewer defects, possibly because carbohydrates were evacuated efficiently in both cases. However, the second InN layer had gallium contamination; hence is supposed to be shifted BG compared to the third one. The TOF-MS does not reveal anything else regarding the use of argon.

Regarding the crystallinity, refer to the small TEM study in figure 4.15. TEM images confirm 20 nm large nanocrystals. The crystallinity seems excellent, as displayed in the diffraction figure and the de-polarised diffraction pattern. Increasing the power to 100 W and including argon in the flow mix allows for a better dissociation & deposition process, hence improving the crystallinity (more peaks, higher peak intensity in the XRD pattern of figure 4.14b).

If the TMI flow is now reduced further (layer n° 4 compared to n° 3), carbo-hydrates are indeed less present (chains of more than two carbon atoms are found in traces only). Such a layer is expected to be cleaner and more “performant” than the previous one, even though it is pretty thin. Lowering the indium flow decreases the layer thickness and increases the absorption on the whole spectrum. The reason for the latter is not fully understood; maybe the thinner layer is less crystalline (still just above the nucleation level), implying more sub-BG absorption? The lower optical bandgap value is just an artefact due to this. Overall, decreasing too much the indium content seems like a bad idea. Why this phenomenon? Maybe there are not enough indium atoms any more, and the layer is more etched than deposited, which makes it more porous overall, hence the increase in absorption. There is another way to look at the problem: by reducing the TMI flow, the absorption edge was effectively reduced, but the low energy absorption was increased, so it is still a step forward. Link with TOF-MS results: assuming the TOF-MS configuration was the same between the two layers, the atomic indium peak $P_{115}$ – $In^+$ falls to lower levels when the TMI flow is decreased in an absolute way (not in a balanced way), meaning that less atomic indium reaches the detector. In terms of crystallinity (see figure 4.14b), the (002) peak strength is decreased while the strength of the other peaks is maintained, all this for a thinner layer. It can be deduced that the preferential (002) orientation arises between 25 to 65 nm, and at the interface, there is a small nano-crystalline layer.

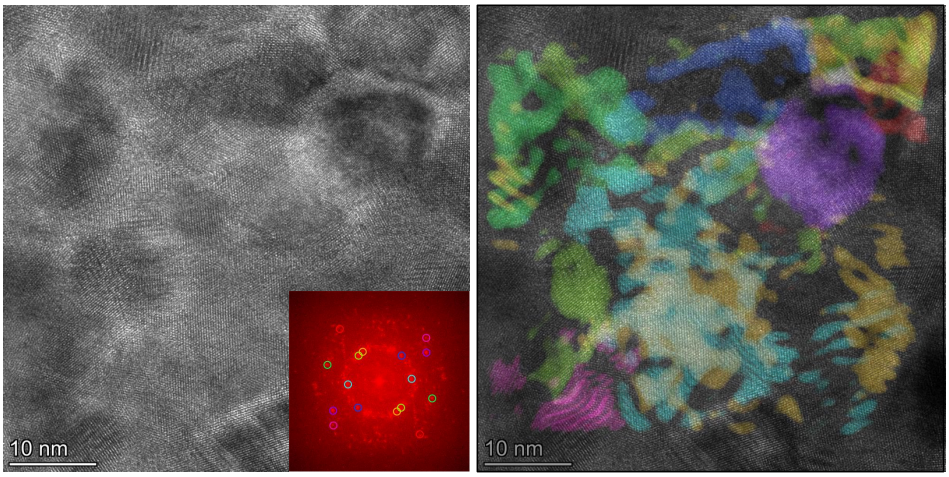


(a) High-resolution TEM micrograph (left), colored with filtered FT-IFT masks (right). The red central figure is the Fourier transform of the HRTEM micrograph.

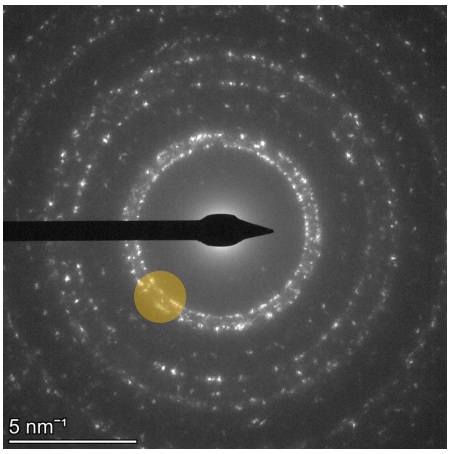


(b) Diffraction pattern.

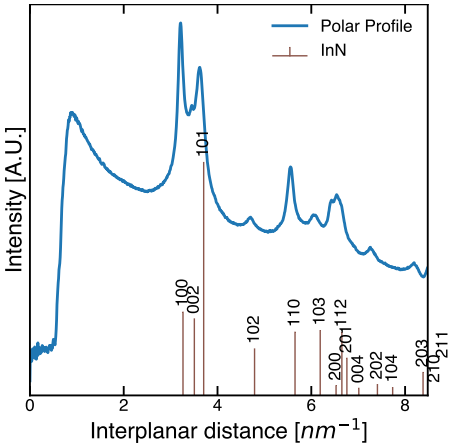


(c) Depolarised diffraction pattern.

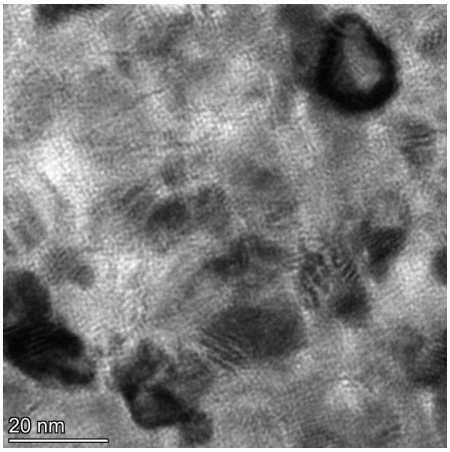


(d) Bright field.

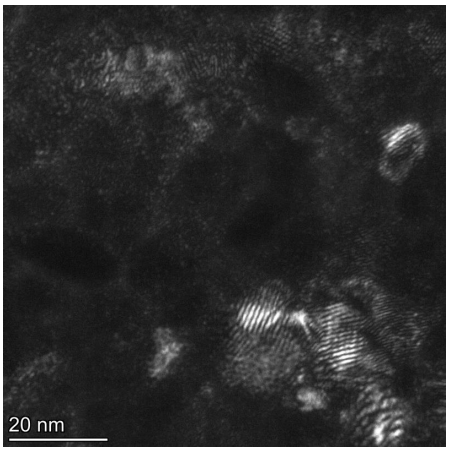


(e) Dark field (with objective apperture shown in figure 4.15b).

Figure 4.15: In/GaN PECVD, TOFMS: InN layer, small TEM study of layer n° 3 deposited on a TEM grid.

See figure 4.16 for unfolding layer n° 5's deposition. Here, the TMI is fully dissociated ($P_{145}$ -– $InMe_2{}^+$ goes to zero) but is not efficiently used ($P_{115}$ -– $In^+$ goes from 0.29 to $0.10 \pm 0.02$ ions/extraction). The usage efficiency of this species may be increased by decreasing further the TMI flow rate so that most of it is used. The carbo-hydrate chains have been observed at noise level, a sign of a suitable deposition process again. However, the addition of ammonia may have etched some gallium off from the surface of the chamber because the $P_{99}$ – $GaMe_2{}^+$ peak was observed varying with plasma light-up and turn-off (pink curve).

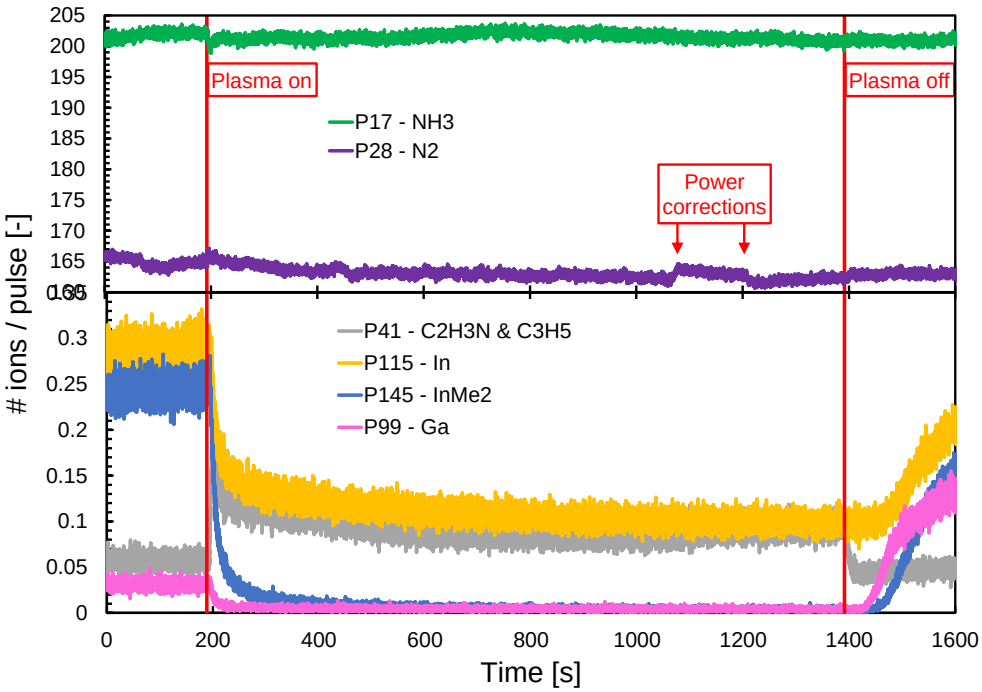


Figure 4.16: In/GaN PECVD, TOFMS: a normal deposition with the TOFMS, fifth layer (InN).

When using ammonia instead of argon, TMI is again fully dissociated but is not efficiently used. There seems to be still a "remnant $P_{115}$ -– $In^+$ peak" that does not react to external stimuli; the TOF-MS detector may be contaminated with indium. In any case, there is now no way to confidently conclude if all the indium dissociated from the TMI was effectively used. Methyl recombines into $C_4H_X{}^+$, which is detected only within noise levels but slightly influenced by the plasma lighting up; sign again of a suitable deposition process, with ammonia this time. Methyl groups up to $P_{78}$ – $C_6H_6{}^+$ / $P_{81}$ – $C_6H_9{}^+$ were observed only at the plasma lighting up and then nothing for the rest of the deposition. Here would be a guess on why such a phenomenon occurs:

1. Plasma is lit up, and the first electrons start heating up.
2. TMI first dissociates quickly, producing its by-products (CH3+ and In+)
3. Considering all the by-products produced within the plasma volume, only the methyl groups produced at the plasma sheath recombine in these carbon-rich chains.
4. The peaks $P_{78}$ & $P_{81}$ quickly shoot up.

5. Since these chains are detected by the TOF-MS, they also "touch" the substrate surface. Certainly, some of them adhere to it and compromise the epitaxy or, at the very least, the crystallinity of the future InN layer.
6. In the meantime, the electrons gain enough speed (energy, temperature) to dissociate other species, liberating more hydrogen (protons!) inside the plasma.
7. Those quickly drift towards the plasma sheath and recombine with the methyl groups, passivating them.
8. The peaks $P_{78}$ & $P_{81}$ quickly disappear.

If this process is confirmed, it would mean that producing a layer this way would inevitably deteriorate the interface between the wafer and the layer itself, influencing the rest of the layer as well. A way to remedy this would be to first light up the plasma with non-contaminating species (such as nitrogen, hydrogen, ammonia, etc.) and then open the MFC of the metallic and other "dirty" contaminating species.

From an optical point of view, switching to ammonia seems to have decreased the optical BG, and layers resemble more to high-quality InN, where the band edge should be lower than 1 eV (see figure 4.14a), but with a low thickness. Due to the lowered BG, switching to FTIR instead of the UV-VIS tool might prove helpful to probe lower energies. These better layers may have been obtained because of the high hydrogen concentration, which helps dissociation and waste evacuation while having less di-nitrogen (less dilution) compared to the other InN ones. Radical nitrogen atoms are also more available, thanks to ammonia. All this could explain why the two InN layers deposited with ammonia present better characteristics than the previous ones. When using ammonia, an excessive TMI flow will result in more defects, a higher absorption coefficient over the whole spectrum, and a higher deposition rate. However optically good as they look, these layers are no longer InN. Indeed, the XRD pattern presented in figure 4.14b shows alien peaks for the fifth InN layer, and a SEM top view coupled with an EDS study proves that the sixth layer is composed of oxidised InN droplets with a radius of $< 50$ nm. Adding ammonia may completely alter the plasma dynamics and create undesirable layers; an equilibrium state must be found again, or the deposition could last slightly longer to have a thicker and hopefully more stable layer.

Link with TOF-MS results: the fact that the two layers deposited with ammonia are too metallic may have been predicted by the TOF-MS analysis. Indeed, the fact that the $P_{17} - NH_3{}^+$ peak did not change at plasma lighting on or off indicates that insufficient nitrogen was present, and atomic indium was too much incorporated in the layer.

#### 4.3.4.3 InGaN layers

This section presents the TOF-MS analysis of two InGaN layers (n° 9 and 10). Their absorption coefficient can be checked in figure 4.12. One is a bit thinner than the other and slightly less crystalline. For the thin one (layer n° 9), $P_{55} - C_4H_7{}^+$ has the same behaviour as $P_{41} - C_3H_5{}^+$, which means that the plasma here produces longer carbohydrates, which is not a good sign.

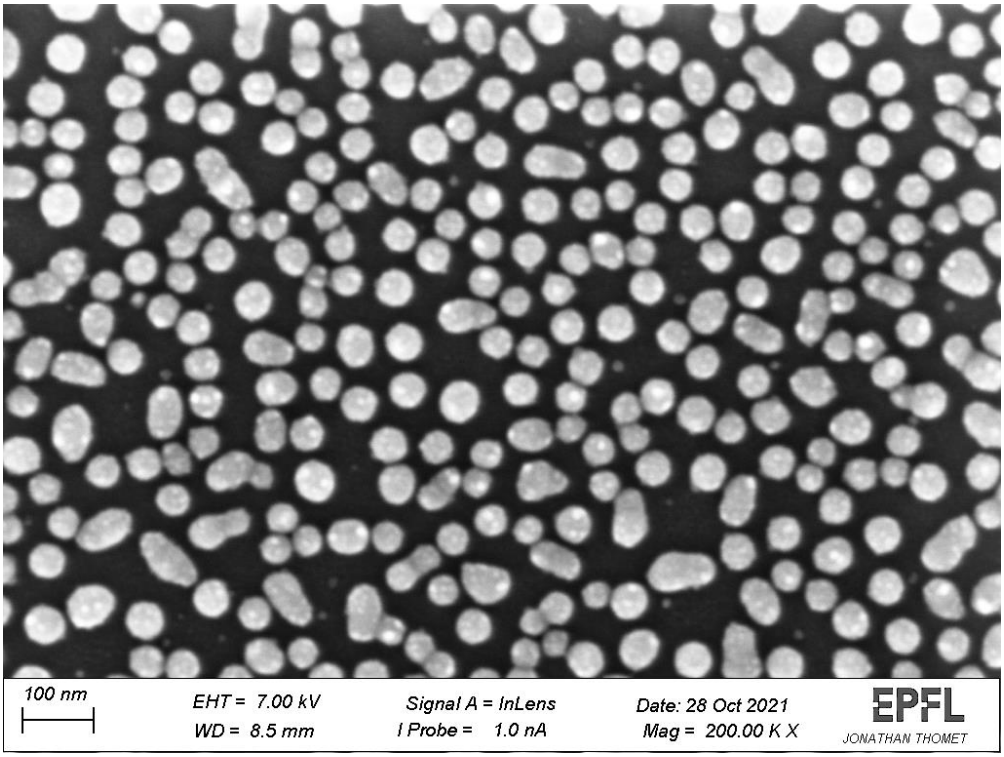


Figure 4.17: In/GaN PECVD, TOFMS: sixth layer (InN) in an SEM top view on a silicon substrate, InN droplets.

Gallium seems fully used up, going from 0.55 to 0.02 ion/ext. It is uncertain why it is used so efficiently here compared to GaN layers; this means, however, that the layer is expected to be Ga-richer than predicted, and indeed it is (verified by EDS). TMI is dissociated, but because of the constant $P_{115} - In^+$ peak, it cannot be said that atomic indium was fully used up. When the TMG flow is reduced and the TMI flow is increased (layer 10), the $P_{55} - C_4H_7{}^+$ peak is way lower, maybe due to less TMG. The metallic precursors are better used because the atomic signature peaks reach shallow values (less than 0.02 ion/ext.).

Regarding InGaN layer's optical properties, the band edge and Urbach energy are excellent, among the sharpest of the set. Still, there is some FCA in both cases, a sign of a layer degeneration, with a larger effect with more indium, as expected. Given their optical BG, and compared to other layers, considering Vegard's curvature, these two layers are expected to have ~ 5 % and ~ 40 % indium. XRD and EDS confirms that as true (see figure 4.18, XRD determines an indium content $X_{\mathrm{In}} = \frac{\mathrm{In}}{\mathrm{In+Ga}}$ (In & Ga in at. %, $X_{\mathrm{In}}$ in %) of 4 % and 37 % respectively, while EDS determines 3 % and 42 % respectively).

We can compare peak intensities since the TOF-MS setup and deposition conditions were the same. And indeed, $P_{145} - InMe_2{}^+$ is way higher in the thin InGaN layer than in the thick one (0.20 vs 0.06 ion/ext.). On the other hand, $P_{99} - GaMe_2{}^+$ went from 1.4 to 1.7 ion/ext before the deposition of the two layers, respectively, which is surprising. The other precursors all

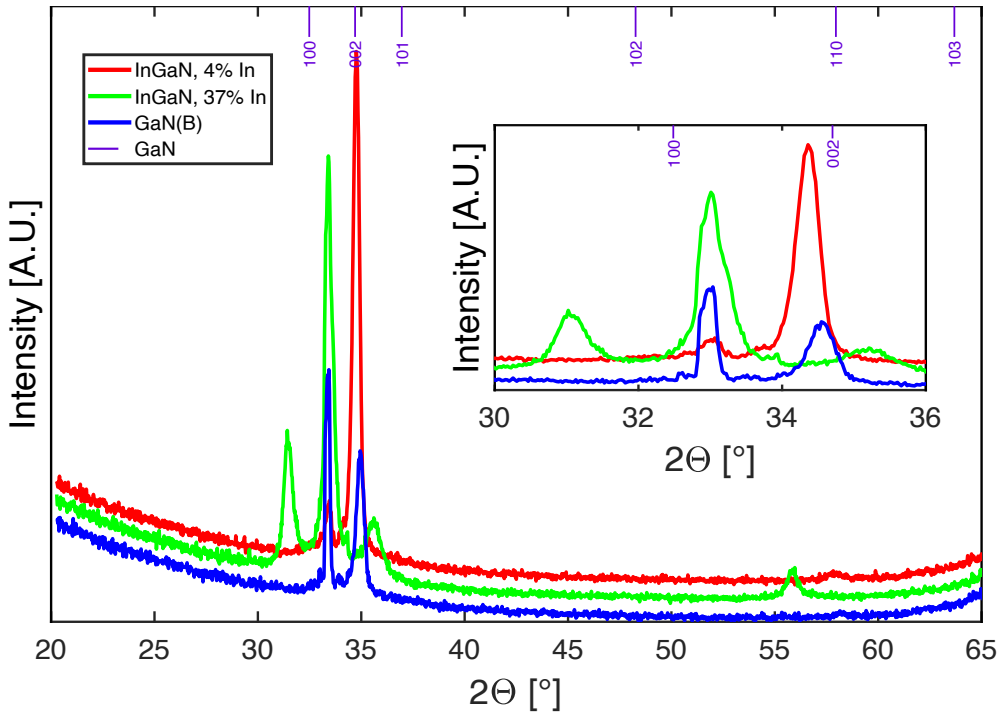


Figure 4.18: In/GaN PECVD, TOFMS: InGaN layers by XRD on a silicon substrate. The sharp peak at 33.3° is attributed to the silicon wafer, not the layers.

maintain the same values in the two experiments. Maybe when more nitrogen-bubbled TMI travels through the same pipe as TMG, it sucks a bit more of TMG out of its bottle? Still, the TMI difference mentioned just earlier completely makes up for it in terms of indium content.

The difference in crystallinity is also visible with a SEM top view, where the thinner layer n° 9 (figure 4.19a) displays more uniform rounded shape crystallites, compared to the more pointy shapes for the thick one (see figure 4.19b and the ~ 30 nm crystallite size also assessed by TEM in figure 4.19c). The rate at which bad by-products reach the detector is pretty low, which hints towards a good plasma deposition reflected in the high crystallinity of the layer. The In/Ga atom usage seems particularly efficient, given nitrogen is over-abundant, which may be why this layer is quite good in structure. This is all coherent, with the thickness playing a major role in the crystallinity formation within the thick layer. The interesting part about layer n° 10 is its homogeneity with respect to indium content (37 %) linked to the crystallite size extracted from XRD and SEM topview. It is well known that indium is extremely mobile, often leading to a phase separation and InN clusters [114], but the layer does not show any phase separation. Indeed, at the global scale, EDS (110) and XRD both confirm that $X_{\mathrm{In}} = \frac{\mathrm{In}}{\mathrm{In+Ga}} \cong 40\,\%$. In particular, the XRD measurement allows the extraction of values presented in table 4.7, showing no preferential orientation.

These values are then compared to the crystallite size extracted from figure 4.19b (see the procedure in figure 4.20). In particular, the average crystallite diameter is $19.15 \pm 5.38$ nm

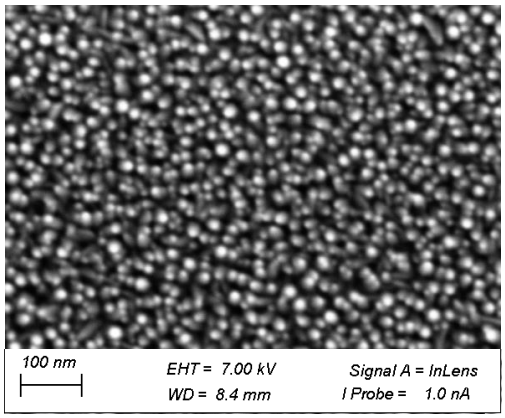


(a) SEM micrograph on silicon, layer n° 9.

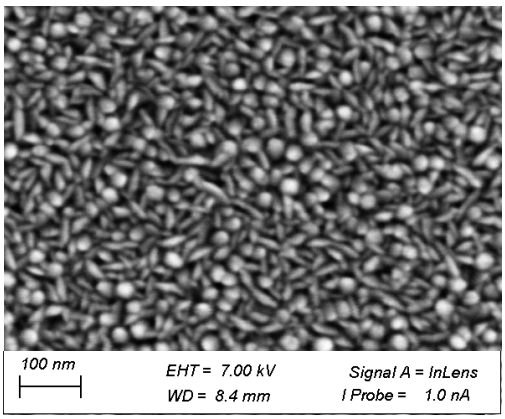


(b) SEM micrograph on silicon, layer n° 10.

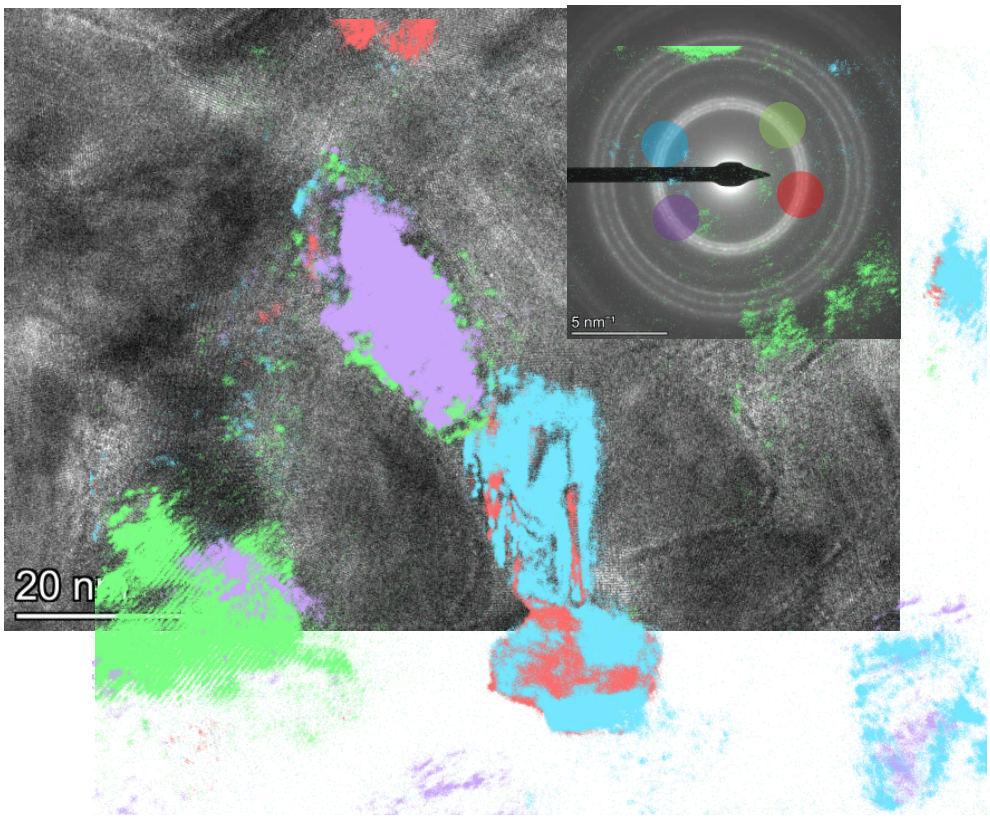


(c) Coloured TEM DFs on top of a HRTEM micrograph and their corresponding diffraction spot on the diffraction figure, layer n° 10 on a TEM grid. The DFs are slightly off compared to the HRTEM because of some movement of the sample holder between the different captures, hence the non-existing HRTEM at the bottom and the right of the figure.

Figure 4.19: In/GaN PECVD, TOFMS: InGaN layer, small electron microscopy study.

according to SEM measurements. If there were a phase separation, the actual XRD peak would be composed of two (or more) sub-peaks slightly offset, with each a different width (and associated crystallite size) than the one of the actual peak. This is not confirmed by the

Table 4.7: In/GaN PECVD, TOFMS: InGaN XRD results.

| Peak | Amp. [A.U.] | $2\theta$ [°] | Cr. Sz. [nm] |
|---|---|---|---|
| (100) | $960.7 \pm 24.6$ | $31.493 \pm 0.008$ | $17.45 \pm 0.02$ |
| (101) | $335.7 \pm 22.0$ | $35.555 \pm 0.023$ | $13.15 \pm 0.02$ |
| (110) | $194.7 \pm 22.3$ | $55.594 \pm 0.039$ | $14.98 \pm 0.02$ |

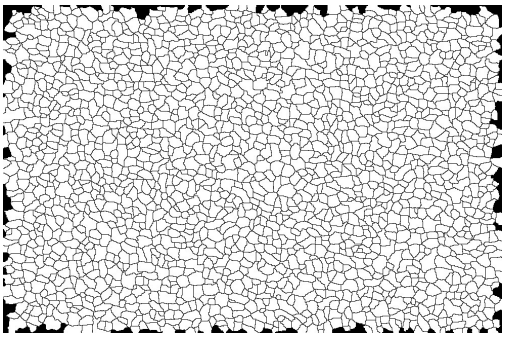

(a) Crystallite border detection, extracted from figure 4.19b. This grain boundary was extracted without thresholding the original image. Each grain is processed as a circle, whose diameter is put in the histogram on the right. This choice was made for simplicity reasons, just to probe the order of magnitude of the crystallite sizes.

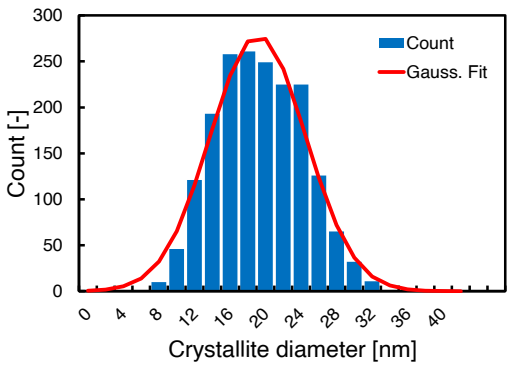


(b) Diameter histogram and gaussian fit of the crystallite size of figure 4.20a. The average crystallite diameter is $\mu = 19.15$ nm with a standard deviation of $\sigma = 5.38$ nm.

Figure 4.20: In/GaN PECVD, TOFMS: process to obtain the crystallite size distribution and main values extracted from it: crystallite border detection (a) → each surface is considered as a circle from which diameter is extracted → histogram of all diameters (b).

SEM analysis, which probes similar grain sizes in the top view. This proves that within the resolution of both instruments, the crystals are homogeneous on a global (XRD) and a local (SEM) scale, without phase separation. The problems start to arise at higher deposition or annealing temperatures.

#### 4.3.4.4 Special GaN layers

The three last layers presented in table 4.6a were produced with an addition of a particular precursor, whose effect is discussed in this section.

The eleventh layer was deposited with the additional precursor: $2 \pm 0.01$ sccm of $PH_3$. The idea was to produce something slightly different with system B: a GaNP layer. The TOF-MS did not reveal any anomalies: the expected dissociation processes occurred without incident. The newly introduced precursor also produced some by-products after dissociation in the plasma that was detected in trace quantities: $P_2^+$, $P_2H_2{}^+$ and $P_2H_4{}^+$ for example, a sign of

a good dissociation of this precursor. A barely visible $P_{55} - C_4H_7{}^+$ peak was present (other possible species: $C_3H_3O^+$ or $CHN_3{}^+$), but it did not react at the plasma lighting up.

Compared to gallium, it was expected to be a P-rich layer, but that is a sweet euphemism. EDS measurement concluded that the layer is mainly constituted of NP, with slight traces of incorporated gallium. This explains the complete lack of crystallinity (by XRD, not shown here), the immense optical BG value compared to GaN usual values (see figure 4.12), and the considerable thickness of the layer (NP seems to be deposited way faster than GaN). Upon re-analysis of the data, there is indeed a tiny $P_{45} - NP^+$ peak along with a $P_{45} - CH_2P^+$ one. But it is so tiny that it is considered within the noise range.

The effect of p-doping on the conductivity was tested with the twelfth layer, adding $0.02 \pm 0.0004$ sccm of TMB. Figure 4.21 shows the evolution of some peaks of interest.

The dark brown curve at the bottom follows the evolution of the most substantial peak of the TMG species; it goes to zero as soon as the plasma is started, the slight delay between the plasma start-up and the signal reaching the zero value is attributed to the specie still present between the deposition chamber and the TOF-MS. This means that the TMG is fully dissociated, and since peak 69 (not shown here) also goes to zero, all the gallium atoms are fully used, and nothing is wasted. In other words, the metallic precursor is the limiting factor with respect to the growth rate.

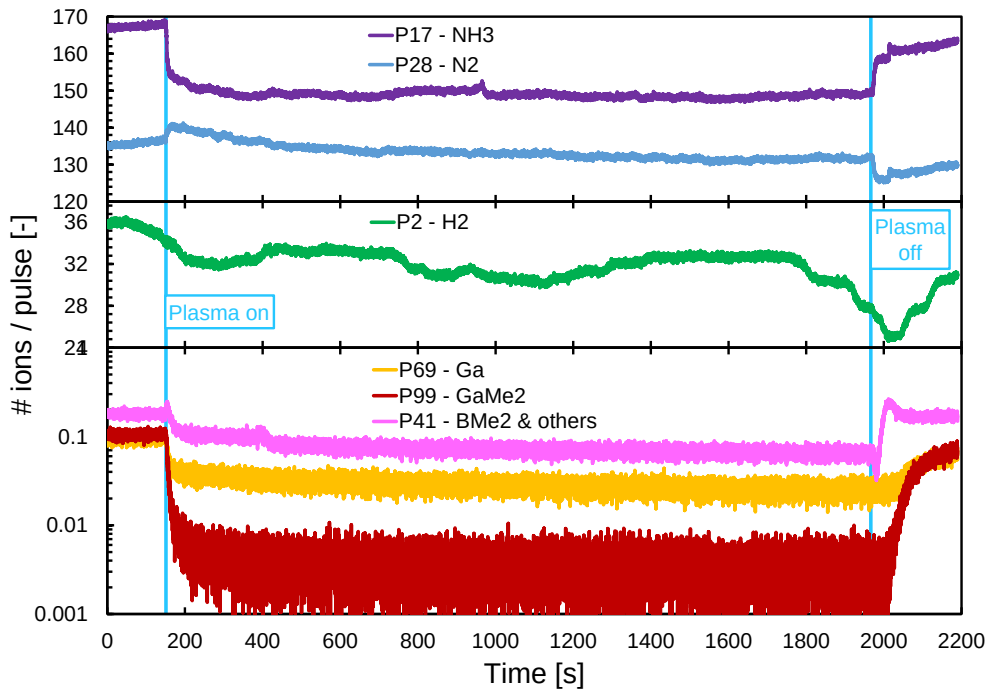


Figure 4.21: In/GaN PECVD, TOFMS: TMB dissociation.

The blue curve (ammonia, $P_{17}$) undergoes a relatively significant drop when the plasma is started, a sign of a partial dissociation of the precursor. In particular, the nitrogen provided by the ammonia will primarily be used and not the one barely provided by $N_2$. And as soon as the plasma is turned off, the peak level returns to normal. Here, even the nitrogen radicals dissociated from ammonia are not the limiting factor because some of it even has time to recombine into $N_2$, as shown by the increase of the pink nitrogen $P_{28}$ peak at the plasma light-up. The red line (hydrogen, $P_2$) is susceptible to plasma changes, whatever their origin. This is why we see such fluctuations in figure 4.21, and the result is difficult to interpret.

Following the peak n° 41, the first intuitive interpretation is the following: "the TMB is only partially dissociated", whereby comparing the values when the plasma is on or off, only two-thirds of it are integrated into the layer, and the rest is wasted. However, when zooming in on the peak 41 before and after the plasma light-up, it is proven that the $Me_2B^+$ peak decreases. Another dominant species is responsible for the non-zero signal during the deposition: $C_2H_3N^+$ (see figure 4.22 for the $P_{41}$ comparison and the non-zero green signal of $P_{41}$ in figure 4.21).

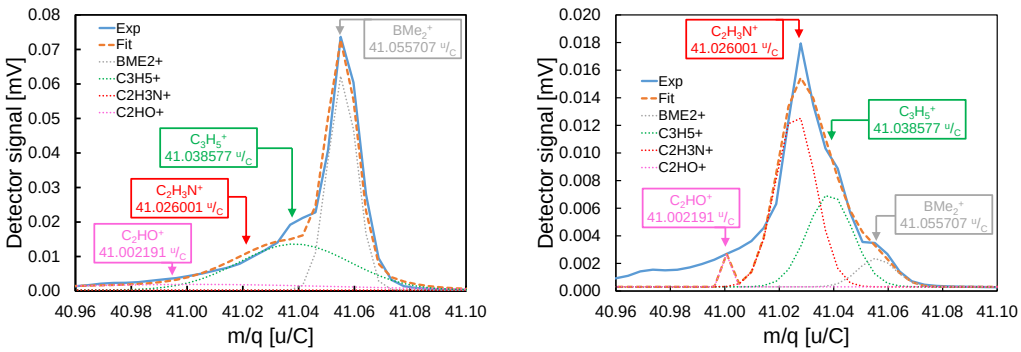


(a) Plasma off, an average of all the timestamps before the plasma is turned on.

(b) Plasma on, average of all the timestamps between 800 and 1800 s.

Figure 4.22: In/GaN PECVD, TOFMS: B-doped GaN, Zoom in on $P_{41}$ that is the cumulation of at least three different species that are more or less present depending on the plasma status. Please note that the y-axis has different values.

There are many candidates for a $m/q = 41$u/C value, but four caught our attention. They could be identified after minute calibrations, and by process of elimination: $BMe_2{}^+$, $C_3H_5{}^+$, $C_2H_3N^+$ and $C_2HO^+$. Deconvoluting $P_{41}$ allows differentiating between all species present. When the plasma is lit up, the $BMe_2{}^+$ peak takes 4 % of its initial value, and the previously absent $C_2H_3N^+$ peak becomes the dominant one. The two other peaks are merely reduced to about 25 % of their initial value.

This small result allows us to deduce a few conclusions. Firstly, the TMB is fully dissociated (or at least 90 % of it) and not partially as was previously thought. Since the layer is not conductive enough for electrical measurement, at least the partially integrated dopant hypothesis can be discarded. Second: this deposition allows the discovery of another plasma by-product ($C_2H_3N^+$) of which we were unaware, and that is, in retrospect, also observed in all other

depositions that included carbon, hydrogen and nitrogen. But in truth, this species may not be a plasma by-product, but one of the signals emitted by a more complex molecule being ionised at the entrance of the TOF-MS, this one being the plasma by-product. Determining the original molecule assembled at the plasma sheath is tedious work that was not performed in the framework of this thesis. And third: this shows us that the TOF-MS used for this observation is sensitive enough to detect such minute differences. The most impressive part is that it is done for a wide range of $^{m}/_{q}$ values simultaneously.

The effect of n-doping on the conductivity was also tested with the thirteenth layer, with the addition of $0.06 \pm 0.01$ sccm of silane injected for five seconds every minute, to test if n-doping could have any effect on the conductivity. This method of pulsed injection had to be used because our MFC and dopant dilution did not allow for a low enough flow to be still considered "doping". The unfolding of this deposition is presented in figure 4.23.

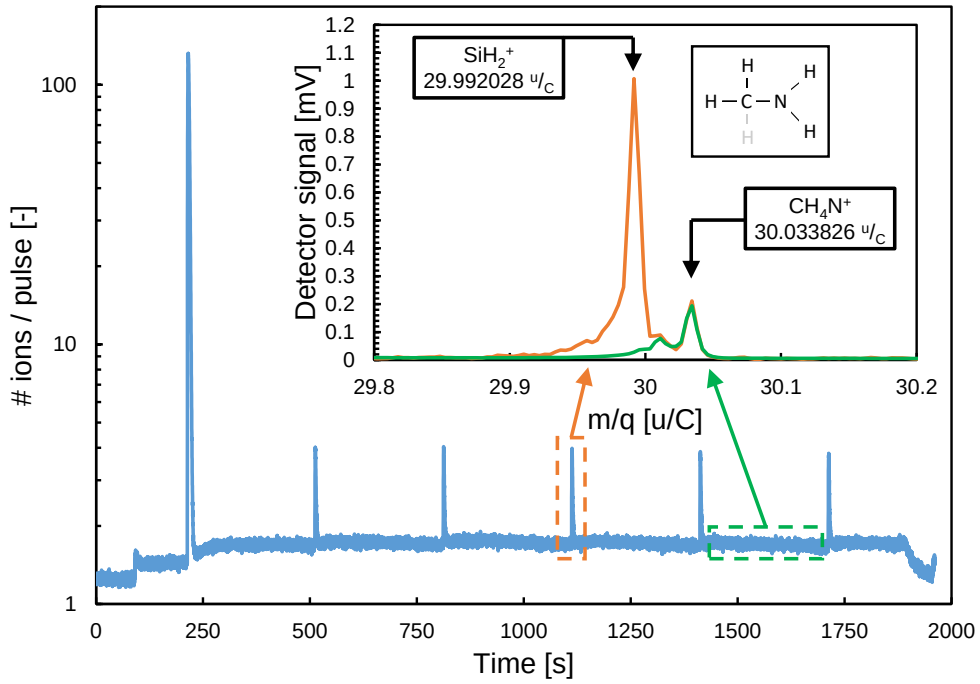


Figure 4.23: In/GaN PECVD, TOFMS: $SiH_4$ dissociation, following $P_{30} - SiH_2{}^+$ & $CH_4N^+$. The plasma is started at the small shoulder around 100 s and turned off at the other shoulder around 1900 s. Every blue peak represents the injection of a burst of silane into the plasma to dope the layer, where the first one was violently massive, far exceeding the error value. The silane is detected at the TOF-MS only during its injection inside the plasma, a sign of a full dissociation when not injected. If the signal does not go back to zero between two bursts, it is because of the presence of another plasma by-product: $CH_4N^+$, decomposed from the $CH_5N^+$ molecule, called "methylamine" and shown in the small top-right rectangle.

During this deposition, another by-product was discovered: $P_{30}$ – $CH_4N^+$, that is produced at the TOF-MS ioniser from the decomposition of the $CH_5N$ molecule. This species was retrospectively also present during all the other depositions.

Now, every time silane is injected in the plasma for a few seconds, some species peak in the detector ($P_2$ – $H_2{}^+$, $P_{28}$ – $N_2{}^+$ and $P_{30}$ – $SiH_2{}^+$), and some drops are detected ($P_{13}$ – $CH^+$, $P_{14}$ – $N^+$, $P_{17}$ – $NH_3{}^+$ $P_{41}$ – $C_2H_3N^+$ and $C_3H_5{}^+$). Some species even do not change noticeably ($P_{26}$ – $C_2H_2{}^+$, $P_{69}$ – $Ga^+$, $P_{99}$ – $GaMe_2{}^+$). The explanation linked to this phenomenon is yet to be validated, but for the time being, here is what is proposed to happen inside the plasma for these brief seconds:

1. Peak $P_{30}$ – $SiH_2{}^+$ increases because silane enters the plasma and is only partially dissociated, hence its peak at the TOF-MS.
2. This, in turn, increases the concentration of hydrogen present in the plasma, hence the $P_2$ – $H_2{}^+$ peak.
3. More hydrogen allows for an easier breakdown of the molecules, such as ammonia, hence its drop. The newly available nitrogen will recombine into $P_{28}$ – $N_2{}^+$ at the plasma sheath, hence its peak. Indeed the $P_{28}$ – $N_2{}^+$ peak seem to start slightly after the $P_{17}$ – $NH_3{}^+$ drop.
4. More hydrogen means that by-products are evacuated faster and better, hence the drop in $P_{41}$ – $C_2H_3N^+$ and $C_3H_5{}^+$.
5. The gallium is already entirely consumed, so there are no changes when the hydrogen concentration increases.

Looking at its optical absorption (figure 4.12), this layer is of poor quality, given its low bandgap and enormous Urbach energy. On top of that, it has some low energy absorption. This may be due to a too-high silicon content, disrupting the GaN bonds, thus allowing for even more sub-gap states. Indeed, we see that the first burst of silane was massive! This probably disrupted the first GaN matrix, where crystals are still tiny and oriented in all directions before growing into ordered columns. That could explain the lowest bandgap, the high sub-gap absorption, and the low energy absorption. It would be worth trying again, with a more insufficient silane flow and less often. The EDS measurement of the silicon content was, however, not conclusive because the silicon wafer dominated the signal coming from the layer. The XRD crystallinity is also extremely poor (not shown here).

### 4.3.5 InGaN PECVD, TOFMS: key takeaways & next steps

This section presents the plasma dynamics of a few deposition processes and their impact on the layer characteristics, thanks to a time-of-flight mass spectrometer. Many plasma by-products were identified and linked to quality metrics and layer contamination. The influence of pressure, plasma frequency and power were explored as well.

Here are a few conclusions that can be deduced from all the results presented in this section:

- Abundant non-reactive precursors (Ar, $N_2$) undergo small to no change when the plasma is lit on or off. However, they remain more sensitive to power and pressure corrections.
- Higher power concentration allows for a better dissociation of the molecules because it breaks stronger bonds more efficiently. For example, $N \equiv N$ has a bond energy of 226 kcal/mol, which is challenging to dissociate compared to ammonia, 86 kcal/mol for the $N-H$ bond [68, 16].
- Hydrogen is sensitive to plasma changes, and this may be mainly due to its lightweight and reaction with many other species.
- Higher hydrogen flow promotes by-product and waste evacuation. Shorter carbo-hydrate chains are detected when hydrogen is over-available.
- When carbo-hydrate wastes are well evacuated and carbon-poor, this results in better optical and structural characteristics; less sub-BG states, less low energy absorption and better crystallinity (but not preferential). This can be achieved by increasing the hydrogen content of the plasma or the plasma power.
- Argon etches the layer and prevents crystallinity. Using $N_2$ as an "almost neutral precursor" is better.
- The lower the base pressure, the better (obviously). It must be below $10^{-5}$ mbar to eliminate contamination from the previous deposition process.
- The twelfth layer proved that the TOF-MS could detect up to four close peaks, tickling the tool's sensitivity limit.
- It is qualitatively (not quantitatively) possible to predict which InGaN layer will contain more indium than another with the TOF-MS by comparing under the same experimental conditions the height of the $P_{99}$ – $GaMe_2{}^+$ and the $P_{145}$ – $InMe_2{}^+$ peaks.
- The TOF-MS explains why the GaN:Si layer failed: the first burst of silane was massive, which contaminated the first layers of the film with extremely high carbon content and subsequent contamination.
- Although the GaN:B layer would need further study, boron in the layer is quickly confirmed by the TOF-MS (thanks to TMB by-products reaching the detector).
- The TOF-MS can detect layer contamination before the use of EDS or any other tool. For example, a supposed GaN layer contained 20 % indium, confirmed by EDS.
- TMI/G are completely dissociated, but In and Ga are not fully used. This was observed by comparing $P_{69}$ and $P_{99}$ for Ga, and $P_{115}$ and $P_{145}$ for In. Increasing $N^+$ availability (higher flow or higher power) or decreasing In/Ga concentration helped boost this efficiency, but a 100 % usage was never reached.

This section aimed to better understand the plasma dynamics; that goal is achieved, and a link between some of the observations and the deposition events and layer characteristics could also be established.

## 4.4 Design of experiment with all the PECVD layers

### 4.4.1 Motivation

Over 250 layers were deposited by PECVD in System B and characterised by different tools in four years. Three master students contributed with one or two tens of layers that they deposited and described in the framework of their semester project on developing InGaN PECVD layers under my and Mathieu Boccard's supervision.

The idea of this section is to use the powerful DOE tool to process all those results and see how some of the layer characteristics can be expressed as a function of the deposition conditions. For example, the optical BG can be empirically expressed as a function of the precursor flows and the RF plasma parameters. This mathematical description has the advantage of being quantitative *and* qualitative, which can then be related to physical events and dynamics. An obvious example: all the models describing the layer thickness (be it InN, GaN or InGaN) have a positively linear "time" effect, which means that the thickness will increase with a longer deposition time, which is consistent with what is already observed.

There are ten deposition parameters (six precursor flows and four RF plasma parameters) that can combine to express one of the five-layer characteristics that are modelled here (thickness, optical BG, crystallite size, Urbach energy, indium content), potentially for all the three compositions (InN, GaN and InGaN). The procedure presented in the next section explains how to find the model that best describes the layer characteristics. The quality of the resulting models that are presented further is also assessed. Ultimately, this part of the thesis aims to express layer characteristics as a function of their deposition parameters.

Once this empirical but quantitative link has been established between multiple layers' characteristics and their deposition conditions, the deposition process can be optimised for that precise layer characteristic. For example, the crystallite size may be maximised or the Urbach energy minimised alone. That optimisation process can, however, be performed for different characteristics simultaneously, where incidentally, pushing a button is beneficial for multiple layer characteristics at once. Or maybe a trade-off between specific input parameters must be decided to achieve an optimum result. This is performed at the end of this section, where a deposition process that will grant the desired characteristics is presented, with expected values according to the models.

### 4.4.2 Procedure

The thickness will be discussed, as well as the BG, the Urbach energy, the crystallite size according to the unstrained Scherrer equation and the indium content. All those sections first present the results for GaN, then InN, and InGaN in some cases.

DOE analysis can be pretty dense at times, and the details of the results presented here are reported in appendix B.2 for the reader's curiosity. Given that the experiment was not designed

beforehand, the appearance of extreme outliers may call for their deletion (with a justification), and the whole fitting procedure may have to be re-processed again. The modelling process follows this flow of operations:

1. A physical quantity (a layer characteristic) is chosen.
2. The whole dataset is filtered by layer quality and composition:
   - Layer quality: good, acceptable (or "fair"), unusable. The quality is an objective estimation of multiple characteristics of one layer at a time, where a good layer has an Urbach energy below 200 meV, an optical BG of more than 2.5 eV for a GaN layer and less than 2.2 eV for an InN layer, is crystalline when measured with the XRD, and has a growth rate that is below 10 nm/min. These values are subjectively chosen. An acceptable or fair layer has one or two of these limits that are overcome (it depends on the severity of the excess), and unusable layers have three or more than these limits overcome; they can mainly be identified by a considerable Urbach energy.
   - Layer composition: InN, GaN, InGaN.
   - If a potentially good layer was not characterised for the chosen physical quantity, it is not considered in the fitting process.
   - For example, the model for the GaN thickness (section 4.4.3.1) uses only the good GaN layers; out of the > 250 layers that were deposited and that make up all the dataset, only the GaN of good quality for which a thickness measurement has been performed are considered for the rest of the procedure; that is 45 layers.
     Another example: the model for the crystallite size of InGaN was based on the set of layers with all types of composition (InN, GaN and InGaN) and with fair quality, meaning the good and acceptable layers, but not the unusable ones. Since the crystallite size could not be or was not measured for all these, only 79 layers remained in the final dataset.
3. After the filtering by layer, only the input parameters that show some variance are retained. Typically, the RF was not varied and will not appear in the results. The possible input parameters are the following: gas flows (TMG denoted as "*Ga*", TMI denoted as "*In*", $N_2$, $H_2$, $NH_3$, *Ar*) and plasma characteristics (pressure "*Pr*", power "*Po*", temperature "*T*", and time "*t*"), for a total of ten possible input parameters. This means ten factors in a linear model but 65 in the full quadratic one.
4. The input parameters are standardised. See the paragraph describing this procedure on page 58.
5. Obviously, the 250 layers were not part of a "grand" experiment designed from the start, so a higher correlation between the input parameters can be expected (see explanation below equation 3.42. A complex starting model (usually the full quadratic one) is fitted to the data, whose factor's VIFs are first estimated (see equation 3.43). All those over 100 are discarded one after the other, preferentially keeping the more uncomplicated effects over the complex ones. The correlation matrix can also help determine which factors to toss in priority (see equation 3.42).

6. The next step is to estimate the p-values of the remaining factors (see equation 3.55). The effect with the highest p-value above 5 % is taken out of the model, which is fitted again to the data. And so on, until there are no p-values above 5 % anymore. This step is labelled as "the decrementing step".
7. The goodness of fit is then evaluated with different tools, all described in section 3.3.2: $R^2_{adj}$ (desired as close to 100 % as possible), *RMSE* (desired as small as possible, or at least one order of magnitude smaller than the range of the observed physical quantity), model p-value $p_M$ (desired smaller than 5 %) and lack of fit p-value $p_{LF}$ (desired greater than 5 %).
8. At this point, if a relatively good model is proposed with some downsides (too high VIF or p-value of one effect, one of the quality metrics is not satisfactory, too many outliers, etc.), the next step becomes a matter of personal choice. For example, the factors that do not make sense can be eliminated: having the time input variable appear in the model describing the growth rate does not make sense if we consider it time-independent. The three previous steps may have to be re-performed again.
9. Various more detailed plots related to the fit are also extracted (see figure 3.11c), which may help identify some outliers or understand a potentially bad quality metric of one of the previous points. Following this analysis, if the description of the physical quantity can be improved, the model or the dataset is modified, and a whole new fitting process may be undertaken until no more improvement can be conducted.

In the following sections, only the model, a summary of the dataset, the standardisation process and the final quality metrics of the fit are presented. The p-values and VIF of each factor and potentially some interesting detailed plot will only be shown in Appendix B.2. The model presented here will be discussed and interpreted further. Please remember that the orthogonal parameter space opened by the range of the input parameters is only partially explored; indeed, a corner would yield a different experimental result from the one predicted. On the contrary, the model should remain valid within a linear combination of the most external points of the parameter space (see figure 4.6b for such an example of non-square parameter space). Finally, the outlier outcomes are shown in every figure, where here, an outlier is defined as such when it exhibits a residual larger than 1.5 times the *RMSE*.

### 4.4.3 Thickness

As mentioned in sections 3.2.2 and 3.2.5, the thickness is determined either by ellipsometry or by profilometry on a glass substrate. The ellipsometry measurement is more precise than the profilometer one (see the error discussion in the last paragraph of section 3.2.2.3 page 39); the thickness difference between the two methods is mainly due to a different measurement location on a slightly inhomogeneous layer since the profilometer needs a lift-off step that would hinder the ellipsometry measurement. For some layers, only one of these characterisations was performed, and, in some cases, the ellipsometry measurement was only performed on one of the two substrates (glass or silicon). Since the profilometer is less

precise and does not perform the measurement in the same spot as all the other techniques, its result will be taken as a last resort. And since most of the ellipsometry measurements were performed on glass, these results will prioritise the ones performed on silicon.

The thickness models were developed on actually deposited layers. Still, forged ones could also have been introduced in the fitting procedure (see limits of a DOE in table 4.8a for example). In the GaN case (hereafter), introducing no TMG or having a deposition time of 0 min should produce a layer of zero thickness. Such "fabricated results" were, however, not introduced.

#### 4.4.3.1 GaN

The model for the thickness of GaN layers was extracted using only the good-quality layers. Adding interaction or quadratic terms did not yield any worthy improvements, but the quality of it can still be considered fair. The fit is expressed by (4.1):

$$Thk_{\mathrm{GaN}} = 420.0 + 217.5Ga + 61.2H_2 - 144.5NH_3 + 130.8Ar - 75.3Pr + 122.4t \tag{4.3}$$

The thickness linearly depends on every input parameter, except for $N_2$ and $Po$ (p-value higher than 5 %). According to $R^2_{adj}$ and $p_M$ (see table 4.8b), the model remains fair but not quite perfect. That is also reflected in the *RMSE* value, where an error of about 50 nm on a predicted value between about 40 and 500 nm would not be qualified as desirable, even though it is still one order of magnitude lower than the range of experimental values. The good news, however, is that the lack of fit p-value above 5 % means that we cannot reject the null hypothesis assuming that the model is under-fitting the data. Or in other words: the lousy quality of the model is mainly due to noise and cannot substantially be improved further.

Further insight can be obtained thanks to the standardisation of the parameters, where each of the coefficients presented in the previous equation can only take values between −1 and 1, corresponding to their real maximum and minimum values shown in table 4.8a. Since the model is entirely linear (no interaction or quadratic terms), increasing an effect with a positive coefficient will linearly increase the predicted thickness of the GaN layer. In more detail, increasing the TMG, $H_2$ or argon flow rates will increase the layer thickness and deposition time. This is all expected since the TMG provides more metallic atoms to the layer, hydrogen fastens the breaking down of the TMG molecules (and, surprisingly, an interaction term $Ga \cdot H_2$ was not kept here), and increasing the deposition time will indeed produce a thicker layer. The sign of the *Ar* effect is surprising here because this precursor dilutes the metallic precursor in the plasma and should not induce a thicker layer when present. On the other hand, increasing the ammonia flow will also increase the dilution of the gallium atoms in the plasma, decreasing the predicted thickness, as expected. The pressure should not play a significant role in the thickness of the GaN layer, but surprisingly, increasing it results in a thinner layer. Increasing the pressure will prevent the plasma ions $Ga^+$ and $N^-$ from travelling

Table 4.8: In/GaN PECVD, DOE: GaN thickness model, input variable standardisation and model quality metrics. There were 45 good layers considered for this model.

(a) Details of the considered layers for the presented model: statistics on their fabrication characteristics.

| Input parameter | Unit | Minimum value | Maximum value | Mean value |
|---|---|---|---|---|
| $Ga$ | sccm | 0.075 | 2.0 | 0.48 |
| $N_2$ | sccm | 0 | 150 | 50.9 |
| $H_2$ | sccm | 0 | 127.3 | 74.1 |
| $NH_3$ | sccm | 0 | 30 | 11.7 |
| $Ar$ | sccm | 0 | 25 | 2.2 |
| $Pr$ | $\mu$bar | 450 | 550 | 496.4 |
| $Po$ | W | 15 | 100 | 36.9 |
| $T$ | °C | 100 | 400 | 232.7 |
| $t$ | min | 6 | 121 | 23.9 |
| $Thk_{\mathrm{GaN}}$ | nm | 39.5 | 500.3 | 150.0 |

(b) Quality metrics of the model.

| Quality metric | Value |
|---|---|
| $R^2_{adj}$ | 76.2 % |
| $p_M$ | $< 10^{-8}$ % |
| $p_{LF}$ | 24.3 % |
| $RMSE$ | 47.0 nm |

further, slowing down the recombination rate, hence the layer thickness. The pressure effect is among the weakest ones.

Some effects are absent from the model due to their too-high p-value or a too-high colinearity with other terms in the model. In the first case, it means that within the explored range of these absent parameters, their variation has a non-significant effect on the output parameter (here, the thickness). This can be addressed by widening the range of said parameter until an effect becomes strong enough. In the second case, it means that these deposition parameters are too similar to one or many others within the whole dataset. In terms of design, the two dimensions describing these parameters in the parameter space are said to be too parallel or not orthogonal enough. This can be addressed by adding new measurement points to the design to make it as orthogonal as possible.

As already mentioned in the introduction of this section, most of the vertexes and even edges of the parameter space are not fully explored. For example, no layer with the minimal value of each table parameter 4.8a was deposited; it would not even produce a GaN layer, but simply deposit gallium since no nitrogen is implied. This edge is, however, considered valid according to the model; it lies within the parameter space and should theoretically give a GaN layer thickness of 107.9 nm. This incoherence can be addressed by stating that the parameter space is too extended compared to the physical reality. The source of this incoherence lies in the nitrogen source, which is different for two different layers considered for this model: either $N_2$ or $NH_3$, resulting in an "unexplorable" parameter space edge where these two factors are at their minimum value of zero. Or in other words, there is an actual physical phase change (or "step") where the plasma does not produce a GaN layer anymore but a Ga one. This step-like change (and other similar behaviours) is generally poorly handled by the DOE method.

Another way to search for problematic extrema and physical incoherences of the model would be to try to reach a negative thickness within the defined parameter space. This is done by minimising every term of equation 4.3, reaching down to −331.7 nm. In particular, this layer could physically exist: minimum TMG flow and maximum $NH_3$ flow defined by the parameter space, with the highest pressure and the lowest deposition time. But again, the model here poorly handled the following step-like behaviour: a smooth decrease of the thickness abruptly followed by a plateau. The best way to address this type of incoherence (abrupt change in the output variable) is to reduce the parameter space so that it does not cover it.

Lastly about the standardisation of the parameters: it also allows a fair comparison of the influence of each factor on the output variable, where the most influential factor has the highest value (here $Ga$ followed by $NH_3$), and the least influential factors have the lowest value (here $H_2$ followed by $Pr$). It can be seen on table B.5 page 241 in appendix B.2 that the influential factors are firmly attached to the model by a low p-value, making them the least irrelevant. In contrast, the least influential ones have among the highest p-values of the model. The temperature does not even appear in the model, meaning it has a minor influence on the thickness of the GaN layer. If one wants to test the model, the temperature should be set at a standardised value of zero, meaning 250 °$C$. The same reasoning stands for $N_2$ and $Po$.

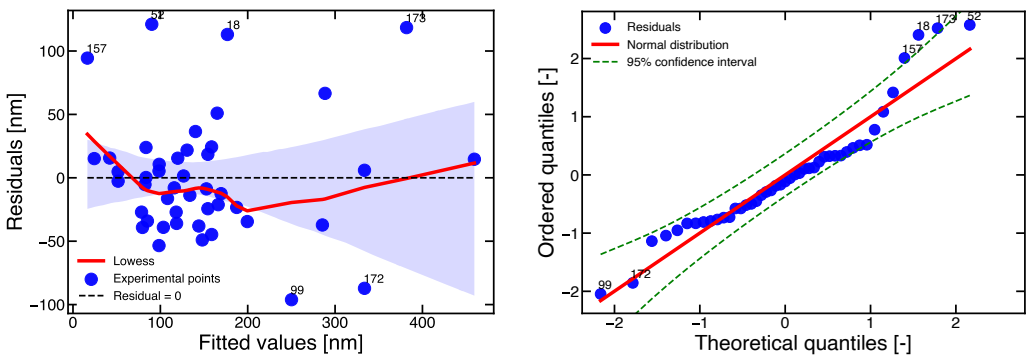


(a) Residual vs fitted values, 95 % confidence interval (CI) and locally weighted scatterplot smoothing (LOWESS).

(b) Q-Q plot.

Figure 4.24: In/GaN PECVD, DOE: residuals vs fitted values plot and quantile-quantile normal plot of the GaN thickness model. The layer numbers inducing the highest error are displayed in both cases.

The noise in the dataset is also shown in the residuals vs fitted values plot (figure 4.24a), where the values are noisily scattered far from the baseline $y = 0$. However, the locally weighted scatterplot smoothing (LOWESS) curve hints towards an unaccounted-for effect because some quadratic trend seems to appear. Or in other words: the linearity is terrible but still acceptable. The homoscedasticity can be estimated by how conic the 95 % confidence interval (CI) is. In this graph, the spreading of the points is more pronounced far from the central cloud of points, which means there is some heteroscedasticity in the model. This kind of heteroscedasticity still seems acceptable. In the Q-Q plot (figure 4.24b), we can again identify the same outliers

as in the residuals *versus* fitted values plot. Is there a problem with these outliers? For example, layer n° 157 were produced just after a cleaning of the deposition system, and layers n° 172 and 173 are part of the first batch of tests of layers deposited with argon. The three of them are clean, with good optical and crystalline properties. Still, the noise in the model may come from this kind of instability: being deposited just after a cleaning of the system or being deposited for the first time. So it was decided to keep them nonetheless.

In conclusion, even if the model is noisy, it shows an overall acceptable agreement with the experimental data, good prediction across the whole range of thicknesses considered (fair linearity), and an uneven noise distribution around the predictor (bad homoscedasticity). It can be used with caution for future depositions of GaN layers inside system B within the parameter space defined by all the considered points, and the trends shown here have some chances to remain valid for other systems or outside of this parameter space (but still inside equilibrium).

#### 4.4.3.2 InN

The model for the thickness of InN layers was extracted using all the usable layers, except one that was first deemed fair (layer n° 27) but induced a considerable noise in the model. Final count: 47 layers were used to base the model on. By analysing that layer, it was indeed part of a problematic batch of depositions, where the growth rate was different under similar deposition conditions. Layer n° 20 is in the same set and does induce too much noise, so it was also discarded.

$$Thk_{\mathrm{InN}} = 272.9 + 332.7In + 33.7N_2 - 24.3Po + 29.4t + 125.2In^2 \tag{4.4}$$

Because of a too-high p-value or because of a too-high correlation with other effects, the linear effects of $H_2$, $NH_3$, $Ar$, $Pr$ and $T$ could sadly not be included in the model. Such a problem was already discussed in section 4.4.3.1, page 108. Despite their absence, the model remains simple, with one quadratic effect but only six effects in total. Its quality is excellent: it explains more than 95 % of the experimental data without underfitting it (see table 4.9b). The quality of the model is also perceived in the low *RMSE* value compared to the range of the output variable.

The standardisation of the parameters allows the same analysis as with the GaN, where the TMI flow is the most significant effect, having a strong positive linear term and a weaker positive quadratic term. Having reasonable control over the flow of TMI inside the chamber seems crucial for a well-controlled layer thickness. The other effects are weaker, but the time is still present here (obviously): increasing the deposition time will still increase the thickness of the InN layer. It is, however, shocking that the nitrogen has a positive effect and the power has a negative effect on the InN thickness; a higher dilution prompted by a more increased

Table 4.9: In/GaN PECVD, DOE: InN thickness model, input variable standardisation and model quality metrics. There were 47 fair layers considered for this model.

(a) Details of the considered layers for the presented model: statistics on their fabrication characteristics.

| Input parameter | Unit | Minimum value | Maximum value | Mean value |
|---|---|---|---|---|
| $In$ | sccm | 0.4 | 8.0 | 2.1 |
| $N_2$ | sccm | 0 | 150 | 18.3 |
| $H_2$ | sccm | 50 | 120 | 88.9 |
| $NH_3$ | sccm | 0 | 30 | 18.1 |
| $Ar$ | sccm | 0 | 5 | 0.2 |
| $Pr$ | $\mu$bar | 480 | 520 | 498 |
| $Po$ | W | 20 | 100 | 33.3 |
| $T$ | °C | 200 | 300 | 236 |
| $t$ | min | 10 | 150 | 25.6 |
| $Thk_{\mathrm{InN}}$ | nm | 26 | 684 | 106 |

(b) Quality metrics of the model.

| Quality metric | Value |
|---|---|
| $R^2_{adj}$ | 97.6 % |
| $p_M$ | $< 10^{-30}$ % |
| $p_{LF}$ | 48.5 % |
| $RMSE$ | 15.3 nm |

nitrogen flow is expected to decrease the deposition rate, and a higher power is expected to break down more molecules, making the plasma ion-richer, the deposition rate faster, hence a thicker layer. Maybe the solution would be to postulate that increasing the power also induces more plasma by-products, which will hinder the deposition, but that is a feeble argument. For the nitrogen effect, the growth rate is limited by the availability of the metallic precursor. Still, the TOF-MS shows that the indium part of the dissociated TMI precursor is not used. It can be postulated here that increasing the nitrogen flow will increase the concentration of nitrogen radicals, enabling the easier capture of indium radicals and increasing the growth rate.

The physical limits are the same as for GaN, where here it would be theoretically possible to produce a InN layer without any nitrogen source (all minimum values still give a non-zero thickness of 26.6 nm). The most negligible valid possible thickness allowed by the model is −22 nm. Not as bad as GaN, but still problematic. The same reasoning applies as for GaN, please refer to the text in section 4.4.3.1, page 109 for more details.

The Q-Q plot shows a satisfactory noise of the data around the Gaussian distribution (see figure 4.25b). The same goes for the residuals *versus* fitted values plot, where the cloud of points is not larger than about ±20 nm (see figure 4.2a). This is also reflected in a low *RMSE* value of about 15 nm, forty times smaller than the range of experimental values. The furthest outliers are layers n° 114 and 120. As mentioned before, because of the already excellent quality of the model and for scientific integrity, these layers were not removed from the dataset; they were produced without any noticeable problems.

In conclusion, the model is excellent. A slight downside, however, is that there seems to be a slight non-linearity within it. Indeed, when looking at the LOWESS red curve of figure 4.25a, the leading cloud of points looks OK, but it dodges quickly when far from it. This non-linearity

mainly concerns the *Po* effect, as shown in figure B.6b of appendix B.2, page 242. With only the residuals *versus* fitted values plot, since the cloud of points is highly dense, judging the homoscedasticity of the model would prove difficult here, even only looking at the 95 % CI. Still, this model can be used with confidence for future depositions of InN layers inside system B within the parameter space defined by all the points considered, and the trends showed here to have a high chance to remain valid for other systems or outside of the parameter space (but still inside equilibrium).

Finally, compared to the GaN thickness model, a similar behaviour is expected since the ranges of the input parameters are identical, and the TMG molecule resembles the TMI one. However, the only similar elements between the two models are the flow of the metallic precursor and the deposition time. The interest in probing the thickness instead of the growth rate is that the time linearity can be checked, proving that the layer does not grow at a different pace after a specific time. Except for these, the reason behind the presence or the absence of effects in one or another model may be attributed to high co-linearity between factors or reflected in the choices made when faced with a high VIF value. Or they could be attributed to a bad fitting of the GaN thickness model because of the too-noisy data.

#### 4.4.3.3 InGaN

Two competing models can describe the thickness of the InGaN layers more or less accurately. The first (denoted by a ①) was extracted using the high-quality layers of all types of content (GaN, InN and InGaN), while the second ② was extracted only using the InGaN layers of high quality. We will analyse both simultaneously; each has upsides and downsides.

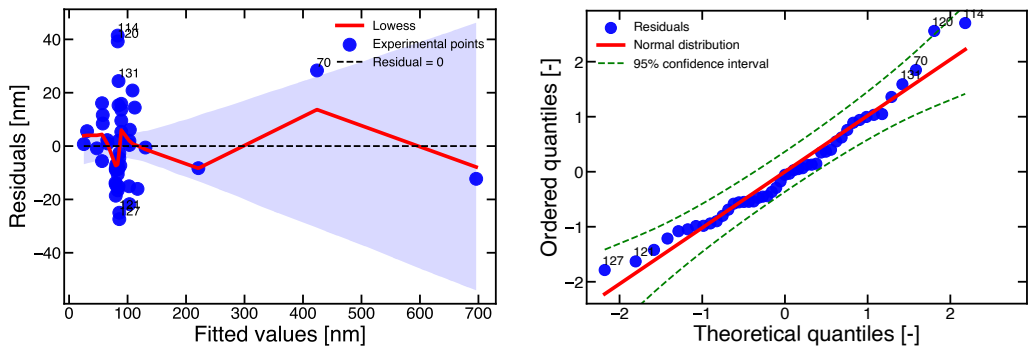


(a) Residual vs fitted values, 95 % CI and LOWESS.

(b) Q-Q plot.

Figure 4.25: In/GaN PECVD, DOE: Residuals vs fitted values plot and quantile-quantile normal plot of the InN thickness model. The layer numbers inducing the highest error are displayed in both cases.

$$
\begin{aligned}
Thk_{\mathrm{InGaN}_{①}} &= 451.4 + 153.9\,Ga + 229.9\,In - 40.4\,Po + 89.7\,t \\
&\quad + 49.3\,N_2 \cdot NH_3 - 99.7\,N_2 \cdot Ar - 350.3\,Pr \cdot T + 114.1\,Pr \cdot t + 101.4\,In^2 \qquad (4.5a) \\
Thk_{\mathrm{InGaN}_{②}} &= 170.3 + 155.4\,Ga - 277.5\,H_2 + 225\,Ga \cdot Po - 154.5\,Ga \cdot t \\
&\quad - 77.3\,In \cdot T + 190.5\,In \cdot t + 123.9\,N_2 \cdot T - 245.7\,H_2 \cdot NH_3 + 141.1\,Po \cdot T \qquad (4.5b)
\end{aligned}
$$

At first glance, the first model looks more convenient than the second for fewer terms and more linear effects. However, the constant is at a high starting point (further than ② from the mean value), and there is an unlikely squared term. Furthermore, the $Pr \cdot t$ interaction effect does not relate to any physical reality and is most likely present only to fit the data better. On the other hand, the second model has other upsides: a constant closer to the mean value without any quadratic terms (which is good), but there are more effects (or more terms), most of them being non-linear but rather interaction terms, making this model more complex (which is terrible).

Regarding their quality, model ① is terrible. In contrast, model ② can be considered as fair (see table 4.10b): while both do not underfit the data, ② explains more experimental points than ① with a comparable *RMSE* with respect to the experimental range (see the last line of table 4.10a).

Regarding the standardisation of the parameters, there is a lot to unpack here. In short, model ① has an expected strong positive linear dependency on the TMG and TMI flows; the layer thickness also linearly depends on time (which is also expected). Surprisingly there is a substantial unexpected joint effect of the pressure and the temperature, where the layer thickness will decrease if both input parameters are increased or decreased simultaneously. Apart from the second to the last effect, the other terms do not stand out, and a link to plasma dynamics can be found for each of them. However, the second to last term ($+114.1\,Pr \cdot t$) is surprising because, during the plasma deposition, there should not be a dependence between these two physical quantities: time and pressure. This term certainly only helps mathematically just to improve the model.

Model ② is a bit worse than model ① with regard to standardisation of the parameters because there is indeed a linear dependency on the TMG flow, but not on the TMI one, which makes less sense with respect to the thickness of an InGaN layer; symmetry is lost here. However, the *In* factor can be found in other interaction effects, so at least this input parameter is still present in the model. Here also, most of the effects can be explained by specific plasma dynamics, except for $a_{N_2 \cdot T}$, $a_{Ga \cdot t}$ and $a_{In \cdot t}$. The first of these three is expected to be negative; when increasing the nitrogen flow and the temperature simultaneously, the thickness of the layer is expected to decrease because of a higher dilution (effect of the nitrogen) slowing down the deposition rate and because of a higher adatom mobility (effect of the temperature)

Table 4.10: In/GaN PECVD, DOE: InGaN thickness models, input variable standardisation and model quality metrics of the two models. There were 121 good layers considered for model ①, and 36 layers deposited in different conditions for model ②, not allowing for the extraction of a lack of fit p-value.

(a) Details of the considered layers for the presented models: statistics on their fabrication characteristics. There was no variance for the argon flow or the pressure in model ②.

| Input parameter | Unit | Minimum value | | Maximum value | | Mean value | |
|---|---|---|---|---|---|---|---|
| | | ① | ② | ① | ② | ① | ② |
| $Ga$ | sccm | 0 | 0.03 | 2.0 | 0.80 | 0.22 | 0.13 |
| $In$ | sccm | 0 | 0.2 | 6.0 | 3.0 | 0.97 | 0.99 |
| $N_2$ | sccm | 0 | 0 | 250 | 250 | 62.9 | 124 |
| $H_2$ | sccm | 0 | 50 | 150 | 150 | 83.5 | 87 |
| $NH_3$ | sccm | 0 | 0 | 30 | 30 | 11.3 | 4.3 |
| $Ar$ | sccm | 0 | 0 | 25 | 0 | 0.91 | 0 |
| $Pr$ | $\mu$bar | 450 | 500 | 550 | 500 | 498 | 500 |
| $Po$ | W | 15 | 20 | 100 | 100 | 35.0 | 33 |
| $T$ | °C | 100 | 200 | 400 | 250 | 234 | 236 |
| $t$ | min | 5 | 5 | 150 | 30 | 23.4 | 21 |
| $Thk_{\text{InGaN}}$ | nm | 26 | 69 | 500 | 380 | 136 | 161 |

(b) Quality metrics of the models.

| Quality Metric | Value ① | Value ② |
|---|---|---|
| $R^2_{adj}$ [%] | 65.3 | 81.0 |
| $p_M$ [%] | $< 10^{-20}$ | $< 10^{-6}$ |
| $p_{LF}$ [%] | 16.6 | - |
| $RMSE$ [nm] | 49.0 | 25.4 |

inducing a better alignment of the crystal resulting in a denser layer, hence the lower growth rate. But maybe the joint effect has a negative linear impact on the thickness, related to a physical phenomenon we are unaware of for the time being. For the two others, again, there cannot be a physical dependent interaction between the physical quantities involved, even more surprisingly, with one positive and the other negative. These two terms are believed to be present in the model just for a better mathematical fitting and cannot be linked to a fundamental plasma dynamic going on.

The physical limits are even more problematic than for GaN and InN, where here the parameter space extends to an edge where it would be theoretically possible to produce a InGaN layer without any precursor, with a thickness of −166.9 nm (①) or 495.4 nm (②) (all values in table 4.10a set to their minimum). This is due to different sources for the same type of precursor (metallic source and nitrogen source) being all mixed since GaN and InN layers are also taken into account for determining the InGaN thickness. A solution to that would be to reduce the dataset to only InGaN layers that are only produced with either only nitrogen or only ammonia. Also, the most extreme possible thicknesses are shown in table 4.11: we see there that the range of predicted values far exceeds the range of experimentally observed ones. This other problem can be addressed by reducing the volume of the parameter space by probing smaller ranges of values for each parameter.

Table 4.11: In/GaN PECVD, DOE: InGaN thickness models, problematic extrema in reaching the minimum and maximum possible thicknesses in nm.

| Model | ① | ② |
|---|---|---|
| Min | −574.5 | −1266.0 |
| Max | 1680.1 | 1606.6 |

As it can be analysed from the LOWESS curve in figures 4.26a and 4.26c, the linearity seems acceptable for model ①, but bad for model ②. Looking at the 95% interval, the homoscedasticity for model ① looks reasonable but fair for model ②. The acceptable linearity of model ① is reflected in its lack of fit p-value that slightly approaches the threshold value of 5 %. These two figures can also be linked to the *RMSE* value, where the y-axis range is entirely different. The range of experimental thicknesses considered is admittedly diverse, and so is the volume of the input parameter space, which explains that difference; model ② has a quantitative better *RMSE* value, but it is not that far better than the one of model ① when comparing with the range of experimental outcomes.

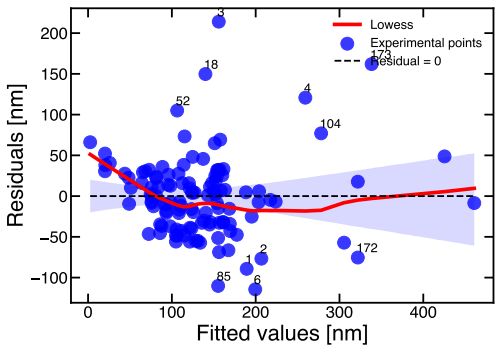


(a) Residual vs fitted values, 95 % CI and LOWESS, ①.

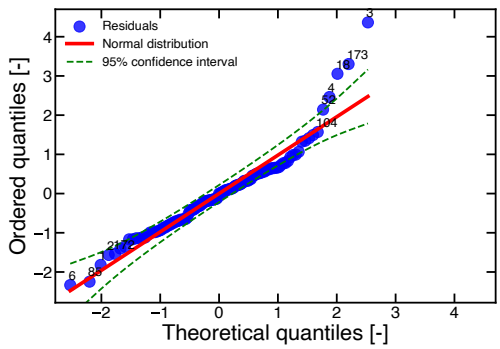


(b) Q-Q plot, ①.

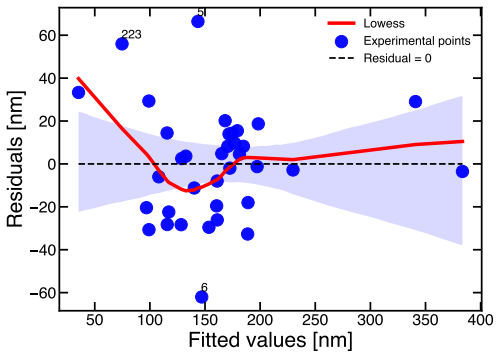


(c) Residual vs fitted values, 95 % CI and LOWESS, ②.

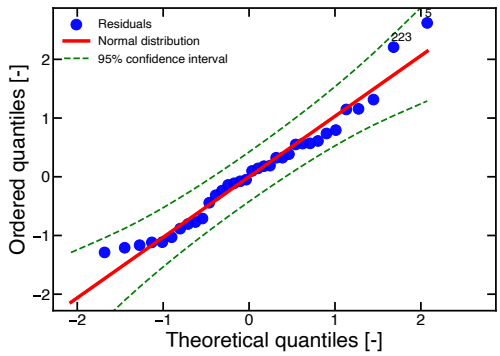


(d) Q-Q plot, ②.

Figure 4.26: In/GaN PECVD, DOE: Residuals vs fitted values plot and quantile-quantile normal plot of the two InGaN thickness models. The layer numbers inducing the highest error are displayed in all cases.

The Q-Q plots show that for most of the points; the residuals are closely behaving like noise (see figures 4.26b and 4.26d). Both plots display diverging tails at high predicted values, where those outlier points are responsible for most of the noise in the level. The outliers of each model are different because one model has difficulty predicting some results that the other can easily predict, and vice versa. By particularly analysing these outliers, nothing, in particular, comes up: their input parameter is not extreme, neither is their thickness, and there is no valid reason to discard any of them. The only peculiar thing is that they were all non-InN layers, but that may come from the fact that the thickness model for InN layers was of excellent quality compared to the GaN one.

In conclusion, compared to the GaN and InN thickness models, even though the quality is worse, model 1 seems to be the best choice because of its similarity with the previous models and because of its effects that are more related to experimentally explained plasma dynamics phenomenons. Another argument against model 2 is also presented in annexe B.2: two of the VIFs take a value above 10, a sign of solid collinearity. Because of its low quality, much caution is needed when using model 1 for future InGaN depositions in system B.

Taking all the thickness models into account, they are mostly made of linear effects in a simple form. The main expected effects are present and amongst the strongest (the metallic precursors and the time), with some interaction and quadratic effects here and there. The same trends are observed in the three models, where given the similarity between the three possible compositions, such behaviour is expected. A physical phenomenon can explain almost all the effects expressed in these optimised models. The quality is overall acceptable with an honourable mention for the InN thickness model, but slightly noisier when describing the InGaN thickness.

### 4.4.4 Optical bandgap

As mentioned just after equation 3.18 page 40, there are multiple ways to determine the BG of a material, sometimes linked to different tools. For the model presented here, the optical bandgap $E_{04}$ extracted from the spectrometer on a glass substrate was chosen as the first choice. If that measurement was unavailable, then the optical bandgap $E_{04}$ given by the ellipsometry modelisation of the layer deposited on glass was preferred, or on silicon, if the former was also unavailable. The Tauc-Lorentz bandgap given by the ellipsometry (see equation 3.10 page 37 and related explanation) or the bandgap provided by the spectrometer's Tauc-plot (also in the description just after equation 3.18, section 3.2.2.4) were discarded, since they substantially differ from the optical bandgap measurement [201], and less of these measurements were performed (see their difference in figure 5.34c as an example).

Due to imperfections in the layer (defects, contaminations, etc.), the bandgap of GaN or InN can vary. The following sections aim to empirically determine which button to turn to achieve a more desired optical quality, where a BG of 3.4 eV and 0.7 eV are aimed for the two materials respectively. Only the good layers were probed in both cases.

#### 4.4.4.1 GaN bandgap

The model for the GaN optical BG was extracted using all the good GaN layers of all contents: 45 layers. See tables 4.12a for more details about the dataset used.

$$1000 \cdot E_{04}^{\mathrm{GaN}} = 2903 - 294H_2 - 381Ar - 278N_2 \cdot Ar - 203NH_3 \cdot Ar \tag{4.6}$$

Looking at table 4.12b, it can be established with confidence that this model is the worst one presented here; the $R^2_{adj}$ value can hardly be lower, and the $p_M$ value is becoming dangerously close to 5 %. In other words, this model can correctly predict less than 20 % of the data, and we are close to being unable to reject the null hypothesis stating that "this model is as good as a constant term". The error on the predicted BG is about a fifth of the full range of experimental results. The only comfort is that there is no underfitting of the data ($p_{LF} > 5\,\%$). Or in other terms, the badness of the model is mainly due to noise in the output parameter.

Table 4.12: In/GaN PECVD, DOE: GaN bandgap model, input variable standardisation and model quality metrics. There were 45 good layers considered for this model.

(a) Details of the considered layers for the presented model: statistics on their fabrication characteristics.

| Input parameter | Unit | Minimum value | Maximum value | Mean value |
|---|---|---|---|---|
| $Ga$ | sccm | 0.075 | 2.0 | 0.48 |
| $N_2$ | sccm | 0 | 150 | 50.9 |
| $H_2$ | sccm | 0 | 127.3 | 74.1 |
| $NH_3$ | sccm | 0 | 30 | 11.7 |
| $Ar$ | sccm | 0 | 25 | 2.2 |
| $Pr$ | $\mu$bar | 450 | 550 | 496.4 |
| $Po$ | W | 15 | 100 | 36.9 |
| $T$ | °C | 100 | 400 | 232.7 |
| $t$ | min | 6 | 121 | 23.9 |
| $E_{04}^{\mathrm{GaN}}$ | eV | 2.335 | 3.445 | 3.095 |

(b) Quality metrics of the model.

| Quality metric | Value |
|---|---|
| $R^2_{adj}$ | 18.5 % |
| $p_M$ | 1.52 % |
| $p_{LF}$ | 86.6 % |
| $RMSE$ | 0.19 eV |

Regarding the effects, the constant is placed at 2.903 eV. From there, an increase to 3.4 eV is desired, so since all the coefficients are negative, reducing the value of their associated input parameter might help obtain a higher bandgap, up to a maximum predicted value of 4.059 eV, substantially higher than the maximum value observed (no argon nor hydrogen, maximum nitrogen and ammonia). Standardising the parameters allows for further analysis, where the most influencing effect is the argon flow, which is also present in interaction effects. The two interaction effects tell us that reducing the flow of this parameter while increasing the flow of nitrogen or ammonia will yield an even higher BG. So, in conclusion: less hydrogen, less argon, more nitrogen, and more ammonia for a less-defective GaN layer. Except for hydrogen, these

make sense because they will increase the dilution, reduce the growth rate, and give more time to the adatoms to arrange themselves, generating fewer defects. One of the roles of hydrogen is to associate with the plasma by-products and evacuate them, so decreasing it should make more carbon assimilate inside the layer, making this effect the only counter-intuitive one of this model.

This model only shows two small non-problematic ones regarding extrema and problematic physical limits. The first one is the same as already mentioned: a GaN layer could theoretically be produced without a nitrogen source because two were used separately in the dataset. The second one is that the minimum reachable value is 1.747 eV, which is not that far lower than the minimum value observed (compared with the maximum predicted value in the previous paragraph).

See figure 4.27: the residuals *versus* fitted values plot shows a relatively even spread across the whole range of fitted values (acceptable linearity and homoscedasticity), with only two high leverage outliers at the bottom (layers n° 44 and 241). However, even without the outliers, compared to the range of experimental output values, the spread is pretty large and is reflected by the relatively large *RMSE*. In the Q-Q plot, we can conclude that almost all the residuals follow a normal distribution (because they lie on a straight line), except for the outliers; their outcome value is more extreme than expected if they came from a normal distribution.

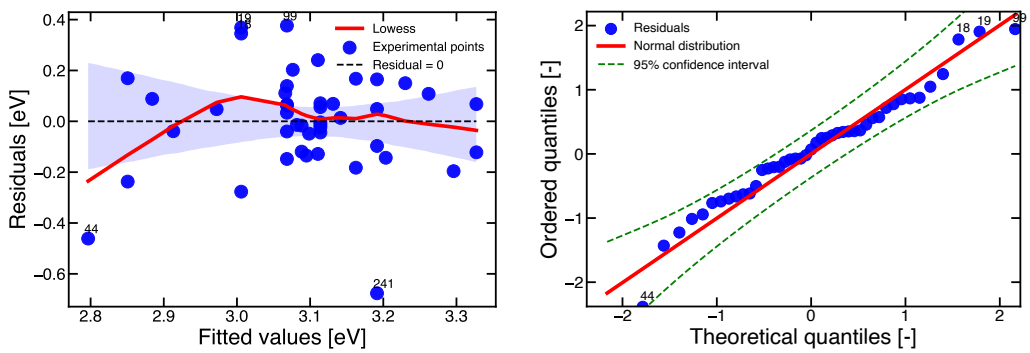


(a) Residual vs fitted values, 95 % CI and LOWESS.

(b) Q-Q plot.

Figure 4.27: In/GaN PECVD, DOE: Residuals vs fitted values plot and quantile-quantile normal plot of the GaN optical bandgap model. The layer numbers inducing the highest error are displayed in both cases.

In conclusion, the model is terrible but shows acceptable linearity and homoscedasticity. This means it may help optimise GaN layers using system B within the parameter space defined by all the points considered with high prudence.

#### 4.4.4.2 InN bandgap

For the optical BG of InN layers, two competing models can describe the layers produced, where the first (denoted by a ①) approaches the experimental values better. Still, the effects of the second (represented by a ②) make way more sense physically. Both were extracted using the excellent quality InN layers, which will be analysed simultaneously.

$$1000 \cdot E_{04}^{\mathrm{InN}①} = 1812 + 97In + 66N_2 - 135Po - 95T + 90N_2 \cdot H_2 + 55NH_3 \cdot Po - 258In^2 \tag{4.7a}$$

$$1000 \cdot E_{04}^{\mathrm{InN}②} = 1594 - 146Po - 97T + 106N_2 \cdot H_2 + 58NH_3 \cdot Po \tag{4.7b}$$

In both cases, the constant $a_0$ is close to the mean value of the output variable, which is a first good sign (see table 4.13a). However, model ① implies that the BG value has a robust quadratic dependency on the TMI flow, which may make sense, knowing that if there is not enough nitrogen in the plasma during the deposition, the layer will mainly appear metallic, and eventually oxidise. However, given the negative curvature of this quadratic effect, if a lowest $BG_{\mathrm{InN}}$ value is desired, this can be achieved either by ultimately increasing the TMI flow or entirely decreasing it (the best case here, because of the added linear effect). In that regard, nitrogen flow should also be reduced (which is not expected to improve the InN layer quality). In contrast, temperature, power and hydrogen flow should be increased (which is expected to enhance the InN layer quality). The last interaction term tells us that the ammonia flow should decrease if power is increased.

In comparison, model ② is in fact model ① but with three less effects ($N_2$, $In$ and $In^2$). The signs are identical, but the effect strength is slightly different to compensate for the absent ones. Hence the tendencies remain the same: the better way to reach a lower InN BG is by increasing the nitrogen flow, the temperature and the power and decreasing the hydrogen and ammonia flows. Given the previously described phenomenons, this makes more sense physically. Regarding physical limits, the parameter space again extends to a region that produces an InN layer without any nitrogen source. Still, surprisingly that is the only irregularity of these two models.

Table 4.13b shows that the first model explains substantially more experimental points than the second one (8 % difference). However, removing three effects did not trigger an alarming decline in the lack of fit p-value: the second model is still well-fitted. Despite a bad $R^2_{adj}$ value, the *RMSE* gives a relatively precise estimate of the calculated output (compare with the GaN value in table 4.12b).

If we now analyse the plots in figure 4.28 without considering the outliers yet, the residuals vs fitted values plots show good linearity across the whole range for the two models in general

Table 4.13: In/GaN PECVD, DOE: InN optical bandgap models, input variable standardisation and model quality metrics. There were 41 good layers considered for these models.

(a) Details of the considered layers for the presented models: statistics on their fabrication characteristics.

| Input parameter | Unit | Minimum value | Maximum value | Mean value |
|---|---|---|---|---|
| $In$ | sccm | 1 | 6 | 2 |
| $N_2$ | sccm | 0 | 150 | 25 |
| $H_2$ | sccm | 50 | 120 | 91 |
| $NH_3$ | sccm | 0 | 30 | 17 |
| $Ar$ | sccm | 0 | 5 | 0.2 |
| $Pr$ | $\mu$bar | 480 | 520 | 499 |
| $Po$ | W | 20 | 100 | 35 |
| $T$ | °C | 200 | 300 | 235 |
| $t$ | min | 10 | 150 | 25 |
| $E_{04}^{\mathrm{InN}}$ | eV | 1.24 | 1.96 | 1.69 |

(b) Quality metrics of the models.

| Quality Metric | Value ① | Value ② |
|---|---|---|
| $R^2_{adj}$ [%] | 75.6 | 67.6 |
| $p_M$ [%] | $< 10^{-7}$ | $< 10^{-6}$ |
| $p_{LF}$ [%] | 93.7 | 87.9 |
| $RMSE$ [eV] | 0.064 | 0.077 |

but consult appendix B.2 for more details about that. At first glance, there could be some heteroscedasticity in the first model since the 95 % CI shade is more conic than for model ②. The two quantile-quantile normal plots are also satisfying, where apart from the outliers, the residuals behave like Gaussian noise.

Regarding the outliers, layer n° 133 is present in both cases, with also layer n° 180 for model ② (left-most point in the residuals *versus* fitted values plot of model ①, figure 4.28a). No valid reason was found for removing these layers from the dataset. Their "out-of-the-group" behaviour can be explained by their low $E_{04}$ values compared to other layers, where layer n° 180 has by far the lowest of the whole dataset and was produced with the lowest TMI flow rate.

In conclusion, these models are "fair enough" and have to be used with a grain of salt in the future. They show good linearity and homoscedasticity features, no under-fitting, and a decent error. Compared to the unreliable model for the GaN BG, model ② seems more similar and makes more sense because of the absence of the solid quadratic $In^2$ term, but its quality is substantially reduced compared to model ①. The best final choice here would be to use only the part of model ① related to low TMI flow rates and not rely on it for high TMI flow rates.

#### 4.4.4.3 InGaN bandgap

In this section, two models describing the optical BG of InGaN layers will be presented simultaneously: $BG_{\mathrm{InGaN_{SysB}}}$ established with the deposition parameters, and $BG_{\mathrm{InGaN_{X_{In}}}}$ related only to the indium content and the growth rate $g$. However, the growth rate was deemed irrelevant for this model (too high p-values for every linear, interaction or quadratic effect containing $g$);

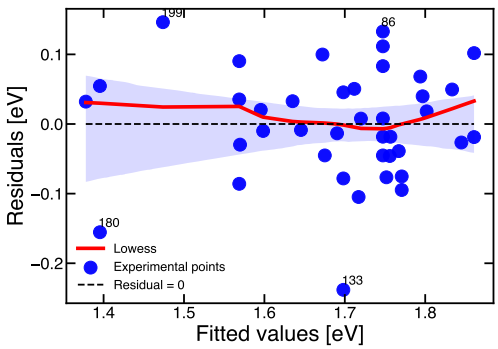


(a) Residuals vs fitted values, ①.

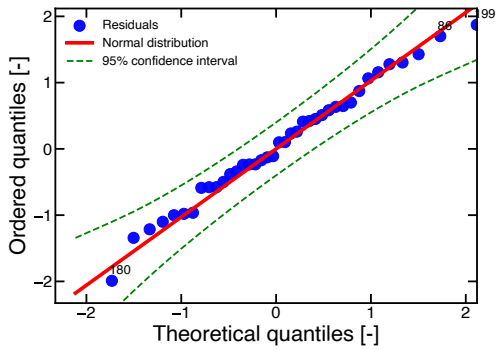


(b) Q-Q plot, ①.

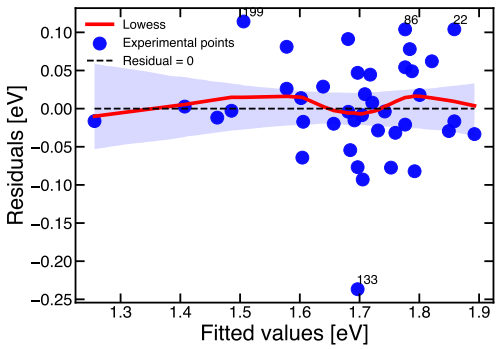


(c) Residuals vs fitted values, ②.

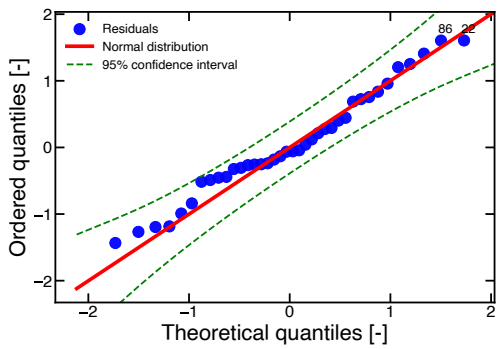


(d) Q-Q plot, ②.

Figure 4.28: In/GaN PECVD, DOE: Residuals vs fitted values plot and quantile-quantile normal plot of the two InN optical bandgap models. The layer numbers inducing the highest error are displayed in all cases.

this model will then entirely depend on $X_{\text{In}} = \frac{\text{In}}{\text{In+Ga}}$ (In & Ga in at. %, $X_{\text{In}}$ in %) extracted by EDS only. This model can be compared to the one developed in section 4.2. For that model, the effects presented can be traced back to the deposition parameters using one of the two models for the indium content in section 4.4.7.

$$1000 \cdot E_{04}^{\text{InGaN}_{SysB}} = 1665 - 380In - 365N_2 + 936In \cdot T - 874N_2 \cdot T - 460Ga^2 + 876In^2 \tag{4.8a}$$

$$1000 \cdot E_{04}^{\text{InGaN}_{X_{\text{In}}}} = 1807 - 707X_{\text{In}} + 587X_{\text{In}}^2 \tag{4.8b}$$

On top of being extremely simple, the model based on EDS is also perfect as it can predict more than 90 % of the experimental data correctly (see table 4.14b). Suppose this model is combined with the $X_{\text{In}}$ model based on the deposition parameters predicting more than 80 % of the experimental result. That is still more than 70 % of the experimental values predicted. This model shows a positive curvature, coherent with the classical Vegard's law expressed in

equation 2.14. Based on it, empirical fitting values for Vegard's law can be extracted from the present model, where $BG_{\mathrm{GaN}} = 3.10 \pm 0.23\,\mathrm{eV}$, $BG_{\mathrm{InN}} = 1.69 \pm 0.11\,\mathrm{eV}$, and the bowing parameter $b = 2.35 \pm 0.26\,\mathrm{eV}$, decent results! In addition to that, the other quality metrics ($RMSE$, $p_{LF}$, $p_M$) are also very satisfactory.

Table 4.14: In/GaN PECVD, DOE: InGaN optical bandgap models, input variable standardisation and model quality metrics. There were 110 good layers considered for the model based on the indium content $X_{\mathrm{In}} = \frac{\mathrm{In}}{\mathrm{In+Ga}}$ (In & Ga in at. %, $X_{\mathrm{In}}$ in %), and 121 good layers for the one based on the deposition parameters.

(a) Details of the considered layers for the presented models: statistics on their fabrication characteristics. See table 4.18a for the model details based on EDS measurements.

| Input parameter | Unit | Min. value | Max. value | Mean value |
|---|---|---|---|---|
| $Ga$ | sccm | 0 | 2 | 0.2 |
| $In$ | sccm | 0 | 6 | 1 |
| $N_2$ | sccm | 0 | 250 | 64 |
| $H_2$ | sccm | 0 | 150 | 84 |
| $NH_3$ | sccm | 0 | 30 | 11 |
| $Ar$ | sccm | 0 | 25 | 0.9 |
| $Pr$ | $\mu$bar | 450 | 550 | 498 |
| $Po$ | W | 15 | 100 | 35 |
| $T$ | °C | 100 | 400 | 234 |
| $t$ | min | 5 | 150 | 23 |
| $E_{04}^{\mathrm{InGaN}}$ | eV | 1.18 | 3.44 | 2.32 |

(b) Quality metrics of the models.

| Quality Metric | Value SysB | Value $X_{\mathrm{In}}$ |
|---|---|---|
| $R^2_{adj}$ [%] | 76.0 | 91.0 |
| $p_M$ [%] | $< 10^{-31}$ | $< 10^{-54}$ |
| $p_{LF}$ [%] | $< 10^{-6}$ | 14.6 |
| $RMSE$ [eV] | 0.332 | 0.207 |

On the other hand, the model based on the deposition parameters could not even be forced to be symmetric with respect to the $Ga$ and $In$ input parameters: it made the collinearity of some of the terms or their p-value to the peak. Its quality is not that good (only 76 % predicted, as shown by the $R^2_{adj}$ value in table 4.14b), and the data are under-fitted. This lower quality is also reflected in the low $RMSE$ value. But all in all, this is still quite competitive with the combined two models of the InGaN BG and the indium content $X_{\mathrm{In}} = \frac{\mathrm{In}}{\mathrm{In+Ga}}$ (In & Ga in at. %, $X_{\mathrm{In}}$ in %), where the $BG_{\mathrm{InGaN_{SysB}}}$ model still has a better overall $R^2_{adj}$ value and a better $RMSE$ value than the combined ones. Nothing can be said about the combined lack of fit p-value since it could not be extracted from the indium content model (see table 4.18b).

Based on the deposition parameters, the downside of the model is that the empirical effects can hardly be related to physical phenomena. For example, in the explored parameter space of the model, the InGaN BG will be reduced by the same amount if the TMG flow is either reduced or increased to its extreme values. On the other hand, the TMI input parameter makes sense in that model since it is highly correlated to the indium content of the layer, and the terms behave in the same way as the $X_{\mathrm{In}}$ effects of the other suitable model. The different effects of the $BG_{\mathrm{InGaN_{SysB}}}$ model allow for an adjustment of the BG relative to, for example, a

different growth rate that will influence the quality of the layer, hence "improving" the BG. And that is the pivot point of this model: it is difficult to express a BG "improvement" across the whole range of indium content. Indeed, a better quality InN crystal will yield fewer defects, inducing a lower BG; while for GaN, fewer defects will make the BG go from 3.1 eV to 3.4 eV, effectively increasing it. Add noise to the data, which is why this model's quality is lower: too many factors to consider to have a reliable and sound model to describe the BG over the whole range of indium content.

This is also reflected in the range of output values allowed by the parameters space, spanning from -0.034 eV to 4.366 eV. As already mentioned in the section on the GaN thickness, the DOE method poorly handles phase change or abrupt step-like variations (a negative optical BG does not exist). Again, according to the model, producing a layer without any precursors would be possible because of the different ways to make the different types of layers. But here, the problem is even more profound; the DOE method usually benefits from the simplicity of a linear combination of the different effects to produce the output variable. However, in this particular case, it would be wiser to have a non-linear dependency of $E_{04}^{\mathrm{InGaN}_{SysB}}$ on the TMG and TMI precursors, but rather something similar to $E_{04} \sim \frac{In}{In+Ga}$, which should reflect the indium content of the layer $X_{\mathrm{In}}$.

Comparing the two Q-Q plots in figure 4.29, we see that the points follow the fitted line better in the one based on the deposition parameters, with a few bunches of outliers. For the model based on the indium content $X_{\mathrm{In}}$, the points seem to follow a specific curved trend, hinting that the model could fit the data better if that curvature were considered. This should be reflected in a low lack of fit p-value – and this value is indeed close to the 5 % threshold for that model – but the strange thing here is that the "better-behaving" Q-Q plot based on the deposition parameters holds a strongly confirmed alternative hypothesis to the null hypothesis for the lack of fit p-value (the alternative hypothesis is "there is a lack of fit"), which sounds strange. However, the Q-Q plot is only a visual tool to detect at first glance if there is any problem quickly; given the noisy model based on system B, maybe that is the reason why the lack of fit cannot be detected directly here.

We see different interesting things in the two residuals *versus* fitted values plots of the same figure. First of all, the $X_{\mathrm{In}}$ one (figure 4.29c): the two lines formed by the points correspond to the GaN (right line), and InN fitted bandgaps values extracted a few paragraphs above, where all the points in-between correspond to InGaN layers. Some points are more to the left than the InN line: those are the InGaN fitted points that have a BG lower than the fitted InN one because of the bending of the Vegard's law. There are here a few residuals proposed for this model, but they are kind of part of the bending of the pattern described for the corresponding Q-Q normal plot; this means that if the bending were taken into account in the model if the data was better fitted, those "outliers" would be put back in line. These outliers correspond to the BG values of non-InGaN layers that are far from the fitted ones mentioned at the beginning of the present section, hence their high residual. Apart from that, both the linearity and the homoscedasticity seem excellent! Indeed, the LOWESS is flat, and the 95 % CI is straight.

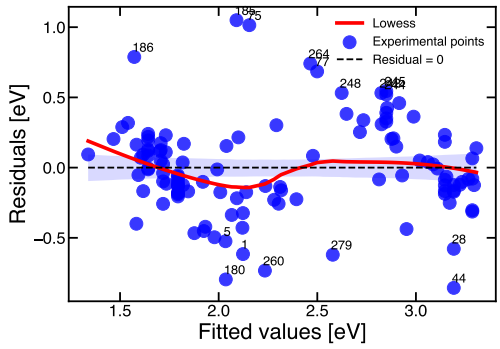


(a) Residual vs fitted values, 95 % CI and LOWESS, system B.

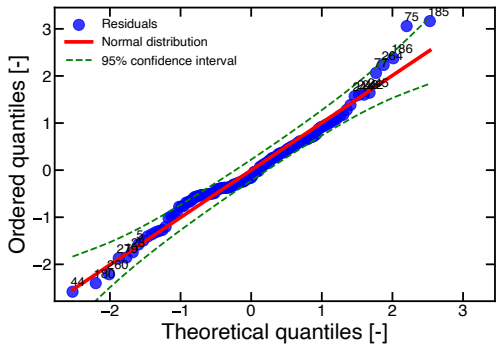


(b) Q-Q plot, system B.

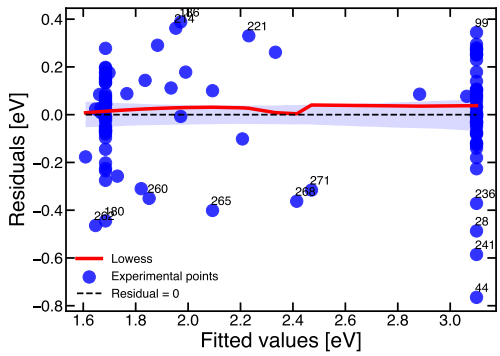


(c) Residual vs fitted values, 95 % CI and LOWESS, $X_{\mathrm{In}}$.

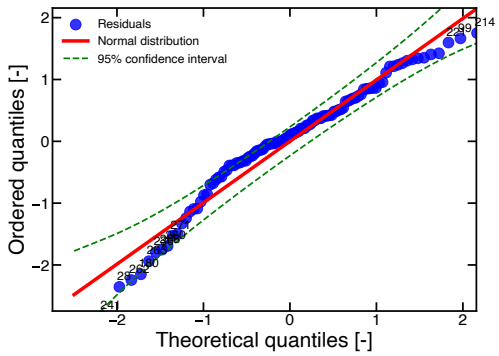


(d) Q-Q plot, $X_{\mathrm{In}}$.

Figure 4.29: In/GaN PECVD, DOE: Residuals vs fitted values plot and quantile-quantile normal plot of the two InGaN optical bandgap models. The layer numbers inducing the highest error are displayed in all cases.

For the one related to the deposition parameters model, notice that the range upon which the residuals are spread out is more extensive. Here, we can also kind of guess two oblique clouds of points, also corresponding to the InN and GaN fitted values, with the InGaN ones in-between. The outliers are better defined and correspond again to the outer layers in the model. Because of the outliers' high leverage on the model (see figure B.13c), discarding them could yield a completely different result, but no valid reason was found for such a decision; they were then kept. About leverage points, also take a look at appendix B.2 where again, layer n° 70 is by far the highest leverage point of them all, inducing non-linearity although well predicted by the model.

In conclusion, both models are valid if we relate the InGaN BG to the deposition parameters. In contrast, the one using EDS is more complicated for similar quality; however, if the goal is to link the InGaN BG to the indium content $X_{\mathrm{In}} = \frac{\mathrm{In}}{\mathrm{In+Ga}}$ (In & Ga in at. %, $X_{\mathrm{In}}$ in %), then the second model presented here is excellent and can be used with confidence.

Considering all the optical BG models, they are mostly made of interaction effects, which complexifies the description. The TMG flow is strongly present in the InN and InGaN ones. Completely different trends are observed between the three models, and this is due to the other behaviour of the optical bandgap at different indium content values. Hence, the incoherence between them is expected. Again, a physical phenomenon can explain almost all the effects expressed in these optimised models. The quality is terrible for the GaN optical BG model and barely acceptable for the two others, with underfitting and a hefty *RMSE* for the InGaN optical BG model.

### 4.4.5 Unstrained XRD crystallite size

The crystallite size of the deposited layers can be extracted by XRD measurement on a silicon substrate, using the width of the thinnest peak (usually the (002) one) and Scherrer's equation (equation A.10 page 225). The goal is to determine which buttons to turn to increase the crystallite size inside the layers. Usually, if a layer grows to be crystalline, there is first a nucleation step from which crystals can stem, increasing in size with the growing layer. So at least the time effect (highly correlated to the thickness; see the models presented in section 4.4.3) is expected to appear here.

#### 4.4.5.1 GaN

Sadly, there were not crystalline enough GaN layers produced under different conditions to perform a reliable study on the crystallite size, even not a linear one. But the one on InN seems interesting, and its conclusions may be applied to future GaN layers!

#### 4.4.5.2 InN

The model for the crystallite size of InN layers was extracted using all the usable layers, except one that was first deemed good (layer n° 274) but induced considerable noise in the model. The resulting crystallite size was overestimated by comparing its crystallite size with other almost identically grown layers, hence why this layer was discarded.

$$CrSz_{\mathrm{InN}} = 29.60 - 8.41\,In + 6.46\,H_2 - 7.15\,NH_3 - 6.31\,Po + 15.41\,T + 14.68\,t \tag{4.9}$$

Because of a too-high p-value or a too-high correlation with other effects, the linear effects of $N_2$, $Ar$ and $Pr$ were not included in the model. Despite their absence, the model remains simple and makes sense of its expected effects. Its quality is bad (see table 4.15b): it explains just less than 60% of the experimental data, without underfitting it ($p_{LF} > 5\,\%$). The quality of the model is also perceived in the average *RMSE* value compared to the range of the output variable.

Table 4.15: In/GaN PECVD, DOE: InN crystallite size, input variable standardisation and model quality metrics. There were 45 fair layers considered for this model.

(a) Details of the considered layers for the presented model: statistics on their fabrication characteristics.

| Input parameter | Unit | Minimum value | Maximum value | Mean value |
|---|---|---|---|---|
| *In* | sccm | 1 | 8 | 2.1 |
| $N_2$ | sccm | 0 | 150 | 17.8 |
| $H_2$ | sccm | 50 | 120 | 90.2 |
| $NH_3$ | sccm | 0 | 30 | 18.4 |
| *Ar* | sccm | 0 | 5 | 0.2 |
| *Pr* | $\mu$bar | 480 | 520 | 498 |
| *Po* | W | 20 | 100 | 33.7 |
| *T* | °C | 200 | 300 | 235 |
| *t* | min | 10 | 150 | 25.9 |
| $CrSz_{\mathrm{InN}}$ | nm | 7.9 | 37.6 | 22.5 |

(b) Quality metrics of the model.

| Quality metric | Value |
|---|---|
| $R^2_{adj}$ | 56.1 % |
| $p_M$ | $< 10^{-4}$ % |
| $p_{LF}$ | 39.4 % |
| *RMSE* | 4.52 nm |

The standardisation of the parameters also allows a deeper analysis of each effect. All the flags are green here: the constant is close to the mean output value, and the effects behave in an expected way. In detail, to increase the crystallite size, one should increase the hydrogen flow, temperature, and time. One of the roles of hydrogen is to recombine with plasma by-products, easing their evacuation, and inducing fewer defects in the layer, hence allowing a larger crystallite size. The temperature will affect the adatoms' speed, causing a faster travel and re-arrangement speed, producing larger crystallite sizes. And as mentioned at the beginning of this section, increasing time will also increase the crystallite size. On the contrary, a highest TMI or ammonia flow, or a highest RF power will induce a smaller crystallite size, where TMI will introduce more plasma by-products that are more likely to be assimilated in the layer. And depending on its value, the highest power may start etching or damaging the part of the already deposited layer, preventing large crystallites from forming. The negative effect of ammonia is not understood here.

Regarding the physical limitations of this model, the usual suspects show up: it allows an InN layer to be produced without a nitrogen precursor source, and the minimum value the model reaches is negative (-28.82 nm to be precise). As already discussed, these can be addressed by reducing the parameter space to avoid abrupt physical phase changes. Theoretically, the largest reachable crystallite should have a size of 88.02 nm, far more than the maximum observed value.

See figure 4.30: the Q-Q plot shows a satisfactory noise of the data around the Gaussian distribution. However, the residuals *versus* fitted values plot display an expanded cloud of points, also reflected in a hefty *RMSE* value of about 5 nm, only a sixth of the range of experimental values. However, after removing layer n° 274, the good news about this model is that there are

no apparent outliers. The model seems fair, with good linearity and fair homoscedasticity, including the effects independently, without underfitting the data. It remains noisy because the output variable is extracted from a fitting procedure. So, it must be used with a grain of salt for future depositions of InN layers inside system B within the parameter space defined by all the points considered. The trends showed here also have a high chance of remaining valid for other systems or outside the parameter space (but still inside equilibrium).

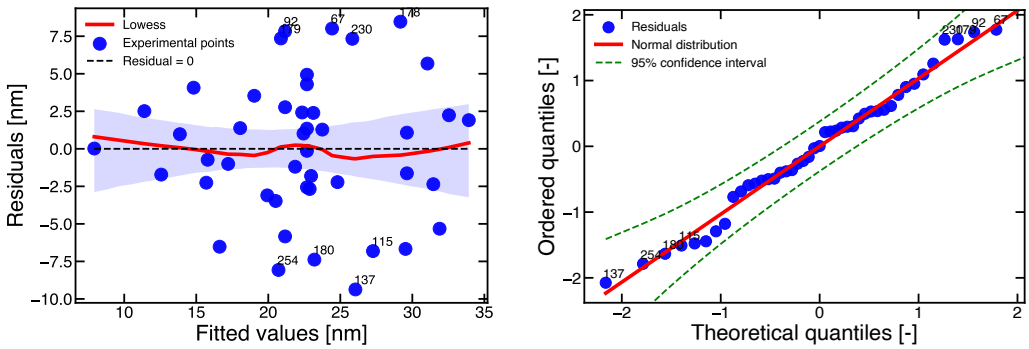


(a) Residual vs fitted values, 95 % CI and LOWESS.

(b) Q-Q plot.

Figure 4.30: In/GaN PECVD, DOE: Residuals vs fitted values plot and quantile-quantile normal plot of the InN crystallite size model. The layer numbers inducing the highest error are displayed in both cases.

#### 4.4.5.3 InGaN

The model for the crystallite size of InGaN layers was extracted using all the fair layers of all kinds of contents (GaN, InN. InGaN). Following the previous section's lead, layer n° 274 was highly problematic again and was also removed from the dataset here. As a reminder, the crystallite size of layer n° 274 was strangely much larger than that of layers deposited in similar conditions, inducing a lot of noise in the previous model.

$$\begin{aligned} CrSz^{\text{InGaN}} &= 36.89 + 13.88Ga + 22.42Po + 18.54t + 10.83Ga \cdot Po + 22.08Ga \cdot T \\ &+ 8.03In \cdot N_2 - 5.76N_2 \cdot H_2 + 12.17Po \cdot t + 27.22T \cdot t - 38.72T^2 \end{aligned} \tag{4.10}$$

Because of a too-high p-value or a too-high correlation with other effects, most of the linear expression of the input parameters could sadly not be included in the model. This model looks complicated with a lot of effects and comes with a few downsides that raise some red flags: it is not symmetric with respect to TMG and TMI, and not all the effects can find their explanation in a physical phenomenon related to crystallite size. Its quality is acceptable (see table 4.16b): it explains just more than 70% of the experimental data, without underfitting it

($p_{LF} > 5\,\%$). The quality of the model is also perceived in the decent *RMSE* value compared to the range of the output variable.

The standardisation of the parameters also allows a deeper analysis of each effect. Still, we will only mention that the most substantial effect here seems to come from the $T^2$ effect, where other interaction terms must be considered to fully describe the real influence of temperature on the crystallite size. The constant $a_0$ also seems pretty close to the average value of the output variable, but compared to it, all the effects seem strong, and a combination of two effects could push the expected crystallite size below zero, which does not make sense and is another red flag.

Table 4.16: In/GaN PECVD, DOE: InGaN crystallite size model, input variable standardisation and model quality metrics. There were 79 fair layers considered for this model.

(a) Details of the considered layers for the presented model: statistics on their fabrication characteristics.

| Input parameter | Unit | Minimum value | Maximum value | Mean value |
|---|---|---|---|---|
| $Ga$ | sccm | 0 | 1 | 0.15 |
| $In$ | sccm | 0 | 8 | 1.45 |
| $N_2$ | sccm | 0 | 150 | 36.7 |
| $H_2$ | sccm | 30 | 140 | 87.3 |
| $NH_3$ | sccm | 0 | 30 | 16.3 |
| $Ar$ | sccm | 0 | 5 | 0.13 |
| $Pr$ | $\mu$bar | 480 | 520 | 498 |
| $Po$ | W | 20 | 100 | 39.4 |
| $T$ | °C | 200 | 400 | 243 |
| $t$ | min | 10 | 150 | 27.8 |
| $CrSz^{\mathrm{InGaN}}$ | nm | 2.5 | 75.7 | 20.9 |

(b) Quality metrics of the model.

| Quality metric | Value |
|---|---|
| $R^2_{adj}$ | 71.9 % |
| $p_M$ | $< 10^{-14}$ % |
| $p_{LF}$ | 9.8 % |
| *RMSE* | 6.41 nm |

In terms of extrema and physical limits, similar to the two previous InGaN models, this one also predicts an excellent optical BG value for a layer deposited using only hydrogen as a precursor. The lowest possible valid crystallite size indicated by the model is −142.76 nm while the largest one is 136.89 nm. This range of the output parameter is way wider than the range of observed experimental values; both problems can be addressed by reducing the parameter space reflected by the present dataset to avoid abrupt physical phase changes.

See figure 4.31: both figures show the same most extreme points. The Q-Q plot shows a satisfactory noise of the data around the Gaussian distribution, with solid extremities. This means that the extreme values of the recorded crystallite sizes are predicted with more difficulty by the model. The residuals *versus* fitted values plot displays an expanded cloud of points, also reflected in a hefty *RMSE* value of about 6 nm, one order of magnitude smaller than the experimental values. However, after removing layer n° 274, the good news about this model is that there are no apparent outliers. Overall, the model seems fair, with acceptable linearity

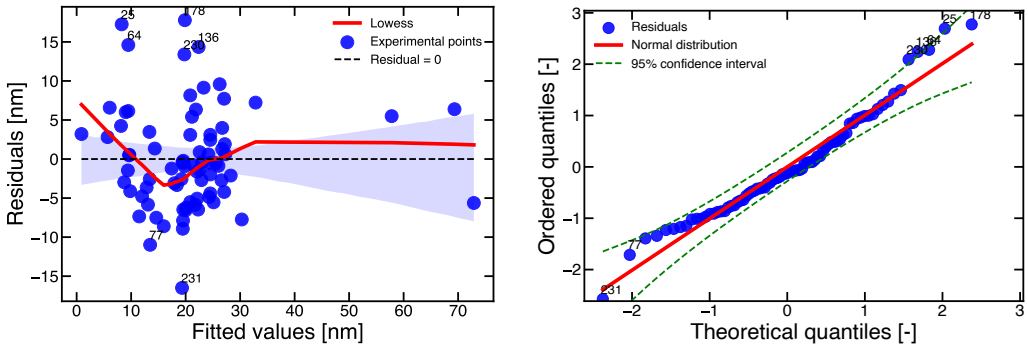


(a) Residual vs fitted values, 95 % CI and LOWESS.

(b) Q-Q plot.

Figure 4.31: In/GaN PECVD, DOE: Residuals vs fitted values plot and quantile-quantile normal plot of the InGaN crystallite size model. The layer numbers inducing the highest error are displayed in both cases.

and acceptable homoscedasticity, including the effects independently. We cannot claim that the data is under-fitted ($p_{LF} > 5\,\%$), but a trend or a curvature is still detectable in the Q-Q plot. The model remains noisy because the output variable is extracted from a fitting procedure. So, it must be used with a grain of salt for future depositions of InGaN layers inside system B within the parameter space defined by all the points considered. The trends showed here also have a high chance of remaining valid for other systems or outside the parameter space (but still inside equilibrium).

Considering the two available crystallite size models, the one describing InN crystallites is extremely simple with only linear terms. In contrast, the one telling InGaN is highly complex with mainly interaction terms. However, the complexity gives the InGaN model less noise in the data, even though the*RMSE* is way more significant. However, imposing a $Ga = -1$ (no TMG flow) in the InGaN crystallite size model will not result in the model describing InN crystallite size.

### 4.4.6 InGaN Urbach energy

The Urbach energy is another quality metric of a layer describing the sharpness of the band edge (see equation 3.19). It is a direct measure of the optical quality of the layer, where perfect crystals can reach a value below 100 meV, sometimes around 50 meV. Since defects tend to smoothen said band edge, it is an indirect measure of the imperfection of the probed material. The model for the InGaN Urbach energy was extracted using all the good In/GaN layers deposited on a glass substrate. See tables 4.17a for more details about the dataset used.

$$E_U^{\mathrm{InGaN}} = 611.4 + 59.9\,Ga + 54.0\,N_2 + 54.4\,Ar + 63.1\,Ga \cdot Po - 128.5\,N_2^2 - 177.1\,NH_3^2 \qquad (4.11)$$

Looking at table 4.17b, one can quickly realise that this model is pretty bad: less than 40 % of the experimental data can be correctly predicted, the model is under-fitted, and the error on the measurement is more than one-tenth of the whole output range. We can also see that the model only depends on TMG flow, without ever mentioning indium, which applies only to non-InN layers. Another bad sign here is that the constant is higher than the highest recorded Urbach energy of the dataset.

By interpreting the model, lower Urbach energy can be reached by increasing the nitrogen flow rate, the ammonia flow rate and the power while decreasing the TMG and argon flow rates. This should produce an Urbach energy of 74.4 meV. On the assumption that the layer quality is related to the growth rate, again, this model makes sense since it will induce a lower growth rate, producing fewer defects, implying lower Urbach energy. In detail, the growth rate is reduced when the dilution is maximised. Because of their high colinearity or irrelevance, TMI, hydrogen, pressure, temperature and time are not part of the model. The quadratic effects are the strongest here, while the linear ones are the weakest. Except for the usual abnormalities already described in other InGaN-related models (a layer can be produced without precursors, to solve this, the parameter space must be reduced), nothing seems out of the ordinary.

Table 4.17: In/GaN PECVD, DOE: InGaN Urbach energy model input variable standardisation and model quality metrics. There were 120 good layers considered for this model.

(a) Details of the considered layers for the presented model: statistics on their fabrication characteristics.

| Input parameter | Unit | Minimum value | Maximum value | Mean value |
|---|---|---|---|---|
| $Ga$ | sccm | 0 | 2 | 0.2 |
| $In$ | sccm | 0 | 6 | 1 |
| $N_2$ | sccm | 0 | 250 | 62 |
| $H_2$ | sccm | 0 | 150 | 83 |
| $NH_3$ | sccm | 0 | 30 | 11 |
| $Ar$ | sccm | 0 | 25 | 0.9 |
| $Pr$ | $\mu$bar | 450 | 550 | 498 |
| $Po$ | W | 15 | 100 | 35 |
| $T$ | °C | 100 | 400 | 234 |
| $t$ | min | 5 | 150 | 23 |
| $E_U^{\mathrm{InGaN}}$ | meV | 46 | 569 | 325 |

(b) Quality metrics of the model.

| Quality metric | Value |
|---|---|
| $R^2_{adj}$ | 36.2 % |
| $p_M$ | $< 10^{-7}$ % |
| $p_{LF}$ | 0.008 % |
| $RMSE$ | 78.5 meV |

See the Q-Q plot in figure 4.32: the residuals behave normally, so this result can be considered reasonable. The most extreme points, usually outliers, are not far from the normal distribution represented by the red line. Just with this result, it seems strange that the model is underfitting the data (see $p_{LF} < 5$ % in table 4.17b), but looking at the residuals *versus* fitted values plot, we can understand. Indeed, the points are assembled in patches around specific fitted values, which stretch far away from the $y = 0$ dashed line. If the model fits the data better, those

patches will disappear, and the spreading will not be as severe as here. The extensive spreading of the residuals in this figure also explains the bad $R^2_{adj}$ and the hefty *RMSE*.

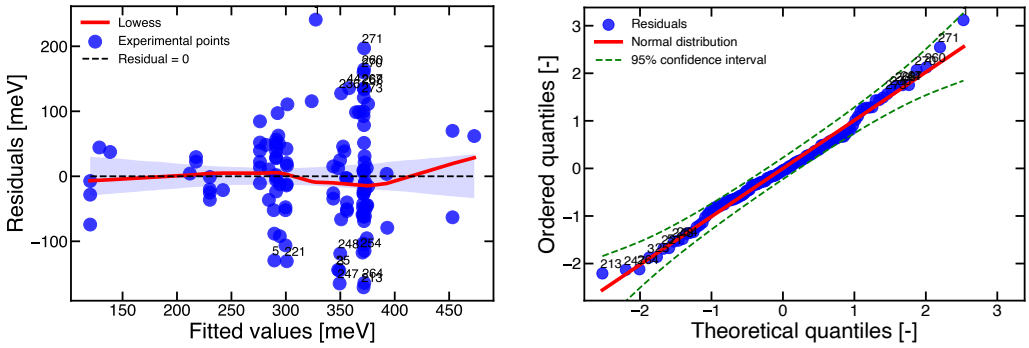


(a) Residual vs fitted values, 95 % CI and LOWESS.

(b) Q-Q plot.

Figure 4.32: In/GaN PECVD, DOE: Residuals vs fitted values plot and quantile-quantile normal plot of the InGaN Urbach energy model. The layer numbers inducing the highest error are displayed in both cases.

In conclusion, the Urbach energy could not be correctly predicted, and this model is to be used only with much caution. The reason for that is an underfitting of noisy data. The Urbach energy is extracted from a fitting procedure of the absorption coefficient. Because sometimes the material is imperfect, the fitting becomes incorrect, generating noise in the dataset.

### 4.4.7 Indium content

Again, the "indium content" $X_{\text{In}}$ refers to the atomic percentage of indium over the total of III-materials in the layer, where $X_{\text{In}} = \frac{\text{In}}{\text{In+Ga}}$ (In & Ga in at. %, $X_{\text{In}}$ in %). So the values should only vary between 0 and 100 %. The determination of the indium content of the layers was done by two methods: SEM combined with EDS (see page 49) and XRD (see section 3.2.2.5 page 42), both with layers deposited on a silicon substrate. Both methods are indirect: they use a fitting process matching a database to extract the desired information. However, these two methods are expected to complement one another within a certain error margin. Taking all the InGaN layers that were crystalline and for which an EDS measurement was performed, we see that. Indeed, the match between the two is acceptable, within a 5 % error margin (refer to figure 4.4b section 4.1 page 73). The XRD method is preferred in the section where the figure is presented because of its higher precision. However, here, the EDS method is selected because there are overwhelmingly more data than the few InGaN layers that were crystalline enough to extract the indium content reliably.

The model to determine the indium content $X_{\text{In}}$ of the layers as a function of the deposition parameters is extracted using all the sound layers of all contents: InGaN as well as GaN and InN. See table 4.18a for more details about the used dataset. The output parameter $X_{\text{In}}$ is expressed in per cent and described as follows:

$$X_{\mathrm{In}} = 74.0 - 44.5Ga + 89.7In - 21.9Ga \cdot NH_3 - 28.6In \cdot NH_3 - 13.1N_2 \cdot H_2 \tag{4.12}$$

This model is not the one that best fits the data, but it is the one that makes the most sense of it and here is why. First, there is a symmetry between the TMG and TMI flows, where their simple linear influence on the indium content makes sense. On the other hand, a high ammonia flow seems to help gallium be integrated more in the layer (and less for indium). In contrast, a low ammonia flow favours indium integration (and less for gallium). Finally, the interaction between hydrogen and nitrogen seems to favour the integration of gallium in the layer again, diminishing the indium content value without changing anything to the TMG or TMI flows. As expected, the other non-precursor input parameters' influence is not relevant enough in the indium content prediction of the layer. It is also a good thing that no quadratic effect was observed here.

Standardising the parameters allows for further analysis, where the metallic precursors have the most decisive influence (with the highest factor, particularly for TMI). In contrast, the interaction term between hydrogen and nitrogen has the weakest influence. However, an interesting feature of this model comes from the lack of fit p-value: zero. This is not because the model is under-fitting the data but because all the repeated experiments have precisely the same output value (see equation 3.59 and related explanation in section 3.3.2). In this model, the output value is the indium content $X_{\mathrm{In}} = \frac{\mathrm{In}}{\mathrm{In+Ga}}$ (In & Ga in at. %, $X_{\mathrm{In}}$ in %), and the different groups of GaN or InN layers that were deposited in the same conditions hold the same result: 0 or 100 % indium content. So $SS_{PE} = 0$ (no variation on the repeated output parameter), and the lack-of-fit is entirely relevant: $p_{LF} = 0$. In other words, the F-test compares a high variation set with a no variation set. So the zero value here is artificial; it does not mean that the model is highly under-fitting the data and should be ignored.

The usual abnormalities already described in other InGaN-related models are encountered here again: a layer can be produced without precursors. To solve this, the parameter space has to be reduced. But here again, the problem is even more profound; the DOE method usually benefits from the simplicity of a linear combination of the different effects. However, in this particular case, the indium content is expected to be proportional to the TMG:TMI flow ratio, which is expressed by a non-linear dependency of $X_{\mathrm{In}}$ on these precursors. Similarly to $E_{04}^{\mathrm{InGaN}_{SysB}}$, the indium content model would be better suited if its relation to the precursor at least included a term in the form of $\frac{In}{In+Ga}$. In terms of extreme values, a few things have to be taken into account when considering the linear model again: the large amplitude of each factor, the "not-centred" constant, and the two abrupt plateaus that the model has to deal with at its extremities (no $X_{\mathrm{In}}$ value lower than 0 or higher than 100 %). With all that in mind, the most significant value that the model predicts within the parameter space is still 228.0 %. Its lowest possible value is −80.0 %. This shows how important it is to explore the extremities

Table 4.18: In/GaN PECVD, DOE: Indium content model, input variable standardisation and model quality metrics. There were 110 good layers considered for this model.

(a) Details of the considered layers for the presented model: statistics on their fabrication characteristics.

| Input parameter | Unit | Minimum value | Maximum value | Mean value |
|---|---|---|---|---|
| $Ga$ | sccm | 0 | 2 | 0.2 |
| $In$ | sccm | 0 | 6 | 1.0 |
| $N_2$ | sccm | 0 | 150 | 56 |
| $H_2$ | sccm | 50 | 140 | 82 |
| $NH_3$ | sccm | 0 | 30 | 12 |
| $Ar$ | sccm | 0 | 25 | 1.0 |
| $Pr$ | $\mu$bar | 450 | 550 | 498 |
| $Po$ | W | 15 | 100 | 36 |
| $T$ | °C | 100 | 400 | 236 |
| $t$ | min | 6 | 150 | 24 |
| $X_{\mathrm{In}}$ | % | 0 | 100 | 46 |

(b) Quality metrics of the model.

| Quality metric | Value |
|---|---|
| $R^2_{adj}$ | 82.5 % |
| $p_M$ | $< 10^{-36}$ % |
| $p_{LF}$ | **0 %** |
| $RMSE$ | 18.2 % |

and edges of a parameter space or at least have fabricated values for hypothetical layers with well-known results; this is not the case here.

The Q-Q plot shows a skewing of the fitted line due to the four outliers in the corners of the graph (see figure 4.33b). Overall, the noise can be considered good, but this model would reach a far better quality without the trouble-makers: layers n° 70, 105, 185 and 186. The same goes for the residuals *versus* fitted values plot, where the cloud of points is no larger than ±25 %. This is also reflected in a relatively hefty *RMSE* value of about 18 %; pretty imprecise, given that the indium content control is a critical element of fabricating a high-quality InGaN layer for solar cell integration. In other words, the *RMSE* is only a fifth of the whole output range. In figure 4.33a, some points seem to form two lines at the extremities of the cloud of points: those are the GaN and InN layers, where the output parameter could not take a value greater than 100 % or lower than 0 %. The outliers in the present model display extreme values for some of the deposition parameters: n° 70 is the InN layer with the highest TMI flow rate of the dataset, n° 105 is the GaN layer with the most increased TMG flow rate, n° 185 and 186 are InGaN layers with the highest $NH_3$ flow rate, with n° 186 amongst the lowest TMG flows. As mentioned before, because of the relatively good quality of the model and for scientific integrity, these layers were not removed from the dataset because no valid reason was found for such action.

In conclusion, the model is acceptable and shows good homoscedasticity. The linearity, though, seems terrible, and a trend appears from the LOWESS in figure 4.33a, which was not considered. This also may be due to the different deposition conditions that led to the same outcome of either 0 % or 100 % indium content for GaN or InN layers, respectively,

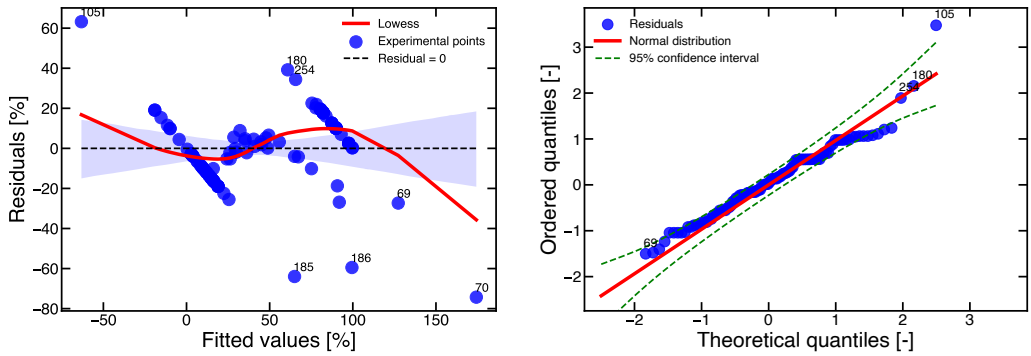


(a) Residual vs fitted values, 95 % CI and LOWESS.

(b) Q-Q plot.

Figure 4.33: In/GaN PECVD, DOE: Residuals vs fitted values plot and quantile-quantile normal plot of the indium content model. The layer numbers inducing the highest error are displayed in both cases.

that the model has a hard time taking into account. This nonlinearity is also reflected in the substantially high error in the output value. This means that this model can be used with caution for future depositions of InGaN layers inside system B within the parameter space defined by all the points considered, and the trends showed here to have a high chance to remain valid for other systems or outside of the parameter space (but still inside equilibrium). The result of this model can also be used for later calculation, where for example, one can make the bandgap of InGaN layers depend on its indium content $X_{\mathrm{In}}$ (see section 4.4.4.3).

### 4.4.8 InGaN PECVD DOE: key takeaways & next steps

As a synthesis of all the results presented in this section about all the layers produced, please refer to table 4.19, where all the dependencies are summarised.

From the get-go, one can notice that the GaN characteristics are poorly modelled: the $E_{04}$ model is the worst one of the lot, and no model for the GaN crystallite size could be produced. Because of the scarcity of quality results for GaN, no link or optimisation process can be established here confidently. However, GaN is expected to behave the same as InN, and the results concerning the latter may be applied to the former. It may also be possible to consider InGaN's models and impose TMI flow of zero, meaning that the *In* input variable takes a value of -1. Under this condition, a higher optical BG for GaN than the defective 3.1 eV is achieved with low nitrogen flows (implying non-zero ammonia flows) and high temperatures. Because of the quadratic nature of the effect, the TMG flow is here best kept around the average value of the whole dataset (1 sccm, according to table 4.14a). If these trends were included in the InGaN crystallite size model, it could be maximised by increasing the hydrogen flow, the power and the deposition time. This will produce a GaN layer with a decently low Urbach energy as long as the argon flow is reduced to a minimum and the ammonia flow is increased to

Table 4.19: In/GaN PECVD, DOE: synthesis of all the DOE models. A diagonal arrow ↗↘ refers to a dominant linear effect on the output variable, a curved line ∩∪ refers to a dominant quadratic effect, an "×" refers to a dominant interaction effect, and a "-" means that this input parameter was absent from the model. The orientation of the sign indicates the sign the dependency.

| Input | | GaN | | InN | | | InGaN | | | | |
|---|---|---|---|---|---|---|---|---|---|---|---|
| parameter | Unit | *Thk* | $E_{04}$ | *Thk* | $E_{04}^{①}$ | *CrSz* | *Thk*① | $E_{04}^{\text{SysB}}$ | *CrSz* | $E_U$ | $X_{\text{In}}$ |
| *Ga* | sccm | ↗ | - | - | - | - | ↗ | ∩ | × | × | × |
| *In* | sccm | - | - | ∪ | ∪ | ↘ | ∪ | ∪ | × | - | × |
| $N_2$ | sccm | - | × | ↗ | × | - | × | × | × | ∩ | × |
| $H_2$ | sccm | ↗ | ↘ | - | × | ↗ | - | - | × | - | × |
| $NH_3$ | sccm | ↘ | × | - | × | ↘ | × | - | - | ∩ | × |
| *Ar* | sccm | ↗ | × | - | - | - | × | - | - | ↗ | - |
| *Po* | W | - | - | ↘ | × | ↘ | ↗ | - | × | × | - |
| *Pr* | $\mu$bar | ↘ | - | - | - | - | × | - | - | - | - |
| *T* | °C | - | - | - | ↘ | ↗ | × | × | ∩ | - | - |
| *t* | min | ↗ | - | ↗ | - | ↗ | × | - | × | - | - |
| $R^2_{\text{adj}}$ | % | 76.2 | 18.5 | 97.6 | 75.6 | 56.1 | 81.0 | 76.0 | 71.9 | 36.2 | 82.5 |
| $p_M$ | $< 10^{(...)}$ % | -8 | 1 | -30 | -7 | -4 | -6 | -31 | -14 | -7 | -36 |
| $p_{LF}$ | % | 24.3 | 86.6 | 48.5 | 93.7 | 39.4 | - | $< 10^{-6}$ | 9.80 | 0.01 | 0 |
| *RMSE* | | 47.0 | 0.19 | 15.3 | 0.06 | 4.52 | 25.4 | 0.33 | 6.41 | 78.5 | 18.2 |

a maximum. With all these considerations, the layer thickness revolves at a bit more than 300 nm (see table 4.20), which could be tweaked ±75 nm by playing a bit with the pressure.

Considering the InN, an optimised layer would have the largest crystallite size for the lowest optical bandgap energy (with respect to the defective InN bandgap energy of ~ 1.6 eV, aiming for 0.7 eV). The optical BG model has a lot of interaction terms that can be played with compared to the rigid only-linear crystallite size model, so the latter will serve as a basis, and the correction for a better optical bandgap will be made with the InN optical bandgap model. This means that for large crystals, one wants to decrease the TMI and ammonia flow while increasing the hydrogen flow to the maximum values within the parameter space of the two models. It is also better to decrease the power and increase the temperature and the deposition time to allow the layer to produce more extended crystals. Now considering the optical BG, there is an interaction term between nitrogen and hydrogen, but since nitrogen is not part of the *CrSz* model, nitrogen can be reduced. The other interaction term involves the ammonia flow and the power where here, if one is decreased, the other must be increased to help decrease the optical BG of InN layers; and this goes against the *CrSz* model that wants to decrease both. However, since the nitrogen flow is reduced, the ammonia flow is increased to maximum values to still produce InN layers. Considering this, the power can be reduced to favour larger crystallites or increased to favour lower optical bandgaps. In table 4.20, the preference went to the optical BG.

If we now apply this reasoning to the flawed Urbach energy model but only for InN layers (this means that the input parameter $Ga = -1$), what is obtained? The two quadratic terms will take extreme values, and $E_U$ will decrease because of them. And because of the interaction term between the TMG flow and the power, knowing that $Ga = -1$, increasing the power will also help decrease the Urbach energy here. Finally, the argon flow also must be reduced to the minimum value allowed by the parameter space. And if this reasoning is also applied to the thickness, we see that it will be diminished under these conditions; a more prolonged deposition will be required for a fixed thickness. All in all, the choices made for the crystallite size and the bandgap will also reduce the Urbach energy; this is not surprising because by simply improving the overall quality of the layer, all its characteristics will also undergo an improvement. The pressure, however, does not seem to play any role in the deposition of InN layers, as long as it takes values within the ranges explored in all the associated models (between 480 and 520 $\mu$bar). What is strange here, however, is that the predicted crystallite size is larger than the layer thickness, which is physically impossible given how the crystallite size is extracted from the XRD measurement. This is sadly one of the limitations of this procedure, but it may partly be explained by postulating that the crystallite is more significant than its height.

Regarding InGaN layers, the optical BG mainly depends on the indium content $X_{\mathrm{In}} = \frac{\mathrm{In}}{\mathrm{In+Ga}}$ (In & Ga in at. %, $X_{\mathrm{In}}$ in %), and that has already been presented in section 4.4.4.3. The indium content mainly depends on non-zero flows of TMG and TMI; the *Ga* and *In* input parameters were arbitrarily chosen with the express condition not to be an extreme value in any considered model. But a more interesting trade-off must be found for simultaneously optimising the crystallite size and the Urbach energy. The interaction terms of one model are not interaction terms in the other, except for the $Ga \cdot Po$ effect present in both models, which means that the extraction of the path leading to optimum results is easier than it looks.

Considering said interaction effect of $Ga \cdot Po$, the sign in the two models is identical (positive), which means that depending on the choice, either a large crystallite size is prefered, but that will induce a higher Urbach energy or a low Urbach energy is preferred, but at the cost of smaller crystallites. However, the effect swings with a larger amplitude in the InGaN crystallite size model, which means that increasing the power seems to remain the better idea (smaller Urbach energy and crystallite size). Regarding all the other effects, the solution to decrease the Urbach energy and increase the crystallite size simultaneously is straightforward: reduce the nitrogen and the argon flows and increase all the other input parameters (hydrogen and ammonia flows, time and temperature). This all should result in a thick InGaN layer. Given all these choices, the indium content model predicts that this will produce a layer containing $59.7 \pm 18.2$ % of indium. Using the optical bandgap model based on $X_{\mathrm{In}}$ extracted by EDS, this will entail an optical BG of $1.692 \pm 0.382$eV.

Another contradiction can be exposed when comparing the two InGaN optical BGs models. Indeed, only a few match when trying to identify the terms between them. The dissimilarity is such that even the error of the models cannot explain the amplitude of such a difference.

Given the quality metrics of the models, the better choice is to use the combination of the $X_{\mathrm{In}}$ and $E_{04}^{X_{\mathrm{In}}}$ models rather than the $E_{04}^{\mathrm{SysB}}$ one, because the latter is of lower quality and shows a clear underfitting feature. Still, such a gap between these two results is difficult to explain; this is undoubtedly due to the choice of all extreme values for all the input variables used to predict these layer characteristics. This also shows precisely why designing an experiment in advance is so important; the corners of the parameter space are crucial. This could not be done in advance because the accessibility and usefulness of the parameter space were unknown beforehand. This is where all the input parameters take extreme values, which makes them high leverage points by design. In other words: the input parameters chosen for these three optimised layers refer to three points outside the non-cubic parameter space established by combining all the layers' characteristics.

The full description of these "best layers" is summarised in table 4.20, gathering the three types of layers: GaN, InN and InGaN. The input parameters were chosen to optimise all the quality metrics simultaneously. However, they were also chosen to stay within the parameter space on which all the involved models are defined. Within the parameter space of all the models altogether, the layers produced under these conditions are expected to be the cream of the crop in terms of quality metrics. However, since the predicted values are estimated from a point outside the non-cubic parameter space, there is a high chance that the models are more off than the errors reported in said table. Since this whole DOE study was performed after all the layers were deposited, these deposition conditions were not physically tested yet and can be the object of future research.

Finally, as fully described in section 4.4.3.1 on the GaN thickness and echoed in the following ones, the parameter space is not fully explored in all of the DOEs. Said parameter space can be associated with a volume whose dimensions equal the number of input parameters (here, 10). Since the input parameters are standardised and orthogonal, the length of every edge is the same size and perpendicular to its neighbouring advantages; a 10-D hypercube. In this volume, experimental measurements are displayed as scattered points, where at least one point touches every hypercube face.

On the other hand, the 10-D volume enclosed only by the experimental points would resemble some bizarre patatoid (consider, for example, the volume surrounded by only the blue points in figure A.3c with respect to its hypercube – in three dimensions in this example). While the model is always well-defined within that potatoid, results that originate outside of this input parameter volume (say a green or a red point in this example) are often ill-defined and will often give strange results. For instance, considering any of the presented models here, the range of the $NH_3$ and $N_2$ flows both reach zero because in every dataset, there exists at least one layer produced with only nitrogen ($NH_3$ = 0 sccm), and one layer produced with only ammonia ($N_2$ = 0 sccm) (which corresponds to two blue points in figure A.3c). But no layer was produced with both conditions simultaneously (a green point in figure A.3c). This unexplored parameter space is at the origin of the main limitation of all these DOE studies.

Table 4.20: In/GaN PECVD, DOE: best-predicted layers, extracted from the combined models. The InGaN layer is expected to contain 59.7 ± 18.2 % indium. These layers were neither deposited, much less characterised. The errors on the predicted values correspond to the *RMSE* value of the related model. The values in orange are outside of the range of the dependent variable.

| Input parameter | Unit | GaN | InN | InGaN |
|---|---|---|---|---|
| *Ga* | sccm | 1 | 0 | 0.8 |
| *In* | sccm | 0 | 1 | 1.0 |
| $N_2$ | sccm | 0 | 0 | 0 |
| $H_2$ | sccm | 120 | 120 | 140 |
| $NH_3$ | sccm | 30 | 30 | 30 |
| *Ar* | sccm | 0 | 0 | 0 |
| *Po* | W | 100 | 100 | 100 |
| *Pr* | $\mu$bar | 500 | 500 | 500 |
| *T* | °C | 400 | 300 | 300 |
| *t* | min | 120 | 150 | 150 |
| Predicted $E_{04}$ | eV | 3.224 ± 0.332 | 1.126 ± 0.064 | 2.738 ± 0.332 |
| Predicted crystallite size | nm | 118.18 ± 6.41 | 61.10 ± 4.52 | 116.63 ± 6.41 |
| Predicted $E_U$ (±78.5) | meV | 197.4 | 74.4 | 172.8 |
| Predicted thickness | nm | 319.8 ± 47.0 | 52.9 ± 15.3 | 580.8 ± 49.0 |

In our case, all the surfaces of the hypercube parameter volume are touched at least once by the real potatoid parameter space. Ideally, the experimental points explore the edges of the hypercube and, most importantly, its corners, making the potatoid volume match the hypercube. This is done by adding more experimental points to the existing one or better designing the experiment in a smaller parameter volume. Usually, the second option is preferred since it has more chances to avoid phase changes such as "negative thickness" or "no nitrogen source".

## 4.5 PECVD results: wrap-up & conclusions

In the first section, the effect of different deposition parameters on layer characteristics was presented for InN, GaN and InGaN. It was observed that the quality metrics of the layers were improved when the growth rate was reduced, that the InGaN BG follows the quadratic Vegard's law, whose bowing is also improved at lower growth rates, and that the indium content $X_{\mathrm{In}} = \frac{\mathrm{In}}{\mathrm{In+Ga}}$ (In & Ga in at. %, $X_{\mathrm{In}}$ in %) was dependent on the TMG:TMI ratio. InN layer still has too many defects that generate donors within the crystal, which in turn increase their BG by B-M effect. The same is true for GaN layers, where the BG was slightly reduced compared to desired values.

The TOF-MS tool allowed for a deeper analysis of the plasma dynamics, where the synthesis and dissociation of different by-products could be discovered. Many results could be extracted, among which the importance of a low base pressure, the synthesis and dissociation of ammonia, the significance of the wafer-layer interface of lighting the plasma before introducing carbon-rich precursors, the conditions for more efficient dissociation of the precursors, etc. (see the exhaustive list in the conclusions of the TOF-MS study, in section 4.3.5).

These results were then compared to a computation of the whole dataset of all the layers deposited during this *Ph.D.*, from which a quantitative description could be extracted that matched most of the results obtained in the first three sections previous to the DOE study. This optimisation process allowed the determination of ideal deposition conditions within the explored parameter space that may lead to a perfect layer whose characteristics are described at the end of said section.

The layers deposited by PECVD are deemed acceptable for a first contact application only, even though they do not reach literature values and may induce a drop in cell performances. Rather than optical, this is primarily due to poor electrical properties that are hypothesised to stem from a poor crystallinity of the layer. The InGaN PECVD contact path is explored in section 6.1. The optimisation of these properties is then worth considering for future research, as well as deeper analysis and optimisation of the doping aspect, which was not the main focus of this chapter. The development of InGaN layers as an absorber was abandoned at this point due to time constraints, and based on these conclusions: only the contact path is considered for the rest of this study.

# 5 InGaN by PVD

The goal of this chapter is essentially the same as the previous one but with another low-$T$ deposition technique: PVD sputtering. This chapter also aims to answer the three first research questions, which are the following:

1. Is it possible to produce InGaN materials at low temperatures?
2. If yes, how compatible are the characteristics of these layers for PV application?
3. If they are compatible enough, how stable do they remain when p- or n-doping is added?

The targeted layer characteristics are the ones presented in table 2.1, with the same quality metrics as in the previous chapter: the Urbach energy $E_U$ should be inferior to at least 100 meV, and the crystallite size *CrSz* should be in the same range as the thickness of the considered layer. In detail for GaN, the aims are the following: a BG of 3.4 eV, a refractive index of 2.50 (a sign of a dense layer), and a measurable resistivity of $10^5\,\Omega$ cm (or below, also possible thanks to doping). Depending on the best performances achieved in this chapter, these key values will also help determine if the sputtered III-N layer can be used as an absorber or as a contact.

This chapter first starts by presenting different studies related to GaN and InGaN layers deposited by PVD. The first section explores the effect of simple deposition parameters such as the temperature or the applied power on basic GaN layer characteristics such as the bandgap, the growth rate, or the crystallinity. The n-doping of the GaN layer is then explored, either with germanium or silicon, and the last section explores the integration of indium in the GaN layer, either by a co-sputtering process or by using an $In_{50}Ga_{50}N$ target.

The layers presented in the first three sections were deposited and characterised by Julien Hurni during his Master's project in PV-lab under my supervision.

## 5.1 Sputtered GaN layer characteristics

In this section, the aim is to obtain a crystalline layer of gallium nitride by RF sputtering. The material's crystallinity is essential as it is a dominant factor in allowing doping in the next step.

Therefore, this layer must have high crystallinity and transparency in the visible and infrared spectrum. The structural properties (crystallinity and morphology) were characterised by X-ray diffraction (XRD) as well as scanning and transmission electron microscopy (SEM and TEM). Ellipsometry and UV-VIS spectroscopy measured optical properties such as refractive index, absorption coefficient and bandgap. Two batches of layers were deposited for this experiment, the first one where the goal thickness was set to 100 nm, and the second one where the goal temperature was set to 400 °C (see table 5.1). For the parameters that were swept, the pressure was set to 0.85, 3.0 or 12.0 $\mu$bar (±2 % relative), the temperature was set to 200, 300 or 400 ± 2 °C, and the aimed thicknesses were 50, 100 and 350 ± 5 nm.

### 5.1.1 Optical properties

Table 5.1 shows the refractive index at 633 nm $n_{633}$, the optical bandgap computed from UV-VIS measurement $E_{04}$ and the Urbach energy $E_U$. Figure 5.1 displays the different absorption curves. Fitting the slope with respect to equation 3.19, the absorption coefficient around $E_{04}$ gives the Urbach energy related to the material's optical quality. Pressure strongly influences the film's density, which is seen by an increase in the refractive index at low pressure extracted from the ellipsometry modelling. High pressure increases the optical bandgap while reducing the Urbach energy. The different colours (red, orange, and blue) represent respectively different substrate temperatures (200, 300, and 400 ± 2 °C) and thicknesses (50, 100, and 400 ± 5 nm). Increasing temperature reduces the optical BG and the Urbach energy while increasing the refractive index at high pressure. For thin layers (~ 50 nm), the films show very little change of refractive index, absorption, and Urbach energy with temperature, but increasing thickness reduces the absorption coefficient and increases $E_{04}$.

The deposition pressure has a significant influence on the different optical properties of the deposited layers. The refractive index is dependent on material density [120] and this relationship is observed in figure 5.2 where an almost linear dependency of $n_{633}$ *versus* pressure can be extracted. Optical bandgap and Urbach energy dependence with pressure indicate that higher pressure gives better optical quality material.

### 5.1.2 Growth rate

The growth rate ($g$, in nm/min) is calculated by dividing the thickness by the deposition time. Looking at figure 5.3a, the logarithmic decay of growth rate is in good agreement with the frequency of collision in plasma, which is linked to the logarithm of the pressure [109]. The temperature almost does not affect the growth rate, as seen by the fitting function's slope in figure 5.3b.

Knox-Davies *et al.* [95] proposed a model explaining the growth rate decrease when increasing substrate temperature by adatoms desorption from the substrate. In our case, since there is just a slight variation of the growth rate between 200 °C and 400 ± 2 °C, and a slight increase of

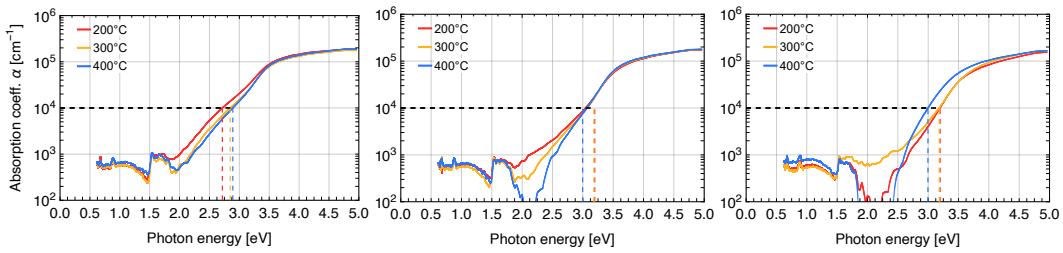


(a) Temperature dependence for a pressure of $0.85 \pm 0.02\,\mu$bar (left), $3.00 \pm 0.06\,\mu$bar (center) and $12.0 \pm 0.3\,\mu$bar (right).

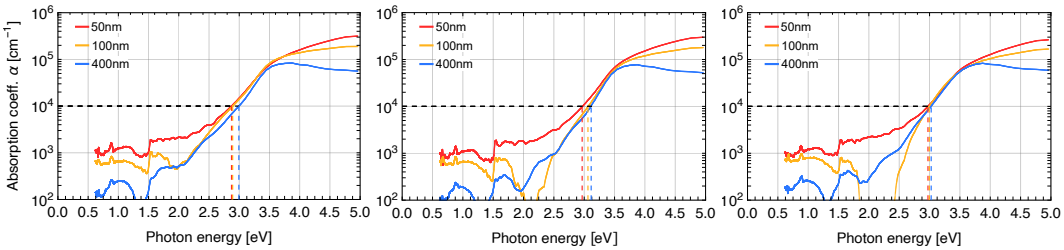


(b) Thickness dependence for a pressure of $0.85 \pm 0.02\,\mu$bar (left), $3.00 \pm 0.06\,\mu$bar (center) and $12.0 \pm 0.3\,\mu$bar (right).

Figure 5.1: PVD GaN, characteristics: optical properties dependence on temperature and thickness on a glass substrate. See extracted values in table 5.1

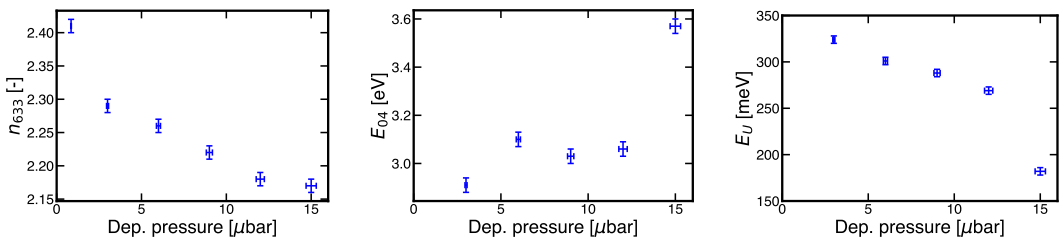


(a) Refractive index $n_{633}$. (b) Optical BG $E_{04}$. (c) Urbach energy $E_U$.

Figure 5.2: PVD GaN, characteristics: effect of the pressure on the refractive index, the optical BG and the Urbach energy. The layers were deposited on a glass substrate at $200 \pm 2\,°$C with a goal thickness of 100 nm.

the refractive index towards higher temperatures, those higher temperatures could increase the film density and reduce the thickness compared to samples grown at a lower temperature. The increase in film density can be caused by the relaxation and realignment of the structure by reducing the defects and the voids. XRD results of figure 5.5 show a slight increase in the degree of crystallinity (DOC) but also a reduction of the (002) peak relative intensity on a silicon substrate at different temperatures. Since there is no clear peak position shift at the different substrate temperatures, the lattice thermal expansion coefficient mismatch does not influence growth on Si wafers.

Table 5.1: PVD GaN, characteristics: optical and structural properties dependence on temperature, pressure and thickness on a glass substrate. The upper half aims for a constant thickness of ~ 100 nm, the bottom half maintains a constant temperature of 400 ± 2 °C.

| $Pr$ ±2 % [$\mu$bar] | $T$ ±2 [°C] | $Thk$ ±5 [nm] | $n_{633}$ ±0.01 [−] | $E_{04}$ ±0.03 [eV] | $E_U$ ±4 [meV] | $CrSz$ ±0.01 [nm] | $a$ ±0.002 [Å] | $c$ ±0.002 [Å] |
|---|---|---|---|---|---|---|---|---|
| 0.85 | 200 | 101 | 2.41 | 2.72 | 370 | 19 | 3.243 | 5.241 |
| 0.85 | 300 | 104 | 2.38 | 2.85 | 370 | 23 | 3.231 | 5.222 |
| 0.85 | 400 | 96 | 2.38 | 2.89 | 310 | 18 | 3.240 | 5.254 |
| 3.00 | 200 | 104 | 2.28 | 3.05 | 270 | 31 | 3.203 | 5.190 |
| 3.00 | 300 | 101 | 2.29 | 3.07 | 270 | 48 | 3.214 | 5.197 |
| 3.00 | 400 | 98 | 2.33 | 3.07 | 250 | 23 | 3.207 | 5.203 |
| 12.0 | 200 | 109 | 2.18 | 3.20 | 180 | 56 | 3.200 | 5.191 |
| 12.0 | 300 | 96 | 2.21 | 3.00 | 250 | 31 | 3.203 | 5.190 |
| 12.0 | 400 | 106 | 2.24 | 3.18 | 210 | 31 | 3.195 | 5.189 |
| 0.85 | 400 | 46 | 2.40 | 2.87 | 360 | 16 | - | - |
| 0.85 | 400 | 96 | 2.38 | 2.89 | 310 | 18 | 3.239 | 5.254 |
| 0.85 | 400 | 356 | 2.35 | 2.99 | 310 | 19 | 3.232 | 5.243 |
| 3.00 | 400 | 50 | 2.40 | 2.97 | 280 | 25 | - | - |
| 3.00 | 400 | 98 | 2.33 | 3.07 | 250 | 24 | 3.207 | 5.201 |
| 3.00 | 400 | 385 | 2.33 | 3.11 | 170 | 22 | 3.207 | 5.215 |
| 12.0 | 400 | 53 | 2.40 | 2.97 | 300 | 22 | 3.214 | 5.196 |
| 12.0 | 400 | 106 | 2.24 | 3.00 | 210 | 31 | 3.195 | 5.189 |
| 12.0 | 400 | 347 | 2.27 | 3.03 | 250 | 15 | 3.235 | 5.213 |

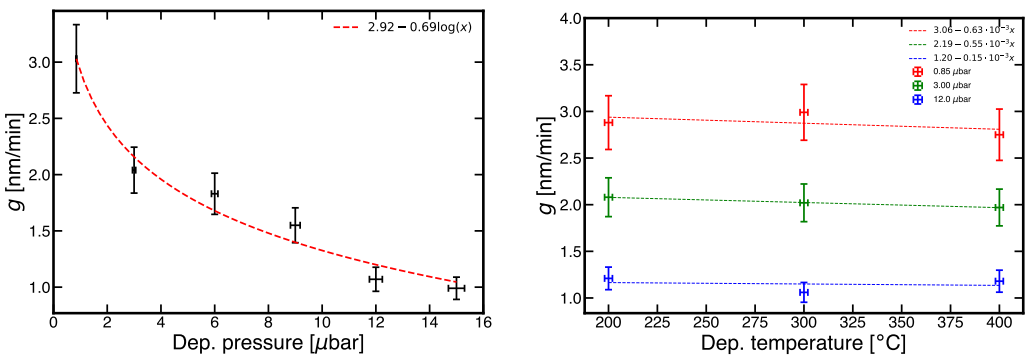


(a) Pressure dependence.

(b) Temperature dependence.

Figure 5.3: PVD GaN, characteristics: growth rate dependence on pressure and temperature on a glass substrate.

### 5.1.3 Structural properties – XRD

The effect of the pressure, temperature, and film thickness on the crystallinity was investigated using X-ray diffraction on silicon and sapphire substrates. Figure 5.4 shows typical diffrac-

tograms at constant deposition pressure ($3.00 \pm 0.06\,\mu$bar) for different substrate temperatures, thicknesses, and substrate materials. Diffraction peak at 33.0°, 69.1°, 41.2° and 91.1° are peaks from the substrates (Si(200), Si(400), $Al_2O_3$(006), $Al_2O_3$(012)), respectively. Diffraction figures of deposition at $0.85 \pm 0.02$ and $12.0 \pm 0.3\,\mu$bar are shown in appendix B.3.1, figure B.23 to B.26. Preferential orientation (PO), degree of crystallinity (DOC), and crystallite size (*CrSz*) can be extracted from these types of diffractograms.

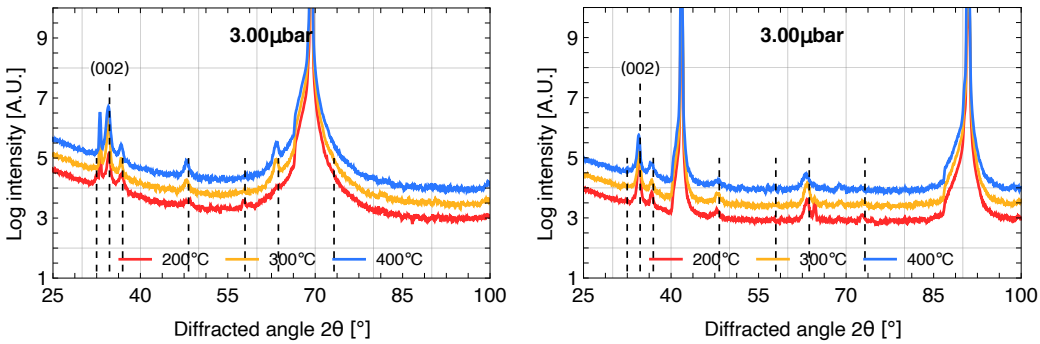


(a) Temperature dependence on silicon, layers with a goal thickness of 100 nm.

(b) Temperature dependence on sapphire, layers with a goal thickness of 100 nm.

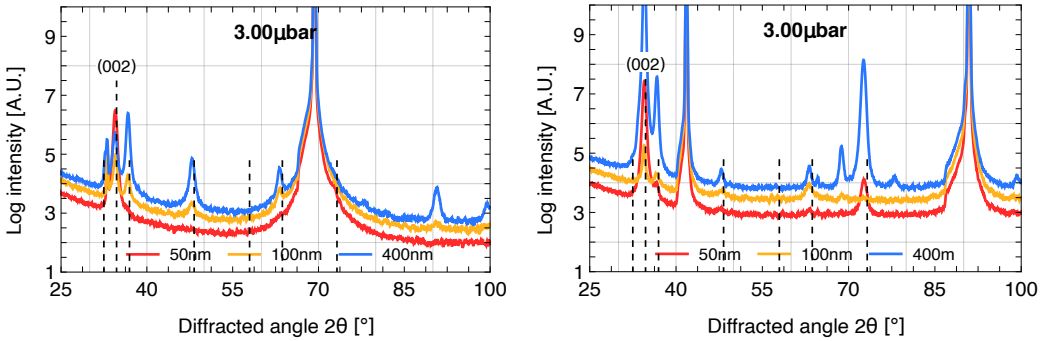


(c) Thickness dependence on silicon, $400 \pm 2$ °C growth temperature.

(d) Thickness dependence on sapphire, $400 \pm 2$ °C growth temperature. The non-referenced peaks on the blue curve highlight the presence of a $Ga_2O_3$ phase.

Figure 5.4: PVD GaN, characteristics: structural properties dependence on temperature, thickness and substrate. The pressure was set at $3.00 \pm 0.06\,\mu$bar and the RF power at $150 \pm 0.1$ W. Other pressure results are presented in appendix B.3.1. The dashed lines correspond to the GaN diffraction peaks of interest. See extracted values in table 5.1.

Using the theory presented in section 3.2.2.5, the crystallite size and the lattice parameters can be extracted from the different fitted plots. These results are presented in table 5.1 and in figure 5.5. Figure 5.5 recalls the percentage of (002) peak intensity, crystallite size, and degree of crystallinity at different pressures, temperatures, and thicknesses. A strong preferential orientation (PO) along the c-axis (peak (002)) is observed from the diffractograms of figure 5.4. By comparing silicon and sapphire substrates (figure 5.5), the PO is very similar between both substrates, but sapphire substrate tends to give higher peak intensities. The deposition parameters influence much more PO than the substrate type. This is because the deposition

parameters used to produce the results presented here were not optimised to efficiently create an epitaxial GaN layer, as in section 5.4. Indeed, in section 5.4, the epitaxial GaN layer deposited on sapphire was produced in the Clusterline at the CSEM, while the ones presented here were produced in the Univex at PV-lab. In the out-of-equilibrium case presented here, the PO seems less influenced by the substrate than by the deposition parameters. Low pressure also appears to give better crystallinity for very thin films, while DOC gradually becomes better for thicker films at higher deposition pressure. Temperature decreases the preferential orientation and the DOC. The crystallite size varies from 15 nm to 100 nm depending on the substrate temperature, pressure, and thickness. Low pressure tends to give smaller crystallite sizes.

Figure 5.6 shows the influence of pressure on the diffracted (002) peak of 50 nm-thick films. Low deposition pressure leads to denser films and increases the stress in the crystal. This effect is seen by the shift of the (002) peak compared to an unstressed GaN material. The strain in the layers is calculated by comparing the interplanar distance $d_{\mathrm{hkl}}$ of the powder peak *versus* the experimental one. The strain is given by equation A.9 in appendix A.3.1 where a negative value indicates tensile stress in the layer while a positive one implies compressive stress; here it is all positive. These curves also confirm the previous results that low pressure decreases crystallite size but gives a better degree of crystallinity.

The deposition pressure significantly influences the deposited layers' different optical and structural properties. Stress/strain analysis of figure 5.6 also shows a strong link between stress and deposition pressure as seen by the shift of the peak's centre. A similar trend is observed comparing the present crystallinity results with other studies [113, 122]. However, since the growth rate between these studies and our results are substantially different ($1-3$ nm/min compared to $10-15$ nm/min) and the fact that most other reports use a mixture of $\mathrm{Ar}-\mathrm{N}_2$ as a reactive gas, more in-depth comparison of crystallinity is difficult.

### 5.1.4 Structural properties – SEM & TEM

SEM cross-sections of figure 5.7 show the effect of three different deposition pressures on the film's structure. Low deposition pressure increases film density, as observed with increased refractive index. In contrast, increasing pressure leads to more columnar growth with bigger crystallite size, as shown by the XRD results. These micrographs show that columns are oriented perpendicularly to the surface and not oriented by the sputtered particle flux due to the substrate rotation during the growth. SEM pictures of the top surface (figure 5.8) show structural differences between various deposition parameters. High temperature and pressure lead to well-defined triangular features at the surface, and films grown at low-$T$ yield circular grain features. Rough measurements of grain sizes from the micrographs concord with the results computed by XRD. Feature size decreases at low deposition pressure and low temperature.

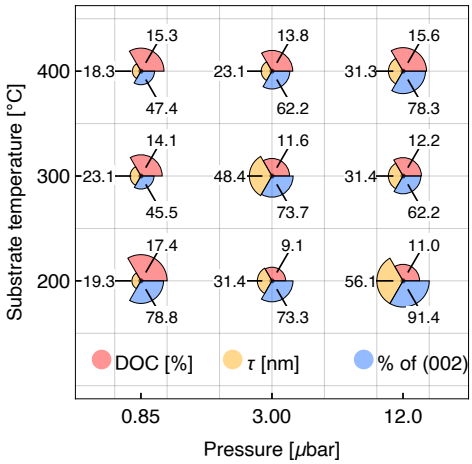


(a) Effect of temperature with a silicon substrate.

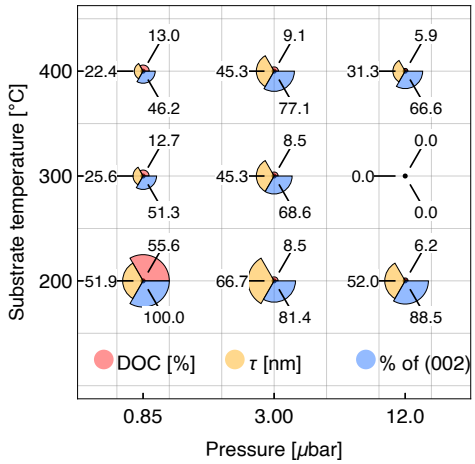


(b) Effect of temperature with a sapphire substrate.

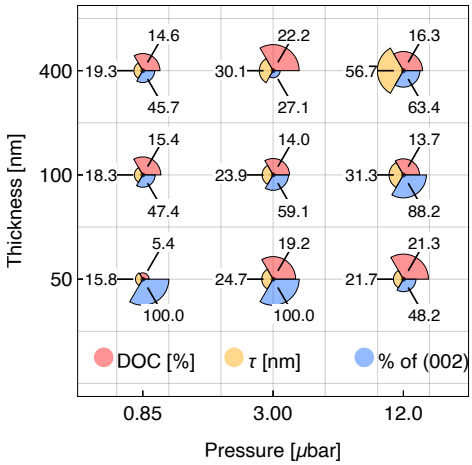


(c) Effect of thickness with a silicon substrate.

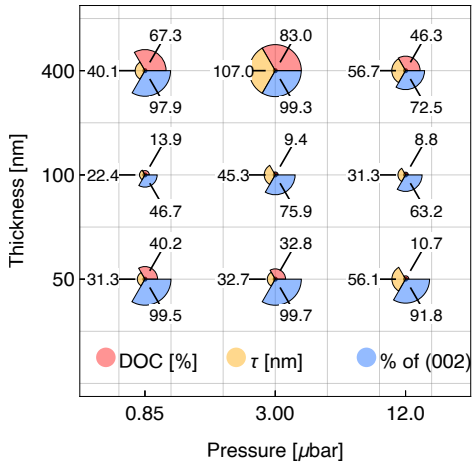


(d) Effect of thickness with a sapphire substrate.

Figure 5.5: PVD GaN, characteristics: crystallite size (±0.01 nm), preferential orientation and degree of crystallinity (±0.2 % absolute) for different substrate temperature (±2 °C), pressure (±2 % relative) and film thickness (±5 nm). The goal thickness for the upper part of the figure is 100 nm, and the set temperature for the bottom part of the figure is 400 ± 2 °C.

TEM micrograph of a sample grown at 3.00 ± 0.06 $\mu$bar, 200 ± 2 °C and with a thickness of 55 ± 5 nm is displayed in figure 5.9. Grain size analysis from the bright field images is in good agreement with XRD analysis and gives grain sizes around 15 nm (20.4 and 21.7 nm for XRD data). Since Scherrer's equation gives the size of the X-ray coherence domain, not the grain size, bigger crystallite size measurements by XRD are expected. Thus, even considering the thickness difference, the crystallite size is supposed to be smaller, which is in good agreement with TEM measurements. The diffraction pattern and its intensity profile confirm the high

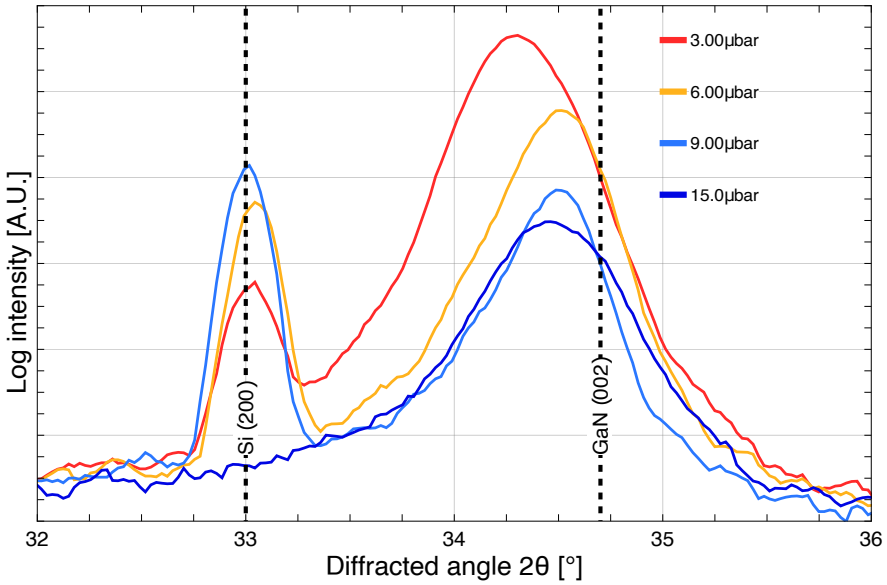


Figure 5.6: PVD GaN, characteristics: diffractogram of $50 \pm 5$ nm thick films for different deposition pressure at RF power of $150 \pm 0.1$ W and silicon substrate temperature of $200 \pm 2$ °C.

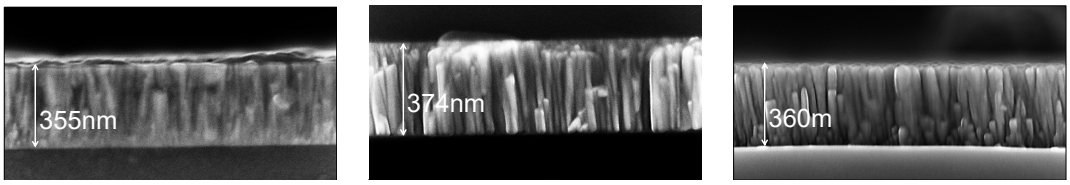


Figure 5.7: PVD GaN, characteristics: SEM cross-section for pressure of $0.85 \pm 0.02\,\mu$bar (left), $3.00 \pm 0.06\,\mu$bar (centre) and $12.0 \pm 0.3\,\mu$bar (right), all deposited at $400 \pm 2$ °C on a silicon substrate.

degree of crystallinity of these layers due to sharp diffracted peaks for minimal interplanar distances detected (peak at 13 $nm^{-1}$ that corresponds to 0.77 Å of interplanar distance). Peak analysis, however, shows very different results compared to XRD analysis. XRD data shows high preferential orientation along the (002) plane, which is absent from the profile of figure 5.9. At the same time, the (100) peak has a bigger intensity than the (101) one, which is supposed to be the main diffracted peak of gallium nitride. Since films are grown on amorphous carbon, the preferential orientation observed on Si and Sa may be directly caused by the substrate and not due to growth conditions. Nevertheless, the complete disappearance of the (002) peak is yet unexplained.

Figure 5.10 shows a TEM image and its corresponding Fourier Transform (FT). The colourised figure showing the respective crystal orientation can be extracted by identifying the diffracted point with their corresponding interplanar distances and applying colourised masks on the inverse operation. TEM crystallite size of approximately 15 nm is obtained, which again concords with XRD and SEM measurements. High crystallinity is also seen on the FT image

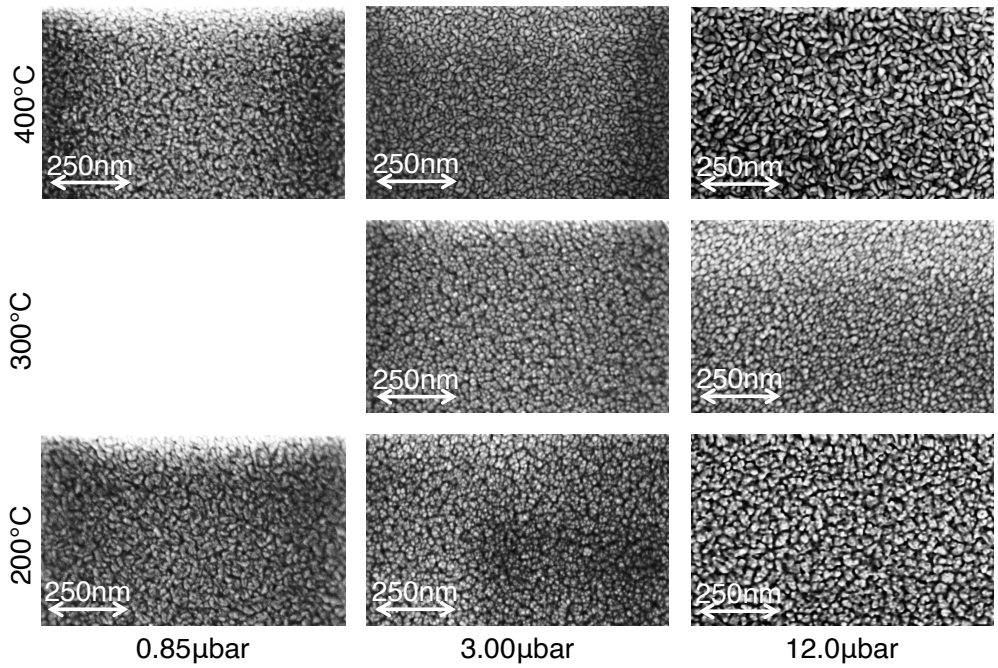


Figure 5.8: PVD GaN, characteristics: SEM top view at different pressures and temperatures, for a goal thickness of 100 nm deposited on a silicon substrate. The micrographs were taken at an acceleration voltage of 5 kV, current of 200 pA and working distance of 5 mm.

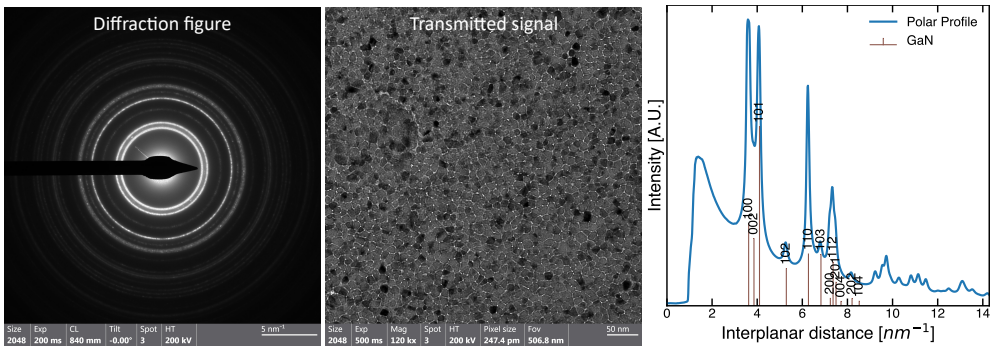


Figure 5.9: PVD GaN, characteristics: depolarisation of a TEM diffraction profile for a layer deposited on a TEM grid. On the left is the diffraction pattern, at the centre is its corresponding BF micrograph, and the polarised figure on the far right resembles the XRD data.

due to well-defined diffracted points. By looking at the different colours and the position of the points in the FT image, most of the crystallites are oriented along the (100) and (101) in figure 5.10. This result is again in contradiction with the preferred orientation found with XRD measurements. The weak (002) peak orientation indicates a growth rate much lower than the two other orientations, which may lead to the evolutionary deletion of the (002) plane on the amorphous carbon substrate.

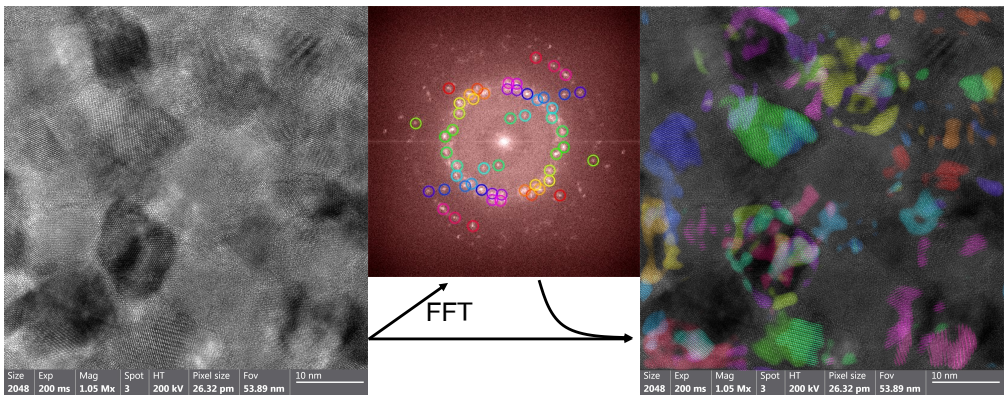


Figure 5.10: PVD GaN, characteristics: FT followed by a masked inverse FT on an HRTEM micrograph to enhance the crystallites and their respective orientations for a layer deposited on a TEM grid.

The influence of temperature on crystalline properties of layers grown on silicon substrates is small, even though SEM top surface images (figure 5.8) show very different surface features. The change in surface morphology could be linked to a different preferential orientation, but such a change is not observed in temperature evolution diffractograms (figure 5.4). Thus, it is still not clear what causes the surface morphology variations. The effect of temperature on crystalline properties on sapphire substrates is very different, and it induces a significant decrease in crystallite size, DOC and PO. This is possibly linked to a mismatch of the thermal expansion coefficient of GaN and $Al_2O_3$ that induces more stress in the structure on the first few tens of nanometers during growth. Figure 5.4 displays an increase in the layers' stress by increasing the substrate temperature (see figures B.23 and B.24 in appendix B.3 for the complete analysis including a zoom-in on the (002) peak). This stress buildup is less marked on silicon substrates, which would explain the different behaviour of crystallinity evolution with substrate temperature for both substrates.

The deposition pressure has a major influence on the deposited layers' different optical and structural properties. SEM cross-section images (figure 5.7) display the effect of pressure on the film density that is considerably increased by reducing the deposition pressure. Surface morphology from SEM top view images (figure 5.8) and crystallite size computation (figure 5.5) shows that grain size is increased with higher deposition pressure. Higher deposition pressure decreases the ionic bombardment of the substrate, as described by Maruyama *et al.* [113]. Reducing the ionic bombardment creates fewer defects during growth since both GaN molecules and nitrogen ions have less kinetic energy to damage the layer due to a smaller mean-free path.

The two pie-chart of figure 5.11 can be extracted using the different diffractograms of the layers deposited on a silicon substrate. Each colour represents an orientation, and the "size" of each pie corresponds to the percentage of the peak relative intensity. Numbers in nm on the charts are the corresponding crystallite size. Different top surface SEM images are plotted

along with the pie charts to show the influence of each orientation on the surface morphology. Gallium nitride growth starts (50 ± 5 nm films) by offering a solid preferential orientation along the c-axis because (002) orientation corresponds to the lowest free energy of wurtzite gallium nitride [63]. By increasing thickness, several other orientations appear ((101) at 37°, (102) at 48° and (103) at 63°), which is a typical indication of kinetic growth phenomena [130, 138]. Crystallographic orientation (101) and (102) gradually replaces (002) growth due to surface diffusivity anisotropy (evolutionary selection) between the different orientations. Crystallographic planes with the fastest growth rate perpendicular to the substrate surface survive through the film growth [141]. According to Thornton model on w-ZnO [173], round feature shape on surface SEM morphology indicates low adatoms mobility (surface diffusion) and assuming equivalent behaviour between w-GaN and w-ZnO, triangular shape are attributed to higher adatoms mobility [130]. By looking at the shape of the different features with SEM pictures and by identifying that higher substrate temperature and low pressure induce higher surface diffusivity, the morphology of the surface can be linked to the different crystallographic orientations and to the deposition parameters and films thickness as presented in figure 5.11.

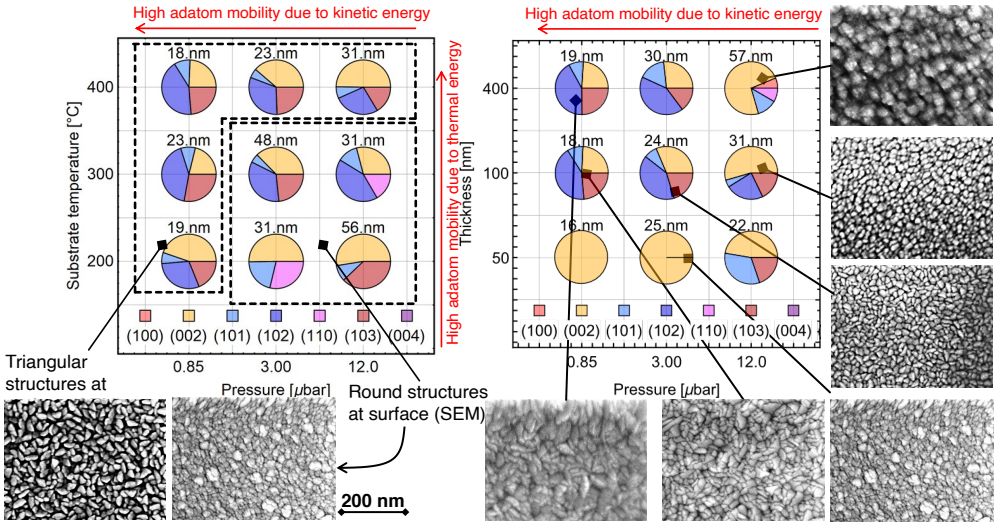


Figure 5.11: PVD GaN, characteristics: effect of the substrate on the structure. The goal thickness of the nine layers in the left-hand part of the figure is 100 nm, and the deposition temperature of the nine layers in the right-hand part of the figure is 400 ± 2 °C.

### 5.1.5 Link with Thornton Diagram

Thornton zone diagram displayed in figure 5.12 shows the influence of the ratio of substrate temperature $T_S$ over the melting temperature of the deposited material and the energy of the incoming particles on film structure and surface morphology. Using the previous discussion on temperature and pressure effect and the fact that peak positions in the diffractograms indicate compressive stress (smaller $d_{hkl}$ values), a first growth zone can be identified from the Thornton diagram [89] (black arrow parallel to temperature axis). Indications about the nature

of stress (tensile or compressive) allow excluding the first zone (zone 1), composed of tapered crystallite with voids. By moving along the temperature black arrow, two different zones are crossed: transition zone, characterised by columnar grains and zone 2, mainly composed of re-crystallised grains [8]. 400 °C is likely not high enough to land far in the re-crystallised zone (zone 2) but could explain the surface morphology changes seen in SEM top view.

Reducing deposition pressure increases the energy of the incoming particles, which means that the deposition zone is shifted along the energy axis of Thornton's diagram (second black arrow). XRD and TEM results show that nanocrystalline structures with well-defined grains are obtained at low pressure. Furthermore, deposition on silicon and sapphire substrates has shown strong (002) preferential orientation. Deposition at low pressure ($0.85-3.00\,\mu$bar) results in film growth in region three which would typically not be accessible without the assistance of the higher bombardment energy. Higher particle energies allow reducing the substrate temperature needed to obtain recrystallised grain structure and thus will enable the growth of high crystallinity material at low temperatures. Epitaxial growth at low energy is possible in the small triangular region that is possibly reached at the current deposition parameters ($150\pm0.1$ W, $0.85\pm0.02\,\mu$bar, $200\pm2$ °C) on sapphire substrates. Indeed, looking at figure 5.5 and the diffractogram presented in figure B.24 of appendix B.3.1 deposited at $0.85\pm0.02\,\mu$bar and $200\pm2$ °C, the layer grown at these conditions displays a very high degree of crystallinity with big crystallite size. Moreover, the only two diffracted peaks of the diffractogram are (002) and the (004) reflection. Growth at these conditions on sapphire substrates is likely to be heteroepitaxial growth.

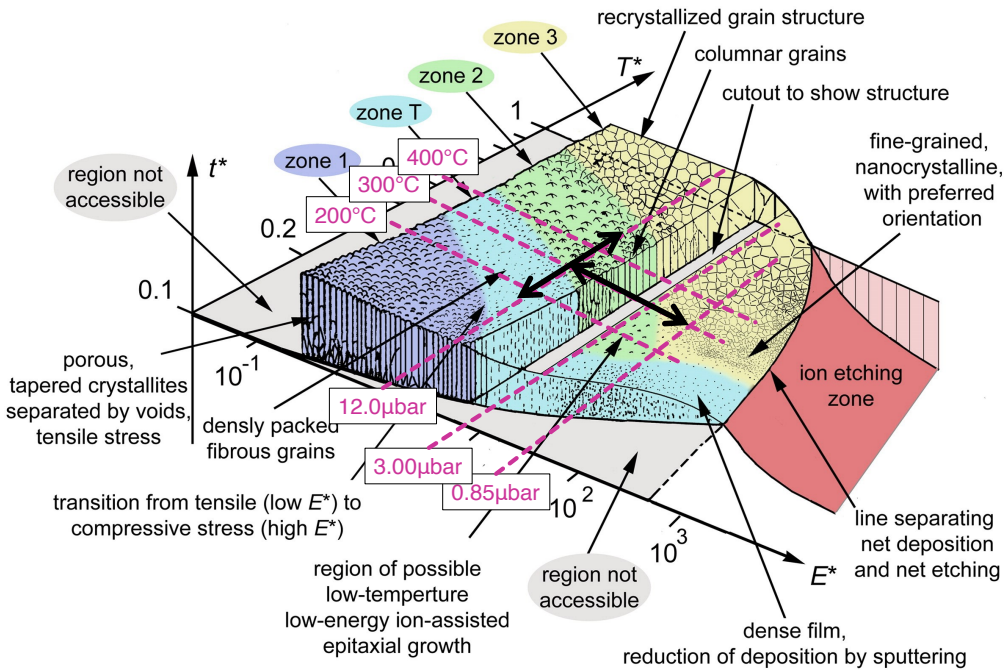


Figure 5.12: PVD GaN, characteristics: link with the Thornton Diagram [173].

Combining the various discussions presented above, the following can be outlined:

- The Urbach energy and optical bandgap are strongly linked with the structural properties and defects in the material. Bigger crystallite size tends to increase $E_{04}$ and decrease $E_U$, thus giving better optical properties.
- The refractive index increases almost linearly with the film density but seems not to be affected by the increase of defects due to stress/strain and the reduction of crystallite size.
- Growth rate values follow a logarithmic dependency with deposition pressure described by Livadiotis *et al.* [109].

### 5.1.6 Sputtered GaN: key takeaways & next steps

This section presented the investigations on the nanocrystalline growth of gallium nitride by RF sputtering. Samples with various deposition pressures, substrate temperatures and film thicknesses have been deposited, and XRD, SEM, TEM, ellipsometry and UV-VIS absorption characterise their structural and optical properties. The influence of the different deposition parameters was discussed, and it was found that low pressure leads to high crystallinity, but high transparency is only attained at high deposition pressure. Substrate temperature and deposition pressure considerably influenced adatom mobility, growth rate, preferential orientation, morphology and film density. Quasi-epitaxial growth of GaN on sapphire substrates was demonstrated at low deposition pressure and low substrate temperature.

Growth rate and refractive index are strongly linked to the deposition pressure and, thus, to the adatom's kinetic energy. Low deposition pressure of $0.85 \pm 0.02\,\mu$bar displayed very high density and increased refractive index compared to samples grown at higher pressure. Optical bandgap and Urbach energy are respectively increased and decreased at high pressure. A better optical quality material is found at high pressure because of the reduction of ion bombardment on the substrate, which results in fewer surface defects.

Knowing the effect of the deposition parameters on layer properties and that a stable deposition process has been established, the integration of dopant can be considered either with germanium or silicon.

## 5.2 Effect of the germanium doping on the GaN layer characteristics

GaN is intrinsically n-doped due to oxygen impurities in the PVD process. Regarding the n-doping, germanium and silicon are considered and can push the free electron concentration up to $10^{20}$ cm$^{-3}$. However, germanium doping does not add any tensile stress when doping GaN, and higher carrier concentrations have been reported. However, germanium doping will also imply lower mobility and conductivity than silicon doping [61, 178].

This section seeks n-type doping using germanium (Ge), introduced into the material by co-sputtering. The layers' optical, electronic, and structural properties are studied for different

dopant concentrations, deposition pressures, and precursor gases. Again, UV-VIS spectroscopy and XRD measure the optical and crystallographic characteristics. The different samples' conductivity and activation energy are measured in the dark at various temperatures.

### 5.2.1 Growth rate and thickness

Growth rate dependency with germanium target power and deposition pressure is shown in figure 5.13 with and without the addition of $H_2$ in the plasma. As for GaN, increasing deposition pressure reduces the growth rate due to the mean free path reduction that limits the kinetic energy of the ions hitting the target. Data can be fitted using a logarithmic function that, again, agrees with the probability of collision in plasma [109].

The growth rate varies pretty linearly by changing the power on the germanium target. Thus, assuming slight structural variation (no significant change of density and growth structure), increasing the germanium target power increases the dopant concentration linearly. Fitting the power data point for low germanium target power ($5-30\pm0.1$ W) leads to a good linear fit that allows growth comparison with $N_2$ and $N_2$ + $H_2$ plasma. As seen in figure 5.13a, the slopes of the fitted functions are very similar, indicating no substantial change in the growth conditions. Since the growth rate increases considerably from 0 to $100\pm0.1$ W of germanium target power, layers grown at high germanium target power are not doped GaN but more likely a mixture of GaN+Ge+GeN that indeed changes the structural properties. It isn't easy to extract the germanium content from growth rate variation. Increasing above $50\pm0.1$ W the germanium target power results in a quadratic dependence of deposition speed with power. However, this power range is out of this work's doping conditions of interest.

Samples grown on silicon substrates at a deposition pressure of $3.00\pm0.06\,\mu$bar, $Po_{\mathrm{GaN}} = 150\pm0.1$ W, $Po_{\mathrm{Ge}} = 20\pm0.1$ W, and substrate temperature of $200\pm2$ °C were annealed at different temperatures (no annealing, 300, 450, 600, $750\pm2$ °C) under nitrogen atmosphere. Figure 5.13c shows the growth rate after different annealing temperatures of about 50 nm thick films. As demonstrated by the minimal slope of the linear fit, the effect of annealing temperature on film density is small but still present as it seems to increase the film density (thickness reduction) by increasing the annealing temperature. The difference in fit offset between $N_2$ and $N_2$ + $H_2$ plasma indicates a lower sputtering yield by adding hydrogen in the plasma that is easily explained considering that hydrogen atoms are too light to participate to target bombardment, thus reducing the growth rate. As there is no considerable difference between $N_2$ and $N_2$ + $H_2$ at different annealing temperatures, either the hydrogen does not influence the growth (small incorporation of H in the films) or the annealing is not efficient enough to desorb hydrogen atoms and re-organise the films, which should lead in a change of film density, and thus of growth rate.

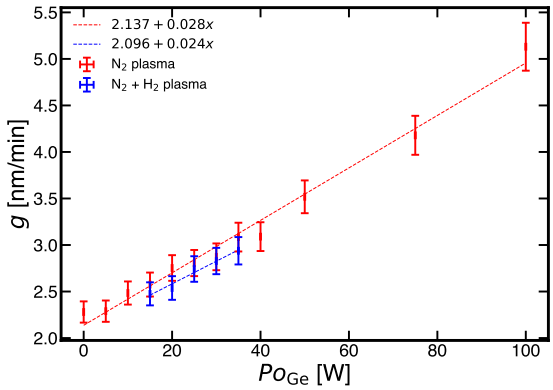


(a) Growth rate dependence with germanium target power at $3.00 \pm 0.06\,\mu$bar.

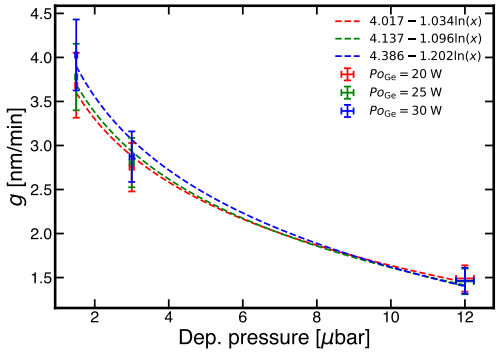


(b) Growth rate dependence with pressure, with $T = 200 \pm 2\,°$C.

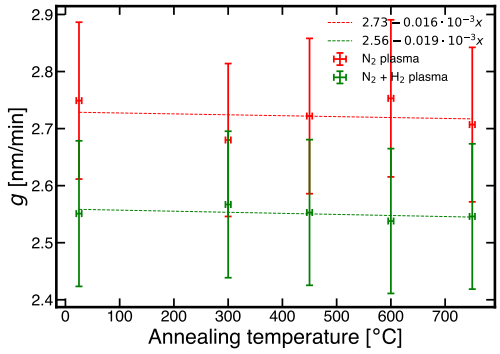


(c) Growth rate dependence with annealing temperature. $Po_{\mathrm{Ge}} = 20 \pm 0.1$ W, $T = 200 \pm 2\,°$C, $p_d = 3.00 \pm 0.06\,\mu$bar.

Figure 5.13: Ge-doped PVD GaN: growth rate evolution with different doping and deposition pressure and annealing temperature for a gallium nitride target power of $150 \pm 0.1$ W and glass substrate deposition temperature of $200 \pm 2\,°$C. The three most-right points of figure a correspond, in fact, to a phase separation (phase apparition would be more correct) due to the too-high germanium content.

### 5.2.2 Optical properties

The optical properties of doped layers were computed by ellipsometry and UV-VIS spectroscopy. Different annealing temperatures, germanium target power, plasma and deposition pressures characterised the layer thickness of about 50 nm on glass and silicon. Tables B.16 and B.15 (in Appendix B.3.1) shows the optical BG and Urbach energy computed from the absorption plots displayed in figure B.27 (in the same Appendix). As for layers without doping, the pressure increases the optical bandgap while decreasing the Urbach energy. Curves from figure B.27b show that the annealing temperature has little influence on the absorption properties. Graphs shown in figure 5.14 are computed from the absorption curves in the appendix and display the effect of doping concentration, gas composition, annealing temperature and deposition pressure on the optical bandgap and the Urbach energy. Similarly, as with the

silicon, the doping concentration is assumed to be linearly related to the Ge target power (see figure 5.18a). The germanium target power influences $E_{04}$ and $E_U$ by decreasing first the optical bandgap for $25 \pm 0.1$ W of germanium target power, and then increasing for higher germanium content. The Urbach energy is increased by adding germanium because doping causes defects in the layers (see the two left graphs of figure 5.14).

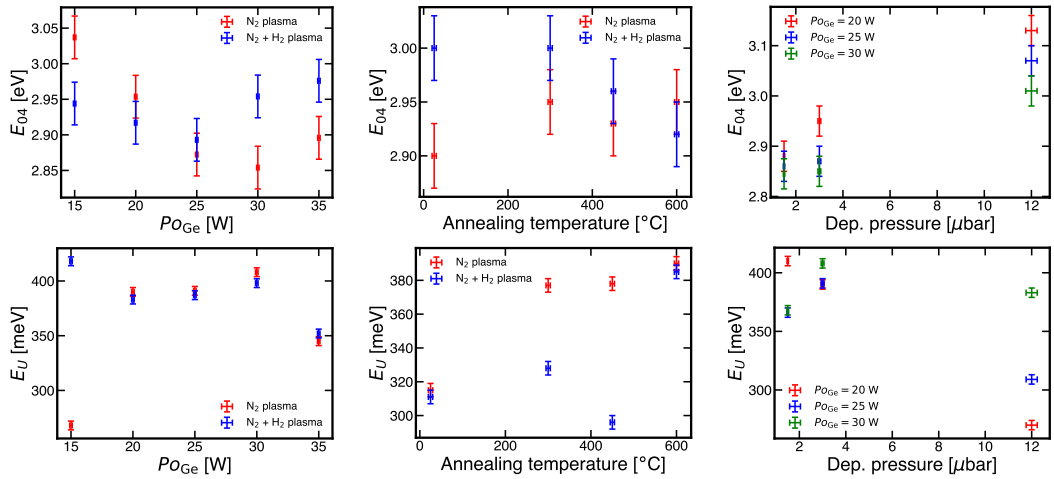


Figure 5.14: Ge-doped PVD GaN: absorption coefficient dependence on deposition pressure, annealing temperature and germanium concentration for layers deposited on a glass substrate.

### 5.2.3 Structural properties

The effect of germanium doping and annealing temperature on crystallinity is shown in figure 5.15 that displays the (002) peak intensity for various germanium target power, annealing temperature and plasma. The forbidden silicon peak (200) is a reference for the setup alignment and allows stress comparison between the different samples. Increasing the germanium concentration leads to a substantial decrease in layers' crystallinity. Comparing samples grown in $N_2$ and $N_2 + H_2$ atmosphere shows that hydrogen seems to reduce crystallinity and increases the peak broadening. Augmenting Ge target power does not affect the stress, as seen by the peak position, which does not change. For very high germanium target power, a small diffraction peak at 34° could belong to a germanium phase. The effect of annealing is presented in figure 5.15c. Increasing temperature shifts the (002) peak to higher diffracted angles from its rest position. $T_A$ has, however, no influence on the (002) peak broadening from which a crystallite size of about 30 nm can be extracted.

### 5.2.4 Electrical properties

Conductivity in the dark at different temperatures is presented in figure 5.16 for different annealing temperatures on sapphire substrates. Arrhenius plot of the effect of pressure, plasma gas and germanium target power is displayed in figure B.28 (Appendix B.3.1). Conductivity

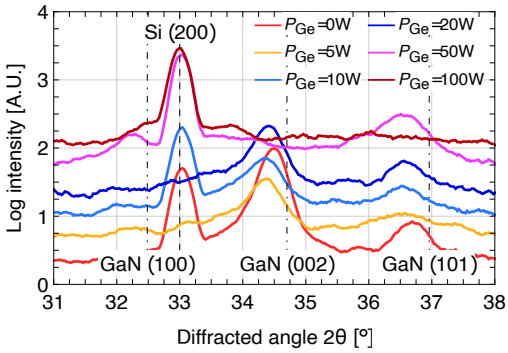


(a) Doping effect, $N_2$ plasma.

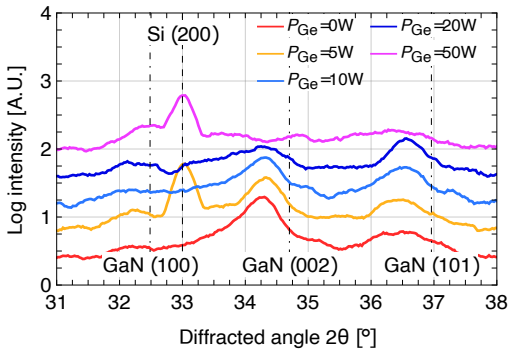


(b) Doping effect, $N_2 + H_2$ plasma.

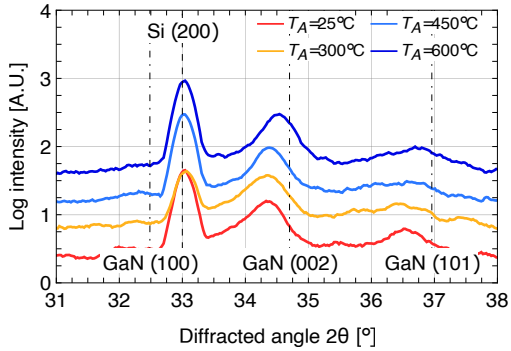


(c) Annealing effect, $N_2$ plasma.

Figure 5.15: Ge-doped PVD GaN: XRD vs annealing and doping level, deposited on a silicon substrate.

data points are fitted by equation 3.35 where $k_B T$ is the thermal energy, $\sigma_0$ is a constant, $\sigma$ is the electrical conductivity and $E_A$ the activation energy that represents the difference between the CB and Fermi level (n-type material) or the Fermi level and the VB (p-type material). The slope of the linear part of the conductivity gives the activation energy; using the fitted function, the conductivity at $20 \pm 2\,°C$ can be extracted. Tables B.16 and B.15 (same appendix) present the different activation energies and conductivities displayed in the different graphs of figure 5.17.

Figure 5.17a shows the effect of different germanium target power on conductivity and activation energy for samples that are annealed at $600 \pm 5\,°C$ after deposition. The optimum doping concentration is around $20 \pm 0.1$ W of germanium target power. This concentration gives a resistivity as low as $12 \pm 0\,\Omega$ cm and a low activation energy ($80 \pm 0$ meV). Increasing the germanium content further decreases the electrical performances drastically. The influence of deposition pressure for $600 \pm 5\,°C$ annealing (figure 5.17b) shows that low pressure gives the best conductivity ($2.3 \pm 0\,\Omega$ cm) and lowest activation energy ($50 \pm 0$ meV). Changing the pressure varies the film density, the crystallinity and, most likely, the germanium concentration. The doping efficiency is strongly dependent on the crystallinity; thus, the increase of the crystallinity gives better electrical properties. Figure 5.17c presents the effect of both annealing temperature and plasma on the electrical properties of the films. Best resistivity

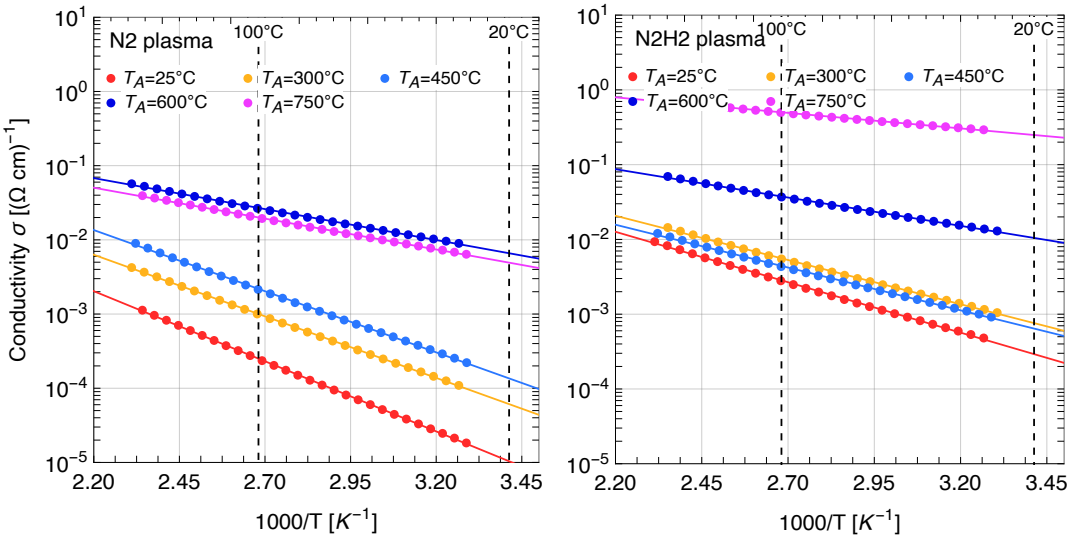


Figure 5.16: Arrhenius plot of sample conductivity at different temperatures for various annealing conditions on a silicon substrate. The annealing temperature is precise to ±5 °C.

and activation energy is achieved with $N_2$ + $H_2$ incorporation and the highest annealing temperature. Annealing activates the dopants and thus increases electrical performances. Since hydrogen passivates nitrogen vacancies during growth and is removed by annealing, nitrogen starts to act as an intrinsic dopant.

### 5.2.5 Germanium doping: key takeaways & next steps

The effect of germanium concentration, deposition pressure, annealing temperature and reactive gas on the electrical performances of Ge-doped GaN has been described. An optimum germanium target power of 20 W has shown promising results in resistivity (2.3 ± 0 Ω cm) and activation energy (50 ± 0 meV). Increasing the germanium target power has dramatically affected the degree of crystallinity, which is strongly reduced. Low deposition pressure displayed better electrical properties than other pressure, possibly linked to the better crystallinity obtained at these sputtering conditions. Comparison between $N_2$ and $N_2$ + $H_2$ gas during sputtering shows an increase of conductivity by adding hydrogen in the layers. The effect of various annealing temperatures on electrical and structural properties has been investigated. It was found that increasing the annealing temperature reduces the stress in the lattice but does not improve the crystallinity. Best resistivity was found for an annealing temperature of 750 ± 5 °C at 4.0 ± 0 Ω cm. Even though the resistivity values are much higher than the objective (< 0.1 Ω cm), germanium-doped gallium nitride grown at low temperatures was demonstrated.

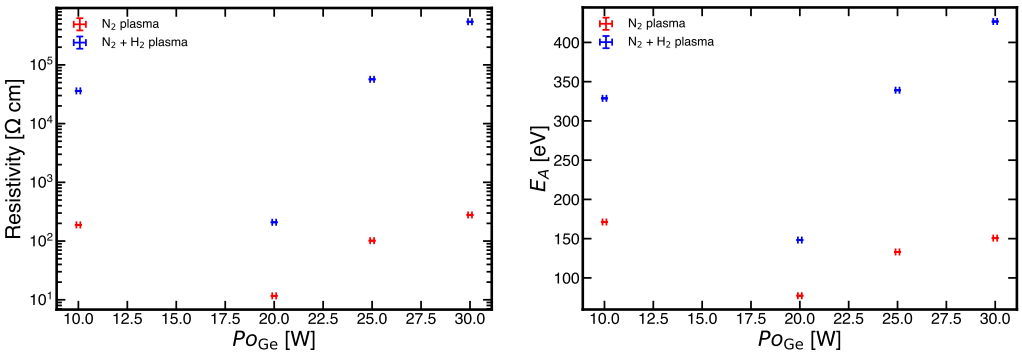


(a) Electric properties as a function of the germanium content, reflected by the power applied to the Ge target.

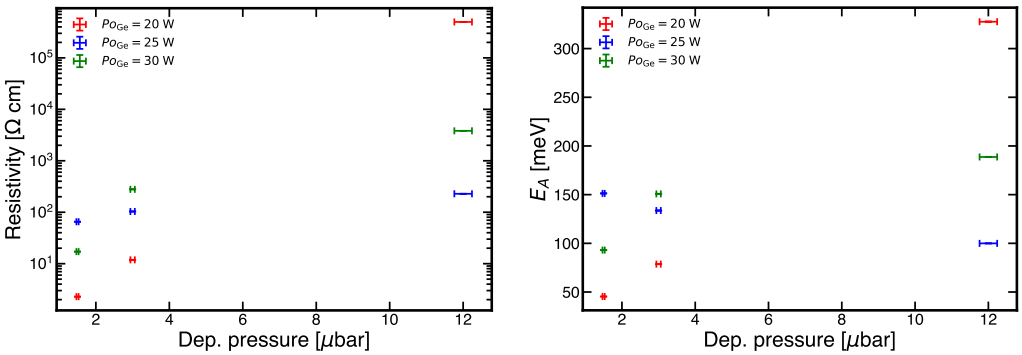


(b) Electric properties as a function of the deposition pressure.

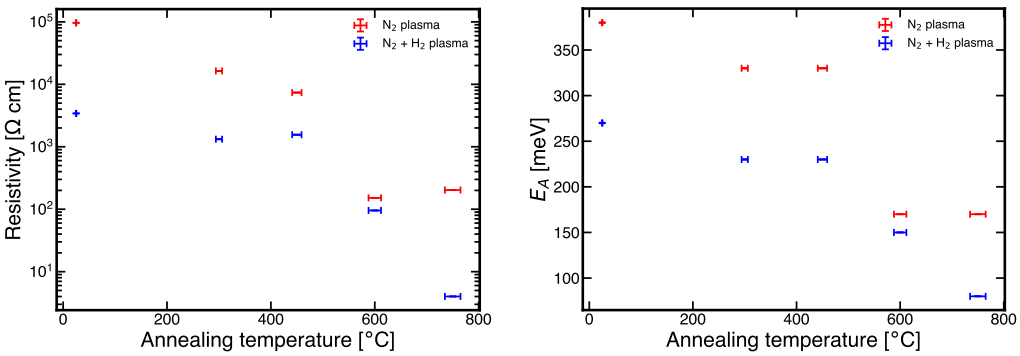


(c) Electric properties as a function of the annealing temperature.

Figure 5.17: Resistivity and activation energy for various deposition pressures, germanium contents and annealing temperatures for layers deposited on a silicon substrate. One physical quantity is varied while all the others remain constant. The constant values are the following: $P_{\mathrm{GaN}} = 150 \pm 0.1\,\mathrm{W}$, $T = 200 \pm 2\,°\mathrm{C}$, $T_A = 600 \pm 5\,°\mathrm{C}$, $p_d = 3.00 \pm 0.06\,\mu\mathrm{bar}$ and $P_{\mathrm{Ge}} = 20 \pm 0.1\,\mathrm{W}$.

Table 5.2: Ge-doped PVD GaN: comparison with literature.

| Characteristic | Symbol | Units | Ge-doped GaN | a-Si(n) literature | GaN(n) literature |
|---|---|---|---|---|---|
| Resistivity | $\rho$ | $\Omega\,\mathrm{cm}$ | $50 \pm 0.05$ | 0.1 [203] | $2 \cdot 10^{-4}$ [178] |
| Activation energy | $E_A$ | meV | $50 \pm 0.05$ | $100 - 400$ [203] | $20 - 40$ [70] |
| Free carrier abs. | FCA | $\mathrm{cm}^{-3}$ | $4.0 \pm 0.2 \cdot 10^{18}$ | - | $5.1 \cdot 10^{18}$ [178] |
| Mobility | $\mu$ | $\frac{\mathrm{cm}^2}{\mathrm{Vs}}$ | $0.3 \pm 0.02$ | - | 61 [178] |
| Optical bandgap | $E_{04}$ | eV | $2.88 \pm 0.03$ | 1.80 [190] | 3.43 [142] |
| Urbach energy | $E_U$ | meV | $410 \pm 4$ | 55 [190] | $20 - 200$ [142, 95] |

Several points have not been cleared up. First, the influence of the GaN deposition power has not been investigated with germanium doping. It is undoubtedly a vital deposition parameter that is, in a way, linked with the deposition pressure. A few depositions of GaN with Ar+$N_2$ have been performed (not shown here); samples grown in a mixture of Ar (50%) + $N_2$ (50%) have a growth rate almost 5 times faster while maintaining the same high crystallinity. It could therefore be an interesting experiment to look at different Ar-$N_2$ composition and their effect on optical and structural properties and doping performances. To confirm the discussion about preferential orientation and its relationship with sputtering parameters and surface morphology, another set of depositions at different pressures, temperatures and thicknesses should be performed to compare with the current data.

The ellipsometric measurements in this section presenting the germanium doping only used a simple Tauc-Lorentz oscillator. The ellipsometric model should be improved by creating a multimodel combining a Tauc-Lorentz model and a Drude model and including the transmittance and reflectance data from UV-VIS spectroscopy. Raman spectroscopy should be performed on the different samples to allow a comparison with XRD results. Furthermore, fitting the various Raman peaks enables the extraction of free carrier concentration and mobility. Understanding the issue with Hall effect measurements and performing the measurements on the doped sample could increase our understanding of doping capabilities and would be a way to confirm the resistivity measurements performed with dark lateral conductivity.

## 5.3 Effect of the silicon doping on the GaN layer characteristics

The goal of this section is to improve even further the resistivity and mobility compared to germanium doping. After a doping regime is reached by tuning the etching gas mix and Si target power, optimum silicon concentration, substrate temperature and annealing temperature can be found. The substrate influence can also be probed between c-Si and glass, and the best result will be integrated into a solar cell architecture as n-contact. *N.B.*: similarly to InGaN where the indium content was compared to gallium only ($X_{\mathrm{In}} = \frac{\mathrm{In}}{\mathrm{In+Ga}}$, In & Ga in at. %, $X_{\mathrm{In}}$ in %), the silicon content is also here only compared to gallium ($X_{\mathrm{Si}} = \frac{\mathrm{Si}}{\mathrm{Si+Ga}}$ at. %).

### 5.3.1 Silicon content influence

As a first test, the power applied to the silicon target was varied, and layer properties were probed. The silicon content linearly depends on the power applied to the silicon target during deposition, as shown in figure 5.18a. Regarding resistivity, figure 5.18b shows an optimum between 3 – 4 % of silicon with low activation energy. The resistivity value at this silicon content is comparable to the germanium optimum one, but with much less incorporation (4 ± 1 % instead of 8 ± 1 % corresponding to a power of 20 ± 0.1 W, see figure 5.17a and particularly its legend to understand why a further error of ±0.4 % is retained in place of the ±1 % here in the text). Regarding the optical properties, the small step around 1.4 eV in figure 5.18c is due to the instrument; that is when the detector is changed inside the spectrometer. For GaN, the

optical BG values are pretty low with a considerable Urbach energy (inset of figure 5.18c), a sign of highly defective layers. The tail at low energy represents the FCA and increases with increasing silicon content.

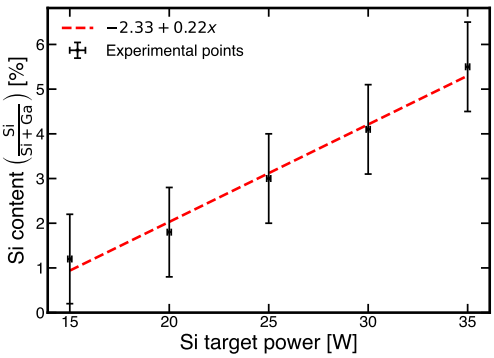


(a) EDS silicon content vs target power on a silicon substrate. Because of the clear linear relationship, the silicon content in subsequent results is expressed about the target power (±0.4 % propagated uncertainty) instead of EDS (±1 % error).

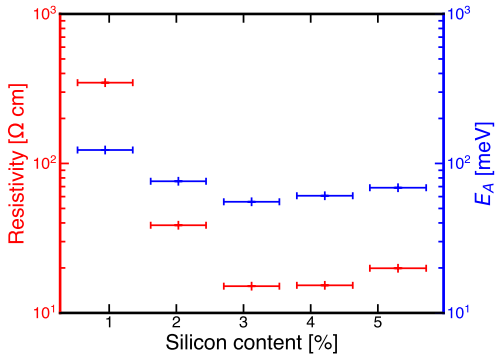


(b) DLC results vs silicon content on a silicon substrate.

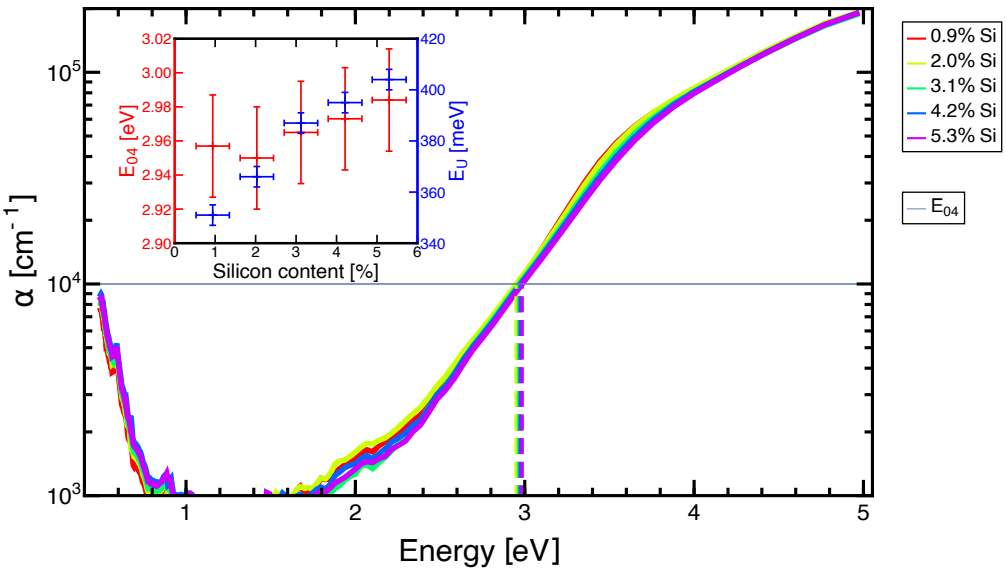


(c) Absorption coefficient vs silicon content on a glass substrate.

Figure 5.18: Si-doped PVD GaN: silicon content dependence of the target power, and influence on the resistivity, the activation energy, the Urbach energy and the optical BG.

The crystallinity was characterised using XRD and Raman spectroscopy. The results can be consulted in figures 5.19 and 5.20. Regarding the Raman crystallinity, increasing the silicon content will mainly influence the $L^+$, $A_{1,LO}$ and $E_{1,LO}$ GaN peaks, and also the silicon peak located around 520 $cm^{-1}$. As expected, the silicon peak intensity increases with increasing silicon content and the free carrier concentration ($L^+$ peak intensity). The $E/A_{1,LO}$ peak is

widened and shifted with increasing silicon content, meaning there is a loss of crystallinity and a stress increase or a lattice parameter change, contrary to what is obtained by XRD.

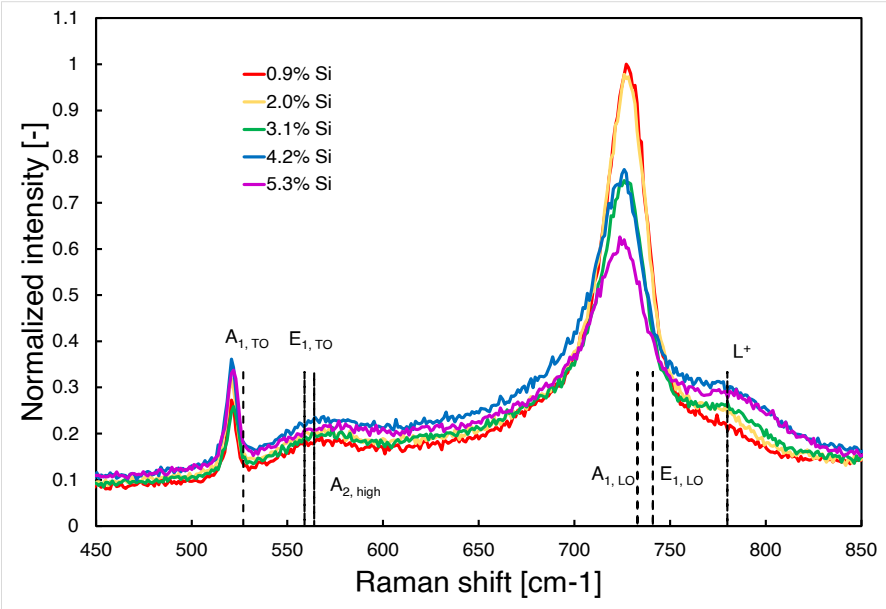


(a) Raman spectra.

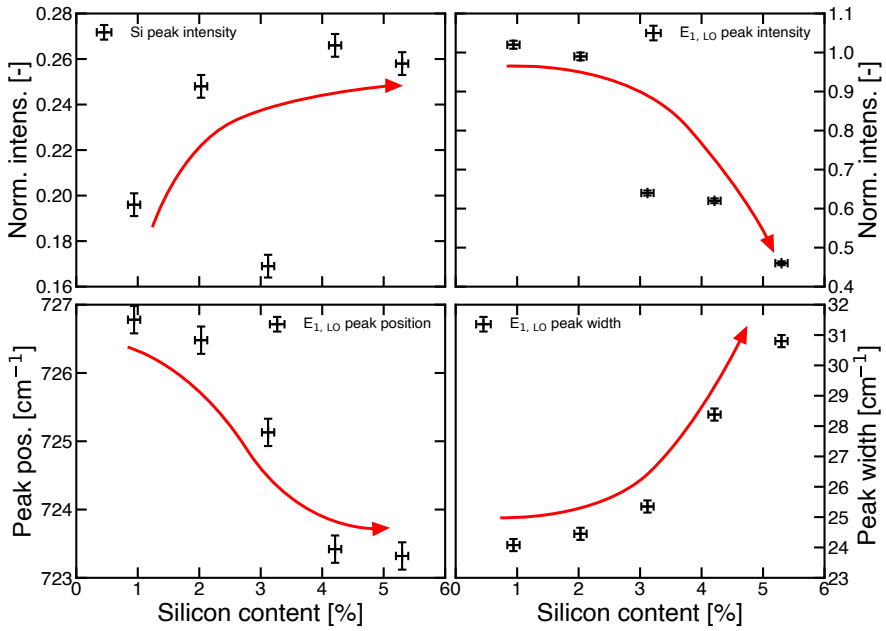


(b) Peak evolution vs silicon content.

Figure 5.19: Si-doped PVD GaN: silicon content influences the Raman crystallinity for layers deposited on a silicon substrate.

For XRD, only the peaks (002) and (101) are considered. Here, the same kind of impact is observed: the (002) preferential orientation peak decreases in intensity to increase the

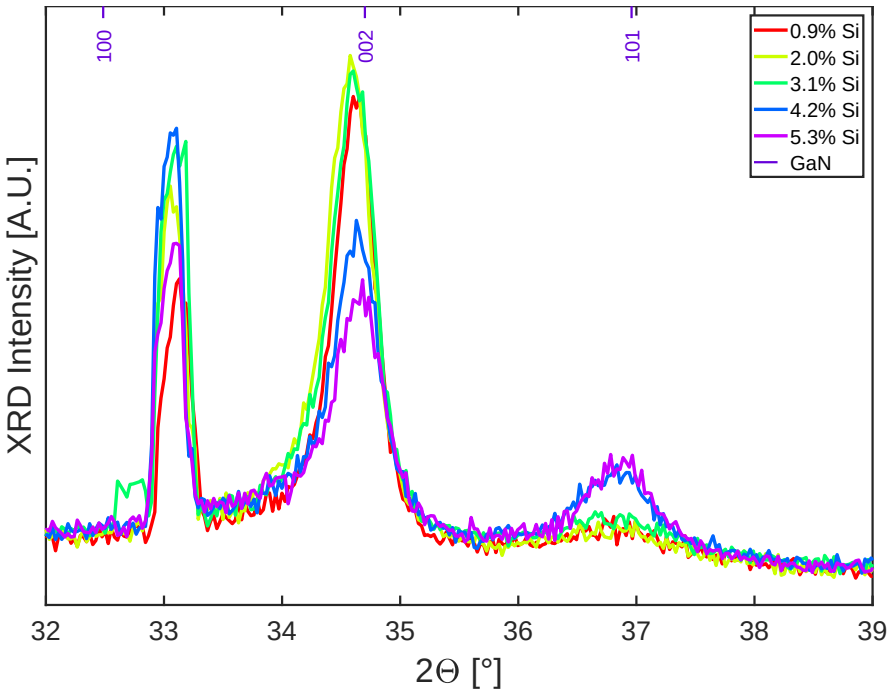


(a) XRD pattern.

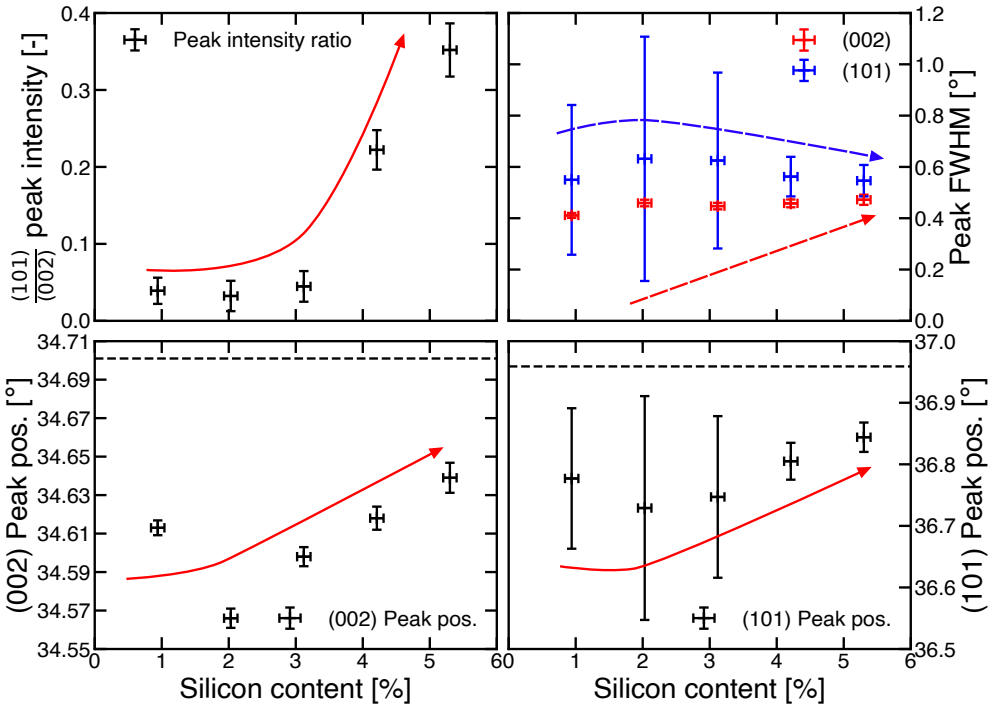


(b) Peak evolution vs silicon content. The dashed line in the two bottom graphs shows the expected reference peak position.

Figure 5.20: Si-doped PVD GaN: silicon content influences the XRD crystallinity for layers deposited on a silicon substrate.

(101) peak with the increasing silicon content. This means that the preferential orientation is slowly lost with the randomisation of the crystal orientation. This is also proven by the widening of the (002) peak and the sharpening of the (101) peak. Regarding peak position, both peaks tend to return to their reference positions, which means that with increasing silicon content, the compressive stress is relaxed or that there is a lattice parameter variation due to Si incorporation. This contradicts the Raman conclusion stating an increase of stress with increasing silicon content. To address this contradiction, one could presume that the XRD reference peaks were not well aligned or that something went wrong with either the calibration or the XRD post-processing analysis. Indeed, if the peak reference (the dashed line in the two bottom plots of figure 5.20b) was placed slightly below the points instead of above, the tensile stress would increase, corroborating the Raman result.

### 5.3.2 Substrate temperature influence

In this characterisation set, the silicon content of all layers remains identical at the optimal value of $4.2 \pm 0.42$ %. Other parameters were kept constant except for the substrate temperature during deposition, which varied between room temperature (RT) and $400 \pm 2$ °C.

Figure 5.21a shows extremum values for the refractive index and the growth rate when the substrate temperature reaches $300 \pm 2$ °C. This may mean that up to that temperature, the layer porosity increases, and above that temperature, the "bad" adatoms are desorbed. However, there is no increase of crystallinity as determined by XRD or Raman above this temperature. It could also be due to a change in the crystallographic orientation (different growth rate depending on the preferential orientation), but that was also not confirmed with XRD or Raman. The problem resides in a modelling artefact using the ellipsometric measurements, where the refractive index and the thickness are strongly correlated in the fitting process, implying that the link between the two parameters may come from the ellipsometric modelling rather than from deposition conditions, making this result less reliable.

Figure 5.21b shows a substantial decrease of the activation energy and the resistivity with temperature, where values such as $1.1\,\Omega \pm 0.2$ % cm and 33 meV$\pm 0.2$ % can be reached at $400 \pm 2$ °C. Figure 5.21c shows the same glitchy feature at 1.4 eV as in the previous subsection, due to the instrument. The inset shows improved optical properties with rising deposition temperature: higher BG and lower Urbach energies. The FCA is also reduced, going on par with the reduced resistivity; this can be explained by an increase in electron mobility (Hall effect, not shown here).

The Raman crystallinity (figure 5.22) analysis is based on the same groundwork as in the previous subsection, where here the optimum crystallinity is found around 300 °C as shown by the $E_{1,LO}$ peak intensity change. The change in width and position of this same peak means that the vibration mode changes, implying that the stress is increased when deposited at higher temperatures. The silicon peak ($\sim 520\,\mathrm{cm}^{-1}$) increases in intensity with increasing

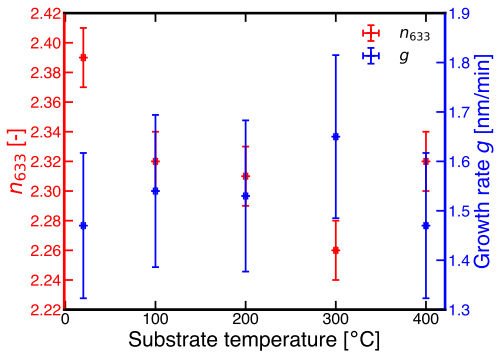


(a) Refractive index and growth rate for layers deposited on a glass substrate.

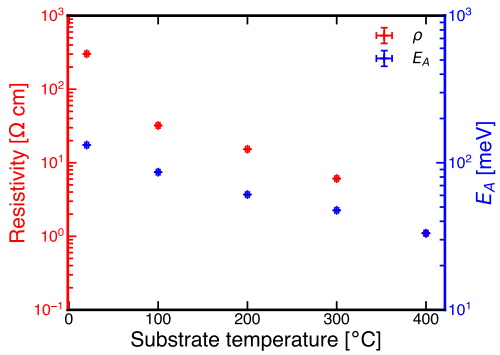


(b) DLC results vs substrate temperature for layers deposited on a silicon substrate.

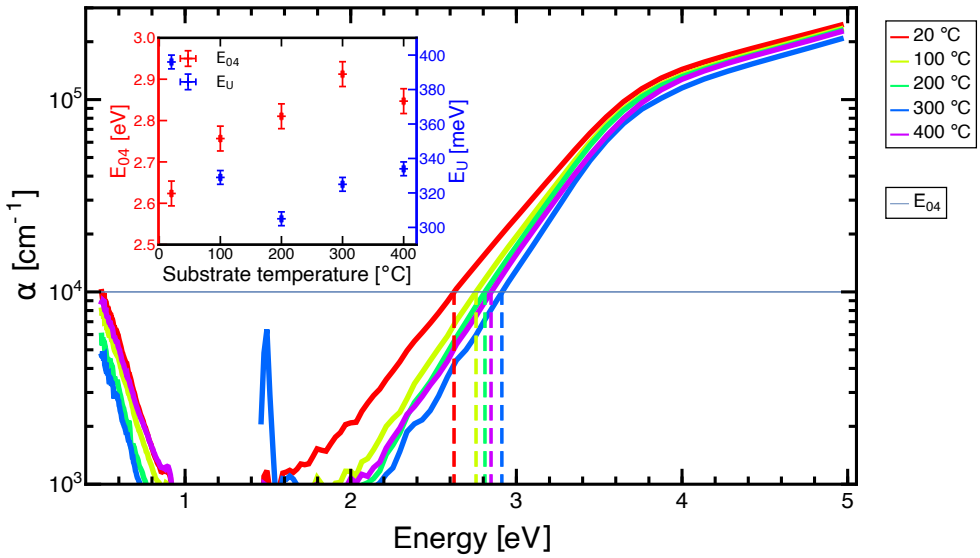


(c) Absorption coefficient vs substrate temperature for layers deposited on a glass substrate.

Figure 5.21: Si-doped PVD GaN: substrate temperature influence on the index of refraction, the growth rate, the resistivity, the activation energy, the Urbach energy and the optical BG.

temperature, which means that the network created by the silicon atoms is more tightly bounded at higher temperatures.

For XRD, again only the peaks (002) and (101) are considered, in figure 5.23. We see that the crystallinity is at its highest at RT, decreasing with increasing substrate temperature, as well as a change in the preferential orientation from (002) to (101). Considering the evolution of the two peak positions, the stress is at its minimum when the temperature is at $200 \pm 2\,°C$. Given all the previous considerations, this last substrate temperature is chosen for the next set of experiments.

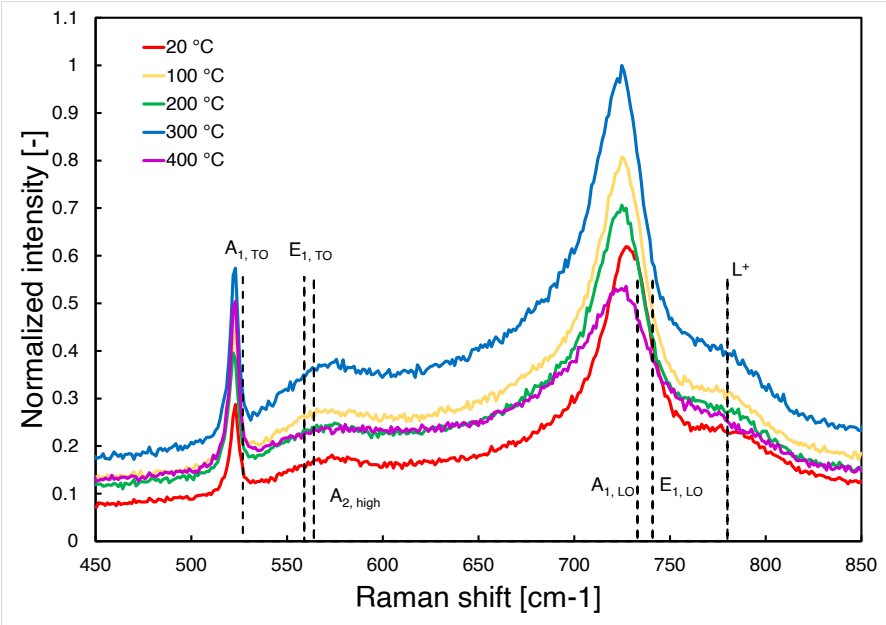


(a) Raman spectra.

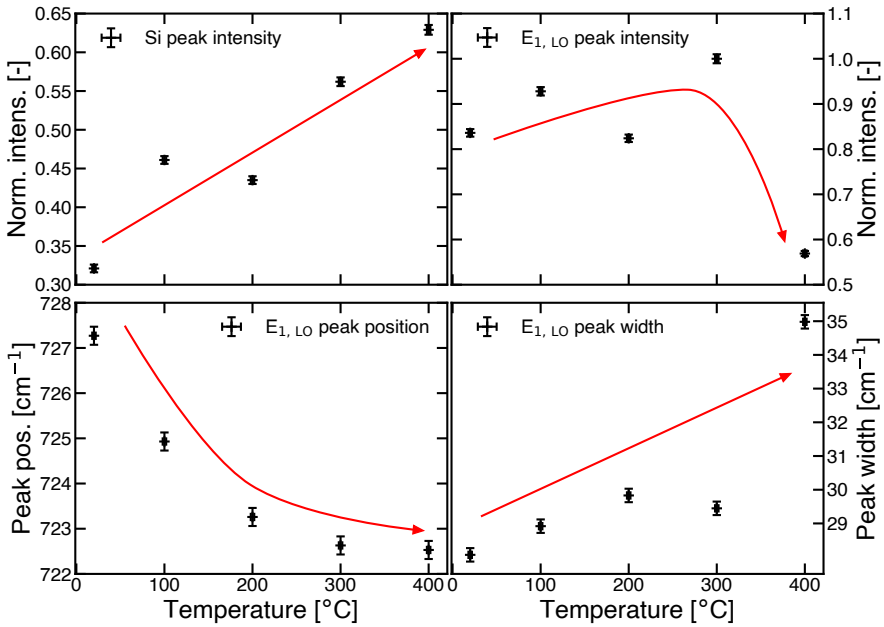


(b) Peak evolution vs substrate temperature.

Figure 5.22: Si-doped PVD GaN: substrate temperature influences the Raman crystallinity for layers deposited on a silicon substrate.

### 5.3.3 Annealing temperature influence

In this characterisation set, the silicon content remains identical at the optimal value of $4.2 \pm 0.42$ %, and the deposition temperature is set to $200 \pm 2$ °C. After being deposited, the

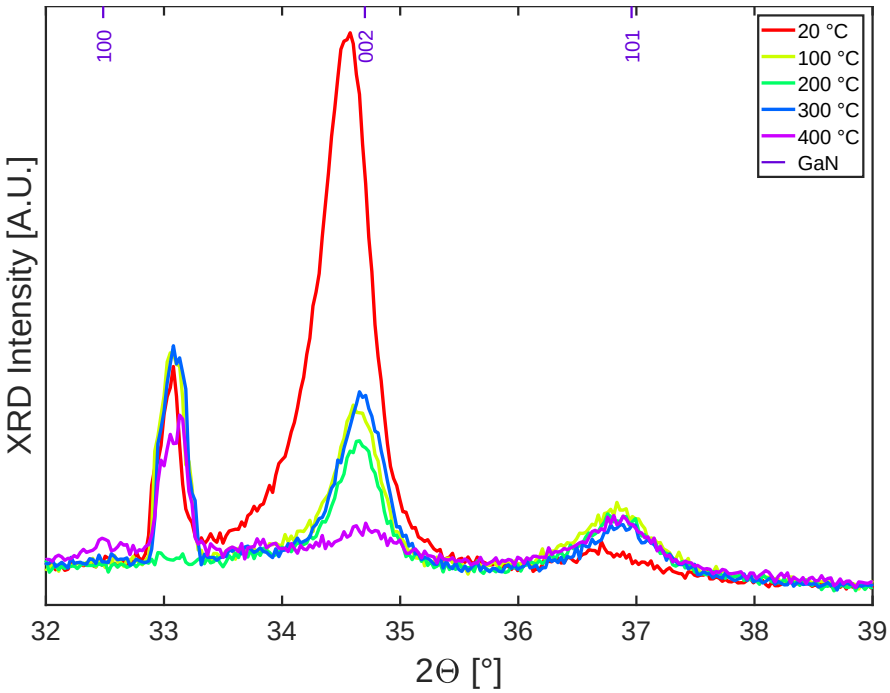


(a) XRD pattern.

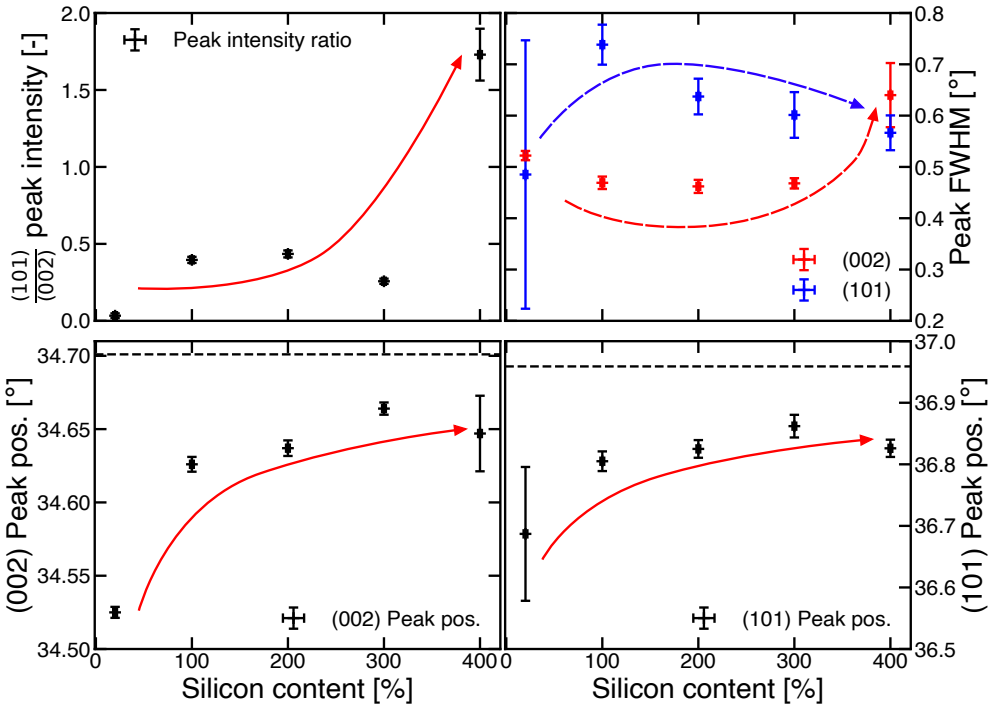


(b) Peak evolution vs substrate temperature.

Figure 5.23: Si-doped PVD GaN: substrate temperature influences the XRD crystallinity for layers deposited on a silicon substrate.

layers are annealed at different temperatures for 15 minutes ±1 s under $N_2$ atmosphere. Only the spectrometer and the DLC setup were used to characterise this set of layers, and the results can be viewed in figure 5.24.

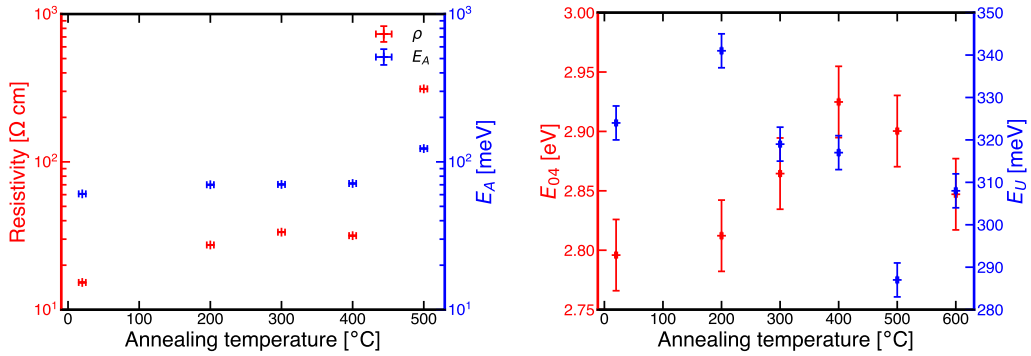


(a) DLC results vs annealing temperature for layers deposited on a silicon substrate.

(b) Optical BG and Urbach energy extracted from figure 5.24c.

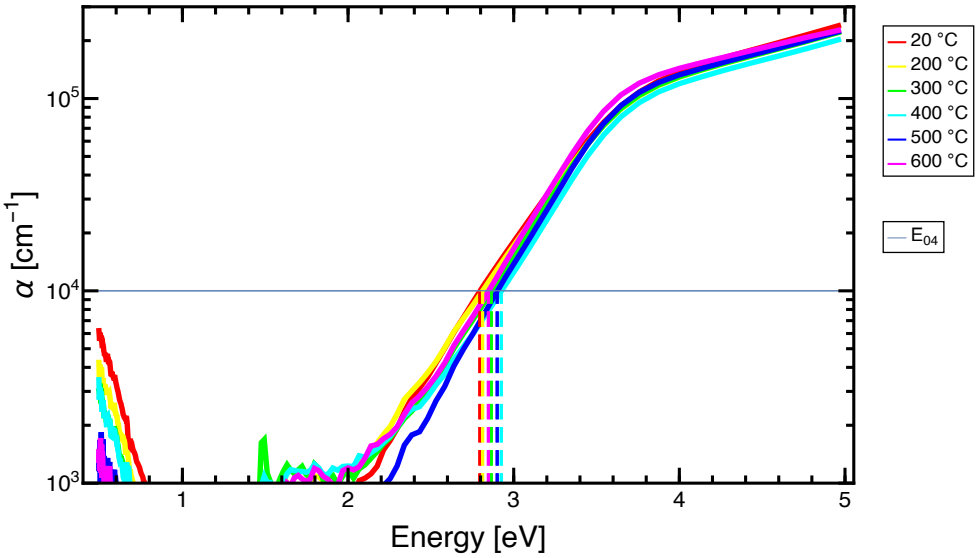


(c) Absorption coefficient vs annealing temperature for layers deposited on a glass substrate.

Figure 5.24: Si-doped PVD GaN: annealing temperature influence on the resistivity, activation energy, BG and Urbach energy.

Increasing the annealing temperature will increase the resistivity and the activation energy (figure 5.24a); that is the opposite trend as with the germanium doping (see figure 5.17c). This means that in terms of electrical characteristics, it is better not to anneal the layer after the deposition at 200 ± 2 °C, even at 200 ± 5 °C. This is extremely surprising, and trying to find an explanation is complicated. Maybe with the dilatation factor difference between the c-Si substrate and the GaN layer, the annealing-induced stress slightly degrades the crystallinity, increasing the grain boundary density and decreasing the electrical properties. Regarding the optical properties, the optimal optical BG is met for an annealing temperature of 400 ± 5 °C, and the Urbach energy seems to decrease slightly with the annealing temperature. The FCA

is also reduced, and the mobility is increased (Hall effect, not shown here), but this time not enough to counter the substantial resistivity increase.

### 5.3.4 Silicon doping: key takeaways & next steps

It can be concluded that the best GaN layer properties are found for a silicon content of about 4.2 %, a deposition temperature of about 200 °C, without post-deposition annealing. In such a configuration, a low resistivity of $15 \pm 0\,\Omega\,\mathrm{cm}$, an activation energy of $60 \pm 0$ meV, an optical BG of $2.90 \pm 0.3$ eV with an Urbach energy of $360 \pm 4$ meV. This is similar to germanium doping (see subsection 5.2.5) but with less dopant concentration.

As a comparison of the experiments related to doping of sputtered GaN, silicon doping has shown good resistivity ($< 0.2\,\mathrm{m}\Omega\,\mathrm{cm}$) and good electron mobility ($> 100\,\mathrm{cm^2/Vs}$) [11] compared to germanium doping ($\rho = 3 \pm 0\,\Omega\,\mathrm{cm}$) [171]. The samples presented in the next section 5.4, deposited with the Clusterline sputtering deposition system at CSEM, could reach $14 \pm 0\,\Omega\,\mathrm{cm}$ of resistivity and $29 \pm 4$ meV in Urbach energy in comparison.

It would be interesting also to probe how the layer thickness influences the layer characteristics. A higher ratio of $N_2/Ar$ is expected to increase the optical BG further (this was not tested with germanium doping as well). And the final step would be to test such a layer in a solar cell architecture as a contact; its characteristics are far from the best values reported in the literature, but we may be able to prove it is feasible.

## 5.4 Effect of the silicon doping on the GaN epitaxy on sapphire

Gabriel Christmann deposited the layers presented in this section in the Clusterline at the Centre Suisse d'Électronique et de Microtechnique (CSEM), and their optical properties and crystallinity was investigated by Julien Hurni during his Master's project in PV-lab under Mathieu Boccard's and my supervision. The FIB lamellae were milled and extracted by Sofia Libraro (another *Ph.D.* student of PV-lab), and all the electron microscopy studies and synthesis were performed by myself.

### 5.4.1 Motivation

Sapphire and GaN are known to have good compatibility in terms of epitaxy: their crystals are both hexagonal and although their lattice parameters are vastly different, the aluminium atoms of the basal-plane unit cell of sapphire align well with the gallium atoms of the basal-plane unit cell of GaN. In sapphire, the distance between two Al atoms is of 4.7580 Å [5] and of 4.3881 Å in GaN (see table 2.1). This allows us to define the "fractional mismatch" $f$ between an epitaxial layer $e$ deposited on top of a substrate $s$ using their interatomic distance $a$ as [164]:

$$f = \frac{a_e - a_s}{\frac{a_e + a_s}{2}} \tag{5.1}$$

Generally, one needs $f < 0.1$ for a good epitaxy, where we obtain $f = 0.0809$. If epitaxy is achieved, the GaN layer will undergo some stress proportional to this fractional mismatch but should stay epitaxial. See figure 5.25 for better visualisation of the possible epitaxy between the two materials.

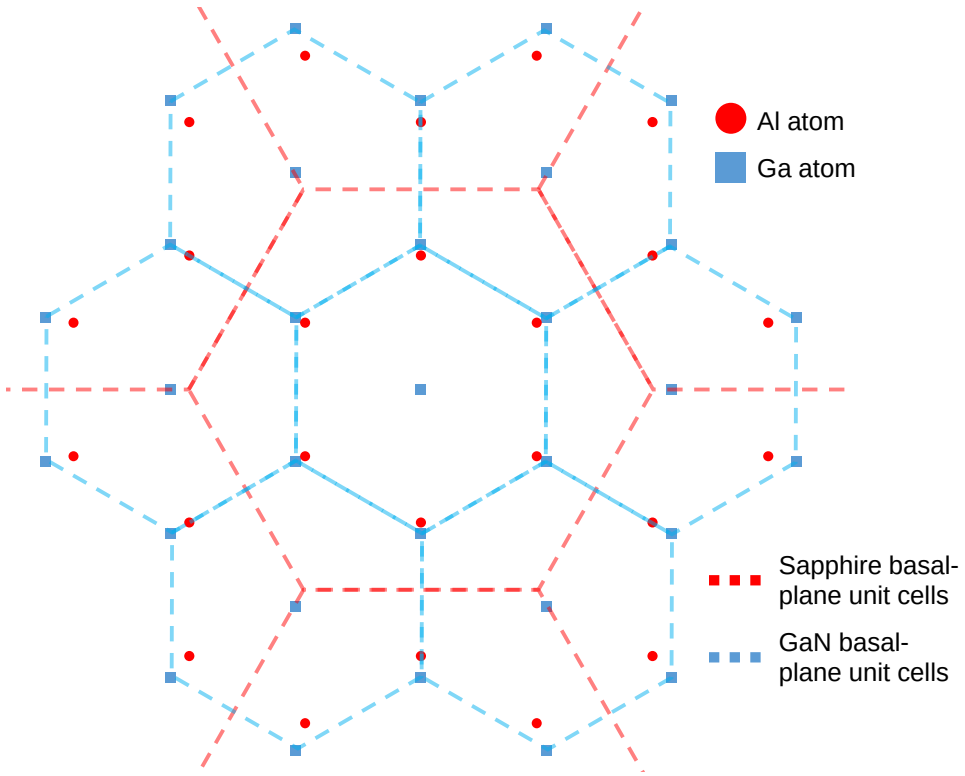


Figure 5.25: PVD GaN(Si) on Sa, epitaxy: sapphire and GaN epitaxial relationship: atoms and unit cell of the two materials. The matching is not perfect.

Because of that compatibility, sapphire is an excellent material on top of which GaN can be grown epitaxially and form large crystals that will decrease the defect density, thus improving the overall quality of the material. This section then presents the effect of silicon doping on the structure of a GaN layer sputtered on a (001) sapphire substrate at low temperatures. Four layers were probed: one with intrinsic GaN and the others increasingly doped with silicon.

### 5.4.2 Basic characteristics

Four layers were deposited in similar conditions of co-sputtering, except for the silicon doping. The power on the GaN target was set to $150 \pm 0.1$ W, at a temperature of $300 \pm 2$ °C and a pressure

of $1.00 \pm 0.02\,\mu$bar. The gas mixture was composed of argon ($50 \pm 0.3$ sccm) and nitrogen ($25 \pm 1$ sccm) for the doped layers, and only $25 \pm 1$ sccm of $N_2$ for the undoped layer. The silicon target was etched with powers of 0, 50, 100 and $200 \pm 0.1$ W. The layers were deposited on both sapphire and glass. After the deposition, these four layers were characterised, annealed, and characterised again. The annealing process occurred at $600 \pm 5\,°$ for 15 minutes $\pm 1$ s under nitrogen atmosphere.

The thickness of the layers was characterised by ellipsometry on silicon, their optical properties by spectroscopy on glass (note that their crystallinity differs than with the sapphire substrate, results not shown here), their electrical properties by dark lateral conductivity and their crystallography by XRD on glass and sapphire. Some of these basic characterisations were performed before and after annealing at $600 \pm 5\,°$C during fifteen minutes and under $N_2$ atmosphere, and all the results are summarised in table 5.3. Better visualisation and understanding can be achieved with visible results in figure 5.26.

Table 5.3: PVD GaN(Si) on Sa, epitaxy: synthesis of the basic characteristics of the GaN layers as deposited and after annealing. Each was doped with silicon, its concentration depending on the power used for the sputtering process. The (101) crystallite size for the undoped layer could not be fitted.

| | | Physical quantity | Unit | Silicon target power ±0.1 W | | | |
|---|---|---|---|---|---|---|---|
| | | | | ①, 0 W | ②, 50 W | ③, 100 W | ④, 200 W |
| | Thickness | | ±10 nm | 179 | 269 | 284 | 312 |
| As deposited | Optical | $E_{04}$ | ±0.03 eV | 3.04 | 3.16 | 3.18 | 3.20 |
| | | $E_T$ | ±0.03 eV | 3.27 | 3.34 | 3.44 | 3.46 |
| | | $E_U$ | ±4 meV | 240 | 250 | 340 | 420 |
| | Electrical | $\rho$ | ±0.001 % Ωcm | $3.0 \cdot 10^8$ | 37 | 14 | $2.8 \cdot 10^5$ |
| | | $E_A$ | ±0.001 % meV | 593 | 36 | 29 | 268 |
| | Structural | 002 *CrSz* | ±0.01 nm | 48.16 | 15.21 | 12.58 | 11.02 |
| | | 101 *CrSz* | ±0.01 nm | 0? | 15.09 | 27.93 | 55.99 |
| Annealed | Optical | $E_{04}$ | ±0.03 eV | 3.12 | 3.21 | 3.24 | 3.31 |
| | | $E_T$ | ±0.03 eV | 3.29 | 3.30 | 3.38 | 3.51 |
| | | $E_U$ | ±4 meV | 190 | 150 | 230 | 340 |
| | Electrical | $\rho$ | ±0.001 % Ωcm | $6.3 \cdot 10^8$ | 13'000 | 1'300 | $2.2 \cdot 10^8$ |
| | | $E_A$ | ±0.001 % meV | 604 | 217 | 226 | 572 |

Here are the changes observed under an increasing power applied for the etching of the silicon target during the sputtering process:

- Increase of the two types of BG: optical $E_{04}$ and the one extracted from the Tauc plot $E_T$,
- Increase of the Urbach energy ($E_U$), which means more defects
- Strong increase of the FCA above 100 W of power,

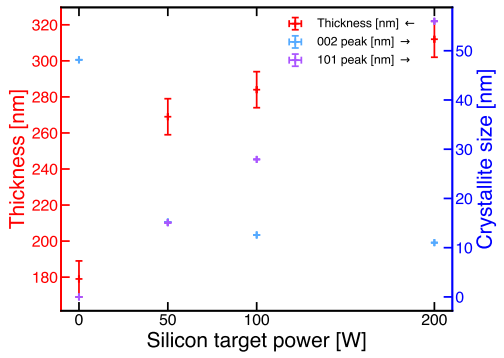


(a) Structural properties of the PVD GaN doped layers. The (101) crystallite size for the undoped layer could not be computed and is here extrapolated.

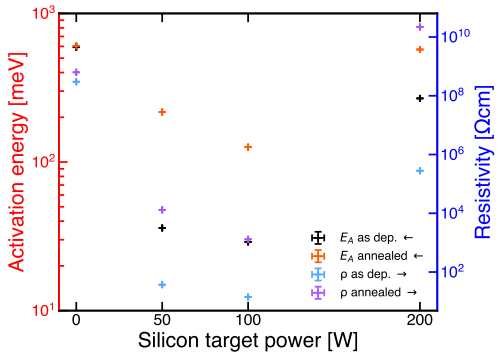


(b) Electrical properties of the PVD GaN doped layers deposited on a silicon substrate.

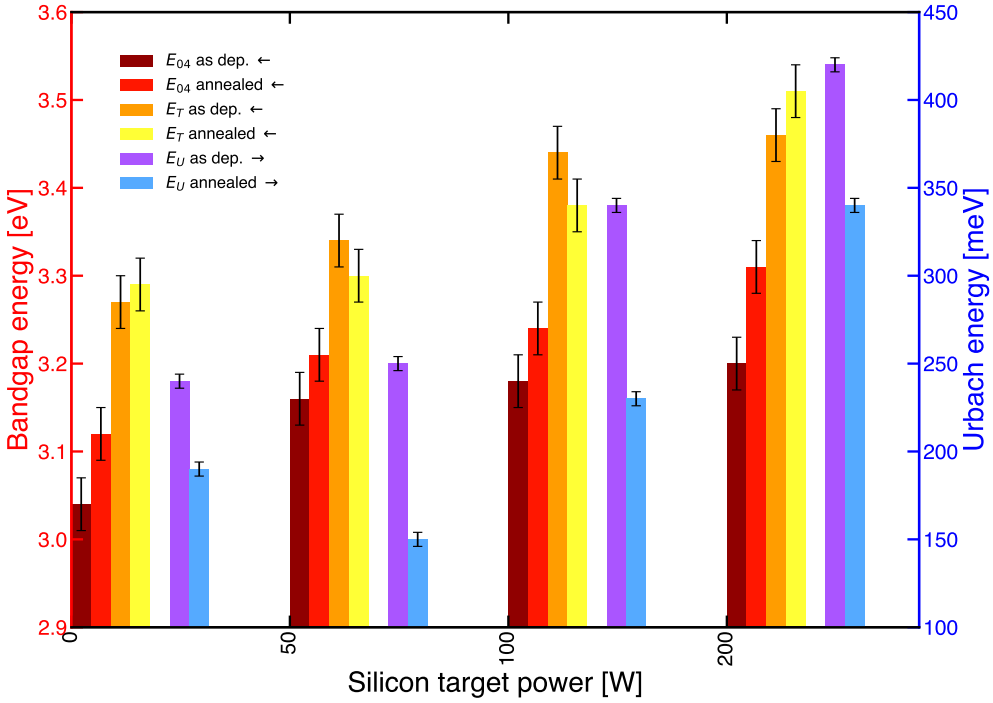


(c) Optical properties of the PVD GaN doped layers deposited on a glass substrate.

Figure 5.26: PVD GaN(Si) on Sa, epitaxy: structural, electrical and optical properties of the doped GaN layers deposited by sputtering, as a function of the power applied on the silicon target.

- Lowest activation energy and resistivity found between 50 and 100 W,
- Disappearance of the (002) preferential orientation and crystallite size in favour of a more randomised arrangement and orientation of crystals.

The annealing also has some effect on the doped GaN layers:

- Increase of the two types of BG (where the BG extracted from the Tauc-plot is always inferior to $E_{04}$, see section 3.2.2.4),
- Decrease of the Urbach energy, which means fewer defects,
- Deterioration of the electrical properties: increase of the activation energy and the resistivity. Regarding the undoped layer: a substantial increase in the free carrier concentration but increased mobility.

### 5.4.3 TEM study

After these first results, TEM lamellae of layers ① and ③ were prepared by FIB, and TEM and TKD analyses were performed. The lamella preparation required an Al protective layer to preserve the top layers of interest during the milling by gallium ions.

First of all, the TEM allowed for an EDS measurement, where less silicon than the detector limit was observed in layer ①, and about 1 % in layer ③. The GaN layer is expected to be stoichiometric, but due to the beam of gallium atoms used by the FIB, a higher proportion of gallium is found inside the GaN layer. Table 5.4 summarises these results. As EDS measurements are less reliable for lighter elements (such as nitrogen), the conclusion on the stoichiometry of the GaN layer is to accept it with a grain of salt. This unreliability is also visible when observing the carbon content of both layers, where both display strange results: one is overshooting while the other does not seem to contain any.

Table 5.4: PVD GaN(Si) on Sa, epitaxy: EDS characterisation of two layers. There is about 1 % of silicon in layer n° ③ and more gallium than nitrogen in both layers because of the milling process in the FIB. EDS values are precise within a ±1 % absolute error margin.

| Layer | C | $n$ | O | Si | Cu | Ga | Ga:N |
|---|---|---|---|---|---|---|---|
| ① | 58.9 | 10.4 | 3.0 | 0.2 | 4.8 | 22.7 | ~ 60 : 40 |
| ③ | 0 | 32.2 | 7.1 | 1.1 | 7.2 | 52.4 | ~ 70 : 30 |

The interface between the cleaned sapphire substrate and the GaN layer can be analysed in figure 5.27. An excellent epitaxy is achieved with layer ①, slightly visible thanks to the broad horizontal lines originating from the interface but visible on the related diffraction pattern (figure 5.27c): the c-axis of the sapphire substrate and the GaN layer are both aligned. On the other hand, the GaN crystallites in layer ③ look significant but seem orientated more randomly. This is also visible in the associated diffraction figure, where for layer ①, the epitaxy is visible: the two c-axis are perfectly aligned, and there is no parasitic diffraction point that would come from a randomly orientated crystal. As for layer ③, the randomness is present and reflected by ring patterns, implying random directions of the c-axis of the GaN crystal with respect to the sapphire substrate. This comparison is the first proof that adding silicon to the deposition process, even slightly, will disrupt the equilibrium of the grain growth birthing at the interface.

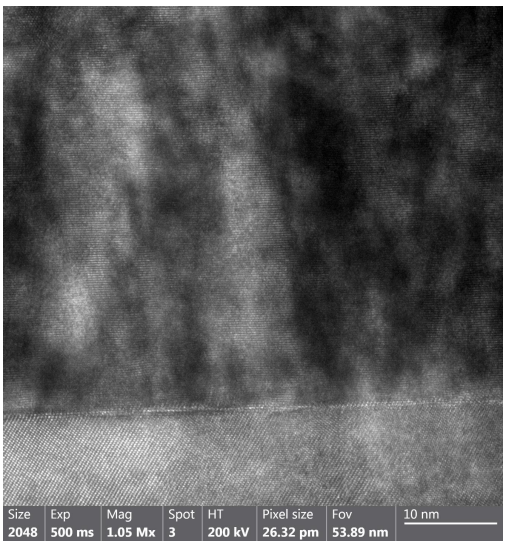


(a) HRTEM micrograph, interface of layer ①.

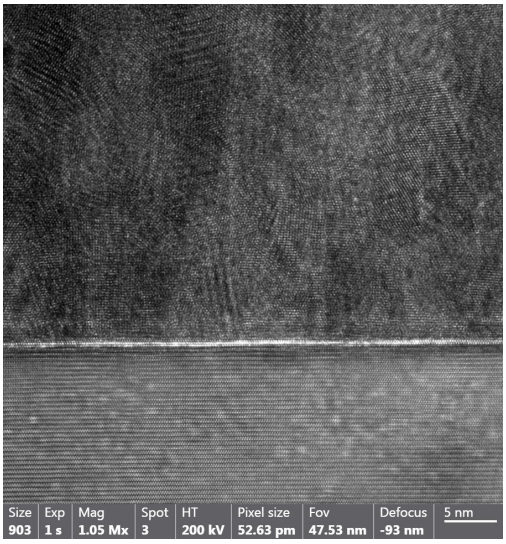


(b) HRTEM micrograph, interface of layer ③.

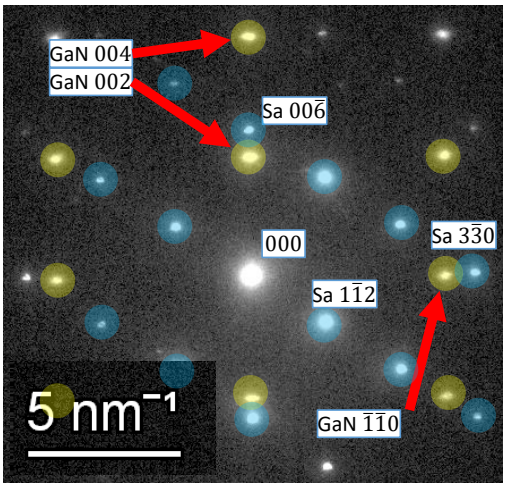


(c) Diffraction pattern and reflection identification, layer ①. The blue semi-transparent dots are sapphire reflections; the yellow ones are GaN reflections.

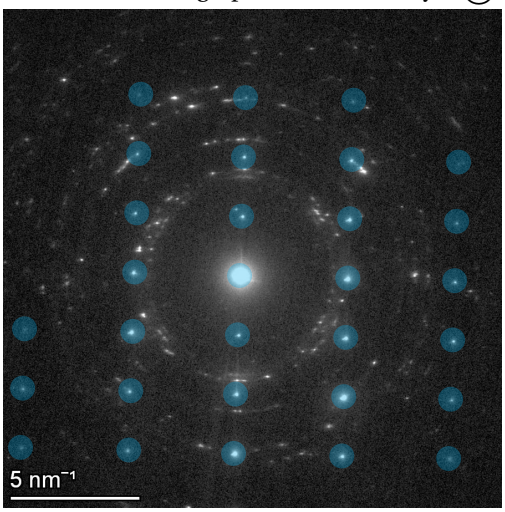


(d) Diffraction figure and reflection identification, layer ③. The blue semi-transparent dots are sapphire reflections, and the circular patterns are reflections of GaN crystallites randomly orientated.

Figure 5.27: PVD GaN(Si) on Sa, epitaxy: HRTEM micrographs and their associated diffraction patterns of the GaN-Sa interfaces of the undoped and one doped layers. The sapphire substrate (bottom of each HRTEM picture) allows for an excellent GaN epitaxy when the dopant is absent.

The TEM analysis was pushed further for both layers. Still, since layer ① was highly epitaxial, the excellent results were straightforward and explanatory enough with what is presented in figures 5.27a and 5.27c. Indeed, the lower energy state for the GaN adatoms was to align their c-axis along the sapphire's c-axis. See appendix B.3.4 for one dark field image of layer ①. For

layer ③, however, see figure 5.28 extracted using both a selected area electron diffraction (SAED) and a narrower objective aperture.

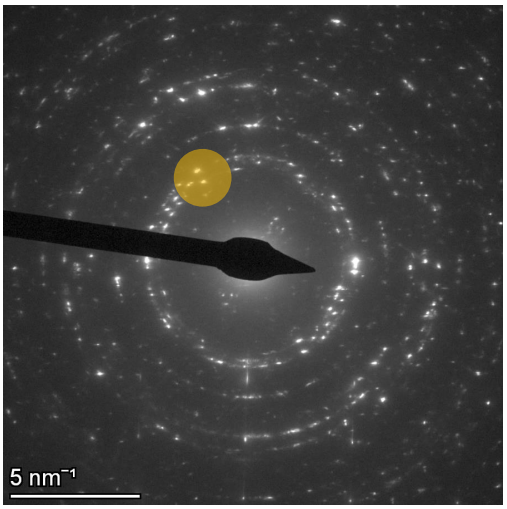


(a) Diffraction figure and dark field spot.

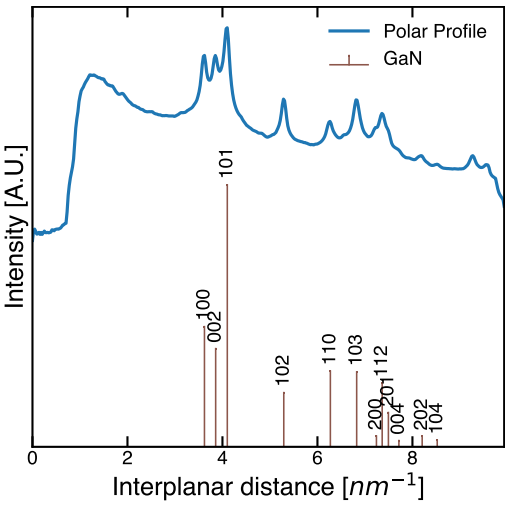


(b) Polarised profile of the diffraction figure.

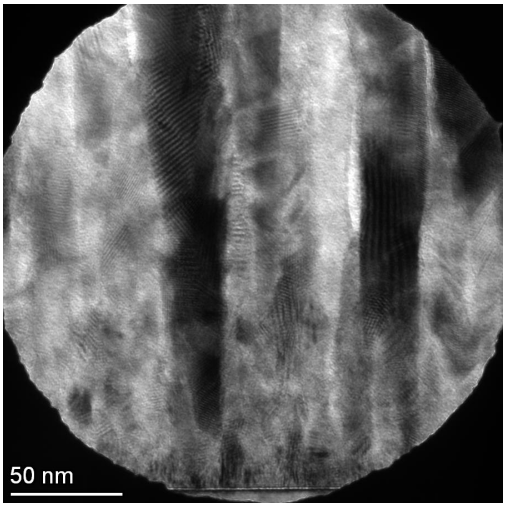


(c) Bright field image.

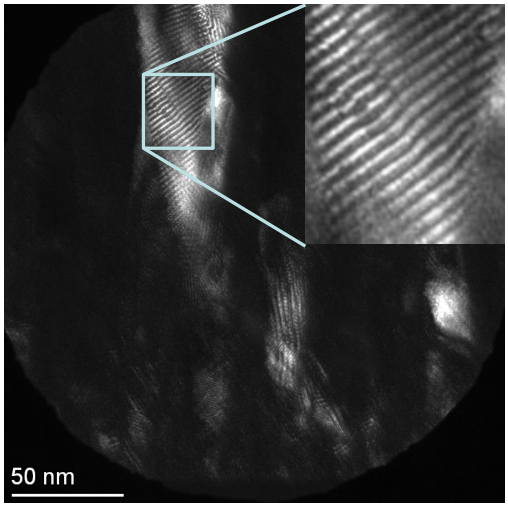


(d) Dark field image, extracted from selected spot in figure 5.28a.

Figure 5.28: PVD GaN(Si) on Sa, epitaxy: deeper TEM analysis of the doped GaN layer.

Part of the electron beam still passes through the sapphire substrate (small line at the bottom of the bright field image, figure 5.28c), and some electrons diffracted by the sapphire substrate still appear in the diffraction pattern (figure 5.28a), but with a far smaller intensity thanks to the narrower selected area aperture; only the randomly oriented GaN reflections remained. The obtained bright field image is shown in figure 5.28c by placing the objective aperture on the transmitted electron beam. The black areas are highly diffracting electrons, proving the presence of highly ordered crystals. From this image alone, we can see a classical growth of the crystalline layer. There are first some unordered nucleation points at the interface, where the growth direction will naturally select the most accessible crystal orientation for the adatom

arrangement. This will eventually lead to columnar-like structures, where the angular opening of the cones depends on the deposition conditions and crystal characteristics [189, 104].

By de-polarizing the diffraction pattern and simply summing all the intensity by radius length, a polarised profile of the diffraction could be obtained (figure 5.28b), which in substance is similar to an XRD profile. Suppose we capture a dark field image instead of a bright field image by moving the objective aperture on the orange circle. In that case, the obtained dark field is shown in figure 5.28d, and the crystals visible here in white can be identified as either one or a combination of these three orientations: (100), (002), (101). In particular, a Moiré pattern appears at the top of the crystal (in the zoomed-in frame). These fringes appear because of the interference of diffracting crystal lattice planes that are overlapping and which might have different spacing and orientation. Here, since the orientation of the crystal is random and there are three possible orientations, further identification of the orientation and implied diffraction sounds difficult. However, the Moiré fringes reveal another feature of that particular crystal: a stacking fault, starting in the middle of the framed zoom-in and going northwest. The stacking fault in such crystals can appear due to different sources: either during growth or after it, because of too high stress on the overall crystal structure or the cool-down after taking the sample out of the deposition chamber, etc.

### 5.4.4 TKD study

See section 3.2.3.3 for a deeper understanding of TKD and EBSD.

The undoped layer probed by TKD shows interesting features, where here again, the epitaxy of the layer is visible: the grains that are started at the interface retain the orientation of the sapphire substrate along their growth but not across the whole layer (see figure 5.29b). Indeed, after reaching a certain height, a new GaN crystal with a different orientation stems from the epitaxial ones, and the growth continues perpendicularly to the interface. This is mainly due to the growing concentration of faults in the crystal, such as dislocations, vacancies, etc. These mainly originate because of the stress in the ever-increasing epitaxial GaN layer, which makes the growth less and less energy favourable for the adatoms to continue to assemble epitaxially. A thinner layer would carry more stress but fewer randomly oriented crystals. As already observed by TEM, the grains are elongated and span almost the whole thickness of the layer. They are about 80 nm thick.

A small charging effect could not be avoided during the acquisition process of the TKD maps of the doped layer ③. This is visually corrected in the post-processing phase, hence the bent images in figure 5.30. However, the green crystal of figure 5.30b representing the sapphire is supposed to have its c-axis perpendicular to the interface (like in figure 5.29b). This means that this charging effect may also have impacted the EBSD acquisition, and these results are to take with a grain of salt.

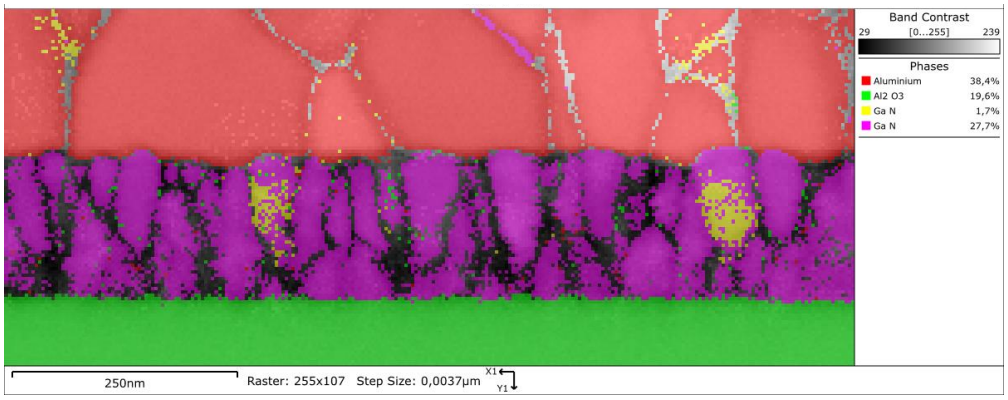


(a) TKD phase map: sapphire substrate at the bottom, GaN layer in the middle, aluminium protective layer on top. The yellow spots correspond to a bad signal assignment to cubic GaN.

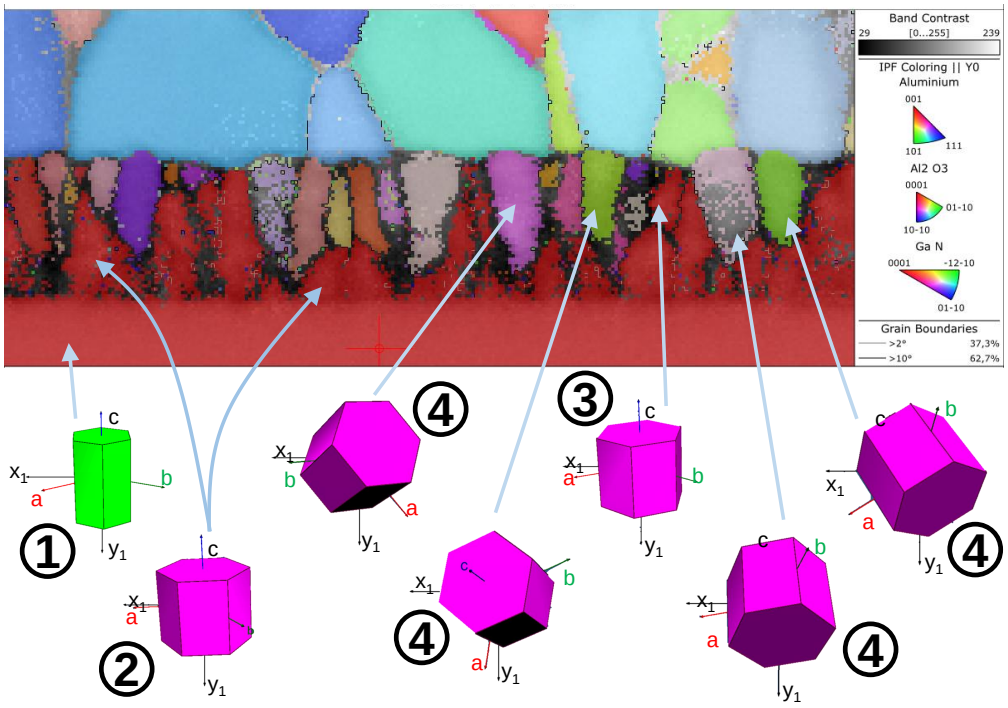


(b) TKD inverse pole figure: orientation. Crystal n° 1 is the sapphire substrate, crystals n° 2 are epitaxial with the sapphire substrate and align perfectly along the c-axis of the unit cell, crystal n° 3 can also be considered epitaxial (same orientation of the c-axis) but with a 15° rotation with respect to the GaN crystal below it (probably a stacking fault), crystals n° 4 are randomly orientated GaN crystals.

Figure 5.29: PVD GaN(Si) on Sa, epitaxy: TKD study of the undoped GaN layer: phase and orientation maps.

In contrast with the undoped layer, we can see here that no epitaxial GaN crystal stems from the interface. On the contrary, columnar structures seem to appear in the middle of the growth and their orientation is usually maintained along the rest of the thickness. The nucleation

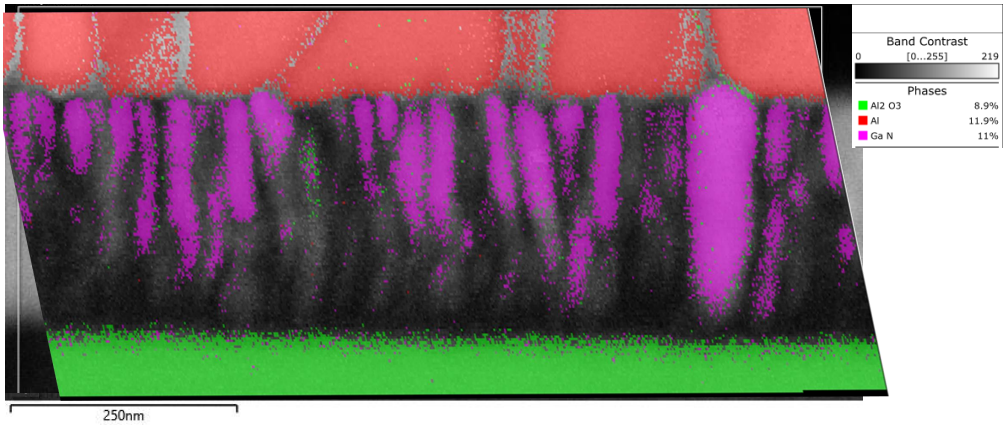


(a) TKD phase map: sapphire substrate at the bottom, GaN layer in the middle, aluminium protective layer on top.

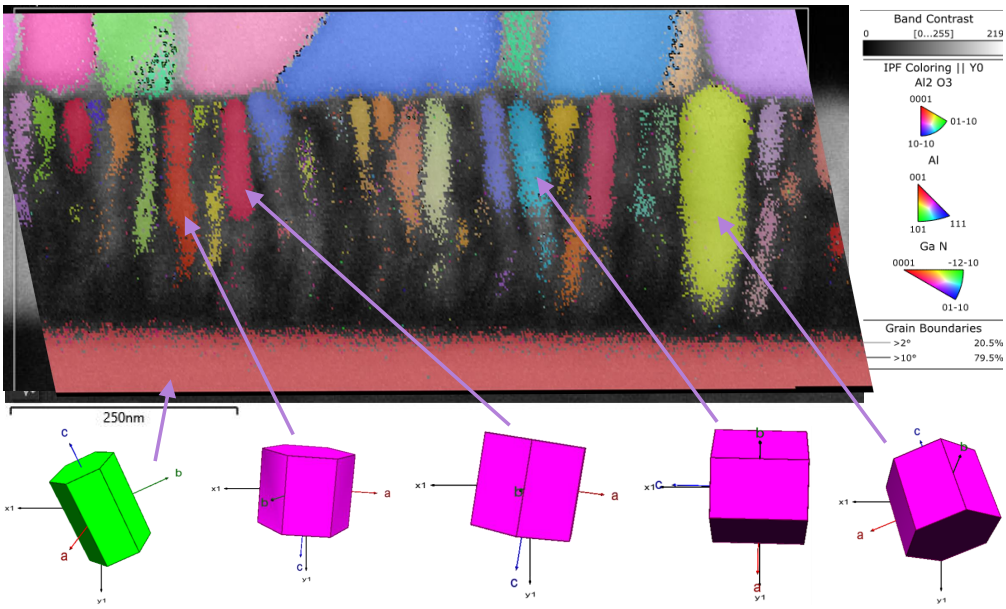


(b) TKD inverse pole figure: orientation. The green unit cell on the far left represents the sapphire substrate orientation, and the other purple ones represent the randomly oriented GaN crystals.

Figure 5.30: PVD GaN(Si) on Sa, epitaxy: TKD study of the doped GaN layer: phase and orientation maps. A strong charging effect during the imaging acquisition may induce some errors in the data processing; for example, the c-axis of the sapphire substrate is supposed to be perpendicular to the interface.

centres are also visible at the bottom of each identified crystal. This means that the GaN matrix above the interface was not epitaxial, as already observed by TEM, but the layer remains highly crystalline. Compared to the undoped layer, these crystals are substantially thinner but have about the same length.

### 5.4.5 GaN epitaxy on sapphire: key takeaways

In conclusion, the optical and electrical properties are acceptable, even for highly doped layers. The crystallinity on sapphire is exceptionally high due to the close lattice matching, especially without silicon doping. The (002) texturisation of the undoped layer changes to a preferential (101) orientation with increasing silicon content. The electrical properties are acceptable for device integration, especially at $100 \pm 0.1$ W. And there is a trade-off with the annealing: it improves the optical properties while deteriorating the electrical properties.

Another key takeaway point here is that for layer n° 3, the lowest energy state during the nucleation of the doped GaN layer did not allow for a good epitaxy (as shown in all the small black areas at the bottom of figure 5.28c). And since the two layers were grown in almost identical conditions, this can only be due to either the presence of the silicon dopant or maybe because of the presence of argon in the gas mixture for the sputtering process producing layer n° 3 (but that is less likely). Further optimisation of the process with dopants has to be undertaken to achieve a perfectly epitaxial layer on sapphire finally.

## 5.5 Effects of the indium content on the layer characteristics

This experiment is a collaboration with Julie Dréon, another *Ph.D.* student at PV-lab, who was working on $MoO_x$ contacts.

### 5.5.1 Motivation

As already seen, InN has a small BG, but is a degenerated material ($N_D \approx 10^{21}\,\mathrm{cm}^{-3}$) with high conductivity. On the other hand, GaN has a wide BG but is so resistive that its electron concentration is difficultly quantifiable. The idea of this section is to explore the possibility of combining the two materials (hence, InGaN) and have both of the good properties of the two: a wide BG with high conductivity. That material could then be an electron contact in a solar cell (concept further developed in section 6.3).

The results presented here are part of a three-step experiment. The first step uses only a single InGaN target deposited on a glass wafer, a polished silicon wafer and TEM grids, with rotation of the sample holder for uniform deposition. After selecting the best layer, the second step involves co-sputtering on the same substrates and textured solar cells without rotation. This was deemed problematic (see figure 5.33 for the two problems encountered) and is not presented here. Still, a second try – third step – was undertaken where the solar cells were built on flat silicon wafers, and the mask was used after, for the indium tin oxyde (ITO) layer. Again, the term "indium content" $X_{\mathrm{In}}$ refers to the atomic indium percentage relative to all the III-materials within the layer $X_{\mathrm{In}} = \frac{\mathrm{In}}{\mathrm{In+Ga}}$ (In & Ga in at. %, $X_{\mathrm{In}}$ in %).

### 5.5.2 Single InGaN target

The first test batch was used to find optimal deposition parameters for a deposition process we did not fully master yet. It only used an $In_{50}Ga_{50}N$ target that was sputtered at different powers and temperatures with the rotating sample holder for homogeneous depositions on a polished silicon wafer, a glass wafer, and TEM grids. Ellipsometry and spectroscopy characterised the optical properties, the Hall effect performed electrical measurements, XRD assessed the layer crystallinity. The results of these characterisations are displayed in table 5.5, and those values are extracted from the different tools, some of which are presented in figure 5.31.

Table 5.5: PVD InGaN: first experimental results extracted from different tools. "Dep." stands for "Deposition", "Ellipso" stands for ellipsometry, and "Si" and "Gl" refer to the silicon and glass substrate respectively.

| | Layer | ① | ② | ③ | ④ | Error |
|---|---|---|---|---|---|---|
| Dep. | Po [W] | 150 | 75 | 150 | 75 | 0.1 |
| | T [°C] | 25 | 25 | 300 | 300 | 2 |
| | t [min] | 17.6 | 49 | 17.6 | 49 | 5 s |
| Ellipso Si | $n_{633}$ [−] | 2.493 | 2.465 | 2.501 | 2.432 | 0.01 |
| | $E_{04}$ [eV] | 1.537 | 1.635 | 1.538 | 1.921 | 0.03 |
| | *Thk* [nm] | 101.51 | 107.98 | 42.13 | 91.85 | 10 |
| | *g* [nm/min] | 5.77 | 2.20 | 2.39 | 1.87 | 10 % |
| Ellipso Gl | $n_{633}$ [−] | 2.475 | 2.364 | 2.420 | 2.408 | 0.01 |
| | $E_{04}$ [eV] | 1.471 | 1.517 | 1.774 | 1.752 | 0.03 |
| | *Thk* [nm] | 93.59 | 113.16 | 45.87 | 84.72 | 10 |
| | *g* [nm/min] | 5.32 | 2.31 | 2.61 | 1.73 | 10 % |
| Spectro | $E_T$ [eV] | 1.554 | 1.608 | 1.413 | 1.805 | 0.03 |
| | $E_{04}$ [eV] | 1.572 | 1.453 | 1.905 | 2.044 | 0.03 |
| | $E_U$ [meV] | 374.5 | 272.5 | 338.6 | 191.9 | 4 |
| Hall | $\rho$ [Ω cm] | - | $9.61 \cdot 10^{-3}$ | $2.75 \cdot 10^{-2}$ | $1.61 \cdot 10^{-3}$ | 0.1 % |
| | $N$ [cm$^{-3}$] | - | $1.80 \cdot 10^{20}$ | $1.02 \cdot 10^{20}$ | $2.00 \cdot 10^{20}$ | 0.1 % |
| | $\mu$ [cm$^2$/Vs] | - | 3.8 | 2.9 | 13.0 | 0.1 % |
| XRD | *CrSz* [nm] | - | 18.11 | 12.36 | 11.16 | 0.01 |
| | $X_{In}$ [%] | - | 59.8 | 62.3 | 81.1 | 0.5 |

Given these results, layer ① was discarded because it was not crystalline and too resistive to extract any results from the Hall effect setup. Layer ④ was the next one to be discarded, also because of the XRD results: the (002) InGaN peak is almost entirely InN (see the purple peak in figure 5.31b), with the smallest grain size. This may signify phase separation, where some InN is mixed within the InGaN layer. The indium content $X_{In}$ is expected to be closer to 50 % since that is the indium content of the target. That is why layer ② is selected for the next step: the indium content the closest to 50 %, the largest crystallite size, and better Hall characteristics

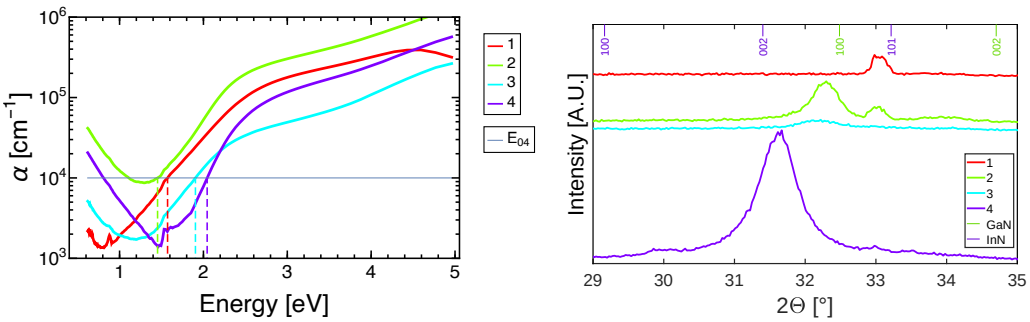


(a) Absorption coefficient from the spectrometer measurement for layers deposited on a glass substrate.

(b) XRD (002) peak for layers deposited on a silicon substrate.

Figure 5.31: PVD InGaN: XRD and spectroscopy results of the first experiment.

than layer n° 3, a sharper band edge (see $E_U$), and the closest agreement between the optical bandgaps given by the ellipsometer measurements on glass or by the spectrometer.

The origin of the indium-richer layer compared to the target is yet unknown. Either indium is more easily sputtered than gallium, or gallium is more easily captured and randomly diffused by the surrounding plasma, or gallium sticks less to the substrate, or there is a phase separation inside the layer, or there might even be another reason. This is also observed by EDS (see next section) and could be the subject of future research.

### 5.5.3 Co-sputtering

The indium content $X_{\mathrm{In}}$ will affect the layer characteristics. To test $X_{\mathrm{In}}$, the Univex was set according to figure 5.32 without rotation to have an indium content gradient, using different substrates for testing (glass wafer, double-side polished silicon wafer, TEM grids, and solar cells), based on sample 2 from the previous experimental batch. This is the second step of the experiment, where the solar cell results are discussed in section 6.3 while the layer results are discussed here.

From the start, co-sputtering on a textured solar cell yielded no reliable result because of the two problems mentioned in figure 5.33. Both can be attributed to the directional deposition feature of the sputtering process. For this reason, the experiment was redone with the same setup but using flat solar cells without mask – called the third step. The sample holder was large enough to hold two half absorbers (one p-doped, one n-doped) on which the InGaN contact was deposited. See section 6.3 for more details on the solar cells. Three sputtering setups were tested (GaN target only, $In_{50}Ga_{50}N$ target only, and co-sputtering with the two targets), with two different deposition times (expected median thicknesses: 10 and 50 nm, referred to as “thin” and “thick” respectively). This means that there are six different setups: co-sputtering InGaN-GaN (thick and thin depositions), single InGaN target (thick and thin depositions), and single GaN target (thick and thin depositions). The sample holder was again

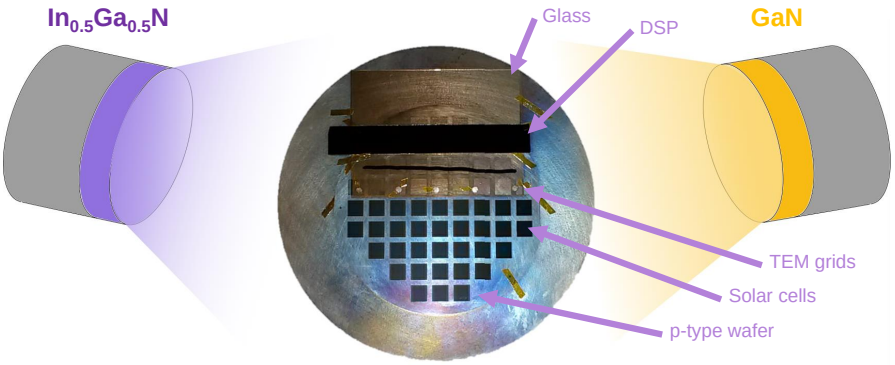


Figure 5.32: PVD InGaN, co-sputtering, indium content gradient on different substrates: glass wafer, double-side polished silicon wafer, five TEM grids, and solar cells. See figure 5.33 for more details on why the solar cells were unusable.

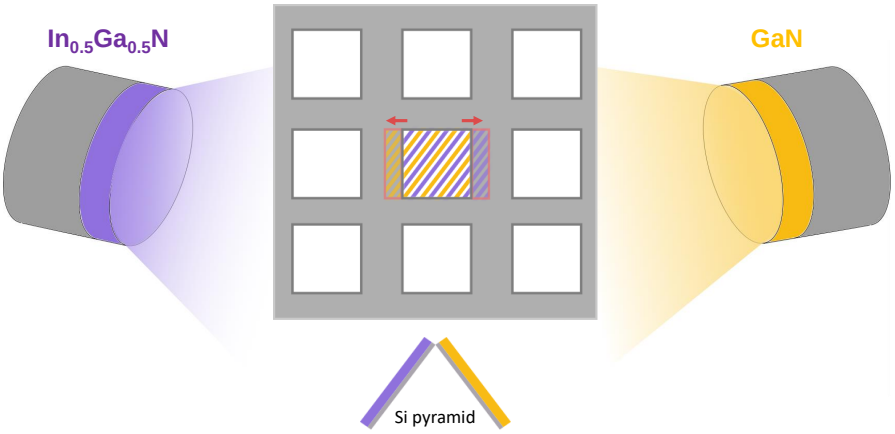


Figure 5.33: InGaN PVD co-sputtering on solar cells. 1st problem: the mask induced some shadowing only due to its thickness, the slight gap between the mask and the cell, and the incident angle difference originating from the two targets. 2nd problem: the non-rotation of the sample holder induced a different composition on each face of each pyramid of the textured solar cells.

not rotating to allow for a gradient of thickness or indium content and was large enough to include silicon and glass reference substrates.

For the basic characterisations, the flat substrates were separated into twelve zones on which only localised measurements on the three thick depositions were performed. Only the thick depositions were used for characterisation because of the inaccuracy of the optical tools with a reduced thickness; ellipsometry typically has a hard time measuring precisely layers' characteristics below 20 nm. The results are presented in figure 5.34. In figure 5.34a, only the values for the co-sputtering setup are shown. For the two other figures, the three setups are presented simultaneously, where the respective placement of each target is signified at the corner. Note that the ellipsometry results are less reliable when the measured layer has

a thickness below 20 nm, hence the semi-transparent part of the curves in the two bottom figures.

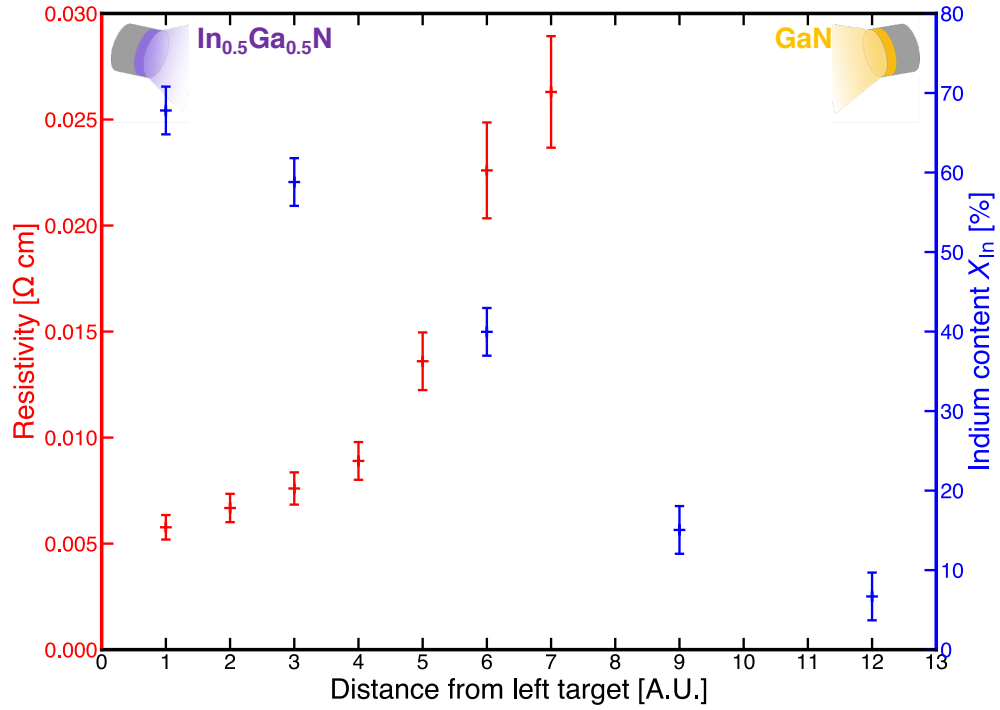


(a) Indium content (co-sputtering mode) and resistivity for the single sputtering deposition using only the InGaN target for layers deposited on a silicon substrate.

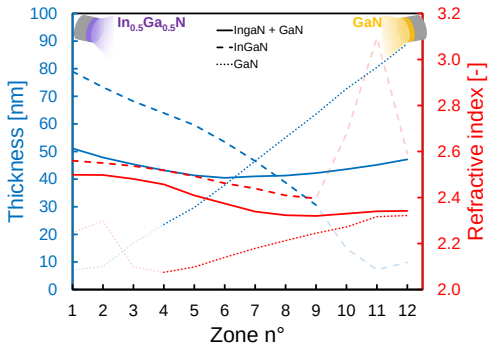


(b) Thickness and refractive index for layers deposited on a glass substrate.

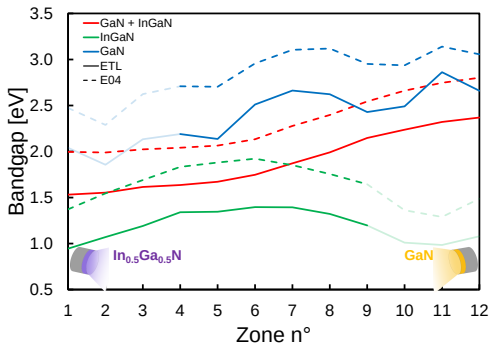


(c) Tauc-Lorentz and optical bandgaps for layers deposited on a glass substrate.

Figure 5.34: PVD InGaN, co-sputtering: indium content, resistivity, ellipsometry Tauc-Lorentz and optical bandgap, ellipsometry thickness and refractive index $n_{633}$. The lack of sample holder rotation allowed a gradient (in thickness for single target deposition, in indium content for co-sputtering). Please consult the end of section 3.2.2.4 for a reminder on the difference between the T-L and the optical BGs. No error bars are shown in figures b and c to help with readability: the thickness has an uncertainty of ±10 nm, the refractive index of ±0.01, and the two BG types of ±0.03 eV.

As expected, the indium content $X_{\mathrm{In}} = \frac{\mathrm{In}}{\mathrm{In+Ga}}$ (In & Ga in at. %, $X_{\mathrm{In}}$ in %, figure 5.34a, extracted using EDS) decreases when approaching the GaN target and getting away from the InGaN target. The indium content of the region that is the closest to the InGaN target is just less than 70 %, and just less than 10 % more than what was determined by XRD in the first batch (see figure 5.31b). This proves that the XRD measurement and post-processing were not ill-calibrated. Since the material does not change for the sputtering with only the InGaN target, the resistivity is not expected to increase. It underlines a change in the material that could not be identified: the indium content, the thickness, the crystal structure, or something else. After zone n° 7, the layer becomes too thin, and the resistivity cannot be measured by the 4-PP tool. Still, for the ones that we could measure, we find here resistivities that are comparable to the first experimental batch but above literature values, which might become the limiting factor for an electron selective contact in a solar cell.

The three thicknesses of the three "thick" depositions behave as expected: thinner when far from the target in a mono-target deposition and flat for the co-sputtering setup. The thickness of 50 nm aimed for in the middle of the substrate is reached; it is a satisfying and reassuring result because this parameter is well-controlled. The refractive index being an indirect measurement of the density of the layer [112], we see here that the matter deposited close to the target is denser than at the furthest point for the two simple sputtering depositions. Referring to table 2.1, GaN is expected to have a value of 2.50, and 2.95 for InN; here the values are slightly lower than that, meaning that the three layers are not perfectly well-packed. For the co-sputtering deposition, a decrease of the refractive index with decreasing indium content is expected and observed.

Analysing figure 5.34c, the BGs are expected to be proportional to the indium content $X_{\mathrm{In}}$ for the co-sputtered deposition (observed). Following Vegard's law, the expected proportionality should be quadratic, but the values were not precise and reliable enough to assert such a relationship. For the two single sputtering depositions, the BGs are expected to remain constant, which is sadly not observed here, and this unexpected behaviour is not explained without difficulty. For the GaN target alone, maybe there is an effect of the thickness or of the distance from the target, where the matter deposited far from the target is less dense and with more defects, which will be reflected in a decreased optical BG. However, that reasoning does not hold with the BG obtained using the single InGaN target, wherein the zones close to the target are even lower than the selected layer of the first experimental batch.

### 5.5.4 PVD InGaN: key takeaways & next steps

At first, four layers were deposited to probe the temperature and power influence. The best layer was selected for the next step, where co-sputtering and single sputtering were performed without spinning the sample holder. Almost all the layer characteristics behave as expected, and the extracted values were within acceptable ranges, even though the lowest recorded resistivity is still two orders of magnitude higher than the one of the standard (n) a-Si:H layer

usually used as a selective electron contact in solar cells. The question asked in the motivation section is thus answered: it seems possible to "mix the two good properties of the two materials into one", where a wide BG with an acceptable resistivity was obtained. The six depositions performed in the last step of this study were also integrated into a total of twelve solar cells, which are reported in section 6.3 and whose J-V curves are analysed there. However, since the resistivity value will be the limiting factor, we can expect that the thinnest layers with the highest indium content may be the most efficient.

This experiment could be pushed further, aiming to reduce resistivity even more. In the first batch's spectroscopic measurements, there is still some FCA and a not-satisfying Urbach energy; both should be reduced to a minimum for better optical properties. The crystallinity is also poor, given the crystallite size extracted from the XRD, and it could also be improved. This may be achieved with additional Ge- or Si-doping of the layer (a co-sputtering with three targets), maybe by annealing the layers for a better dopant activation or with a lower growth rate. A higher temperature is expected to favour a better crystallinity, and it would also be worth understanding why that was not the case in the first batch of the present experiment.

## 5.6 PVD results: Wrap-up and conclusions

In the first section, the strong influence of the pressure was highlighted, where a low pressure could lead to high crystallinity but low transparency compared to high pressure. A better optical quality material is found at high pressure because of the reduction of ion bombardment on the substrate, which results in fewer surface defects. Substrate temperature and deposition pressure considerably influenced adatom mobility, growth rate, preferential orientation, morphology and film density. The best conditions with germanium doping allowed to reach a relatively good resistivity of $2.3 \pm 0\,\Omega$ cm and an activation energy of $50 \pm 0$ meV, but the Ge atomic content of the layer reached $10 \pm 3$ %, a sign of a lousy dopant activation. With silicon doping, on the other hand, a lower dopant concentration of $4.2 \pm 0.4$ % could lower the resistivity to only $15 \pm 0\,\Omega$ cm with an activation energy of $60 \pm 0$ meV.

Epitaxy on sapphire was achieved, due to the close lattice matching, especially without silicon doping. The (002) texturisation of the undoped layer changes to a preferential (101) orientation with increasing silicon content. Increasing the indium content $X_{\mathrm{In}} = \frac{\mathrm{In}}{\mathrm{In+Ga}}$ (In & Ga in at. %, $X_{\mathrm{In}}$ in %) of the layer decreases the resistivity, but still to values at least two orders of magnitude greater than the standard (n) a-Si:H layer used in solar cells.

Sadly, because of time constraints, no DOE was performed on all or part of the layers deposited by PVD. It will, however, be the subject of a later study that will lead to the publication of an article in collaboration with Julien Hurni. The germanium doping study still has some open questions that were not explored, such as the influence of the deposition power linked to the pressure and the effect of different Ar:$N_2$ ratios in the sputtering gas on the layer properties and doping performances. This can be the subject of a subsequent study.

The layers fabricated with PVD sputtering have suitable enough properties to be integrated into a solar cell, even though losses in crystallinity and conductivity when doped may lead to a worse cell performance than cell performances using a-Si:H contacts. Increasing $X_{\mathrm{In}}$ helps in that regard but with worse performances than the already known (n) a-Si:H layer (if contact is considered). This is developed in sections 6.2 and 6.3. The development of InGaN layers as an absorber was abandoned due to time constraints: only the contact path is considered for the rest of this study.

# 6 InGaN contacts

One of the most important conclusions of the two previous chapters is that PECVD or sputtered InGaN material developed during the present thesis was not performant enough to act as an absorber in a solar cell. In detail, p-doping was not achieved, and the resistivity was too high even with the help of doping, with sometimes some FCA. This is due to a too-low crystallinity and a too-high defect and impurity density; those could not be optimised further.

Nevertheless, InGaN may still be integrated into a solar cell, but as a contact. This chapter aims to answer the fourth and last research question: "How well does such a material compare with standard c-Si solar cell technology?". The two same fabrication means used in the previous chapters were used to test if such an operation was possible: PECVD and PVD sputtering. This chapter first presents PECVD results of undoped InGaN layers as contacts for c-Si solar cells, then PVD results of both doped GaN and undoped InGaN layers. A small study on a-Si:H contacts deposited at 400 ° is presented in appendix C.

The band diagrams presented in this chapter were all produced using the PC1D version 5 software provided by the University of New South Wales, Australia [179]. The values for the InN and GaN BG, dielectric constant, mobilities and electron affinity *EA* are taken from table 2.4, where, because of the defects mentioned previously, the intrinsic doping is set to n-type with a concentration of $1 \cdot 10^{20}\,\mathrm{cm}^{-3}$ and to $1 \cdot 10^{22}\,\mathrm{cm}^{-3}$ when GaN is doped with either germanium or silicon. Table 6.1 shows the values considered for the other elements of the solar cell: ITO, doped c-Si and a-Si. The band diagrams presented in this work aim to give a basic understanding and intuition of the dynamics of the charge carriers inside the solar cell. A more suited tool for precisely calculating all the parameters (band bending depth, tunnelling, recombination, etc.) would be something like NextNano. Such software was not used because of a lack of reference files for ITO and a-Si; manually creating these reference files could not be done because of time constraints.

Table 6.1: Contacts: band alignment physical quantities for non-III-V materials on a flat surface (a 1.7 factor is applied when deposited on a textured wafer). The c-Si lines account for the silicon wafer

| Material | Thk. [nm] | $\varepsilon_\Gamma$ [-] | $\mu_e$ [$\frac{cm^2}{Vs}$] | $\mu_h$ [$\frac{cm^2}{Vs}$] | $E_g$ [eV] | $n$ or $p$ [$cm^{-3}$] |
|---|---|---|---|---|---|---|
| ITO front | 120 | 4.0 | 50 | 50 | 3.9 | $10^{20}$ (n) |
| ITO back | 240 | | | | | |
| a-Si:H(n) | 12 | | | | | $10^{19}$ |
| a-Si:H(i) | 8 | 11.9 | 20 | 4 | 1.7 | - |
| a-Si:H(p) | 15 | | | | | $10^{19}$ |
| c-Si(n) | 200'000 | 11.9 | 1400 | 450 | 1.1 | $10^{15}$ |
| c-Si(p) | | | | | | $10^{15}$ |

## 6.1 In/GaN contacts by PECVD

The solar cells presented in this section were deposited and characterised by Nils Toggwyler, who was partially realising his semester's project under my supervision.

In chapter 4, the fabrication of InGaN layers by a low-$T$ PECVD process was presented, with structural, optical and electrical characteristics that were deemed acceptable for integration in a solar cell structure. This section shows the integration results as an electron back contact (passivating and selective). First, the deposition conditions and the architectures are presented, followed by the solar cell performances and comparison with current c-Si solar cell performances.

### 6.1.1 Setup of the experiment

After some testing, five different compositions (or "indium contents" $X_{\text{In}} = \frac{\text{In}}{\text{In+Ga}}$, In & Ga in at. %, $X_{\text{In}}$ in %, ranging from a pure InN layer to a pure GaN layer) distributed in three different architectures were selected and tested for an In/GaN contact, *i. e.* 15 tested configurations. To decrease the defect and contamination density, the aim is for all the layers to have a deposition rate of, at the very most, 6 nm/min. This deposition rate allows for a good quality layer, as seen in section 4.2. All layers were grown with the following base parameters:

| Pressure | Frequency | Temperature | Power | Time | $N_2$ | $H_2$ |
|---|---|---|---|---|---|---|
| ±2 $\mu$bar | ±0 MHz | ±2 °C | ±2 W | ±1 s | ±1 sccm | ±0.6 sccm |
| 500 | 110 | 250 | 30 | 1000 | 60 | 50 |

Every layer was deposited on a double-side polished n-doped (100) silicon wafer. The three architectures that were tried were all compared to one reference architecture. They can be seen in figure 6.2, in which the reference architecture is also presented. They are named the "n(-)",

"n(i)" and "n(i/n)" architectures, and this notation will only be used in the present section. Given their configuration, the n(n/i) architecture only probes the conductivity of the In/GaN layer, the n(i) probes both the conductivity and the selectivity, and the n(-) probes the three characteristics necessary for a good contact at the same time: the passivation, the selectivity and the conductivity. As standalone layers, the five tested candidates have the characteristics displayed in table 6.2 before their integration in the solar cell as thinner component (by reducing the deposition time).

Table 6.2: In/GaN PECVD contact: characteristics of five In/GaN PECDVD layers before their integration as a contact. $X_{\mathrm{In}}$ is probed by EDS on layers deposited on a silicon substrate, and $E_{04}$ is probed by spectroscopy on layers deposited on a glass substrate.

| N° | TMG ±0.006 sccm | TMI ±0.04 sccm | Thickness ±10 nm | $X_{\mathrm{In}}$ ±3 % | $E_{04}$ ±0.03 eV |
|---|---|---|---|---|---|
| 1 | 0.096 | 0 | 91.1 | 2 | 2.95 |
| 2 | 0.066 | 0.34 | 85.9 | 28 | 2.58 |
| 3 | 0.057 | 0.46 | 101.8 | 39 | 2.25 |
| 4 | 0.051 | 0.60 | 70.3 | 42 | 2.21 |
| 5 | 0 | 1.46 | 75.6 | 98 | 1.68 |

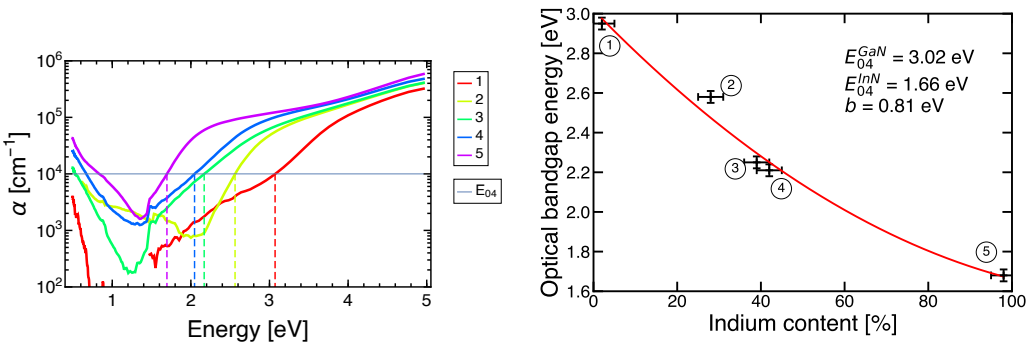


(a) Absorption coefficient of the five tested layers.

(b) Optical bandgap as a function of the indium content $X_{\mathrm{In}}$ in percent showing Vegard's law with a low bowing parameter.

Figure 6.1: In/GaN PECVD contact: absorption coefficient $\alpha$ and optical BG $E_{04}$ of the five tested layers.

The absorption coefficient, from which the optical BG $E_{04}$ was extracted in table 6.2, is displayed in figure 6.1a. Again, Vegard's law is respected, as shown in figure 6.1b: the quadratic trend is clearly visible with a low bowing parameter. And without surprise, FCA is still present in the layers, increasingly with the indium content. This means that the layers are degenerated, as modelled in figure 6.2, making the band diagrams in figure 6.2 reliable.

In terms of band diagrams (see figure 6.2 again), we can see how the reference architecture provides an excellent selectivity of the charge carriers while at the same time minimising the thermal and tunnelling emission of both charge carrier types over and respectively through

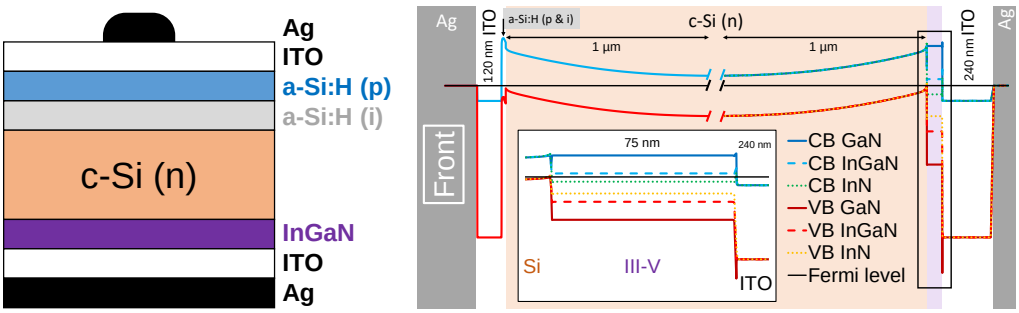


(a) n(-) architecture.

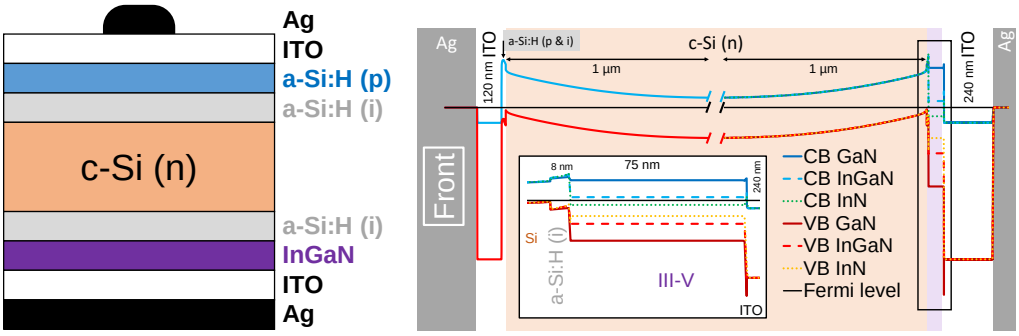


(b) n(i) architecture.

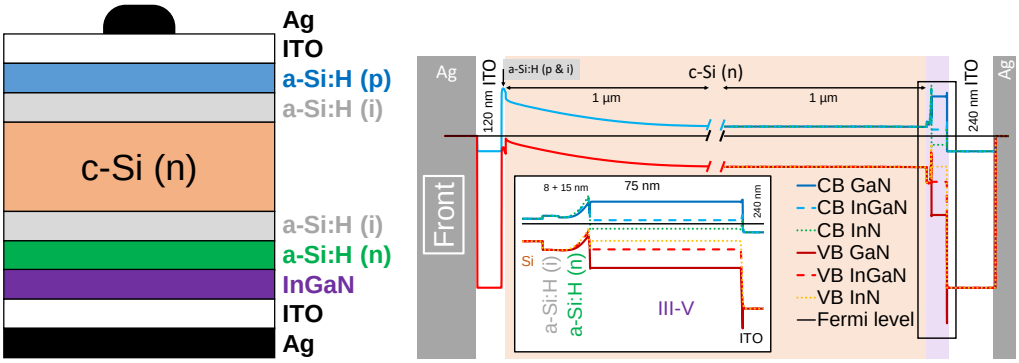


(c) n(i/n) architecture.

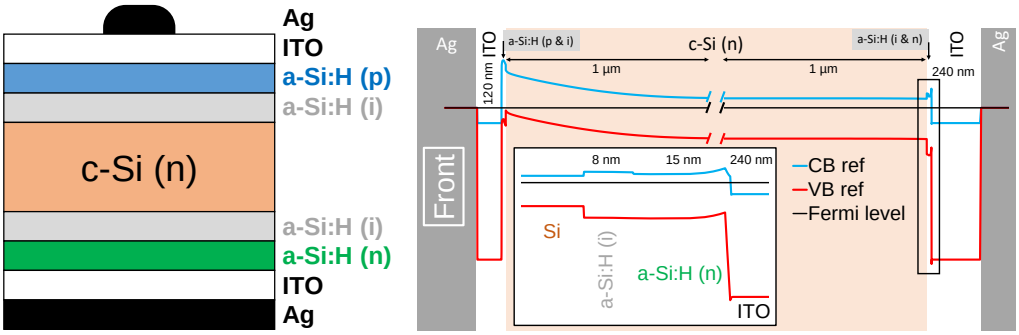


(d) Reference architecture.

Figure 6.2: In/GaN PECVD contact: three tested architectures and the reference one on a flat wafer (left) and their corresponding band diagrams (right), in which the inset is a zoom-in on the black square, where the In/GaN layer is located (at the back contact).

the thin barrier junctions (see band diagram 6.2d). In comparison, the n(i/n) architecture (see figure 6.2c) should improve the transmission of electrons through the electron contact as long as the indium content is not too low so that the tunnelling emission is not prevented; further experiment should be done to confirm this with a thinner In/GaN layer. In particular, we already see that this remains valid for indium contents of at least about 50 % (see in particular the $In_{50}Ga_{50}N$ conduction band minimum, the dashed blue line in figure 6.2c, aligning at precisely the same level as the n-doped c-Si wafer), which is kind of a reminder of the potential ohmic junction discussed in the State of the Art chapter, mainly related to figure 2.4b.

In the first and second architecture (figures 6.2a & 6.2b), the band diagrams show us that surprisingly, in this kind of configuration, the In/GaN layer is selective "against" electrons, in the same way as the front p-contact, by the rising of the CB at both sides. So a lack of selectivity is expected here, where a better configuration would be to use a p-doped c-Si wafer instead (see, for example, the band diagram presented in figure 6.14a, considered one of the best configuration tested). The other challenges mentioned in the previous paragraph are also still present, where a higher gallium content might hinder the electron extraction at the back. The main difference between these two architectures lies in the passivating power of the In/GaN layer compared to the standard a-Si:H(i) layer, which a band diagram cannot describe.

### 6.1.2 Results

The J-V curves and cell characteristics for the three architectures and the five different contents are displayed in figure 6.3.

Independent of the architecture, the better efficiency (figure 6.3h) and *FF* (figure 6.3g) is obtained for a higher indium content. Or, to put it differently, the efficiency decrease is sharper for $X_{In} < 30 - 40\,\%$. This takes us back to the undoped case presented in figure 2.4b, page 16 and related explanation: it is suspected that this is due to a mix between the defective InGaN layer, the Fermi stabilisation energy, and the energy difference to the vacuum level of silicon. All in all, since the imperfect InGaN layer is degenerated for $X_{In} > 30\,\%$, the transport between it and the silicon is eased for electrons, hence resulting in better contact. The band diagram makes this visible by lowering the conduction band minimum in the III-V region below the Fermi level, promoting better tunnelling and thermionic emission of the negative charge carriers. The $V_{OC}$ (figure 6.3e) is, in fact, not expected to change with a different indium concentration because the In/GaN layer is not part of the p-n junction; no noticeable trend or optimum value can be found here. The same goes with the $J_{SC}$ (figure 6.3f), an indication of more or less recombination within the absorber; it should not be dependant on $X_{In}$.

In terms of architecture, it is better to compare the different J-V curves (figures 6.3a to 6.3c). The first noticeable effect of the In/GaN layer is that only the n(i/n) architecture shows better performance than the reference cell. This is also displayed by the dashed lines in the four figures at the bottom of figure 6.3: the reference represented by the dashed line is only worse than a few instances of the n(i/n) architecture. This means that the a-Si:H(n) – In/GaN – ITO

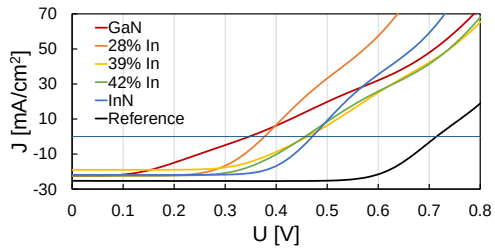


(a) J-V curves of the n(-) architecture for different indium contents $X_{In}$.

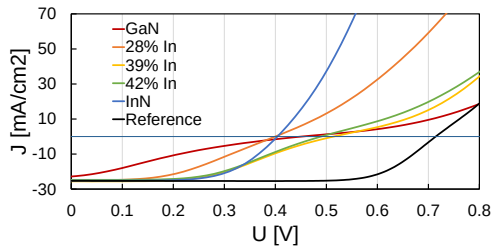


(b) J-V curves of the n(i) architecture for different indium contents $X_{In}$.

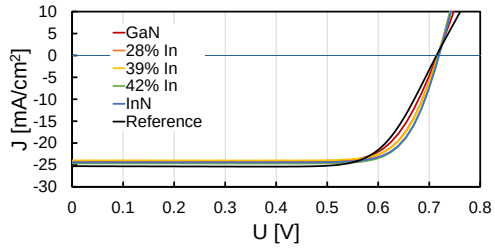


(c) J-V curves of the n(n/i) architecture for different indium contents $X_{In}$.

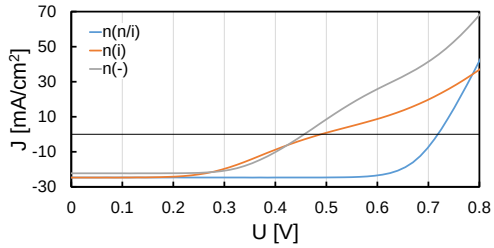


(d) J-V curves for the $In_{42}Ga_{58}N$ layer in different architectures.

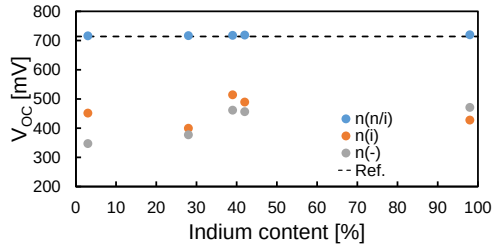


(e) $V_{OC}$.

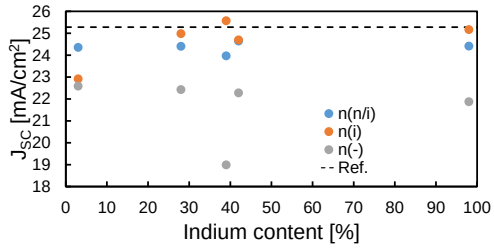


(f) $J_{SC}$.

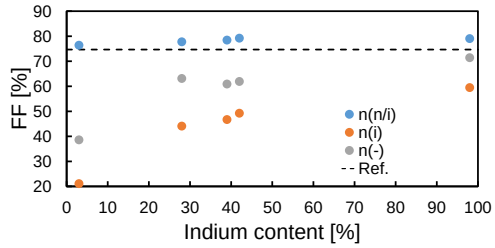


(g) $FF$.

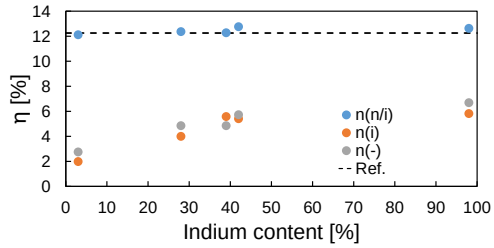


(h) Efficiency $\eta$.

Figure 6.3: In/GaN PECVD contact: J-V characteristics. The dashed lines in the four figures at the bottom correspond to the reference architecture performances. The electrical measurements are precise to less than ±2 ‰relative, so no vertical error bar is shown here. The indium content has an uncertainty of ±3 %.

combination works better than the reference Si:H(n) – ITO one. Compared to the reference cell, the gain is mainly due to a better $FF$ while the $J_{SC}$ has slightly lower values. The better $FF$ can be attributed to a lower contact resistivity, allowing a better collection of the electrons

at that side of the solar cell. The lower $J_{SC}$ could be attributed to parasitic absorption in the additional In/GaN layer.

Comparing the n(i/n) and n(i) architecture, the vast difference in $V_{OC}$ and *FF* resulting in a far lower efficiency is a result of a worsening of the selectivity, as predicted by the band diagram analysis. So the n(i/n) architecture remains the best choice, with as much indium as possible. As an example of such a selectivity issue and its impact on the J-V curve, see figure 6.3d.

The n(i) and the n(-) architectures have comparable efficiencies and $V_{OC}$ but differ in terms of $J_{SC}$ and *FF*. Compared to that, the constant $V_{OC}$ in the n(n/i) architecture means that here the passivation is not the limiting factor, but the selectivity is; the indium content does not play a significant role in the n(n/i) architecture. The comparison between n(-) and n(i) assesses the quality of the passivation of the In/GaN layer compared to the a-Si:H(i) one. The lower $J_{SC}$ here indicates that a higher recombination rate occurs when the In/GaN layer is at the contact. Another feature of some of the JV curves is an S-shape, according to Fébba *et al.* [57], it is due to a barrier for electron extraction. This S-shape is mainly observed in architectures n(-) and n(i) (figures 6.3a and 6.3b). This implies that the In/GaN layer has poor selectivity and passivating power, functioning as a resistive layer. Related to the band diagram, the latter may be alleviated by thinning the III-V contact, promoting a better tunnelling emission of the electrons.

Two other tests were performed to answer two questions: "What is the effect of the operating temperature on the J-V curves under equal illumination?" and "What is the effect of the annealing temperature on the layers?". The two J-V curves related to these small tests are displayed in figure 6.4, where only the $In_{42}Ga_{58}N$ of the n(i) architecture is presented here. The annealing was performed at $210 \pm 5$ °C for 30 minutes not to degrade the other a-Si layers. This anneal is performed on the finished solar cells; after the 15 min deposition of the GaN layer at 250 °C that should still have had an impact on the subjacent a-Si layers. It is observed that instead of improving the cell performances, an anneal of the solar cells degrades them by decreasing the $V_{OC}$. Since the GaN layer remains stable under extreme temperatures, it is safe to assume that the annealing only affects the amorphous layers, resulting in a $V_{OC}$ decrease because of a further crystallisation that reduces the BG, and possibly on the ITO as well (which would lead to a conductivity decrease and a loss in *FF*). This crystallisation began during the GaN layer deposition but is exacerbated by the longer annealing time.

Regarding the effect of temperature, as expected, the S-shape disappears slowly due to improved conductivity, with a better *FF*. This means that the temperature gives more energy to the charge carriers, which can more easily access the contact by thermionic emission (see said barriers in the band diagrams in figure 6.2). This is sadly achieved at the expense of a worse $V_{OC}$ because the BG energy of the absorber decreases with increasing temperature, like in all solar cells (see equation 2.10 page 9 and related explanation).

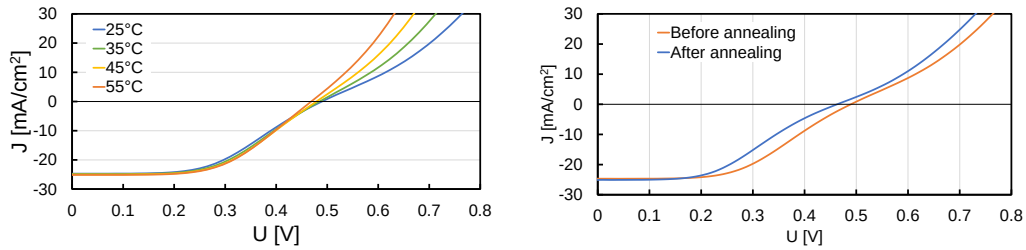


(a) Working temperature effect before annealing.

(b) Before and after annealing at 210 °C, measurement performed at room temperature.

Figure 6.4: In/GaN PECVD contact: effect of temperature (a) and annealing (b) on the J-V curve & cell performances for the n(i) architecture and 42 ± 3 % indium.

### 6.1.3 In/GaN PECVD contact: key takeaways & next steps

The cell testing revealed poor electron selectivity of InGaN grown by PECVD, which impacts their passivating capacity in the n(-) and n(i) architectures. Their corresponding band diagram confirms this (see figures 6.3a & 6.3b). This is also confirmed by the n(n/i) architecture showing the highest performance, where the In/GaN layer is not implied in the contact's selectivity, as demonstrated by its corresponding band diagram. The difference in performance between the two former architectures confirms that the passivating capacity of the In/GaN layer is not the limiting factor in extracting charge carriers efficiently. The S-shape of the J-V curves supports an electron barrier phenomenon. This was confirmed by increasing the operating temperature to promote thermionic emission of the absorber to the contact, improving the *FF*. The tunnelling emission through one of the barriers in the band diagram can also be promoted by thinning the In/GaN layer. The overall performance of the cells was also weak: almost 13 % efficiency for the best one. However, even though the poor reference cell performance could mask the benefits of using an InGaN contact, the potential for improvement was still demonstrated. Further optimisation looks promising because the development of this technology in PV-lab is still in its early stages and should be explored further to develop alternative materials for the photovoltaic sector. In particular, ammonia was not used here as a nitrogen source, which should help further decrease the growth rate, allowing more crystalline InGaN layers with better performances.

## 6.2 Doped GaN contacts by PVD

The solar cells presented in this section were deposited and characterised by Julien Hurni, under Mathieu Boccard's supervision, in the framework of his internship that followed his master's thesis at PV-lab. They were included in this thesis with his permission because they were closely related to the present research and will be integrated into a joint publication currently under preparation.

The material developed in chapter 5 was deemed good enough for cell integration, and a small test with germanium doping and an extensive study on silicon doping were undertaken. These constitute the two parts of this section on doped GaN as an electron back contact (passivating and selective).

### 6.2.1 Doped with germanium

#### 6.2.1.1 Experimental setup

Two architectures were tested, shown in figure 6.5, where either an ITO layer doubled with a silver contact was used on both faces or simply an aluminium contact at the back and a silver contact on top of an ITO layer at the front. The rest of the solar cell is a standard heterojunction cell, with silicon and ITO reference layers used in PV-lab's standard fabrication procedure. The GaN layer is here tested as a selective electron contact placed at the back, forming a heterojunction solar cell using an n-type wafer.

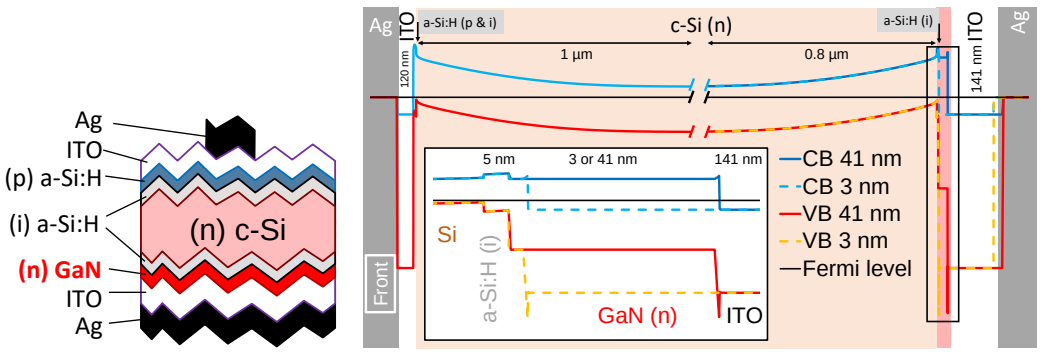


(a) ITO-Ag architecture and corresponding band diagram

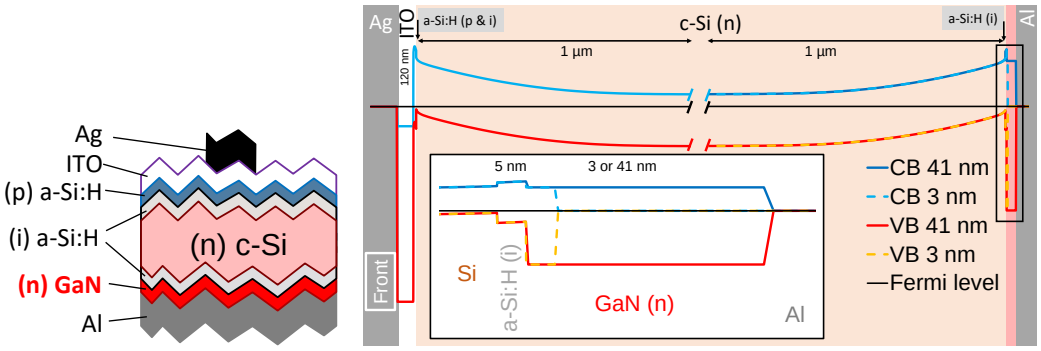


(b) Al architecture and corresponding band diagram

Figure 6.5: Ge-doped GaN PVD contact: two architectures for the characterisation of the Ge-doped GaN PVD contact: "ITO-Ag" (a) or "Al" (b). The inset in the band diagram is a zoom-in on the black square, where the In/GaN is located (at the back contact). The legend refers to the thickness of the GaN (n) layer (see inset for a clearer difference); that thickness difference is the reason why some of the bands are not perfectly aligned like is the case on the ITO-Ag interface in the top figure.

The procedure follows what was presented in chapter 5, where the Ge-doped GaN layer is deposited with different goal thicknesses (between 5 and 70 ± 5 nm on flat, equivalent to a thickness varying between 3 and 41 ± 5 nm on the textured wafer) with different sputtering gas mixtures (either $N_2$ or $N_2$ (50 %) + $H_2$ (50 %)), then annealed at either 200 or 600 ± 5 °C for 15 minutes under $N_2$ atmosphere, and the ITO and metals are eventually evaporated. The goal of the low-$T$ anneal is to increase the thermal budget of the stack to passivate the different interfaces better, but the dopants within the GaN layer are less activated. On the contrary, a high-$T$ annealing will activate the dopants but potentially kill the a-Si layers. The PV characteristics were then probed on sixteen tested configurations.

The band diagram of four of those architectures are presented in figure 6.5, where similarly to the band diagrams of the n(-) and n(i) configuration of the previous section, a selectivity problem can already be detected. Indeed, on the back side, the electrons are also prevented from reaching the electron contact. This is visible by the slow rise of the CB of the c-Si wafer before reaching the electron contact at the back. This will negatively impact the selectivity of the contact for electrons. Still, this negative effect is expected to be dampened using a thinner GaN(n) layer, promoting a slightly better tunnelling emission.

#### 6.2.1.2 Results

The J-V characteristics of the sixteen different combinations of architectures and deposition parameters are presented in figure 6.6. The name code is used as the following example: N2H2_70_Ta600_ITO-Ag corresponds to the use of $N_2$ (50 %) $H_2$ (50 %) sputtering gas, a layer thickness of 70 nm and an annealing temperature of 600 °C for the ITO-Ag architecture (see figure 6.5). Except for layer N2_05_Ta600_Al, which surprisingly displays a standard J-V curve, all the J-V curves are strongly S-shaped, characteristic of poor electrical properties. The influence of film thickness is extracted by comparing the various sputtering conditions.

**The $J_{SC}$** diminishes drastically with increasing thickness; that can be partially explained by the increase of series resistance that limits the current flow. In other words, considering the band diagram, the extraction of electrons out of the absorber through the contact is prevented by a too-thick barrier. Even though the selectivity is problematic, conductivity is at least the second limiting factor. The difference between N2_70 and N2H2_70 in terms of $J_{SC}$ is attributed to a lower resistivity of the Ge-doped GaN layers by adding hydrogen that improves the doping performances as demonstrated in section 5.2.

**The $V_{OC}$** is expected to be degraded for samples annealed at high temperatures. This effect should come from the low thermal stability of a-Si, affecting the $V_{OC}$, and eventually degradation of the ITO, which worsens the *FF*. Indeed, for annealing temperature superior to 250 ± 5 °C, a-Si layers start to degrade, thus reducing the passivation and ultimately decreasing the open circuit voltage [65]. However, the reduction of the $V_{OC}$ between high and low annealing temperatures is unclear. However, increasing the layer thickness reduces the discrepancy between $V_{OC}$ for architectures annealed at 200 and 600 ± 5 °C.

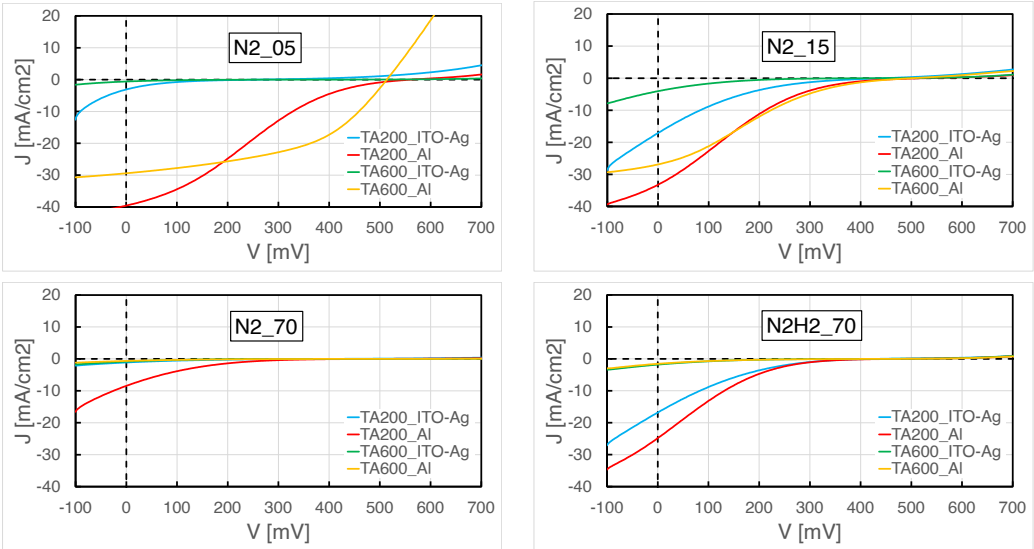


(a) J-V curves.

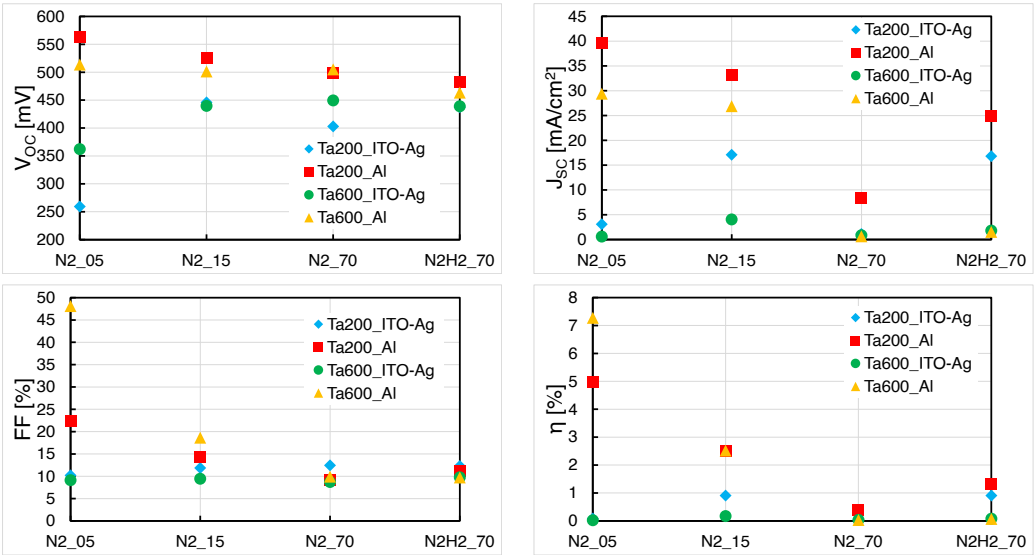


(b) Cell performances.

Figure 6.6: Ge-doped GaN PVD contact: J-V curves and cell performances. The labelling code is the following: N2H2_70_Ta600_ITO-Ag corresponds to the use of $N_2$ & $H_2$ sputtering gas, a layer thickness of $70 \pm 5$ nm and an annealing temperature of $600 \pm 5$ °C for the ITO-Ag architecture (see figure 6.5).

**The architecture** difference between Al and ITO-Ag is very pronounced. Indeed, ITO-Ag architecture suffers from very low $J_{SC}$ and $V_{OC}$ compared to the Al architecture. Several mechanisms could cause this. Deposition of ITO and Ag by sputtering induces much more damage to the layers underneath, which can explain a change of the characteristic of the GaN films due to sputtering defects. Another explanation could be that the band alignment of GaN and ITO creates a blocking contact that prevents electron extraction.

Still, the simulated band diagram shows only a slight bump at the GaN-ITO interface, contrary to the smooth GaN-Al transition. So, in the end, the difference seems to be more related to defects than band alignment.

**The *FF* and the efficiency** of the different cells can be compared. Best *FF* and $\eta_{std}$ are attained for very thin GaN layers and with aluminium back contact. Surprisingly, the sample annealed at 600 ± 5 °C has better characteristics ($FF$ = 45.3 % and $\eta_{std}$ = 8.3 %) than the one annealed at 200 ± 5 °C ($FF$ = 22.1 % and $\eta_{std}$ = 6.0 %). From the $V_{OC}$ and $J_{SC}$, one would expect that a sample annealed at 200 ± 5 °C would have better properties, but higher series resistances shown by the slope at the $V_{OC}$ value of sample Ta_200 changes the shape of the J-V curve and therefore diminish the fill factor and the efficiency. In this case, the *FF* and $\eta$ trends cannot be related to a band diagram analysis.

#### 6.2.1.3 Ge-doped GaN PVD contact: key takeaways & next steps

Different solar cells using a Ge-doped GaN layer as electron-selective contacts were fabricated and tested. The influence of this layer's thickness, the annealing temperature, and the contact architecture were analysed. Given the solar cell performances, the annealing temperature and its impact on the charge carrier dynamics and the doping activation is not the limiting factor of solar power generation. The metallic contact type and the GaN layer thickness seem to have a more significant impact. It was found that the sample with a small thickness of Ge-doped GaN annealed at 600 ± 5 °C with an aluminium back contact presents the best characteristics. $V_{OC}$ of 514 mV is measured, which, although very low compared to the set objective of 730 mV, is promising as it results from the very first batch of experiments. The measured $J_{SC}$ is also below the goal (35 mA/cm² instead of 40 mA/cm²). Nevertheless, despite a very low *FF* (47 %) linked to a very high series resistance, an efficiency of about 8 % is measured. Although these values are lower than expected to replace the (n) a-Si layers in the immediate future, these results show that optimised Ge-doped GaN layers could be used for this type of application.

The architectures are chosen to test the selectivity and the conductivity of the GaN contact. Four of the sixteen associated band diagrams confirm the poor selectivity of the electron contact the GaN is part of, visible thanks to an inadequate band bending. These handicaps in the architecture can be partially alleviated by thinning the GaN electron contact, thus promoting a more efficient tunnelling (and eventually thermionic) emission. But the best way to make use of this band arrangement would be to use a p-doped c-Si wafer instead of an n-doped (see figure 6.14b). It would also be interesting to find the best trade-off between the crystallinity linked to a better dopant activation (achieved with a low-pressure deposition) and the sputtering damage reduction when the Si-doped GaN layer is deposited at high pressure. That could be the goal of a later experiment.

Eventually, more solar cells should be produced and analysed to understand which effects limit the different solar cells' parameters most. The S-shaped J-V curves should be fitted to extract majority and minority carriers' currents and develop an understanding of the physics

happening in these types of defective devices. Other architectures should also be tested, and it would be essential to improve the doping performances.

### 6.2.2 Doped with silicon

#### 6.2.2.1 Experimental setup

Doping of sputtered GaN with silicon has shown good resistivity (< 0.2 mΩ cm) and good electron mobility (> 100 $cm^2/Vs$) in the literature [11] compared to germanium doping ($\rho$ = 3 Ω cm, activation energy of $E_A$ = 50 meV) [171]. The epitaxial layer produced by the Clusterline at CSEM, which is described in section 5.4 could be optimised, reaching a resistivity of 14 Ω cm and activation energy of 29 meV in comparison. Here, the layer containing 4.4 at. % of silicon developed in section 5.3 with the Univex at PV-lab is used as a contact in different cell architectures, and their performances are compared to literature results. A total of twelve architectures was tested in which the Si-doped GaN layer can take one of the following roles (where the capital "N" stands for the n-doped c-Si wafer, and where this specific notation is only used in the present section):

- Spectator in a p-i-N-i-n-GaN stack or simply "i-n",
- Electron selector in a p-i-N-i-GaN stack or simply "i",
- Electron passivating contact in a p-i-N-GaN stack or simply "-".

The solar cell is engineered along four different architectures:

- A reference architecture without GaN: "Ref",
- ITO on both sides with a 20 nm Si-doped GaN layer at the back: "DITO",
- A front side ITO with a 100 nm Si-doped GaN layer at the back: "FITO",
- No ITO with a 100 nm Si-doped GaN layer at the back: "NITO".

These are all detailed in figure 6.7. The error bars on electrical characterisations are dropped here because they are precise enough that the uncertainty on measurement is insignificant compared to the measured value (less than ±2 ‰ relative).

#### 6.2.2.2 Lifetime

The solar cells are produced according to a particular recipe, whose steps are carefully engineered as follows (ignore an action if the corresponding layer is not part of the architecture presented in figure 6.7:

1. (i) a-Si:H layer deposition on both sides,
2. (p) a-Si:H layer deposition at the front, possibly (n) a-Si:H layer deposition at the back,
3. Lifetime measurement "Before ITO/Ag",
4. ITO & Ag layer deposition at the front with a mask,
5. Lifetime measurement "After ITO/Ag" on a not-metallised spot,

6. Si-doped GaN (4.4 at. % Si) layer deposition in the full area at the back,
7. Lifetime measurement "After GaN" on a not-metallised spot,
8. ITO & Ag layer deposition at the back in the full area,
9. J-V measurement of the solar cell under STC,
10. Anneal followed by a second J-V measurement of the solar cell under STC.

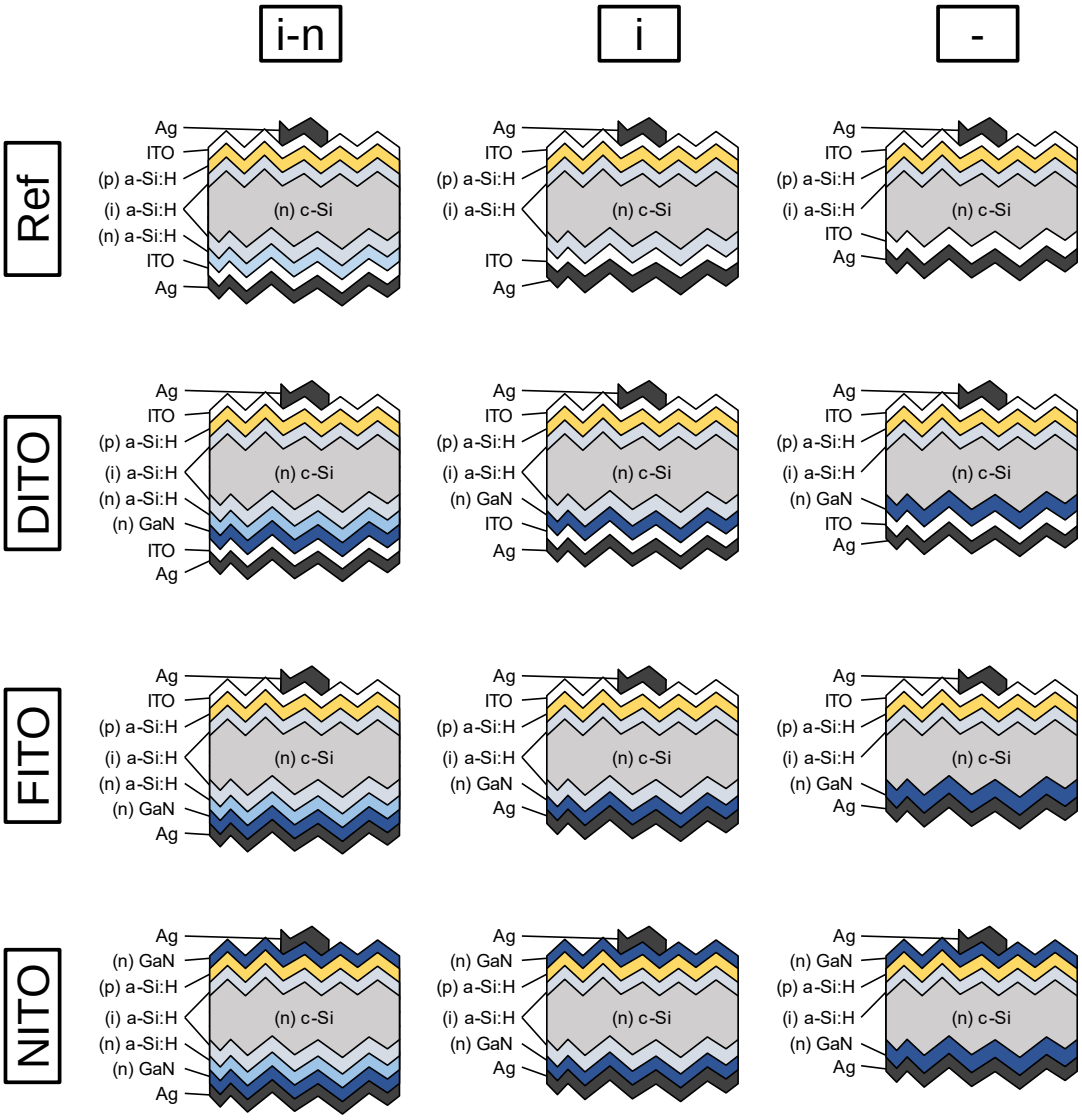


Figure 6.7: Si-doped GaN PVD contact: architectures. The rows represent the four tested architectures (reference without GaN "REF", double side ITO "DITO", front side ITO "FITO" and no ITO "NITO"). In contrast, the columns represent the three probed roles of the GaN layer. When the GaN layer (painted in dark blue in the figure) assumes only a contacting role ("i-n" column), the passivation and selectivity are taken care of by the a-Si:H(i) and a-Si:H(n) layers respectively. As an electron selector, the selectivity and contacting role are handled by the GaN layer, while the a-Si:H(i) layer assumes the passivation. In the last configuration "-", the GaN layer simultaneously takes the three roles of passivation, selectivity and contact.

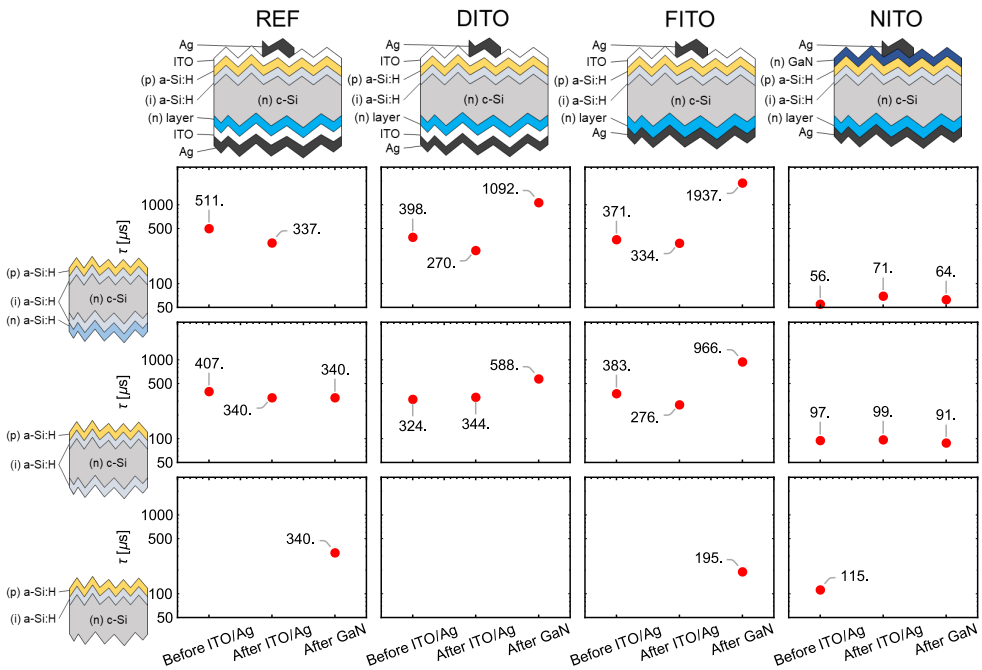


Figure 6.8: Si-doped GaN PVD contact: lifetime for the twelve architectures at three strategic moments: before and after applying the contacts (ITO/Ag), and after depositing the Si-doped GaN layer (Si content: 4.4 at. %). See figure 6.7 for more details on the architectures: the general x-axis of the present figure represents the architecture type (Réf., DITO, FITO, NITO), while the y-axis represents the role of the GaN layer ("i-n", "i" or "-"). The errors here are not shown because they are shorter than the point diameter (< 0.2 % relative).

The lifetime of each of the twelve architectures, characterised by the Sinton (see section 3.2.4.5), is displayed in figure 6.8, at different production steps. By analysing all these values, it is observed that overall the lifetime is low, even for the reference cells; a lifetime of at least 1 ms is expected for high-quality solar cells. The i-n reference architecture usually reaches a lifetime of 5 ms; a problem may have occurred either during the a-Si batch deposition or because of the unlucky pick of a bad c-Si wafer batch. Indeed these depositions were all performed the same week with wafers taken out of the same box. The heterojunction group in PV-lab sometimes had to discard a whole box of wafers either because of its lousy passivation performances or because of a bug or problem during the batch deposition of the a-Si layer in the KAI-M. It seems that these first results are one of those cases. But all results are still expected to be coherent and comparable.

It is also observed that the lifetime decreases after the ITO/Ag sputtering due to sputtering damage. On the other hand, the lifetime increases after the GaN sputtering because even though there is some sputtering damage during that deposition (and possibly some breakdown of the Si – H bond by the UV emission of the plasma near the target), it is performed at 200 °C, which helps re-passivate the amorphous layers.

Finally, removing the (n) layer at the back considerably decreases the lifetime, indicating a poor passivation capacity of the sputtered Si-doped GaN (compare first and second row). The NITO contact (last column) damages the p-side (front) and prevents the lifetime from recovering. This may be due to either a too-long deposition (thermal energy budget is exceeded) or maybe a scratch on the n-side during the Univex sputtering.

#### 6.2.2.3 I-V curves at standard test conditions

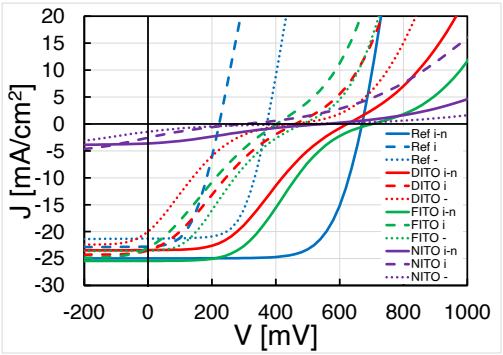


(a) J-V curves, as deposited.

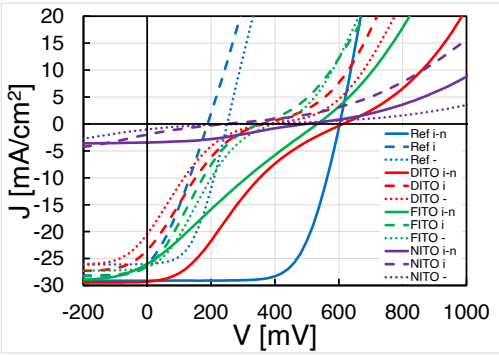


(b) J-V curves, annealed.

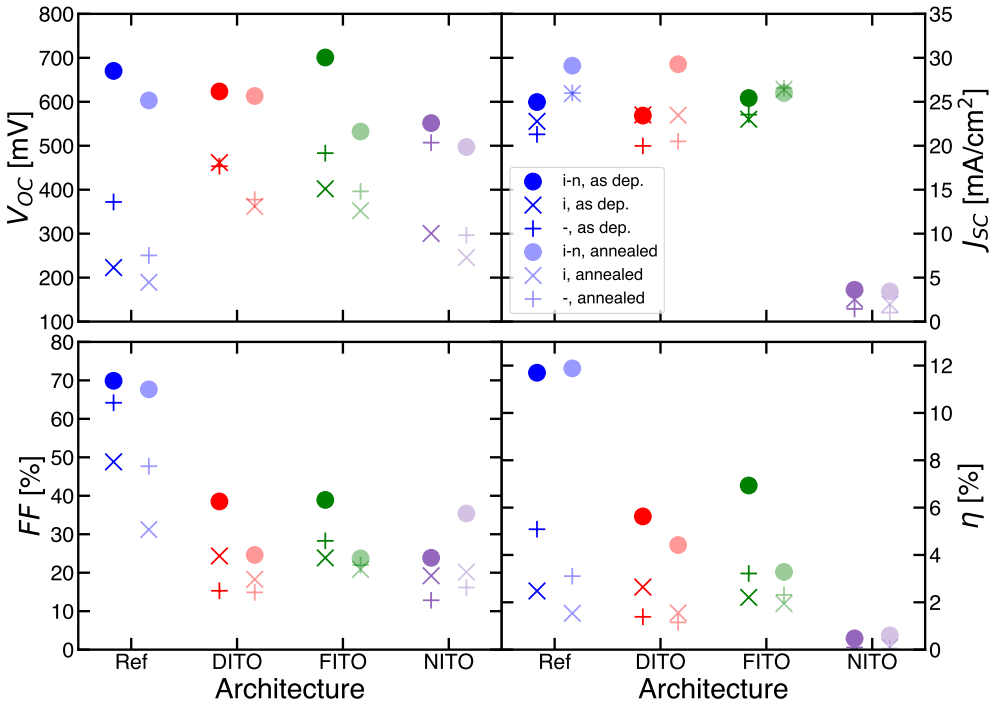


(c) Cell performances. The ±2 ‰ relative error bars are not shown here because they are shorter than the point width.

Figure 6.9: Si-doped GaN PVD contact: J-V curves and key performances for the twelve architectures, as-deposited and annealed at 200 °C. The GaN layer contains 4.4 at. % of silicon.

Each of the twelve configurations was characterised by the current-voltage cell characterisation before and after annealing at 200 °C, and the resulting J-V curves are displayed in figure 6.9. Here is what can be observed:

**REF** no GaN

- The $V_{OC}$ and *FF* are low, but there is no S-shape, whatever the architecture.
- Reduction of the $V_{OC}$ and *FF* after annealing. For the N-i configuration, this is severe enough that even the current density is impacted, probably due to the absence of the a-Si:H(n) layer.
- The efficiency $\eta$ of the i-n reference solar cell usually resides at higher values; this degradation can be attributed to the defective wafer that is part of a batch of faulty wafers used for all the solar cells in this part of the experiment. This means that although the actual performances could be more impressive, all the results have the potential to increase their efficiency substantially.

**DITO** 20 nm GaN

- N-i-n architecture: the $V_{OC}$ is similar to the reference, but the J-V curve is S-shaped with a low *FF*. This indicates low layer conductivity or high series resistance ($\sim 15\,\Omega\,\mathrm{cm}$).
- N-i architecture: the low $V_{OC}$ without the (n) a-Si layer indicates a low electron selectivity of the GaN layer. Different reasons for such a behaviour can be proposed: a bad CB alignment or poor doping, for example (see figure 6.10).
- Follow-up on the previous point: a slight increase of the $V_{OC}$ in the N- architecture without the (i) a-Si layer; this may be due to a better band alignment or the S-shape effect.
- Reduction of the $V_{OC}$ and *FF* after annealing. Here, the annealing worsens all the architectures, but the N-i-n configuration has an increased $J_{SC}$.

**FITO** 100 nm GaN.

- The behaviour and trends are the same as with the DITO architectures, with slightly less S-shaping (*i.e.* lower series resistance) and with slightly different values. Please refer to the conclusions of the DITO point here above.

**NITO** 100 nm GaN

- In this configuration, the $J_{SC}$ is extremely reduced because the GaN layer is placed at the front, which increases the parasitic absorption compared to the larger BG of the ITO.
- On top of that, the Si-doped GaN(n) front layer is not designed to transport holes as a majority carrier and is not conductive enough (compared to the ITO) to laterally move the holes to the metallic contact.
- Finally, the reduced $J_{SC}$ value can also be attributed to high recombination within the absorber because of the short lifetime presented in figure 6.8, which hints towards a passivation problem.
- For the N- architecture, there is somehow a $V_{OC}$ improvement compared to REF/N-, DITO/N- and FITO/N- architectures. The reason for this feature is not understood.

#### 6.2.2.4 I-V curves: irradiance & operating temperature influence

Instead of thoroughly analysing the differences between the 12 architectures and their corresponding band diagrams, we will focus on one of the most performant ones. The "champion" one is the DITO i-n architecture, whose band diagram is presented in figure 6.10, with the second most extended lifetime of 1092 $\mu$s (see figure 6.8) and an efficiency of almost 6 % (see figure 6.9). In this configuration, the Si-doped GaN layer (Si content: 4.4 at. %) influences the contact quality by its conductivity only; the passivation and the selectivity are already taken care of by the two a-Si layers. The high resistivity of the GaN layer coupled with a good CB alignment with the a-Si:H(n) layer will slightly hinder the electron extraction; a thinner layer may be more beneficial than a thicker one. Overall, a performant cell is expected out of that architecture.

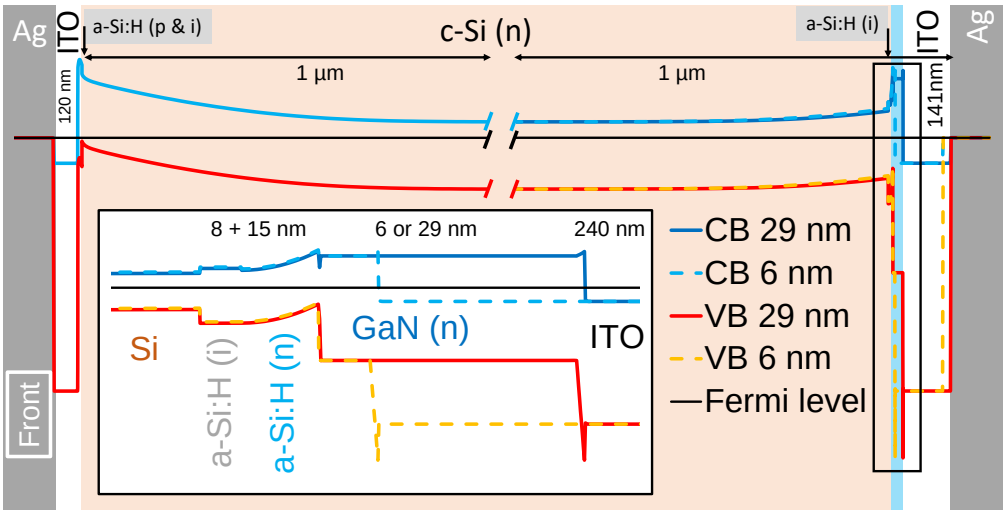


Figure 6.10: Si-doped GaN PVD contact: DITO i-n band diagram. The legend refers to the thickness of the GaN (n) layer (see inset for a clearer difference, referencing the DITO i-n architecture in figure 6.7); that thickness difference is the reason why some of the bands are not perfectly aligned like is the case on the ITO-Ag interface.

As an overall conclusion, the cell characteristics are bad (except for some champion cells), and the Si-doped GaN layer induces an S-shaping of the J-V curves, which means that the series resistance is increased. This is particularly flagrant in the NITO configuration in which the GaN layer cannot replace the highly conductive ITO in any way. An attempt to anneal these structures was made, but inconclusive, which could not be explained in the present framework and is therefore not shown here.

Only the DITO configuration was characterised by the current-voltage cell characterisation under different working temperatures (25, 35, 45, 55 °C). Different illuminations (1, 5, 10, 50, 100 % of the STC illumination 1000 W/m$^2$), and the resulting J-V curves are displayed in figure 6.11. The corresponding band diagram is also shown in figure 6.10. As expected, the experimental $V_{OC}$ follows a logarithmic increase with respect to the $J_{SC}$, which is linearly

proportional to the irradiance (see equation 2.10 page 9 and other related physical quantities). See also equation 6.1.

$$\begin{aligned} V_{OC} &\propto \ln\left(\frac{I_{SC}}{I_0}\right) \\ I_{SC} &\propto T, irradiance \\ I_0\left(n_i^2\right) &\propto \exp(T) \end{aligned} \tag{6.1}$$

However, the exponential decrease of the *FF* with illumination shows here that the limiting factor in this cell configuration is the series resistance, as already mentioned in the previous section. Considering the band diagram of the DITO i-n solar cell (figure 6.10, no other influence rather than the high resistivity can be reported. Indeed, increasing the irradiance will further split the quasi-fermi levels, and they will probably re-assemble on the experimental GaN layer, a sign of high resistivity and an imperfect selectivity, as previously presented. This is especially highlighted by the S-shape of the J-V curve that remains similar whatever the illumination (see figure 6.11a). Some other conclusions can be drawn from these results:

- Refering to equation 6.1, it is expected and observed that the $V_{\mathrm{OC}}$ decreases linearly with the temperature ($V_{OC} \propto \ln\left(\exp(-T)\right) \propto -aT + b$), whatever the illumination degree. So everything is functioning correctly from this point of view. In terms of band diagrams, the VB and the CB slightly change energy levels with varying temperatures, which will usually reduce the BG at higher temperatures.
- The *FF* is not expected to change with temperature for a suitable solar cell; its linear increase with increasing temperature is a sign of a charge transport limited by a barrier. That barrier has already been mentioned in the previous sections (see for example fifth paragraph of section 6.1.2), but this is one more proof of its presence.
- The $J_{\mathrm{SC}}$ is barely increasing with temperature because of the associated BG reduction that increases the photo-generated current (see lower right panel of figure 6.7), see equation 2.5 page 7).
- The second saturation current (plateau at the far right of the plots, at a higher voltage in figure 6.11a) also depends on temperature. This is due to thermionic emission, and checking if the values follow that law still must be done. The saturation current is given by:

$$J_{SAT}(T,V) = AT^2 \exp\left(\frac{\Phi}{k_B T}\right) \tag{6.2}$$

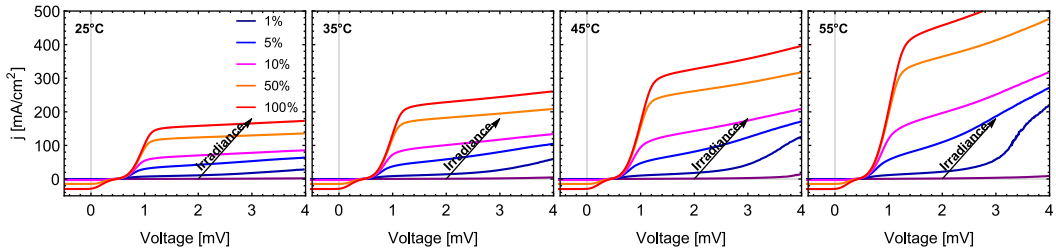


(a) J-V curves for various working temperatures and illuminations.

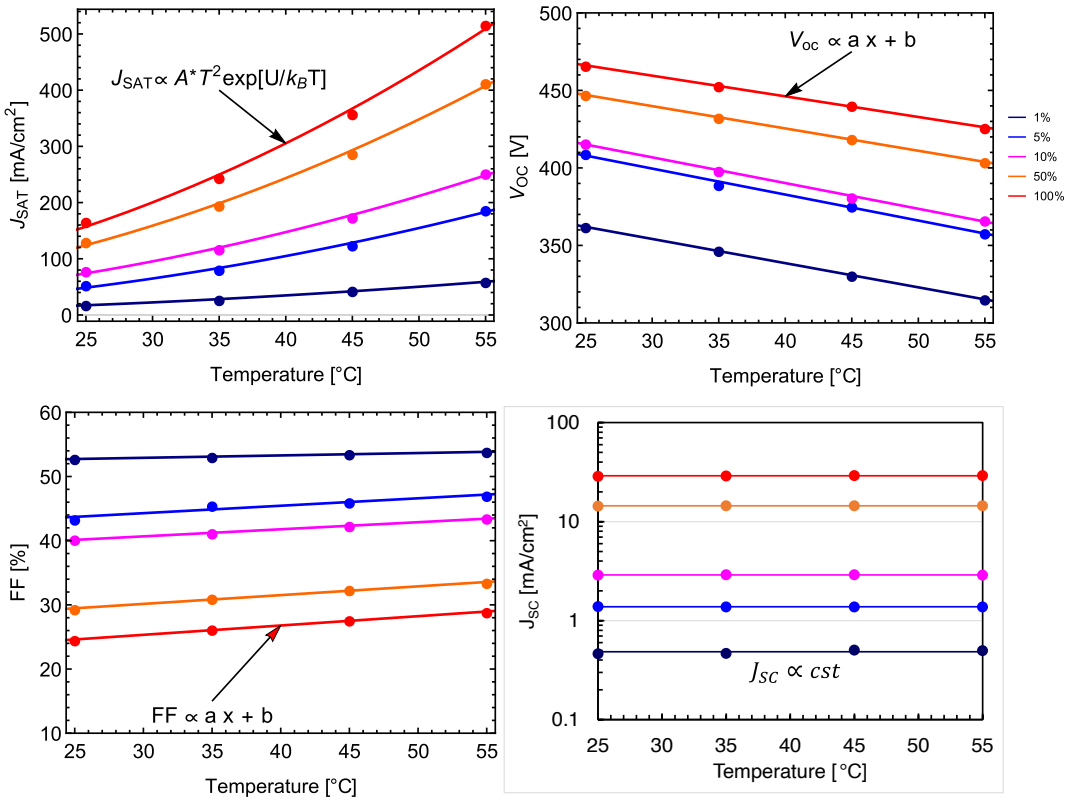


(b) Solar cell key performance values vs working temperature and illumination.

Figure 6.11: Si-doped GaN PVD contact: temperature & irradiation influence on the DITO i-n architecture (see figure 6.7). No vertical error bar is shown here because they are shorter than the point width (0.2 % relative). The temperature is set with a ±2 °C precision.

#### 6.2.2.5 Back contact, doping level and thickness influence

This section explores the application in a solar cell of the Si-doped GaN layers developed in section 5.3. The solar cell performances are evaluated as a function of the doping level and the thickness of the contact.

Figure 6.12 displays the lifetime of charge carriers inside the DITO/i-n architecture (see figure 6.7), for different doping levels and different thicknesses. We see that the lifetime is now acceptable and has the same behaviour as in the analysed figure 6.8: it reduces after the

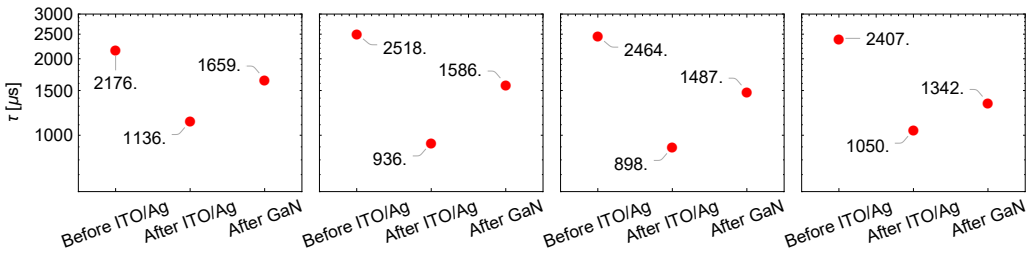


(a) Lifetime for different silicon content (0.0, 2.0, 4.2 and 6.5 at. % Si) levels and a constant thickness of 20 nm.

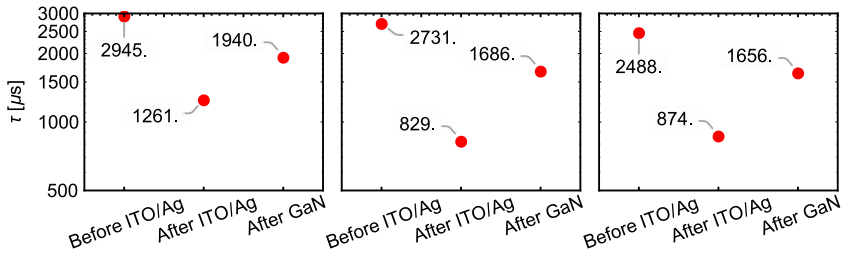


(b) Lifetime for different thicknesses (10, 20 and 50 nm if they were deposited on a flat wafer) and a constant silicon content of 4.4 %.

Figure 6.12: Si-doped GaN PVD contact: doping level and thickness influence on the lifetime on the DITO i-n architecture (see figure 6.7). The errors here are not shown because they are shorter than the point diameter (< 0.2 % relative).

ITO/Ag front deposition (sputtering damage). It improves after the Si-doped GaN sputtering at the back (passivation recovery from the 200 °C deposition temperature). A different batch of wafers explains these better performances than the ones used for the previously presented results. The depositions also occurred 3 – 4 weeks later; fewer problems arose, and better passivation was achieved. Regarding the thickness, a thinner GaN layer seems to result in a more sustainable lifetime, and a slight decrease with increasing doping level is also noted.

The J-V curves of these different combinations are displayed in figure 6.13. If we consider the influence of the silicon content (figure 6.13a), we see in figure 5.18b that increasing the silicon content to 3 – 4 % should yield a better conductivity and activation energy. Here, the inverse is observed: the $V_{OC}$ is reduced with increasing silicon content. So the problem may lie in the interface between the GaN and its neighbouring layers rather than on the GaN layer itself or in the fact that here the GaN layer is thinner, which may have a different effect on the resistivity and activation energy with respect to the silicon content. When considering only the architectures containing doped GaN(n) layers, the optimal one is still found with a silicon content of about 4 % (see efficiency values of figure 6.13a). But such fine-tuning of a trade-off makes it difficult to judge the involved parameters, even with the help of the band diagram. It should be a mix of surface recombination, resistivity and band edge effects.

If we now consider the influence of the thickness (see figure 6.13b), increasing it will hinder the $V_{OC}$ and $FF$. This is most likely due to reducing the effect of the Si-doped GaN layer on the metal's work function. Indeed, increasing the resistance between the absorber and the contact

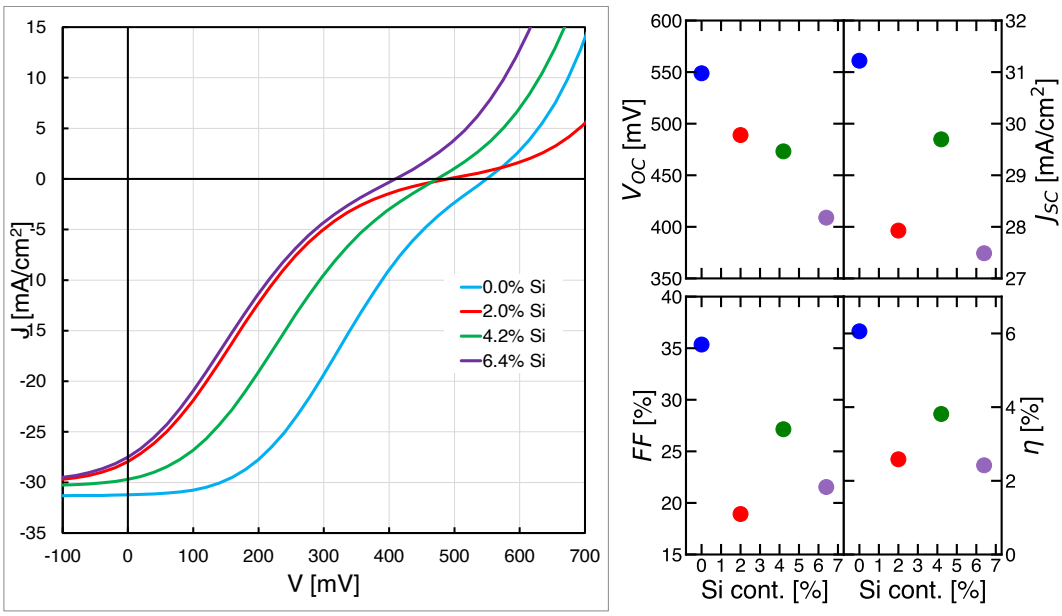


(a) Silicon content influence.

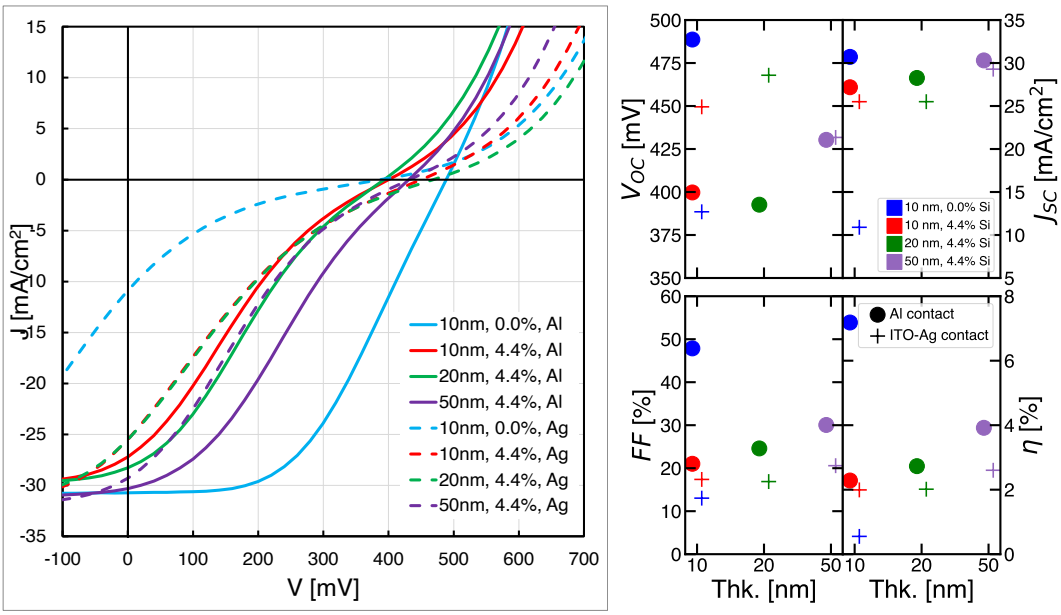


(b) Thickness influence.

Figure 6.13: Si-doped GaN PVD contact: doping level and thickness influence on the J-V curve for the DITO i-n architecture (see figure 6.7) with either an ITO/Ag or an aluminium back contact. The errors here are not shown because they are shorter than the point diameter (< 0.2 % relative).

will dampen the *FF*, even to a point where the $V_{OC}$ is affected. Finally, a better $V_{OC}$ and *FF* were reached when using the aluminium back contact rather than the ITO/Ag one. By a thorough measurement, a contact resistivity $\rho_C$ of $\rho_C^{\mathrm{ITO/Ag}} \cong 10-50\,\Omega\,\mathrm{cm}^2$ and $\rho_C^{\mathrm{Al}} \cong 0.5-1.0\,\Omega\,\mathrm{cm}^2$ was

obtained for the two types, and indeed the aluminium is more performant. This is similar to the germanium-doping results (section 6.2.1).

#### 6.2.2.6 Si-doped GaN PVD contact: key takeaways & next steps

Even though the cell performances were overall poor because of an unknown experimental mishap or because of a slightly defective wafer, implementing the Si-doped GaN layer (Si content: 4.4 at. %) in a DITO (ITO on both sides with a 20 nm GaN layer at the back) or FITO (a front side ITO with a 100 nm GaN layer at the back, see figure 6.7) configuration did improve the lifetime of the charge carriers, without additional benefit. The low lifetime is also a reminder of how sensitive to defects and contamination silicon is. However, given the S-shape of the J-V curve induced by the addition of the GaN layer, the $V_{\mathrm{OC}}$ was undoubtedly decreased. Still, the brutal decline of the *FF* dominated this slight improvement, and the efficiency was reduced to lower values compared to the reference cells. In particular, the NITO configuration proved that GaN is not conductive enough to replace highly conductive ITO. The too-high resistivity of the layer was also reflected by the behaviour of the *FF* at different irradiances (figure 6.11). But overall, since the whole batch of results was mediocre, as reflected by the reference architecture, all these results have a considerable amelioration potential with a luckier set of wafers from the supplier or fewer instabilities in the KAI-M.

Annealing was also tested, but it also worsened the photovoltaic performances and should be avoided. It seems to degrade both the $V_{\mathrm{OC}}$ and the *FF*. GaN is known to be sturdy under such stresses due to high temperatures. So the $V_{\mathrm{OC}}$ degradation is believed to originate from the amorphous silicon layers, losing in selectivity. At the same time, the *FF* is also degraded, possibly because of a conductivity decrease due to a degradation of the ITO. But overall, these cells exhibit such J-V curve S-shaping that it is difficult to trust the $V_{\mathrm{OC}}$ and, to a certain extent, the *FF*.

The second batch of experiments probed the thickness and the silicon content of the GaN layer and the metallic contact type. This second batch showed better performances than the first one but still worse than the reference cell, again because of an S-shape of the J-V curve, symptomatic of the high series resistance of the whole stack. Extracted from that second batch, the best combination is found for undoped GaN contact at 20 nm thickness ($V_{OC}$ = 550 mV, $FF$ = 33 %), and for doped GaN contact at 10 nm thickness and 4.2 % content ($V_{OC}$ = 500 mV, $FF$ = 48 %).

This S-shaping of the J-V curve is, in fact, the consequence of a GaN layer that is far from being conductive enough ("-" architecture, referring to figure 6.7), does not passivate enough ("i" architecture) and is not selective enough ("i-n" architecture). Instead of exploring further the architectures and different effects of its fabrication processes, it would be better to first go back to improving the performances of the layer itself: lower the Urbach energy, reduce the FCA, increase the optical BG, increase the crystallinity and increase the stability under doping.

## 6.3 InGaN contacts by PVD

### 6.3.1 Introduction

This section presents the continuation of my collaboration with Julie Dréon (see section 5.5.3), another *Ph.D.* student working on $MoO_x$ layers in PV-lab who obtained her *Ph.D.* in 2022.

The incorporation of InGaN in a solar cell by PECVD and doped GaN by PVD sputtering was tested in the two previous sections. This section presents the results of the integration of undoped InGaN layers deposited by PVD in solar cells with two different configurations (electron or hole selective front contacts) and how they compare to the current PV technology. The InGaN layers used in the solar cell architectures presented in this section are developed in the second half of section 5.5.3. Please refer to it for more details. In particular, the so-called "thin" co-sputtered layers are about 10 nm thick, while the "thick" ones are about 50 nm thick. For the single target deposition, the thickness varies between 5 and 20 nm for the "thin" ones and between 10 and 100 nm for the "thick" ones.

Three sputtering setups were used to test different properties where the sample holder was never rotated. In the co-sputtering setup, an InGaN and a GaN target were sputtered simultaneously and with a power that kept the deposited thickness constant across the whole wafer. This is expected to create an indium content gradient across the wafer, and the effect of the indium content $X_{\mathrm{In}} = \frac{\mathrm{In}}{\mathrm{In+Ga}}$ (In & Ga in at. %, $X_{\mathrm{In}}$ in %) can be analysed. On the second setup (and the third one), only the GaN (or only the InGaN) target was used to create a thickness gradient and analyse its effect on cell properties. See section 5.5 for more result details.

### 6.3.2 Architectures

In addition to the reference substrates, the Univex sample holder was large enough to hold two 4" wafers cut in half (see figure 5.32, showing one of two halves at the bottom). For the six depositions presented in section 5.5.3, two studied architectures were also introduced in the Univex, analysing twelve configurations of architectures and layers. These architectures are described in figure 6.14, where the InGaN/GaN layer is at the front. Referring to figure 6.7, it would resemble the DITO/i architecture, where the InGaN/GaN layer has both a role of selectivity and of contact.

After the InGaN/GaN layer deposition on the whole half-wafer at once, the ITO was applied through a mask on both sides, followed by the metallic contact. The J-V curve of each solar cell was then measured with a mask that perfectly fits the size of the ITO so as not to create charge carriers outside the solar cell.

The two band diagrams of figure 6.14 show what can be expected regarding performance. In both cases, the selectivity and the conductivity of the InGaN layer were tested; the passivation is taken care of by the a-Si layer. In the so-called "electron contact architecture" (corresponding to the role assigned to the InGaN layer), we see that there is almost no band bending in the

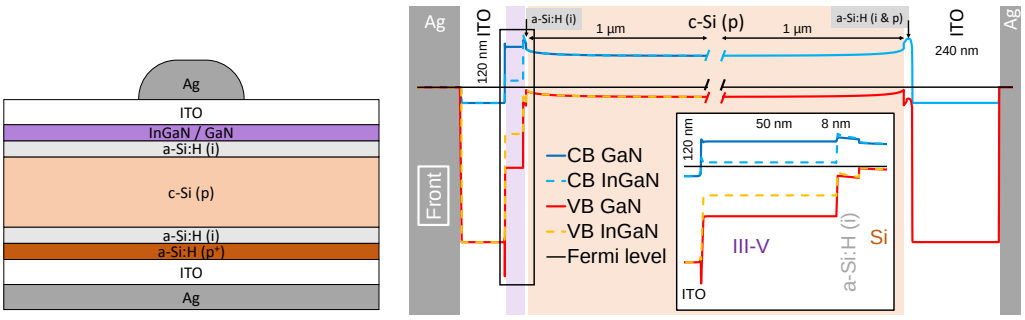


(a) Electron contact architecture and corresponding band diagram.

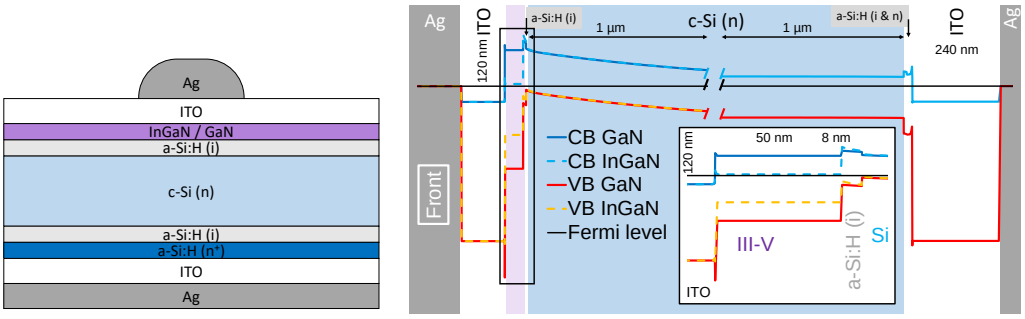


(b) Hole contact architecture and corresponding band diagram.

Figure 6.14: InGaN contact: basic architecture tested and corresponding band diagram, where the InGaN layer acts either as an electron contact or as a hole contact.

wafer's c-Si region for the CB, which means that electrons are expected not to be repelled. This indicates that the architecture allows good electron selectivity at the front contact. The same could be said for the holes since the band bending seems to favour their emission at that side, but they would have to face a solid repelling barrier, being the deep InGaN's VB. The holes are far better off on the back contact, where they can be absorbed by the ITO and generate current at that contact. In terms of indium content, since the naturally doped GaN aligns its CB with the one of a-Si, this means that the thin barrier that was first opposed to the electron exiting at this side by thermionic or tunnelling emission is more or less thickened (because of the different thicknesses tested), preventing said extractions. But with a little bit of indium, that barrier is slowly lifted; it is expected that the higher the indium content, the better the contact because of that. In other words, the single InGaN target is expected to deliver the best results.

In contrast, the hole architecture will bend the wafer's c-Si's VB to favour hole extraction. However, since this study does not consider doping, the GaN contact has to act here as a hole extractor with its intrinsic n-type doping. This means that the holes are opposed with the same barrier as in the electron contact, where the InGaN's VB falls deep in energy and is too thick to be penetrated by tunnelling. In short, this architecture is doomed to fail because there is no p-region, and the holes always remain the minority carrier; they will easily recombine before reaching a contact. Increasing the indium content could alleviate part of this issue by reducing the height of the hole barrier, but that will certainly not lead to a record-breaking solar cell.

### 6.3.3 Results

The cell performances are displayed in figure 6.15. They are extracted from the J-V curves that are presented in annexe B.4, figures B.30 and B.31. The qualitative analysis and main conclusions are based on the modelisation proposed by Antognini in his PhD thesis [10, 151].

As expected, the InGaN contact acts better as an electron than a hole contact. This is due to both the work function and the stabilisation Fermi level energy $E_{FS}$ being closer to (or maybe even within) the CB; the defects and impurities thus tend to be donor-like until $E_F$ reaches $E_{FS}$. This is the primary reason why p-doping of In/GaN materials remains difficult, why In/GaN is naturally n-doped, and hence why it acts better as an electron selective contact. Indeed, considering figure 6.14a, if the InGaN layer is n-doped, there is not even a p-n junction to make the minority carriers drift towards the contact. The band diagram analysis presented in the previous section then holds.

If now the thickness influence is considered, comparing the J-V curves of the thin with the thick layers, the most noticeable difference is only displayed when the GaN target is used (top J-V curves in the result figures), where here a thinner layer will allow the solar cell to begin to produce power, once it has reached 5 nm. For the GaN target, there is, in fact, almost no charge carrier extraction (zero $J_{SC}$ value), which means that all the generated charge carriers recombine before being extracted. In other words, the GaN layer prevents the extraction of charge carriers until they recombine within the solar cell; decreasing the thickness of the said layer will ultimately allow some charge carriers to reach the metallic contact through tunnelling emission. This is undoubtedly a combination of the following factors: poor selectivity and bad resistivity. The poor selectivity will offer recombination centres at interfaces where the charge carriers can recombine instead of reaching the metallic contact, decreasing the $V_{OC}$ and provoking this S-shaping of the J-V curve. Nothing can be said about the passivation here because it was not measured, where good selectivity and resistivity should imply good passivation. However, the passivation is assumed to be acceptable because of the use of reference a-Si:H(i) layers deposited against the thick absorber and because no step of the fabrication process included a temperature above 230 °C. The high resistivity of the layer has already been demonstrated in the layer characterisation section (section 5.5.3). In other words, even if a charge carrier would cross the absorber – InGaN junction, it would also be slowed down and hindered in its path towards the contact, reducing the $V_{OC}$ even further.

The counterproductive effect of the resistivity is mitigated by the increase of the indium content $X_{In} = \frac{In}{In+Ga}$ (In & Ga in at. %, $X_{In}$ in %), as shown in the co-sputtering configuration (bottom J-V curves in the result figures), where the thickness is considered constant. Increasing $X_{In}$ will allow more charges to be collected (an increase of the $J_{SC}$), an increase of the $FF$, a reduction of the S-shape and overall an increase of the efficiency of the solar cell, as observed for layers deposited by PECVD (see section 6.1) and reported in the literature [145]. On the two problematic points mentioned in the previous paragraph, the resistivity and the electron barrier are lowered (hence improving the cell performance) when adding indium. The S-shape,

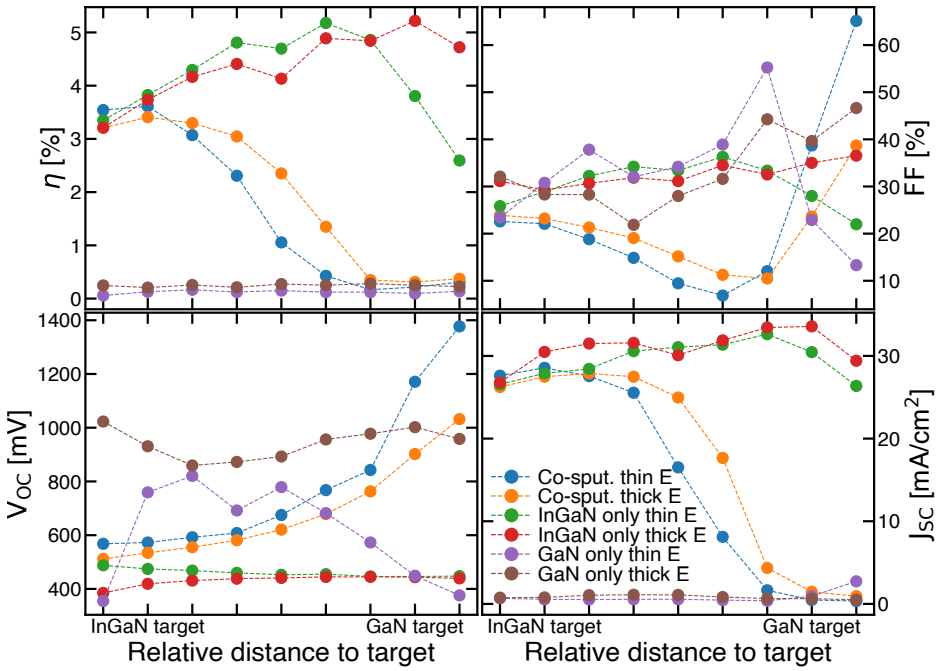


(a) Electron architecture "E" (see figure 6.14a). See J-V curves in figure B.31.

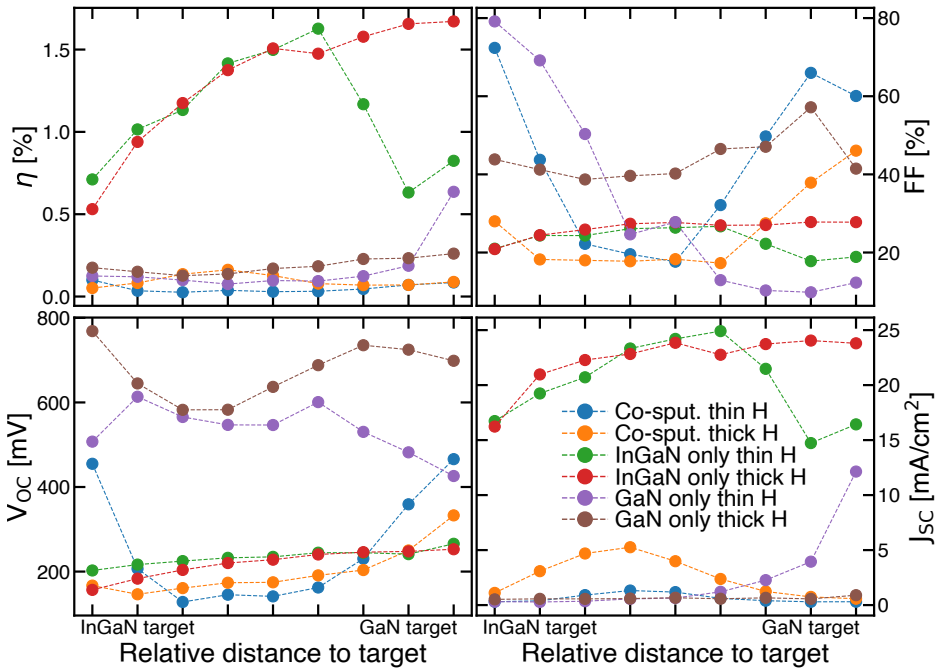


(b) Hole architecture "H" (see figure 6.14b). See J-V curves in figure B.30.

Figure 6.15: InGaN PVD contact: cell performances for "thin" (5–20 nm) or "thick" (10–100 nm) In/GaN layer as a function of the relative distance to the sputtering targets. The InGaN target is figuratively located on the left of each x-axis, while the GaN one is on the right. Depositions are performed either in single or co-sputtering mode. The error bars (< 0.2 % relative) are shorter than the point diameter, hence not shown.

though reduced, is still present, and the $J_{SC}$ is still not at its optimal value. This means that due to the presence of gallium, the resistivity of the InGaN layer, the main contributor to the series resistance of the solar cell, is still too high, preventing charges from reaching the contact. With increasing indium content, not only is the resistivity reduced, but by considering the band diagrams, the barriers for both charge carriers are lowered.

Table 6.3: InGaN PVD contact: best result compared to literature results. The best solar cell contains an $In_5Ga_5N$ layer of about 10 nm deposited in a single sputtering setup in an electron architecture. The texturisation of the cell in the literature result allows for a higher $J_{SC}$.

| Cell | $V_{OC}$ [mV] | $J_{SC}$ [mA/$cm^2$] | $V_{MPP}$ [mV] | $J_{MPP}$ [mA/$cm^2$] | $FF$ [%] | $\eta$ [%] |
|---|---|---|---|---|---|---|
| InGaN(n)-i-p-i-p flat, present work | 454.9 | 31.36 | 234.3 | 22.1 | 36.29 | 5.18 |
| Si p-i-n-i-n texturised, [75] | 744.5 | 39.58 | | | 78.3 | 22.3 |

Compared to the chosen literature reference, the texturisation allows for better light trapping, which can explain most of the $J_{SC}$ difference between the two solar cells. Even though adding indium helps, the higher resistivity of the InGaN contact still lowers the cell performances. However, power is still extracted from the cell and could be improved further, given a finer tuning. For example, this exact thickness could be used with a textured wafer on a rotating sample holder during its sputtering to improve the $J_{SC}$. The Clusterline, a PVD sputtering system at the CSEM, could deposit epitaxial GaN on sapphire. Since epitaxy is possible by sputtering but was not achieved with the Univex at PV-lab (the system used for the present work), there is room for layer improvement leading to better contact performances.

### 6.3.4 InGaN PVD contact: key takeaways & next steps

InGaN and GaN targets were used for (co-)sputtering of an (In)GaN contact in a total of twelve different configurations using a compositional gradient, allowing the measurement of each nine solar cells for a grand total of 108 J-V curves. In that regard, only the four most significative band diagrams are presented, from which it is correctly predicted that the InGaN layer acts far better as an electron contact than a hole contact. If the resistivity had been adequate, a trade-off between the thickness and the indium content should have been found, optimising the tunnelling emission through the contact. But since resistivity is the main limiting factor in the layers produced with the Univex, a thinner layer with a high indium contact is preferred.

It was thus observed that the most efficient configuration was the one with the highest indium content and the thinner thickness in an electron contact architecture. These results are good news: a first efficiency of more than 5 % was achieved, even though such solar cell performances still compare poorly with the literature numbers. The improvement should focus on the layer quality rather than its compatibility with the rest of the solar cell; the resistivity must be reduced by improving the crystallinity of the InGaN layer.

## 6.4 Contacts: wrap-up and conclusions

In this chapter, the layers developed in chapters 4 and 5 were integrated into solar cells as contacts only since they were not performant enough to act as an absorber.

First, GaN, InN and InGaN layers deposited by PECVD were integrated as an electron contact, where their passivation and selectivity impact on the solar cell was tested. Strong S-shaped J-V curves hinted towards a high resistivity of the contact, and due to these low performances, poor passivation and poor selectivity were deduced. A band diagram analysis also confirmed these two results. Nevertheless, an efficiency of almost 13 % could still be reached when the indium content was maximised and when the InN electron back contact layer was a simple contact between the passivating and selective layers and the metallic contact. Compared to the reference cell, an improvement was observed thanks to that InN layer. By analysing the modelled band diagrams, it is observed that above about 40 % indium ($X_{\mathrm{In}} = \frac{\mathrm{In}}{\mathrm{In+Ga}}$, In & Ga in at. %, $X_{\mathrm{In}}$ in %), the cell performances did not vary as much as under that value, hinting towards the fact that the CB of the underlying layer aligned with the In/GaN one at that indium content value (see the undoped case in figure 2.3c).

Then, different PVD layers were tested, first a germanium-doped GaN as electron selective back contact in sixteen configurations, then a silicon-doped GaN electron back contact in twelve configurations, and finally an undoped InGaN as electron or hole selective front contact in 12 structures of 9 cells each. With the germanium doping, the first of these three achieved an efficiency of 8 %, well below expected and present values of the usual (n)a-Si:H layer taking this place and role. It was concluded that a thinner selective contact with an aluminium layer produced the best results because of a better thermionic and tunnelling emission through the selective barrier. It was also observed that the GaN layer induces an S-shaping of the J-V curves, probably due to sputtering damage on the underlying layers, which could be mitigated by increasing the deposition pressure. However, by doing that, the GaN crystallinity is expected to be lost, weakening the dopant activation. Annealing reduces the resistance between a Ge-doped PVD GaN layer and metallic contact. An optimal annealing temperature of 400 °C was found, and an aluminium metallic contact is preferred over an ITO/Ag one. However, the resistivity of such contact was still five orders of magnitude under literature values, most likely because of the poor electrical performances of the GaN layer.

Experiments on twelve electron back contact configurations highlighted once again that the Si-doped GaN contacting layer was not conductive enough and that this factor was the limiting one for now. The ill-performing wafer batch of this experiment allows the conjecture that far better solar cell performances can be achieved with a less defective wafer. It is also observed that the GaN layer induces an S-shaping of the J-V curves, probably due to sputtering damage, with the exact causes and proposed solutions. The irradiance and temperature sweeps confirm the existence of an electron extraction barrier at the back while also confirming that the solar cell behaves as expected from a reverse biased p-n junction (see figure 6.11b). This led to the study of the influence of the thickness and the doping concentration on the J-V curves and

cell performances, where similarly to section 5.3.1, an optimal silicon content of about 4 at. % is found, and where the thinnest possible layer favours charge carrier extraction by easing the thermionic and tunnelling emission.

The thin undoped InGaN electron selective front contact, in agreement with the PECVD results, performed best when the indium content was maximised, simultaneously decreasing the resistivity, allowing the solar cell to reach an efficiency above 5 %. Again, the layer thickness and the indium content are key parameters to alleviate that electron barrier extraction.

The In/GaN contact compares poorly to literature values and state-of-the-art performances. However, the processes and layers presented here are not optimised, and particularly an improvement of the crystallinity/epitaxy should enormously boost the conductivity of the layer, impacting not only its performances as a contacting material but the transport of the charges to the metallic contact as well. Please refer to the two previous chapters' conclusions for clues on how to improve even further the crystallinity. The band diagrams of all these different architectures also highlighted that, as a naturally n-doped material, the In/GaN layer electron selectivity is terrible when used with an n-doped c-Si wafer. This means that when using InGaN in a single junction solar cell, it is preferable to create the p-n junction at the side where the InGaN layer is located, being front or back. This, in turn, implies that the c-Si wafer should be p-doped.

# 7 Conclusion

In the context of climate change, PV technology is a critical enabler in the transition towards cleaner energy sources. Nowadays, the solar panel market is dominated by PERC technology, with growing competition from the TOPCON technology based on monocrystalline silicon. These have by-design efficiency limits that can be overcome with different solutions, one of them being the tandem technology: coupling a c-Si bottom absorber with a higher bandgap top absorber. In that regard, InGaN is a serious candidate because of its potential compatibility with silicon. However, the challenges tied to InGaN growth can partially be alleviated by switching to lower-temperature deposition processes, which is the subject of this thesis. Using quality metrics and reference performances, the following research questions were established as crucial guidelines for the present research:

1. Is it possible to produce InGaN materials at low temperatures?
2. If yes, are the characteristics of these layers compatible with PV applications?
3. If they are compatible, how stable do they remain when p- or n-doping is added?
4. If stability is sufficient, and once integrated, how well do these layers compare with standard choices (e.g. a-Si) in c-Si solar cells?

The first three questions were addressed by exploring a PECVD deposition process in chapter 4. Among others, the main result of the PECVD study was that lowering the growth rate generally improves all quality metrics of the layers. It was also observed that the bandgap of InGaN follows the quadratic Vegard's law with respect to indium content $X_{\mathrm{In}} = \frac{\mathrm{In}}{\mathrm{In+Ga}}$ (In & Ga in at. %, $X_{\mathrm{In}}$ in %), but that the bowing of said law is influenced by the growth rate as well. Using a TOF-MS allowed for a deeper analysis of the plasma dynamics and the critical importance of different factors leading to a deposition of layers with better quality metrics. In particular, this is achieved by promoting a stronger precursor dissociation, by a more efficient evacuation of the plasma by-products, and by starting the plasma before injecting the precursors containing carbon. Eventually, most of the different layer characteristics and quality metrics were modelled as a function of all but one deposition parameter with acceptable accuracy, allowing the identification of the optimal processing conditions. In concluding that chapter, the InGaN-absorber path was discarded because of the following

reasons: p-doping could not be achieved, optical properties were not satisfactory enough (insufficient sharpness in the band edge, FCA still present, degeneracy level increase with increasing indium content), as well as concerns related to crystallinity and resistivity. However, some promise remained for applying these layers as selective contacts, which we investigated further. In answer to the first three research questions asked above:

1. Yes, it is possible to produce InGaN materials at low-$T$ using PECVD,
2. The layer characteristics are sufficient for applications as a selective contact but not as a photovoltaic absorber, and
3. Only the n-doping could be achieved.

Similarly, the feasibility of low-temperature InGaN deposition by PVD sputtering was also explored. Among others, the main results of the PVD study highlighted the vital role of pressure on the basic layer characteristics. They demonstrated acceptable performances for Ge doping, better than Si doping. Epitaxy of undoped GaN on sapphire could be achieved but was unstable under an increasing silicon doping level. Increasing the indium content of the layer helped decrease the resistivity, but still to values at least two orders of magnitude greater than standard (n)a-Si:H layers. For the same reasons as with PECVD, but mainly because p-doping could not be achieved, the possibility of using these InGaN layers as absorbers was discounted, and we investigated selective-contact applications instead. In conclusion, we find the same answers to the research questions above for sputtering but with better conductivity features compared to PECVD.

By testing both PECVD and PVD layers in devices, it was observed that the obtained layer properties (be it optical, electrical or structural) did not improve cell performances compared to state-of-the-art literature values. However, for each technique used and presented (undoped In/GaN by PECVD, doped GaN and undoped InGaN by PVD), power could be extracted from the solar cell under STC, in one case even higher than the one of the reference cell it was compared to (InGaN by PECVD, see figure 6.3h). The main two issues with these contacts are their insufficient conductivity (decreasing the $V_{OC}$ and worsening the $FF$) and their lousy selectivity (decreasing the $J_{SC}$, worsening the $FF$ and inducing S-shaping of the J-V curve). However, **optimisation at all the levels seems possible, and better cell performances are expected if more time and research are dedicated to InGaN materials for PV applications**. The fourth research question is then answered in the following way: it compares poorly with standard c-Si solar cells but has a vast potential for improvement.

Several scientific questions remain unanswered and may represent pathways towards further optimisation. Concerning PECVD, InGaN was only produced using $N_2$ as a nitrogen source, not ammonia. The use of the latter has demonstrated improvement for GaN and InN and may slow the growth rate further, leading to better-quality InGaN layers. In general, the crystallinity and the epitaxy of the layers deposited by PECVD can still be improved, leading to a better understanding of the doping impact. The study of the doping with PECVD was also not explored as much as the layer characteristics, and a deeper focus on this subject

may prompt better layer properties for solar cell integration. Only one study varying the indium concentration and the architecture was conducted on solar cells. When integrated, the InGaN layer thickness, its doping level or the annealing of the whole solar cell may still yield improved performance with further optimisation. Regarding PVD sputtering, the doping was only tested with the GaN layer; including indium in the mix may also yield electrical and structural improvements of the layer, leading again to more efficient solar cells. Thanks to the DOE method, the impact and potential interaction effects of the less numerous deposition parameters of the sputtering process on the layer characteristics may be better understood. And here again, the crystallinity and the epitaxy of the layers deposited by PVD can still be improved until epitaxy is reached. All the above entails that low-$T$ InGaN layers retain significant promise for selective-contact applications.

# A Further theoretical development

This appendix aims to give a deeper understanding of some of the methods and tools presented in the chapter 3 of this thesis. Each section begins by recalling to which section the subject is linked.

## A.1 Raman: other parasitic vibrational modes

This section is linked to the Raman characterisation method, section 3.2.2.1, and is an addition to table 3.2 mentioning the major In/GaN vibration modes detected with this tool. And indeed, other parasitic modes can be observed when using the Raman, some of which are presented in table A.1.

## A.2 Ellipsometry: from Fresnel coefficients to the complex index of refraction

This section is linked to the ellipsometry characterisation method found in section 3.2.2.3 and better explains the fundamental physics on which the ellipsometry measurement is built. Concretely, the measured parameters before and after interaction with the probed sample are the so-called "ellipsometric angles" $\Delta$ and $\Phi$, which are linked to the complex Fresnel coefficients $r_\perp$ and $r_\parallel$, where $\delta_{p,s}$ is the phase value of the electric field regular (respectively parallel) to the probed surface.

$$\rho = \frac{r_\parallel}{r_\perp} = \tan(\Psi)\, e^{i\Delta} \tag{A.1}$$

$$\tan(\Psi) = \frac{|r_\parallel|}{|r_\perp|}, \qquad 0° \leqslant \Psi \leqslant 90° \tag{A.2}$$

$$\Delta = \delta_\parallel - \delta_\perp, \qquad 0° \leqslant \Delta \leqslant 360° \tag{A.3}$$

Table A.1: Experimental methods, Raman: other parasitic vibrational modes encountered during Raman or FTIR characterisation, with references. The abbreviations TA, LA, TO and LO stand for "Transverse Acoustic", "Longitudinal Acoustic", "Transverse Optical" and "Longitudinal Optical", respectively.

| Signature mode | Wavenumber $[\mathrm{cm}^{-1}]$ | Reference |
|---|---|---|
| Mg – H | 2168 | [26] |
| Mg – H | 2219 | [26] |
| N – H surface bending | 870 | [19] |
| N – $H_2$ bending & rocking | 1200 – 1500 | [19] |
| N – H Fuchs-Kliewer phonon | 1430 | [19] |
| N – H stretching | 3260 | [19] |
| N – N – N bending | 640 | [43] |
| N – N – N symmetric stretching | 1304 – 1350 | [43] |
| N – N symmetric stretching | 1571 | [43] |
| N – N asymmetric stretching | 1694 | [43] |
| N – N – N asymmetric stretching | 1986 – 2112 | [43] |
| $H_2O$ translational (2) | 65 | [34] |
| $H_2O$ translational (4) | 162 | [34] |
| $H_2O$ librational $A_2$ | 430 | [34] |
| $H_2O$ librational $B_2$ | 650 | [34] |
| $H_2O$ librational $B_1$ | 795 | [34] |
| OH bending | 1581, 1641 | [34] |
| OH stretching | 3051, 3233, 3393, 3511, 3628 | [34] |
| a-Si (TA) | 150 | [17] |
| a-Si (LA) | 310 | [17] |
| a-Si (LO) | 380 | [17] |
| a-Si (TO) | 480 | [17, 51] |
| $\mu$c-Si | 510 | [51] |
| Si – Si (TO), c-Si | 520 | [17, 51] |
| Si – H bending | 640 | [69] |
| Si – $H_2$ wagging | 640 | [69] |
| Si – H stretching 1 & 2 | 2000 & 2090 | [69] |
| Si – $H_2$ stretching | 2095 | [69] |
| Si – C stretching | 770 – 800 | [90] |
| Si – $CH_2$ wagging | ~ 1000 | [90] |
| Si – $CH_3$ bending | 1250 | [90] |
| C – $H_2$ symmetric stretching | 2850 | [85] |
| C – $H_3$ symmetric stretching | 2850 | [85] |
| C – $H_2$ asymmetric stretching | 2920 | [85] |
| C – $H_3$ asymmetric stretching | 2960 | [85] |

For detailed mathematical developments, we invite the reader to consult the excellent and complete work of Fujiwara [64]. The Fresnel coefficients are defined as such for reflection $r$ and transmission $t$:

$$r_{\parallel} = \frac{\tilde{n}_i \cos(\theta_t) - \tilde{n}_t \cos(\theta_i)}{\tilde{n}_i \cos(\theta_i) + \tilde{n}_t \cos(\theta_t)} \tag{A.4a}$$

$$r_{\perp} = \frac{\tilde{n}_i \cos(\theta_i) - \tilde{n}_t \cos(\theta_t)}{\tilde{n}_i \cos(\theta_i) + \tilde{n}_t \cos(\theta_t)} \tag{A.4b}$$

$$t_{\parallel} = \frac{2\tilde{n}_i \cos(\theta_i)}{\tilde{n}_t \cos(\theta_i) + \tilde{n}_i \cos(\theta_t)} \tag{A.4c}$$

$$t_{\perp} = \frac{2\tilde{n}_i \cos(\theta_i)}{\tilde{n}_i \cos(\theta_i) + \tilde{n}_t \cos(\theta_t)} \tag{A.4d}$$

Here, the angles $\theta_i$ and $\theta_t$ of the incident and of the transmitted light are related by Snell's law:

$$\tilde{n}_i \sin(\theta_i) = \tilde{n}_t \sin(\theta_t) \tag{A.5}$$

Equation A.5 presents Snell's law, valid for both perpendicular and parallel polarisations, where the $i$ or $t$ index refers to the medium containing the incident and transmitted light respectively, $\tilde{n}$ is the complex index of refraction, and $\theta$ is the angle of the photon trajectory with respect to the normal of the surface. The parallel or perpendicular component of the Fresnel coefficients are considered with respect to the plane spanned between the incident and the reflected beam; see figure A.1 for a better visual representation, with the kind permission of Dr. Mittleman [121].

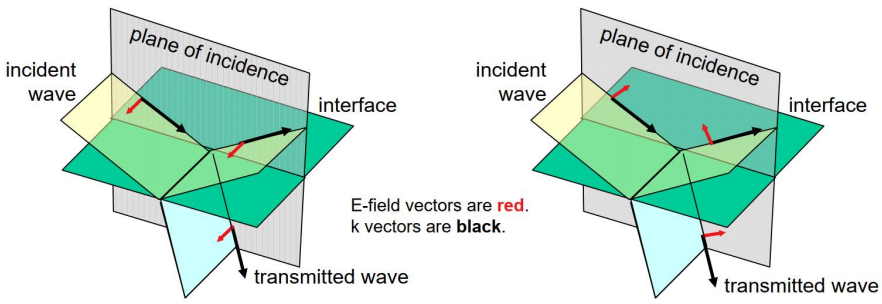


Figure A.1: Experimental methods, ellipsometry: Electro-magnetic wave encountering an interface, where the electric field is perpendicular (left image) or parallel (right image) to the plane of incidence. The combination of these two electric fields give rise to the photon polarisation. Taken with the kind permission from Mittleman's lecture [121].

The measured $\Delta$ and $\Psi$ values are thus linked to the Fresnel coefficients, which can define $\rho$ (see equation A.1). $\rho$ is linked to the complex dielectric constant of the probed material $\tilde{\varepsilon}_t$ by the following relationship:

$$\widetilde{\varepsilon}_t = \widetilde{n}_t^2 = \widetilde{n}_i^2 \sin^2(\theta_i) \cdot \left[1 + \left(\frac{1-\rho}{1+\rho}\right)^2 \tan^2(\theta_i)\right] \tag{A.6}$$

where the complex dielectric constant $\widetilde{\varepsilon}$, the complex index of refraction $\widetilde{n}$ and the extinction coefficient $k$ are all linked in the following ways:

$$\begin{array}{lll}
\widetilde{\varepsilon} = \varepsilon_r + i\varepsilon_i & \varepsilon_r = n^2 - k^2 & \varepsilon_i = 2nk \\
\widetilde{n} = n + ik & n^2 = \frac{1}{2}\left(\sqrt{\varepsilon_r^2 + \varepsilon_i^2} + \varepsilon_r\right) & k^2 = \frac{1}{2}\left(\sqrt{\varepsilon_r^2 + \varepsilon_i^2} - \varepsilon_r\right) \\
\widetilde{\varepsilon} = \widetilde{n}^2 & n \sim \varepsilon_r & k \sim \varepsilon_i
\end{array}$$

The reflectance $R$ is the fraction of the incident power reflected at the interface. At the same time, the transmittance $T$ is the fraction of the incident power that is transmitted through the interface. Assuming that the media are non-magnetic and substituting Snell's law, the reflectance $R$ and transmittance $T$ for parallel and perpendicular electric fields are defined as

$$R_\parallel = |r_\parallel|^2 = \left| \frac{n_i \sqrt{1 - \left(\frac{n_i}{n_t}\sin(\theta_i)\right)^2} - n_t \cos(\theta_i)}{n_i \sqrt{1 - \left(\frac{n_i}{n_t}\sin(\theta_i)\right)^2} + n_t \cos(\theta_i)} \right|^2 \tag{A.7a}$$

$$R_\perp = |r_\perp|^2 = \left| \frac{n_i \cos(\theta_i) - n_t \sqrt{1 - \left(\frac{n_i}{n_t}\sin(\theta_i)\right)^2}}{n_i \cos(\theta_i) + n_t \sqrt{1 - \left(\frac{n_i}{n_t}\sin(\theta_i)\right)^2} +} \right|^2 \tag{A.7b}$$

$$T_\parallel = 1 - R_\parallel \tag{A.7c}$$

$$T_\perp = 1 - R_\perp \tag{A.7d}$$

which interestingly allows for two special cases: the normal incidence case (developed under the spectroscopy section, page 39) and Brewster's angle. Brewster's angle refers to an incident angle at which $R_\parallel = 0$. This means that the reflected light is fully polarised perpendicularly to the plane of incidence. This condition is fulfilled only for an angle $\theta_B$ such that:

$$\theta_B = \arctan\left(\frac{n_t}{n_i}\right) \tag{A.8}$$

In the particular case of the air ($n_i = 1$) to glass ($n_t = 1.5$) interface or air to silicon ($n_t = 3.41$) interface, this corresponds to an angle of 56.3° and 73.6°, respectively. Depending on the substrate used for the layer deposition, these will be the incident angles used for ellipsometry characterisation since they provide the highest difference between the two polarisation directions, allowing for a better signal-to-noise ratio. The rest of this development is presented in section 3.2.2.3.

## A.3 XRD: other powerful tools

This section is linked to the XRD characterisation method found in section 3.2.2.5 and follows the mathematical development of the end of said section. Indeed, the width of the XRD peaks can be studied deeper and in combination with their position on the XRD pattern to give richer information on the grain size and the stress in the layer. The rocking curve is also presented.

### A.3.1 The Williamson-Hall plot

The strain $\varepsilon$ in the layer also contributes to peak broadening (see equation A.9). Assuming that the crystallite size and the strain contributions to line broadening are independent of one another and that both have a Cauchy-like profile (implying that their linear combination will also have a Cauchy-like profile), then the total peak width $\beta_{hkl}$ is the sum of the two contributions (see equation A.10, combining equations 3.25 and A.9).

$$\varepsilon = \frac{\beta_{hkl}}{4\tan(\theta)} \tag{A.9}$$

$$\beta_{hkl} = \frac{K\lambda}{D\cos(\theta)} + 4\varepsilon\tan(\theta) \tag{A.10}$$

$$\beta_{hkl}\cos(\theta) = \frac{K\lambda}{D} + \varepsilon \cdot 4\sin(\theta) \tag{A.11a}$$

$$\beta_{hkl}\cos(\theta) = \frac{K\lambda}{D} + \sigma \cdot \frac{4\sin(\theta)}{E_{hkl}} \tag{A.11b}$$

$$\beta_{hkl}\cos(\theta) = \frac{K\lambda}{D} + \sqrt{u} \cdot \sqrt{\frac{32\sin^2(\theta)}{E_{hkl}}} \tag{A.11c}$$

The set of equations A.11 is arranged in a $y = b + ax$ fashion, where XRD peaks will generate the (x, y) points on which a linear regression can be computed. The result of which will give the y-intercept $b$ from which the crystallite size $D$ can be deduced, and the slope $a$ from which the strain $\varepsilon$ (sub-equation A.11a, called the "uniform deformation model" UDM) or the stress $\sigma$ (sub-equation A.11b, called the "non-uniform deformation model" NUDM) or the energy density $u$ (sub-equation A.11c, called the "uniform deformation energy density model" UDEDM) can be deduced. This is called the "Williamson-Hall plot". The UDM assumes that the strain is uniform in all crystallographic directions, thus considering the isotropic nature

of the crystal. In other words, the material properties are independent of the direction along which they are measured, which does not sound appropriate for In/GaN. The NUDM is often used when the crystal shows anisotropic properties, expressed by the $E_{hkl}$ factor. $E_{hkl}$ is Young's modulus in the direction perpendicular to the set of the crystal lattice plane $(hkl)$ (see next paragraph). Finally, because of the presence of defects and dislocations, the assumed linear relationship between the stress and the strain, as the NUDM assumes, does not always perfectly describe reality (compare equations A.11a and A.11b, see also equation A.12). The energy density notion is thus better suited to take the uniform anisotropic lattice strain in every crystallographic orientation into account. In the present thesis, the UDEDM will be used because of the high defect density of the material and because of the anisotropic properties of the crystal.

### A.3.2 The Young's modulus

The Young's modulus $E_{hkl}$ is a mechanical property that measures the tensile or compressive stiffness of a solid material when a force is applied lengthwise, perpendicularly to the $(hkl)$ set of planes [195, 147]. It quantifies the relationship between the stress $\sigma$ (force per unit area) and the strain $\varepsilon$ (proportional deformation) in the linear elastic regime of a material.

$$\varepsilon_{hkl} = \frac{\sigma}{E_{hkl}} \tag{A.12}$$

Young's modulus entirely depends on the crystal structure. For Wurtzite structures [147] such as In/GaN, it is expressed as

$$E_{hkl} = \frac{\left(h^2 + \frac{(h+2k)^2}{3} + \left(\frac{al}{c}\right)^2\right)^2}{S_{11}\left(h^2 + \frac{(h+2k)^2}{3}\right)^2 + S_{33}\left(\frac{al}{c}\right)^4 + (2S_{13} + S_{44})\left(h^2 + \frac{(h+2k)^2}{3}\right)\left(\frac{al}{c}\right)^2} \tag{A.13}$$

where the elastic compliances $S_{ij}$ are

$$S_{11} = \frac{1}{2}\left(\frac{C_{33}}{C_{33}(C_{11}+C_{22}) - 2C_{13}^2} + \frac{1}{C_{11}-C_{12}}\right) \tag{A.14a}$$

$$S_{12} = \frac{1}{2}\left(\frac{C_{33}}{C_{33}(C_{11}+C_{22}) - 2C_{13}^2} - \frac{1}{C_{11}-C_{12}}\right) \tag{A.14b}$$

$$S_{33} = \frac{C_{11}+C_{12}}{C_{33}(C_{11}+C_{22}) - 2C_{13}^2} \tag{A.14c}$$

$$S_{13} = \frac{-C_{13}}{C_{33}(C_{11}+C_{22}) - 2C_{13}^2} \tag{A.14d}$$

$$S_{44} = \frac{1}{C_{44}} \tag{A.14e}$$

where the elastic stiffness constants $C_{ij}$ (see table A.2) are chosen along the $[11\bar{2}0]$, $[1\bar{1}00]$ and $[11\bar{2}0]$ directions for the $x-$, $y-$ and $z-$axes respectively.

Table A.2: Experimental methods, XRD: Elastic stiffness constants for indium nitride [195] and for gallium nitride [196, 148], in GPa.

| | $C_{11}$ | $C_{12}$ | $C_{13}$ | $C_{44}$ | $C_{55}$ |
|---|---|---|---|---|---|
| GaN | 373 | 141 | 80 | 87 | 94 |
| InN | 225 | 109 | 108 | 265 | 55 |

The elastic stiffness constants and the elastic compliances are used in a tensor that relates the stress $\sigma$ and the strain $\varepsilon$ in the film, where according to the stress directions sketched in figure A.2, the tensor is as follows for Wurtzite structures:

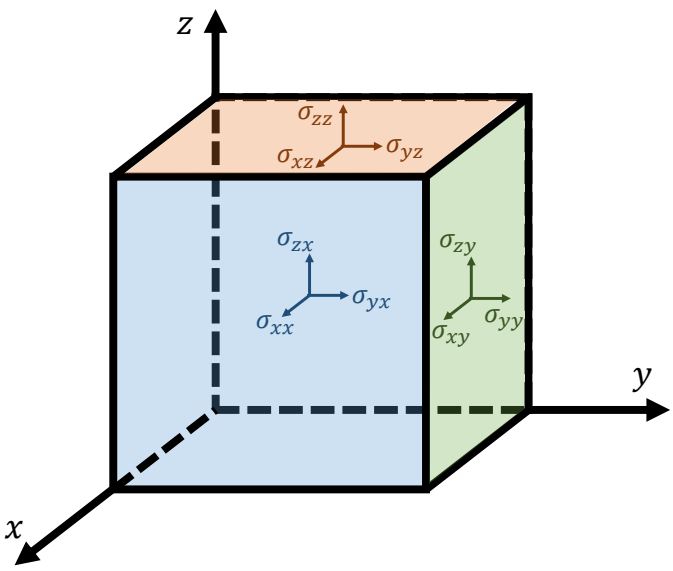


Figure A.2: Experimental methods, XRD: Elaborates of stress.

$$\begin{pmatrix} \sigma_{xx} \\ \sigma_{yy} \\ \sigma_{zz} \\ \sigma_{yz} \\ \sigma_{xz} \\ \sigma_{xy} \end{pmatrix} = \begin{pmatrix} C_{11} & C_{12} & C_{13} & 0 & 0 & 0 \\ C_{12} & C_{11} & C_{13} & 0 & 0 & 0 \\ C_{13} & C_{13} & C_{33} & 0 & 0 & 0 \\ 0 & 0 & 0 & C_{44} & 0 & 0 \\ 0 & 0 & 0 & 0 & C_{44} & 0 \\ 0 & 0 & 0 & 0 & 0 & (C_{11}-C_{12})/2 \end{pmatrix} \cdot \begin{pmatrix} \varepsilon_{xx} \\ \varepsilon_{yy} \\ \varepsilon_{zz} \\ \varepsilon_{yz} \\ \varepsilon_{xz} \\ \varepsilon_{xy} \end{pmatrix} \tag{A.15}$$

where in particular,

$$\varepsilon_{xx} = \frac{a - a_0}{a_0}, \quad \varepsilon_{yy} = \frac{m - m_0}{m_0}, \quad \varepsilon_{zz} = \frac{c - c_0}{c_0} \tag{A.16}$$

where $m_0 = \sqrt{3}a_0$ and $a_0$ and $c_0$ are the strain-free lattice parameters. Indeed, the set of equations A.14 just expresses the inverse of the tensor in equation A.15, where $S_{ij} = \left(C^{-1}\right)_{ij}$.

### A.3.3 The rocking curve

XRD is a rich and powerful technique with several possible configurations. Another useful result that it can provide is the so-called "rocking curve" (also called an "omega scan"). The rocking curve is an intensity graph sketched at a constant $2\theta$ angle, but the probed sample is tilted (or "rocked"), hence the name of omega scan. The $2\theta$ value is usually chosen to reflect the highest intensity peak, allowing the extraction of the mosaicity of the layer. A perfectly mosaic layer is constituted of many small crystallites that are randomly oriented, which will result in a flat rocking curve. However, if, for the probed reflection, the crystallites have a preferential orientation (or if the mosaicity is not perfect, meaning that the layer is slightly texturised), this will appear as a peak in the rocking curve. The FWHM determines the amount of texture, where the sharper the peak, the higher the layer's texture. Its position will give away the preferential orientation. Given the nature of the measurement, it is also possible to probe the defects, the dislocations, and the curvature of the layer by analysing the peak asymmetry.

## A.4 Design of experiment deepening

This section is linked to the DOE mathematical tool found in section 3.3 and presents other aspects of that field that were not necessarily used in this thesis.

The development presented in section 3.3.1.2 (orthogonality, correlation, variances, VIFs, etc.) can be anticipated before doing any measurement when conceiving the experiment matrix $E$ with a specific goal in mind. Three of the designs presented in the following section (see figure A.3) produce a diagonal correlation matrix, while the central composite design (CCD) does too, but only in particular cases. Other experimental plans that are not presented here can, of course, be designed, some of which are not necessarily orthogonal (see, for example, the Doehlert design applied by Cerqueira *et al.* [35]). But each of them has its usefulness and inconvenience.

### A.4.1 Designs

> The quality of a design of experiments is measured by the variability of the estimate of its coefficients and consequently by the variability of the response

estimate.

(Bouzid *et al.* in [6], p. 152)

An experiment describes under which conditions the multiple runs will be performed. This means that the final chosen model will depend on the design of said experiment, which is selected depending on the circumstances surrounding the measurements. Is the relationship between a result and an input variable already well-known? Is there enough time or money, or other resources available to perform all the runs of a design? Usually, three designs are chosen consecutively when probing a dependent variable: a screening design that narrows the field of variables under assessment, a factorial design that studies the response of every combination of factors and factor levels in an attempt to zone in on a region of values where the process is close to optimisation, and a response surface designed to model the response. For a precise model, more experiments are required, and a trade-off between time and quality must be decided. It is then essential to know the strengths and limitations of every design. Optimising one input parameter at a time is typically called a "star design", proving to be one of the most expensive. On the other hand, a good strategy is first to minimise the trace and the determinant of the dispersion matrix and minimise the variance of the coefficients (see equations 3.41 and 3.43, respectively). The designs presented here do precisely that.

#### A.4.1.1 Full Factorial Design

The full factorial design (FFD, see figure A.3a) is the most used and well-known design of the DOE method. The concept is to have one measurement at each corner of the experimental design space. In other words, each input parameter only ever takes two different values. This means that the number of runs $n$ increases exponentially with the number of input variables $k$ to be tested: $n = 2^k$. For $k = 3$, this means that eight runs are performed. Though expensive, going back to equation 3.37, this design allows for the complete determination of the main effect's coefficients $a_i$, the first order interaction effect's coefficients $a_{ij}$, and the second order interaction effect's coefficients $a_{ijm}$, which are often not significant. Since this design has only corner points, the quadratic effect's coefficients cannot be determined. This also means that the centre of the design has the higher response variance since it is the furthest away from all the experimental points. This is why this design is used as a second step in determining the output's dependencies rather than as a response surface design. Although complete and powerful, the considerable drawback of this design is that it becomes quickly expensive with the increasing number of input variables. On the plus side, since this design is entirely orthogonal, the correlation matrix is completely orthogonal, and the VIFs are all equal to one.

#### A.4.1.2 Fractional Factorial Design

The fractional factorial design (FrFD, see figure A.3b) is based on the FFD but used when the number of runs is too expensive, *i.e.* when the number of input parameters is too high. This is why this kind of design is usually used as a screening in the early stages of the three-step

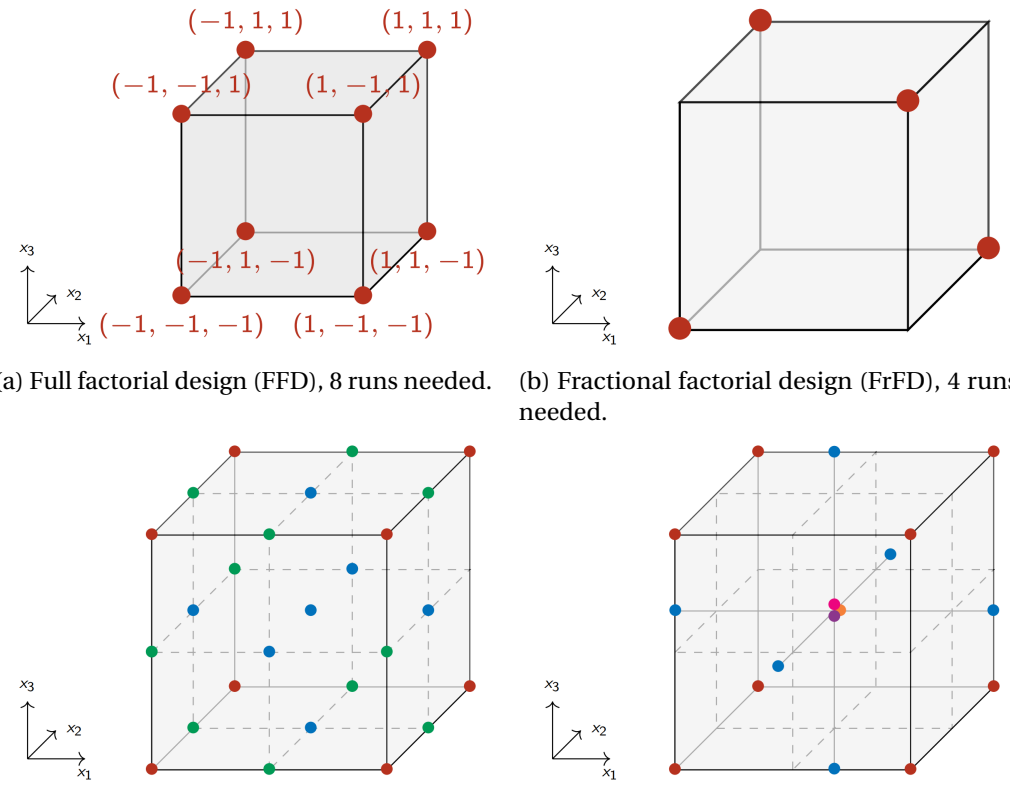


(a) Full factorial design (FFD), 8 runs needed.

(b) Fractional factorial design (FrFD), 4 runs needed.

(c) $3^k$ Design (3kD), 27 runs needed.

(d) Central composite design (CCD), with three central points and a radius $\alpha = 1.353$, 15 runs needed.

Figure A.3: Experimental methods, DOE: four 3D designs represented in the experimental design space. All kinds of designs can be conceived, including non-square-shaped ones, but these are the ones that will be examined here. The input variable range has been standardised in all cases; the coordinates of the vertices can be seen in figure A.3a. The number of runs necessary for each design can be obtained by counting all the coloured points. With the kind permission of Dr. Fürbringer [62].

consecutive approach. The number of runs $n$ still depends on the number of input variables $k$ but can be reduced by a factor $2^g$ in such a way that the experimental design space remains unchanged (see figure A.3b). Here, $g$ refers to the number of "design generators" or simply "generators". The total number of runs is then $n = 2^{k-g}$. The generators generate relationships for the design, where $g$ standardised input variables are defined as a function of the other $k-g$ standardised input variables. In the following equation, we compare two essay matrices: one from a FFD with three input variables, and the other from a $2^{4-1}$ FrFD where the generator for the fourth input parameter is a multiplication of the three first ones, expressed as "4=123". This is deduced from the identity equation where, in the same notation, $\mathbb{1} = 1234$.

$$E_{\mathrm{FFD}_3} = \begin{pmatrix} 1 & 1 & 1 \\ 1 & 1 & -1 \\ 1 & -1 & 1 \\ 1 & -1 & -1 \\ -1 & 1 & 1 \\ -1 & 1 & -1 \\ -1 & -1 & 1 \\ -1 & -1 & -1 \end{pmatrix} \qquad E_{\mathrm{FrFD}_{4-1}} = \begin{pmatrix} 1 & 1 & 1 & 1 \\ 1 & 1 & -1 & -1 \\ 1 & -1 & 1 & -1 \\ 1 & -1 & -1 & 1 \\ -1 & 1 & 1 & -1 \\ -1 & 1 & -1 & 1 \\ -1 & -1 & 1 & 1 \\ -1 & -1 & -1 & -1 \end{pmatrix} \tag{A.17}$$

We see that the number of runs is the same, but a fourth input parameter could be probed with the FrFD, which would have taken twice as many runs with the $\mathrm{FFD}_4$. The three first input parameters are chosen similarly between the two designs. However, when the FFD allowed for a complete determination of the primary and interaction effects, the FrFD injects aliases in the model; it is unclear if a variation in the modelled outcome $y$ is the consequence of the change of one effect or another. The chosen generators determine these aliases, whereas, in this example, we only have one: $4 = 123$. Still, with a $n$ run experiment, deducing $n$ contrasts $I_{n-1}$ is possible. The contrasts described here below follow the $E_{\mathrm{FrFD}_{4-1}}$ example used here above.

$$\begin{aligned} I_0 &= a_0 + a_{1234} \\ I_1 &= a_1 + a_{234} \\ I_2 &= a_2 + a_{134} \\ I_3 &= a_3 + a_{124} \\ I_4 &= a_4 + a_{123} \\ I_5 &= a_{12} + a_{34} \\ I_6 &= a_{13} + a_{24} \\ I_7 &= a_{14} + a_{23} \end{aligned} \tag{A.18}$$

As shown in table A.3, it is possible to generalise to any $k$ and $g$ combinations, given that $g$ is not too high. The highlighted number describes the FrFD, where the subscribed capital roman numeral represents its "resolution", which corresponds to the length of the shortest generator. Highest-order interactions are less likely to occur or are less potent than lowest-order interactions and can be dismissed more easily. This is why higher resolution FrFD is preferred. The FrFD can then be chosen and designed so that known interaction terms are irrelevant and dismissed from the contrast so that the whole model is de-aliased, even though fewer runs were performed.

Compared to the FFD, the FrFD still preserve orthogonality, which means that the correlation matrix is diagonal, and the VIFs are all equal to one (if not ill-chosen concerning the gener-

Table A.3: Experimental methods, XRD: the table of the $2^{n-g}$ FrFD plan for 3 to 8 input parameters, and up to $2^7 = 128$ runs. The highlighted number describes the chosen FrFD, where the subscribed capital roman numeral describes its resolution [24, 23].

| | | Number of input parameters $k$ | | | | | |
|---|---|---|---|---|---|---|---|
| | | 3 | 4 | 5 | 6 | 7 | 8 |
| Number of runs | 4 | $2^{3-1}_{III}$<br>$\pm 3 = 12$ | | | | | |
| | 8 | $FFD_3$ | $2^{4-1}_{IV}$<br>$\pm 4 = 123$ | $2^{5-2}_{III}$<br>$\pm 4 = 12$<br>$\pm 5 = 13$ | $2^{6-3}_{III}$<br>$\pm 4 = 12$<br>$\pm 5 = 13$<br>$\pm 6 = 23$ | $2^{7-4}_{III}$<br>$\pm 4 = 12$<br>$\pm 5 = 13$<br>$\pm 6 = 23$<br>$\pm 7 = 123$ | |
| | 16 | $2 \times FFD_3$ | $FFD_4$ | $2^{5-1}_{V}$<br>$\pm 5 = 1234$ | $2^{6-2}_{IV}$<br>$\pm 5 = 123$<br>$\pm 6 = 234$ | $2^{7-3}_{IV}$<br>$\pm 5 = 123$<br>$\pm 6 = 234$<br>$\pm 7 = 134$ | $2^{8-4}_{IV}$<br>$\pm 5 = 234$<br>$\pm 6 = 134$<br>$\pm 7 = 123$<br>$\pm 8 = 124$ |
| | 32 | $4 \times FFD_3$ | $2 \times FFD_4$ | $FFD_5$ | $2^{6-1}_{VI}$<br>$\pm 6 = 12345$ | $2^{7-2}_{IV}$<br>$\pm 6 = 1234$<br>$\pm 7 = 1245$ | $2^{8-3}_{IV}$<br>$\pm 6 = 123$<br>$\pm 7 = 124$<br>$\pm 8 = 2345$ |
| | 64 | $8 \times FFD_3$ | $4 \times FFD_4$ | $2 \times FFD_5$ | $FFD_6$ | $2^{7-1}_{VII}$<br>$\pm 7 = 123456$ | $2^{8-2}_{V}$<br>$\pm 7 = 1234$<br>$\pm 8 = 1256$ |
| | 128 | $16 \times FFD_3$ | $8 \times FFD_4$ | $4 \times FFD_5$ | $2 \times FFD_6$ | $FFD_7$ | $2^{8-1}_{VIII}$<br>$\pm 8 = 1234567$ |

ators). But the cutback on the number of runs is pretty substantial: it can be divided by a power of two! However, depending on the resolution of the FrFD and the circumstances of the experiment, even the main effects may not be fully de-aliased. This design will be used cleverly, where aliases can be dismissed by playing intelligently with the generators and the input parameters.

#### A.4.1.3 $3^k$ Design

The $3^k$ design (3kD, see figure A.3c) is, in fact, the same as the FFD, orthogonal but with central points on all input parameter values. This means that the number of runs increases like $3^k$ instead of $2^k$ for the FFD. This is extremely expensive but may be necessary for an experiment with highly interacting input parameters. Indeed, with such a high number of runs, here is the exhaustive list of coefficients that are entirely determined: the main effect's coefficients $a_i$, the first-, second- and third-degree interaction effect's coefficients ($a_{ij}$, $a_{ijk}$, $a_{ijkl}$), the quadratic effect's coefficients $a_{ii}$ and the interaction coefficient between one main and one quadratic effect $a_{iij}$. This design also allows for a low standardised response variance at its centre, which,

added to its cost, makes it preferred in the last stages of the three-step consecutive approach of experimental design.

#### A.4.1.4 Central Composite Design

This small section is based on Box's and Hunter's work [24] and a technical report from the University of Illinois [39]. While all the previous designs mainly focus on a rigid and expensive diagonal dispersion matrix, second-order (quadratic) models can be designed without needing to use a complete three-level factorial experiment, where here the response variable is the main focus of the said design, instead of the VIFs. This is why the central composite design (CCD) is also often used as an alternative cheaper response-surface design at the third step of the three-step consecutive approach. The CCD is based on the FFD ($2^n$ runs) and a star design. A star design is composed of one or many central points $N_0$ and a point in the centre of every design face (see the blue points in figure A.3d, $2k$ face points). The total number of runs $n$ is given in equation A.19. The exciting feature of the CCD is the $\alpha \geqslant 1$ value, which describes how wide the star design is, or how far from the origin are the face-centred runs, where $\alpha = 1$ places them on the FFD surface. Here, a choice can be made for $\alpha$, depending on the purpose of the design.

A critical characteristic of a design can be its "iso-variance per rotation", or "rotatability". A rotatable design provides the preferred property of constant prediction variance at all points that are equidistant from the design centre, thus improving the quality of the prediction and, in other words, referring to equation 3.44, $\mathrm{var}_y(x_i) = \mathrm{var}_y\left(\sqrt{\sum_i x_i^2}\right)$, and if two input parameters are swapped, the standardised response variance does not change. This is an incredibly convenient design quality in exploratory work when the investigator is ignorant of the response surface and its relative orientation to the orthogonal effect axes. This is achieved with a value of $\alpha_{\mathrm{rot}}$ depending only on the number of input parameters $k$ (see equation A.20).

Another essential characteristic is the orthogonality of a design, which can be constructed by blocks. An "orthogonally blocked design" refers to experiments whose design matrix $D$ is a composition of sub-matrices placed on the diagonal of $D$, with zeros everywhere else. Orthogonally blocked designs let model terms and block effects be estimated independently, minimise the variation in the regression coefficients, and reduce the VIFs. This is the case in all the other designs presented here since the surfaces or edges of the space parameter are all orthogonal to one another, leading to only diagonal elements in the dispersion matrix (see equation 3.41) or in the correlation matrix (see equation 3.42). This aspect of the design is valuable to the experimenter concerned with isolating potential effects due to such factors as different experimenters, changes in apparatus, and environmental conditions. For an orthogonally blocked design, it is best to choose the $\alpha_{\mathrm{ort}}$ described in equation A.21, where more central points will increase its value.

$$n_{CCD} = 2^k + 2k + N_0 \tag{A.19}$$

$$\alpha_{\text{rot}} = 2^{k/4} \tag{A.20}$$

$$\alpha_{\text{ort}} = \left( \frac{2^k \left( \sqrt{2^k + 2k + N_0} - \sqrt{2^k} \right)^2}{4} \right)^{\frac{1}{4}} \tag{A.21}$$

It is often impossible to have both orthogonality and rotatability, except for some rare cases (for example, $k = 2$ and $N_0 = 4$, then $\alpha_{\text{rot}} = \alpha_{\text{ort}} = \sqrt{2}$). To achieve orthogonal blocking, it is often necessary to sacrifice rotatability. In human factors applications, however, the potential gains from orthogonal blocking probably outweigh the risk of forfeiting rotatability. Other than $\alpha$, the researcher can also play on the number of central points with a replicated experiment. Those allow for additional degrees of freedom to estimate the experimental error better. It will also determine the estimate's precision at the centre of the design, which is often the value of interest. All in all, the appropriate number of replications for the central point will be the one that leads to the standard error of the estimates that is roughly constant inside the whole design. With too few central points, the variance will increase drastically at the centre of the design compared to the border and vice versa.

### A.4.2 Cook's distance

Another useful tool in the DOE toolkit is called "Cook's distance"[42] and relates to the influence that one point has on the overall regression. In other words, deleting a point with a high influence (or a long Cook's distance) may lead to a completely different result. That does not mean that the first fit result was wrong or bad, but Cook's distance indicates which points are worth investigating to ensure they are trustworthy. For the $i^{\text{th}}$ outcome, the Cook's distance $D_i$ is defined as

$$D_i = \frac{\Sigma_{j=1}^{n} \left( f_j - f_{j(i)} \right)^2}{p s^2} \tag{A.22}$$

where $f_j$ is the fitted value of the $j^{\text{th}}$ outcome, and $f_{j(i)}$ is the fitted value of the $j^{\text{th}}$ outcome if the $i^{\text{th}}$ outcome did not exist. $n$ is the number of outcomes, $p$ is the number of effects in the model and $s$ is the mean squared error defined in equation 3.50 page 61. These values have no units, and the threshold above which a measurement point is considered to merit closer inspection is usually defined as $4/n$. You can find such a study with a plot.

# B Deeper analysis of some results

It was unnecessary to show the figures presented here to prove a point developed in different locations of this thesis. Here are more thorough analyses of some of the results on deposited layers.

## B.1 More details on the influence of deposition parameters on the InGaN layers deposited by PECVD

This section aims to give more details and more results on the characterisation of InGaN layers deposited by PECVD in section 4.2.

### B.1.1 Plasma dynamics

Given the plasma conditions described in the experimental setup, all the used precursors will be dissociated to a certain degree, where $N_2$ is the most difficult to break down and, thus, requires a high flow rate to compensate for the lack of nitrogen radicals. An accurate description of the plasma dynamics with such a complex mix of precursors would include kinematics of dissociation, adsorption, nitridation, carbidization, and synthesis, at different rates and equilibria. Only a simplified version of the deposition process is presented here but see section 4.3 for more details. When entering the plasma region, a TMI (or TMG) molecule will dissociate into its central indium (or gallium) radical atom and three unstable methyl radicals. $N_2$ will also undergo dissociation to produce nitrogen radicals in the plasma, which in turn will bind with the indium (or gallium) radical to form InN (or GaN). This small molecule will eventually drift towards the substrate, which will adsorb into a weakly bound precursor state and either form a chemical bond or desorb from the substrate. The behaviour of the InN (or GaN) species in the adsorbed precursor state will determine crystallite quality and size [130]. Both properties are governed by the parameters shown in tables 4.2 and 4.4, and agreement with reported works is observed [135, 205, 206, 134, 159]. During all these processes, hydrogen radicals are produced from $H_2$ dissociation, from ammonia dissociation, or the

dissociation of the methyl groups of the dissociated TMI (or TMG). Their primary role is to passivate surface defects and to help eliminate plasma by-products, particularly the organic ones.

### B.1.2 Substrates and data extraction

Since the InGaN layers are simultaneously deposited on glass and silicon substrate, the results presented in section 4.2 may differ depending on the substrate. Thus, specific substrates were used to extract some of the material parameters. The crystallite size (XRD) and the indium content (XRD & EDS) were extracted from the layer deposited on silicon wafers exclusively. The growth rate (ellipsometry & profilometer) and the optical BG (ellipsometry & spectroscopy) were extracted from the layer deposited on the glass wafer exclusively.

It is assumed that the indium content $X_{\mathrm{In}} = \frac{\mathrm{In}}{\mathrm{In+Ga}}$ (In & Ga in at. %, $X_{\mathrm{In}}$ in %) of the InGaN layer does not depend on the substrate. Indeed, once the first few atomic layers are deposited, the substrate no longer influences the composition. However, a loss of crystallinity was observed in the InGaN layers deposited on glass, because of its amorphous nature, compared to layers deposited on silicon.

It is assumed, however, that contrary to the crystallinity level of silicon, the InGaN BG does not depend on the crystallographic arrangement of the layer, be it crystalline or amorphous, whatever the indium content. Indeed, literature reports that the amorphous InN BG was observed at 1.7 eV instead of 0.7 eV [30, 93], but that makes it equivalent to a highly defective crystalline InN layer with intrinsic doping as discussed above (*c.f.* also ref. [188]), which are the kind of layers obtained and presented in this thesis. For amorphous GaN, values between 3.1 and 3.4 eV were reported, similar to that of crystalline GaN [131, 21, 197, 175]. The corollary of the previous assumption is that the substrate, inducing a different crystal structure as experimentally observed in the present work, will, in fact, not influence the spectroscopic and ellipsometric measurements.

Finally, the deposition rate was slightly lower on silicon (~10% thinner layers), most probably due to a more efficient arrangement in the crystal structure. The thicknesses reported in the present thesis are exclusively the ones measured on glass, and that slight difference in growth rate must be considered when comparing the two substrates.

The indium content $X_{\mathrm{In}}$ of the layers was determined using two methods that validated one another. On one side, for the layers that were crystalline enough, the XRD 110 peak position varies with the sinus of the interatomic distance (see figure 4.4a), which varies linearly with $X_{\mathrm{In}}$. This allowed for a precise $X_{\mathrm{In}}$ determination when compared with pure InN and GaN layers. On the other hand, EDS measurements allowed for a straightforward measure of the In:Ga ratio, from which the indium content of the layers was deduced. The error between the two methods was less than 3 % (see figure 4.4b).

### B.1.3 ANOVA tables of the different InN DOEs

Please also visit section 3.3 for an introduction to this mathematical method. For the DOE on InN layers deposited using ammonia, the last six input parameters of table 4.4 are explored. The chosen design is a FrFD $2^{6\text{-}2}$ with three central points, for a total of 19 layers characterised. The coefficients are not normalised here to relate better to the physical input parameters rather than explore their inter-correlation. For the growth rate $g$, see equation B.1a and corresponding table B.1. For the optical BG $E_{04}$, see equation B.1b and corresponding table B.2. For the crystallite size, see equation B.1c and corresponding table B.3. See also the overall quality of the three models in table B.4.

$$g = 4.432 - 0.537NH_3 - 0.164H_2 - 0.148Po - 0.455T \tag{B.1a}$$

$$1000E_{04} = 1719 - 61H_2 - 47Po - 42T + T(36Pr + 31Po) \tag{B.1b}$$

$$Sz_{Gr} = 20.924 - 1.000NH_3 + 3.160H_2 + 3.691T + 1.031t - 1.079Pr \cdot T \tag{B.1c}$$

Table B.1: In/GaN PECVD, deposition parameters: Anova table for the growth rate $g$ of InN layers.

| Factor | SS | DF | MS | F | p-value |
|---|---|---|---|---|---|
| $a_{NH_3}$ | 4.618 | 1 | 4.618 | 40.89 | $1.67 \cdot 10^{-5}$ |
| $a_{H_2}$ | 0.428 | 1 | 0.428 | 3.79 | $7.19 \cdot 10^{-2}$ |
| $a_{Po}$ | 0.351 | 1 | 0.351 | 3.11 | $9.96 \cdot 10^{-2}$ |
| $a_T$ | 3.315 | 1 | 3.315 | 29.36 | $9.06 \cdot 10^{-5}$ |
| Residuals | 1.581 | 14 | 0.113 | - | - |
| Lack of fit | 1.037 | 12 | 0.086 | 0.32 | $9.21 \cdot 10^{-1}$ |
| Pure error | 0.544 | 2 | 0.272 | - | - |

Table B.2: In/GaN PECVD, deposition parameters: Anova table for the optical BG $E_{04}$ of InN layers.

| Factor | SS | DF | MS | F | p-value |
|---|---|---|---|---|---|
| $a_{H_2}$ | 0.059 | 1 | 0.059 | 17.76 | $1.20 \cdot 10^{-3}$ |
| $a_{Po}$ | 0.035 | 1 | 0.035 | 10.53 | $7.02 \cdot 10^{-3}$ |
| $a_T$ | 0.029 | 1 | 0.029 | 8.61 | $1.25 \cdot 10^{-2}$ |
| $a_{Pr \cdot T}$ | 0.021 | 1 | 0.021 | 6.34 | $2.70 \cdot 10^{-2}$ |
| $a_{Po \cdot T}$ | 0.016 | 1 | 0.016 | 4.72 | $5.06 \cdot 10^{-2}$ |
| Residuals | 0.040 | 12 | 0.003 | - | - |
| Lack of fit | 0.032 | 11 | 0.003 | 0.36 | $8.76 \cdot 10^{-1}$ |
| Pure error | 0.008 | 1 | 0.008 | - | - |

In the ANOVA tables, the p-value for the different factors is displayed in green if they are below a value of 5% and in red if they are above 5%. As a reminder of section 3.3.2.2, the 5% p-value

Table B.3: In/GaN PECVD, deposition parameters: Anova table for the crystallite size of InN layers.

| Factor | SS | DF | MS | F | p-value |
|---|---|---|---|---|---|
| $a_{NH_3}$ | 16.008 | 1 | 16.008 | 3.64 | $7.87 \cdot 10^{-2}$ |
| $a_{H_2}$ | 159.782 | 1 | 159.782 | 36.34 | $4.24 \cdot 10^{-5}$ |
| $a_T$ | 218.020 | 1 | 218.020 | 49.59 | $8.77 \cdot 10^{-6}$ |
| $a_t$ | 16.999 | 1 | 16.999 | 3.87 | $7.10 \cdot 10^{-2}$ |
| $a_{Pr \cdot T}$ | 18.624 | 1 | 18.624 | 4.24 | $6.02 \cdot 10^{-2}$ |
| Residuals | 57.153 | 13 | 4.396 | - | - |
| Lack of fit | 50.246 | 11 | 4.568 | 1.32 | $5.08 \cdot 10^{-1}$ |
| Pure error | 6.907 | 2 | 3.453 | - | - |

threshold is the standard chosen p-value to reject the following null hypothesis: "this factor has no effect on the physical quantity observed", where here the physical quantity is either $g$, $E_{04}$ or the crystallite size. However, even though some factors express a dismissing coefficient, they are retained because the overall model quality is optimal when including them. For the lack of fit, however, it is preferable to be unable to reject the null hypothesis following that "there is no lack of fit". Hence, the lack of fit p-values are displayed in red when they are below 5%, and in green when above.

Table B.4: In/GaN PECVD, deposition parameters: evaluation of the different models, with the adjusted R-squared value $R^2_{adj}$, the Root Mean Square Error RMSE, and the F-statistic vs constant model p-value $FC_p$.

| Model | $R^2_{adj}$ | RMSE | $FC_p$ |
|---|---|---|---|
| $g$ | 0.803 | 0.336 | $1.40 \cdot 10^{-5}$ |
| $E_{04}$ | 0.716 | 0.058 | $7.11 \cdot 10^{-4}$ |
| $Sz_{Gr}$ | 0.837 | 2.100 | $1.24 \cdot 10^{-5}$ |

### B.1.4 3D view of the fit

Since the optical BG was fitted as a function of two parameters (the growth rate $g$ and the indium content $X_{\text{In}}$), the fitted model can be represented as a 3D surface, displayed in figure B.1. Two of the three projections of this plot were used in section 4.2: the back wall projection corresponds to figure 4.5 which shows Vegard's law, and the floor projection corresponds to figure 4.6b which offers the explored parameter space.

## B.2 Details of the InGaN PECVD DOEs

Please find here more details and a deeper analysis of the results presented in section 4.4, where the DOE method was applied to all the layers deposited during my four years of *Ph.D.*, for three significant physical quantities. In particular, all the "residuals vs fitted values" plots

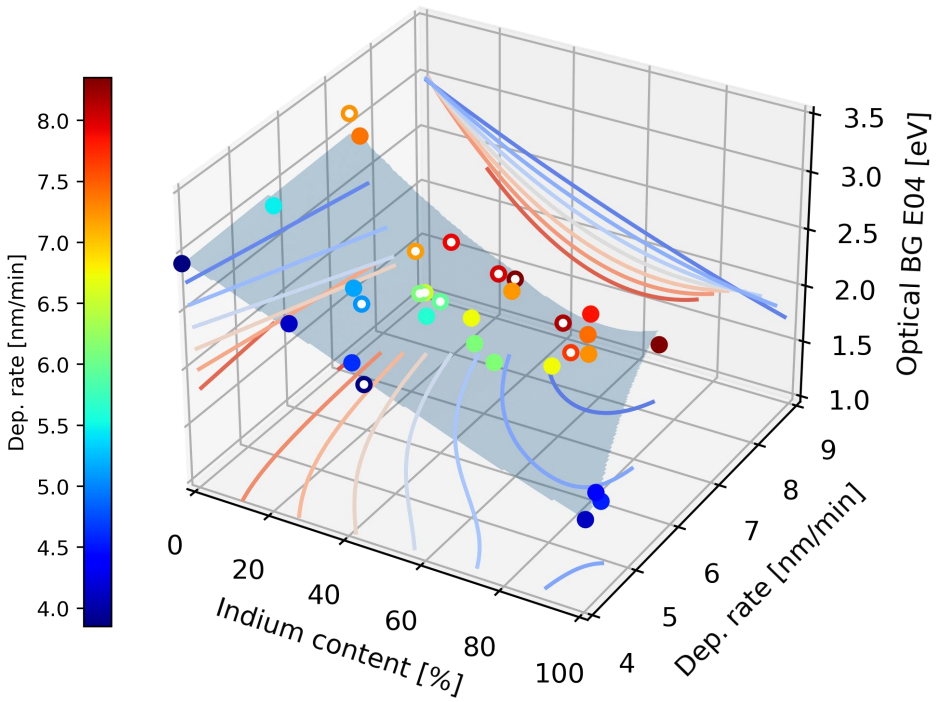


Figure B.1: In/GaN PECVD, deposition parameters: 3D fit of the experimental points for the In/GaN layers deposited with an $N_2$ nitrogen source. Its characteristics were determined by ellipsometry and spectroscopy (optical BG $E_{04}$ and thickness), and XRD and EDS ($X_{\mathrm{In}} = \frac{\mathrm{In}}{\mathrm{In+Ga}}$, In & Ga in at. %, $X_{\mathrm{In}}$ in %). The open symbols correspond to layers whose crystallinity was not good enough for $X_{\mathrm{In}}$ to be determined by XRD.

presented previously were extracted using a Python code; a Matlab tool allows for a smoother and more manageable but slightly different way to look at that result: a model added plot (see more details about this in the last paragraph just before section 3.3.2.2, page 63). Please also note that for all the Cook distance plots presented here, the numbers in parenthesis are formatted as "(layer n°, Cook distance)" and the horizontal red dashed line represents the threshold above which points are worth examining, at $y = 4/n$.

## B.2.1 Thickness

### B.2.1.1 GaN

See the model for the prediction of GaN layers' thickness in equation 4.3, page 107, or consult table B.5. Figure 4.24a is the residuals *versus* fitted values plot, which is similar to the model added plot displayed in figure B.2. However, with the added model plot here, we can see that most of the experimental thicknesses are out of the 95 % confidence interval of the values predicted by the model, but they are evenly dispersed around it. So again, the data is noisy, making it difficult to improve the model. The partial regression plots and the component – component plus residual plots do not yield more information than this: also noisy data, with

an acceptable prediction over the whole set (fair linearity) and a non-standard dispersion away from the model (heteroscedasticity).

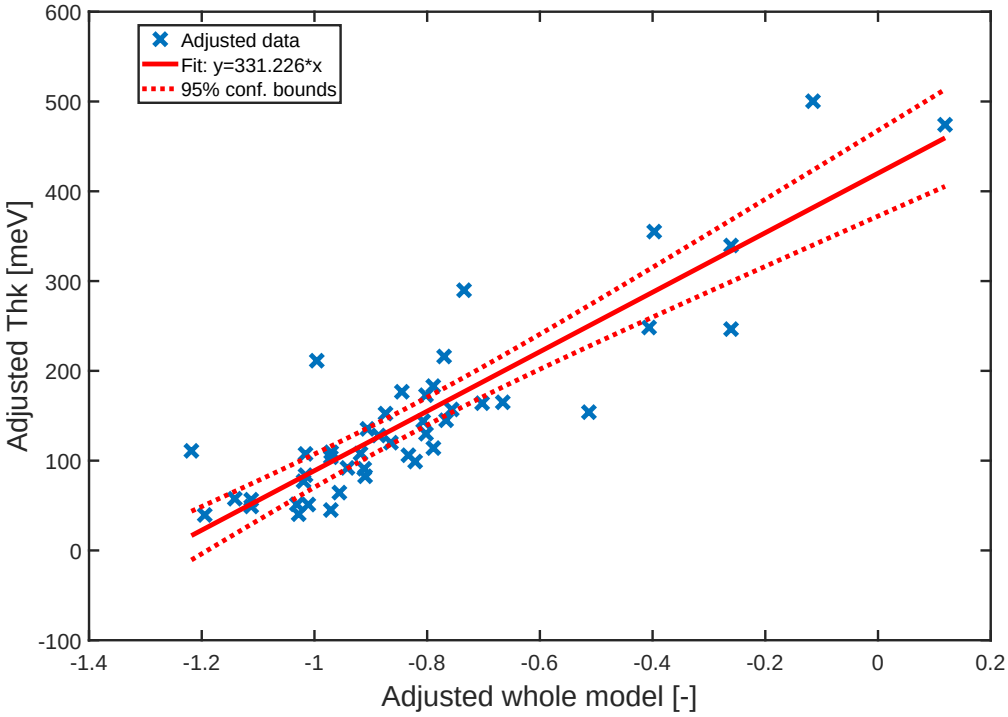


Figure B.2: In/GaN PECVD, DOE: GaN thickness model, added model plot. Compare with figure 4.24a on page 109.

It is also worth examining the Cook distance of the different points (see figure B.3), where here again, the most influential points are the furthest away from the model (except for the longest Cook distance, layer n° 142, which can be considered "within the packed cloud of points"). Again, the examination of these points has already been done, and the decision was to keep them because of their quality, and there was no potential reason to eliminate them. Indeed, it would be worth re-doing all the processes without them, but that would also compromise one's scientist's integrity by only selecting the outcomes that produce an appealing result.

Finally, table B.5 shows more details of the chosen coefficients, where no p-value above 5 % or no VIF value above ten was allowed.

#### B.2.1.2 InN

See the model for the prediction of InN layers' thickness in equation 4.4, page 110, or consult table B.6. Figure 4.25a is the residuals *versus* fitted values plot, which is similar to the model added plot displayed in figure B.4. However, with the added model plot here, we can see a sharp 95 % confidence interval, with most of the points evenly dispersed around it. This means that the noise in the data is small and normally distributed. The partial regression plots and the component – component plus residual plots do not yield more information than this. Still,

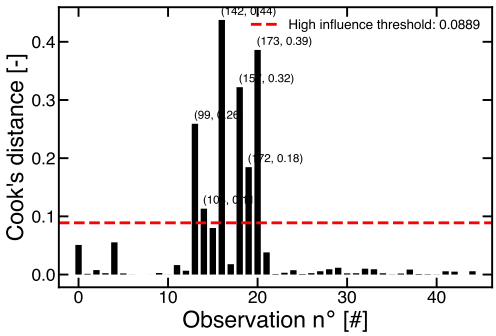


Figure B.3: In/GaN PECVD, DOE: GaN thickness model, Cook distance.

| Coefficient | Value | p-value [%] | VIF |
|---|---|---|---|
| $a_0$ | 420.0 | - | - |
| $a_{Ga}$ | 217.5 | $2.2 \cdot 10^{-5}$ | 3.46 |
| $a_{H_2}$ | 61.2 | 0.864 | 2.22 |
| $a_{NH_3}$ | -144.5 | $4.2 \cdot 10^{-6}$ | 4.23 |
| $a_{Ar}$ | 130.8 | $5.3 \cdot 10^{-6}$ | 2.09 |
| $a_{Pr}$ | -75.3 | 1.446 | 1.41 |
| $a_t$ | 122.4 | 0.068 | 2.22 |

Table B.5: In/GaN PECVD, DOE: GaN thickness model. Details of the coefficients: value, irrelevance (p-value) and correlation (VIF).

the ones for the *In* coefficient are incredibly satisfying and can be discovered in figure B.6. The figure also shows a normal dispersion away from the model (good homoscedasticity).

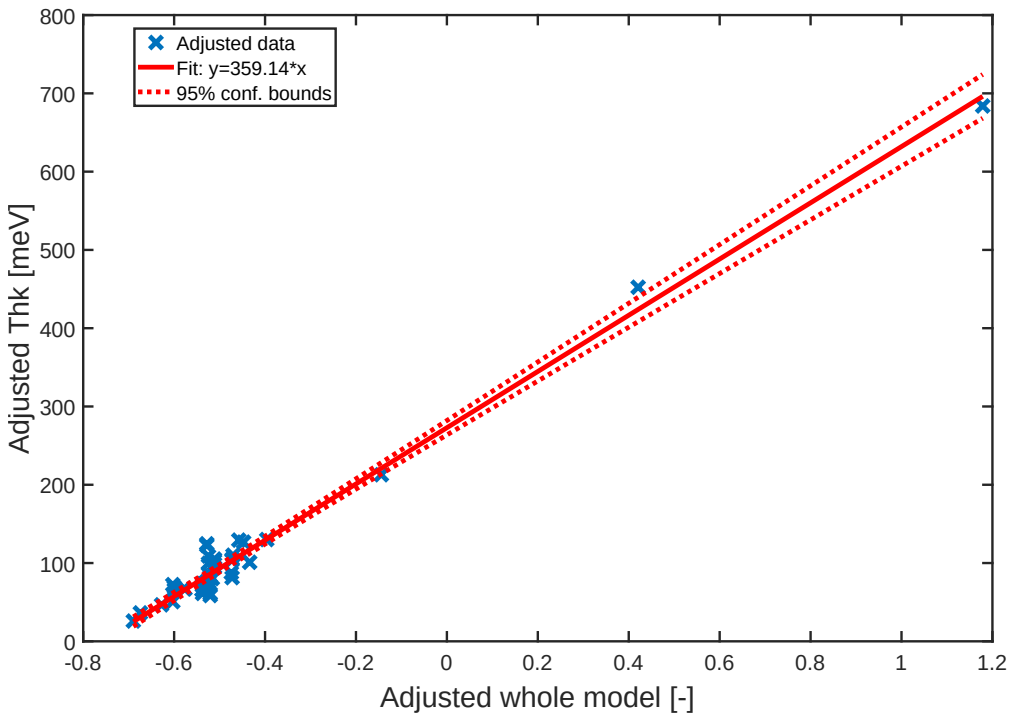


Figure B.4: In/GaN PECVD, DOE: InN thickness model, added model plot. Compare with figure 4.25a on page 112.

It is also worth examining the Cook distance of the different points (see figure B.5). Here, the most influential point is n° 201, which is the longest deposition time of the dataset by far but is correctly predicted by the model. That is where its strong influence comes from. On the other

hand, layers n° 70 and 71 have the thickest InN layer but are also very well predicted, and no problem happened during the deposition process.

Finally, table B.6 shows more details of the chosen coefficients, where no p-value above 5 % or no VIF value above ten was allowed.

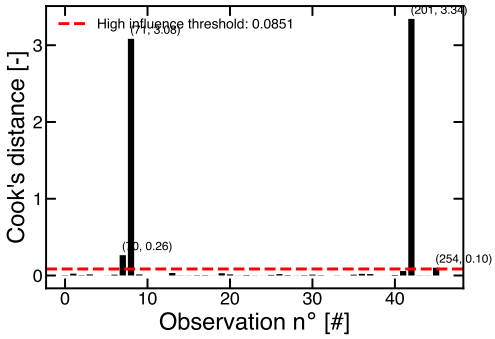


Figure B.5: In/GaN PECVD, DOE: InN thickness model, Cook distance.

| Coefficient | Value | p-value [%] | VIF |
|---|---|---|---|
| $a_0$ | 272.8 | - | - |
| $a_{In}$ | 332.7 | $3.9 \cdot 10^{-33}$ | 1.06 |
| $a_{N_2}$ | 33.7 | $7.1 \cdot 10^{-6}$ | 1.20 |
| $a_{Po}$ | -24.3 | $1.2 \cdot 10^{-3}$ | 1.43 |
| $a_t$ | 29.4 | 0.335 | 1.36 |
| $a_{In^2}$ | 125.2 | $1.2 \cdot 10^{-9}$ | 1.07 |

Table B.6: In/GaN PECVD, DOE: InN thickness model. Details of the coefficients: value, irrelevance (p-value) and correlation (VIF).

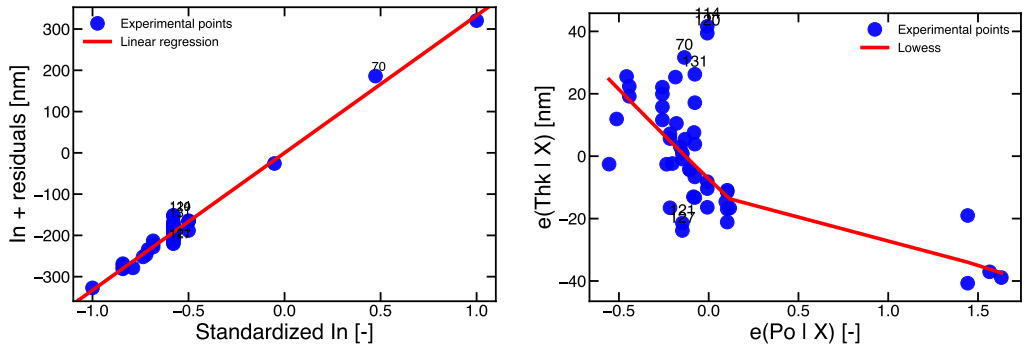


(a) Component – component plus residual plot for the *In* effect with a linear fit.

(b) Partial regression plot for the *Po* effect with a locally weighted scatterplot smoothing (LOWESS).

Figure B.6: In/GaN PECVD, DOE: InN thickness model, two plots detailing the *In* and *Po* effects. All the points are well-aligned for *In*, implying that the effect is relevant for the model, and no undesirable influence was unaccounted for. On the contrary, there is some non-linearity for the *Po* effect.

#### B.2.1.3 InGaN

See the models for the prediction of InGaN layers' thickness in equation 4.5, page 113, or consult table B.7. Figures 4.26a and 4.26c are the residuals *versus* fitted values plots, which are similar with the model added plots displayed in figures B.7a and B.7b.

Comparing the two added model plots, we notice they are both relatively good (the 95 % intervals are pretty narrow). In contrast, model ①'s is narrower while spreading on a more extensive range. Here again, the spreading of the cloud of points is slightly placed below the fitted line, where the outliers are mostly placed on top of the fitter line. It is also worth examining the Cook distance of the different points (see figures B.7c and B.7d). For model ①, the most significant points are n° 70, 105, 173, and the most important of them all: layer n° 201. These points have nothing in common and are reliable; there is no reason to discard them. But as already mentioned for InN, layer n° 201 is the longest deposition of the dataset, hence its heavy influence on the model; if we were to look at the partial regression plot of the time effect, that point appears on the far right side, precisely on the fitted line. All these graphs (Cook distance, the partial regression plot, and the component – component plus residual plot) are linked to show us this precise layer's importance. But as another example, also take a look at figure B.8a, where for the $In^2$ effect, layer 70 is more important here, having the highest indium flow far above all the other layers. We can also notice that in this plot (like in any other for this model), the outliers are ever-present: layers n° 3, 4, 18, 52 and 173, the noise-makers of this model.

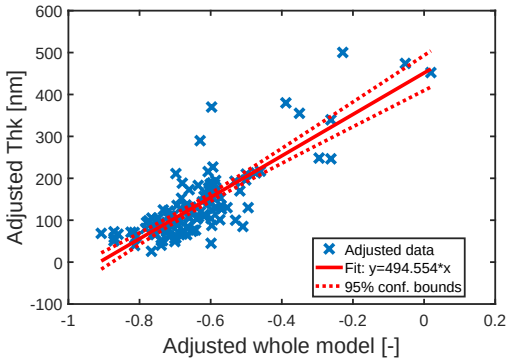


(a) Added model plot, model ①.

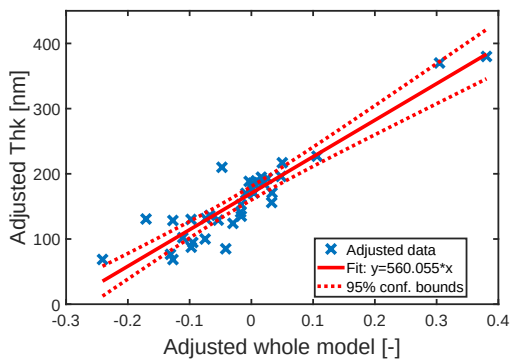


(b) Added model plot, model ②.

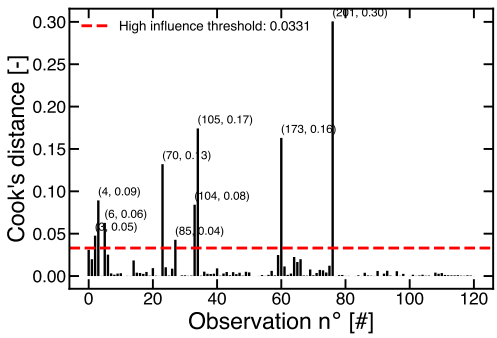


(c) Cook distance, model ①.

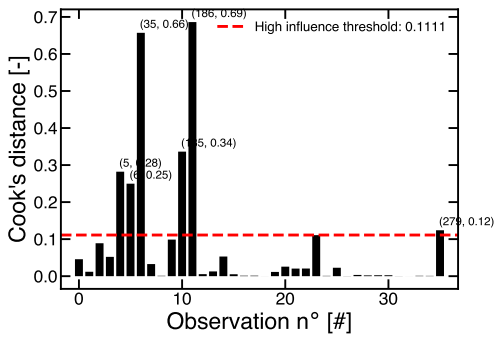


(d) Cook distance, model ②.

Figure B.7: In/GaN PECVD, DOE: InGaN thickness models, Added model plots (top) and Cook distance. Compare the added model plots with figures 4.26a and 4.26c on page 115.

For model ②, the only outliers are layers n° 5, 6 and 223, where layers n° 5 and 6 are above Cook's threshold. After careful examination of these particular two layers, they were produced

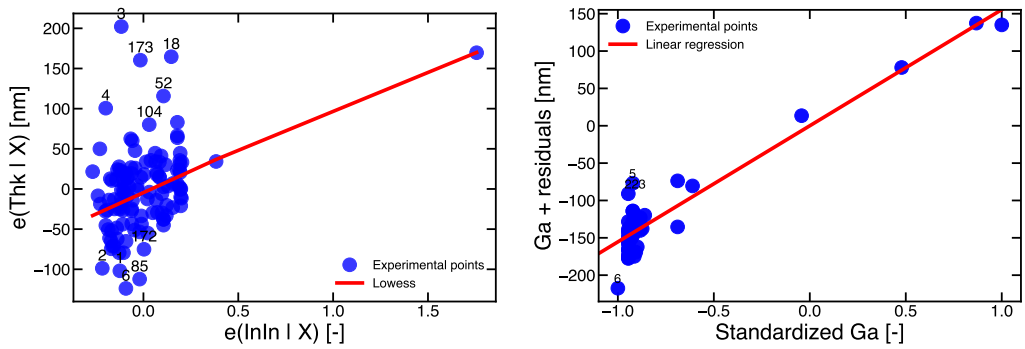


(a) Partial regression plot of the $In^2$ effect with a LOWESS, model ①. The far right point corresponds to the highest TMI flow rate.

(b) Component – component plus residual plot for the *Ga* effect with a linear fit, model ②. Proof of non-linearity for this effect in particular.

Figure B.8: In/GaN PECVD, DOE: InGaN thickness models, the study of the $In^2$ effect of model ① and the *Ga* effect of model ②.

with amongst the lowest TMG flows, often away from the fitted line, as shown in the component – component plus residuals plot displayed for the *Ga* effect in figure B.8b (bottom-left corner). Again, there is no valid reason to discard these layers that are behaving perfectly fine in the first model. However, in the case of model ②, removing them would substantially improve the model quality. In the top-right part of figure B.8b, we can also see the layers that were grown with the highest TMG flow of the dataset, and the model fits them pretty well.

Table B.7 shows more details of the chosen coefficients, where no p-value above 5 % or no VIF value above ten should be allowed. However, without the two intra-correlated factors in model ②, higher p-values rose and were discarded, leading to an even more uncomplicated and under-fitted model. So exceptionally, this imperfect model was still considered because of its relatively high quality. The correlation between these two coefficients is most noticeable in the correlation matrix, typed in bold red face in the following matrix:

$$C_{\mathrm{InGaN}_{②}} = \begin{array}{c} \\ a_0 \\ a_{Ga} \\ \boldsymbol{a_{H_2}} \\ a_{H_2 \cdot NH_3} \\ a_{In \cdot T} \\ a_{N_2 \cdot T} \\ a_{Ga \cdot Po} \\ a_{Po \cdot T} \\ a_{Ga \cdot t} \\ a_{In \cdot t} \end{array} \begin{array}{c} \begin{array}{cccccccccc} a_0 & a_{Ga} & a_{H_2} & \boldsymbol{a_{H_2 \cdot NH_3}} & a_{In \cdot T} & a_{N_2 \cdot T} & a_{Ga} \cdot Po & a_{Po \cdot T} & a_{Ga \cdot t} & a_{In \cdot t} \end{array} \\ \begin{pmatrix} 1 & 0.38 & -0.29 & -0.32 & -0.17 & 0.49 & 0.13 & 0.36 & 0.16 & 0.26 \\ & 1 & -0.26 & -0.17 & -0.24 & 0.04 & 0.86 & 0.38 & -0.62 & 0.38 \\ & & 1 & \boldsymbol{0.92} & 0.42 & -0.82 & -0.37 & -0.77 & 0.33 & -0.66 \\ & & & 1 & 0.56 & -0.81 & -0.32 & -0.78 & 0.20 & -0.66 \\ & & & & 1 & -0.41 & -0.32 & -0.75 & 0.22 & -0.66 \\ & & & & & 1 & 0.12 & 0.68 & 0 & 0.61 \\ & & & & & & 1 & 0.46 & -0.60 & 0.52 \\ & & & & & & & 1 & -0.33 & 0.65 \\ & & & & & & & & 1 & -0.41 \\ & & & & & & & & & 1 \end{pmatrix} \end{array} \tag{B.2}$$

Table B.7: In/GaN PECVD, DOE: InGaN thickness model. Details of the coefficients: value, irrelevance (p-value) and correlation (VIF). Some of the VIF's values of model ② are greater than 10, hinting towards high colinearity between the two effects.

| Coefficient | Value | | p-value [%] | | VIF | |
|---|---|---|---|---|---|---|
| | ① | ② | ① | ② | ① | ② |
| $a_0$ | 451 | 170 | - | - | - | - |
| $a_{Ga}$ | 154 | 155 | $4.5 \cdot 10^{-9}$ | $1.62 \cdot 10^{-5}$ | 2.30 | 4.67 |
| $a_{In}$ | 230 | | $5.9 \cdot 10^{-13}$ | | 3.50 | |
| $a_{H_2}$ | | -278 | | $3.1 \cdot 10^{-6}$ | | **15.17** |
| $a_{Po}$ | -40.4 | | 0.005 | | 1.24 | |
| $a_t$ | 89.7 | | 0.008 | | 1.27 | |
| $a_{Ga \cdot Po}$ | | 225 | | $4.0 \cdot 10^{-8}$ | | 5.55 |
| $a_{Ga \cdot t}$ | | -154 | | $3.4 \cdot 10^{-7}$ | | 2.41 |
| $a_{In \cdot T}$ | | -77.3 | | 0.044 | | 4.98 |
| $a_{In \cdot t}$ | | 191 | | $5.0 \cdot 10^{-5}$ | | 4.12 |
| $a_{N_2 \cdot NH_3}$ | 49.3 | -246 | 0.022 | $4.6 \cdot < 10^{-6}$ | 1.42 | **11.63** |
| $a_{N_2 \cdot Ar}$ | -99.7 | | $4.3 \cdot -18$ | | 1.41 | |
| $a_{N_2 \cdot T}$ | | 124 | | 0.001 | | 5.70 |
| $a_{Po \cdot T}$ | | 141 | | $1.2 \cdot 10^{-6}$ | | 6.72 |
| $a_{Pr \cdot T}$ | -350 | | 1.163 | | 1.43 | |
| $a_{Pr \cdot t}$ | 114 | | 0.016 | | 1.52 | |
| $a_{In^2}$ | 101 | | 0.001 | | 3.44 | |

### B.2.2 Optical bandgap

#### B.2.2.1 GaN bandgap

See the model for the prediction of GaN layers' optical BG in equation 4.6, page 117, or consult table B.8. Figure 4.27a is the residuals *versus* fitted values plot, which is similar to the model added plot displayed in figure B.9a. The 95 % confidence interval is spread quite widely, and we recognise the two outliers of the model at the bottom of the graph. Most of the experimental optical bandgap values are out of the 95 % confidence interval of the values predicted by the model, but they are evenly dispersed around it. So again, the data is noisy, making it difficult to improve the model. The partial residual plot for the *Ar* effect (see figure B.9b) also shows some deviation from linearity, where the LOWESS is slightly bent in the middle. Non-linear relationships between an effect and the output variable can be dealt with via basis expansions (*e.g.* polynomial regression) or regression splines [44].

It is also worth examining the Cook distance of the different points (see figure B.10), where the two outliers again display high leverage on the model. The examination of these points has already been done, and the decision was to keep them because of their quality, and there was no potential reason to eliminate them. Finally, table B.8 shows more details of the chosen coefficients, where no p-value above 5 % or no VIF value above ten was allowed.

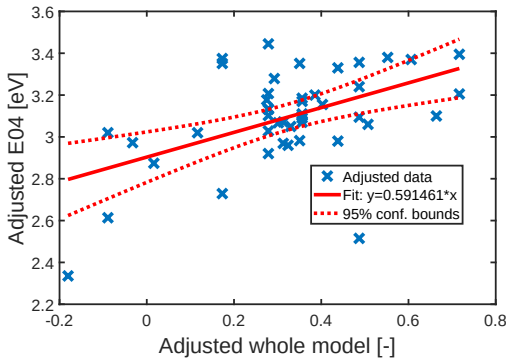


(a) Added model plot for the GaN optical bandgap model. Compare with figure 4.27a on page 118.

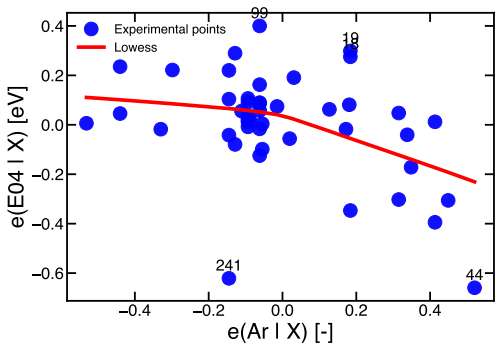


(b) Partial residual plot of the $a_{Ar}$ factor of the GaN optical bandgap model with a LOWESS.

Figure B.9: In/GaN PECVD, DOE: GaN optical bandgap model, added model plot and partial residual plot of the $a_{Ar}$ effect.

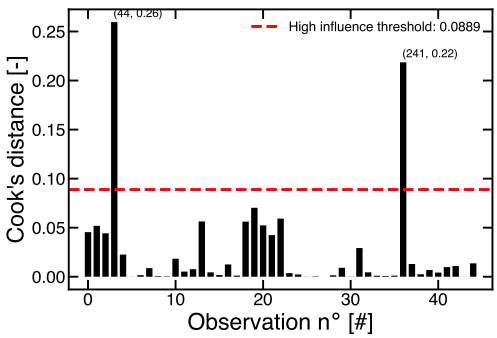


Figure B.10: In/GaN PECVD, DOE: GaN optical bandgap model, Cook distance.

| Coefficient | Value | p-value [%] | VIF |
|---|---|---|---|
| $a_0$ | 2.903 | - | - |
| $a_{H_2}$ | -0.294 | 0.717 | 3.03 |
| $a_{Ar}$ | -0.391 | 0.536 | 5.79 |
| $a_{N_2 \cdot Ar}$ | -0.278 | 0.108 | 4.95 |
| $a_{NH_3 \cdot Ar}$ | -0.203 | 1.049 | 3.48 |

Table B.8: In/GaN PECVD, DOE: GaN optical bandgap model. Details of the coefficients: value, irrelevance (p-value) and correlation (VIF).

#### B.2.2.2 InN bandgap

See the models for the prediction of InN layers' BG in equation 4.7, page 119, or consult table B.9. Figures 4.28a and 4.28c are the residuals *versus* fitted values plots, which are similar with the model added plots displayed in figures B.11a and B.11b.

Comparing the two added model plots, we notice they are both relatively good (the 95 % intervals could be narrower). For a deeper analysis, see the comments about the residuals *versus* fitted values plot on page 121. If we now examine the Cook distance of the different points (see figures B.11c and B.11d), we notice that layer n° 199 is a high leverage point in both cases and thankfully not an outlier in both cases as well. For model ①, the influential layer is n° 180 (an outlier), and n° 70 for model ② (not an outlier). Layer n° 70 has the highest TMI flow by far, so it is placed "far from the cloud of points" and thus greatly impacts the fitting procedure. This is also reflected with the component – component plus residual plot

(figure B.12b, where that special point is placed far to the right, away from the others). On the contrary, layer n° 180 has the lowest TMI flow rate of the dataset but remains consistent enough, and layer n° 199 was produced with the highest ammonia flow at the highest power of the dataset. All these particular layers were reliably produced in stable conditions and yielded results that are not out of the ordinary; there is no particular reason to discard them.

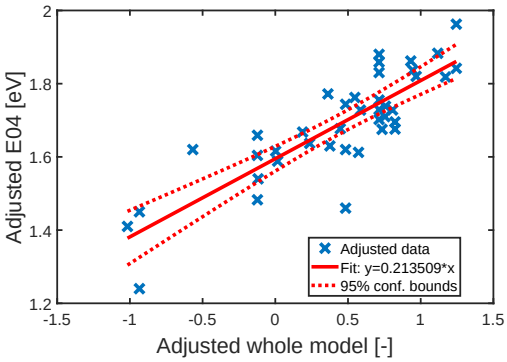


(a) Added model plot, model ①.

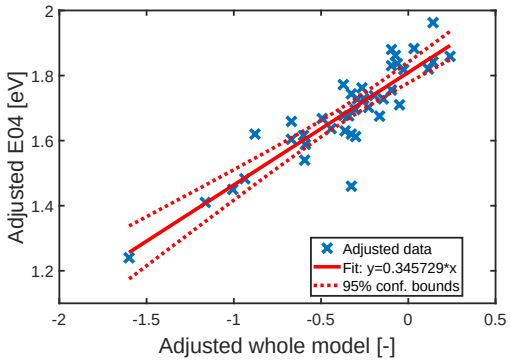


(b) Added model plot, model ②.

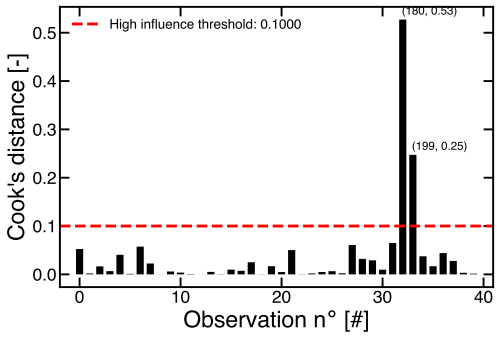


(c) Cook distance, model ①.

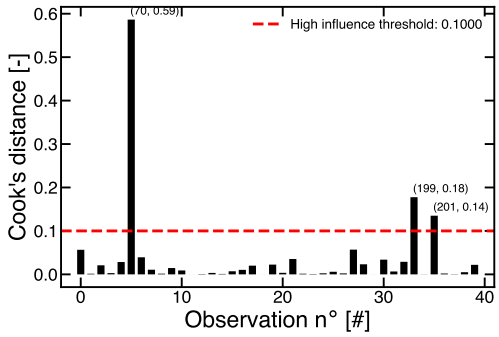


(d) Cook distance, model ②.

Figure B.11: In/GaN PECVD, DOE: InN optical bandgap models, added model plots (top) and Cook distance. Compare the added model plots with figures 4.28a and 4.28c on page 121.

See also figure B.12a: the partial residual plot for the $N_2$ effect: the one displaying the least linearity of model ②. Overall, both models look linear, which looks like a minor imperfection amongst the relatively good quality of this model. Other partial regressions show good linearity and homoscedasticity. Table B.9 shows more details of the chosen coefficients, where as announced, one effect of model ① has its p-value just slightly above 5 %, but no VIF value above ten was allowed. However, without this high p-value effect, higher p-values rose and were discarded, leading to model ②. So exceptionally, this imperfect model was still considered because of its relatively high quality. The rest is excellent: all acceptable p-values and shallow VIF values.

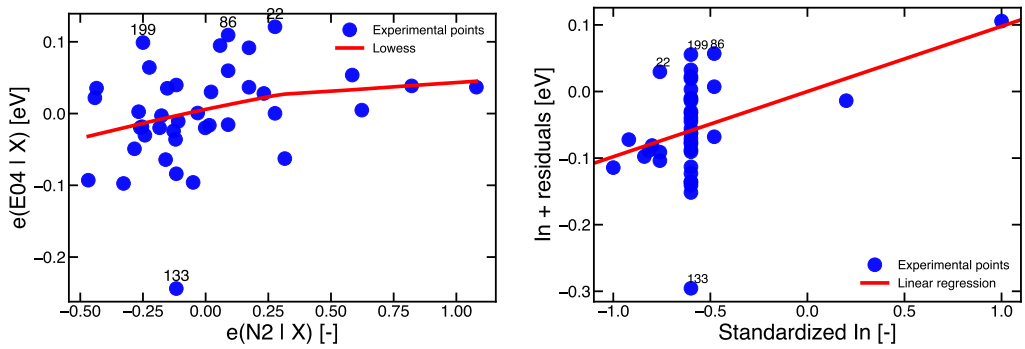


(a) Partial regression plot of the $N_2$ effect with a LOWESS.

(b) Component − component plus residual plot for the *In* effect with a linear fit.

Figure B.12: In/GaN PECVD, DOE: second InN optical bandgap model, the study of two particular effects $N_2$ and *In*.

Table B.9: In/GaN PECVD, DOE: InN optical bandgap model. Details of the coefficients: value, irrelevance (p-value) and correlation (VIF). The $a_{N_2}$ effect has a p-value higher than 5 % for model ①.

| Coefficient | Value | | p-value [%] | | VIF | |
|---|---|---|---|---|---|---|
| | ① | ② | ① | ② | ① | ② |
| $a_0$ | 1.810 | 1.595 | - | - | - | - |
| $a_{In}$ | 0.098 | | 3.47 | | 1.39 | |
| $a_{N_2}$ | 0.061 | | **8.79** | | 2.70 | |
| $a_{Po}$ | -0.133 | -0.147 | $2.3 \cdot 10^{-5}$ | $2.1 \cdot 10^{-5}$ | 1.24 | 1.14 |
| $a_T$ | -0.098 | -0.096 | 0.130 | 0.325 | 1.28 | 1.14 |
| $a_{N_2 \cdot H_2}$ | 0.090 | 0.107 | 0.083 | 0.020 | 1.23 | 1.02 |
| $a_{NH_3 \cdot Po}$ | 0.055 | 0.059 | 2.586 | 1.596 | 1.57 | 1.16 |
| $a_{In^2}$ | -0.260 | | 0.153 | | 1.57 | |

#### B.2.2.3 InGaN bandgap

See the models for the prediction of InGaN layers' BG in equation 4.8, page 121, or consult table B.10. Figures 4.29a and 4.29c are the residuals *versus* fitted values plots, which are similar with the model added plots displayed in figures B.13a and B.13b.

Comparing the two added model plots, the points in the one related to the deposition parameters are more spread out, and the 95 % confidence interval is wider than the one related to the indium content $X_{\text{In}} = \frac{\text{In}}{\text{In+Ga}}$ (In & Ga in at. %, $X_{\text{In}}$ in %). This is coherent with the better quality metrics of the second model described in table 4.14b. If we now examine the Cook distance of the different points (see figures B.13c and B.13d), we notice that for the $X_{\text{In}}$ model, the high leverage points are not too far from the threshold, which means that the points are overall well equilibrated between one another. The sad part is that the layers that exceed the threshold are, in fact, the outlier ones. This is problematic because an outlier can be considered an

exceptional case, and in the case of this model, the whole fit seems to revolve around those outliers / exceptional cases. In comparison, for the model related to the deposition parameters, the infamous layer n° 70 (highest TMI flow of the dataset) is two orders of magnitude above the next most influential point of the model (notice the logarithmic y-scale). The good thing here is that the model predicts this high leverage point well, and it was repeatedly said that there is nothing wrong with that layer. Some of the other leverage points are outliers, but one layer, n° 70, overshadows their weight on the model.

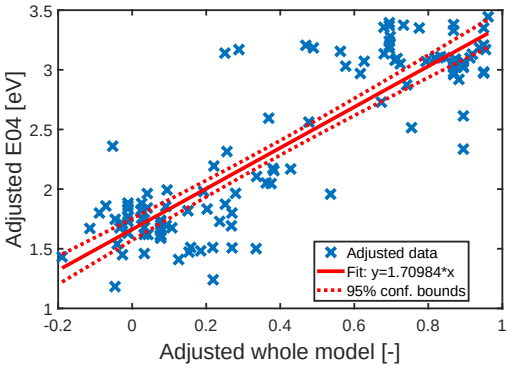


(a) Added model plot, system B model.

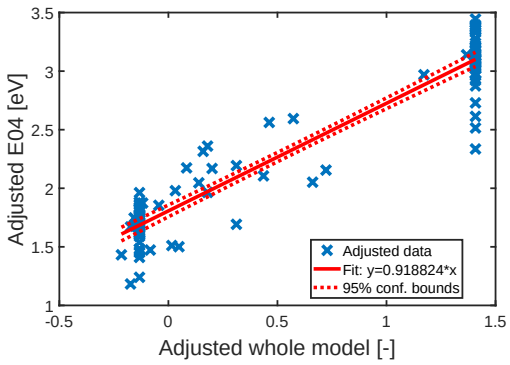


(b) Added model plot, $X_{\text{In}}$ model.

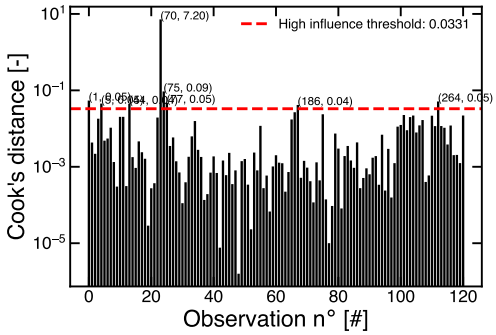


(c) Cook distance, system B model.

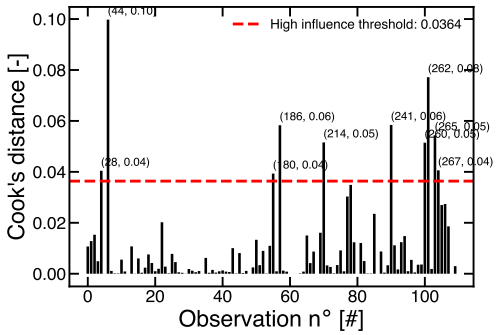


(d) Cook distance, $X_{\text{In}}$ model.

Figure B.13: In/GaN PECVD, DOE: InGaN optical bandgap model, added model plots (top) and Cook distance. Compare the added model plots with figures 4.29a and 4.29c on page 124.

See also figure B.14: the partial residual plot for the *In* effect for the model related to deposition parameters. We understand here why layers n° 70 and 69 are amongst the most influential ones, compromising the linearity of this particular effect. The overall model seems linear, looking at the added model plot (figure B.13a) or the LOWESS of the residuals *versus* fitted values plot (figure 4.29a), but that layer, in particular, is not well fitted by that effect when it takes high values.

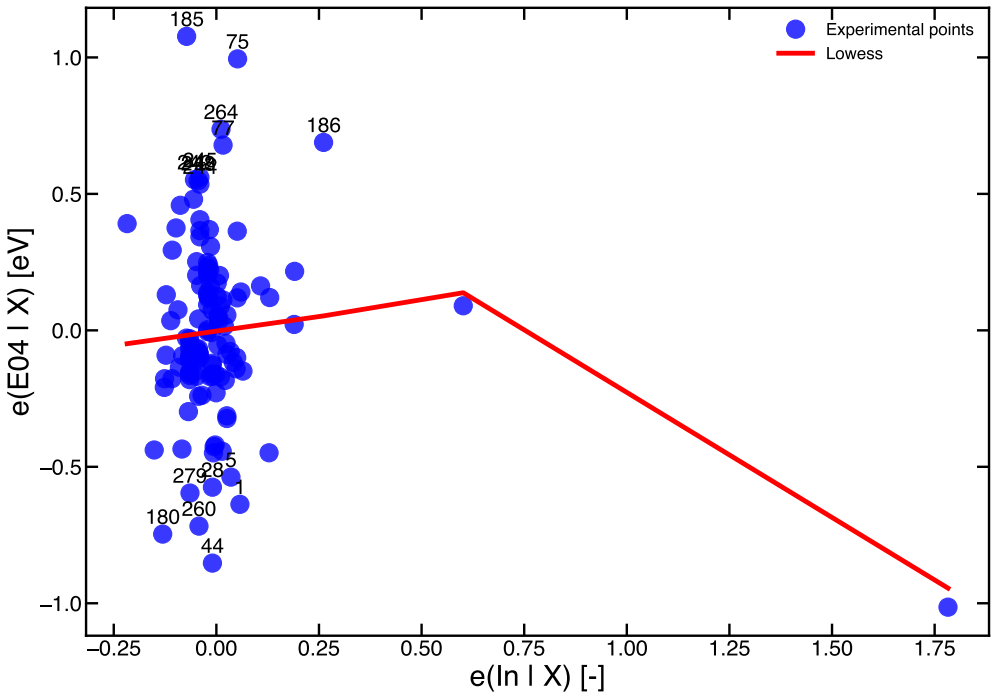


Figure B.14: In/GaN PECVD, DOE: InGaN optical bandgap model related to system B: partial residual plot for the *In* effect. The LOWESS highlights the non-linearity of this effect.

Table B.10: In/GaN PECVD, DOE: InGaN optical bandgap models. Details of the coefficients: value, irrelevance (p-value) and correlation (VIF).

| Coefficient | Value | | p-value [%] | | VIF | |
|---|---|---|---|---|---|---|
| | SysB | $X_{\text{In}}$ | SysB | $X_{\text{In}}$ | SysB | $X_{\text{In}}$ |
| $a_0$ | 1.662 | 1.807 | - | - | - | - |
| $a_{In}$ | -0.380 | | 2.624 | | 3.45 | |
| $a_{N_2}$ | -0.367 | | 0.007 | | 2.70 | |
| $a_{In \cdot T}$ | 0.943 | | 0.093 | | 3.92 | |
| $a_{N_2 \cdot T}$ | -0.881 | | 0.405 | | 4.19 | |
| $a_{Ga^2}$ | -0.460 | | 0.174 | | 2.46 | |
| $a_{In^2}$ | 0.876 | | $6.4 \cdot 10^{-6}$ | | 3.59 | |
| $a_{X_{\text{In}}}$ | | -0.708 | | $5.7 \cdot 10^{-54}$ | | 1.00 |
| $a_{X_{\text{In}^2}}$ | | 0.586 | | $2.9 \cdot 10^{-17}$ | | 1.00 |

### B.2.3 Unstrained XRD grain size

#### B.2.3.1 InN

See the model for the prediction of InN layers' crystallite size in equation 4.9, page 125, or consult table B.11. Figure 4.30a is the residuals *versus* fitted values plot, which is similar to the model added plot displayed in figure B.15. However, with the added model plot here, we can

see a wide 95 % confidence interval, with most of the points evenly dispersed outside of it. This means that the noise in the data is significant but normally distributed. The partial regression plots and the component – component plus residual plots do not yield more information than this.

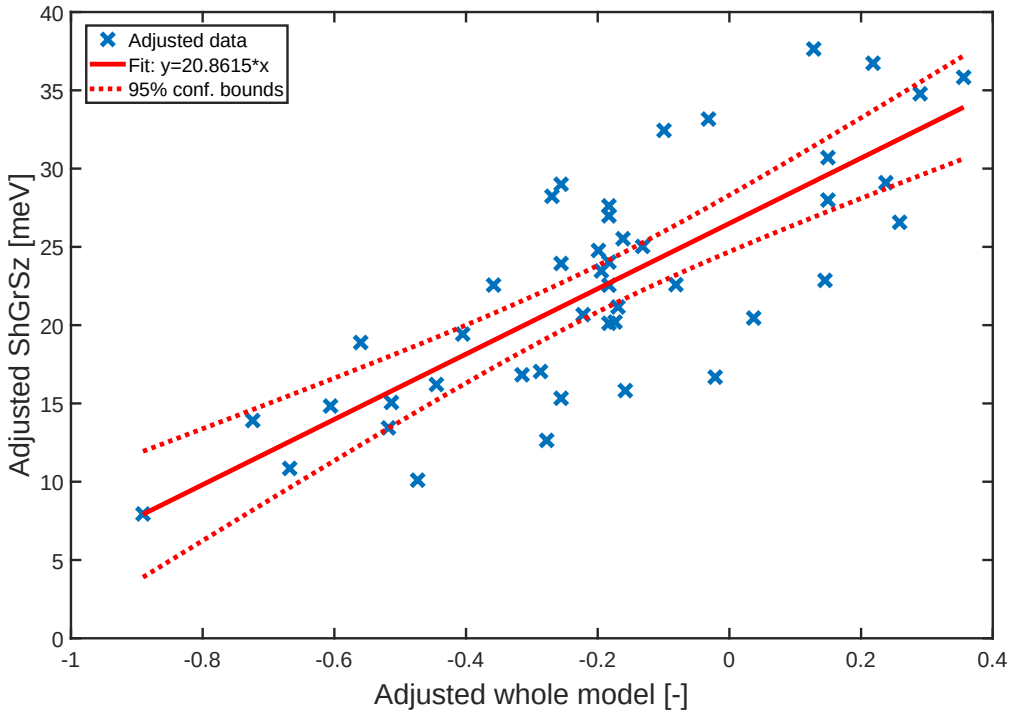


Figure B.15: In/GaN PECVD, DOE: InN crystallite size model, added model plot. Compare with figure 4.30a on page 127.

It is also worth examining the Cook distance of the different points (see figure B.16). Here, the most influential point is n° 201, which is the longest deposition time of the dataset by far but is correctly predicted by the model. That is where its strong influence comes from. Overall, there seems to be an even distribution of the leverage between many points, which is satisfying but relates to the noisiness of the model again. There were no outliers, but the points exhibited in the Cook distance plot are those with the highest residuals. But since the lack of fit p-value does not allow us to conclude that the model is underfitting the data, the source of that deviation must come from noise.

Finally, table B.11 shows more details of the chosen coefficients, where no p-value above 5 % or no VIF value above ten was allowed.

#### B.2.3.2 InGaN

See the model for the prediction of InGaN layers' crystallite size in equation 4.10, page 127, or consult table B.12. Figure 4.31a is the residuals *versus* fitted values plot, which is similar to the model added plot displayed in figure B.17. However, with the added model plot here, we can

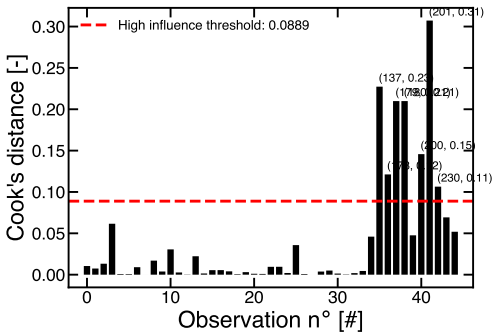


Figure B.16: In/GaN PECVD, DOE: InN crystallite size model, Cook distance.

| Coefficient | Value | p-value [%] | VIF |
|---|---|---|---|
| $a_0$ | 26.50 | - | - |
| $a_{In}$ | -8.13 | 0.152 | 1.17 |
| $a_{H_2}$ | 5.83 | 0.017 | 1.22 |
| $a_{NH_3}$ | -4.67 | 0.429 | 1.78 |
| $a_{Po}$ | -4.74 | 0.555 | 1.72 |
| $a_T$ | 12.87 | $2.35 \cdot 10^{-5}$ | 1.55 |
| $a_t$ | 11.19 | 0.169 | 1.86 |

Table B.11: In/GaN PECVD, DOE: InN crystallite size model. Details of the coefficients: value, irrelevance (p-value) and correlation (VIF).

see a narrow 95 % confidence interval, with most of the points evenly dispersed outside of it and a few points at the far right inside of it. This means that the noise in the data is significant but normally distributed, and the model has an acceptable prediction accuracy over its whole range. The partial regression plots and the component – component plus residual plots do not yield more information than this as well: they show acceptable linearity and homoscedasticity, usually with the extremes of the plots filled with the most outlier points mentioned in the related section, page 127.

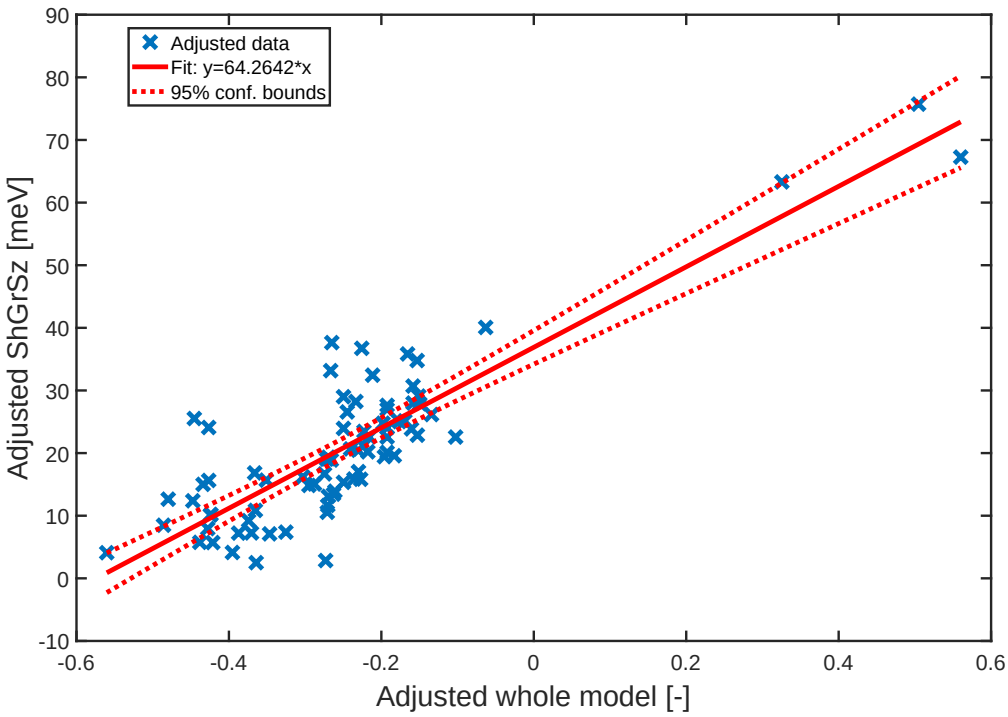


Figure B.17: In/GaN PECVD, DOE: InGaN crystallite size model, added model plot. Compare with figure 4.31a on page 129.

It is also worth examining the Cook distance of the different points (see figure B.18). Here, the most influential result by far is n° 197, which shows two extreme characteristics: it is the second longest GaN deposition, and it is one of these rare good layers that were deposited at 400 °C. On top of that, it is correctly predicted by the model. It is often part of the cloud of points (except for partial regression plots, including the temperature and deposition time). That is where its strong influence comes from. Apart from this result, there seems to be an even distribution of the leverage between many points, which is satisfying but relates to the noisiness of the model again. There were no outliers, but the points exhibited in the Cook distance plot are, in fact, the points with the highest residuals. But since the lack of fit p-value does not allow us to conclude that the model is underfitting the data, the source of that deviation must come from noise.

Finally, table B.12 shows more details of the chosen coefficients, where no p-value above 5 % or no VIF value above ten was allowed.

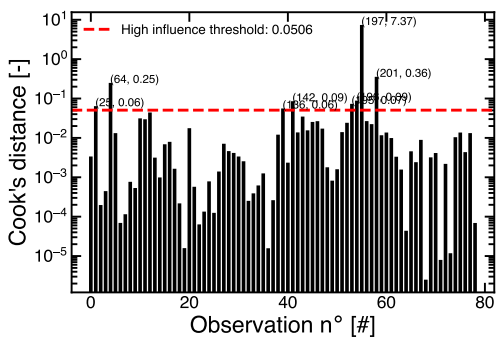


Figure B.18: In/GaN PECVD, DOE: InGaN crystallite size model, Cook distance.

| Coefficient | Value | p-value [%] | VIF |
|---|---|---|---|
| $a_0$ | 36.89 | - | - |
| $a_{Ga}$ | 13.88 | 0.001 | 4.85 |
| $a_{Po}$ | 22.42 | $8.15 \cdot 10^{-8}$ | 8.24 |
| $a_t$ | 18.54 | 0.064 | 3.88 |
| $a_{Ga \cdot Po}$ | 10.83 | $7.62 \cdot 10^{-7}$ | 1.61 |
| $a_{Ga \cdot T}$ | 22.08 | 0.001 | 5.39 |
| $a_{In \cdot N_2}$ | 8.03 | 0.003 | 1.53 |
| $a_{N_2 \cdot H_2}$ | -5.76 | 1.779 | 1.48 |
| $a_{Po \cdot t}$ | 12.17 | 0.122 | 6.26 |
| $a_{T \cdot t}$ | 27.22 | 0.005 | 6.25 |
| $a_{T^2}$ | -38.72 | $2.37 \cdot 10^{-8}$ | 3.88 |

Table B.12: In/GaN PECVD, DOE: InGaN crystallite size model. Details of the coefficients: value, irrelevance (p-value) and correlation (VIF).

### B.2.4 InGaN Urbach energy

See the model for the prediction of InGaN layers' Urbach energy in equation 4.11, page 129, or consult table B.13. Figure 4.32a is the residuals *versus* fitted values plot, which is similar to the model added plot displayed in figure B.19. The linearity of the model is good, as well as the homoscedasticity.

It is also worth examining the Cook distance of the different points (see figure B.20), where each point's influence seems evenly distributed here. The values that exceed the threshold of $n/4$ are not that far from said threshold and are not outliers, except for layer n° 1. That layer has

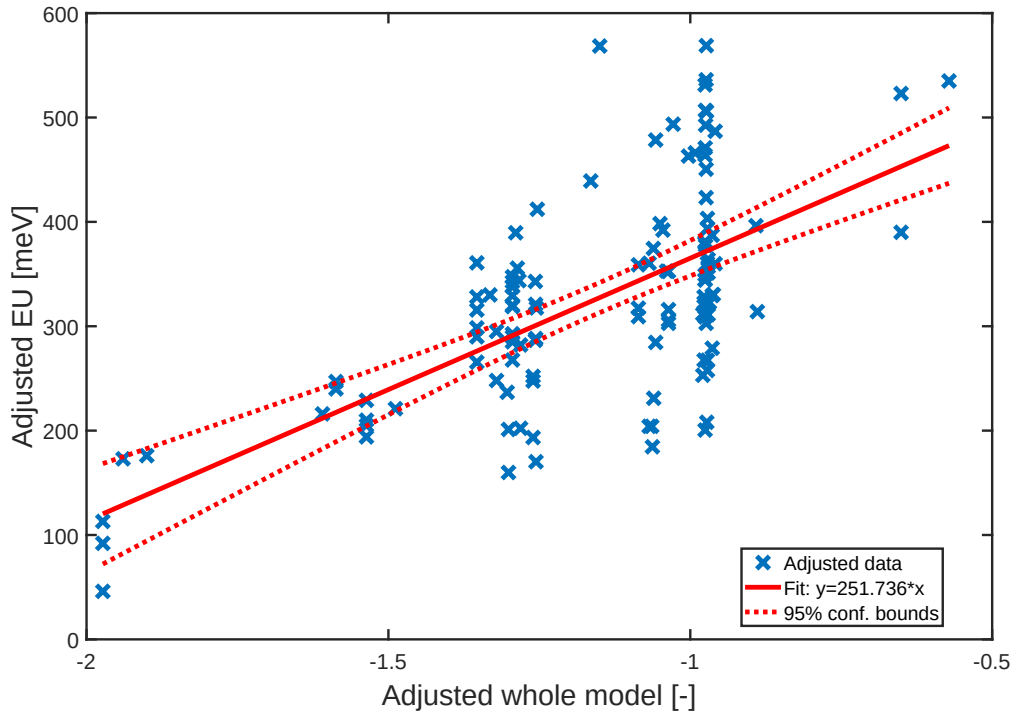


Figure B.19: In/GaN PECVD, DOE: InGaN Urbach energy model, added model plot. Compare with figure 4.32a on page 131.

the highest Urbach energy value and is, therefore, more difficult to predict than the central cloud of points. But that layer remains valid and sound so that it will be kept in that dataset. Finally, table B.13 shows more details of the chosen coefficients, where no p-value above 5 % or no VIF value above ten was allowed.

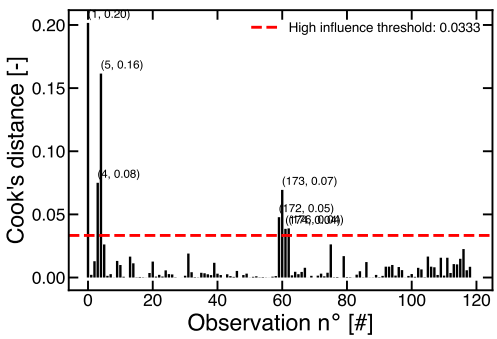


Figure B.20: In/GaN PECVD, DOE: InGaN Urbach energy model, Cook distance.

| Coefficient | Value | p-value [%] | VIF |
|---|---|---|---|
| $a_0$ | 611.4 | - | - |
| $a_{Ga}$ | 59.1 | 2.684 | 1.48 |
| $a_{N_2}$ | 56.0 | 1.037 | 2.86 |
| $a_{Ar}$ | 54.4 | 1.006 | 1.06 |
| $a_{Ga \cdot Po}$ | 63.1 | 0.419 | 1.69 |
| $a_{N_2^2}$ | -132.2 | 0.006 | 3.60 |
| $a_{NH_3^2}$ | -179.8 | $3.0 \cdot 10^{-4}$ | 4.26 |

Table B.13: In/GaN PECVD, DOE: InGaN Urbach energy model. Details of the coefficients: value, irrelevance (p-value) and correlation (VIF).

### B.2.5 Indium content

See the model for the prediction of the indium content of InGaN layers in equation 4.12, page 132, or consult table B.14. The "indium content" referred to here corresponds to the atomic indium content relative to only the III-materials of the layer, $X_{\mathrm{In}} = \frac{\mathrm{In}}{\mathrm{In+Ga}}$ (In & Ga in at. %, $X_{\mathrm{In}}$ in %). Figure 4.33a is the residuals *versus* fitted values plot, which is similar to the model added plot displayed in figure B.21. In the latter, one recognises the two series of points forming two lines, corresponding to the GaN and InN layers. Again, most of the experimental points are outside the 95 % confidence interval of the model, proving once again that the model is a bit noisy. The partial regression plots and the component – component plus residual plots do not yield more information than this as well: also noisy data, with a lousy prediction over the whole set (bad linearity) and an acceptable dispersion away from the model (some heteroscedasticity), slightly skewed because of the outliers. One possible solution to this kind of problem is to use weighted regression. This type of regression assigns a weight to each data point based on the variance of its fitted value. This gives small weights to data points with higher variances and shrinks their squared residuals. When the proper weights are used, this can eliminate the heteroscedasticity problem [44].

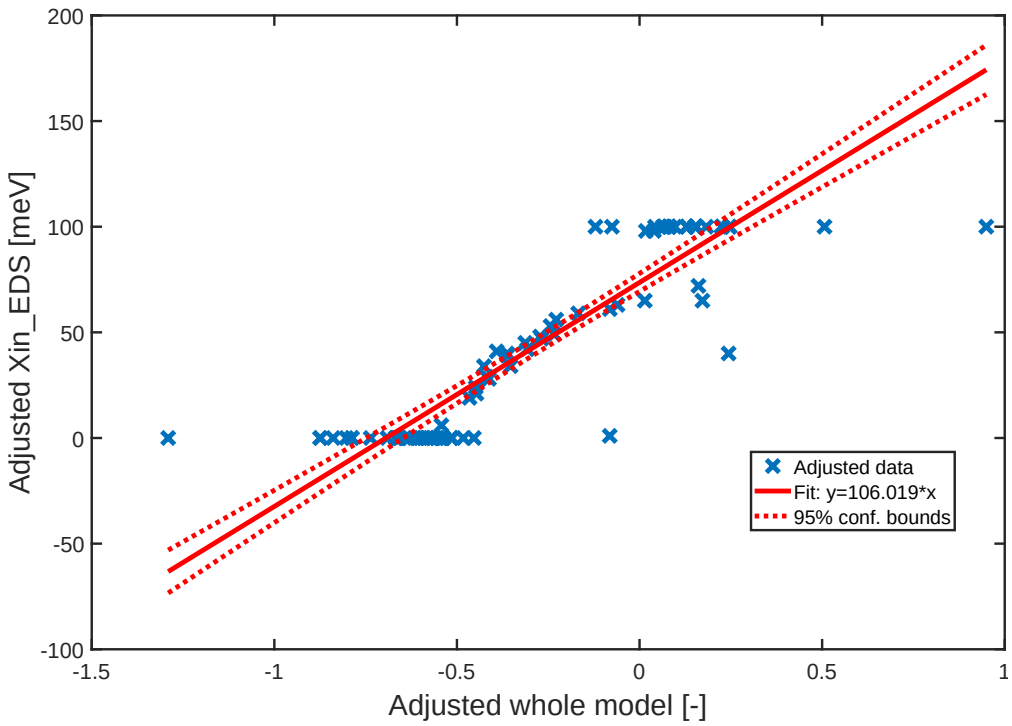


Figure B.21: In/GaN PECVD, DOE: indium content model, added model plot. Compare with figure 4.33a on page 134.

It is also worth examining the Cook distance of the different points (see figure B.22), where here again, the most significant points are the usual suspects: layers n° 69, 70, 185 and 186. Here would be why this model is less reliable: the outliers of the fitting procedure are those that most influence the results. Or in other words: it is probable (but maybe not) that without

those exceptional points, a completely different model would fit the data better. Again, the examination of these points has already been done, and the decision was to keep them because of their quality, and there was no valid reason to eliminate them. This high and bad influence can also be perceived in the skewed fitted line of the Q-Q plot displayed in figure 4.33b.

Finally, table B.14 shows more details of the chosen coefficients, where no p-value above 5 % or no VIF value above ten was allowed.

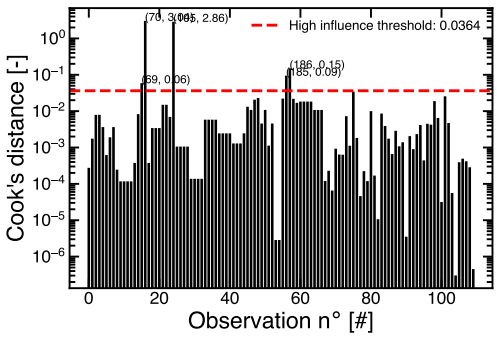


Figure B.22: In/GaN PECVD, DOE: indium content model, Cook distance.

| Coefficient | Value | p-value [%] | VIF |
|---|---|---|---|
| $a_0$ | 73.6 | - | - |
| $a_{Ga}$ | -44.1 | $4.4 \cdot 10^{-5}$ | 2.42 |
| $a_{In}$ | 89.0 | $3.3 \cdot 10^{-19}$ | 2.20 |
| $a_{Ga \cdot NH_3}$ | 20.8 | 0.0070 | 3.49 |
| $a_{In \cdot NH_3}$ | -27.8 | 0.0012 | 3.91 |
| $a_{N_2 \cdot H_2}$ | -13.3 | 1.09 | 1.46 |

Table B.14: In/GaN PECVD, DOE: indium content model. Details of the coefficients: value, irrelevance (p-value) and correlation (VIF).

## B.3 GaN by PVD: lost figures

This section aims to completely present all the results obtained through the different characterisation methods in section 5.1.

### B.3.1 Effects of deposition parameters – Pressure on structural properties

Figure 5.4 presents the structural properties dependence on temperature, thickness and substrate for a pressure deposition of 3.00 $\mu$bar. Figures B.23 to B.26 present the same kind of plots, but for the two other pressures of this experiment: 0.85 $\mu$bar and 12.0 $\mu$bar, on sapphire and silicon, including a zoom-in on the angle of interest.

### B.3.2 Effect of germanium doping – optical properties

The points presented in figure 5.14 are summarised in tables B.15 and B.16, and extracted from the optical plots of figure B.27.

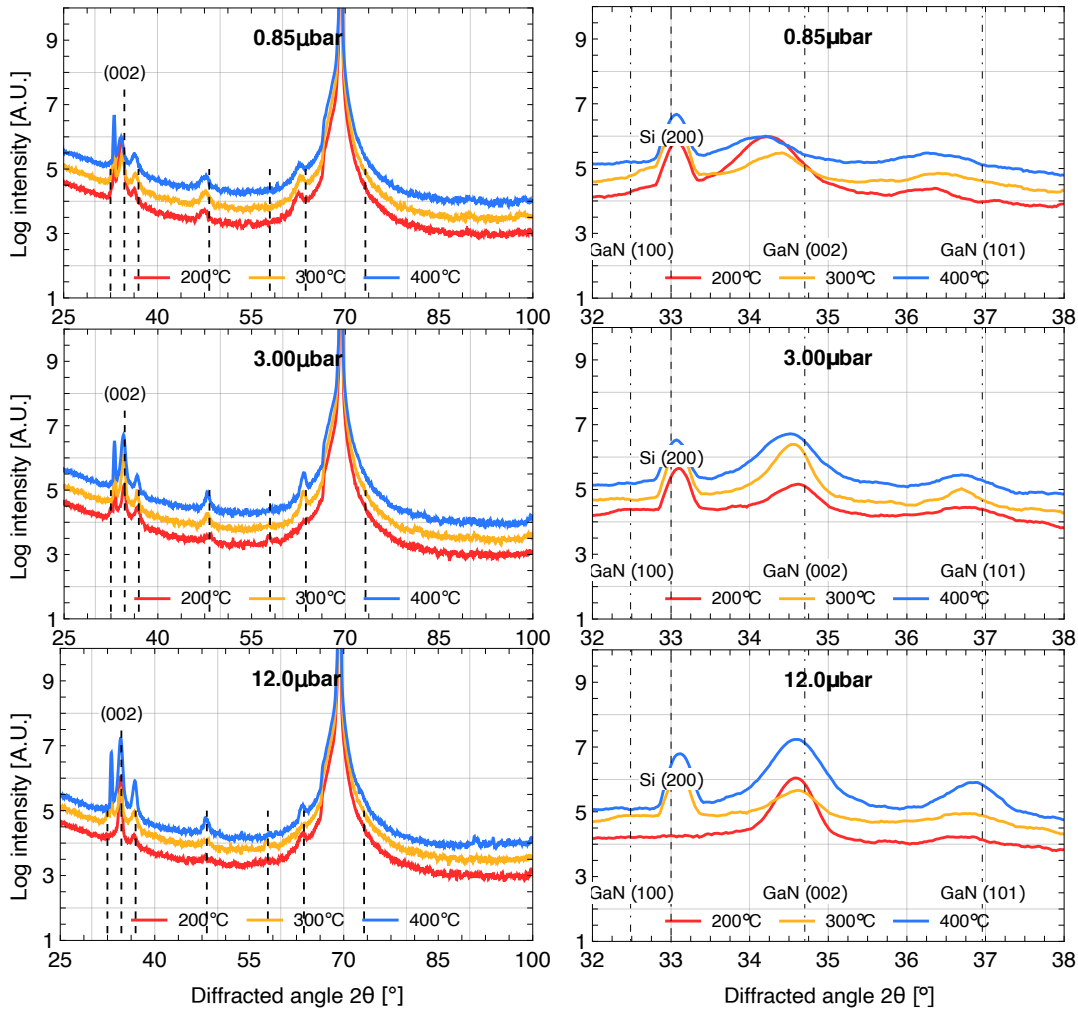


Figure B.23: PVD GaN, characteristics: XRD temperature and pressure variation on silicon for a fixed thickness (100 nm).

### B.3.3 Effect of germanium doping – electrical properties

The points presented in figure 5.17 are summarised in tables B.15 and B.15 and are extracted from the Arrhenius plots of figure B.28 presented here.

### B.3.4 Dark fields of a GaN/Sa PVD epitaxial layer

Find in figure B.29 a small TEM study of the epitaxy of the undoped layer presented in section 5.4. A narrower SAED was used here compared to figure 5.27.

Figure B.29a is the TEM image of the probed area without any objective aperture, not a bright field image. Its associated diffraction figure is presented in figure B.29b, where two spots were selected with the objective aperture, one selecting a diffraction point of the sapphire substrate

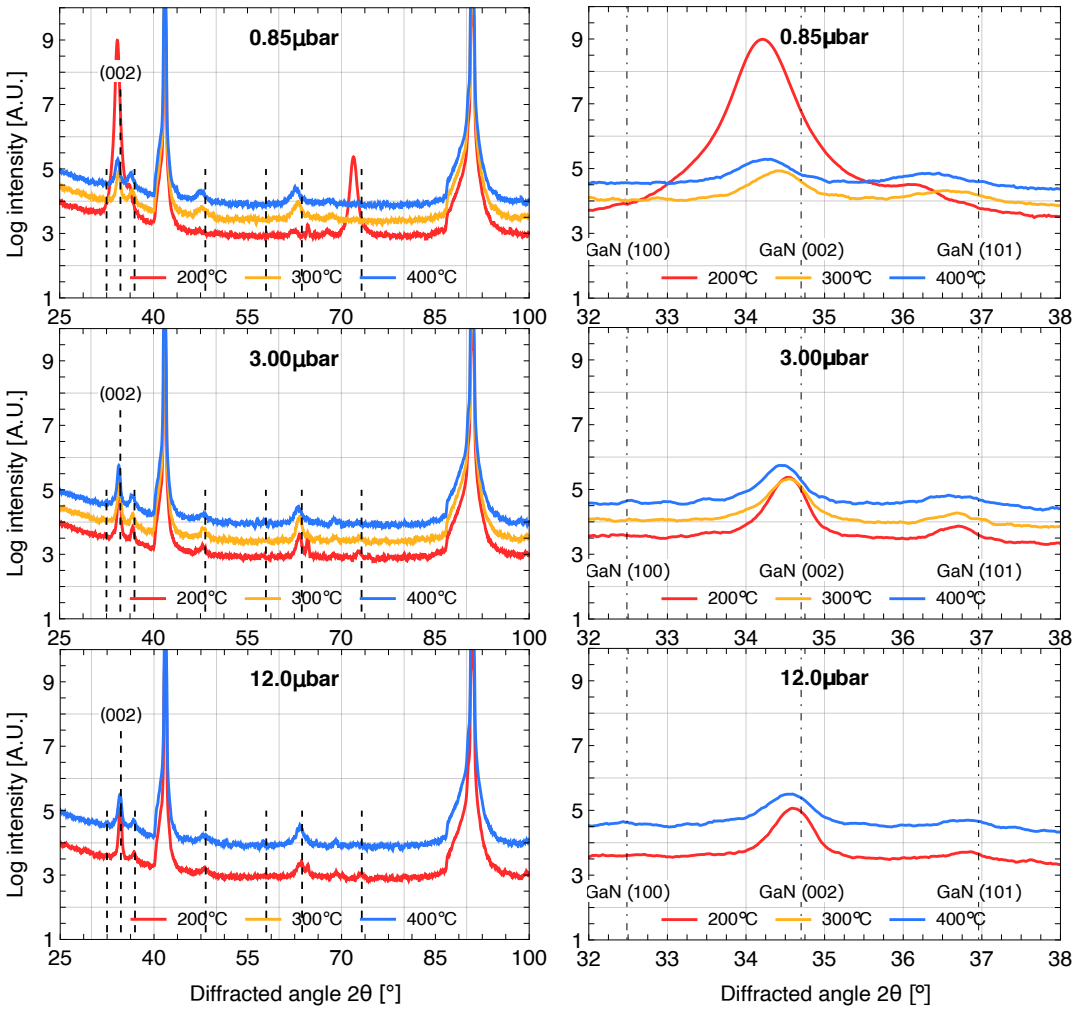


Figure B.24: PVD GaN, characteristics: XRD temperature and pressure variation on sapphire for a fixed thickness (100 ± 10 nm).

(blue spot, associated with the DF in figure B.29c) and one selecting a diffraction point of the epitaxial GaN layer (orange spot, associated with the DF in figure B.29d).

The grains are clearly visible with the TEM image: about 50 nm wide and 150 nm tall, the layer thickness. Even though a SAED was used here to reduce the probed area, the diffraction figure shows the same patterns as figure 5.27c, because of the high crystallinity of even only one GaN crystals. In the DF of the sapphire substrate, we see that near the interface, the colour is wavering a bit; this is a sign of some tension due to the epitaxy. Indeed, the darker shades are centred just under the centre of a GaN crystal (when compared with the TEM image), while the brighter shades are positioned just under a grain boundary. Finally, the last figure is extracted using only one GaN point in the diffraction figure, but each point of the GaN mesh gave produced a similar DF. We see some large Moiré patterns, a sign of a minimal difference between two superposed crystal patterns, but also some long thin dark vertical lines. These

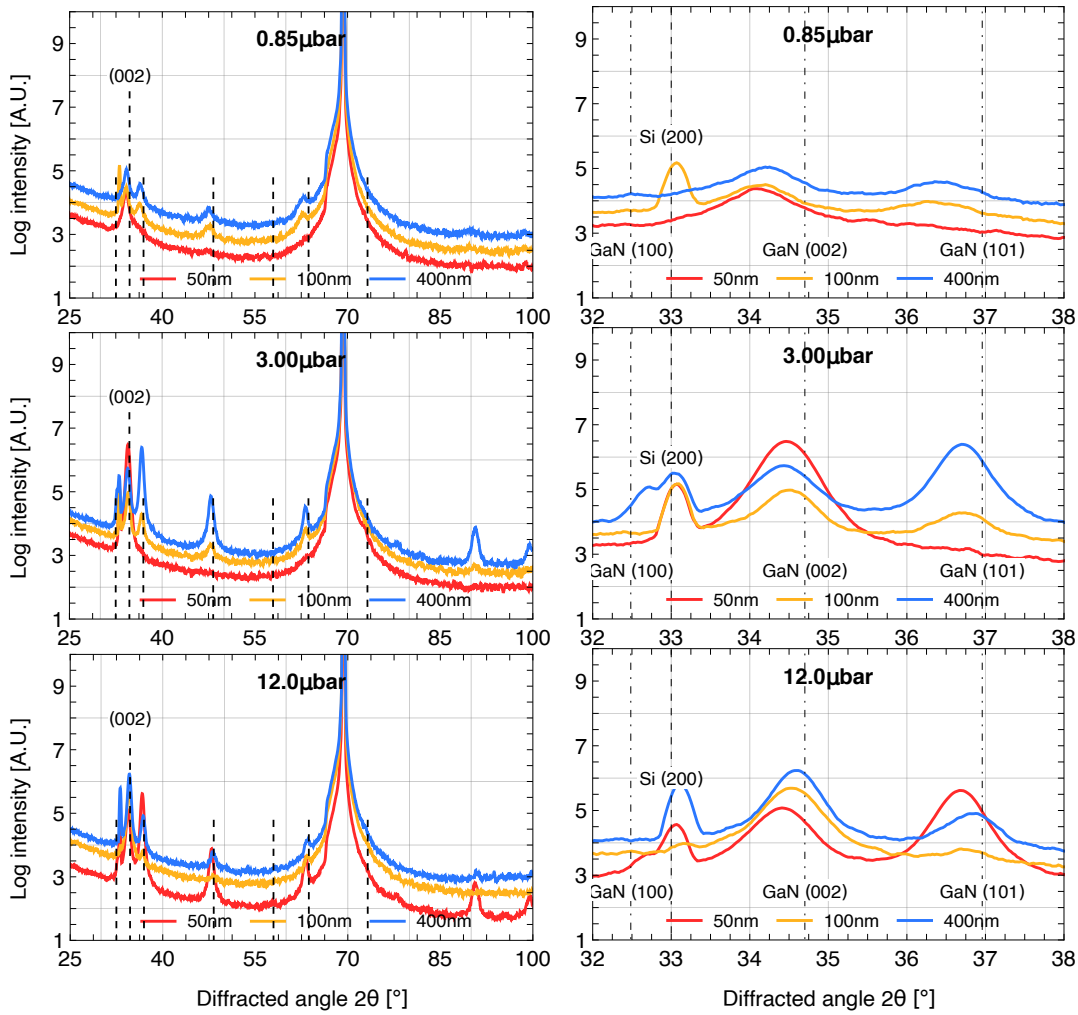


Figure B.25: PVD GaN, characteristics: XRD thickness and pressure variation on silicon for a fixed deposition temperature (400 ± 2 °C).

lines were not identified, but it is believed that they are threading dislocations and birthing at the interface; they could be the product of the release of the high tensile stress produced by the epitaxy between the substrate and the layer.

## B.4 InGaN contacts by PVD, J-V curves

In section 6.3, six layers were deposited in the Univex without rotating the sample holder to induce a gradient. The six layers were a thin and thick version of a single InGaN target, a single GaN target, and a co-sputtering deposition with the two targets simultaneously. For each of these six depositions, a p-doped and an n-doped silicon wafer was used, and the gradient could be fragmented into 9 “zones” that were later characterised as solar cells. This totals 108 solar cells, each of which has its own J-V curve, displayed here in figures B.30 and B.31 for the

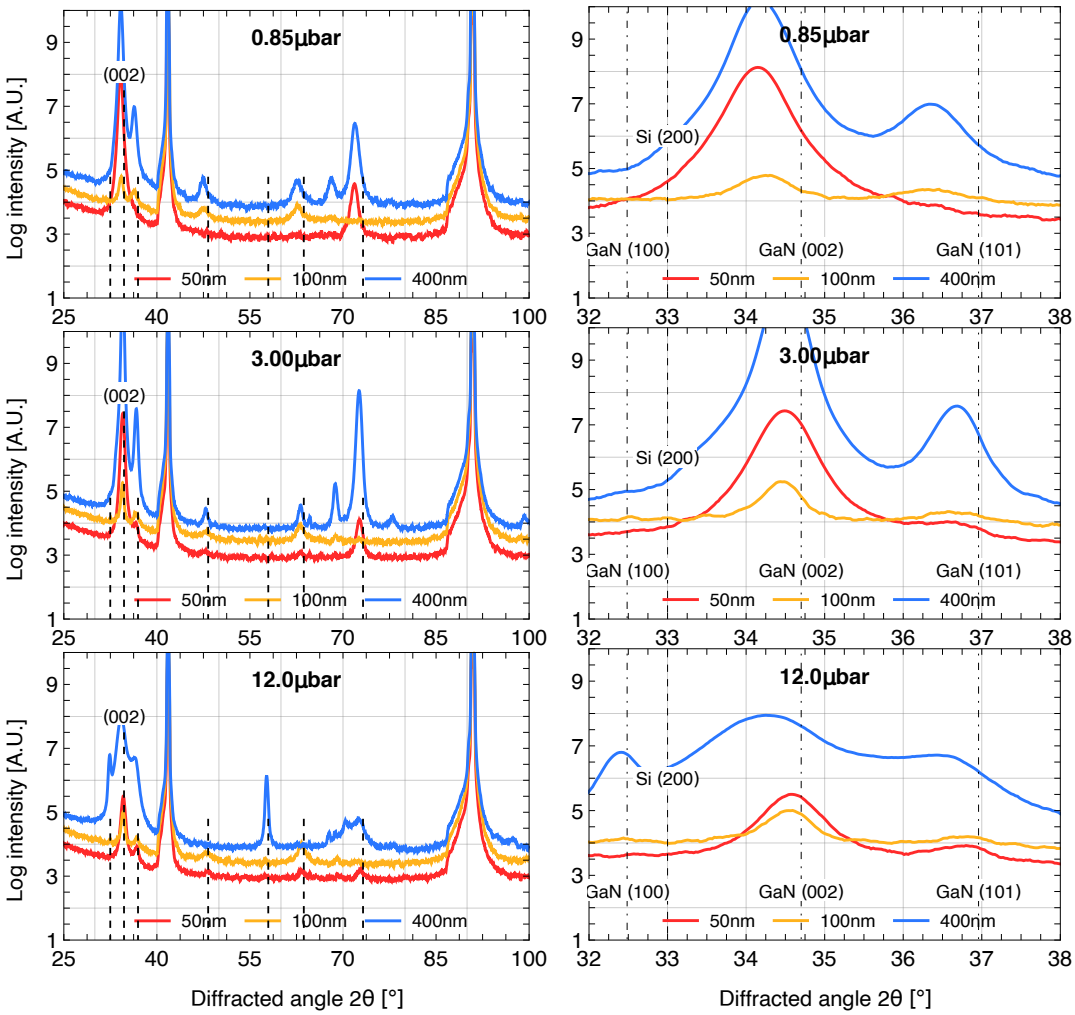


Figure B.26: PVD GaN, characteristics: XRD thickness and pressure variation on sapphire for a fixed deposition temperature (400 ± 2 °C).

hole and the electron architecture respectively (see figure 6.14 and related explanation). The cell performances are extracted from all those and presented in figure 6.15.

Table B.15: Ge-doped PVD GaN: optical and electrical parameters, a variation on the germanium power for layers deposited on glass. The deposition pressure is fixed at $Pr = 3.00 \pm 0.06\,\mu$bar and the annealing temperature at $T_A = 600 \pm 5\,°$C.

| $Po_{\mathrm{Ge}}$ ±0.1 [W] | Gas | g ±10 % [nm/min] | $E_{04}$ ±0.03 [eV] | $E_U$ ±4 [meV] | $\rho_0$ ±0.1 % [Ω cm] | $E_A$ ±0.1 % [meV] |
|---|---|---|---|---|---|---|
| 0 | $N_2$ | 2.28 | 3.05 | 240 | $6.1 \cdot 10^7$ | 560 |
| 5 | $N_2$ | 2.29 | 3.00 | 360 | $2.9 \cdot 10^1$ | 560 |
| 10 | $N_2$ | 2.48 | 3.01 | 410 | $6.1 \cdot 10^6$ | 560 |
| 15 | $N_2$ | 2.58 | 3.04 | 270 | $1.9 \cdot 10^6$ | 170 |
| | $N_2H_2$ | 2.49 | 2.94 | 420 | $3.6 \cdot 10^4$ | 330 |
| 20 | $N_2$ | 2.75 | 2.94 | 390 | $1.2 \cdot 10^2$ | 80 |
| | $N_2H_2$ | 2.54 | 2.92 | 380 | $2.1 \cdot 10^2$ | 150 |
| 25 | $N_2$ | 2.81 | 2.87 | 390 | $1.0 \cdot 10^1$ | 130 |
| | $N_2H_2$ | 2.74 | 2.89 | 390 | $5.9 \cdot 10^4$ | 340 |
| 30 | $N_2$ | 2.87 | 2.85 | 410 | $2.9 \cdot 10^2$ | 150 |
| | $N_2H_2$ | 2.83 | 2.95 | 400 | $5.4 \cdot 10^5$ | 430 |
| 35 | $N_2$ | 3.08 | 2.90 | 340 | - | - |
| | $N_2H_2$ | 2.94 | 2.98 | 350 | - | - |
| 40 | $N_2$ | 3.09 | 2.84 | 340 | - | - |
| 50 | $N_2$ | 3.52 | 2.97 | 310 | $1.9 \cdot 10^2$ | 490 |
| 75 | $N_2$ | 4.18 | 2.92 | 320 | - | 0 |
| 100 | $N_2$ | 5.13 | 3.05 | 260 | - | 0 |

Table B.16: Ge-doped PVD GaN: optical and electrical parameters, a variation on the germanium power for layers deposited on glass.

| $Po_{\mathrm{Ge}}$ ±0.1 [W] | $Pr$ ±2 % [$\mu$bar] | $T_A$ ±5 [°C] | Gas | g ±10 % [$nm/\mathrm{min}$] | $E_{04}$ ±0.03 [eV] | $E_U$ ±4 [meV] | $\rho_0$ ±0.1 % [Ω cm] | $E_A$ ±0.1 % [eV] |
|---|---|---|---|---|---|---|---|---|
| 20 | 3.00 | 25 | $N_2$ | 2.75 | 2.90 | 310 | $9.7 \cdot 10^4$ | 380 |
| | | | $N_2H_2$ | 2.55 | 3.00 | 310 | $3.4 \cdot 10^3$ | 270 |
| 20 | 3.00 | 300 | $N_2$ | 2.68 | 2.95 | 380 | $1.6 \cdot 10^4$ | 330 |
| | | | $N_2H_2$ | 2.57 | 3.00 | 330 | $1.3 \cdot 10^3$ | 230 |
| 20 | 3.00 | 450 | $N_2$ | 2.72 | 2.93 | 380 | $7.4 \cdot 10^3$ | 330 |
| | | | $N_2H_2$ | 2.55 | 2.98 | 300 | $1.6 \cdot 10^3$ | 230 |
| 20 | 3.00 | 600 | $N_2$ | 2.75 | 2.95 | 390 | $1.5 \cdot 10^2$ | 170 |
| | | | $N_2H_2$ | 2.54 | 2.92 | 390 | $9.6 \cdot 10^1$ | 150 |
| 20 | 3.00 | 750 | $N_2$ | 2.71 | - | - | $2.0 \cdot 10^2$ | 170 |
| | | | $N_2H_2$ | 2.55 | - | - | $4.0 \cdot 10^0$ | 80 |
| 20 | 1.50 | 600 | $N_2$ | 3.68 | 2.88 | 410 | $2.3 \cdot 10^0$ | 50 |
| 25 | 1.50 | 600 | $N_2$ | 3.78 | 2.86 | 370 | $6.5 \cdot 10^1$ | 150 |
| 30 | 1.50 | 600 | $N_2$ | 4.03 | 2.85 | 370 | $1.7 \cdot 10^1$ | 90 |
| 20 | 3.00 | 600 | $N_2$ | 2.75 | 2.95 | 390 | $1.3 \cdot 10^1$ | 80 |
| 25 | 3.00 | 600 | $N_2$ | 2.81 | 2.87 | 390 | $1.0 \cdot 10^2$ | 130 |
| 30 | 3.00 | 600 | $N_2$ | 2.87 | 2.85 | 410 | $2.9 \cdot 10^2$ | 150 |
| 20 | 12.0 | 600 | $N_2$ | 1.49 | 3.13 | 270 | $4.9 \cdot 10^5$ | 330 |
| 25 | 12.0 | 600 | $N_2$ | 1.46 | 3.07 | 310 | $2.2 \cdot 10^2$ | 100 |
| 30 | 12.0 | 600 | $N_2$ | 1.46 | 3.01 | 380 | $3.9 \cdot 10^3$ | 190 |

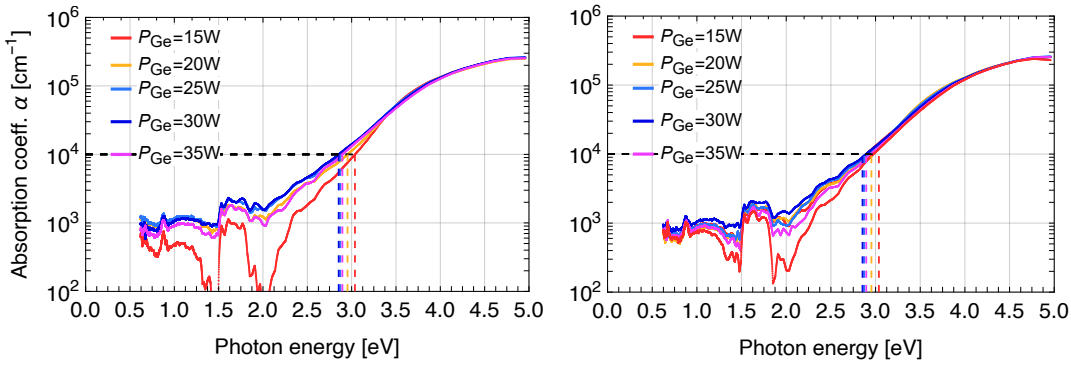


(a) Absorption coefficient for different doping concentrations given by germanium power. $P_{\mathrm{GaN}} = 150 \pm 0.1\,\mathrm{W}$, $T_A = 600 \pm 5\,°\mathrm{C}$, $p_d = 3.00 \pm 0.06\,\mu\mathrm{bar}$. The layers in the left figure were produced using an $N_2$ plasma, the ones in the right figure with a mix of $N_2$ and $H_2$ plasma.

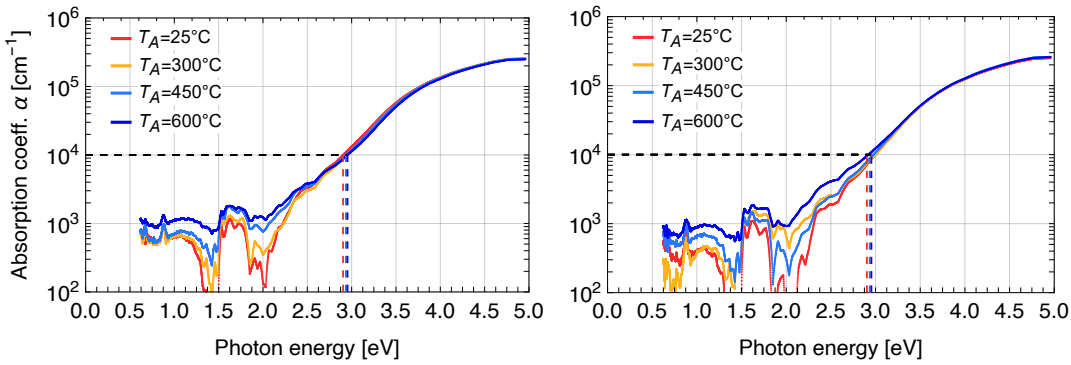


(b) Absorption coefficient for different annealing temperatures. $P_{\mathrm{GaN}} = 150 \pm 0.1\,\mathrm{W}$, $P_{\mathrm{Ge}} = 20 \pm 0.1\,\mathrm{W}$, $p_d = 3.00 \pm 0.06\,\mu\mathrm{bar}$. The layers in the left figure were produced using an $N_2$ plasma, the ones in the right figure with a mix of $N_2$ and $H_2$ plasma.

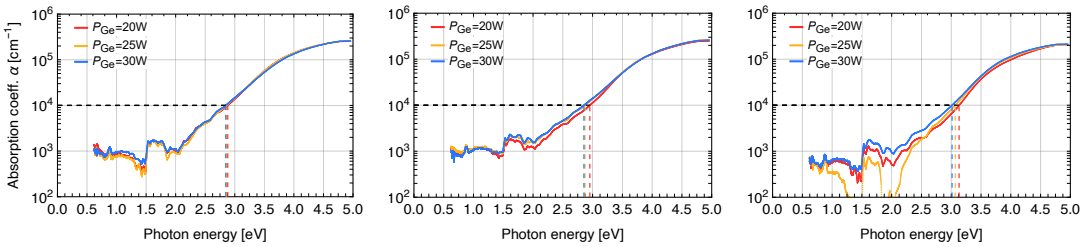


(c) Absorption coefficient for different deposition pressures, only with the $N_2$ plasma. $P_{\mathrm{GaN}} = 150 \pm 0.1\,\mathrm{W}$, $T_A = 600 \pm 5\,°\mathrm{C}$.

Figure B.27: Ge-doped PVD GaN: absorption coefficients for layers deposited on glass.

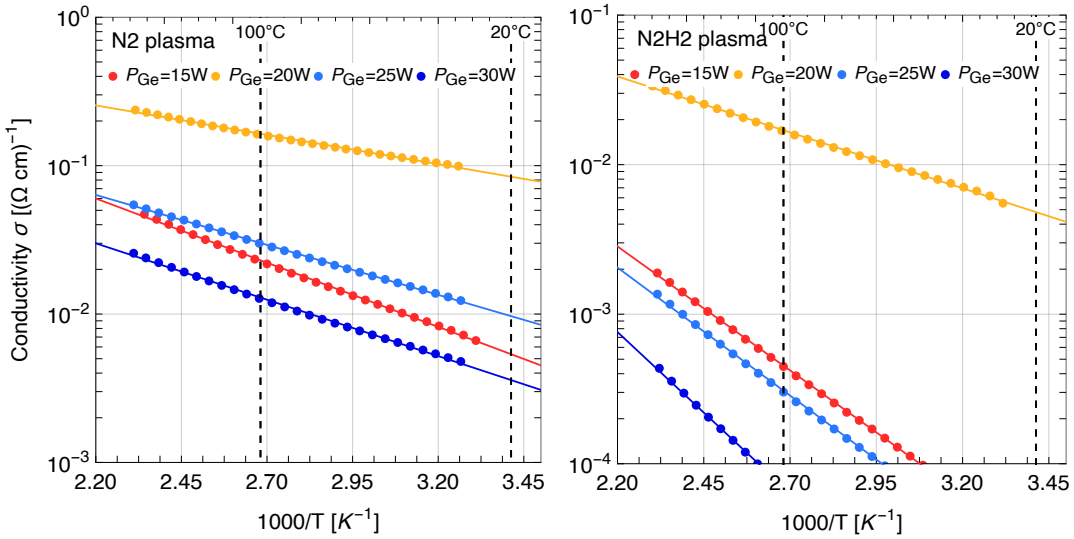


(a) Germanium content variation for a constant $P_{GaN} = 150 \pm 0.1$ W, substrate temperature $T = 200 \pm 2$ °C, deposition pressure $3.00 \pm 0.06\,\mu$bar, annealing temperature $T_A = 600 \pm 5$ °C. The etching gas is either only $N_2$ (left) or a mix of $N_2$ and $H_2$ (right).

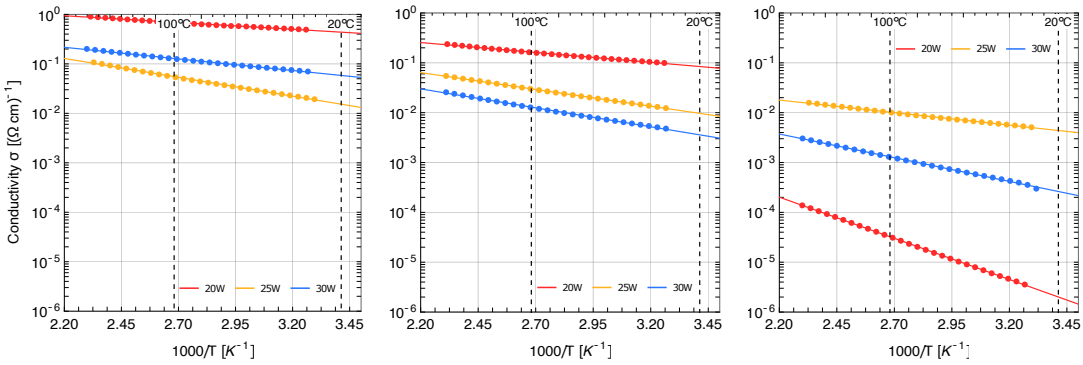


(b) Deposition pressure variation for constant $P_{GaN} = 150 \pm 0.1$ W, $P_{Ge} = 20 - 30 \pm 0.1$ W, substrate temperature $T = 200 \pm 2$ °C, annealing temperature $T_A = 600 \pm 5$ °C, using $N_2$ for etching.

Figure B.28: Ge-doped PVD GaN: Arrhenius plots for layers deposited on a silicon wafer.

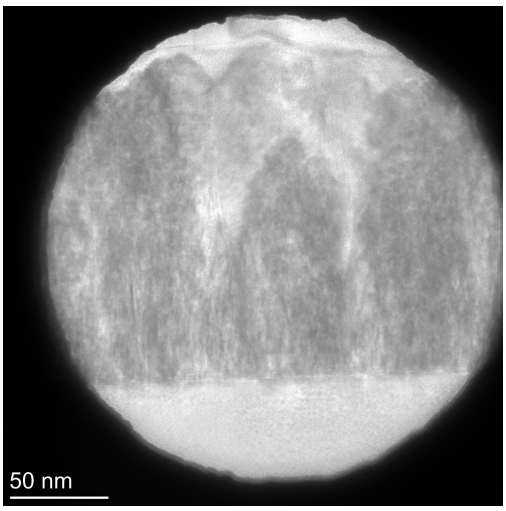


(a) TEM image of the probed area.

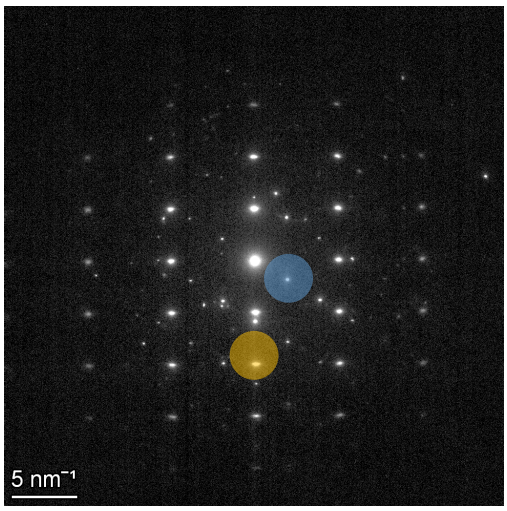


(b) Associated diffraction figure.

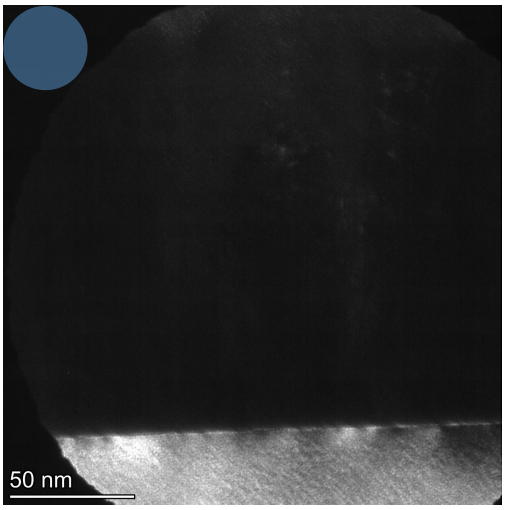


(c) DF of the sapphire substrate.

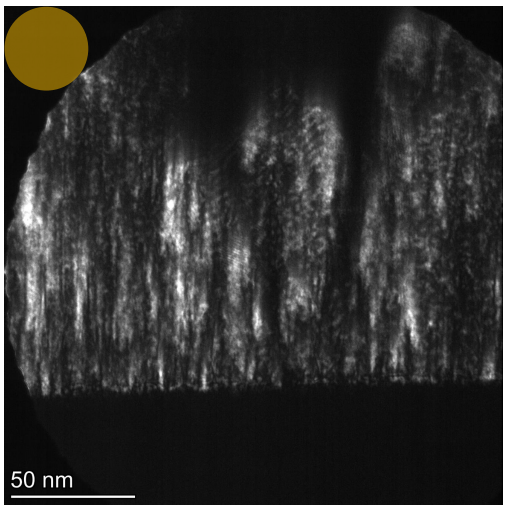


(d) DF of the GaN layer.

Figure B.29: PVD GaN(Si) on Sa, epitaxy: deeper TEM analysis of the undoped GaN layer, FIB-TEM lamella.

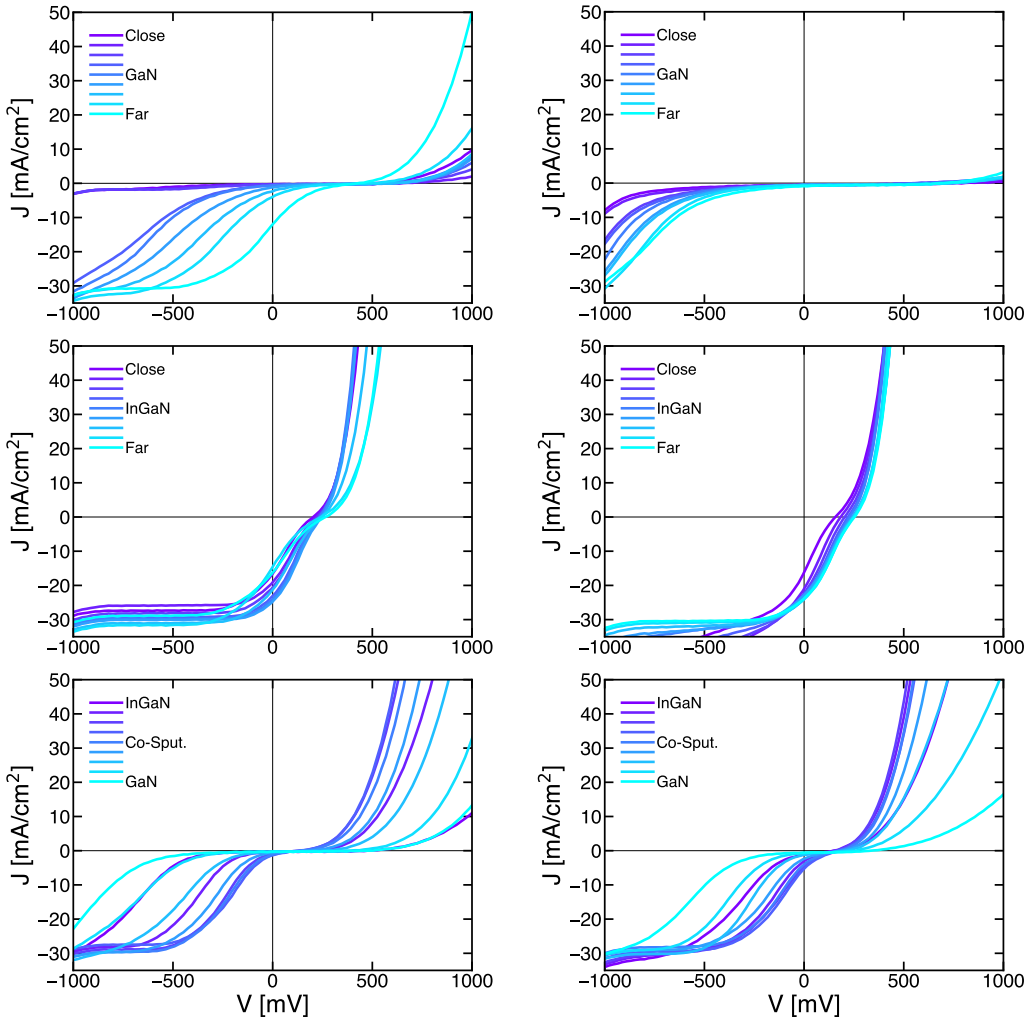


(a) Thin In/GaN layer.

(b) Thick In/GaN layer.

Figure B.30: InGaN PVD contact: J-V curves for the hole architecture (see figure 6.14b). The sample holder was not rotating, allowing a gradient of the sputtered material: close or far from the target mentioned in the figure. For the co-sputtering setup, the curve's colour indicates how close the cell is to one or the other targets.

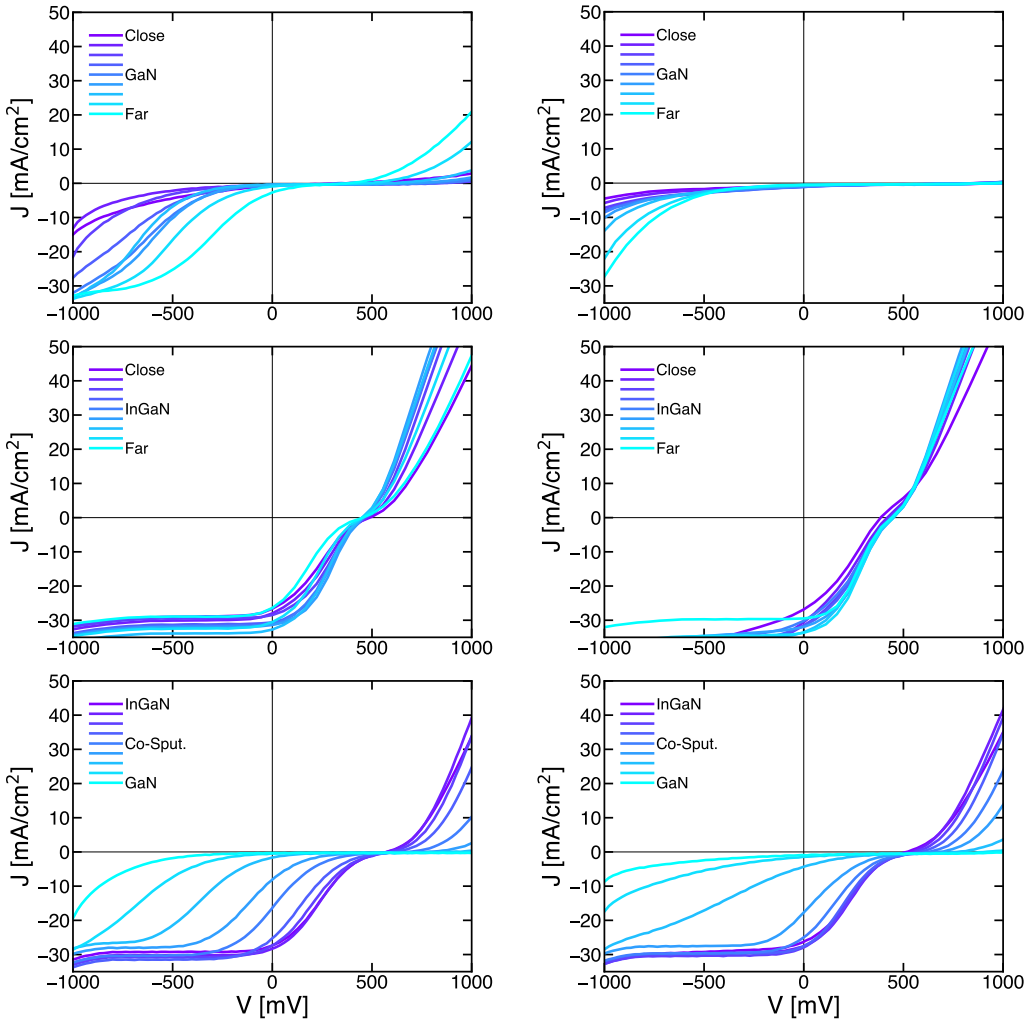


(a) Thin In/GaN layer.

(b) Thick In/GaN layer.

Figure B.31: InGaN PVD contact: J-V curves for the electron architecture (see figure 6.14a). The sample holder was not rotating, allowing a gradient of the sputtered material: close or far from the target mentioned in the figure. For the co-sputtering setup, the curve's colour indicates how close the cell is to one or the other targets.

# C Other noteworthy results

## C.1 A-Si:H contacts

In chapters 4 & 5, we understood that low-$T$ InGaN layers still need more research and development, even for only a contact. However, System B allowed for deposition temperatures, potentially useful for crystalline silicon solar cells with tunnel oxide passivated contact (TOPCON). In PV-lab, these are generally manufactured by depositing in-situ doped layers of a-$SiC_x$ with low carbon content at temperatures around 200 – 250 °C. Subsequently, they are annealed at temperatures between 800 – 900 °C. This annealing step crystallises the layers and activates the dopants. After annealing, dangling bonds at the Si-$SiO_x$ interface are passivated by hydrogenation. Typically, this is achieved by deposing a layer of $SiN_x$:H and a second anneal to release hydrogen. It would be a significant simplification if combined into a single annealing step. However, the outflow of hydrogen in the as-deposited a-$SiC_x$ layer makes the stack prone to delamination, often called blistering. To reduce the hydrogen content of the doped a-$SiC_x$ layers, a deposition process at 400 °C was investigated. For a visual understanding, please refer to figure C.1.

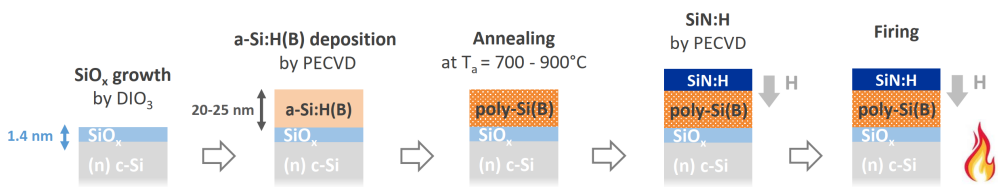


Figure C.1: A-Si:H PECVD contact: Fabrication process of *in situ* doped poly-Si(B) contact. If the second step is executed at a high enough temperature, the hydrogen content could be low enough; hence the third step may be skipped.

### C.1.1 A-Si:H at 400 °C: optimization

Producing an a-Si:H layer at 400 °C with System B proved difficult because of a stronger blistering effect at higher temperatures. The process could be stabilised by adding some

carbon, using methane as a precursor during the deposition. The deposition parameters for the final baseline are shown in the following table:

| Precursors [sccm] | | | |
|---|---|---|---|
| $SiH_4$ | $H_2$ | Ar | $CH_4$ |
| $1.0 \pm 0.01$ | $80 \pm 0.6$ | $25 \pm 0.3$ | $0.50 - 0.75 \pm 0.04$ |

| Pressure [$\mu$bar] | Frequency [MHz] | Temperature [°C] | Power [W] | Time [min] |
|---|---|---|---|---|
| $800 \pm 2$ | $70 \pm 0$ | $400 \pm 2$ | $20 \pm 3$ | $10 - 12 \pm 1$ s |

At $400 \pm 2$ °C, this massive dilution of silane with hydrogen seemed necessary, decreasing the growth rate and increasing the deposition time. For production means, it may become necessary to use another precursor mix that quickens the deposition process and remains stable at such high temperatures. At this stage, with such a stabilised layer, it is already possible to have an idea about the hydrogen content levels when measuring the Si–H bond concentration by FTIR (see equation 3.7 page 35 and related development). In parallel, layer crystallinity was assessed by Raman analysis. These results are presented in figure C.2, where the hydrogen content decreases independently of the thickness (label of each point) with increasing temperature. There also seems to be an optimum temperature around 300 °C with respect to the Raman crystallinity.

Next, boron was added to obtain p-type films, and its effect was probed by different means, all presented in figure C.3 as a function of the TMB flow added to the precursor mix. The doping effect appears to be as expected:

- The thickness increases because more metallic precursors are deposited at a time than without the dopant (figure C.3a).
- The resistivity increases because before the second annealing, the dopants are not activated yet (figure C.3b).
- The activation energy decreases because the p-dopants push the Fermi level closer to the VB (figure C.3b again).
- And the $Si - H$ bond concentration decreases because some hydrogen atoms are captured by the dopant instead of the silicon atoms (figure C.3d).

However, some optimal conditions seem to appear in terms of Raman crystallinity before annealing (figure C.3c) and in terms of the FTIR peak position (figure C.3d). About the FTIR peak position and referring to table A.1, a signature close to 2000 $cm^{-1}$ corresponds to a high density of $Si - H$ bond concentration while a signature close to 2090 $cm^{-1}$ corresponds to a high density of $Si - H_2$ bond concentration. The former kind of bond is usually found within the layer (in the matrix of the amorphous material). At the same time, the latter is a bond that generally forms at the surface of voids or in porous materials, where the outer silicon

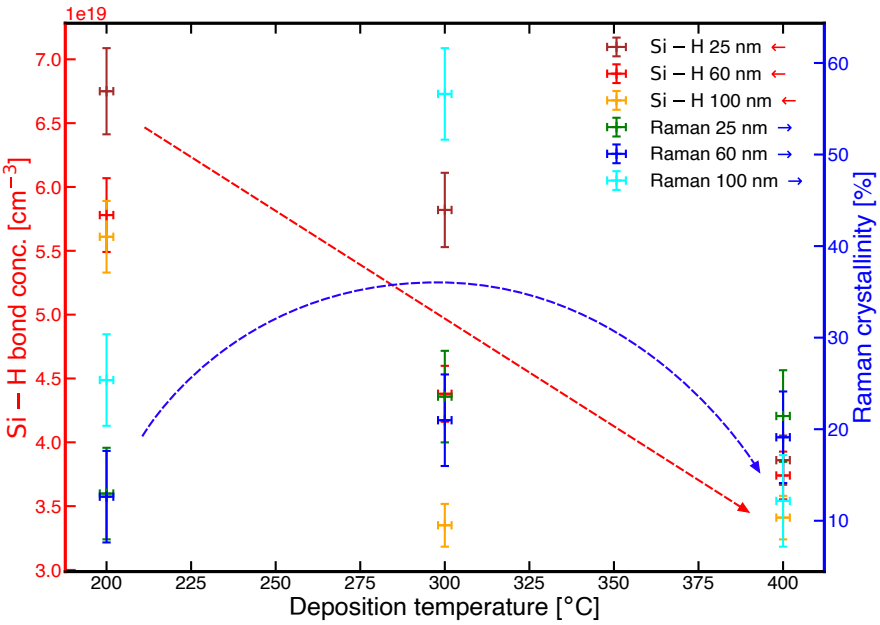


Figure C.2: A-Si:H PECVD contact: decrease of the hydrogen content with increasing temperature, and optimum Raman crystallinity around 300 °C for layers deposited on a silicon wafer. Dashed curves are added to help the reader's eye.

atoms have more dangling bonds that can be passivated by hydrogen. In other words, the peak observed in the FTIR spectrum around 2050 cm$^{-1}$ is a composition of these two signals, where its position is an indirect measure of a porous film structure. It is then obviously preferred to aim for a low porosity density, reflected by a peak position closer to 2000 cm$^{-1}$, found here for a TMB flow between 0.01 and 0.04 sccm. Regarding the Raman crystallinity, we can already see that a slow deposition of a-Si:H with a high dilution does not result in a completely amorphous layer (blue points in figure C.3c). The first annealing step ( corresponding to the third step in figure C.1) has a crystalization effect for low TMB flow (proved by the orange points in the same figure); if this annealing step is to be skipped, a higher Raman crystallinity of the "as deposited" layer is here prefered. The better Raman crystallinity before annealing is observed for a TMB flow between 0.01 and 0.02 sccm. If the layer is then annealed, this optimum disappears, and the expected trend is observed again, where the concentration of dopant atoms will more or less hinder the crystallisation of the a-Si:H matrix.

Based on all these studies, optimal conditions include the addition of methane to the precursor mix to stabilise the layer deposited at 400 ± 2 °C, and a TMB flow of 0.02 ± 0.0004 sccm for the doping level. Before annealing, this corresponds to a layer resistivity of 0.26 ± 0 Ωcm and an activation energy of 405 ± 0.4 meV.

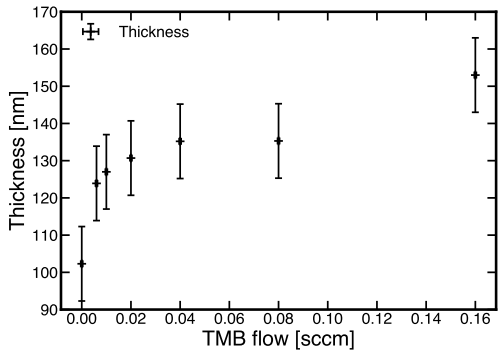


(a) Ellipsometry thickness for layers deposited on a glass wafer.

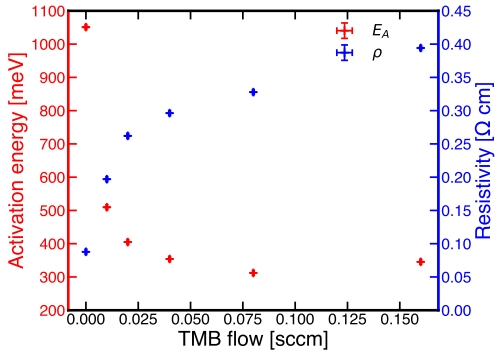


(b) Dark lateral conductivity for layers deposited on a silicon wafer.

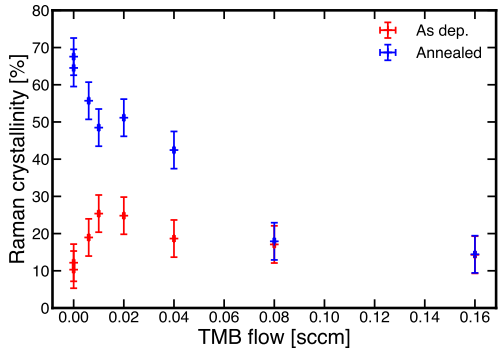


(c) Raman crystallinity for layers deposited on a silicon wafer.

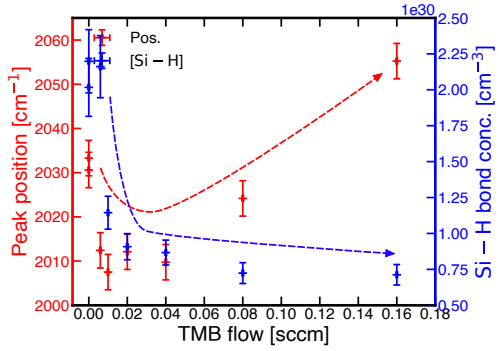


(d) FTIR results for layers deposited on a silicon wafer.

Figure C.3: A-Si:H PECVD contact: effect of the doping on the a-Si:H layer characteristics: thickness by ellipsometry, Raman crystallinity, resistivity, activation energy and Si – H bond concentration and type.

### C.1.2 Passivation & lifetime

As the objective of the a-Si:H layer deposited at 400 °C is to passivate the absorber; a full solar cell stack is not necessarily needed here for the evaluation, and a simple passivation test with the Sinton is enough to compare with a reference architecture (see section 3.2.4.5 for a reminder of the Sinton operation). See figure C.4 for the details of the architecture used to test the passivation. Since the plasmabox of System B is not large enough for a full 4" wafer, the depositions and measurements were only done on quarter wafers. Two references were also used: a quarter four-inch wafer and a full wafer, which were processed with the same architecture, but with another PECVD deposition system: the KAI-M PECVD reactor. The passivation results are presented in table C.1, where the following codes are used:

- The SiC layer was deposited on both sides of the silicon wafer either in System B at 400 ± 2 °C, or at 200 ± 2 °C in the KAI-M PECVD reactor for the reference layers.
- The first annealing was performed either in the dirty UTP 1100 oven or in the clean RTP jetfirst 200 oven.

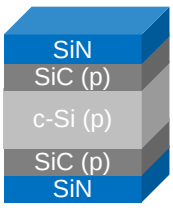


Figure C.4: A-Si:H PECVD contact: Architecture used to test the passivating capability of the a-Si:H layer deposited at $400 \pm 2\,°C$ in the System B.

- The SiN layer was deposited on both sides of the substrate either in the XL PECVD system of PV-lab or with the help of Meyer Burger, using their standard recipe for SiN.
- The second annealing was performed either with a hotplate (30 min ±5 s at $450 \pm 5\,°C$) or in the CAMINI firing furnace.

Table C.1: A-Si:H PECVD contact at 400 °C: passivation results for the architecture presented in figure C.4.

| N° | SiC | Anneal | SiN | Anneal | Lifetime [$\mu$s] | $iV_{OC}$ [mV] |
|---|---|---|---|---|---|---|
| 1 | SysB | UTP | M-B | Camini | $2.86 \pm 0.03$ | $558 \pm 6$ |
| 2 | SysB | - | M-B | Camini | $1.07 \pm 0.02$ | $528 \pm 6$ |
| 3 | SysB | UTP | XL | Hotplate | $1.79 \pm 0.02$ | $531 \pm 6$ |
| 4 | SysB | - | XL | Hotplate | $1.98 \pm 0.02$ | $549 \pm 6$ |
| 1/4 ref. | 200 °C KAI | RTP | XL | Hotplate | $105 \pm 2$ | $657 \pm 7$ |
| Full ref. | 200 °C KAI | RTP | M-B | Camini | $526 \pm 6$ | $702 \pm 8$ |

As presented in table C.1, the obtained passivation is here extremely bad for the layers deposited in System B. Sadly, because of a lack of time, the layers could not be developed further: only an analysis of these poor results may give some clue for an outlook and possible next exploration steps. Blisters did develop during the second annealing when the first one was not performed (layers 2 and 4), meaning that although increasing the deposition temperature did reduce the hydrogen content of the SiC layer, there was still too much of it to avoid the first annealing. Curing of the SiC layer was also tried, where after the deposition on one side, the wafer was left in the vacuum of System B, close to the 400 °C heating bodies for 2 h and 14 h and probed for Si – H content by FTIR. The curing did decrease the hydrogen content of the layer, but not sufficiently to prevent blistering at a later step. Finally, comparing layer 1 with the complete reference or layer 3 with the quarter reference, we can conclude that the most probable source of the problem is System B. Indeed, the intrinsic wafer's passivation is, in fact, wholly killed when the SiC layers are deposited, resulting in such insufficient lifetimes. This may come from either one of the deposition parameters (maybe the argon that damages the wafer at the beginning of the deposition?) or because, despite thorough cleaning, System B remained dirty, and the silicon was contaminated. Indeed, the lifetime of the four tested recipes is so bad that comparing them is not worth comparing. Another potential problem could be using a "dirty" oven, which could contaminate the device during the annealing. However, comparing the two reference recipes, we can conclude that cleaving the wafer may also contribute to this decrease in passivation or at least damages the substrate. This is, however, a strange result in itself, given its lifetime and the drift velocity of charge carriers in silicon

($\sim 1300\,\frac{\mathrm{cm}^2}{\mathrm{Vs}}$ for electrons at room temperature and at low carrier concentration [86, 106]), the electrons should be able to travel for a few millimetres before recombination. The plasmabox of System B is a $8 \times 8$ square space and only allowed for quarter wafers, but these are still far larger than the potential travelling distance; therefore, cleaving the wafer was not expected to decrease the lifetime that much. The last possible source of these bad results may be a lousy manipulation or damage induced by the cleavage.

### C.1.3 A-Si:H contacts: key takeaways & next steps

After the InGaN contacts developed and presented in previous chapters, System B's high deposition temperature was used to deposit passivating amorphous silicon layers in the hope of skipping the following annealing step before the SiN layer. The stabilisation of such a deposition required using methane as an additional precursor, and the p-doping level was probed and optimised by different means (refer to figure C.3 for more details). The passivation was then tested, but the results were not conclusive and different clues as to why were presented.

The main results and outlooks are that even though a stable a-Si:H layer can be deposited at 400 °C, its hydrogen content is still too high for the subsequent annealing steps, producing blisters and bubbling. It may be possible to increase the temperature further to reach low enough hydrogen content during the deposition directly, but that remains to be tested. It is also concluded that System B is too dirty for this kind of process (certainly some leftovers of all the In/GaN depositions), and a more successful result may be achieved in a cleaner PECVD deposition system.

# Bibliography


[1] Daisuke Adachi, José Luis Hernández, and Kenji Yamamoto. "Impact of carrier recombination on fill factor for large area heterojunction crystalline silicon solar cell with 25.1% efficiency". In: *Applied Physics Letters* 107.23 (2015), pp. 22–25. ISSN: 00036951. DOI: 10.1063/1.4937224. URL: http://dx.doi.org/10.1063/1.4937224.

[2] Sadao Adachi. "Cubic Gallium Nitride ($\beta$-GaN)". In: *Optical Constants of Crystalline and Amorphous Semiconductors: Numerical Data and Graphical Information*. Boston, MA: Springer US, 1999, pp. 188–197. ISBN: 978-1-4615-5247-5. DOI: 10.1007/978-1-4615-5247-5_20. URL: https://doi.org/10.1007/978-1-4615-5247-5_20.

[3] Joel W. Ager et al. "Electrical properties of InGaN-Si heterojunctions". In: *Physica Status Solidi (C) Current Topics in Solid State Physics* 6.SUPPL. 2 (2009), pp. 413–416. ISSN: 18626351. DOI: 10.1002/pssc.200880967.

[4] Joel W. Ager III et al. "Group III-nitride alloys as photovoltaic materials". In: *Fourth International Conference on Solid State Lighting* 5530.June 2014 (2004), p. 308. ISSN: 0277786X. DOI: 10.1117/12.561935.

[5] Björn Agnarsson. "Surface studies on $\alpha$–sapphire for potential use in GaN epitaxial growth". PhD thesis. KTH, 2009. ISBN: 9789174152869.

[6] Bouzid Ait-Amir, Philippe Pougnet, and Abdelkhalak El Hami. "Meta-Model Development". In: *Embedded Mechatronic Systems 2*. Elsevier, 2015, pp. 151–179. ISBN: 9781785480140. DOI: 10.1016/B978-1-78548-014-0.50006-2. URL: https://linkinghub.elsevier.com/retrieve/pii/B9781785480140500062.

[7] M. Anani et al. "InxGa1-xN refractive index calculations". In: *Microelectronics Journal* 38.2 SPEC. ISS. (2007), pp. 262–266. ISSN: 00262692. DOI: 10.1016/j.mejo.2006.11.001.

[8] André Anders. "A structure zone diagram including plasma-based deposition and ion etching". In: *Thin Solid Films* 518.15 (2010), pp. 4087–4090. ISSN: 00406090. DOI: 10.1016/j.tsf.2009.10.145. URL: http://dx.doi.org/10.1016/j.tsf.2009.10.145.

[9] Lucio Claudio Andreani et al. "Silicon solar cells: Toward the efficiency limits". In: *Advances in Physics: X* 4.1 (2019). ISSN: 23746149. DOI: 10.1080/23746149.2018.1548305. URL: https://doi.org/10.1080/23746149.2018.1548305.

[10] Luca Massimiliano Antognini. "Contact Design for Silicon Heterojunction Solar Cells". PhD thesis. EPFL, 2022, p. 215. DOI: 10.5075/epfl-thesis-9477.

[11] Yasuaki Arakawa et al. "Electrical properties of Si-doped GaN prepared using pulsed sputtering". In: *Applied Physics Letters* 110.4 (2017). ISSN: 00036951. DOI: 10.1063/1.4975056. URL: http://dx.doi.org/10.1063/1.4975056.

[12] ASTM. "Standard Tables for Reference Solar Spectral Irradiances : Direct Normal and Hemispherical On 37° Tilted Surface". In: *Astm* 03.Reapproved (2013), pp. 1–21. DOI: 10.1520/G0173-03R12. URL: http://enterprise.astm.org/SUBSCRIPTION/filtrexx40.cgi?+REDLINE%7B%5C%%7D7B%7B%5C_%7D%7B%5C%%7D7DPAGES/G173.htm.

[13] Mani Azadmand et al. "Raman spectroscopy of epitaxial InGaN/Si in the central composition range". In: *Japanese Journal of Applied Physics* 58.SC (2019). ISSN: 13474065. DOI: 10.7567/1347-4065/ab0f1e.

[14] Christophe Ballif. "Fundamentals and processes for photovoltaic devices". University Lecture. 2019.

[15] J. Batey and E. Tierney. "Low-temperature deposition of high-quality silicon dioxide by plasma-enhanced chemical vapor deposition". In: *Journal of Applied Physics* 60.9 (1986), pp. 3136–3145. DOI: 10.1063/1.337726. eprint: https://doi.org/10.1063/1.337726. URL: https://doi.org/10.1063/1.337726.

[16] Sidney W. Benson. "Papers — III Bond Energies". In: *Journal of Chemical Education* 42.9 (1965), pp. 502–518.

[17] D. Bermejo and M. Cardona. "Raman Scattering in Pure and Hydrogenated Amorphous". In: *Journal of Non-Crystalline Solids* 32.I 979 (1978), pp. 405–419.

[18] Fabio Bernardini, Vincenzo Fiorentini, and David Vanderbilt. "Spontaneous polarization and piezoelectric constants of III-V nitrides". In: *Physical Review B - Condensed Matter and Materials Physics* 56.16 (1997), R10024–R10027. ISSN: 1550235X. DOI: 10.1103/PhysRevB.56.R10024. arXiv: 9705105 [cond-mat].

[19] R. P. Bhatta et al. "Surface structure, composition, and polarity of indium nitride grown by high-pressure chemical vapor deposition". In: *Applied Physics Letters* 88.12 (2006), pp. 2004–2007. ISSN: 00036951. DOI: 10.1063/1.2187513.

[20] Ashraful Ghani Bhuiyan et al. "InGaN solar cells: Present state of the art and important challenges". In: *IEEE Journal of Photovoltaics* 2.3 (2012), pp. 276–293. ISSN: 21563381. DOI: 10.1109/JPHOTOV.2012.2193384.

[21] A. Bittar et al. "Ion-assisted deposition of amorphous GaN: Raman and optical properties". In: *Applied Physics Letters* 78.5 (2001), pp. 619–621. ISSN: 00036951. DOI: 10.1063/1.1345800.

[22] Andrew W. Blakers et al. "22.8% Efficient Silicon Solar Cell". In: *Applied Physics Letters* 55.13 (1989), pp. 1363–1365. ISSN: 00036951. DOI: 10.1063/1.101596.

[23] George E P Box and Norman R Draper. *Empirical model-building and response surfaces.* Wiley series in probability and mathematical statistics. Oxford, England: John Wiley & Sons, 1987, pp. xiv, 669–xiv, 669. ISBN: 0-471-81033-9 (Hardcover).

[24] George E. P. Box and J. Stuart Hunter. "Multi-Factor Experimental Designs for Exploring Response Surfaces". In: *The Annals of Mathematical Statistics* 28.1 (1957), pp. 195–241. ISSN: 00034851. URL: http://www.jstor.org/stable/2237033 (visited on 05/20/2022).

[25] bp. "bp Statistical Review of World Energy 2021". In: *Statistical Review of World Energy* vol. 67 (2022), pp. 1–60. URL: bp.com/statisticalreview.

[26] M. S. Brandt et al. "Local vibrational modes in Mg-doped gallium nitride". In: *Physical Review B* 49.20 (1994), pp. 14758–14761. ISSN: 01631829. DOI: 10.1103/PhysRevB.49.14758.

[27] S. P. Bremner, M. Y. Levy, and C. B. Honsberg. "Analysis of tandem solar cell efficiencies under AM1.5G spectrum using a rapid flux calculation method". In: *Progress in Photovoltaics: Research and Applications* 16.3 (May 2008), pp. 225–233. ISSN: 10627995. DOI: 10.1002/pip.799. URL: https://www.mendeley.com/catalogue/analysis-tandem-solar-cell-efficiencies-under-am15g-spectrum-using-rapid-flux-calculation-method/%20http://doi.wiley.com/10.1002/pip.799.

[28] M. H. Brodsky, Manuel Cardona, and J. J. Cuomo. "Infrared and Raman spectra of the silicon-hydrogen bonds in amorphous silicon prepared by glow discharge and sputtering". In: *Physical Review B* 16.8 (1977), pp. 3556–3571. ISSN: 01631829. DOI: 10.1103/PhysRevB.16.3556.

[29] Ceyhun Bulutay, Cem Murat Turgut, and N. A. Zakhleniuk. "Carrier-induced refractive index change and optical absorption in wurtzite InN and GaN: Full-band approach". In: *Physical Review B - Condensed Matter and Materials Physics* 81.15 (2010), pp. 1–10. ISSN: 10980121. DOI: 10.1103/PhysRevB.81.155206. arXiv: 0911.2312.

[30] B. Cai and D. A. Drabold. "Ab initio models of amorphous InN". In: *Physical Review B - Condensed Matter and Materials Physics* 79.19 (2009), pp. 1–4. ISSN: 10980121. DOI: 10.1103/PhysRevB.79.195204.

[31] Marco Cantoni and Lucie Navratilova. "3D Electron Microscopy and FIB-Nanotomography". University Lecture. 2020.

[32] Marco Cantoni, Emadeddin Oveisi, and Lucie Navratilova. "Scanning electron microscopy techniques". University Lecture. 2019.

[33] Marco Cantoni et al. "scanning transmission microscopy (STEM) and analytical transmission electron microscopy (ATEM)". University Lecture. 2018.

[34] David M. Carey. "Measurement of the Raman spectrum of liquid water". In: *Journal of Chemical Physics* 108.7 (1998), pp. 2669–2675. ISSN: 00219606. DOI: 10.1063/1.475659.

[35] Uillian Mozart Ferreira Mata Cerqueira et al. "Doehlert design in the optimization of procedures aiming food analysis – A review". In: *Food Chemistry* 364.March (2021). ISSN: 18737072. DOI: 10.1016/j.foodchem.2021.130429.

[36] Handy Chandra et al. "Open-source automated mapping four-point probe". In: *Materials* 10.2 (2017), pp. 1–17. ISSN: 19961944. DOI: 10.3390/ma10020110.

[37] Daming Chen et al. "24.58% total area efficiency of screen-printed, large area industrial silicon solar cells with the tunnel oxide passivated contacts (i-TOPCon) design". In: *Solar Energy Materials and Solar Cells* 206.September 2019 (2020), pp. 1–8. ISSN: 09270248. DOI: 10.1016/j.solmat.2019.110258.

[38] P Chen et al. "Deposition and crystallization of amorphous GaN buffer layers on Si(111) substrates". In: *Journal of Crystal Growth* 213.1 (2000), pp. 27–32. ISSN: 0022-0248. DOI: https://doi.org/10.1016/S0022-0248(00)00248-7. URL: https://www.sciencedirect.com/science/article/pii/S0022024800002487.

[39] Christine Clark and Robert C Williges. *Response surface methodology design variants useful in human performance research*. Tech. rep. ILLINOIS UNIV AT URBANA-CHAMPAIGN SAVOY AVIATION RESEARCH LAB, 1971.

[40] Marvin L. Cohen and T. K. Bergstresser. "Band Structures and Pseudopotential Form Factors for Fourteen Semiconductors of the Diamond and Zinc-blende Structures". In: *Physical Review* 141.2 (Jan. 1966), pp. 789–796. ISSN: 0031-899X. DOI: 10.1103/PhysRev.141.789. URL: https://link.aps.org/doi/10.1103/PhysRev.141.789.

[41] Marvin L. Cohen and James R. Chelikowsky. "Wurtzite Structure Semiconductors". In: *Electronic Structure and Optical Properties of Semiconductors*. Berlin, Heidelberg: Springer Berlin Heidelberg, 1989, pp. 140–160. ISBN: 978-3-642-61338-8. DOI: 10.1007/978-3-642-61338-8_9. URL: https://doi.org/10.1007/978-3-642-61338-8_9.

[42] R. Dennis Cook. "Detection of Influential Observation in Linear Regression". In: *Technometrics* 19.1 (1977), pp. 15–18. ISSN: 15372723. DOI: 10.1080/00401706.1977.10489493.

[43] Aurora Costales, Anil K. Kandalam, and Ravindra Pandey. "Theoretical study of neutral and anionic group III nitride clusters: MnNn (M = Al, Ga, and In; n = 4-6)". In: *Journal of Physical Chemistry B* 107.19 (2003), pp. 4508–4514. ISSN: 15206106. DOI: 10.1021/jp022417s.

[44] Our World In Data. *Solar PV module prices vs. cumulative capacity*. 2020. URL: https://ourworldindata.org/grapher/solar-pv-prices-vs-cumulative-capacity (visited on 08/18/2022).

[45] S. Yu Davydov. "Estimates of the spontaneous polarization and permittivities of AlN, GaN, InN, and SiC crystals". In: *Physics of the Solid State* 51.6 (2009), pp. 1231–1235. ISSN: 10637834. DOI: 10.1134/S1063783409060249.

[46] Louis Albert De Broglie. "On the Theory of Quanta". In: *Quantum* 10.III (1987), p. 81. ISSN: 1941-5982. URL: http://puhep1.princeton.edu/%7B~%7Dmcdonald/examples/QM/debroglie%7B%5C_%7Dthesis%7B%5C_%7D24.pdf.

[47] Louis Albert De Broglie. " XXXV. A tentative theory of light quanta ". In: *The London, Edinburgh, and Dublin Philosophical Magazine and Journal of Science* 47.278 (1924), pp. 446–458. ISSN: 1941-5982. DOI: 10.1080/14786442408634378.

[48] Stefaan DeWolf et al. "High-efficiency silicon heterojunction solar cells: A review". In: *Green* 2.1 (2012), pp. 7–24. ISSN: 18698778. DOI: 10.1515/green-2011-0018.

[49] D. L. Dexter. "Absorption of light by atoms in solids". In: *Physical Review* 101.1 (1956), pp. 48–55. ISSN: 0031899X. DOI: 10.1103/PhysRev.101.48.

[50] Laura Ding et al. "Silicon minority-carrier lifetime degradation during molecular beam heteroepitaxial III-V material growth". In: *Energy Procedia* 92 (2016), pp. 617–623.

[51] C. Droz et al. "Relationship between Raman crystallinity and open-circuit voltage in microcrystalline silicon solar cells". In: *Solar Energy Materials and Solar Cells* 81.1 (2004), pp. 61–71. ISSN: 09270248. DOI: 10.1016/j.solmat.2003.07.004.

[52] Albert Einstein. "Concerning an heuristic point of view toward the emission and transformation of light". In: *American Journal of Physics* 33.5 (1965), p. 367. ISSN: 00029505. URL: http://skfiz.wdfiles.com/local--files/materialy/1905photon.pdf.

[53] Jonathan Emanuel Thomet et al. "Bandgap engineering of indium gallium nitride layers grown by plasma-enhanced chemical vapor deposition". In: *Journal of Vacuum Science & Technology A* 40.6 (2022), p. 063102. ISSN: 0734-2101. DOI: 10.1116/6.0002039.

[54] Stephanie Essig et al. "Raising the one-sun conversion efficiency of III-V/Si solar cells to 32.8% for two junctions and 35.9% for three junctions". In: *Nature Energy* 2.9 (2017). ISSN: 20587546. DOI: 10.1038/nenergy.2017.144.

[55] Chloe A.M. Fabien and W. Alan Doolittle. "Guidelines and limitations for the design of high-efficiency InGaN single-junction solar cells". In: *Solar Energy Materials and Solar Cells* 130 (2014), pp. 354–363. ISSN: 09270248. DOI: 10.1016/j.solmat.2014.07.018. URL: http://dx.doi.org/10.1016/j.solmat.2014.07.018.

[56] Lorenzo Fanni et al. "Increasing Polycrystalline Zinc Oxide Grain Size by Control of Film Preferential Orientation". In: *Crystal Growth and Design* 15.12 (2015), pp. 5886–5891. ISSN: 15287505. DOI: 10.1021/acs.cgd.5b01299.

[57] Davi Febba et al. "Effects of Work Function and Electron Affinity on the Performance of Carrier-Selective Contacts in Silicon Solar Cells Using ZnSnxGe1-xN2as a Case Study". In: *IEEE Journal of Photovoltaics* 11.6 (2021), pp. 1350–1357. ISSN: 21563403. DOI: 10.1109/JPHOTOV.2021.3109585.

[58] F Feldmann et al. "A passivated rear contact for high-efficiency n-type silicon solar cells enabling high Vocs and FF> 82%". In: *28th European PV solar energy conference and exhibition*. 2013.

[59] Z. C. Feng et al. "Raman scattering properties of GaN thin films grown on sapphire under visible and ultraviolet excitation". In: *Journal of Raman Spectroscopy* 32.10 (2001), pp. 840–846. ISSN: 03770486. DOI: 10.1002/jrs.765.

[60] Angela N. Fioretti et al. "Gallium Nitride as Transparent Electron-Selective Contact in Silicon Heterojunction Solar Cells". In: *Conference Record of the IEEE Photovoltaic Specialists Conference* (2019), pp. 2608–2612. ISSN: 01608371. DOI: 10.1109/PVSC40753.2019.8980621.

[61] S. Fritze et al. "High Si and Ge n-type doping of GaN doping - Limits and impact on stress". In: *Applied Physics Letters* 100.12 (2012). ISSN: 00036951. DOI: 10.1063/1.3695172.

[62] Jean-Marie Fuerbringer. "Design of Experiment (a) - Fall semester". University Lecture. 2020.

[63] Norifumi Fujimura et al. "Control of preferred orientation for ZnO films: control of self-texture". In: *Journal of Crystal Growth* 130.1-2 (May 1993), pp. 269–279. ISSN: 00220248. DOI: 10.1016/0022-0248(93)90861-P. URL: https://linkinghub.elsevier.com/retrieve/pii/002202489390861P.

[64] Hiroyuki Fujiwara. "Spectroscopic Ellipsometry: Principles and Applications". In: *Spectroscopic Ellipsometry: Principles and Applications* (2007), pp. 1–369. DOI: 10.1002/9780470060193.

[65] S. Gatz et al. "Thermal stability of amorphous silicon/silicon nitride stacks for passivating crystalline silicon solar cells". In: *Applied Physics Letters* 93.17 (2008), pp. 9–12. ISSN: 00036951. DOI: 10.1063/1.3009571.

[66] John F. Geisz et al. "Measurements of Six-Junction Concentrator Solar Cells". In: *Conference Record of the IEEE Photovoltaic Specialists Conference* 2 (2019), pp. 3415–3419. ISSN: 01608371. DOI: 10.1109/PVSC40753.2019.9198953.

[67] D. Ghosh et al. "Stress and Grain Boundary Properties of GaN Films Prepared by Pulsed Laser Deposition Technique". In: *ISRN Materials Science* 2014 (2014), pp. 1–10. DOI: 10.1155/2014/521701.

[68] George Glockler. "Estimated bond energies in Carbon, Nitrogen, Oxygen, and Hydrogen compounds". In: *The Journal of Chemical Physics* 19.1 (1951), pp. 124–125. ISSN: 00219606. DOI: 10.1063/1.1747958.

[69] D. M. Goldie and S. K. Persheyev. "Quantitative hydrogen measurements in PECVD and HWCVD a-Si:H using FTIR spectroscopy". In: *Journal of Materials Science* 41.16 (2006), pp. 5287–5291. ISSN: 00222461. DOI: 10.1007/s10853-006-0302-6.

[70] W. Götz et al. "Activation energies of Si donors in GaN". In: *Applied Physics Letters* 68.22 (1996), pp. 3144–3146. ISSN: 00036951. DOI: 10.1063/1.115805.

[71] Brendan Gunning et al. "Negligible carrier freeze-out facilitated by impurity band conduction in highly p-type GaN". In: *Applied Physics Letters* 101.8 (2012). ISSN: 00036951. DOI: 10.1063/1.4747466.

[72] E. H. Hall. "On a New Action of the Magnet on Electric Currents". In: *American Journal of Mathematics* 2.3 (Sept. 1879), p. 287. ISSN: 00029327. DOI: 10.2307/2369245. URL: https://www.jstor.org/stable/2369245?origin=crossref.

[73] Max Roser Hannah Ritchie and Pablo Rosado. "Energy". In: *Our World in Data* (2020). https://ourworldindata.org/energy.

[74] Hiroshi Harima. "Properties of GaN and related compounds studied by means of Raman scattering". In: *Journal of Physics Condensed Matter* 14.38 (2002). ISSN: 09538984. DOI: 10.1088/0953-8984/14/38/201.

[75] Jan Haschke et al. "Annealing of Silicon Heterojunction Solar Cells: Interplay of Solar Cell and Indium Tin Oxide Properties". In: *IEEE Journal of Photovoltaics* 9.5 (2019), pp. 1202–1207. ISSN: 21563403. DOI: 10.1109/JPHOTOV.2019.2924389.

[76] S. Hasegawa et al. "Analysis of SiH and SiN vibrational absorption in amorphous SiNx:H films in terms of a charge-transfer model". In: *Physical Review B* 48.8 (1993), pp. 5315–5325. ISSN: 01631829. DOI: 10.1103/PhysRevB.48.5315.

[77] Klaus Hinkelmann. *Design and Analysis of Experiments*. Ed. by Klaus Hinkelmann. Vol. 3. Wiley Series in Probability and Statistics. Hoboken, NJ, USA: John Wiley & Sons, Inc., Jan. 2012, pp. 1–566. ISBN: 9781118147634. DOI: 10.1002/9781118147634. URL: http://doi.wiley.com/10.1002/9781118147634.

[78] Kelsey A. Horowitz et al. "A Techno-Economic Analysis and Cost Reduction Roadmap for III-V Solar Cells". In: *National Renewable Energy Laboratory* November (2018), pp. 1–35. URL: https://www.nrel.gov/docs/fy19osti/72103.pdf.%7B%5C%%7D0Ahttp://www.osti.gov/servlets/purl/1484349/%7B%5C%%7D0Ahttp://www.osti.gov/servlets/purl/1484349/%7B%5C%%7D0Ahttps://www.nrel.gov/docs/fy19osti/72103.pdf.%7B%5C%%7D0Ahttp://www.osti.gov/servlets/purl/1484349/.

[79] L. Hsu and W. Walukiewicz. "Modeling of InGaN/Si tandem solar cells". In: *Journal of Applied Physics* 104.2 (2008). ISSN: 00218979. DOI: 10.1063/1.2952031.

[80] L. Hsu et al. "Electron mobility in InN and III-N alloys". In: *Journal of Applied Physics* 102.7 (2007). ISSN: 00218979. DOI: 10.1063/1.2785005.

[81] J. Humlíček et al. "Ellipsometry and transport studies of thin-film metal nitrides". In: *Thin Solid Films* 332.1-2 (1998), pp. 25–29. ISSN: 00406090. DOI: 10.1016/S0040-6090(98)01014-1.

[82] I. H. Hutchinson. *Principles of Plasma Diagnostics*. Second edition. Massachusetts Institute of Technology, Cambridge, Massachusetts, USA: Cambridge University Press, July 2002, p. 440. ISBN: 9780521803892. DOI: 10.1017/CBO9780511613630. URL: https://www.cambridge.org/core/product/identifier/9780511613630/type/book.

[83] International Energy Agency IEA. "Electricity Market Report". In: *Electricity Market Report* July (2022). URL: https://www.iea.org/reports/electricity-market-report-january-2022.

[84] S. Ito et al. "Resonant Raman and FTIR spectra of carbon doped GaN". In: *Journal of Crystal Growth* 414 (2015), pp. 56–61. ISSN: 00220248. DOI: 10.1016/j.jcrysgro.2014.11.024. URL: http://dx.doi.org/10.1016/j.jcrysgro.2014.11.024.

[85] Teresa Iwasita and Elena Pastor. "A dems and FTir spectroscopic investigation of adsorbed ethanol on polycrystalline platinum". In: *Electrochimica Acta* 39.4 (1994), pp. 531–537. ISSN: 00134686. DOI: 10.1016/0013-4686(94)80097-9.

[86] C. Jacoboni et al. "A review of some charge transport properties of silicon". In: *Solid State Electronics* 20.2 (1977), pp. 77–89. ISSN: 00381101. DOI: 10.1016/0038-1101(77)90054-5.

[87] A. M. Jeffries et al. "Gallium nitride grown by molecular beam epitaxy at low temperatures". In: *Thin Solid Films* 642 (2017), pp. 25–30. ISSN: 00406090. DOI: 10.1016/j.tsf.2017.07.066. URL: https://doi.org/10.1016/j.tsf.2017.07.066.

[88] I. Jonak-Auer, R. Meisels, and F. Kuchar. "Determination of the hydrogen concentration of silicon nitride layers by Fourier transform infrared spectroscopy". In: *Infrared Physics and Technology* 38.4 (1997), pp. 223–226. ISSN: 13504495. DOI: 10.1016/S1350-4495(97)00011-X.

[89] Norbert Kaiser. "Review of the fundamentals of thin-film growth". In: *Applied Optics* 41.16 (June 2002), p. 3053. ISSN: 0003-6935. DOI: 10.1364/AO.41.003053. URL: https://opg.optica.org/abstract.cfm?URI=ao-41-16-3053.

[90] Tsutomu Kaneko et al. "FTIR analysis of a-SiC:H films grown by plasma enhanced CVD". In: *Journal of Crystal Growth* 275.1-2 (2005), pp. 1097–1101. ISSN: 00220248. DOI: 10.1016/j.jcrysgro.2004.11.128.

[91] S. A. Kazazis et al. "Optical properties of InGaN thin films in the entire composition range". In: *Journal of Applied Physics* 123.12 (2018). ISSN: 10897550. DOI: 10.1063/1.5020988. URL: http://dx.doi.org/10.1063/1.5020988.

[92] S. S. Khludkov, I. A. Prudaev, and O. P. Tolbanov. "Physical properties of indium nitride, impurities, and defects". In: *Russian Physics Journal* 56.9 (2014), pp. 997–1006. ISSN: 15739228. DOI: 10.1007/s11182-014-0131-z.

[93] Jebreel M. Khoshman and Martin E. Kordesch. "Optical absorption in amorphous InN thin films". In: *Journal of Non-Crystalline Solids* 352.52-54 (2006), pp. 5572–5577. ISSN: 00223093. DOI: 10.1016/j.jnoncrysol.2006.09.011.

[94] Jan Kirenz. *Linear regression diagnostics in Python*. 2021. URL: https://www.kirenz.com/post/2021-11-14-linear-regression-diagnostics-in-python/linear-regression-diagnostics-in-python/ (visited on 12/06/2022).

[95] E. C. Knox-Davies et al. "Improved optical and electrical properties of low-temperature sputtered GaN by hydrogenation". In: *Journal of Applied Physics* 99.3 (2006). ISSN: 00218979. DOI: 10.1063/1.2171780.

[96] A. G. Kontos et al. "Micro-Raman characterization of InxGa1-xN/GaN/Al2O3 heterostructures". In: *Physical Review B - Condensed Matter and Materials Physics* 72.15 (2005), pp. 1–10. ISSN: 10980121. DOI: 10.1103/PhysRevB.72.155336.

[97] Sarah Kurtz et al. "A comparison of theoretical efficiencies of multi-junction concentrator solar cells". In: *Progress in Photovoltaics: Research and Applications* 16.6 (Sept. 2008), pp. 537–546. ISSN: 10627995. DOI: 10.1002/pip.830. URL: https://onlinelibrary.wiley.com/doi/10.1002/pip.830.

[98] Thomas LaGrange, Duncan Alexander, and Danièle Laub. "Transmission electron microscopy and diffraction". University Lecture. 2019.

[99] M.D. Lammert and R.J. Schwartz. "The interdigitated back contact solar cell: A silicon solar cell for use in concentrated sunlight". In: *IEEE Transactions on Electron Devices* 24.4 (Apr. 1977), pp. 337–342. ISSN: 0018-9383. DOI: 10.1109/T-ED.1977.18738. URL: http://ieeexplore.ieee.org/document/1478930/.

[100] M. Ledinský et al. "Crystallinity of the mixed phase silicon thin films by Raman spectroscopy". In: *Journal of Non-Crystalline Solids* 354.19-25 (2008), pp. 2253–2257. ISSN: 00223093. DOI: 10.1016/j.jnoncrysol.2007.09.073.

[101] Czang-Ho Lee, Andrei Sazonov, and Arokia Nathan. "High-mobility nanocrystalline silicon thin-film transistors fabricated by plasma-enhanced chemical vapor deposition". In: *Applied Physics Letters* 86.22 (2005), p. 222106. DOI: 10.1063/1.1942641. eprint: https://doi.org/10.1063/1.1942641. URL: https://doi.org/10.1063/1.1942641.

[102] M. Leszczynski et al. "Lattice parameters of gallium nitride". In: *Applied Physics Letters* 69.1 (July 1996), pp. 73–75. ISSN: 00036951. DOI: 10.1063/1.118123. URL: http://aip.scitation.org/doi/10.1063/1.118123.

[103] M. Leszczynski et al. "Thermal expansion of gallium nitride". In: *Journal of Applied Physics* 76.8 (1994), pp. 4909–4911. ISSN: 00218979. DOI: 10.1063/1.357273.

[104] Andrea C. Levi and Miroslav Kotrla. "Theory and simulation of crystal growth". In: *Journal of Physics Condensed Matter* 9.2 (1997), pp. 299–344. ISSN: 09538984. DOI: 10.1088/0953-8984/9/2/001.

[105] S. X. Li et al. "Fermi-level stabilization energy in group III nitrides". In: *Physical Review B - Condensed Matter and Materials Physics* 71.16 (2005), pp. 1–4. ISSN: 10980121. DOI: 10.1103/PhysRevB.71.161201.

[106] Sheng S. Li and W. Robert Thurder. "The dopant density and temperature dependence of electron mobility and resistivity in n-type silicon". In: *Solid State Electronics* 20.7 (1977), pp. 609–616. ISSN: 00381101. DOI: 10.1016/0038-1101(77)90100-9.

[107] Alex Lidow et al. *GaN Transistors for Efficient Power Conversion: Second Edition*. Vol. 978-1118844762. 2014, pp. 1–250. ISBN: 9781118844779. DOI: 10.1002/9781118844779.

[108] Hsiang Lin Liu et al. "Infrared and Raman-scattering studies in single-crystalline GaN nanowires". In: *Chemical Physics Letters* 345.3-4 (2001), pp. 245–251. ISSN: 00092614. DOI: 10.1016/S0009-2614(01)00858-2.

[109] G. Livadiotis. "Collision frequency and mean free path for plasmas described by kappa distributions". In: *AIP Advances* 9.10 (2019). ISSN: 21583226. DOI: 10.1063/1.5125714. URL: https://doi.org/10.1063/1.5125714.

[110] Junqing Lu and Chan Gyu Lee. "Numerical estimates for energy of sputtered target atoms and reflected Ar neutrals in sputter processes". In: *Vacuum* 86.8 (2012), pp. 1134–1140. ISSN: 0042207X. DOI: 10.1016/j.vacuum.2011.10.018. URL: http://dx.doi.org/10.1016/j.vacuum.2011.10.018.

[111] R. G. Mani and K. von Klitzing. "Hall effect under null current conditions". In: *Applied Physics Letters* 64.10 (Mar. 1994), pp. 1262–1264. ISSN: 0003-6951. DOI: 10.1063/1.110859. URL: http://aip.scitation.org/doi/10.1063/1.110859.

[112] B. Marler. "On the Relationship between Refractive Index and Density for SiO2-polymorphs". In: *Physics and Chemistry of Minerals* 16.3 (1988), pp. 286–290. ISSN: 03421791. DOI: 10.1007/BF00220696.

[113] Toshiro Maruyama and Hidetomo Miyake. "Gallium nitride thin films deposited by radio-frequency magnetron sputtering". In: *Journal of Vacuum Science & Technology A: Vacuum, Surfaces, and Films* 24.4 (2006), pp. 1096–1099. ISSN: 0734-2101. DOI: 10.1116/1.2208988.

[114] NA El-Masry et al. "Phase separation in InGaN grown by metalorganic chemical vapor deposition". In: *Applied physics letters* 72.1 (1998), pp. 40–42.

[115] Keiichiro Masuko et al. "Achievement of more than 25% conversion efficiency with crystalline silicon heterojunction solar cell". In: *IEEE Journal of Photovoltaics* 4.6 (2014), pp. 1433–1435. ISSN: 21563381. DOI: 10.1109/JPHOTOV.2014.2352151.

[116] Augustin McEvoy, Luis Castaner, and Tom Markvart. *Solar Cells Materials, Manufacture and Operation*. 2nd. Academic Press, 2012, p. 640. ISBN: 978-0123869647. DOI: 10.1016/C2011-0-07789-X.

[117] F. Meillaud et al. "Efficiency limits for single-junction and tandem solar cells". In: *Solar Energy Materials and Solar Cells* 90.18-19 (2006), pp. 2952–2959. ISSN: 09270248. DOI: 10.1016/j.solmat.2006.06.002.

[118] Marius Millot et al. "Determination of effective mass in InN by high-field oscillatory magnetoabsorption spectroscopy". In: *Physical Review B - Condensed Matter and Materials Physics* 83.12 (2011), pp. 1–5. ISSN: 10980121. DOI: 10.1103/PhysRevB.83.125204.

[119] M. A.R. Miranda and J. M. Sasaki. "The limit of application of the Scherrer equation". In: *Acta Crystallographica Section A: Foundations and Advances* 74.1 (2018), pp. 54–65. ISSN: 2053-2733. DOI: 10.1107/S2053273317014929.

[120] Konstantin Mishchik. "Ultrafast laser-induced modification of optical glasses : a spectroscopy insight into the microscopic mechanisms". Theses. Université Jean Monnet - Saint-Etienne, July 2012. URL: https://theses.hal.science/tel-00966418.

[121] Daniel Mittleman. "ENGN 2911T: Ultrafast Optics (fall 2021)". University Lecture. 2021.

[122] Takayuki Miyazaki et al. "Properties of radio-frequency-sputter-deposited GaN films in a nitrogenhydrogen mixed gas". In: *Journal of Applied Physics* 97.9 (2005). ISSN: 00218979. DOI: 10.1063/1.1888027.

[123] B Monemar, P.P. Paskov, and A Kasic. "Optical properties of InN—the bandgap question". In: *Superlattices and Microstructures* 38.1 (July 2005), pp. 38–56. ISSN: 07496036. DOI: 10.1016/j.spmi.2005.04.006. URL: https://linkinghub.elsevier.com/retrieve/pii/S0749603605000558.

[124] M. Monish et al. "Gallium nitride films of high n-type conductivity grown by reactive sputtering". In: *Semiconductor Science and Technology* 35.4 (2020). ISSN: 13616641. DOI: 10.1088/1361-6641/ab73ec.

[125] Vd Mote, Y. Purushotham, and Bn Dole. "Williamson-Hall analysis in estimation of lattice strain in nanometer-sized ZnO particles". In: *Journal of Theoretical and Applied Physics* 6.1 (2012), pp. 2–9. ISSN: 22517235. DOI: 10.1186/2251-7235-6-6.

[126] A. V. Mudryi et al. "Optical properties of indium nitride powder and films". In: *Journal of Applied Spectroscopy* 73.1 (Jan. 2006), pp. 95–98. ISSN: 0021-9037. DOI: 10.1007/s10812-006-0041-0. URL: http://link.springer.com/10.1007/s10812-006-0041-0.

[127] J. F. Muth et al. "Absorption coefficient, energy gap, exciton binding energy, and recombination lifetime of GaN obtained from transmission measurements". In: *Applied Physics Letters* 71.18 (1997), pp. 2572–2574. ISSN: 00036951. DOI: 10.1063/1.120191.

[128] Henning Nagel, Christopher Berge, and Armin G. Aberle. "Generalized analysis of quasi-steady-state and quasi-transient measurements of carrier lifetimes in semiconductors". In: *Journal of Applied Physics* 86.11 (1999), pp. 6218–6221. ISSN: 00218979. DOI: 10.1063/1.371633.

[129] Jenny Nelson. *THE PHYSICS OF SOLAR CELLS (Properties of Semiconductor Materials)*. 1st. ICP, 2003, p. 384. ISBN: 978-1860943492.

[130] S. Nicolay, S. Fay, and C. Ballif. "Growth Model of MOCVD Polycrystalline ZnO". In: *Crystal Growth and Design* 9.11 (2009), pp. 4957–4962. ISSN: 15287483. DOI: 10.1021/cg900732h.

[131] S. V. Novikov et al. "Molecular beam epitaxy of crystalline and amorphous GaN layers with high As content". In: *Journal of Crystal Growth* 311.13 (2009), pp. 3417–3422. ISSN: 00220248. DOI: 10.1016/j.jcrysgro.2009.04.010.

[132] Nathan J. O'Brien et al. "In Situ Activation of an Indium(III) Triazenide Precursor for Epitaxial Growth of Indium Nitride by Atomic Layer Deposition". In: *Chemistry of Materials* 32.11 (2020), pp. 4481–4489. ISSN: 15205002. DOI: 10.1021/acs.chemmater.9b05171.

[133] G. Orsal et al. "Bandgap energy bowing parameter of strained and relaxed InGaN layers". In: *Optical Materials Express* 4.5 (2014), p. 1030. ISSN: 2159-3930. DOI: 10.1364/ome.4.001030.

[134] B. Ouyang et al. "A brief review on plasma for synthesis and processing of electrode materials". In: *Materials Today Nano* 3 (2018), pp. 28–47. ISSN: 25888420. DOI: 10.1016/j.mtnano.2018.11.002. URL: https://doi.org/10.1016/j.mtnano.2018.11.002.

[135] P. Pansila et al. "Growth kinetics for temperature-controlled atomic layer deposition of GaN using trimethylgallium and remote-plasma-excited NH 3". In: *Applied Surface Science* 357 (2015), pp. 1920–1927. ISSN: 01694332. DOI: 10.1016/j.apsusc.2015.09.138. URL: http://dx.doi.org/10.1016/j.apsusc.2015.09.138.

[136] W. Paszkowicz. "X-ray powder diffraction data for indium nitride". In: *Powder Diffraction* 14.4 (1999), pp. 258–260. ISSN: 19457413. DOI: 10.1017/S0885715600010630.

[137] W. Paszkowicz, R. Černý, and S. Krukowski. "Rietveld refinement for indium nitride in the 105–295 K range". In: *Powder Diffraction* 18.2 (2003), pp. 114–121. ISSN: 0885-7156. DOI: 10.1154/1.1566957.

[138] P. Patsalas, C. Gravalidis, and S. Logothetidis. "Surface kinetics and subplantation phenomena affecting the texture, morphology, stress, and growth evolution of titanium nitride films". In: *Journal of Applied Physics* 96.11 (2004), pp. 6234–6235. ISSN: 00218979. DOI: 10.1063/1.1811389.

[139] A. L. Patterson. "The Scherrer Formula for X-Ray Particle Size Determination". In: *Phys. Rev.* 56 (10 Nov. 1939), pp. 978–982. DOI: 10.1103/PhysRev.56.978. URL: https://link.aps.org/doi/10.1103/PhysRev.56.978.

[140] Th Pavloudis et al. "Ordered structures in III-Nitride ternary alloys". In: *Computational Materials Science* 118 (2016), pp. 22–31. ISSN: 09270256. DOI: 10.1016/j.commatsci.2016.02.036. URL: http://dx.doi.org/10.1016/j.commatsci.2016.02.036.

[141] I. Petrov et al. "Microstructural evolution during film growth". In: *Journal of Vacuum Science & Technology A: Vacuum, Surfaces, and Films* 21.5 (2003), S117–S128. ISSN: 0734-2101. DOI: 10.1116/1.1601610.

[142] Marco Piccardo et al. "Localization landscape theory of disorder in semiconductors. II. Urbach tails of disordered quantum well layers". In: *Physical Review B* 95.14 (2017). ISSN: 24699969. DOI: 10.1103/PhysRevB.95.144205. arXiv: 1704.05524.

[143] L. F.J. Piper et al. "Origin of the n-type conductivity of InN: The role of positively charged dislocations". In: *Applied Physics Letters* 88.25 (2006), pp. 1–4. ISSN: 00036951. DOI: 10.1063/1.2214156.

[144] E. Płaczek-Popko. "Top PV market solar cells 2016". In: *Opto-Electronics Review* 25.2 (2017), pp. 55–64. ISSN: 18963757. DOI: 10.1016/j.opelre.2017.03.002. URL: http://dx.doi.org/10.1016/j.opelre.2017.03.002.

[145] C. Jayant Praharaj. "Indium gallium nitride on silicon heterojunction Schottky barrier solar cell characteristics". In: *MRS Communications* 11.4 (Aug. 2021), pp. 432–435. ISSN: 2159-6859. DOI: 10.1557/s43579-021-00050-y. URL: https://link.springer.com/10.1557/s43579-021-00050-y.

[146] X. D. Pu et al. "Temperature dependence of Raman scattering in hexagonal indium nitride films". In: *Journal of Applied Physics* 98.3 (2005). ISSN: 00218979. DOI: 10.1063/1.2006208.

[147] Marzieh Rabiei et al. "Measurement modulus of elasticity related to the atomic density of planes in unit cell of crystal lattices". In: *Materials* 13.19 (2020), pp. 1–17. ISSN: 19961944. DOI: 10.3390/ma13194380.

[148] Mina Rais-Zadeh et al. "Gallium nitride as an electromechanical material". In: *Journal of Microelectromechanical Systems* 23.6 (2014), pp. 1252–1271. ISSN: 10577157. DOI: 10.1109/JMEMS.2014.2352617.

[149] John Robertson. "Self-compensation and the absence of doping in amorphous GaAs". In: *Physical Review B* 33.6 (Mar. 1986), pp. 4399–4401. ISSN: 0163-1829. DOI: 10.1103/PhysRevB.33.4399. URL: https://link.aps.org/doi/10.1103/PhysRevB.33.4399.

[150] P Roca i Cabarrocas. "Plasma enhanced chemical vapor deposition of silicon thin films for large area electronics". In: *Current Opinion in Solid State and Materials Science* 6.5 (2002), pp. 439–444. ISSN: 1359-0286. DOI: https://doi.org/10.1016/S1359-0286(02)00112-2. URL: https://www.sciencedirect.com/science/article/pii/S1359028602001122.

[151] Ellis T. Roe, Kira E. Egelhofer, and Mark C. Lonergan. "Exchange current density model for the contact-determined current-voltage behavior of solar cells". In: *Journal of Applied Physics* 125.22 (2019). ISSN: 10897550. DOI: 10.1063/1.5090519.

[152] Sven Rühle. "Tabulated values of the Shockley-Queisser limit for single junction solar cells". In: *Solar Energy* 130 (2016), pp. 139–147. ISSN: 0038092X. DOI: 10.1016/j.solener.2016.02.015.

[153] Hitoshi Sai et al. "High-efficiency microcrystalline silicon solar cells on honeycomb textured substrates grown with high-rate VHF plasma-enhanced chemical vapor deposition". In: *Japanese Journal of Applied Physics* 54.8S1 (July 2015), 08KB05. DOI: 10.7567/jjap.54.08kb05. URL: https://doi.org/10.7567/jjap.54.08kb05.

[154] Jan Schmidt, Robby Peibst, and Rolf Brendel. "Surface passivation of crystalline silicon solar cells: Present and future". In: *Solar Energy Materials and Solar Cells* 187.June (2018), pp. 39–54. ISSN: 09270248. DOI: 10.1016/j.solmat.2018.06.047. URL: https://doi.org/10.1016/j.solmat.2018.06.047.

[155] Dieter K. Schroder. *Semiconductor material and device characterization*. John Wiley & Sons, 2015, p. 784. ISBN: 0471739065.

[156] L. G. Schulz. *The experimental study of the optical properties of metals and the relation of the results to the Drude free electron theory*. Vol. 6. 21. 1957, pp. 102–144. DOI: 10.1080/00018735700101166.

[157] Reinoud Segers. "Three options to calculate the percentage renewable energy: An example for a EU policy debate". In: *Energy Policy* 36.9 (2008), pp. 3243–3248. ISSN: 03014215. DOI: 10.1016/j.enpol.2008.05.014.

[158] Arvind Shah and Arvind Victor Shah. *Thin-film silicon solar cells*. First edition. EPFL press, 2010, p. 440. ISBN: 9780429136054. DOI: 10.1201/b16327.

[159] Javishk Shah et al. "Ammonia Synthesis by Radio Frequency Plasma Catalysis: Revealing the Underlying Mechanisms". In: *ACS Applied Energy Materials* 1.9 (2018), pp. 4824–4839. ISSN: 25740962. DOI: 10.1021/acsaem.8b00898.

[160] An Shih et al. "Structural and electronic differences between deuterated and hydrogenated amorphous silicon". In: *Journal of Applied Physics* 88.3 (2000), pp. 1684–1687. ISSN: 00218979. DOI: 10.1063/1.373872.

[161] An Shih et al. "Structural differences between deuterated and hydrogenated silicon nitride/oxynitride". In: *Journal of Applied Physics* 89.10 (2001), pp. 5355–5361. ISSN: 00218979. DOI: 10.1063/1.1364645.

[162] R. Singh et al. "Phase separation in InGaN thick films and formation of InGaN/GaN double heterostructures in the entire alloy composition". In: *Applied Physics Letters* 70.9 (1997), pp. 1089–1091. ISSN: 00036951. DOI: 10.1063/1.118493.

[163] R. A. Sinton, A. Cuevas, and M. Stuckings. *Sinton-QSSPC.pdf*. 1996.

[164] D.L. Smith. *Thin-film Deposition: Principles and Practice*. McGraw-Hill, 1995. ISBN: 9780071139137. URL: https://books.google.ch/books?id=LLe6QgAACAAJ.

[165] George W. Snedecor and William G. Cochran. *Statistical Methods*. Eighth Edi. Ames, Iowa, USA: Iowa State University Press, 1989, p. 523.

[166] Michael Elias Stuckelberger. "Hydrogenated amorphous silicon: Impact of process conditions on material properties and solar cell eficiency". PhD thesis. EPFL, 2014. DOI: 10.5075/epfl-thesis-6393.

[167] Touko Sugiura et al. "Raman scattering study of InGaN grown by metalorganic vapor phase epitaxy on (0001) sapphire substrates". In: *Japanese Journal of Applied Physics, Part 1: Regular Papers and Short Notes and Review Papers* 40.10 (2001), pp. 5955–5958. ISSN: 00214922.

[168] Masakatsu Suzuki and Takeshi Uenoyama. "First-principles calculation of effective mass parameters of gallium nitride". In: *Japanese Journal of Applied Physics* 34.7R (1995), pp. 3442–3446. ISSN: 13474065. DOI: 10.1143/JJAP.34.3442.

[169] Bibhu Prasad Swain. "Synthesis and Characterization of Gallium nitride (GaN) thin films deposited by Low pressure chemical vapor deposition (LPCVD) technique." In: 2015.April 2015 (2015), pp. 1–9.

[170] J. Tauc, R. Grigorovici, and A. Vancu. "Optical Properties and Electronic Structure of Amorphous Germanium". In: *physica status solidi (b)* 15.2 (1966), pp. 627–637. DOI: https://doi.org/10.1002/pssb.19660150224. eprint: https://onlinelibrary.wiley.com/doi/pdf/10.1002/pssb.19660150224. URL: https://onlinelibrary.wiley.com/doi/abs/10.1002/pssb.19660150224.

[171] Cao Phuong Thao and Dong Hau Kuo. "Electrical and structural characteristics of Ge-doped GaN thin films and its hetero-junction diode made all by RF reactive sputtering". In: *Materials Science in Semiconductor Processing* 74.October 2017 (2018), pp. 336–341. ISSN: 13698001. DOI: 10.1016/j.mssp.2017.10.024. URL: https://doi.org/10.1016/j.mssp.2017.10.024.

[172] *Theory of solar cells*. URL: https://en.wikipedia.org/wiki/Theory_of_solar_cells (visited on 12/28/2022).

[173] John A. Thornton. "High Rate Thick Film Growth." In: *Annual Review of Materials Science* 7 (1977), pp. 239–260. ISSN: 00846600. DOI: 10.1146/annurev.ms.07.080177.001323.

[174] S. Tripathy et al. "Micro-Raman investigation of strain in GaN and AlxGa 1-xN/GaN heterostructures grown on Si(111)". In: *Journal of Applied Physics* 92.7 (2002), pp. 3503–3510. ISSN: 00218979. DOI: 10.1063/1.1502921.

[175] H. J. Trodahl et al. "Raman spectroscopy of nanocrystalline and amorphous GaN". In: *Journal of Applied Physics* 97.8 (2005), pp. 1–6. ISSN: 00218979. DOI: 10.1063/1.1875743.

[176] Yi-Chia Tsai and Can Bayram. "Band Alignments of Ternary Wurtzite and Zincblende III-Nitrides Investigated by Hybrid Density Functional Theory". In: *ACS Omega* 5.8 (2020). PMID: 32149218, pp. 3917–3923. DOI: 10.1021/acsomega.9b03353. eprint: https://doi.org/10.1021/acsomega.9b03353. URL: https://doi.org/10.1021/acsomega.9b03353.

[177] R. Tsu et al. "Critical volume fraction of crystallinity for conductivity percolation in phosphorus-doped Si:F:H alloys". In: *Applied Physics Letters* 40.6 (1982), pp. 534–535. ISSN: 00036951. DOI: 10.1063/1.93133.

[178] Kohei Ueno et al. "Electron transport properties of degenerate n -type GaN prepared by pulsed sputtering". In: *APL Materials* 5.12 (2017). ISSN: 2166532X. DOI: 10.1063/1.5008913. URL: http://dx.doi.org/10.1063/1.5008913.

[179] Australia University of New South Wales. *Software, data & links.* 2023. URL: https://www.unsw.edu.au/engineering/our-schools/photovoltaic-and-renewable-energy-engineering/our-research/software-data-links (visited on 04/21/2023).

[180] Unknown author. "Coal consumption affecting climate". In: *Rodney and Otamatea Times, Waitemata & Kaipara Gazette* (1912), p. 7.

[181] Franz Urbach. "The Long-Wavelength Edge of Photographic Sensitivity and of the Electronic Absorption of Solids". In: *Phys. Rev.* 92 (5 Dec. 1953), pp. 1324–1324. DOI: 10.1103/PhysRev.92.1324. URL: https://link.aps.org/doi/10.1103/PhysRev.92.1324.

[182] Chris G. Van De Walle. "Universal alignment of hydrogen levels in semiconductors and insulators". In: *Physica B: Condensed Matter* 376-377.1 (2006), pp. 1–6. ISSN: 09214526. DOI: 10.1016/j.physb.2005.12.004.

[183] V. Verlaan et al. "Unambiguous determination of Fourier-transform infrared spectroscopy proportionality factors: The case of silicon nitride". In: *Physical Review B - Condensed Matter and Materials Physics* 73.19 (2006), pp. 1–8. ISSN: 10980121. DOI: 10.1103/PhysRevB.73.195333.

[184] Thomas J. Bruno W. M. Haynes, David R. Lide. *CRC Handbook of Chemistry and Physics.* Ed. by W. M. Haynes, David R. Lide, and Thomas J. Bruno. CRC Press, June 2016. ISBN: 9781315380476. DOI: 10.1201/9781315380476. URL: https://www.taylorfrancis.com/books/9781498754293.

[185] W. Walukiewicz. "Amphoteric native defects in semiconductors". In: *Applied Physics Letters* 54.21 (1989), pp. 2094–2096. ISSN: 00036951. DOI: 10.1063/1.101174.

[186] W. Walukiewicz. "Fermi Level Stabilization in Semiconductors: Implications for Implant Activation Efficiency". In: *MRS Proceedings* 104.181420014 (Feb. 1987), p. 483. ISSN: 0272-9172. DOI: 10.1557/PROC-104-483. URL: http://link.springer.com/10.1557/PROC-104-483.

[187] W. Walukiewicz. "Intrinsic limitations to the doping of wide-gap semiconductors". In: *Physica B: Condensed Matter* 302-303 (2001), pp. 123–134. ISSN: 09214526. DOI: 10.1016/S0921-4526(01)00417-3.

[188] W. Walukiewicz et al. "Structure and electronic properties of InN and In-rich group III-nitride alloys". In: *Journal of Physics D: Applied Physics* 39.5 (2006). ISSN: 00223727. DOI: 10.1088/0022-3727/39/5/R01.

[189] John D Weeks and George H Gilmer. "Dynamics of crystal growth". In: *Advances in chemical physics* 40 (1979), pp. 157–228.

[190] R. B. Wehrspohn et al. "Urbach energy dependence of the stability in amorphous silicon thin-film transistors". In: *Applied Physics Letters* 74.22 (1999), pp. 3374–3376. ISSN: 00036951. DOI: 10.1063/1.123349.

[191] Jérémie Werner, Bjoern Niesen, and Christophe Ballif. "Perovskite/Silicon Tandem Solar Cells: Marriage of Convenience or True Love Story? – An Overview". In: *Advanced Materials Interfaces* 5.1 (2018). ISSN: 21967350. DOI: 10.1002/admi.201700731.

[192] Christian M. Wolff et al. "Highly Efficient Perovskite-on-Silicon Tandem Solar Cells on Planar and Textured Silicon". In: (2022), pp. 1119–1119. DOI: 10.1109/pvsc48317.2022.9938735.

[193] J. Wu et al. "Small band gap bowing in In1-xGaxN alloys". In: *Applied Physics Letters* 80.25 (2002), pp. 4741–4743. ISSN: 00036951. DOI: 10.1063/1.1489481.

[194] J. Wu et al. "Superior radiation resistance of In 1-xGa xN alloys: Full-solar-spectrum photovoltaic material system". In: *Journal of Applied Physics* 94.10 (2003), pp. 6477–6482. ISSN: 00218979. DOI: 10.1063/1.1618353.

[195] Mengyao Xie. *Structural and elastic properties of InN and InAlN with different surface orientations and doping*. 1485. 2012. ISBN: 978-91-7519-754-8.

[196] M. Yamaguchi et al. "Brillouin scattering study of bulk GaN". In: *Journal of Applied Physics* 85.12 (1999), pp. 8502–8504. ISSN: 00218979. DOI: 10.1063/1.370635.

[197] Yi Yang et al. "Blue luminescence from amorphous GaN nanoparticles synthesized in situ in a polymer". In: *Applied Physics Letters* 74.16 (1999), pp. 2262–2264. ISSN: 00036951. DOI: 10.1063/1.123819.

[198] Ping Yin and Xitao Fan. "Estimating R 2 Shrinkage in Multiple Regression: A Comparison of Different Analytical Methods". In: *The Journal of Experimental Education* 69.2 (2001), pp. 203–224. DOI: 10.1080/00220970109600656. eprint: https://doi.org/10.1080/00220970109600656. URL: https://doi.org/10.1080/00220970109600656.

[199] Kunta Yoshikawa et al. "Silicon heterojunction solar cell with interdigitated back contacts for a photoconversion efficiency over 26%". In: *Nature Energy* 2.5 (2017). ISSN: 20587546. DOI: 10.1038/nenergy.2017.32.

[200] Zhengshan J. Yu, Joe V. Carpenter, and Zachary C. Holman. "Techno-economic viability of silicon-based tandem photovoltaic modules in the United States". In: *Nature Energy* 3.9 (2018), pp. 747–753. ISSN: 20587546. DOI: 10.1038/s41560-018-0201-5. URL: http://dx.doi.org/10.1038/s41560-018-0201-5.

[201] A. R. Zanatta. "Revisiting the optical bandgap of semiconductors and the proposal of a unified methodology to its determination". In: *Scientific reports* 9.1 (2019), p. 11225. ISSN: 20452322. DOI: 10.1038/s41598-019-47670-y. URL: http://dx.doi.org/10.1038/s41598-019-47670-y.

[202] Chaomin Zhang et al. "Silicon nitride barrier layers mitigate minority-carrier lifetime degradation in silicon wafers during simulated MBE growth of III–V layers". In: *IEEE Journal of Photovoltaics* 9.2 (2019), pp. 431–436.

[203] D. H. Zhang and D. Haneman. "Band gap and activation energy in amorphous silicon doping-modulated superlattices". In: *Applied Physics Letters* 52.17 (1988), pp. 1392–1394. ISSN: 00036951. DOI: 10.1063/1.99125.

[204] Hairong Zheng and M. P. Sarachik. "Impurity resistivity of the double-donor system si:p,bi". In: *Physical Review B - Condensed Matter and Materials Physics* 60.23 (1999), pp. 15824–15828. ISSN: 1550235X. DOI: 10.1103/PhysRevB.60.15824.

[205] Jie Zheng et al. "Iron nitride thin films deposited by chloride assisted plasma enhanced chemical vapour deposition: Facile stoichiometry control and mechanism study". In: *Journal of Physics D: Applied Physics* 42.18 (2009). ISSN: 00223727. DOI: 10.1088/0022-3727/42/18/185209.

[206] R. Zwierz et al. "Plasma enhanced growth of GaN single crystalline layers from Ga vapour". In: *Crystal Research and Technology* 48.4 (2013), pp. 186–192. ISSN: 02321300. DOI: 10.1002/crat.201200481.

# JONATHAN EMANUEL THOMET

**R&D Engineer**

jonathan.thomet (at) gmail.com | +41 (0)78 868 83 64 | Rue des Fahys 27
2000 Neuchâtel, SWITZERLAND | /jonathan-thomet-53043847/ | 0000-0002-7528-7312


## EXPERIENCE

### Post-doctor
**École Polytechnique Fédérale de Lausanne**

June 2023 – present | PV-lab, Neuchâtel

- Research & development of 3D detectors for high energy particles.

### Doctoral assistant
**École Polytechnique Fédérale de Lausanne**

March 2019 – May 2023 | PV-lab, Neuchâtel

- Research & development of InGaN materials for photovoltaic applications.

### BNF internship
**École Polytechnique Fédérale de Lausanne**

August 2018 – February 2019 | PV-lab, Neuchâtel

- Simulation of amorphous silicon-based microchannel plates multiplication.

### Youth animator
**Buzz pour Jésus**

August 2013 – July 2018 | Paroisse de l'Entre-deux-lacs

- Social, individual and leadership development of the youth center.

## JOURNAL ARTICLES

### As first author

- J. Emanuel Thomet, A. Kamlesh Singh, M. Nelly Rouèche, *et al.*, "Bandgap engineering of indium gallium nitride layers grown by plasma-enhanced chemical vapor deposition," *Journal of Vacuum Science & Technology A: Vacuum, Surfaces, and Films*, vol. 40, no. 6, p. 063 102, 2022.

### As co-author

- C. Hain, P. Schweizer, P. Sturm, *et al.*, "Microwave plasma-assisted reactive hipims of inn films: Plasma environment and material characterisation," vol. 454, Elsevier, 2023, p. 129 188.
- J. Loffler, M. Belhaj, N. Bundaleski, *et al.*, "A comprehensive analysis of electron emission from a-si:h/$al_2o_3$ at low energies," 6, vol. 56, IOP Publishing Ltd, 2023, p. 065 306.
- J. Löffler, J. Thomet, S. Frey, C. Ballif, and N. Wyrsch, "Single photon detection with amorphous silicon-based microchannel plates: A monte carlo model," vol. 1032, Elsevier, 2022, p. 166 589.
- D. Fébba, V. Paratte, L. Antognini, *et al.*, "Effects of work function and electron affinity on the performance of carrier-selective contacts in silicon solar cells using $znsn_xge_{1-x}n_2$ as a case study," 6, vol. 11, IEEE, 2021, pp. 1350–1357.
- W. Lin, M. Boccard, S. Zhong, *et al.*, "Degradation mechanism and stability improvement of dopant-free zno/$lif_x$/al electron nanocontacts in silicon heterojunction solar cells," 11, vol. 3, ACS Publications, 2020, pp. 11 391–11 398.

## EDUCATION

### Ph.D. in Microtechnic
**EPFL**

March 2019 – May 2023

Thesis title: III-nitride semiconductors deposited at low temperature for photovoltaic applications

### M.Sc. in Physics
**EPFL**

Sept 2010 – June 2012

### Applied theology certificate
**HET-Pro**

Sept 2013 – June 2018

## SKILLS & INTERESTS

Cleanroom | PECVD | PVD | Characterization | SEM | TEM

DOE | Comsol | Python | Matlab | Latex | MS Office | Mathematica

R&D methodologies | Leadership | Logistic | Communication | Social

Jogging | Piano | Snowboard | Poetry | Cooking | Meditation

## LANGUAGES

| | |
|---|---|
| French | ●●●●●● |
| English | ●●●●●○ |
| German | ●●●●○○ |

## REFEREES

**Dr. Aïcha Hessler-Wyser**
aicha.hessler (at) epfl.ch
+41 (0)21 693 48 30

**Dr. Nicolas Wyrsch**
nicolas.wyrsch (at) epfl.ch
+41 (0)21 695 43 57